Seyed Sattar Emamian
Mokhtar Awang
Jeeferie Abd Razak
Patrick J. Masset   *Editors*

# Advances in Material Science and Engineering

## Selected Articles from ICMMPE 2021

Springer

# Lecture Notes in Mechanical Engineering

Seyed Sattar Emamian · Mokhtar Awang ·
Jeeferie Abd Razak · Patrick J. Masset
Editors

# Advances in Material Science and Engineering

Selected Articles from ICMMPE 2021

Springer

*Editors*
Seyed Sattar Emamian
University of Twente
Enschede, The Netherlands

Mokhtar Awang
Institute of Transport Infrastructure
Universiti Teknologi PETRONAS
Seri Iskander, Perak, Malaysia

Jeeferie Abd Razak
Faculty of Manufacturing Engineering
Universiti Teknikal Malaysia Melaka
Durian Tunggal, Melaka, Malaysia

Patrick J. Masset
Koszalin University of Technology
Koszalin, Poland

# Preface

This book presents a compilation of research works covering the fields of mechanical, manufacturing, and plant engineering. All manuscripts in this volume were presented during the 7th International Conference on Mechanical, Manufacturing and Plant Engineering 2021 (ICMMPE 2021) which was conducted through a virtual presentation on November 29, 2021. ICMMPE is an annual event held in Malaysia where the main aim is to bring together researchers and industry players in mechanical engineering to share their knowledge and research findings. This book consists of 38 chapters covering from experimental works on mechanical, materials, and manufacturing to numerical modeling studies in mechanical engineering.

It is hoped that the content of this book will benefit the researchers and scholars who are looking for recent findings and breakthrough in mechanical and manufacturing engineering research works. The editors of the proceeding would like to express the utmost gratitude and thanks to all reviewers in the technical team for making this volume a success.

Enschede, The Netherlands
Seri Iskander, Malaysia
Durian Tunggal, Malaysia
Koszalin, Poland

Seyed Sattar Emamian
Mokhtar Awang
Jeeferie Abd Razak
Patrick J. Masset

# Acknowledgments

# Contents

# Design of Permanent Rectification for Flare Stack Structure by Using Finite Element Method

M. S. Yob, A. Hussin, N. A. Mat Tahir, O. Kurdi, and M. M. Izahar

**Abstract** A flare device is built in a refinery or petrochemical plant to ensure the safety and effective disposal of emitted gases or liquids. A flare is expected to operate for 24 h and must be in service for several years without a need to shut it down and is always available for flaring whenever a plant disruption occurs. A proper operating flare system is a vital component to deter a plant disturbance from developing into a disaster. When the flare is exposed to the environment, it can lead the flare to corrosion. It can affect the strength of the flare and needs to maintain the flare by changing the corroded part to a new part. The purpose of this study is to evaluate the stress of flare reinforced by proposed designs I-beam using finite element analysis (FEA). The proposed design was analysed by using FEA at three different boundary conditions focusing on no external disturbance, wind disturbance, and earthquake disturbance. Then, the analysis was validated and compared with experimental analysis conducted on simplified flare design model. The finding shows that the safety factor for the proposed design increases at the welding stress and decreases at the flare (at all three conditions). However, the safety factor still lies in the safe and acceptable condition.

M. S. Yob (✉)
Advanced Manufacturing Centre (AMC), Universiti Teknikal Malaysia Melaka, Hang Tuah JayaDurian Tunggal, 76100 Melaka, Malaysia
e-mail: mshukriy@utem.edu.my

M. S. Yob · N. A. Mat Tahir
Faculty of Mechanical Engineering, Universiti Teknikal Malaysia Melaka, Hang Tuah JayaDurian Tunggal, 76100 Melaka, Malaysia

A. Hussin
Civil and Structural (Design and Integrity Onshore), IRSO East Cost – Engineering, Petronas Carigali Sdn Bhd, 24300 Kerteh, Kemaman, Terengganu, Malaysia

O. Kurdi
Department of Mechanical Engineering, Diponegoro University, Semarang, Indonesia

National Center of Sustainable Transportation Technology, Bandung, Indonesia

M. M. Izahar
Faculty of Education and Social Sciences, University of Selangor, Kampus Bestari Jaya, 45600 Bestari Jaya, Selangor, Malaysia

## 1 Introduction

Petroleum Nasional Berhad (PETRONAS) has appointed SAAEM as a contractor to execute the flare stack rectification work in a gas plant in Terengganu. In order to execute the project, an engineering and design stage has been carried out to prepare the material specification and suitable procedures. As a result, related calculations and analysis will be presented in this technical report. This report specifically elaborates on finite element analysis findings and validation of the structure using experimental study.

Flare was used to provide a safe vapour release during plant operation, upset or emergency situation, and is still used widely nowadays especially in the oil and gas industry, including petrochemical. Flare is designed to deal with a variety of gas compositions depending on the type of plant it is working on. Hydrocarbon is the most typical material released into the flares. In designing flare system and its component, there are several factors that need to be considered including the type of flares. There were three types of flares that were used in the petrochemical industries which are: single-point flares, multi-point flares, and enclosed flares [1]. Each design has its own functions and specifications.

In oil and gas industry, safety is one of the priorities that must be taken care of. Here, safety factor was highlighted when proposing a new design and system. There were many studies conducted on analysing the factor safety in the flare system and its components. Fault tree analysis was used by [2, 3] in order to conduct risk assessment based on historical data. Here, the analysis was able to predict emergency scenario in future.

In the past few years, many researchers had conducted studies on designing the flare system. In 2013, [4] had proposed a steady-state model for a flare system and was able to estimate the pressure safety valve (PSV) back pressure and velocity of the relieving fluid. In another study, [5] analysed the chemical plant flare by using plant-wide dynamic simulation. Xu was able to minimize the flare by using dynamic simulation model that runs through the system and examined the critical potential process operational risk.

By utilizing CFD, Yadav et al. have adopted one-dimensional model to predict bubble size and liquid fluctuation level of the seal drum. By determining the problematic area, countermeasure can be taken. Recently, [6] has conducted dynamic analysis and optimized the flare network system of offshore plant. By implementing his proposed system, he claimed that the optimized parameter was able to minimize the overall capital costs and ensure the safety of the system by avoiding vibration and noise within the system's pipe. On the other hand, [7] had analysed the optimized flare header platform design in liquefied natural gas plant. He utilizes the FEA to investigate the misalignment in flare header plat form and determined that the issue that occurs is due to the cyclic pressure that will turn into failures.

The flare system of an oil and gas plant is always associated with high-temperature process. Due to its slightly endothermic nature, pyrolysis requires a relatively large amount of heat to sustain the reaction at high temperature [8, 9]. According to earlier findings, it had been confirmed that residual stress was able to produce quite significant effects on fatigue performance of weld joints. In 2013, Pan et al. had emphasized on the important role played by residual stresses in determining the failure location. This led to earlier prevention of failures. In order to improve the accuracy of finite element, the modelling of joint was carried by previous researchers to increase the accuracy of finite element model [10–12].

With developed various software analysis, prediction of failures is eased and cost-effective. However, most previous studies are focusing on the network and not on the flare component itself. Hence, this study is focusing on evaluating the stress of flare and reinforcing the corroded area with I-beam and patch plate.

## 2　Methodology

The detailed analysis is carried out to reinforce the corroded area of flare with I-beam and patch plate. The analysis is performed by using finite element analysis (FEA) software (ANSYS) to determine stress distribution to the affected area of flare. In order to validate the finding of finite element model, a physical testing is conducted to compare the stress distribution for a scale model with a finite element model. The detailed arrangement of I-beam to flare rectification is shown in Fig. 1.
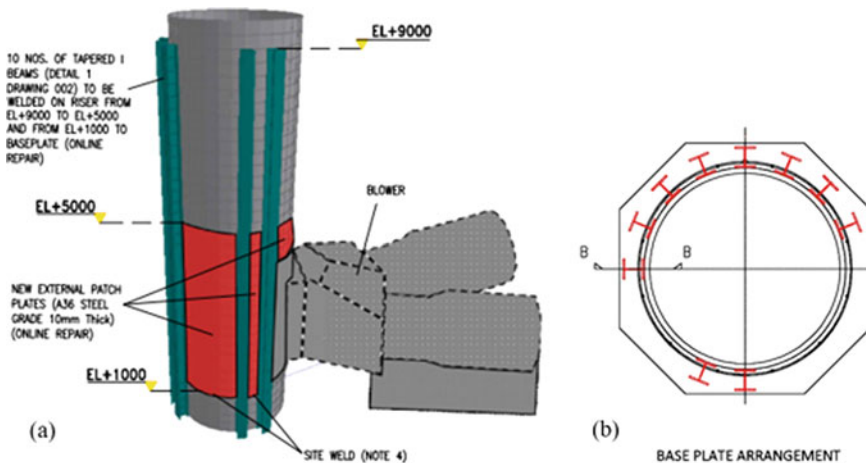


**Fig. 1** Detailed arrangement of I-beam to flare rectification **a** 3D view and **b** top view

**Fig. 2** Loading and
boundary condition for Case
1
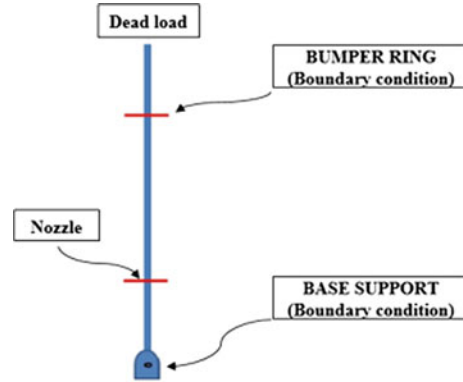


## 2.1 Finite Element Analysis

### 2.1.1 Loading Conditions

In this analysis, the strength of flare structure will be tested under serviceability
and ultimate load (factor with 1.4) for three cases of loading conditions: no external
disturbance, wind disturbance, and earthquake disturbance.

*Case 1*

Case 1 was tested for loading conditions with no external disturbance. The illustration of the loading and boundary was shown in Fig. 2, where the loads acting to
the structure are dead load (stack and risers) and nozzle load.

*Case 2*

Case 2 was tested for loading condition with wind disturbance. The illustration of
the loading and boundary was shown in Fig. 3, where the loads acting to the structure
are dead load (stack and risers), nozzle load, and wind load. The direction of wind
is shown in Fig. 3b. For wind load, the structure is divided into three sections, and
load acting to each section is shown in Table 1.

*Case 3*

Case 3 was tested for loading condition with earthquake disturbance. The illustration of the loading and boundary was shown in Fig. 4, where the loads acting to the
structure are dead load (stack and risers), nozzle load, and earthquake. The direction
of earthquake is shown in Fig. 4b. The earthquake load acting to the structure is
shown in Table 2.

### 2.1.2 Material Properties

In this analysis, the stack, I-beam, and patch plate are defined as mild steel with the
following properties as shown in Table 3.

Fig. 3 Loading and boundary condition for Case 2 **a** with wind load distribution and **b** wind direction (PTS 11.10.01, October 2013)
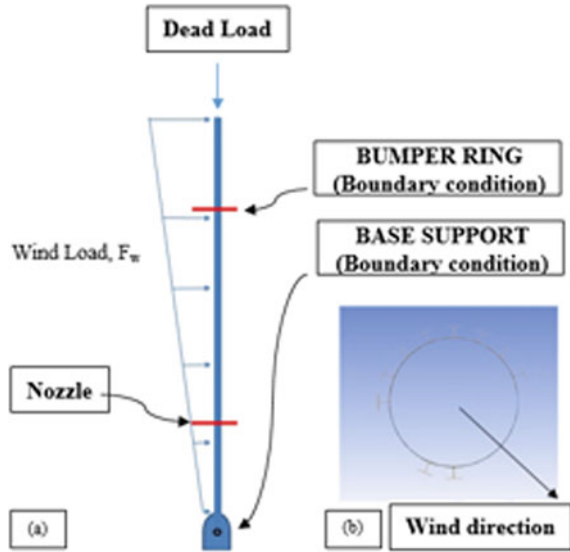
Table 1 Wind load acting to three sections for Case 2

| Elevation (m) | Height (m) | Area (m²) | Midpoint (m) | Average velocity (m/s) | Wind load (N) (serviceability) | Wind load (N) × 1.4 (ultimate) |
|---|---|---|---|---|---|---|
| 0–16 | 16 | 41.44 | 8 | 1.872 | 209.4 | 293.1 |
| 16–83 | 67 | 173.53 | 49 | 17.591 | 32,889.8 | 46,045.8 |
| 83–112 | 29 | 75.11 | 97 | 34.823 | 55,713.7 | 77,999.2 |

Fig. 4 Loading and boundary condition for Case 3 **a** with wind load distribution and **b** eaarthquake direction (PTS 11.10.01, October 2013)
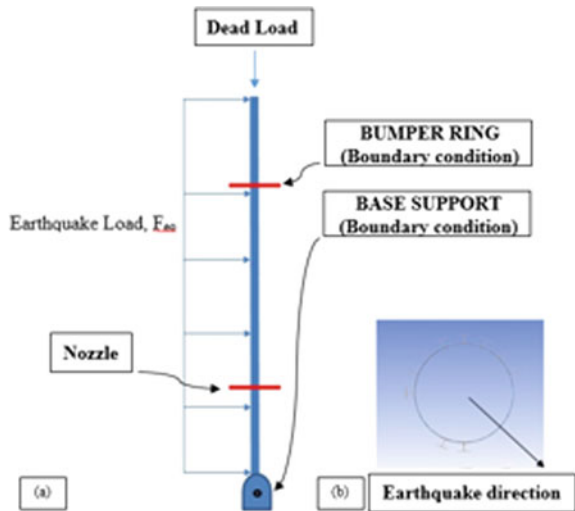
**Table 2** Earthquake load acting for Case 3

| Earthquake load, $F_{eq}$ (N) | |
| --- | --- |
| Total weight (kg) | 169,336.390 |
| Acceleration, $A$ (m/s$^2$) | 0.075 |
| Feq (N) | 12,700.229 |

**Table 3** Material's properties selected for analysis

| Properties | Value |
| --- | --- |
| Materials | Mild steel |
| Yield's strength, $y_{ield}$ | 250 Mpa |
| Young's modulus, $E$ | 200a |

## 2.2 Experimental Validation Setup

In this section, the study was carried out to understand the behaviour of flare structure and to validate the finding from finite element modelling. The test jig for the load test experiment was built and designed by referring the previous study by [13, 14] in order to ensure that the test jig was able to provide accurate force intended on the test piece. The layout of the experiment is shown in Fig. 5, while the simplified scale model and location of strain gauges and boundary condition for scale model are shown in Fig. 5(b).
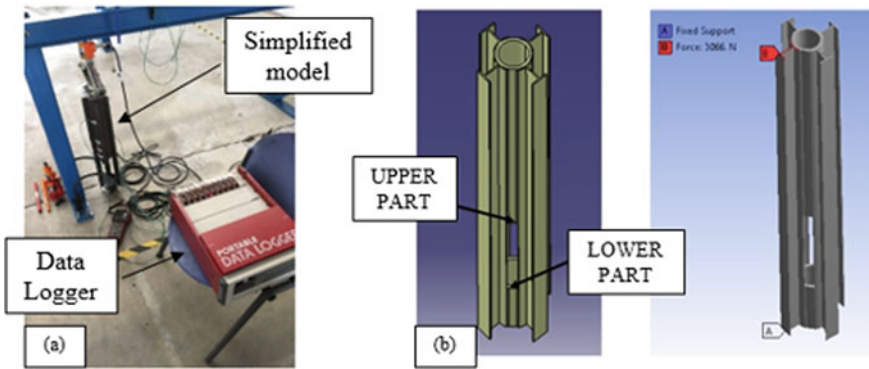


**Fig. 5** Experimental layout **a** actual setup and **b** scale model and location of strain gauges and boundary condition setup

## 2.3 Welding Stress Analysis

It is important to analyse joined parts when two or more components are mashed. There are many types of joints that can be used in building a structure such as welding, bolt and nuts, and others. Analysing this part is crucial due to frequent occurrences of failures within this area caused by the modification of the solid structure, where the stress point may be shifted. In this study, the I-beam is welded to the flare. Hence, the welding stress analysis needs to be conducted in order to ensure that there will be no failure or issue within this region.

## 3 Finding

### 3.1 Finite Element Analysis

By using loading and boundary conditions, stress distribution at rectified area for three cases with I-beam design model from ITB and proposed I-beam designs are shown in Figs. 6, 7 and 8, while the summary of the results is shown in Table 4.

### 3.2 Validation

The data obtained from the experimental setup was collected and, later, compared with the FEA findings. The comparison data was shown in Table 5. From the comparison, it can be seen that the boundary condition and meshing type applied in the FEA produce a good agreement with the experiment. Besides that, it is confirmed that lower part is more critical than the upper part of flare since both experimental and FEA show higher stress value at lower part. The highest difference is recorded at 11.19% for lower part at load 3066 N.

### 3.3 Welding Stress Analysis

From the FEA analysis, it is found that the most dominant loads that affect the stress of structure are dead and nozzle loads. In this study, welding stress analysis has been conducted as the I-beam is welded to the flare. For welding stress analysis, components of dead and nozzle loads in Y-axis are stated in Table 6. They will cause the highest welding shear stress at lower part of flare as shown in Fig. 9. Figure 10 shows the FEA analysis for welding stress for both existing ITB and proposed design by setting the loading condition as shear. From the finding, it is evident that the stress

**Fig. 6** Stress distribution under dead load for Case 1, where (**a** and **b**) are for serviceability ITB design model, (**c** and **d**) are for ultimate ITB design model, (**e** and **f**) are for serviceability proposed design, and (**g** and **h**) are for ultimate proposed design
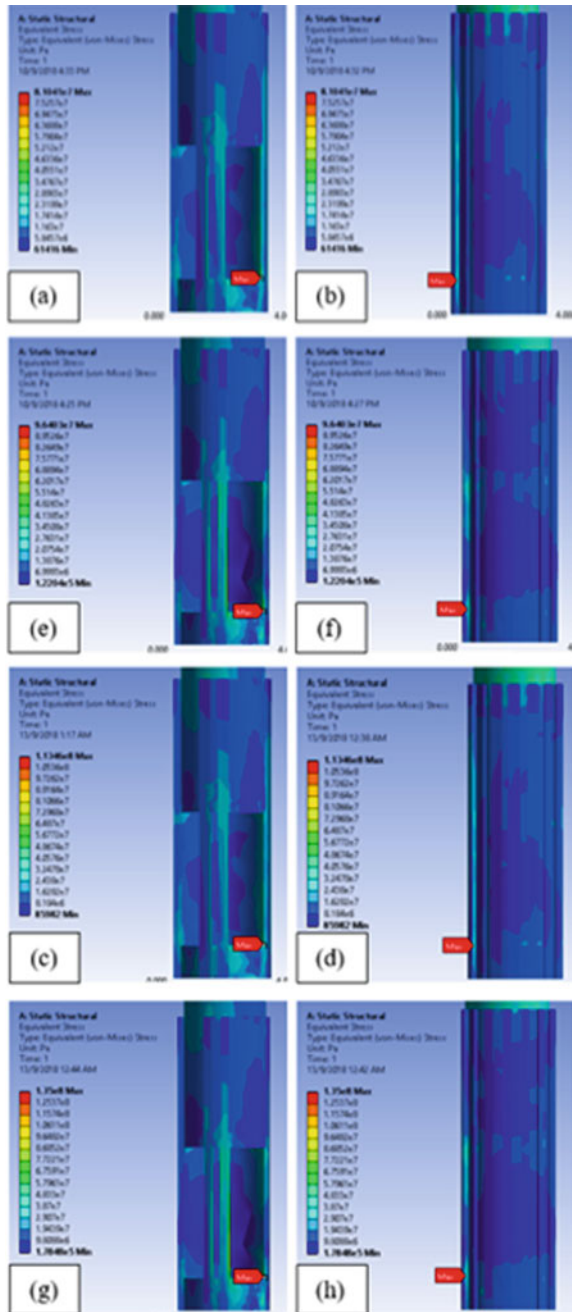
**Fig. 7** Stress distribution under dead load for Case 2, where (**a** and **b**) are for serviceability ITB design model, (**c** and **d**) are for ultimate ITB design model, (**e** and **f**) are for serviceability proposed design model, and (**g** and **h**) are for ultimate proposed design
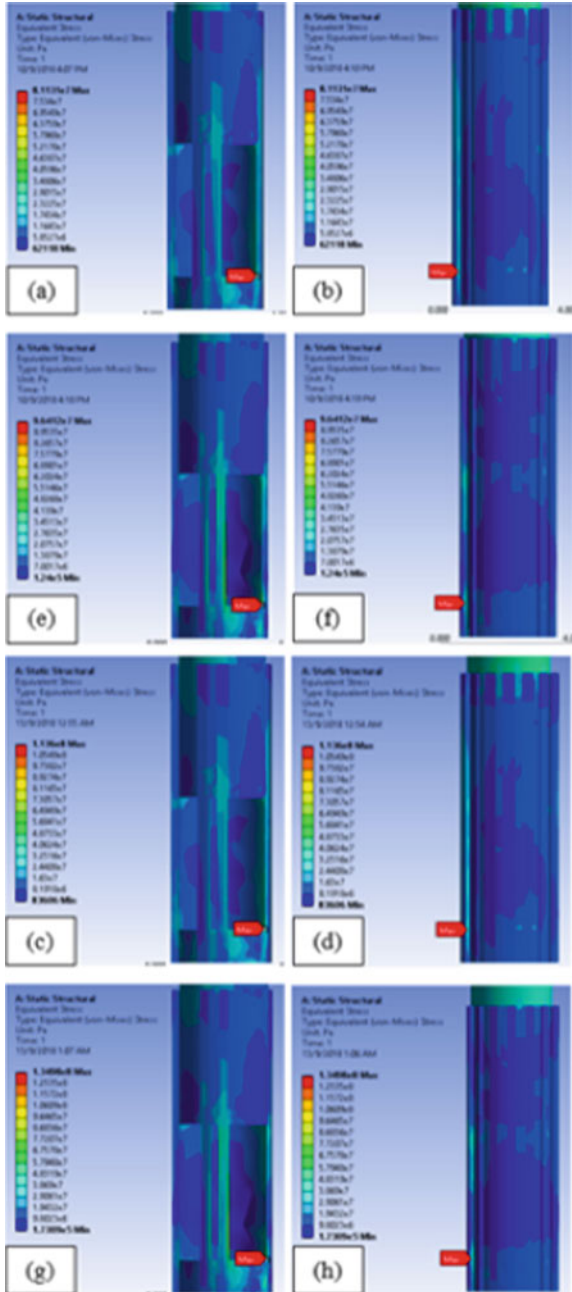
**Fig. 8** Stress distribution under dead load for Case 3, where (**a** and **b**) are for ITB design model and (**c** and **d**) are for proposed design
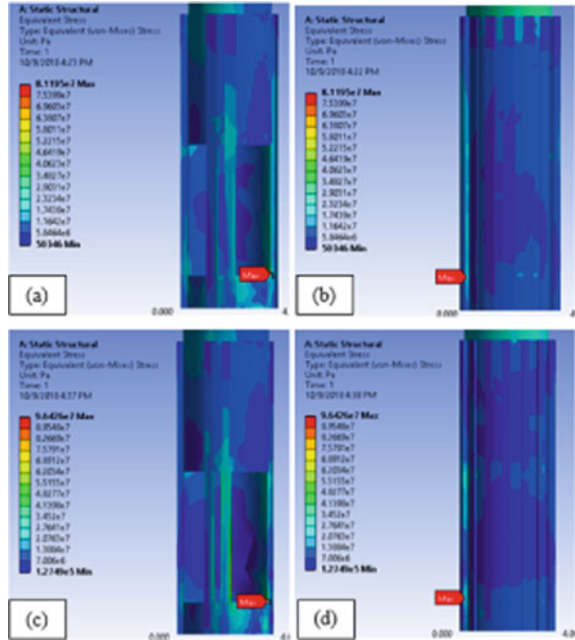


**Table 4** Summary of the analysis results for all cases

| Loading condition | ITB | | Proposed design | |
|---|---|---|---|---|
| | Max stress (MPa) | Factor safety | Max stress (MPa) | Factor safety |
| Case 1—dead load (serviceability) | 81.04 | 3.1 | 96.40 | 2.6 |
| Case 1—dead load (ultimate) | 113.46 | 2.2 | 135.00 | 1.9 |
| Case 2—dead load (serviceability) | 81.13 | 3.1 | 96.41 | 2.6 |
| Case 2—dead load (ultimate) | 113.60 | 2.2 | 134.98 | 1.9 |
| Case 3—dead load + earthquake | 81.20 | 3.1 | 96.45 | 2.6 |

**Table 5** Finite element analysis and experimental finding comparison

| Load (N) | Stress at upper part (MPa) | | | Stress at lower part (MPa) | | |
|---|---|---|---|---|---|---|
| | FEA | Experiment | Difference (%) | FEA | Experiment | Difference (%) |
| 1009 | 1.29 | 1.45 | 11.03 | 1.77 | 1.89 | 6.35 |
| 2013 | 2.45 | 2.63 | 6.84 | 3.47 | 3.88 | 10.57 |
| 3066 | 3.75 | 4.10 | 8.54 | 5.24 | 5.90 | 11.19 |

**Table 6** Load cause shear stress to welding area

| Source of load (ultimate) | Load (N) |
|---|---|
| Dead load | 2,325,666.00 |
| Nozzle ($Y$-axis) | 25,586.17 |

**Fig. 9** Most critical welding shear stress
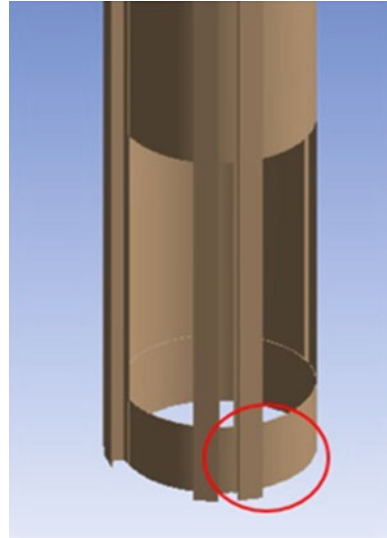


at welding area for existing ITB design is 41.22 MPa and for proposed design is 39.74 MPa.

By referring to Fig. 11, the welding properties for the lower part are set to be as: welding height, h = 6 mm, meanwhile welding length, l = 2 m (1 m for each side). By using formulation from ref [15], welding stress calculated is 27.71 MPa. Table 7 shows comparison between FEA and formulation calculation for both ITB and proposed design.

## 4 Conclusion

The analysis of this flare rectification has been successfully carried out both numerically and experimentally. The numerical analysis is not just limited to design model proposed by PETRONAS but also includes the proposed contractor's design as well. As a summary, the concluding remarks are as follows:

1. The safety factor for design model from ITB is 2.2. Meanwhile, as for proposed design, the safety factor is 1.9. Hence, both designs are safe.
2. As for the welding stress, the proposed flare rectification design has managed to increase the safety factor from 3.0 to 3.1 as shown in Table 6. The values indicate
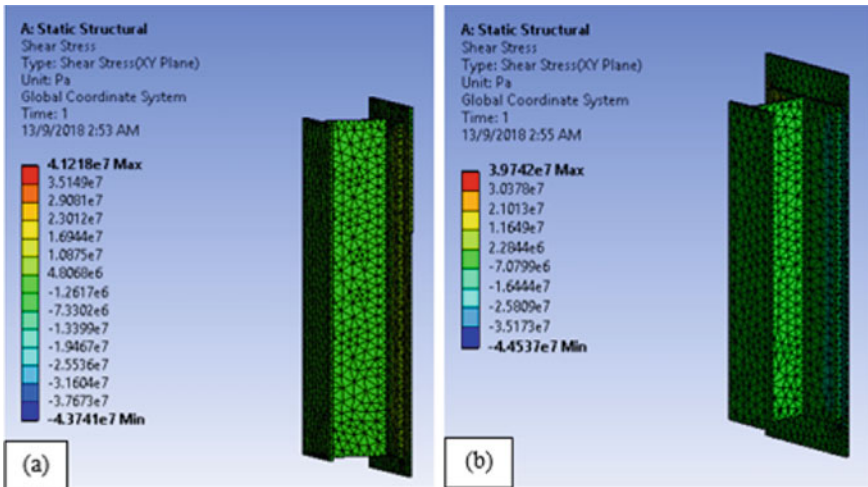
Fig. 10 Welding stress analysis for **a** existing ITB design and **b** proposed design
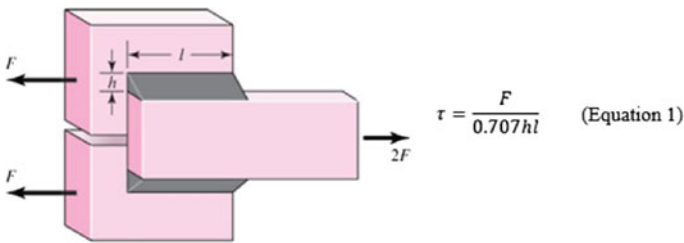


Fig. 11 Welding stress calculation. *Source* Mechanical Engineering Design, Shigley

**Table 7** Comparison of welding stress between FEA and formulation calculation (under shear loading condition)

| Loading condition | ITB | | Proposed design | |
|---|---|---|---|---|
| | Max stress (MPa) | Factor safety | Max stress (MPa) | Factor safety |
| FEA | 41.21 | 3.0 | 39.74 | 3.1 |
| Formulation | 27.71 | 4.5 | 27.71 | 4.5 |

that the proposed design has successfully improved the structure strength and, at the same time, becomes more cost-effective.

3. As for the recommendation, the installation of I-beam can be extended to the service utility area. This will result in reducing the stress concentration to the I-beam located near to the blower area.

# References

1. Bader A, Baukal Jr C, Bussman W (2011) Selecting the proper flare systems. American Institute of Chemical Engineers (AIChE), July, pp 45–50
2. Berrouane MT, Lounis Z (2016) Safety assessment of flare systems by fault tree analysis. J Chem Technol Metall 51(2):12–17
3. Khan F, Rathnayaka S, Ahmed S (2015) Methods and models in process safety and risk management: past, present and future. Process Saf Environ Prot 98:116–1467
4. Sahoo M (2013) High back pressure on pressure safety valves (PSVs) in a flare system. In: Developing the simulation model, identifying and analyzing the back-pressure build-up
5. Xu Y, Dinh H, Xu Q, Eljack FT, El-halwagi MM (2020) Flare minimization for an olefin plant shutdown via plant-wide dynamic simulation. J Clean Prod 254:120129. https://doi.org/10.1016/j.jclepro.2020.120129
6. Jo Y, Cho Y, Hwang S (2020) Dynamic analysis and optimization of flare network system for topside process of offshore plant. Process Saf Environ Prot 134:260–269. https://doi.org/10.1016/j.psep.2019.12.008
7. Mahdi E, Nasser K, Gharbia M (2010) Optimization of flare header platform design in a liquefied natural gas plant. In: Proceedings of 2nd annual gas processing symposium, pp 359–367. https://doi.org/10.1016/S1876-0147(10)02038-0
8. Jahromi SAJ, Javadpour S, Gheisari K (2006) Failure analysis of welded joints in a power plant exhaust flue. Eng Fail Anal 13(4):527–536. https://doi.org/10.1016/j.engfailanal.2005.02.019
9. Ghalambaz M, Abdollahi M, Eslami A, Bahrami A (2017) A case study on failure of AISI 347H stabilized stainless steel pipe in a petrochemical plant. Case Stud Eng Fail Anal 9:52–62. https://doi.org/10.1016/j.csefa.2017.07.001
10. Yob MS, Mansor S, Sulaiman R (2014) Joint stiffness of 3D space frame thin walled structural joint considering local buckling effect. Appl Mech Mater 660:773–777. https://doi.org/10.4028/www.scientific.net/AMM.660.773
11. Yob MS, Mansor S, Sulaiman R (2014) Individual stiffness of 3D space frame thin walled structural joint considering local buckling effect. Appl Mech Mater 554:411–415. https://doi.org/10.4028/www.scientific.net/AMM.554.411
12. Yob MS, Mansor S, Sulaiman R (2013) Finite element modelling to predict equivalent stiffness of 3D space frame structural joint using circular beam element. Appl Mech Mater 431:104–109. https://doi.org/10.4028/www.scientific.net/AMM.431.104
13. Rokhim MI, Yob MS, Kurdi OJO, Izahar MM (2020) Validated finite element model of build-up i-beam using triangular element under 4-point bending load, vol 10, no 3, pp 14593–14600
14. Yob MS, Junaidi R, Mat Tahir NA, Kurdi O, Abd Latif MJ (2020) Validated finite element model of build-up i-beam using triangular element under 4-point bending load. J Mech Eng Technol 12(2):46–53
15. Budynas RG, Nisbett JK, Shigley JE (2020) Shigley's Mechanical Engineering design (11th edn). Chapter 9—Welding, bonding, and the design of permanent joints. McGraw-Hill Education, New York, pp 475–516

# Experimental Investigation of a Swirl Toroidal Trapped Vortex Miniature Combustor

**Azam Che Idris, Mohd Rashdan Saad, and Mohd Rosdzimin Abdul Rahman**

**Abstract** A novel combustor that benefited from the swirl flow movement via tangential injection of air/fuel is presented in this study. This combustor was designed to solve the problem of low rate of fuel atomization and short mixing residence time typically found in a miniature combustor. The air/fuel was pre-heated before entering the combustion chamber by placing the exhaust path in the middle of the air/fuel entrance. The air/fuel mixing was enhanced by the formation of toroidal vortex due to the forced flow turning. The miniature combustor was supplied with n-heptane at the flow rate of 2.0 ml/min and air at the flow rate of 20.0 l/min to keep the equivalence ratio of 0.93. Background-oriented schlieren technique was applied to study the resultant exhaust gas and internal combustion mechanics. Combustion confinement was successfully achieved through enhancement of fuel vaporization-rate and increase in mixing residence time. The formation of multiple toroidal vortex rings was successfully visualized, and they can be attributed to the stable-mixing and confinement of the flame inside the combustion chamber. Temperature measurement of the exhaust gas indicates random pockets of air/fuel may be carried in a coherent fluid–structure and would spontaneously combust as it disintegrates.

**Keywords** Miniature combustor · Swirl combustion · Background oriented schlieren

## 1 Introduction

With the advent of Industrial Revolution 4.0 (IR 4.0) and the Internet of things (IoT), there has been a renewed push towards developing a portable power source that can supply electrical energy to smart autonomous devices. In the defence sector, we are looking towards building a smart soldier system. This system which can

A. Che Idris (✉)
Faculty of Integrated Technologies, Universiti Brunei Darussalam, Bandar Seri Begawan, Brunei
e-mail: azam.idris@ubd.edu.bn

M. Rashdan Saad · M. R. Abdul Rahman
Faculty of Engineering, Universiti Pertahanan Nasional Malaysia, Kuala Lumpur, Malaysia

enhance the combatant with superior communications capability, heightened audio-visual sensing, and augmented physical abilities using the exoskeleton system will require a power source that would not burden the soldier. Amongst the promising portable power source technology is a small internal combustion generator that would produce reasonable power without imposing too much weight. The practical issue involved in a small-scale combustion system has been discussed broadly in [1–3]. The most important challenge in a practical operation of a miniature combustor is flame instability. The instability is related to the small combustor size which have high ratio of surface to volume ratio, high-heat loss [4], and poor fuel/air mixing characteristics.

In most studies with regards to flame instability in a small combustor, the focus was more on the gaseous fuel [4]. The liquid fuel was not given much attention due to the complexity of the atomization process [5]. This has presented a missed opportunity in designing a practical miniature power generator since the liquid fuel has much higher energy density [6]. There are various methods to ensure stability of a liquid fuel combustion including porous media combustion [7–9], liquid film combustion [10–15], and electrospray combustion [16–20].

In this current study, a new concept of liquid fuel miniature combustor is presented. The new combustor design utilized annulus channel for fuel and air injection that will be pre-heated before entering the combustion chamber. The objectives of this study are (i) to prove that the flame can be confined internally within the combustion chamber and (ii) to visualize the internal combustion mechanism. To the authors' knowledge, there has been no previous attempt to visually inspect the flame inside a miniature combustor using the method of schlieren.

## 2  Conceptual Design Considerations

The most important design objectives which guided the design process are (i) enhanced fuel evaporation rate, (ii) optimum air–fuel mixing, and (iii) prolonged residence time of the air–fuel mixture. The formation of swirl toroidal vortex inside the combustion chamber is anticipated by the tangential injection of air and fuel into the annulus. The annulus is expected to promote fuel evaporation since it will receive heat from the exhaust flow channel in the middle of the annulus. The air and fuel will swirl downwards since the top of the annulus is sealed. The air/fuel will experience a sudden expansion and tumble during entry into the chamber. The tumble flow, due to its downward and angular momentum, will wrap into a toroidal vortex that will enhance air–fuel mixing. The swirling toroidal vortex is expected to hold the flame inside the bottom chamber. The cross-section structure of the combustor is shown in Fig. 1.
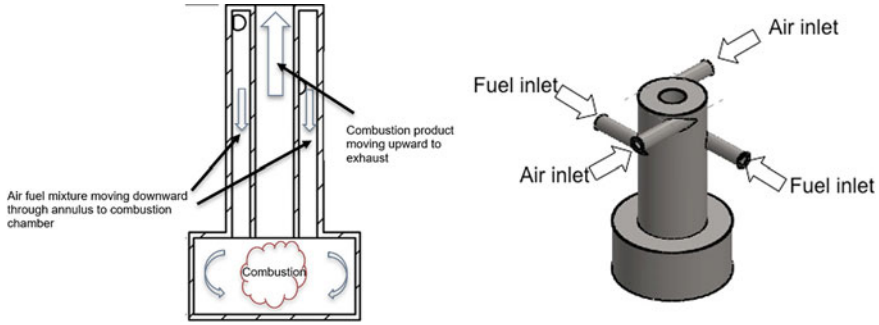
**Fig. 1** Schematic of the swirl toroidal vortex trapped miniature combustor

## 3  Experimental Setup

The combustor was made from two types of material, namely stainless steel (annulus and exhaust) and quartz (combustion chamber wall). Quartz was chosen to enable observation of the flame inside the chamber. The diameter of the inner and outer tubes is 10.0 mm and 22.2 mm, respectively. The chamber at the bottom has a diameter of 42.2 mm. Liquid fuel used in this study was n-heptane. The fuel was supplied to the combustor inlet by using a flow rate syringe pump (Model: LSP01-1A) with an accuracy of less than 0.5% error. A flow metre was used to regulate the flow rate of the air that supply from the air compressor tank to the combustor. A high-resolution camera, Nikon D90, is used to capture the image of the random pattern set at the background of the combustor. The image will be processed with digital image correlation (DIC) software, PIVLab, which can calculate the movement of the random pattern when density gradient appears inside the combustion chamber [21]. This technique is called background-oriented schlieren (BOS) and can be used to measure the temperature of the gas inside the chamber and outside the exhaust port. A high-speed digital camera, Casio Exilim Ex-zr100, was used to capture BOS images at 1000 frame per second. The combustor was operated at fuel flow rate of 2.0 ml/min and air flow rate of 20.0 l/min to keep the equivalence ratio of 0.93 (fuel lean). This is the optimum value where the flame is fully confined inside the combustion chamber.

## 4  Results and Discussion

### 4.1  Aerodynamics Investigation of the Combustion Chamber

The flow structure inside the combustion chamber when it is operating with $\emptyset = 0.93$ is examined by using the technique of BOS. Figure 2 shows the two original images

before they were processed using BOS algorithm. In Fig. 2a, there is no combustion, but the air and fuel have flowed into the chamber. In Fig. 2b, the image is captured during steady combustion, where the flame is totally confined inside the chamber, and no flame is detected at exhaust port. There is a slight blue tint glow of the flame inside the combustion chamber. The movement of the visible pattern inside the combustion chamber is calculated by BOS algorithm, and the results are presented in Fig. 3. The map shows the magnitude of the light refraction in the unit of pixels. We have not been able to calculate density or temperature due to the lack of available calibration data. Qualitatively, it is easy to understand that large magnitude of light refraction is related to large density gradient, which is caused by large temperature change. Figure 3 serves only as a qualitative observation to understand the turbulence mixing inside the chamber.

The upper region inside the chamber which has a large magnitude of light refraction coincides with the location of the observed flame glow. Similarly, the lower region of the chamber which has a low-density gradient has not been observed with
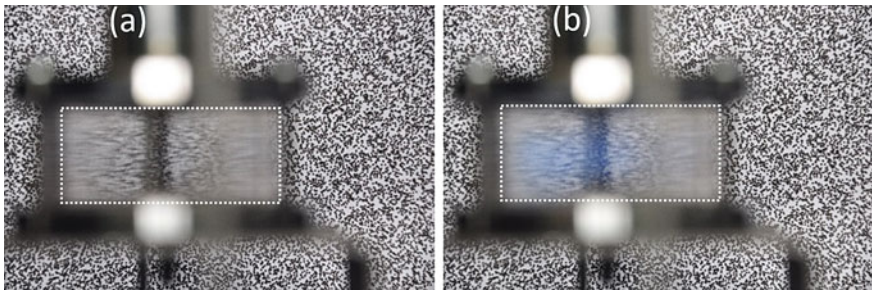


**Fig. 2** Raw unprocessed image of **a** no combustion, **b** steady combustion
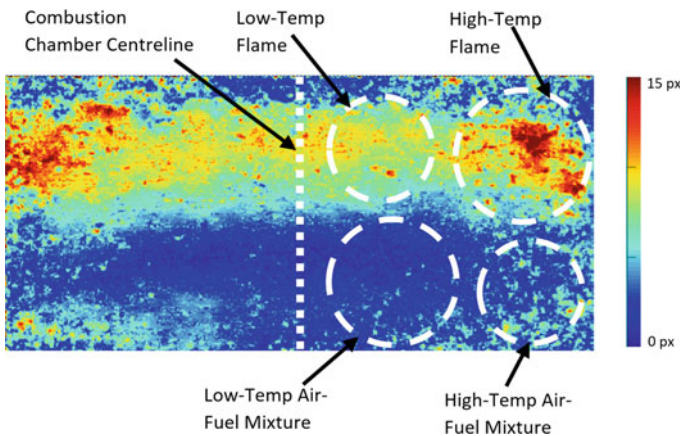


**Fig. 3** Intensity map of light refraction (in pixel unit) inside the combustor

a visible flame in any form. This would mean that the lower region is filled with air and fuel that has not been optimally mixed.

On the upper region, large magnitude of light refraction can be observed near the combustion chamber sidewall. This means that the flame is colder in the mid-region of the chamber. This is thought to be related to the cooling of the flame as it interacts the air/fuel entering the chamber as it expands towards the exhaust port.

The liquid fuel could not mix properly before it enters the chamber and would concentrate in the bottom region of the chamber, with lower temperature fluid around the centre. The interaction between the flame (heading upwards to exhaust) with unburnt air–fuel (flowing downwards from annulus) would cause the flame layer to roll and turn, transforming into contra-rotating toroidal flames [22]. The flame thickness and speed are influenced by the interaction between cold unburnt and hot burnt gas [23]. This observation shows that the highest temperature will be detected on the upper region of the chamber sidewall, and the lowest temperature is at the middle of the chamber bottom surface. Most of the flow can be seen to reverse direction as it enters from the air/fuel annulus. However, some of the flow were trapped inside circulation regions (toroidal flames) whose vector direction pointing normal to the mid-plane.

## *4.2  Aerodynamics Investigation of the Combustor Exhaust*

The flow structure of the exhaust gas when the combustor is operating with $\emptyset = 0.93$ is examined by using the technique BOS. In Fig. 4a, there is no combustion and no gas emanating from the exhaust port. In Fig. 4b, the combustor has been ignited for at least 30 s before the image is taken to ensure flame stability. By assuming a linear relationship between the change in temperature (delta $T$) and the change in refractive index (delta $n$) [24], and by taking a point measurement of temperature inside the whole field; we were able to calibrate all vectors and produce a temperature field image such as in Fig. 5. The hot gas produced by the combustion expanded into the atmosphere in a non-symmetrical cone. Due to this, we are unable to perform Abel transformation to present the temperature field in a 2-dimensional plane. Some coherent flow-structures can be observed, suggesting the formation of a first mode, single-helix jet flow as explained by Fiedler [25]. This flow-structures are aided by the Rayleigh–Taylor instabilities due to the interaction between lower-density hot gas with the higher-density atmospheric air [26].

The investigation of the flow structure of the exhaust gas is important before we could design a suitable nozzle and turbine to extract the kinetic energy in the exhaust flow. It is interesting to note that a peak temperature of more than 1800 degrees Celsius formed some distance away from the exhaust port of the combustor. In the pre-processed image, no flame could be observed at this peak temperature region. However, we speculated that pockets of air/fuel mixture inside the coherent vortical structure, which was isolated from being burned completely in the main combustion
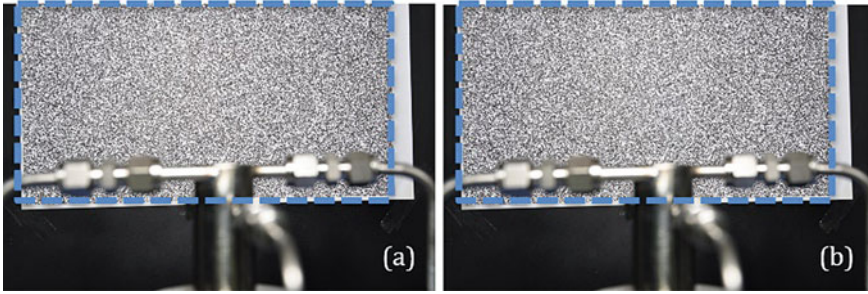
**Fig. 4** Raw unprocessed image of **a** no combustion and **b** steady combustion
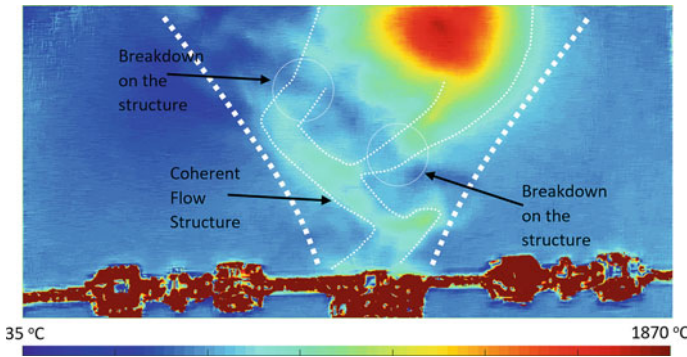


**Fig. 5** Map temperature (in celcius unit) showing the hot gas emanating from exhaust port

chamber, combusted suddenly when the vortical structure dissipated in the expansion process.

## 4.3 Combustion Dynamics

To study the combustion dynamics of this novel combustor, a series of images are captured at 1000 frame per second. For these images, we must use image subtraction technique due to the extremely low-exposure time of each image that increase the overall noise. By using image subtraction technique, we could only observe the flow qualitatively and could not measure the density gradient or temperature like in the previous sections. The original images are presented in Fig. 6 with the first image showing the exhaust port right just after ignition. In the next four images in the series, the flame is swallowed into the combustion chamber, and we could hardly detect any flame forming around the exhaust port. The Fig. 7a shows the process of ignition where the flame originally above the exhaust port moves downward into the chamber via a vortical structure. In Fig. 7b, the flame has been swallowed fully
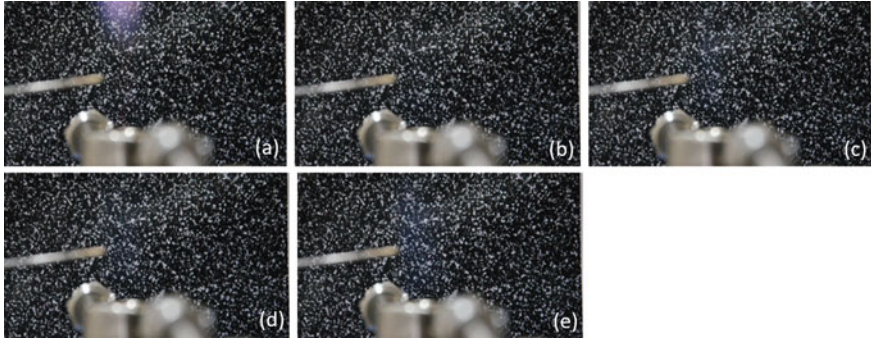
**Fig. 6** Raw images at **a** $t = 0$, **b** 1 ms, **c** 2 ms, **d** 3 ms, and **e** 4 ms
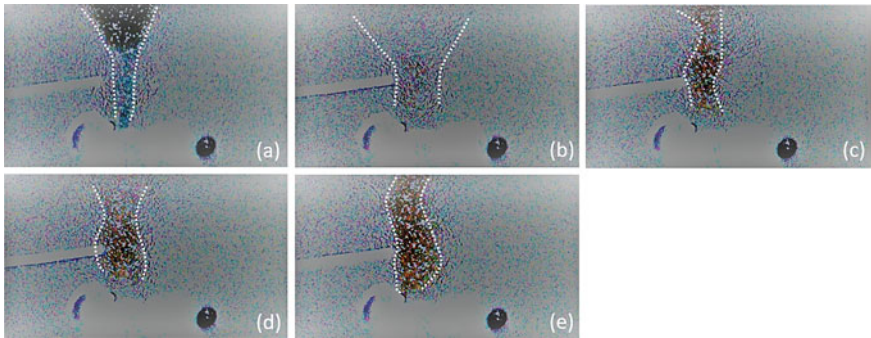


**Fig. 7** Processed images at **a** $t = 0$, **b** 1 ms, **c** 2 ms, **d** 3 ms, and **e** 4 ms

into the chamber and only faint hot gas can be seen in a conical shape. In the next three images, we can observe rapid changes in the shape of the exhaust gas. This suggests that the exhaust gas inherited the angular momentum or the toroidal vortex flame structures inside the combustion chamber. It is estimated that the exhaust gas fluctuates radially with the frequency around 250 Hz.

## 5 Conclusions

The present study investigated a novel liquid fuel miniature combustor using the BOS technique. It is concluded that a stable combustion of the n-heptane liquid fuel inside the miniature combustor is achieved without the need for external heating, liquid spray, secondary injection, or a porous media. The flame is strongly confined inside the combustion chamber at fuel lean regime (equivalent ratio of 0.93). The observed flow structure inside the chamber indicates the formation of multiple toroidal vortex rings, hot, and cold mixing vortices at the bottom and hot and cold flame vortices

at top region of the chamber. Some pockets of air/fuel mix may escape through vortical structure in the exhaust gas and combust outside the chamber. The angular momentum of the internal swirl vortices can be observed by the radial fluctuation of the exhaust gas.

# References

1. Walther DC, Ahn J (2011) Advances and challenges in the development of power-generation systems at small scales. Prog Energy Combust Sci 37:583–610
2. Chou SK, Yang WM et al (2011) Development of micro power generators–a review. Appl Energy 88:1–16
3. Shirsat V, Gupta AK (2011) A review of progress in heat recirculating meso-scale combustors. Appl Energy 88:4294–4309
4. Ju Y, Maruta K (2011) Microscale combustion: Technology development and fundamental research. Prog Energy Combust Sci 37:669–715
5. Li YH, Chao YC et al (2008) Progress in miniature liquid film combustors: double chamber and central porous fuel inlet designs. Exp Thermal Fluid Sci 32:1118–1131
6. Dunn-Rankin D, Leal EM, Walther DC (2005) Personal power systems. Prog Energy Combust Sci 31:422–465
7. Li YH, Chao YC, Dunn-Rankin D (2008) Combustion in a meso-scale liquid-fuel-film combustor with central-porous fuel inlet. Combust Sci Technol 180:1900–1919
8. Sadasivuni V, Agrawal AK (2009) A novel meso-scale combustion system for operation with liquid fuels. Proc Combust Inst 32:3155–3162
9. Li J, Huang J et al (2014) Experimental study of n-heptane/air combustion in meso-scale burners with porous media. Exp Thermal Fluid Sci 52:47–58
10. Sirignano WA, Pham TK, Dunn-Rankin D (2002) Miniature-scale liquid-fuel-film combustor. Proc Combust Inst 29:925–931
11. Pham TK, Amade NS et al (2005) Liquid film combustion in small cylindrical chambers. In: Proceedings of the fourth joint meeting of the US sections of The Combustion Institute, pp 20–23
12. Pham TK, Dunn-Rankin D et al (2007) Flame structure in small-scale liquid film combustors. Proc Combust Inst 31:3269–3275
13. Mattioli R, Pham TK, Dunn-Rankin D (2009) Secondary air injection in miniature liquid fuel film combustors. Proc Combust Inst 32:3091–3098
14. Giani C, Dunn-Rankin D (2013) Miniature fuel film combustor: swirl vane design and combustor characterization. Combust Sci Technol 185:1464–1481
15. Hery Soegiharto AF, Wardana ING et al (2017) The role of liquid fuels channel configuration on the combustion inside cylindrical mesoscale combustor. J Combust
16. Deng W, Klemic JF, Gomez A (2007) Liquid fuel microcombustor using microfabricated multiplexed electrospray sources. Proc combust Inst 31:2239–2246
17. Yuliati L, Seo T, Mikami M (2012) Liquid-fuel combustion in a narrow tube using an electrospray technique. Combust Flame 159:462–464
18. Gan Y, Luo Z et al (2015) The electro-spraying characteristics of ethanol for application in a small-scale combustor under combined electric field. Appl Therm Eng 87:595–604
19. Gan Y, Tong Y et al (2017) Experimental study on electro-spraying and combustion characteristics in meso-scale combustors. Energy Convers Manage 131:10–17
20. Gan Y, Tong Y et al (2018) Electro-spraying and catalytic combustion characteristics of ethanol in meso-scale combustors with steel and platinum meshes. Energy Convers Manage 164:410–416
21. Idris AC, Saad MR et al (2018) Background-Oriented Schlieren (BOS) for Scramjet Inlet-isolator Investigation. IOP Conf Ser: Mater Sci Eng 370:012003

22. Westbrook CK, Dryer FL (1981) Simplified reaction mechanisms for the oxidation of hydrocarbon fuels in flames. Combust Sci Technol 27:31–43
23. Peters N (1986) Laminar flamelet concepts in turbulence combustion. In: Twenty first symposium on combustion, The Combustion Institute, pp 1231–1250
24. Tokgoz S, Geisler R et al (2012) Temperature and velocity measurements in a fluid layer using background-oriented schlieren and PIV methods. Meas Sci Technol 23:115302
25. Fiedler HE (1988) Coherent structures in turbulent flows. Prog Aerosp Sci 25:231–269
26. Kull HJ (1991) Theory of the Rayleigh-Taylor instability. Phys Rep 206:197–325

# Experienced of Thermal Fatigue Failure on Closed Blowdown System Line in Delay Coker Unit

**Mohd Zainuddin Awang Ahmad, Mohd Shukri Yob, Noor Ayuma Mat Tahir, and Mohd Juzaila Abd Latif**

**Abstract**  Delay coker is one of the most important and profitable units in a refinery plant which consists of a closed blowdown system that is designed to contain blowdown from coke drums to quench tower. Due to constant used at various temperature, pressure, and conditions, components are susceptible to various of failures including thermal fatigue, corrosion, and others. Due to cyclic temperature, multiple cracks have been observed on the closed blowdown system (CBS) header piping in a short period. The crack was observed on the welding join between two different thickness pipes. This paper aims to study the structural integrity and risk level of the CBS line with the presence of different thickness intersection. Finite element analysis (FEA) was conducted on this line to evaluate the overall material behaviour and assessed the risk of failure. The acceptance criteria of the analysis were set to be based on ASME VIII-Division 2 part 5.2.2 (elastic stress analysis method) and ASME II-part D. Findings from FEA show that the failure occurred on the CBS line was caused by the presence of the different thickness intersection. Changes in geometry at this intersection causing stress intensification and high-peak stress that is highly susceptible to crack initiation in cyclic service. It is recommended that the petroleum refinery plant to sectionally replace the closed blowdown system line to ensure the pipe wall thickness is uniform throughout the entire length, thus eliminating stress intensification point and subsequently, removing the potential of fatigue failure.

**Keywords**  Thermal fatigue · Closed blowdown system · Finite element analysis · Stress intensification · Structural analysis

M. Z. Awang Ahmad
Petronas IRSO West Coast, Persiaran Penapisan, 76300 Sungai Udang, Melaka, Malaysia

M. S. Yob (✉) · N. A. Mat Tahir · M. J. Abd Latif
Fakulti Kejuruteraan Mekanikal (FKM), Universiti Teknikal Malaysia Melaka, Hang Tuah Jaya, 76100 Durian Tunggal, Melaka, Malaysia
e-mail: mshukriy@utem.edu.my

M. S. Yob · M. J. Abd Latif
Advanced Manufacturing Centre (AMC), Universiti Teknikal Malaysia Melaka, Hang Tuah Jaya, 76100 Durian Tunggal, Melaka, Malaysia

# 1 Introduction

The increase in industrial sector had cause the increase in demand for fuel resources. With the increasing demand, the petroleum industries have been rapidly expanded throughout the world. In order to maximize the products delivery, pipeline has been utilized as means of main transportation for these resources between plants and refineries. In 2006, it has been estimated that the transmission pipelines around the world were assessed at 350,000 km which 19% of it were used to transport petroleum products [1]. These pipe vessels are exposed to high-pressure loading which becomes potentially hazardous [2, 3]. Failures of crude oil, gas, and petrochemical pipe vessels have high risk that could jeopardize the life, environment, and not to mention has significant budget loss. Thus, pipelines are expected to have a high-quality control standard as the carrying materials and attached assets are strongly depending on the pipe integrity [1, 4, 5].

In petroleum refinery plant, there are several processes that are required to convert the crude oil into useful products such as naphtha, gasoline, fuel, and gas. Due to the difference in processing conditions, a refinery plant is divided into several units. Each unit consists of basic components such as pressure vessel, heat exchanger, tank, and boiler which these units are connected by pipe or line. Amongst the units, delayed coker unit (DCU) is a semi-batch process to convert the densest and least desirable of crude oil into profitable product. This process breaks the long hydrocarbon chain molecules of the residual crude oil into gas oil and petroleum coke.

Due to the nature of this process, the coke drums in this unit are subjected to extreme thermal cycling. Typically, these drums exposed to high temperatures up to 482 °C for a long period of time. Then, to cool the remnant material to a safe operating temperature, a rapid steam quenching followed by long water quench was conducted. However, this process is mechanically put the drum shell under repetitive strain. Over full operational cycles, these drums also operate at various pressure (from 0 to 345 MPa) repetitively.

Although the pressure and temperatures of the operating streams are known and controlled, the actual loading on the pressure envelope of the drum is not certain, especially during the water quench stage where large volumetric flow rates are impacted by the distribution, density, porosity, and internal channelling within the remnant residual coke mass. This cyclic repetitive strain shows a huge threat towards the drums body and components [3]. In the closed blowdown system (CBS), there is a huge variation of temperatures (between 130 and 340 °C) at the inlet header to quench tower during steam out, back warming, and water quenching. This process was conducted up to 2 h which then resulting on temperature cyclic.

Susceptible to cyclic stress and strain, welding joints are the most likely to be failed amongst other body. This is because welding process itself is altering the mechanical and physical properties of a material in order to hold other materials together. There are many failure cases reported on the pipelines due to cyclic temperature and pressure [6–11]. Amongst those studies, it was found that the crack growth rate is much higher when the temperature is increase. They also found that the higher stress intensity

factor caused by high temperature fluctuations is one contributor to the increased crack growth rate at the higher temperature [6]. This was discussed as it follows the Paris Law that the crack growth rate increased as the stress intensity increased [6, 7, 12–14].

Besides the cyclic temperature and pressure changes, changes in flow direction and inner diameter of tube pipe also considered as contributing factor to pipe failures [9, 10, 15]. Study by Varnosfaderani et al. [1] diagnoses a crack of blowdown pipe in a petrochemical plant and found that the crack initiates from inner surface to outer surface due to erosion caused by high stress. Other studies also found similar pattern where cracks were initiated from the inner surface [6]. The changes of flow direction due to change in inner diameter and stepped pipe were also proved by other researcher where there were crack observed near the tee joint, stepped pipe, and diameter change area [9–11, 15, 16].

Computational fluid dynamics (CFD) are often used by researcher to study the flow of gas and liquids inside a closed system. Turbulent flow is often seen when there are changes in flow directions and area. The backflow often disrupting the original flow which eventually causing high pressure in certain area in a closed system. Study by Liu et al. [17] found that erosion of the gas passing through the stepped pipe is the main contributor to pipe failure near the flow change area beside the possibility of contaminants (third body abrasion) that travelled along the gas through the analysis using ANSYS (finite volume method) analysis. In addition, ANSYS was also used by Raafat et al. [18], where their analysis on fatigue and thermal stress analysis of submerged steel pipes shows that by controlling the angle of the waves, the maximum can be predicted and not exceeding the allowable stress. Previous, finite element modelling is used to predict behaviour of joining parts and managed to produce satisfactory result [19–21].

As discussed above, with proper planning and analysis on pipe flow, stress and failures can be predicted and prevented. Prevention of failures can reduce the process shutdown and able to eliminate catastrophic. Thus, this paper aims to study the structural integrity and risk level of the CBS line with the presence of different thickness intersection. The outcome of this study was expected to provide a clear and concise analysis on different thickness intersection of petroleum piping for future planning on piping system.

## 2 Problem Statement

### 2.1 Problem to Be Countered

It has been reported that several crack failures around affected region along circumferential weldment occur at 24″ CBS header pipe in one of refinery. The repetitive failures at the same region have led to loss of output due to loss of fluid and system shutdown for rectification work.
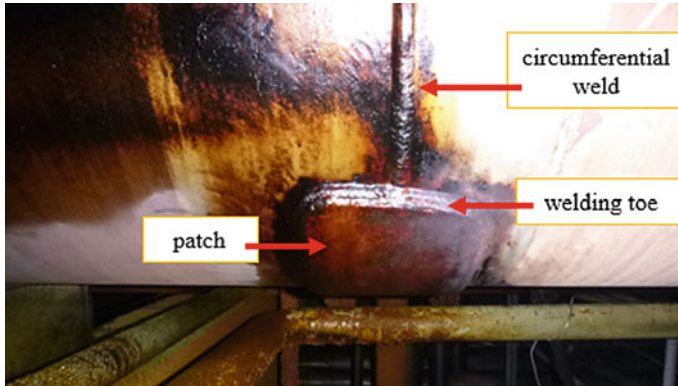
**Fig. 1** Fillet weld patch at different thickness weldment crack

The pipe has two different thickness (17 and 9 mm) at intersection nearest to tee. Between the two different thickness pipe, 30° angle tapered welding was initially weld during the pipe installation. The first occur in 2011 and was suspected to be caused by the high stress because of the change of thickness. However, in 2014, the patch cracked at the weld toe that causing second repairs by applying another patch on top of the existing patch. Unfortunately, the second patch failed within less than one year. The image of the patch is shown in Fig. 1. Other cracks were also observed on the same year at different thickness intersection.

## 2.2 Analysis on Crack

Root cause failure analysis (RCFA) was conducted before deeper analysis using finite element analysis (FEA) was conducted. The FEA was performed by using ABAQUS 6.13 software. The acceptance criteria of the analysis were referred to the ASME VIII-Division 2-Part 5.2.2 (elastic stress analysis method) and ASME-Part D. Simple static analysis (without fatigue analysis) was used to examine the stress variation across the cross section of the pipe. Figure 2 shows the illustration of piping line with different thickness.

## 3 Discussion

The RCFA analysis found that the cracks were due to thermal fatigue due to repetitive temperature changes and stress riser due to the difference in thickness. Detailed inspections conduct initiates that the pipe undergoes thermal cyclic ranging from
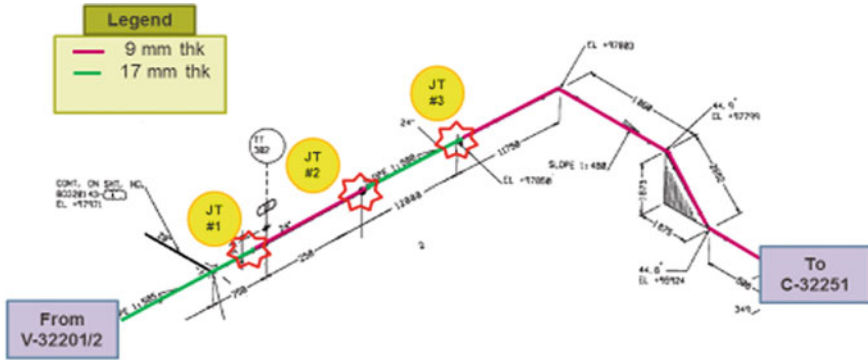
**Fig. 2** Locations of different thickness of pipe

120 to 340 °C at least twice a day. The system has been operated since 1999 which makes the pipe undergoes at least 8750 thermal cyclic until its first failure (crack).

Reaction from Caesar II simulation was then implemented on the FEA model (simplified pipeline) as shown in Fig. 3, while the FEA analysis is shown in Fig. 4. It is expected that stress intensification is expected at locations with changes of geometry such as elbow and tee. Thus, intersection of different thickness also is form of geometry changes will have stress intensification. From the analysis in Caesar II, there were no significant stress intensification observed at the different thickness weldment area. This finding is expected since there is no stress intensification factor (SIF) has been specifically pointed out on the different thickness location based on The American Society of Mechanical Engineers Process Piping Guide (ASME B31.3) [20], and the stress given is purely average stress over cross-sectional area without variation of the thickness.

FEA results in Fig. 4 show that piping with higher thickness gives lower overall stress value along the piping line. Thus, highest peak stress value was obtained on the inner side of the thinner pipe intersection. These were recorded at all different thickness weldment of the 24″ CBS header. Highest peak stress is shown at location 1 under design condition and operating with gradient temperature condition support, the evidence of different thickness intersection is the cause of failure. This finding was also supporting by earlier research where the disruption in inner diameter caused increase in stress intensification which led to failures [7, 16].

## 4   Conclusions

This study shows that the different thickness pipe weldment plays significant factor in thermal cyclic piping system as happened in this CBS piping system. Normally in construction, the different thickness weldment has not been taking as serious issue since there is a guideline in The American Society of Mechanical Engineers Process
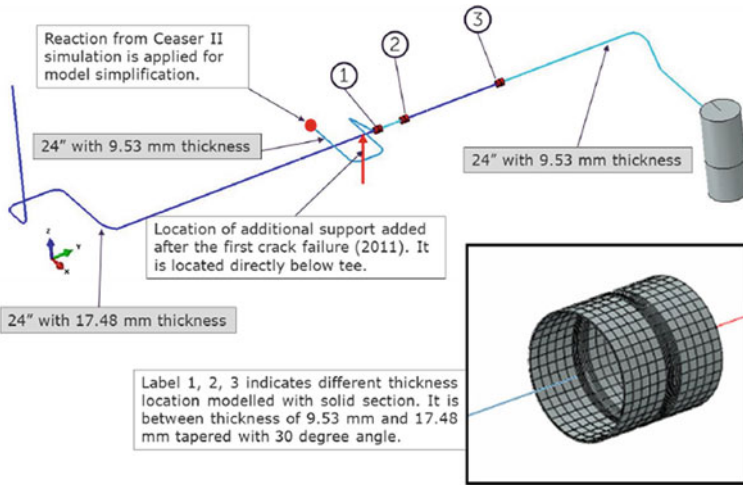
**Fig. 3** FEA model of simplified pipeline
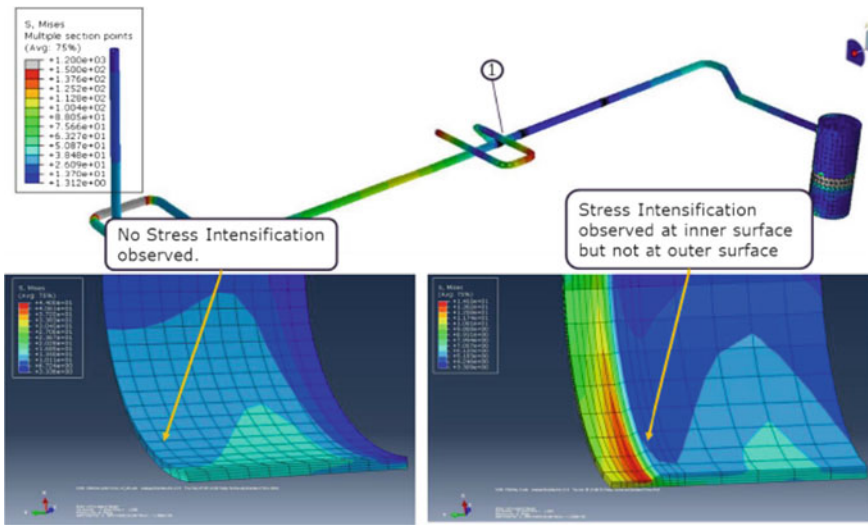


**Fig. 4** FEA analysis on cross section of pipe area at point 1

Piping Guide (ASME B31.3) for welding the two pipes. Based on this study, the fatigue failure analysis shall be taken into consideration whenever this condition required to installed. This is because the amount of peak stress value at the changes of thickness weldment will be the weakest area that will become additional factors for fatigue failure due to thermal cyclic in piping system.

# References

1. Varnosfaderani MA, Eslami A, Saiedi N, Bahrami A (2019) Metallurgical aspects of a blowdown pipe failure in a petrochemical plant. Eng Fail Anal 98:141–149
2. Shafiq U et al (2020) A review on modeling and simulation of blowdown from pressurized vessels and pipelines. Process Saf Environ Prot 133:104–123
3. Barma MC et al (2017) A review on boilers energy use, energy savings, and emissions reductions. Renew Sustain Energy Rev 79:970–983
4. Guan R, Lu Y, Wang K, Su Z (2019) Fatigue crack detection in pipes with multiple mode nonlinear guided waves. Struct Heal Monit 18:180–192
5. Ibrahim RI, Humod AT, Essa NA (2020) Design and implementation of an automatic control system to avoid fouling in pipes with blow down heat recovery in steam boilers. IOP Conf Ser Mater Sci Eng 765:1–14
6. Paffumi E, Nilsson KF, Szaraz Z (2015) Experimental and numerical assessment of thermal fatigue in 316 austenitic steel pipes. Eng Fail Anal 47:312–327
7. Paffumi E, Nilsson KF, Taylor NG (2008) Simulation of thermal fatigue damage in a 316L model pipe component. Int J Press Vessel Pip 85:798–813
8. Coleman K (2006) Thermal fatigue of fossil boiler. Power 3
9. Kamaya M, Miyoshi K (2017) Thermal fatigue damage assessment at mixing tees (elastic-plastic deformation effect on stress and strain fluctuations). Nucl Eng Des 318:202–212
10. Jones DP, Holliday JE, Leax TR, Gordon JL (2004) Analysis of a thermal fatigue test of a stepped pipe. Am Soc Mech Eng Press Vessel Pip Div PVP 482:67–77
11. Radu V, Paffumi E (2010) A stochastic approach of thermal fatigue crack growth (LEFM) in mixing tees. Am Soc Mech Eng Press Vessel Pip Div PVP 3:1031–1040
12. Pugno N, Ciavarella M, Cornetti P, Carpinteri A (2006) A generalized Paris' law for fatigue crack growth. J Mech Phys Solids 54:1333–1349
13. Carpinteri A, Montagnoli F (2020) Scaling and fractality in subcritical fatigue crack growth: crack-size effects on Paris' law and fatigue threshold. Fatigue Fract Eng Mater Struct 43:788–801
14. Bazant ZP, Hubler MH (2014) Theory of cyclic creep of concrete based on Paris law for fatigue growth of subcritical microcracks. J Mech Phys Solids 63:187–200
15. Lee JI, Hu L, Saha P, Kazimi MS (2009) Numerical analysis of thermal striping induced high cycle thermal fatigue in a mixing tee. Nucl Eng Des 239:833–839
16. Cipière MF, Le Duff JA (2002) Thermal fatigue experience in French piping: influence of surface condition and weld local geometry. Weld World 46:23–27
17. Liu E et al (2021) Erosion simulation and improvement scheme of separator blowdown system —a case study of Changning national shale gas demonstration area. J Nat Gas Sci Eng 88:103856
18. Raafat E, Nassef A, El-hadek M, El-Megharbel A (2019) Fatigue and thermal stress analysis of submerged steel pipes using ANSYS software. Ocean Eng 193:106574
19. Yob MS, Mansor S, Sulaiman R (2013) Finite element modelling to predict equivalent stiffness of 3D space frame structural joint using circular beam element. Appl Mech Mater 431:104–109
20. Yob MS, Mansor S, Sulaiman R (2014) Individual stiffness of 3D space frame thin walled structural joint considering local buckling effect. Appl Mech Mater 554:411–415
21. Yob MS, Mansor S, Sulaiman R (2014) Joint stiffness of 3D space frame thin walled structural joint considering local buckling effect. Appl Mech Mater 660:773–777

# Numerical Study on the Effects of Sloshing in a Spherical Tank Using Double-Side Curved Baffle

**Ahmad Mahamad Al-Yacouby, Mostafa M. Ahmed, and M. S. Liew**

**Abstract** The sloshing phenomena is a critical engineering problem encountered by designers in the oil and gas industry and causes damages to the tank walls. Thus, in this study, the effects of sloshing in a spherical tank with double-side curved baffle was investigate using numerical simulation. Two cases were considered in this simulation. A spherical tank without curved baffle was modelled in the first case, then, in the second case, a double-side curved baffle was introduced. The simulation was conducted considering three filling levels of 30%, 50%, and 75% using ANSYS CFX software. The outcome of the study shows that introducing double-side curved baffle has significantly reduced the sloshing force, the sloshing pressure, and the fluid velocity in the tank.

**Keywords** Sloshing effects · Double-side curved baffle · Spherical tank · Filling levels

## 1 Introduction

Sloshing in FLNG tanks has direct effects on the vessel's movement. During the production and offloading process, FLNGs have a wide range of filling levels. Especially in the offloading operation, the filling level inside the tank can vary significantly within a relatively short time therefore the demand for precise and effective tools to predict the coupling responses of liquid loading on FLNG vessels is increasing in the literature [1]. Different numerical and experimental approaches have been carried out in the previous studies to investigate the sloshing effects in different tank shapes using various types of baffles. The nonlinear sloshing effect has been thoroughly investigated and most of the studies concerned with the impact pressures on tank walls caused by the sloshing as reported by Wen-Hua et al. [2], while the studies on the interaction between a floating vessel and the liquid sloshing inside the tanks equipped on it are still limited. Shao et al. [3] have stated that liquid sloshing at

A. M. Al-Yacouby (✉) · M. M. Ahmed · M. S. Liew
Department of Civil and Environmental Engineering, Universiti Teknologi PETRONAS, 32610 Seri Iskandar, Perak Darul Ridzuan, Malaysia
e-mail: ahmad.alyacouby@utp.edu.my

a great amplitude will inevitably lead to unintended consequences. Thus, with any form of sloshing mitigation devices or damping structure, it is essential to minimize the impacts and damaging effects due to sloshing. Baffles are the most considerably utilized tools for mitigating the sloshing impacts due to their simplicity in the design and suitability in the installation process. The numerical investigation of liquid sloshing in a closed, partially filled, T-shaped baffled and unbaffled 2D rectangular tank has been considered by Ünal et al. [4]. The inhibition effect of different baffles on the sloshing phenomenon was investigated by Guan et al. [5] using computational simulations of liquid sloshing in three-dimensional tanks under horizontal and roll excitation. In the sloshing tanks, the horizontal baffle, vertical baffle, and T-baffle were examined, and the baffles' location, dimensions, and liquid depth were investigated.

Various types of porous baffles such as T-baffle, semicircle baffle in two-dimensional tanks have been utilized by Gao et al. [6] to analyze the liquid sloshing behaviors under the external excitation. They have adopted finite element method (FEM) and control variable method to study the impacts of the baffle height, number, length, shape, location, porous effect of the porous baffle, the external load frequency and the tank shape on the liquid sloshing response. An effective immersed cylinder was utilized numerically as a reduction tool on the inhibition sloshing in a moveable container by Iranmanesh [7]. Further, Ma et al. [8] have investigated the influence of baffle location on the liquid sloshing in a laterally moving spherical tank was investigated. Smooth Particles Hydrodynamic (SPH) method was used to simulate weakly compressible viscous flow in the partially filled tank. To monitor the pressure exerted on the tank wall, four probes are placed at various locations within the tank wall. To investigate how the sloshing phenomenon is suppressed, four tank models with different baffle locations are created. The incompressible smoothed Particle Hydrodynamic (ISPH) method was applied by Zheng et al. [9], to simulate the sloshing in a 2D tank with complex baffles. Different sloshing tanks were simulated under varied conditions to investigate the impact of baffle configuration and the excitation frequency. The findings indicate that the complex baffles can considerably influence the impact pressures on the wall induced by the severe sloshing, and the relevant analysis can assist to find the engineering solutions to efficiently repress the problem. According to Chen et al. [10], an in-house mesh-free particle solver MLParticle-SJTU was developed based on improved moving particle semi-implicit (MPS) method, was employed to simulate numerically the impacts of T-baffle on liquid sloshing under surge excitation. The transient sloshing in laterally excited horizontal elliptical containers with T-shaped baffles has been first analyzed by Wang et al. [11], by utilizing an innovative semi-analytical scaled boundary finite element method (SBFEM). Meanwhile, three T-shaped baffle configurations are considered including surface-piercing baffle, bottom-mounted baffle, and their combination form.

The concept of horizontal perforated plate (HPP) used in a rectangular tank to sup-press the sloshing loads using analytical model based on potential theory [12]. The findings helped to clarify the impact of the internal HPP on the sloshing behavior in the vessel tank. The anti-sloshing impact of a vertical porous baffle with various perforations and immersed depths in a rolling rectangular tank was studied by George

**Table 1** Required particulars of spherical tanks and double-side curved baffle

| Spherical tank | |
| --- | --- |
| Internal diameter of spherical tank | 3.6 m |
| *Double-side curved baffle parameters* | |
| Top and bottom width | 0.6 m |
| Height | 1.8 m |
| Radius of the arc | 3.6 m |

and Cho [13], using the analytical, numerical, and experimental models. An effective anti-sloshing tool namely, a bottom-hinged and top-tensioned vertical porous membrane baffle was utilized by Cho and Kim [14], to inhibit the excited sloshing by swaying and rolling rectangular tank based on the 2D hydroelastic linear potential theory.

Thus, the aim of this study is to investigate the effects of double-side curved baffle on the fluid sloshing of a spherical tank considering two case studies. In the first case the tank was modelled without baffle, and in the second case a double side curved baffle was introduced to evaluate the sloshing effects, under three different filling levels of 30%, 50%, 75%. The outline of the remaining sections is: Sect. 2 provides the methodology and theoretical background, Sect. 3 presents the results and discussions, and the conclusion is presented in Sect. 4.

## 2 Methodology

### 2.1 Geometrical Particulars of the Tank and Double-Side Curved Baffle

The spherical tank geometry used in the numerical simulation was based on the particulars reported by Arai et al. [15]. The scaled down parameters for the double-side curved baffle and the tank size are presented in Table 1. The spherical tank and the double-side curved baffle are modelled using ANSYS software, as shown in Fig. 1.

### 2.2 Numerical Background

**Volume of Fluid Method (VOF)**. To manage the numerical diffusion and capture the two-phase interface effectively, the Volume of Fluid (VOF) method is used in ANSYS CFX in conjunction with bounded compression approaches [16]. The fractional function of the VOF as identified by $\varphi$ in a computational cell is obtained by

**Fig. 1** Dimensions of the spherical tank and the double-side curved baffle
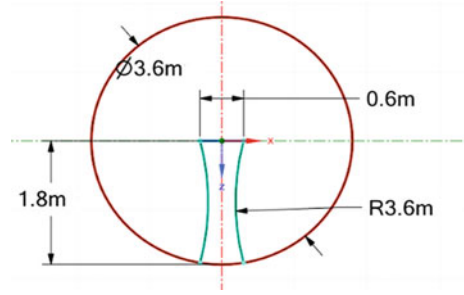


$$\varphi = \begin{cases} 0 & \text{in air} \\ 0 \text{ on free surface} & < \varphi < 1 \\ 1 & \text{in water} \end{cases} \tag{1}$$

The fractional function satisfies the following advection equation:

$$\frac{\partial \varphi}{\partial t} + \left(u_i - u_i^m\right)\frac{\partial \varphi}{\partial x_i} = 0 \tag{2}$$

The interface between the water and air phases is represented by the contour of the fractional function with $\varphi = 0.5$. The fluid density and viscosity are averaged by the provided fractional function in the calculation as follows:

$$\rho = \varphi\rho_W + (1 - \varphi)\rho_A \tag{3}$$

$$\mu = \varphi\mu_W + (1 - \varphi)\mu_A \tag{4}$$

where W and A represent the water and air phases, respectively.

## 3 Results and Discussion

### 3.1 Sloshing Results

The sloshing simulation was investigated under three filling levels, namely of 30%, 50%, and 75% using ANSYS CFX solver. In this study two conditions are considered to evaluate the sloshing effects. The outcome of the sloshing simulation is discussed in the following sections.

**Low Filling Level (30%)**: In the case of 30% filling level, the sloshing effects was investigated under two conditions, tank without baffle, and tank with double-side curved baffle as indicated in Fig. 2. The graphs show that the sloshing parameters starts with fluctuating values at the beginning of the simulation prior to converge

to more stable values at the end. The max values of sloshing force, pressure, and velocity are 8.37 N, 8427.06 Pa and 8.34 m/s respectively. These values correspond to the tank without baffle as summarized in Table 2.

**Medium Filling Level (50%)**: In the case of 50% filling level, the results of sloshing effects are illustrated in Fig. 3. The graphs show the variation of sloshing parameters with time as well as the corresponding contours that show the intensity of forces, pressure and fluid velocity inside the tank. Generally, the maximum values of 3.05 N, 8415.51 Pa and 7. 26 m/s respectively, were observed. These values correspond to the tank without baffle as presented in Table 3. The comparison of the results clearly indicates that the presence of baffle can improve the sloshing effects significantly.

**High-filling Level (75%)**: In the case of 75% filling level, the results of sloshing effects are demonstrated and represented as in Fig. 4 and Table 4. The max sloshing force, the maximum pressure, and the maximum sloshing velocity are 5.09 N, 9519.74 Pa and 6.36 m/s respectively. The comparison of the results clearly indicates that the presence of baffle in the tank has improved the sloshing effects significantly. In addition, the 75% fill level has shown the highest sloshing parameter in the tank as the sloshing pressure, the sloshing force and the sloshing velocity are the highest as compared to other fill levels.

## 3.2 Comparison on Filling Levels Effects on Sloshing Parameters

This section discusses the effects of three filling levels of 30%, 50%, and 75% on the sloshing force, sloshing pressure, and sloshing velocity, under two conditions, such as baffled tank, and unbaffled tank.

**Sloshing Force**. Figure 5 shows the variation of sloshing forces with time for three filling levels of 30%, 50%, 75% for unbaffled and baffled tank. As shown in the aforementioned figure, in the case of 30% filling level, the maximum sloshing force occurred in the unbaffled tank, recorded as 8.38 N, whereas in the baffled tank, the max force occurred is 4.32 N. Similarly, in the case of 50% filling level, the max force in the unbaffled tank was recorded as 13.05 N, while in the baffled tank, the max force was observed as 7.97 N. In the case of high-filling level of 75%, the maximum sloshing force occurred in the unbaffled tank as 5.09 N, whereas in the baffled tank, the max sloshing force was 1.45 N.

**Sloshing Pressure**. Figure 6 shows the variation of sloshing pressure with time for three filling levels of 30%, 50%, 75% for unbaffled and baffled tank. The graph indicates that in the case of low filling level of 30%, the peak pressure in the tank occurred in the case of tank without baffle, recorded as 8427.06 Pa, whereas in the tank with baffle, the fluid pressure was 1401.55 Pa. similarly, in the medium filling level of 50%, the peak pressure in tank without baffle was 8415.51 Pa, while in the case of the tank with baffle, the recorded pressure was 3538.75 Pa. The outcome also indicates
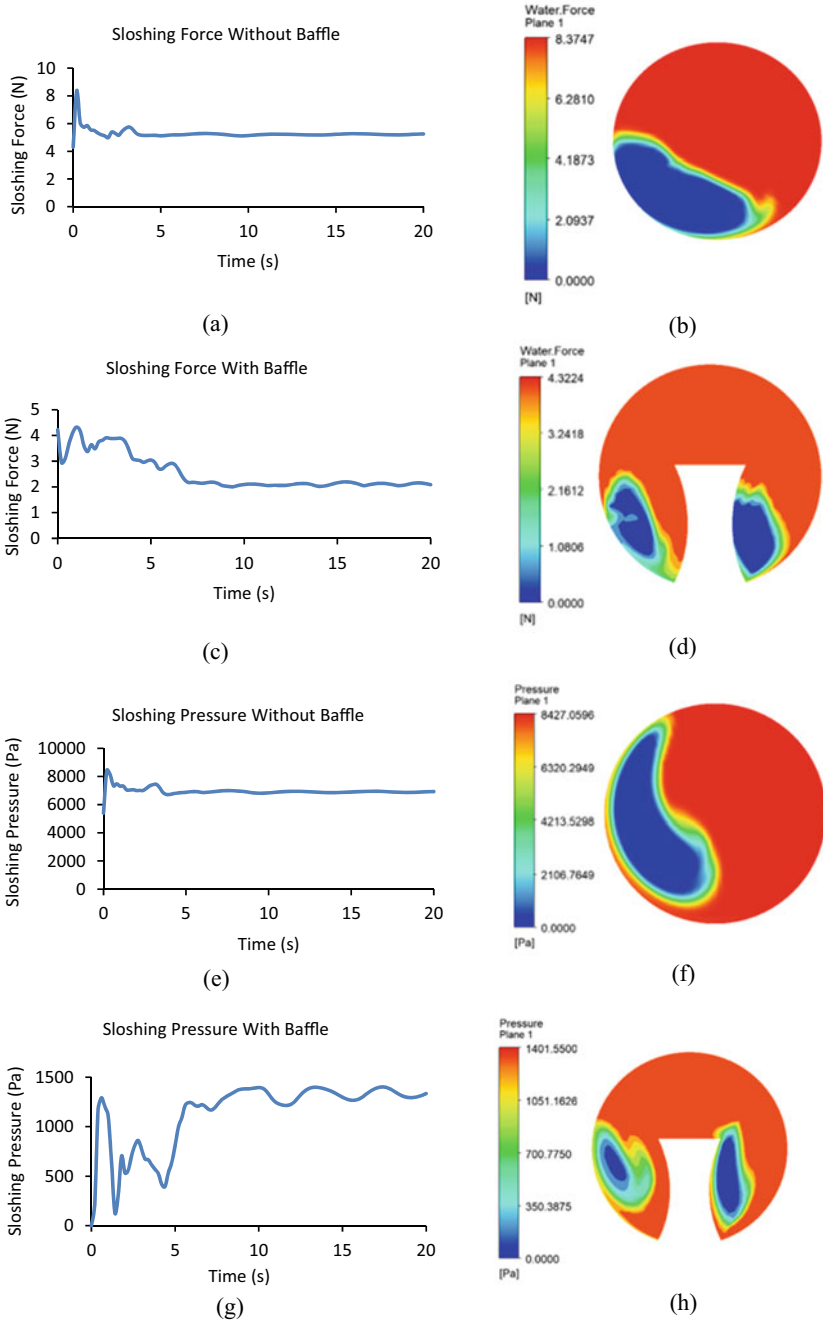
**Fig. 2** Variation of sloshing force, pressure, and velocity in the spherical tank, for unbaffled and baffled cases with 30% filling level

(i)



(j)



(k)



(l)
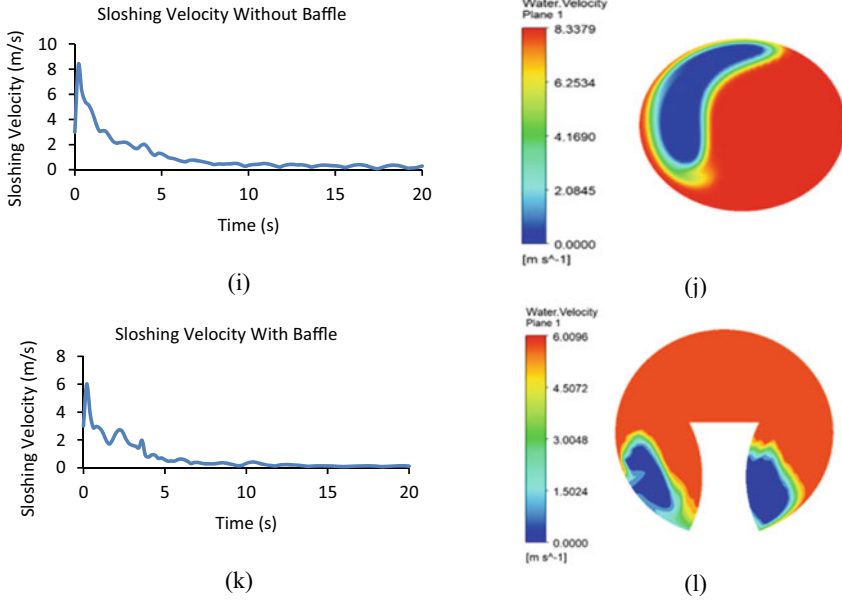
**Fig. 2** (continued)

**Table 2** Maximum values of sloshing pressure, velocity, and force at 30% filling level

| Parameters | 30% filling level | | |
|---|---|---|---|
| | Max sloshing force (N) | Max sloshing pressure (Pa) | Max sloshing velocity (m/s) |
| Tank without baffle | 8.37 | 8427.06 | 8.34 |
| Tank with baffle | 4.32 | 1401.55 | 6.01 |

that in the case of 75% filling level, the peak pressure was observed as 9519.74 Pa in the tank without baffle, whereas in the tank with baffle, the corresponding pressure was 1829.43 Pa.

**Sloshing Velocity**. Figure 7 shows the variation of sloshing velocity with time for three filling levels of 30%, 50%, 75% for unbaffled and baffled tank. The comparison of the results shows that for 30% filling level, the maximum sloshing velocity was recorded as 8.34 m/s corresponding to the case of tank without baffle, whereas in the tank with baffle the sloshing velocity was 6.01 m/s. Similarly, for the 50% filling level, the max velocity was 7.26 m/s in the tank without baffle, while in the tank with baffle, the recorded sloshing velocity was 6.59 m/s. For the case with filling level of 75%, the maximum velocity was 6.27 m/s, corresponding to the tank without baffle, while in the case of the tank with baffle the sloshing velocity was 3.48 m/s as depicted in the figure.
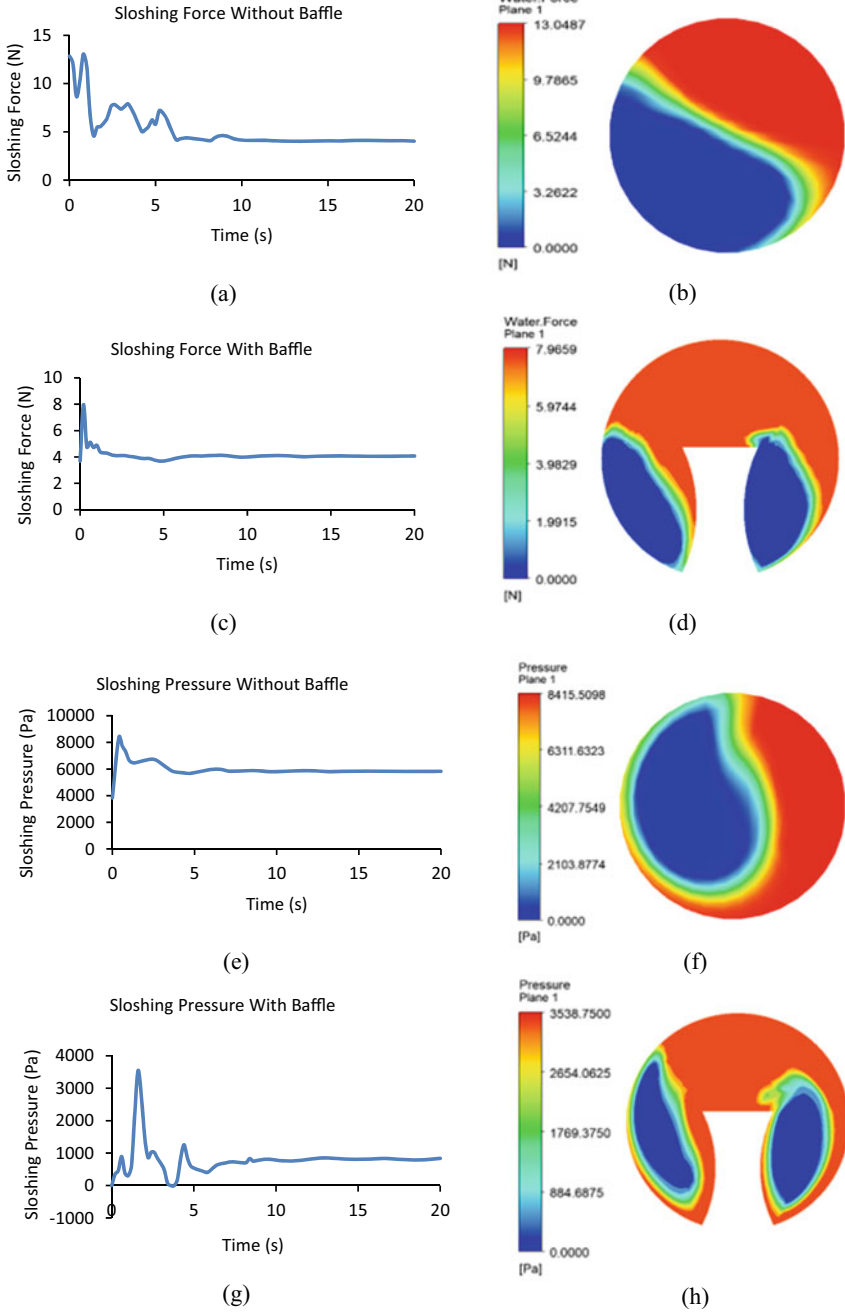
Fig. 3 Variation of sloshing force, pressure, and velocity effects in a spherical tank for unbaffled and baffled tank under 50% filling level

Sloshing Velocity Without Baffle

(i)



Water.Velocity
Plane 1

(j)

Sloshing Velocity With Baffle

(k)



Water.Velocity
Plane 1

(l)
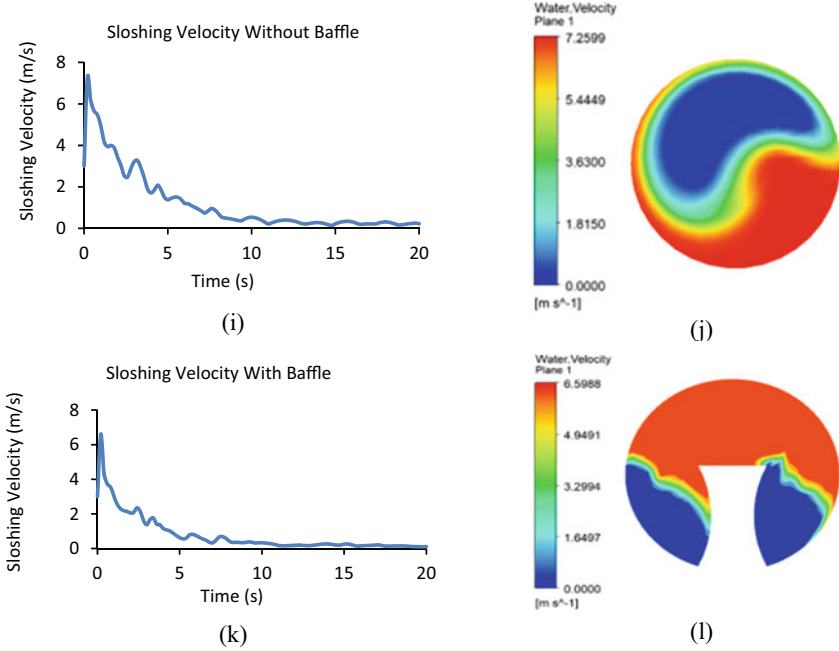
**Fig. 3** (continued)

**Table 3** Maximum values of sloshing force, pressure, and velocity at 50% filling level

| Parameters | 50% filling level | | |
|---|---|---|---|
| | Max sloshing force (N) | Max sloshing pressure (Pa) | Max sloshing velocity (m/s) |
| Tank without baffle | 13.05 | 8415.51 | 7.26 |
| Tank with baffle | 7.97 | 3538.75 | 6.59 |

# 4 Conclusion

In this study, we have carried out two cases of numerical simulations to investigate the effects of sloshing in a spherical tank using double-side curved baffle using numerical simulations. First, we have investigated the sloshing effects in the tank without baffle, and later a baffle was introduced, and the sloshing was investigated numerically under three filling levels of 30%, 50%, and 75%. The result shows that in the case of sloshing force, the maximum effect was observed in the case with fill level of 50%, observed as 13.05 N. While, in the case of sloshing pressure, the max effect was observed in the fill level of 75% recorded as 9519.74 Pa. Finally, in the case of slosh-ing velocity, the maximum effect was noticed in the 30% filling with
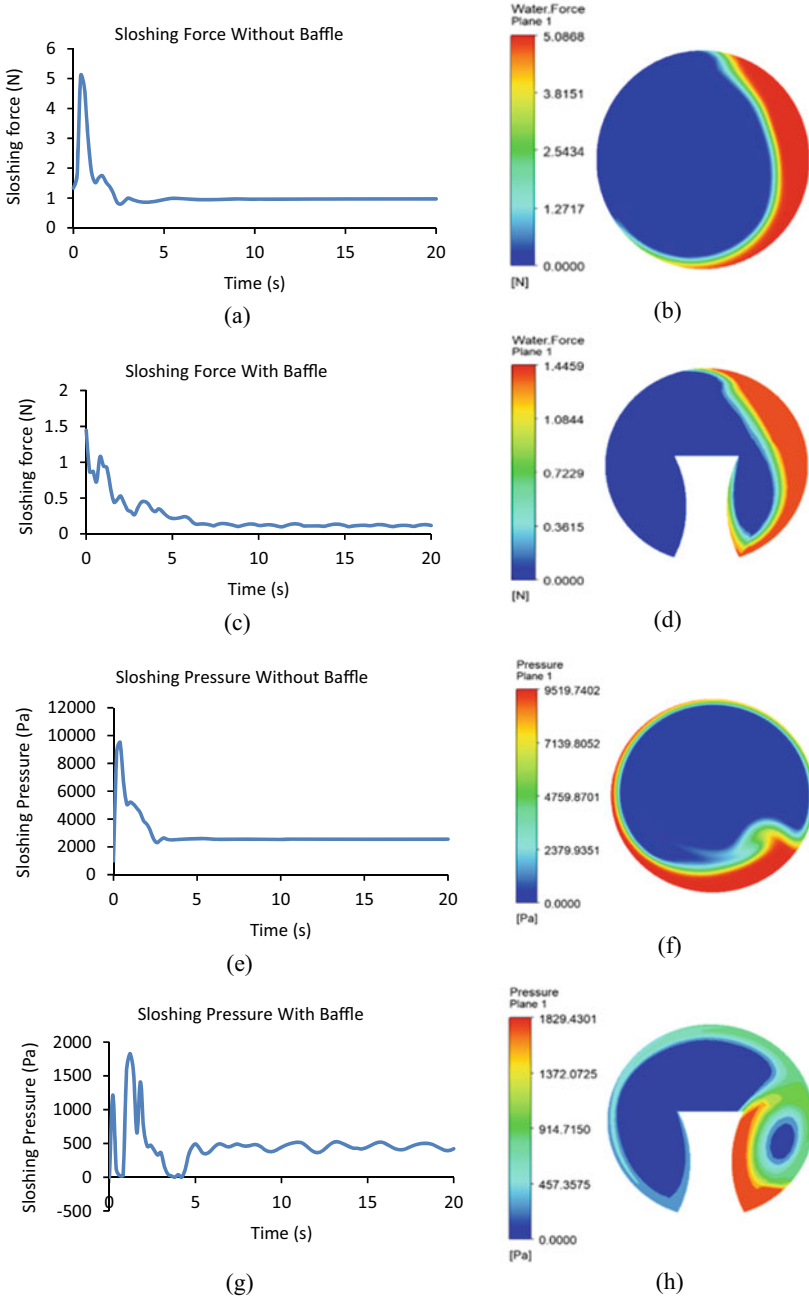
**Fig. 4** Sloshing force, pressure, and velocity effects in spherical tank in unbaffled and baffled tank under 75% filling level

(i)



(j)



(k)



(l)
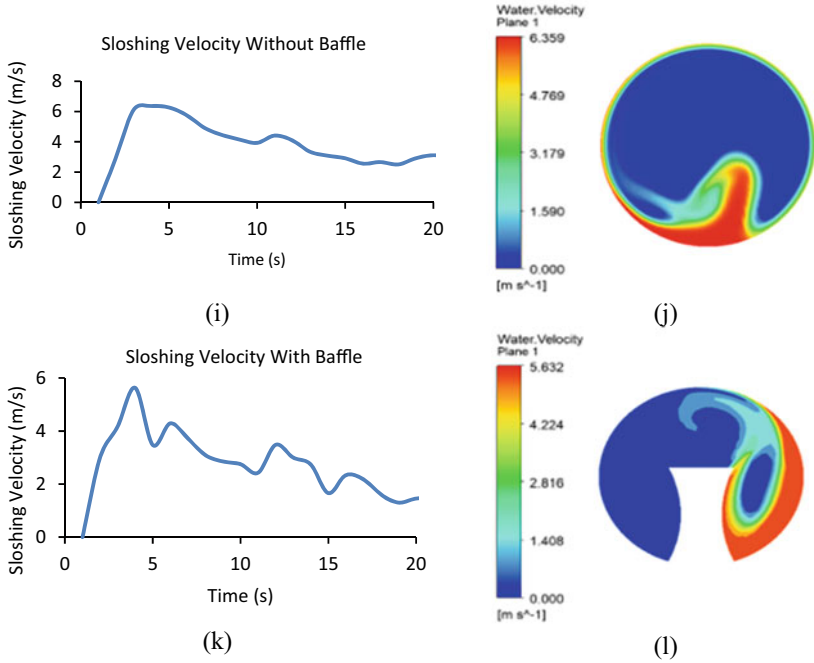
**Fig. 4** (continued)

**Table 4** Max values of sloshing force, pressure, and velocity at 75% filling level

| Parameters | 75% filling level | | |
|---|---|---|---|
| | Max sloshing force (N) | Max sloshing pressure (Pa) | Max sloshing velocity (m/s) |
| Tank without baffle | 5.09 | 9519.74 | 6.36 |
| Tank with baffle | 1.45 | 1829.43 | 5.63 |

**Fig. 5** Variation of sloshing forces with time for three filling levels of 30%, 50%, 75% for unbaffled and baffled tank
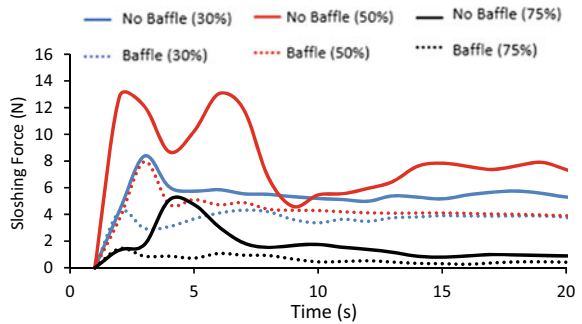
**Fig. 6** Variation of sloshing pressure with time for three filling levels of 30%, 50%, 75% for unbaffled and baffled tank
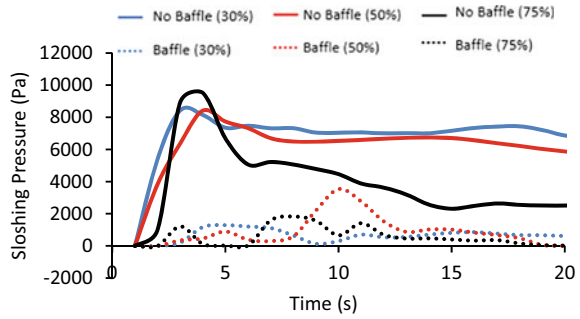


**Fig. 7** Variation of sloshing velocity with time for three filling levels of 30%, 50%, 75% for unbaffled and baffled tank
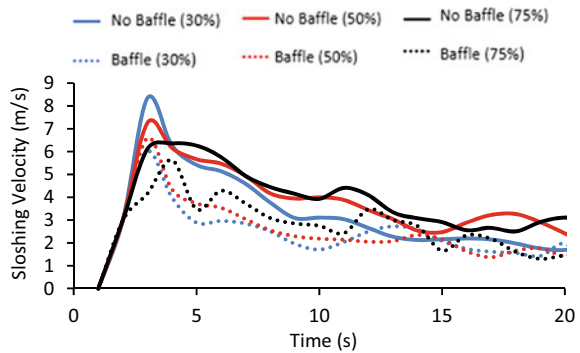


value of 8.34 m/s. Thus, it can be concluded that the presence of double-side curved baffle in the tank has significantly reduced the sloshing effects.

# References

1. Zhao D, Hu Z, Chen G, Chen X, Feng X (2018) Coupling analysis between vessel motion and internal nonlinear sloshing for FLNG applications. J Fluids Struct 76:431–453. https://doi.org/10.1016/j.jfluidstructs.2017.10.008
2. Wen-hua Z, Jian-min Y, Zhi-qiang HU, Long-fei X (2012) Experimental investigation of effects of inner-tank sloshing on hydrodynamics of an FLNG system. J Hydrodyn 24(1):107–115. https://doi.org/10.1016/S1001-6058(11)60224-2
3. Shao J, Li S, Li Z, Liu M (2015) A comparative study of different baffles on mitigating liquid sloshing in a rectangular tank due to a horizontal excitation. Eng Comput (Swansea, Wales) 32(4):1172–1190. https://doi.org/10.1108/EC-12-2014-0251
4. Ünal UO, Bilici G, Akyıldız H (2019) Liquid sloshing in a two-dimensional rectangular tank: a numerical investigation with a T-shaped baffle. Ocean Eng 187(November 2018).https://doi.org/10.1016/j.oceaneng.2019.106183

5. Guan Y, Yang C, Chen P, Zhou L (2020) Numerical investigation on the effect of baffles on liquid sloshing in 3D rectangular tanks based on nonlinear boundary element method. Int J Nav Archit Ocean Eng 12:399–413. https://doi.org/10.1016/j.ijnaoe.2020.04.002
6. Gao H, Yin Z, Liu J, Zang Q, Lin G (2020) Finite element method for analyzing effects of porous baffle on liquid sloshing in the two-dimensional tanks. Eng Comput (Swansea, Wales). https://doi.org/10.1108/EC-12-2019-0567
7. Iranmanesh (2017) A 2D numerical study on suppressing liquid sloshing using a submerged cylinder. Ocean Eng 138(April):55–72. https://doi.org/10.1016/j.oceaneng.2017.04.022
8. Ma L, Wei C, Zhao Y (2018) Research on the suppression effect law of different baffle positions on liquid sloshing in spherical tank. In: Proceedings of 2018 9th international conference on mechanical and aerospace engineering ICMAE 2018, pp 457–461. https://doi.org/10.1109/ICMAE.2018.8467649
9. Zheng X, You Y, Ma Q, Khayyer A, Shao S (2018) A comparative study on violent sloshing with complex baffles using the ISPH method. Appl Sci. https://doi.org/10.3390/app8060904
10. Chen X, Tang Z, Wan D (2016) The effects of T type baffle on liquid sloshing by MPS method. In: Proceedings of 3rd international conference on violent flows, no March, pp 9–11.
11. Wang W, Tang G, Song X, Zhou Y (2017) Transient sloshing in partially filled laterally excited horizontal elliptical vessels with T-shaped baffles. J Press Vessel Technol Trans ASME 139(2):1–13. https://doi.org/10.1115/1.4034148
12. Jin H, Liu Y, Song R, Liu Y (2020) Analytical study on the effect of a horizontal perforated plate on sloshing motion in a rectangular tank. J Offshore Mech Arct Eng 142(4):1–12. https://doi.org/10.1115/1.4046171
13. George, Cho IH (2020) Anti-sloshing effects of a vertical porous baffle in a rolling rectangular tank. Ocean Eng 214(July):107871. https://doi.org/10.1016/j.oceaneng.2020.107871
14. Cho H, Kim MH (2020) Effect of a bottom-hinged, top-tensioned porous membrane baffle on the sloshing reduction in a rectangular tank. Appl Ocean Res 104(August):102345. https://doi.org/10.1016/j.apor.2020.102345
15. Arai M, Cheng LY, Wang X, Okamoto N, Hata R, Karuka G (2016) Sloshing and swirling behavior of liquid in a spherical LNG tank. In: PRADS 2016—Proceedings of the 13th international symposium on PRActical design of ships and other floating structures, no June 2017
16. Jiang SC, Bai W (2020) Coupling analysis for sway motion box with internal liquid sloshing under wave actions. Phys Fluids 32(7). https://doi.org/10.1063/5.0015058

# Analysis on the Performance of Logistics Companies with TOPSIS Model

**Lam Weng Siew, Lam Weng Hoe, Lee Pei Fun, and Mohd Abidin Bin Bakar**

**Abstract** Maritime, packaging, storage, distribution, transportation, and reverse logistics happen around the clock globally. In domestic and international trades, these logistics services are imperative in driving the economy of a country. The greater the trade volume, the more sought after are the logistics companies. To provide timely delivery and make informed decisions during the pandemic, logistics companies depend on a variety of assets to support their operations. Analysis on the financial performance will offer insights on the resilience of logistics companies in the pandemic. This paper aims to analyze and rank the financial positions of logistics companies using Technique for Order Preference by Similarity to Ideal Solution model. The results show that MISC gives the best financial performance among the studied companies. Besides, it provides insights to other companies for further improvement based on the ideal solution identified in this study.

**Keywords** TOPSIS · Logistics companies · Ideal solution · Ranking

## 1 Introduction

The export of diamonds from South Africa to the United Kingdom, intercontinental trade of Norwegian salmon to Australia, and even the shipment of vaccines from the United States to Malaysia rely heavily on logistical processes from the acquisition of raw materials to a storage point prior to transportation and the last-mile delivery to reach consumers. From these scenarios, the role of logistics companies is enlarged as they are entrusted to deliver parcels and consignments successfully in the shortest time with minimum risk regardless of calamity. As the world slows down due to the COVID-19 pandemic, many logistics companies around the world are continuing their operations despite not being in full swing [1]. This reflects the value of logistics activities to the economy of the world and the urgent need for logistics companies to deliver daily supplies as people maintain indoors in the stressful period.

L. W. Siew (✉) · L. W. Hoe · L. P. Fun · M. A. B. Bakar
Department of Physical and Mathematical Science, Faculty of Science, Universiti Tunku Abdul Rahman, Kampar Campus, Jalan Universiti, Bandar Barat, 31900 Kampar, Perak, Malaysia
e-mail: lamws@utar.edu.my

Nonetheless, being the core service industry and the backbone for economy during desperate times, logistics companies face many turbulences when many other physical businesses are not allowed to operate. As individuals and businesses urgently review their budgets, logistics companies experience drastic decline in demand in the early stage but with greater operating costs. Road, waterway, air and railway freight have been disrupted with reduction in manpower, while individual and corporate customers also ship fewer goods as manufacturing plants, and retailers are forced to close to bring down infection risk. Besides, the usual logistics network cannot be executed due to local, regional and cross border traffic limitations. Business model of logistics companies has also changed to contactless delivery which focuses more on health condition and temperature screening of logistics employees and proofs of delivery in the form of pictures instead of signatures and the use of drones [2].

Borgstrom et al. [3] agreed that E-commerce is a major driver for the logistics industry. However, they also mentioned that since logistics companies are mainly providing services, logistics companies rely on a number of assets with huge investments including vehicle fleet, material handling equipment, transport structure, storage space and digitization. This shows that logistics resilience, which is the ability to return to normal state after an interruption or the absorbance of shock while maintaining critical functions, is important in logistics companies particularly in financial perspectives [4]. Being one of the essential industries to operate during this pandemic, disruptions in ports, customs clearance and warehouses would lead to losses in other parties since this is a chain reaction where all parties are dependent on each other for the fulfillment of delivery. As such, logistics resilience is of utmost importance for the satisfaction of the parties in the upstream and downstream of the logistics chain. Resilient logistics companies often plan for financial flexibility by managing their balance sheets to outplay their competitors in recessions. Finance has been identified as a major factor in logistic resilience [5–7].

Therefore, the financial positions of logistics companies in Malaysia will be investigated based on the proposed framework using Technique for Order Preference by Similarity to Ideal Solution (TOPSIS) model. TOPSIS is a decision-making model which solves multi-criteria decision-making (MCDM) problems [8–10]. MCDM problems involve determining the best alternative or solution by considering multiple decision criteria [11–15]. The optimal decision is made in a systematic manner using decision making model [16–21]. In TOPSIS model, the best alternative will have the least divergence from the positive ideal solution (PIS) and the largest geometric distance to the negative ideal solution (NIS). An alternative shows better achievement when it is less diverged from PIS and separate further from NIS. The determination of weights of criteria, normalization, and computing the geometric separation to the ideal solutions is the main steps in TOPSIS [22, 23]. Its broad application can be traced in food processing [24], oil and gas [25], evaluation of strategies [26], selection of logistics companies [27], barriers in logistics [28], and site selection [29]. With regards to this, this paper adopts financial variables to study the financial positions of listed logistics companies in Malaysia using TOPSIS model. Logistics companies majoring various activities such as maritime services, transportation, air logistics, and freight forwarding are evaluated in terms of performances [30, 31]. This section

shall then be followed by data and methodology, empirical results, and a concluding paragraph.

## 2 Data and Methodology

The analysis of financial positions of logistics companies is based on the proposed framework as presented in Table 1. The criteria are current asset (CA), current liability (CL), total asset (TA), total liability (TL), net income after tax (NI), and revenue (Rev) which are extracted from the annual reports of the logistics companies from 2016 to 2020 [32]. All criteria shall be maximized except CL and TL in which lower values are deemed as better performance. The alternatives are the listed logistics companies made up of BIPORT, GDEX, LITRAK, MISC, MMCCORP, and SURIA.

The steps of TOPSIS model are shown as follows [9, 33].

Step-1: Build a matrix $(x_{mn})$ of size $p \times q$:

Step-2: Form a normalized decision matrix $R = (r_{mn})$:

$$r_{mn} = \frac{x_{mn}}{\sqrt{\sum_{i=1}^{p} x_{mn}^2}}, \, m = 1, 2, \ldots, p \text{ and } n = 1, 2, \ldots, q \tag{1}$$

Step-3: Obtain a weighted-normalized decision matrix $(D)$:

$$W = \left(w_1, w_2, \ldots, w_q\right), \text{ where } \sum_{n=1}^{q} w_n = 1 \tag{2}$$

A weighted-normalized matrix, $D$, can be obtained when row elements in the normalized decision matrix $R$ multiples with the weights, $w_n$. In this study, equal weights imply that the criteria are equally important according to TOPSIS model.

Step-4: Calculate PIS $\left(A^+\right)$ with NIS $\left(A^-\right)$:

| Table 1 Proposed framework | Objective | To investigate the financial positions of logistics companies | | |
|---|---|---|---|---|
| | Criteria | CA | Alternatives | BIPORT |
| | | CL | | GDEX |
| | | TA | | LITRAK |
| | | TL | | MISC |
| | | NI | | MMCCORP |
| | | Rev | | SURIA |

$$A^+ = \left\{ (\max D_{mn} | n \in N)(\min D_{mn} | n \in N') \right\} = \left\{ d_1^+, d_2^+, \ldots, d_j^+ \right\} \quad (3)$$

$$A^- = \left\{ (\min D_{mn} | n \in N)(\max D_{mn} | n \in N') \right\} = \left\{ d_1^-, d_2^-, \ldots, d_j^- \right\} \quad (4)$$

Step-5: Compute the geometric separation of alternatives from PIS ($v_n^+$) and NIS ($v_n^-$):

$$v_m^+ = \sqrt{\sum_{n=1}^{j} (d_{mn} - d_n^+)^2}, m = 1, 2, \ldots, i \quad (5)$$

$$v_m^- = \sqrt{\sum_{n=1}^{j} (d_{mn} - d_n^+)^2}, m = 1, 2, \ldots, i \quad (6)$$

Step-6: Determine the multiple composite score ($C_m^*$), which is the relative proximity to the ideal solutions.

$$C_m^* = \frac{v_m^-}{v_m^- + v_m^+} \text{ where } C_m^* \in [0, 1], m = 1, 2, \ldots, i \quad (7)$$

Step-7: Rank each alternative according to the descending order of the multiple composite scores, $C_m^*$, because higher $C_m^*$ resembles greater performance.

The ranking of listed companies is important because it provides insights to the fund managers, investors as well as the companies for potential improvement [34–37].

## 3 Empirical Results

Based on the optimal solution of TOPSIS model, the weighted-normalized decision matrix is obtained and presented in Table 2.

**Table 2** Weighted-normalized decision matrix

|         | CA     | CL     | TA     | TL     | NI     | Rv     |
|---------|--------|--------|--------|--------|--------|--------|
| BIPORT  | 0.0121 | 0.0046 | 0.0087 | 0.0134 | 0.0145 | 0.0036 |
| GDEX    | 0.0052 | 0.0008 | 0.0015 | 0.0006 | 0.0032 | 0.0046 |
| LITRAK  | 0.0096 | 0.0039 | 0.0064 | 0.0106 | 0.0243 | 0.0080 |
| MISC    | 0.1554 | 0.1466 | 0.1505 | 0.1243 | 0.1591 | 0.1493 |
| MMCCORP | 0.0579 | 0.0791 | 0.0708 | 0.1097 | 0.0405 | 0.0733 |
| SURIA   | 0.0033 | 0.0018 | 0.0039 | 0.0023 | 0.0055 | 0.0046 |

**Fig. 1** PIS and NIS for each criterion
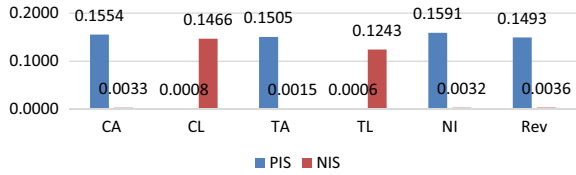


Figure 1 demonstrates the PIS and NIS for each criterion.

As shown in Fig. 1, the PIS with CA, CL, TA, TL, NI, and Rev is 0.1554, 0.0008, 0.1505, 0.0006, 0.1591, and 0.1493, respectively. NIS with criteria CA, CL, TA, TL, NI, and Rev is 0.0033, 0.1466, 0.0015, 0.1243, 0.0032, and 0.0036, respectively. These values are applied to obtain the geometric separations of the logistics companies to PIS and NIS.

Figure 2 presents the geometric separations of logistics companies to PIS and NIS.

As seen in Fig. 2, MISC has the least divergence of 0.1912 to PIS, followed by MMCCORP with 0.2318 separation to PIS, LITRAK with separation of 0.2833 to PIS and BIPORT, SURIA, and GDEX with separations of 0.2880, 0.2985, and 0.3000, respectively. These values are obtained after computation involving the weighted-normalized decision matrix with PIS. MMCCORP, BIPORT, LITRAK, SURIA, GDEX, and MISC have increasing divergence with NIS at 0.1371, 0.1809, 0.1839, 0.1893, 0.1912, and 0.3014, respectively.

Since a logistics company is performing better when it is less diverged from PIS and further from NIS simultaneously, the multiple composite score ($C_m^*$) is obtained and ranked as shown in Table 3.

**Fig. 2** Geometric separation of logistics companies to PIS and NIS
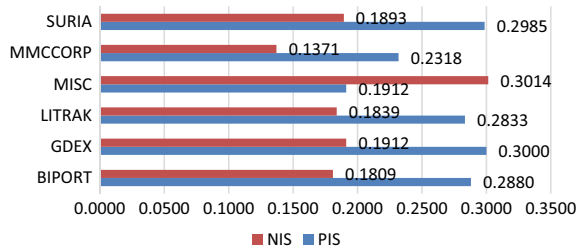


**Table 3** Ranking of multiple composite score of logistics companies

| Company | $C_m^*$ | Ranking |
|---------|---------|---------|
| MISC | 0.6119 | 1 |
| LITRAK | 0.3936 | 2 |
| GDEX | 0.3893 | 3 |
| SURIA | 0.3881 | 4 |
| BIPORT | 0.3858 | 5 |
| MMCCORP | 0.3716 | 6 |

From Table 3, MISC is having the highest multiple composite score of 0.6119, and therefore, MISC obtains the first ranking and the best financial position among the studied logistics companies. The ranking of the financial performance is followed by LITRAK (0.3936), GDEX (0.3893), SURIA (0.3881), BIPORT (0.3858), and MMCCORP (0.3716).

## 4 Conclusion

Assets are supporting tools for logistics industry to expedite the delivery of parcels between players in the supply chain. To achieve this, besides, the management of assets, liabilities, incomes, and revenues is part of a logistics company's finances requiring routine reviews throughout an accounting year. This paper aims to analyze CA, CL, TA, TL, NI, and Rev of logistics companies in Malaysia based on the proposed framework using TOPSIS model. MISC, LITRAK, and GDEX are the best three companies in managing finances. Results from this study can serve as references for the government and analysts to provide inputs to balance the financial statuses of the listed logistics companies to facilitate them to serve the country with greater efficiency. Logistics companies can also scrutinize their financial positions with regards to the competitors. Being a developing country, managing finances in the logistics industry is important to drive the economy of a country.

## References

1. Illahi U, Mir MS (2021) Maintaining efficient logistics and supply chain management operations during and after coronavirus (COVID-19) pandemic: learning from the past experiences. Environ Dev Sustain 23:11157–11178
2. Srinivas SS, Marathe RR (2021) Moving towards "mobile warehouse": last-mile logistics during COVID-19 and beyond. Transp Res Interdisc Persp 10(100339):1–6
3. Borgstrom B, Hertz S, Jensen L (2021) Strategic development of third-party logistics providers (TPLs): "going under the floor" or "raising the roof"? Ind Mark Manage 97:183–192
4. Ferreira C, Cardoso C, Travassos M, Paiva M, Pestana M, Lopes JM, Oliveira M (2021) Disorders, vulnerabilities and resilience in the supply chain in pandemic times. Logistics 5(48):1–16
5. Chen A, Hsieh C, Wee HM (2014) A resilient global supplier selection strategy—a case study of an automotive company. Int J Adv Manuf Technol 87(5):1475–1490
6. Malek A, Ebrahimnejad S, Tavakkoli-Moghaddam R (2017) An improved hybrid grey relational analysis approach for green resilient supply chain network assessment. Sustainability 9(1433):1–28
7. Parkouhi SV, Ghadikolaei AS, Lajimi HF (2019) Resilient supplier selection and segmentation in grey environment. J Clean Prod 207:1123–1137
8. Lam WS, Bakar MA, Lam WH, Liew KF (2017) Multi-criteria decision making in the selection of mobile network operators with AHP-TOPSIS model. J Eng Appl Sci 12(23):6382–6386
9. Lam WH, Lam WS, Liew KF (2019) Performance analysis on telecommunication companies in Malaysia with TOPSIS model. Indonesian J Electr Eng Comput Sci 13(2):744–751

10. Lam WS, Liew KF, Lam WH (2017) Evaluation on the financial performance of the Malaysian banks with TOPSIS model. Am J Serv Sci Manage 4(2):11–16
11. Liew KF, Lam WS, Lam WH (2017) An empirical evaluation on the efficiency of the companies in Malaysia with data envelopment analysis model. Adv Sci Lett 23(9):8264–8267
12. Lam WS, Liew KF, Lam WH (2018) Investigation on the efficiency of financial companies in Malaysia with Data Envelopment Analysis model. J Phys Conf Ser 995(1):012021
13. Lam WS, Bishan RS, Lam WH (2017) An empirical study on the mold machine-tool selection in semiconductor industry with Analytic Hierarchy Process Model. Adv Sci Lett 23(9):8286–8289
14. Lam WS, Lee WK, Lam WH (2015) Multi-criteria decision making in job selection problem using Analytic Hierarchy Process model. Math Stat J 1(2):3–7
15. Lam WS, Jaaman SH, Ismail H (2015) An empirical comparison of different optimization models in enhanced index tracking problem. Adv Sci Lett 21(5):1278–1281
16. Lam WH, Lam WS, Liew KF (2017) Improvement on the efficiency of technology companies in Malaysia with Data Envelopment Analysis model. Lect Notes Comput Sci 10645:19–30
17. Lam WS, Liew KF, Lam WH (2018) An optimal control on the efficiency of technology companies in Malaysia with Data Envelopment Analysis model. J Telecommun Electron Comput Eng 10(1):107–111
18. Lam WS, Lam WH, Jaaman SH, Liew KF (2021) Performance evaluation of construction companies using integrated Entropy-Fuzzy VIKOR model. Entropy 23(3):320
19. Lam WS, Chen JW, Lam WH (2016) An empirical study on the selection of fast food restaurants among the undergraduates with AHP model. Am J Inform Sci Comput Eng 2(3):15–21
20. Lam WS, Leong WB, Lam WH (2015) Selection of mobile network operator based on multi-criteria decision making model using Analytic Hierarchy Process. Math Stat J 1(1):12–18
21. Lam WS, Liew KF, Lam WH (2021) Performance evaluation of construction companies in Malaysia with Entropy-VIKOR model. Eng J 25(1):297–305
22. Chodha V, Dubey R, Kumar R, Singh S, Kaur S (in press) Selection of industrial arc welding robot with TOPSIS and entropy MCDM techniques. Mater Today Proc
23. Zeng J, Lin G, Huang G (2021) Evaluation of the cost-effectiveness of green infrastructure in climate change scenarios using TOPSIS. Urban Forestry Urban Greening 64(127287):1–9
24. Yılmaz VA, Koca I (2020) Development of gluten-free corn bread enriched with anchovy flour using TOPSIS multi-criteria decision method. Int J Gastronomy Food Sci 22(100281):1–10
25. Khojastehmehr M, Madani M, Daryasafar A (2019) Screening of enhanced oil recovery techniques for Iranian oil reservoirs using TOPSIS algorithm. Energ Rep 5:529–544
26. Fan S, Zhang J, Blanco-Davis E, Yang Z, Yan X (2020) Maritime accident prevention strategy formulation from a human factor perspective using Bayesian Network and TOPSIS. Ocean Eng 210(107544)
27. Singh RK, Gunasekaran A, Kumar P (2018) Third party logistics (3PL) selection for cold chain management: a fuzzy AHP and fuzzy TOPSIS approach. Ann Oper Res 267:531–553
28. Gupta H, Barua MK (2018) A framework to overcome barriers to green innovation in SME using BWM and fuzzy TOPSIS. Sci Total Environ 633:122–139
29. Micale R, La Fata CM, La Scalia G (2019) A combined interval-valued ELECTRE TRI and TOPSIS approach for solving the storage location assignment problem. Comput Ind Eng 135:199–210
30. Le T, Wang C, Nguyen H (2020) Using the optimization algorithm to evaluate and predict the business performance of logistics companies—a case study in Vietnam. Appl Econ 1–18
31. Thi HXH (2019) Application of DEA model to evaluate the performance of logistics enterprises in Vietnam. Int Res J Adv Eng Sci 4(4):146–149
32. Bursa Malaysia: Company Announcement. https://www.bursamalaysia.com/market_information/announcements/company_announcement (2021). Last accessed 2021/8/10.
33. Hwang CL, Yoon K (1981) Multiple attribute decision making. Springer, Berlin
34. Lam WS, Lam WH, Liew KF (2018) Data analysis on the performance of technology sector in Malaysia with entropy-TOPSIS model. Commun Comput Inform Sci 886:194–203
35. Lam WS, Lam WH, Jaaman SH (2021) Portfolio optimization with a mean–absolute deviation–entropy multi-objective model. Entropy 23(10):1266

36. Lee PF, Lam WS, Lam WH (2021) Evaluation and improvement of efficiency of logistics companies with data envelopment analysis model. Eng J 25(6):45–54
37. Liew KF, Lam WS, Lam WH (2016) Financial analysis on the company performance in Malaysia with multi-criteria decision making model. Syst Sci Appl Math 1(1):1–7

# The Effects of Double-Side Curved Baffle Height on the Liquid Sloshing of a Spherical Tank—Numerical Study

**Ahmad Mahamad Al-Yacouby, Mostafa M. Ahmed, and M. S. Liew**

**Abstract** The aim of this study is to evaluate the effects of double-side curved baffle on the sloshing effects of a spherical tank. In this study, numerical simulation was adopted using ANSYS CFX software. Two different cases of a double-side curved baffle were put into account in this simulation. Spherical tank with 0.55 m baffle height and 0.80 m baffle height were investigated under three filling levels, namely 30, 50 and 75%. The outcome of the study shows that the peak sloshing pressure, the peak velocity, and the corresponding peak sloshing forces were observed as 9997.8 Pa, 9.94 m/s and 4.99 N respectively. These peak values correspond to baffle height of 0.55 m, with 75% filling level. Based on the simulation results, it can be concluded that the intensity of sloshing pressure, velocity, and force in the spherical tank can be reduced by introducing curved baffle with appropriate geometry.

**Keywords** ANSYS CFX software · Double-side curved baffle · Filling levels · Sloshing problem · Spherical tank

## 1 Introduction

The liquid sloshing is a complex fluid–structure interaction phenomenon encountered in maritime industries. The influence of baffle location on the liquid sloshing in a laterally moving spherical tank was investigated by Ma et al. [1]. Smooth Particle Hydrodynamic (SPH) method was used by them to simulate weakly compressible viscous flow in a partially filled tank. Based on the MPS-FEM coupled method that was developed by Zhang and Wan [2], a fully Lagrangian FSI solver was adopted to investigate numerically the interaction between the severe sloshing motion and a liquid tank with an elastic lateral wall. Air-trapping mechanism was applied numerically by Kim et al. [3], to inhibit sloshing effective pressure in a prismatic tank. They established a small horizontal baffle array to carry out the air-trapping mechanism on one side of the tank to assemble air by the sloshing motion. In the numerical study

A. M. Al-Yacouby (✉) · M. M. Ahmed · M. S. Liew
Department of Civil and Environmental Engineering, Universiti Teknologi PETRONAS, 32610 Seri Iskandar, Perak Darul Ridzuan, Malaysia
e-mail: ahmad.alyacouby@utp.edu.my

of [4], the sloshing effect was investigated and inhibited using horivert baffles which are the combination of horizontal and vertical baffles that are positioned at variable mass area of the square tank. Based on a parameter sensitivity analysis through CFD simulation, an anti-sloshing effectiveness of a ring baffle placed in the LNG independent type C tank was investigated numerically by Liu et al. [5]. A novel approach of coupled SPH with smoothed point interpolation method (S-PIM) was employed by Wang et al. [6] to simulate 2D sloshing problem with several resilient baffles. The Arbitrary Lagrangian–Eulerian approach and linear diffraction-radiation theory were utilized by Du et al. [7], to analyze the coupling between sloshing and vessel responses numerically in a time domain method as well as to compute the sloshing motion and exterior wave forces. The structural response of vertical and horizontal anti-sloshing baffles was numerically studied by Qin et al. [8], using various configurations in a sloshing tank. They considered hydroelasticity to ensure the structural safety using a robust coupled fluid–structure interaction (FSI) approach. Further, different tank shapes with arbitrary geometries were proposed by Hu et al. [9], to investigate the 2D sloshing natural frequencies and mode forms of tanks considering two cases, with and without baffles using Boundary Element Method (BEM). They treated the baffles as double layers engrossed in liquid. In addition, they investigated the impact of vertical and horizontal baffles, and they proposed empirical equations to compute natural frequencies of rectangular tanks considering baffles. A set of model tests were conducted by Saghi et al. [10], to analyze the sloshing effects in a rectangular tank with baffle using OpenFoam. Moreover, in their numerical simulations and experimental works, they put into consideration some criteria such as the horizontal forces induced in the tank region due to the liquid sloshing, entropy generation, and tank zone, to optimize the geometric particulars of the tank. The sloshing effects were also investigated numerically by Ünal et al. [11], in a rectangular tank using T-shaped baffle. They analyzed the sloshing in two conditions, baffled and unbaffled tank. Computational simulations were performed by Guan et al. [12], to evaluate the inhibition impact of varied baffles on the sloshing effect in 3D tanks under horizontal and roll exterior wave forces.

[13] pointed out that sloshing at a considerable amplitude will unavoidably lead to unintended consequences. As a result, with any shape of sloshing mitigation device or damping structure, it is very substantial to diminish the impacts and damaging effects due to sloshing. They also stated that baffles are the most considerably utilized tools for mitigating sloshing impacts due to their easy design and suitability in installation. Various types of porous baffles such as T-baffle and semicircle baffle in 2D tanks were implemented by Gao et al. [14] to analyze the sloshing behaviors under the external excitation. The sloshing phenomena in a rectangular tank subjected to a vibro-impact harmonic motion were studied by Zhang et al. [15]. They modeled the sloshing liquid by the five-lumped-mass model with a linear spring and viscous damping. A flexible baffle of variant heights was used as an effective sloshing reduction strategy. The Incompressible Smoothed Particle Hydrodynamic (ISPH) method was applied by Zheng et al. [16], to simulate the sloshing in a 2D tank with complex baffles. Different sloshing tanks were simulated under various conditions to investigate the impact of the baffle configuration and excitation frequency. The findings indicate

that the complex baffles can considerably influence the impact pressures on the wall induced by the severe sloshing, and the relevant analysis can assist to find the engineering solutions to efficiently curb the sloshing problem. According to [17], an in-house mesh-free particle solver MLParticle-SJTU was developed based on improved moving particle semi-implicit (MPS) method that was employed to simulate numerically the impacts of T-baffle on liquid sloshing under surge excitation. The transient sloshing in laterally excited horizontal elliptical containers with T-shaped baffles was first analyzed by Wang et al. [18], by utilizing an innovative semi-analytical scaled boundary finite element method (SBFEM) considering three T-shaped baffle configurations, including surface-piercing baffle, bottom-mounted baffle, and their combination form. Thus, this study aims to investigate the impacts of sloshing pressure, velocity, and force in a spherical tank using ANSYS CFX software under two different cases. The first case is to evaluate the sloshing effects on the spherical tank considering a baffle height of 0.55 m, while in the second case a baffle with a height of 0.80 m was used. In both the cases, three filling levels of 30%, 50%, and 75% were considered. The outline of the remaining sections is as follows: Sect. 2 provides the methodology and theoretical background, Sect. 3 presents the results and discussions, and the conclusion is presented in Sect. 4.

## 2 Methodology

### 2.1 Geometric Parameters of Double-Side Curved Baffle and Spherical Tank

The geometric parameters of the spherical tank were selected based on the parameters presented in [19], and the scaled down parameters are shown in Table 1. The spherical tank and the double-side curved baffle presented in Figs. 1 and 2, respectively, are modeled using ANSYS software. The model consists of a spherical tank with double-side curved baffle of 0.55 and 0.80 m heights, under three filling levels of 30, 50 and 75%.

**Table 1** Particulars of the spherical tank and the double-side curved baffle

| Spherical tank | |
|---|---|
| Internal diameter of spherical tank | 1 m |
| Double-side curved baffle parameters | |
| Top and bottom width | 0.34 m |
| Radian of double-side curved baffle | $30^{\circ}$ m |
| Height | Case 1, H = 0.55 m |
| | Case 2, H = 0.80 m |

Case 1: 30% Filling Level

Case 2: 50% Filling Level

Case 3: 75% Filling Level
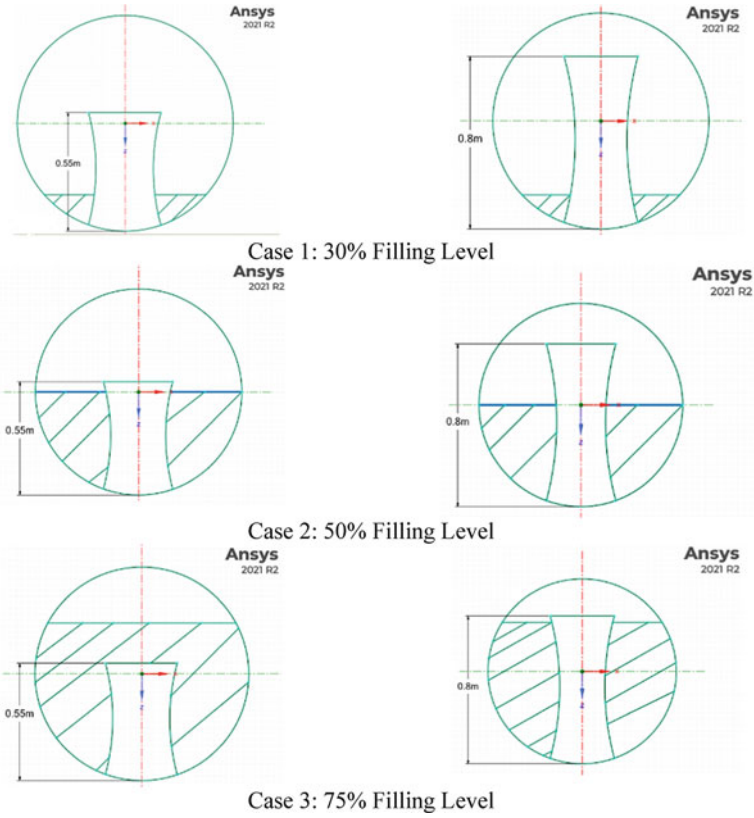
**Fig. 1** Configuration of different heights of double-side curved baffle in the spherical tank under 30, 50 and 75% filling levels

**Fig. 2** Dimensions of the double-side curved baffle and the spherical tank
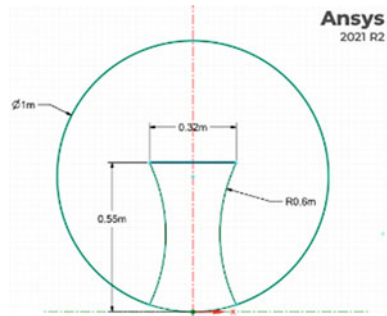
## 2.2 Numerical Analysis in ANSYS CFX Software

In this section, the theoretical background of the numerical simulation adopted in this study is briefly discussed:

**Volume of Fluid (VOF) Method**: To manage the numerical diffusion and capture the two-phase interface effectively, the Volume of Fluid (VOF) method is used in ANSYS CFX in conjunction with bounded compression approaches [20]. The fractional function of the VOF, as identified by $\varphi$ in a computational cell, is obtained by

$$\varphi = \begin{cases} 0 \; in \; air \\ 0 \; on \; free \; surface \; < \varphi < 1 \\ 1 \; in \; water \end{cases} \tag{1}$$

The fractional function satisfies the following advection equation:

$$\frac{\partial \varphi}{\partial t} + (u_i - u_i^m)\frac{\partial \varphi}{\partial x_i} = 0 \tag{2}$$

The interface between water and air phases is represented by the contour of the fractional function with $\varphi = 0.5$. The fluid density and viscosity are averaged by the provided fractional function in the calculation as follows:

$$\rho = \varphi \rho_W + (1 - \varphi)\rho_A \tag{3}$$

$$\mu = \varphi \mu_W + (1 - \varphi)\mu_A \tag{4}$$

where $W$ and $A$ represent the water and air phases, respectively.

**Meshing Analysis**: The spherical tank model including the double-side curved baffle was meshed in ANSYS Meshing as shown in Fig. 3. The number of generated nodes and elements is 7422 and 3559, respectively. The appropriate mesh size was adopted based on mesh convergence analysis.

## 3  Results and Discussion

## 3.1 Sloshing Analysis

The effect of sloshing was investigated under three filling levels, namely 30, 50 and 75%, using ANSYS CFX solver. In this study, two conditions were considered to evaluate the sloshing effects. The spherical tank was modeled with baffle height of

**Fig. 3** Generated mesh of
the spherical tank with
double-side curved baffle
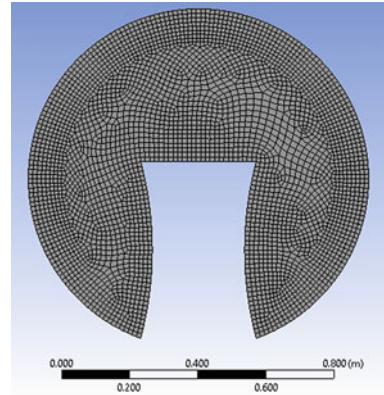


0.55 and 0.80 m, and the effect of these heights on the sloshing pressure, velocity,
and force was investigated as follows:

**Low Filling Level (30%)**. Figure 4 shows the variation of sloshing pressure, velocity,
and sloshing force with baffle heights of 0.55 and 0.80 m, under filling level of 30%.
The figure shows the time series records and the contour of pressure, velocity, and
sloshing force inside the tank. The red color in the contour represents the water
phase, and the blue color represents the air phase, while the yellow color repre-
sents the volume fraction between the two phases (air and water phases), and the
green color represents the total energy of the two phases. At 30% filling level, the
maximum sloshing pressure occurred in the case with 0.55 m baffle height, recorded
as 3433.7 Pa, while in the case of 0.80 m baffle height, the maximum pressure in
the tank was 3281.7 Pa. Similarly, the maximum sloshing velocity for the 0.55 and
0.80 m baffle heights was recorded as 8.2 and 7.7 m/s, respectively. The analysis of
the results also shows that for a 0.55 m baffle height, the maximum sloshing force
was 0.53 N, while in the case of 28 m baffle height, the maximum sloshing force was
0.498 N. This analysis clearly shows that increasing the baffle height from 0.55 to
0.80 m has significantly reduced the sloshing pressure, the sloshing velocity, and the
sloshing force. The maximum values of the sloshing pressure, velocity, and forces
at 30% filling level are summarized in Table 2 and Fig. 4.

**Medium Filling Level (50%)**. In the case of 50% filling level, the results of the
sloshing parameters and their effects on the tank are illustrated in Fig. 5 and summa-
rized in Table 3. Under 50% filling level, the maximum sloshing pressure observed
in the case of 0.55 m baffle height was 4741.5 Pa, while in the case of 0.80 m baffle
height, the maximum pressure was 4180 Pa. Similarly, the results show that for
0.55 m baffle height, the maximum sloshing velocity was 8.10 m/s, whereas in the
case of 0.80 m baffle height, the maximum velocity recorded was 7.5 m/s. From the
graphs, one can also observe that the maximum sloshing forces in the tank for the
0.50 and 0.80 m baffle heights are 2.05 and 1.03 N, respectively. The summary of
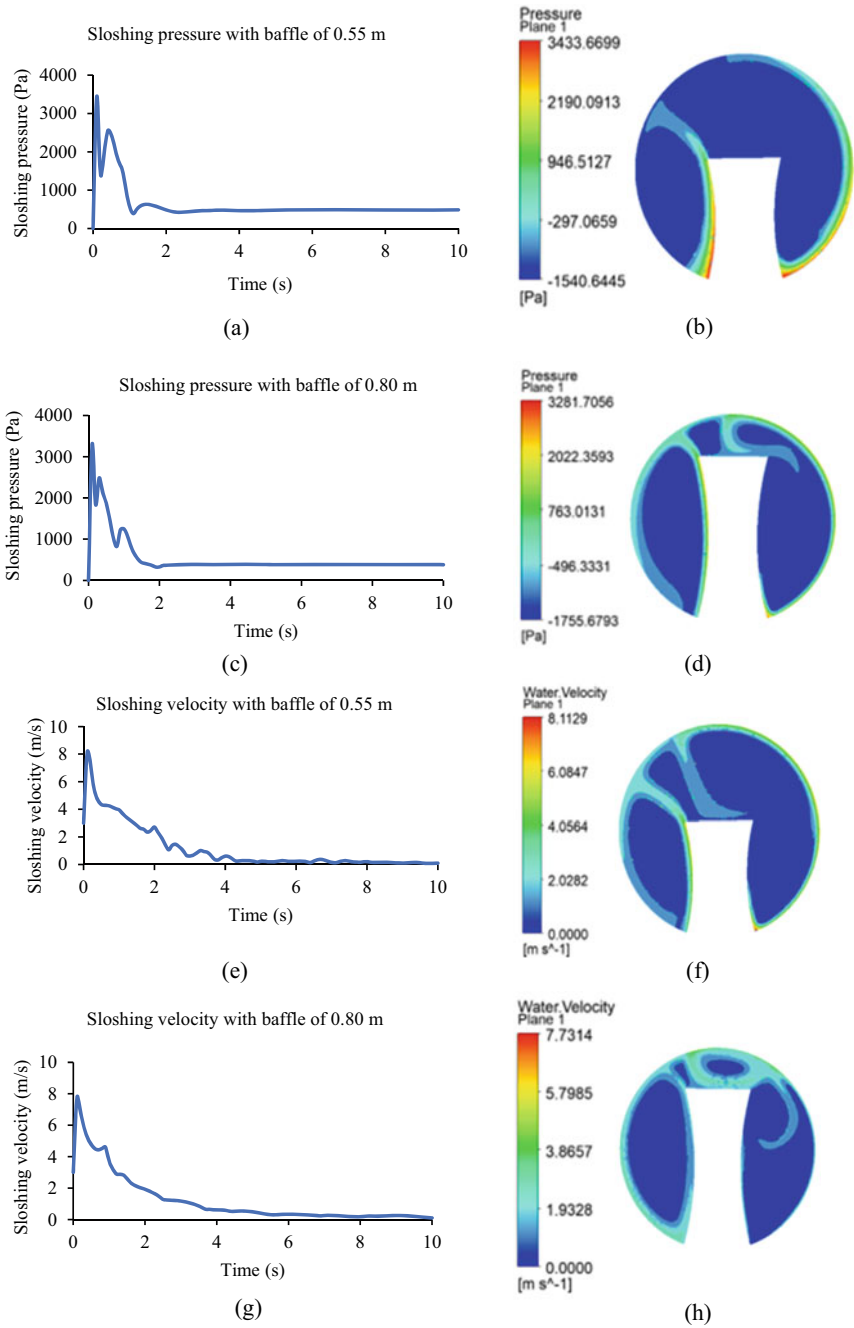
**Fig. 4** Variation of sloshing pressure, velocity, and force with baffle height of 0.55 and 0.80 m under 30% filling level

(i)



(j)



(k)



(l)
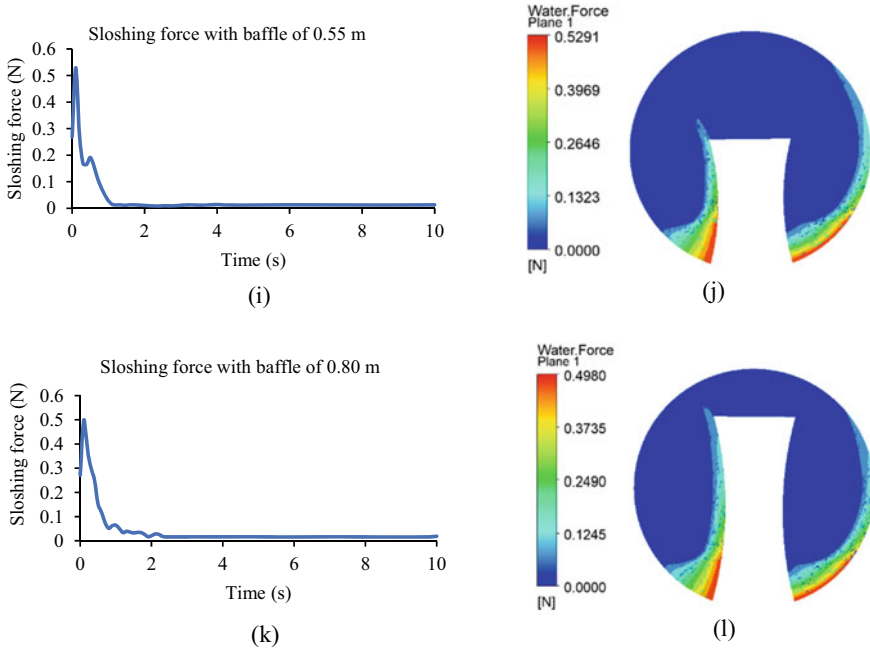
**Fig. 4** (continued)

**Table 2** Maximum values of sloshing pressure, velocity, and force at 30% filling level

| Parameters | 30% Filling Level | | |
|---|---|---|---|
| | Maximum sloshing pressure (Pa) | Maximum sloshing velocity (m/s) | Maximum sloshing force (N) |
| Tank with baffle height of 0.55 m | 3433.70 | 8.20 | 0.53 |
| Tank with baffle height of 0.80 m | 3281.10 | 7.70 | 0.49 |

maximum values of the sloshing pressure, velocity, and forces at 50% filling level is shown in Table 3.

**High Filling Level (75%).** In this study, the effects of high filling level of 75% on the sloshing parameters were investigated considering baffle height of 0.55 m and 0.8 m. The sloshing effect results are represented in Fig. 6 and summarized in Table 4. Under 75% filling, the peak sloshing pressure noticed in 0.55 m baffle was 9997.8 Pa, while in the case of 0.80 m baffle, the maximum pressure was 9944.0 Pa. The peak sloshing velocity noticed in the case of 0.55 m baffle height is 9.94 m/s, whereas in the case of 0.80 m baffle height, the corresponding maximum velocity was 9.77 m/s. Similarly, for the 0.55 m baffle height, the peak sloshing force was
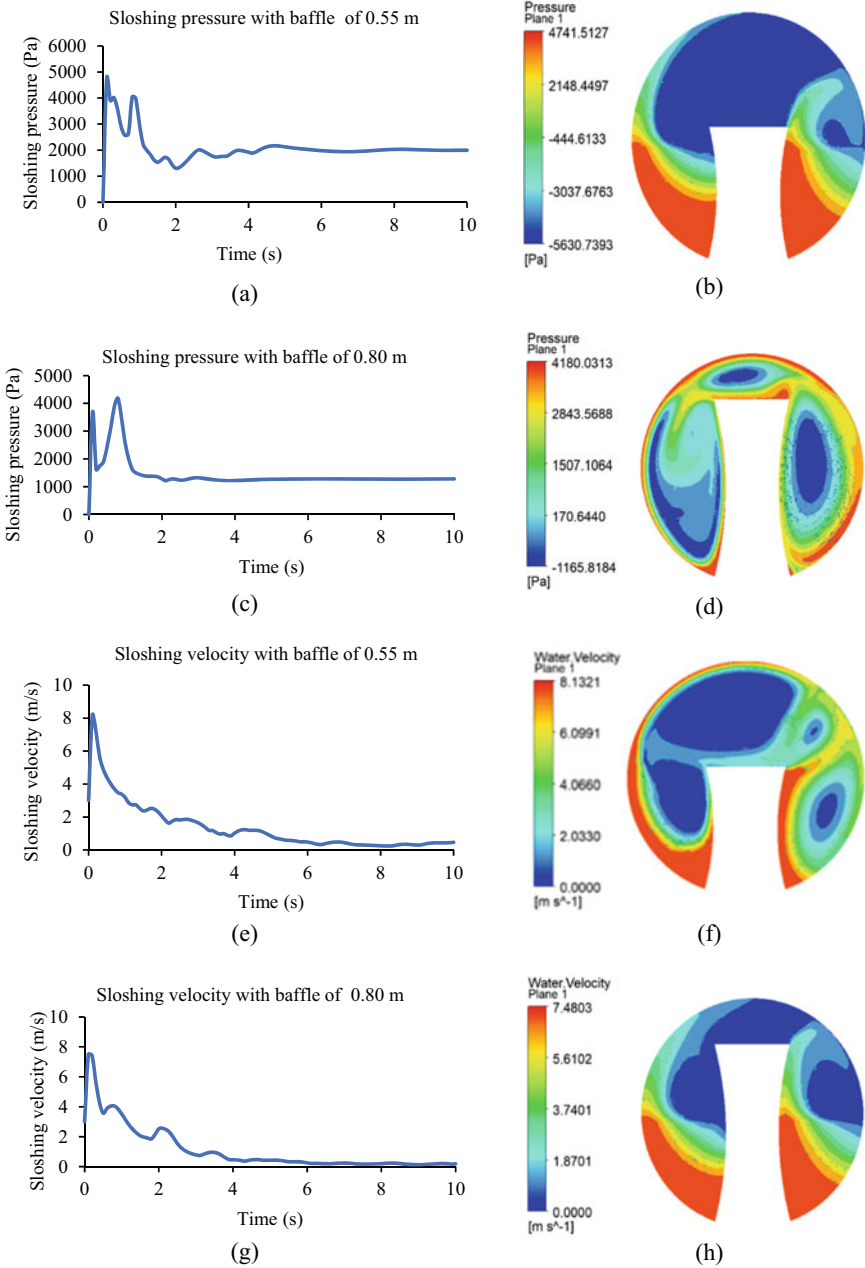
**Fig. 5** Variation of sloshing pressure, velocity, and force with baffle height of 0.55 and 0.80 m under 50% filling level

Sloshing force with baffle 0.55 m



(i)



(j)

Sloshing force with baffle of 0.80 m



(k)



(l)
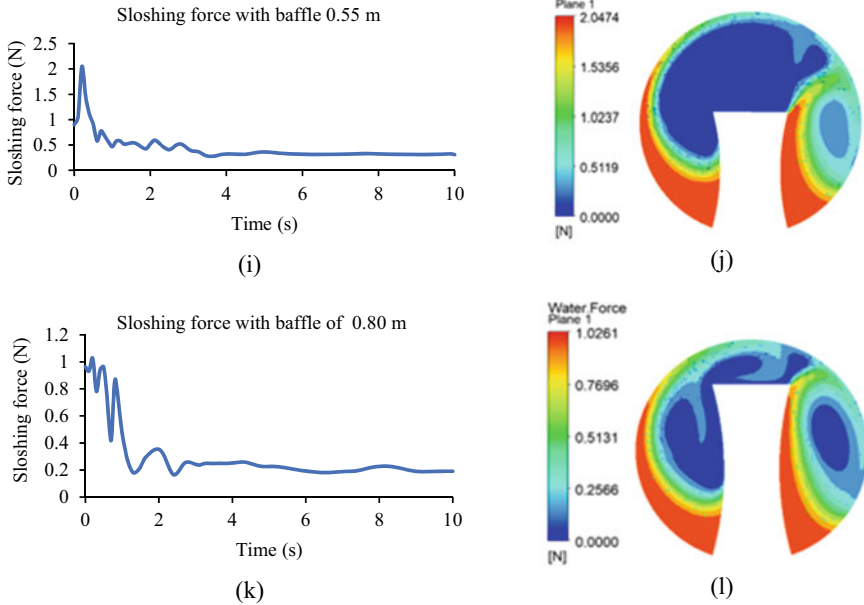
**Fig. 5** (continued)

**Table 3** Maximum values of sloshing pressure, velocity, and force at 50% filling level

| Parameters | 50% Filling level | | |
|---|---|---|---|
| | Maximum sloshing pressure (Pa) | Maximum sloshing velocity (m/s) | Maximum sloshing force (N) |
| Tank with baffle height of 0.55 m | 4741.51 | 8.13 | 2.05 |
| Tank with baffle height of 0.80 m | 4180.03 | 7.48 | 1.03 |

4.99 N, whereas in the case of 0.80 m baffle case, the peak force was 4.74 N. The summary of maximum values of the sloshing pressure, velocity, and forces at 70% filling level is shown in Table 4.

## 3.2   Overall Comparison of Sloshing Parameters

This section discusses the overall comparison of sloshing parameters for the three filling levels of 30, 50 and 75% conducted to evaluate the sloshing pressure, velocity, and sloshing forces inside the tank under two different baffle height conditions of 0.55 and 0.80 m as follows:
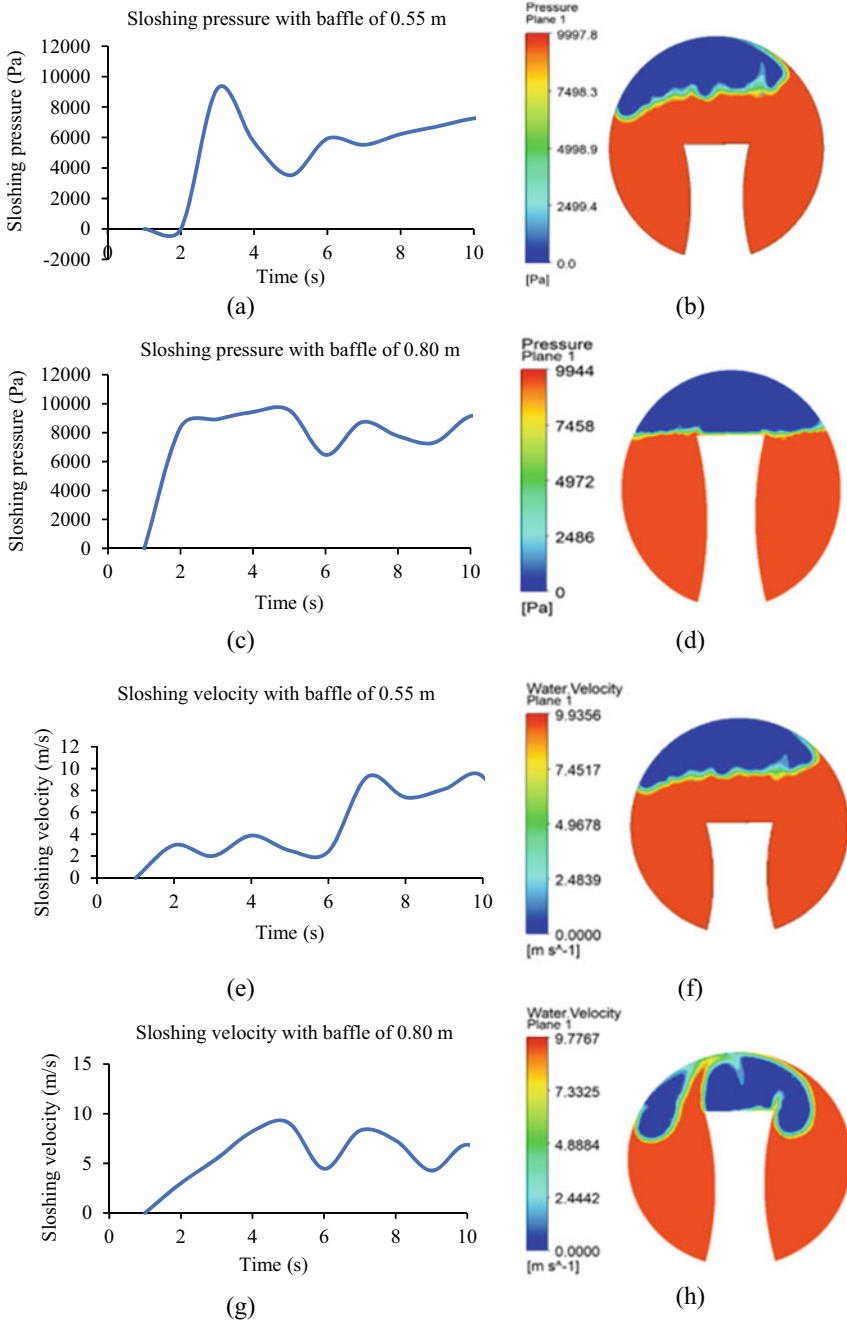
Fig. 6 Effects of sloshing pressure, velocity, and force on baffle heights 0.55 and 0.80 m under 75% filling level

Sloshing force with baffle of 0.55 m



(i)



(j)

Sloshing force with baffle of 0.80 m



(k)



(l)
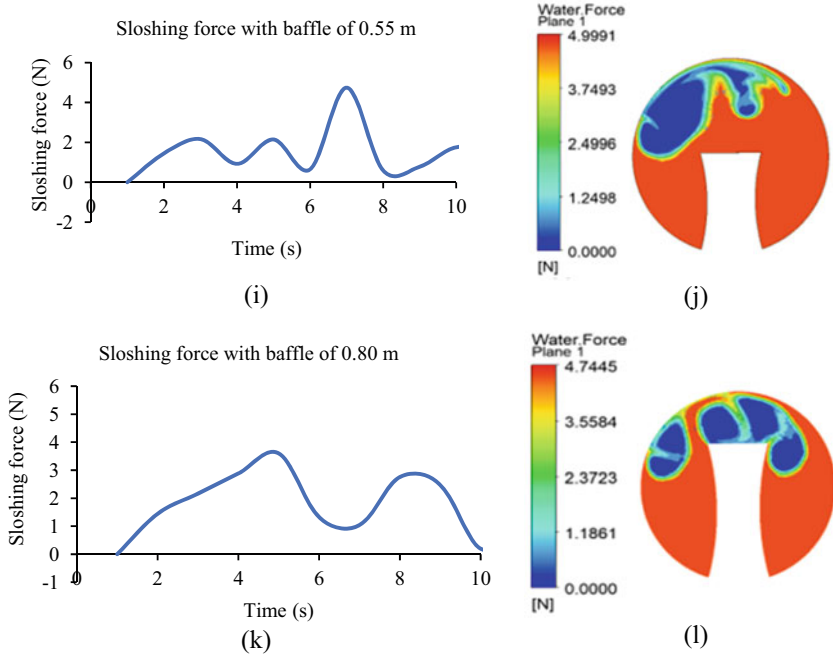
**Fig. 6** (continued)

**Table 4** Maximum values of sloshing pressure, velocity, and force at 75% filling level

| Parameters | 75% Filling level | | |
|---|---|---|---|
| | Maximum sloshing pressure (Pa) | Maximum sloshing velocity (m/s) | Maximum sloshing force (N) |
| Tank with baffle height of 0.55 m | 9997.8 | 9.96 | 4.99 |
| Tank with baffle height of 0.80 m | 9944.0 | 9.78 | 4.74 |

**Sloshing Pressure**. Figure 7 shows the variation of sloshing pressure with time for 0.55 m and 0.80 m baffle heights under filling levels of 30, 50 and 75%. The graphs show the fluctuation of sloshing pressure with times. Generally, the graphs start with minimal values at the beginning of simulation and increase gradually to reach a maximum value, before decreasing gradually with time. As shown in the graphs, in the case of 30% filling level, the maximum sloshing pressure occurred in the case with 0.55 m baffle is 3433.67 Pa at t = 3 s, whereas in the case of 0.80 m baffle, the maximum pressure observed was 3281.71 Pa at 3 s. In the case of 50% filling level, the maximum pressure in the case 0.55 m baffle was 4741.51 Pa at t = 3.1 s, while in the case of 0.80 m baffle height, the maximum pressure is 4180.03 Pa at t = 3.4 s. Similarly, in the case of 75% filling level, the maximum pressure in the tank

**Fig. 7** Variation of sloshing pressure with time for 0.55 and 0.80 m baffle heights under filling levels of 30, 50 and 75%
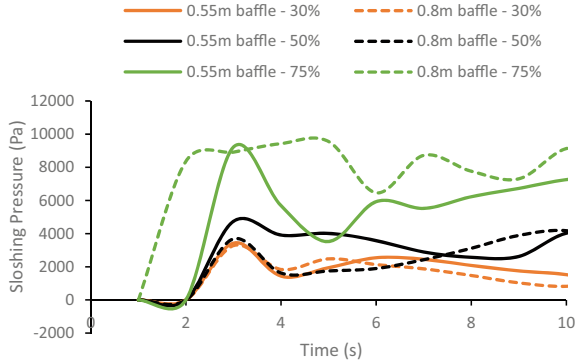


with 0.55 m baffle height was 9997.8 Pa at t = 3 s, while in the case of 0.80 m baffle height, the maximum pressure was 9944 Pa at t = 4.8 s as depicted in the figure.

**Sloshing Velocity**. Figure 8 represents the variation of sloshing velocity with time for 0.55 and 0.80 m baffle heights under filling levels of 30, 50 and 75%. The graphs indicate that the velocity of fluid inside the tank fluctuates from smaller values at the beginning of the simulation to reach a maximum value and gradually decreases to reach stable values at the end. From the graphs, one can observe that both the filling level and baffle height have significant influence on the sloshing velocity. The peak sloshing velocity corresponding to 30% filling level for 0.55 and 0.80 m baffle heights was observed as 8.1 and 7.70 m/s, respectively. Similarly, in the medium filling level of 50%, the peak velocity for 0.55 and 0.80 m baffle heights was recorded as 8.13 and 7.48 m/s, respectively. The results also show that when the filling level was increased to 75%, the peak velocity in the tank for 0.55 and 0.80 m baffle heights is 9.94 and 9.78 m/s, respectively (Fig. 9).

**Fig. 8** Variation of sloshing velocity with time for 0.55 and 0.80 m baffle heights under filling levels of 30, 50 and 75%
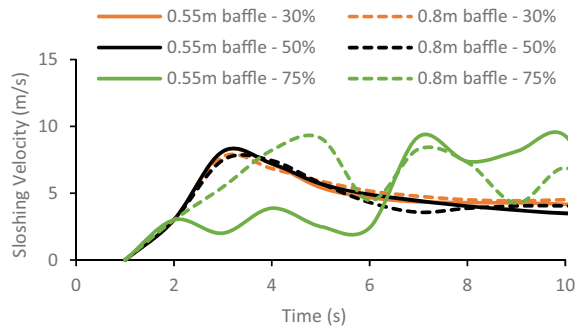
**Fig. 9** Variation of sloshing force with time for 0.55 and 0.80 m baffle heights under filling levels of 30, 50 and 75%
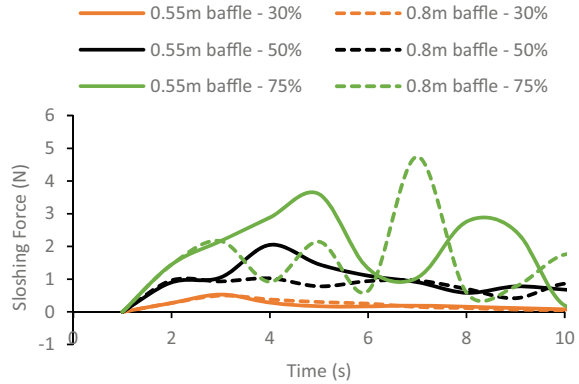


## 4 Conclusion

In this study, the effects of double-side curved baffle height on the liquid sloshing of a spherical tank were investigated using numerical simulations. Two case studies were investigated in this simulation. In the first case, we have investigated the sloshing effects in the tank considering a 0.55 m baffle height and, in the second case, a tank with 0.80 m baffle height, under three filling levels of 30, 50 and 75% of the tank height. The outcome of the study shows that the peak pressure value in the tank was observed in the case of 75% filling level with 0.55 m baffle height, recorded as 9997.8 Pa. Similarly, the peak effect of the sloshing velocity was observed in the case of 75% filling level, with 0.55 m baffle recorded as 9.94 m/s. Finally, in the case of sloshing force, the maximum value was observed as 4.9 N, corresponding to 75% filling level, with 0.5 m baffle height. This indicates that the highest filling level of 75% resulted in higher sloshing effects, as the outcome of the results indicates that increasing the height of double-side curved baffle from 0.55 to 0.80 m reduced the effects of sloshing pressure, sloshing velocity, and the corresponding sloshing force in the tank.

## References

1. Ma L, Wei C, Zhao Y (2018) Research on the suppression effect law of different baffle positions on liquid sloshing in spherical tank. In: Proceedings 2018 9th international conference mechanical aerospace engineering ICMAE 2018, pp 457–461. https://doi.org/10.1109/ICMAE.2018.8467649
2. Zhang Y, Wan D (2018) MPS-FEM coupled method for sloshing flows in an elastic tank. Ocean Eng 152:416–427. https://doi.org/10.1016/j.oceaneng.2017.12.008

3. Kim H, Nanjundan P, Jeon J, Lee YW (2020) Numerical estimation on applying air-trapping mechanism to suppress sloshing loads in a prismatic tank. J Mech Sci Technol 34(7):2895–2902. https://doi.org/10.1007/s12206-020-0621-6

4. Thirunavukkarasu B, Rajagopal TKR (2021) Numerical investigation of sloshing in tank with horivert baffles under resonant excitation using CFD code. Thin-Walled Struct 161:107517. https://doi.org/10.1016/j.tws.2021.107517

5. Liu G, Lin Y, Guan G, yun Yu Y (2018) Numerical research on the anti-sloshing effect of a ring baffle in an independent type C LNG tank. J Zhejiang Univ Sci A 19(10):758–773. https://doi.org/10.1631/jzus.A1700268

6. Wang S, Zhang G, Yan B, Zhang Z, Zong Z (2018) Numerical simulation of liquid sloshing with multiple flexible baffles using a coupled SPH with smoothed point interpolation method. In: Proceedings international offshore polar engineering conference, 2018-June, pp 895–902

7. Du Y, Wang C, Zhang N (2019) Numerical simulation on coupled ship motions with nonlinear sloshing. Ocean Eng 178:493–500. https://doi.org/10.1016/j.oceaneng.2019.02.057

8. Qin H, Mu L, Tang W, Hu Z (2019) Numerical study on structural response of anti-sloshing baffles of different configurations in a sloshing tank considering hydroelasticity. Ocean Eng 188:106290. https://doi.org/10.1016/j.oceaneng.2019.106290

9. Hu Z, Zhang X, Li X, Li Y (2018) On natural frequencies of liquid sloshing in 2-D tanks using boundary element method. Ocean Eng 153:88–103. https://doi.org/10.1016/j.oceaneng.2018.01.062

10. Saghi H, De-zhi N, Pei-wen C, Ming Z (2020) Optimization of baffled rectangular and prismatic storage tank against. 34(5):664–676

11. Ünal UO, Bilici G, Akyıldız H (2018) Liquid sloshing in a two-dimensional rectangular tank: a numerical investigation with a T-shaped baffle. Ocean Eng 187:2019. https://doi.org/10.1016/j.oceaneng.2019.106183

12. Guan Y, Yang C, Chen P, Zhou L (2020) Numerical investigation on the effect of baffles on liquid sloshing in 3D rectangular tanks based on nonlinear boundary element method. Int J Nav Archit Ocean Eng 12:399–413. https://doi.org/10.1016/j.ijnaoe.2020.04.002

13. Shao J, Li S, Li Z, Liu M (2015) A comparative study of different baffles on mitigating liquid sloshing in a rectangular tank due to a horizontal excitation. Eng. Comput. (Swansea, Wales) 32(4):1172–1190. https://doi.org/10.1108/EC-12-2014-0251

14. Gao H, Yin Z, Liu J, Zang Q, Lin G (2020) Finite element method for analyzing effects of porous baffle on liquid sloshing in the two-dimensional tanks. Eng Comput (Swansea, Wales). https://doi.org/10.1108/EC-12-2019-0567

15. Zhang J, Gaidai O, Gui B, Yurchenko D (2020) Influence of the vibroimpact interaction on sloshing dynamics in a rectangular tank. Ocean Eng 217:107821. https://doi.org/10.1016/j.oceaneng.2020.107821

16. Zheng X, You Y, Ma Q, Khayyer A, Shao S (2018) Applied sciences a comparative study on violent sloshing with complex baffles using the ISPH method. https://doi.org/10.3390/app8060904

17. Chen X, Tang Z, Wan D (2016) The effects of T type baffle on liquid sloshing by MPS method. In: Proceedings 3rd international conference violent flows, March, pp 9–11

18. Wang W, Tang G, Song X, Zhou Y (2017) Transient sloshing in partially filled laterally excited horizontal elliptical vessels with T-shaped baffles. J Press Vessel Technol Trans ASME 139(2):1–13. https://doi.org/10.1115/1.4034148

19. Zhao W, Mcphail F (2016) Roll response of an LNG carrier considering the liquid cargo flow. Ocean Eng 129:83–91, 2017. https://doi.org/10.1016/j.oceaneng.2016.11.023

20. Jiang SC, Bai W (2020) Coupling analysis for sway motion box with internal liquid sloshing under wave actions. Phys Fluids 32(7). https://doi.org/10.1063/5.0015058

# Influence of Water-In-Fuel (Diesel and Biodiesel) Emulsions on the Performance and Emission Characteristics of a Single-Cylinder Diesel Engine

**Hussein Saleh Yaser, Hasanain A. Abdul Wahhab, and Hayder A. Dhahad**

**Abstract** The use of fuel emulsification technology is a promising area of study as an alternative fuel for diesel engines. New investigations concluded with a significant decrease in the emissions of NOx, CO, and unburnt hydrocarbons (HC) with the operation of the diesel engine with water-diesel emulsion formulations. In this research a new kinds of emulsions are prepared by mixed surfactant span-80, to result being the long-term stability of emulsions. Then performance and emission tests were carried out by using the W/D and W/BD emulsions in a single-cylinder diesel engine. The results obtained include; the engine performance of IC has been enhanced with addition of 5% water dosage to pure diesel and B20D80 fuel, the BTE increased by 5.6 and 7.7%, respectively. The increase percentage of CO emission is 1.85–4.69% for 5% W/D emulsion compared with the neat diesel, while it is 0.88–3.93% for 5% W/B20D80 emulsion compared with the B20D80 fuel. Also, the total reduction percentage of NOx emission for 5% W/D emulsion is 8.4% compared with pure diesel and it is 9.8% for 5% W/B20D80 emulsion compared with the B20D80 fuel.

**Keywords** Fuel emulsions · Engine performance · Emissions · Fuel technology

## 1 Introduction

Compression ignition (C.I.) engines producing emissions and unburnt hydrocarbons have long been regarded as a main source of air pollution, generally in densely populated cities; therefore, it was the focus of researchers' attention as it is a dangerous source of pollution. There have been numerous researches in the field of reduction of these emissions since diesel engines came to main use [1, 2]. Several off-engine processing methods have been used to reduce CO and HC emissions in the catalytic converter, while NOx can be "oxidized" to obtain some clean products in engine, considering these pollutants the most influential. Newly selective catalytic

H. S. Yaser · H. A. Abdul Wahhab (✉) · H. A. Dhahad
Mechanical Engineering Department, University of Technology, Baghdad, Iraq
e-mail: 20085@uotechnology.edu.iq

reduction technology has been invested in to reduce NOx emissions [3, 4]. Growing efforts within alternative fuel to use water-in-diesel emulsions in diesel engines as a recent area of study. Water/diesel (W/D) emulsion formulations have been reported to reduce emissions of NOx, CO, and particulate matter (PM) without compensating for engine performance [5–8]. Hamadi et al. [9] have interested on reduction of $H_2O$ and HC in IC engines. There are two reasons why the combustion process is affected by the water content. One is the decrease in the maximum temperature inside the engine cylinder, which results in a decrease in the NOx formation. While the phenomenon of micro-explosion is considered the second reason, as this is due to the difference in stability between the components of the emulsion from water and diesel. Several studies have examined the water content at dosages ranging from 5 to 45%. On the other hand, a limited number of reports deal with the stability of emulsions compared to the total research that dealt with emulsions used as alternative fuels in diesel engines. Baskar and Kumar [10] studied engine performance and emissions on a single-cylinder engine with impact of water dosages in water/diesel emulsions. Emulsified diesel fuels of 10, 15, 20, 25 and 30% water/Diesel ratios by volume were tested. The results appeared that increase in the brake thermal efficiency average value for using 30% water dosage is approximately 5% over the use of diesel for the different engine speed ranges. While The NOx and HC emissions decrease as the value of water dosage in the emulsion increased to 30%. Tanaka et al. [11] have interested with NOx and HC emission control using (single cylinder) four-stroke engine. This work focused on the effects of water/diesel emulsion fuel combustion on the brake-specific fuel consumption, brake thermal efficiency, and NOx and HCL emissions in a C.I engine. Experiments were done using diesel fuel and water/diesel emulsion with 10 and 20% water dosages by volume. The literature review appeared that many works have studied the water-in-diesel emulsions, the influence of the water concentration in emulsions on engine performance features and emissions. But the studies on water in biodiesel emulsions has been little attention if compare with water-in-diesel emulsions. In this work, a new kinds of emulsions are prepared by mixed surfactant span-80, to result being the long-term stability of emulsions. Then many experiments to test engine performance and emissions were carried out by using the W/D and W/BD emulsions in a single-cylinder C.I engine. The new results were validated with that results of diesel tests and compared it with available results in the literature.

## 2 Experimental Setup

### 2.1 Mechanical Agitator and Emulsion Preparing

Homogenizer was designed to give wide range of stirring speeds at 5000 to 28,000 rpm. All experiments of preparing W/D and W/BD emulsions are applied under the stirring speed of 15,000 rpm and the mixture is thoroughly mixed for

**Table 1** All properties of emulsions samples used in experiments

| Fuel type | Diesel | 5% Water + D | 5% Water + (B20 + D80) |
|---|---|---|---|
| Cetane No | 54.7 | 36.4 | 36 |
| Density, kg/m$^3$ | 821 | 837 | 848 |
| Calorific value, kJ/kg | 45,133 | 46,300 | 46,340 |
| Viscosity, cSt | 2.3 | 4.34 | 4.92 |
| Cloud point, °C | – | −1 | −2.2 |
| Flash point, °C | 68 | 93 | 109 |

about 15 min. The resulted emulsion from this method was checked for stability. The steps of emulsion preparation; first step, the container, burette, and pipette are thoroughly cleaned. Second step, diesel, and biodiesel were measured in the burette in required volume and poured into the homogenizer container. Third step, it calculated volume of each surfactant (span-80) was measured in the pipette and poured into the homogenizer container, same case was done for water dosage. In this work, two samples of W/D and W/BD emulsions at 5% water dosage were tested. Table 1 presented all properties of these samples.

## 2.2 Engine Specifications and Apparatus

The experiments have carried out by using a four-stroke C.I. engine (single cylinder) with a set of measurement devices and a gas analyzer, as shown in Fig. 1. The CI engine works on the principle of direct and natural fuel injection. It has design features with a cylinder bore of 70 mm, a stroke of 55 mm and a compression ratio of 17:1.The engine specification has been elucidated in Table 2. Several experimental features were been collected; output power (engine load), air mass flow rate, fuel volume flow rate, and engine speed. An orifice system was used to measure the amount of air flowing into the engine, by installing it in the air box, where the pressure difference was recorded using a manometer. While the engine speed was recorded using a digital tachometer. The amount of fuel consumed was measured by using a fixed size with stopwatch. BEA 460 Bosch gas analyzer was used to record exhaust gases (emissions). New software supplied from Bosch was used as the data acquisition system and operation control. All tests were performed for constant engine speed at different engine loads. For each operating test, there are waiting 3–5 min to the engine had stabilized under steady conditions.

**Fig. 1** Diesel engine setup



**Table 2** The specifications of the test engine

| Model of engine | Loben-RB170F |
|---|---|
| Type of engine | Single cylinder, 4-stroke |
| Bore | 70 mm |
| Stroke | 55 mm |
| Displacement | 0.221 L |
| Compression ratio | 17:1 |
| Engine speed | 3000–3600 rpm |
| Cooling system | Air cooled system |
| Injection of fuel | Direct injection |

## 2.3 Uncertainty Analysis

Uncertainty analysis in the tests is very important to provide a high level of confidence in all results. It obtains by determining the repeatability and increasing of interest the results. All tests were repeated thrice. The variants of the predicted values of performance factors and exhaust emissions were used to calculate the uncertainty using the percent relative standard error, Φ, as shown in Eq. 1 [12]:

$$\emptyset\% = \left(\frac{S}{Y}\right) \times 100, \tag{1}$$

where $S$ is the standard error and $Y$ is the mean of the collected data. The standard error is calculated using Eq. 2:

**Table 3** Uncertainties of the measured parameters

| Parameter | Max. value | Accuracy | Uncertainty |
|---|---|---|---|
| Power (kw) | 2.1 | ± 0.08 kw | ± 0.56 |
| Speed (rpm) | 3000 | ± 1 rpm | ± 1.65 |
| BSFC (g/kw hr) | 512 | ± 1.91 g/kw hr | ± 0.87 |
| CO (Vol %) | 23.7% | ± 0.03 Vol % | ± 1.66 |
| HC (ppm) | 57 | ± 2 ppm | ± 1.79 |
| NOx (ppm) | 1110 | ± 2 ppm | ± 3.25 |

$$S = \frac{\alpha}{\sqrt{k}} \tag{2}$$

where $\alpha$ is the standard deviation, and $k$ is the repeatable readings of performance, combustion characteristics, and emission parameters. Overall experimental uncertainty, $\alpha n$, was calculated using Eq. 3:

$$\alpha_n = \sqrt{\alpha_1^2 + \alpha_2^2 + \ldots + \alpha_i^2}, \tag{3}$$

where $\alpha n$ is the total uncertainty, and $\alpha 1$, $\alpha 2$, and $\alpha i$ are the uncertainties of the individual parameters. The accuracies and uncertainties of the measured parameters are given in Table 3.

## 3  Results and Discussion

Figure 2 shows the variation between the brake thermal efficiency (BTE) and engine load for the fuel types; pure diesel (D), biodiesel 20% + diesel 80% (B20D80), 5% W/D emulsion, and 5% W/B20D80 emulsion. At low load conditions, the BTE results show similar BTE values for 5% W/D emulsion on par with pure diesel and it was increased at higher load conditions. Addition of water dosage to the pure diesel affects the cylinder temperature and pressure and it caused inferior combustion. On the contrary, at higher load, the compressed air temperature and pressure are higher. The water dosage will be evaporated at temperature of 100 °C temperature starts to micro-explosion phenomena and it produces secondary atomization in W/D emulsion which further improved the combustion operation [10]. Also, this behavior is similar between B20D80 fuel and 5% W/B20D80 emulsion. More so, the results show the increasing BTE when used emulsions as fuel.

Figure 3 shows the brake-specific fuel consumption (BSFC) changing trend at various engine loads. The BSFC decreased with the increase in engine load for all of the tested fuel samples, thereby demonstrating good combustion. The 20% diesel and 80% biodiesel (B20D80) fuel blends exhibited higher fuel consumption than diesel at all loading conditions. The increase in the BSFC resulted from the low heating value and the high viscosity and density, thereby causing a greater amount of fuel

**Fig. 2** Variation of brake thermal efficiency with engine load at different fuel blends
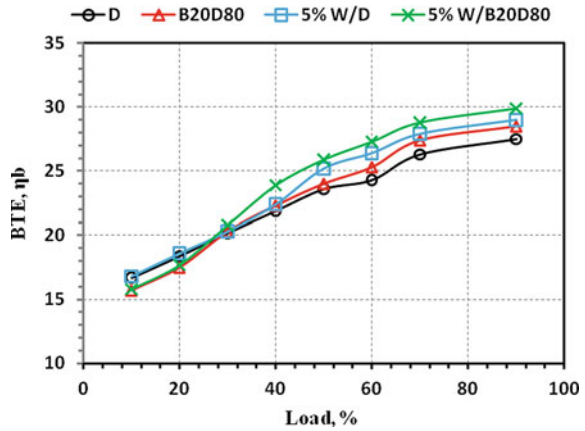


to be injected into the combustion chamber than the diesel fuel. These results are consistent with the findings of [7, 13]. The results appeared increasing BSFC with fueling the engine for the 5% W/D emulsion and the 5% W/B20D80 emulsion.

If the consequences of adding biodiesel to elegant diesel will change the chemical composition of the mixture, then adding a dosage of water to both types from the fuel (i.e., converting it to an emulsion) will have a more impact on the chemical structure and produce a new type of fuel with improved chemical properties. So, the exhaust gases are changing in terms of emission. The resulting CO, HC, and NOx have been measured to specify and evaluate the emissions percentage. All of the parameters have been evaluated at different loading conditions of the test engine, varying from a 10% load to a 90% near of full load. Figure 4 displays the CO emission of diesel fuel (D), a mixture of diesel and biodiesel (B20D80), 5% W/D emulsion, and 5% W/B20D80 emulsion at various engine loads. Results show that the CO emissions increase with the engine load because CO emissions are extremely dependent on the air/fuel ratio. In addition, the results revealed that CO emission is reduced in B20D80

**Fig. 3** Variation of brake-specific fuel consumption (BSFC) with engine load at different fuel blends
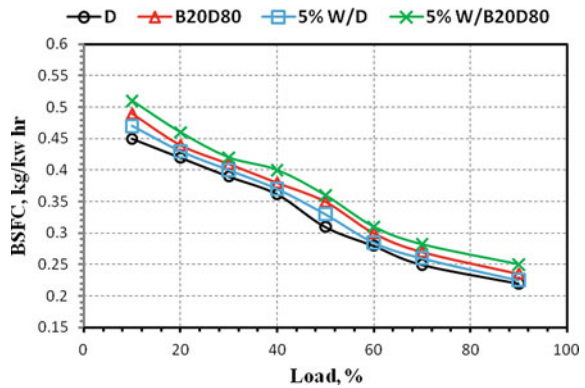
fuel, while the CO emission increased for 5% W/D emulsion and 5% W/B20D80 emulsion in all cases of the loading conditions. This effect is evident during near full loading conditions but is not so vital at low loads because of their low values.

Figure 5 presents the HC emissions at various engine loads for the studied fuel blends. The HC emissions changes are similar to the CO emissions. Thus, the HC emission is the highest for diesel and lessens for the B20D80 fuel, also 5% water dosage blending to D and B20D80 as emulsions formation reduces HC emissions. The reasons for such comportment of HC emissions are described in CO emission. Figure 6 shows the variation of NOx emission at various engine loads of the considered fuel blends. The NOx emission increased with the increase in engine load. However, the value of the NOx emissions for D20B80 is above that of pure diesel. While fuel emulsions helped reduce the NOx emissions of both 5% W/D and 5% W/B20D80 emulsions.
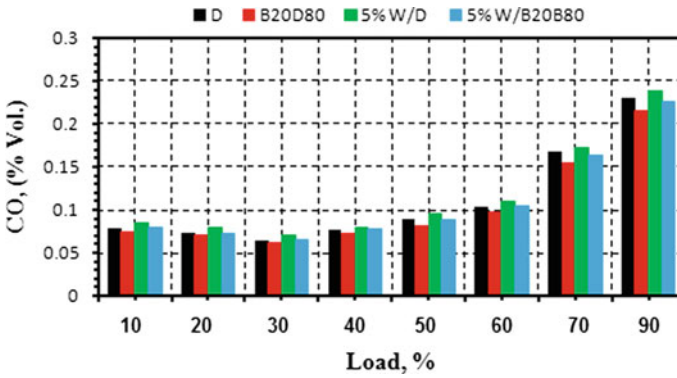


**Fig. 4** The variant of CO emission for tested fuel blend samples at various engine loads
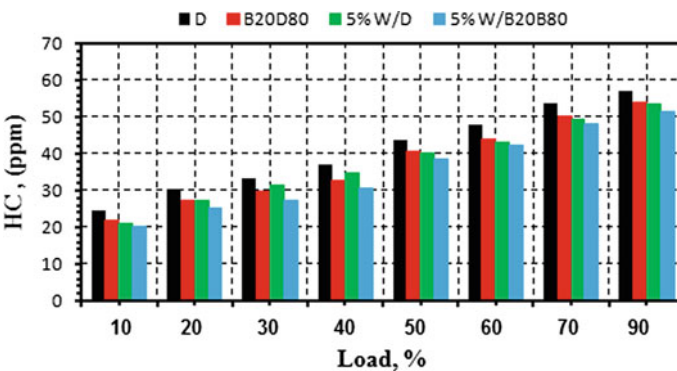


**Fig. 5** The variant of HC emission for tested fuel blend samples at various engine loads
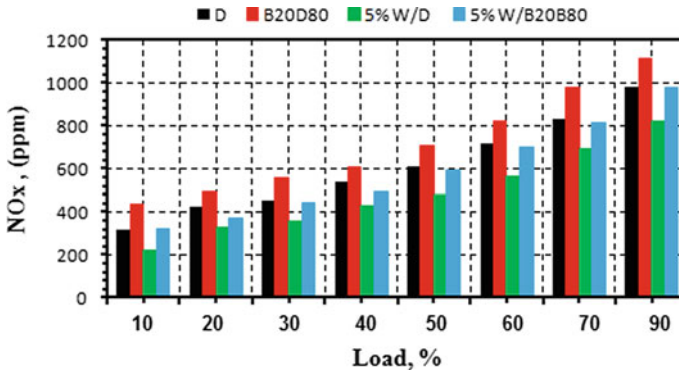
**Fig. 6** The variant of NOx emission for tested fuel blend samples at various engine loads

## 4   Conclusions

The present work aims to investigate the suitability of blended water dosages and blended biodiesel as an additive to neat diesel. The combustion performance and emissions characteristics of fuel emulsions produced by diesel and biodiesel have been investigated and compared with neat diesel as baseline fuels. The physico-chemical properties of all the considered fuel samples are measured according to the ASTM standards. The following conclusions are drawn based on the obtained results:

- The engine performance of IC has been enhanced with the addition of 20% biodiesel. Compared with the neat diesel. Also, the BTE increased for 5% W/D emulsion and 5% W/B20D80 emulsion by 5.6 and 7.7%, respectively.
- The increase percentage of CO emission is 1.85–4.69% for 5% W/D emulsion compared with the neat diesel, while it is 0.88–3.93% for 5% W/B20D80 emulsion compared with the B20D80 fuel. Also, the total reduction percentage of NOx emission for 5% W/D emulsion is 8.4% compared with pure diesel and it is 9.8% for 5% W/B20D80 emulsion compared with the B20D80 fuel.

Further investigations using different emulsion types and amounts of surfactant added to the diesel fuel and blends are recommended.

# References

1. Abdul Wahhab HA, Al-Kayiem HH (2021) Environmental risk mitigation by biodiesel blending from eichhornia crassipes: performance and emission assessment. Sustainability 13:8274
2. Vellaiyan S, Amirthagadeswaran K (2016) The role of water-in-diesel emulsion and its additives on diesel engine performance and emission levels: a retrospective review. Alex Eng J 55(3):2463–2472
3. Vellaiyan S, Amirthagadeswaran K (2016) Influence of water-in-diesel emulsion fuel and compression ratio on combustion, performance and emission characteristics of diesel engine. J Sustain Energy Eng 3(3):238–253
4. Tariq CM (2013) Enhancement of DI compression ignition engine performance and emission using diesel-water emulsion as fuel-eng. Al-Rafidain Eng J (AREJ) 21(4):29–41
5. Abdul Wahhab HA, Mashkour M, S, Madodi (2020) Investigation of water-diesel emulsion characteristics using optical technique. J Appl Fluid Mech 13(1):349–355
6. Hegde RR et al (2016) Factors affecting emissions from diesel fuel and water-in-diesel emulsion. Energy Sour Part A: Recovery, Utilization, and Environ Effects 38(12):1771–1778
7. Khalid A et al (2017) Effect of biodiesel-water-air derived from biodiesel crude palm oil using premix injector and mixture formation in burner combustion. Energy Procedia 111:877–884
8. Annamalai M et al (2016) An assessment on performance, combustion and emission behavior of a diesel engine powered by ceria nano-particle blended emulsified bio-fuel. Energy Convers Manage 123:372–380
9. Hamadi AS, Dhahad HA, Khudhur AG (2018) An experimental investigation of combustion emissions and diesel engine performance of water in diesel nano emulsion fuel. J Petrol Res Stud 8(3):147–157
10. Baskar P, Kumar AS (2017) Experimental investigation on performance characteristics of a diesel engine using diesel-water emulsion with oxygen enriched air. Alex Eng J 56(1):137–146
11. Tanaka H et al (2006) Effect of ambient pressure on micro-explosion of an emulsion droplet evaporating on a hot surface. JSME Int J, Ser B 49(4):1345–1350
12. Ithnin AM et al (2018) Emulsifier-free gl emulsion fuel: Its stability behavior, engine performance and exhaust emission. Fuel 215:454–462
13. Vigneswaran R et al (2018) Experimental investigation of unmodified diesel engine performance, combustion and emission with multipurpose additive along with water-indiesel emulsion fuel. Energy Convers Manage 172:370–380

# Survey to Water-In-Diesel Emulsion Characteristics as an Alternative Fuel for CI Engine

Hussein Saleh Yaser, Hasanain A. Abdul Wahhab, and Hayder A. Dhahad

**Abstract** This paper presents the previous literature on the performance and emissions behavior of compression ignition engines (CI) through the investment of water and fuel emulsions. Diesel engines (CI) are the most widely used internal combustion engines for their high efficiency, as they are characterized by the spread of millions of them within commercial and industrial applications, etc. Therefore, alternative fuels that require complete changes to these types of engines will be uneconomical. Water/fuel emulsions are the best alternative fuel for a compression ignition engine, as it can be prepared for the injection system within the operating procedure without any modifications to the engine. The benefits of this type of fuel lie in the simultaneous reduction of both nitrogen oxides and particulate matter. More so, it increases the combustion efficiency. Micro-explosion is the most important phenomenon of water/fuel emulsion inside the internal combustion engine cylinder. Therefore, this alternative fuel contributed mainly to reducing emissions and improving combustion efficiency. It has operational features, the most important of which are; the type of emulsion, the water dosage, the diameter and penetration length of the dispersed liquid, and the atmospheric conditions. This document discusses many studies were interested with the investment of fuel emulsions to enhancing the combustion process and reduction emissions in diesel engine. It also presents the effect of main parameters on different fuel emulsions. This review includes an explanation of the most important advantages of using emulsifier as an alternative fuel and the most important improvements that have been made to the combustion process inside the engine.

**Keywords** Fuel emulsions · Engine performance · Emissions · Fuel technology

## 1 Introduction

Diesel engines are one of the most important means that provide fuel for ideal energy conversion efficiency, as they have better fuel economy, so this type of engines

H. S. Yaser · H. A. Abdul Wahhab (✉) · H. A. Dhahad
Mechanical Engineering Department, University of Technology, Baghdad, Iraq
e-mail: 20085@uotechnology.edu.iq

dominates the mass transit, agricultural sectors, and heavy industries. Despite its preferred advantages, despite its many advantages, it remains main source of environmental pollution [1, 2]. The combustion products emitted by diesel engines are black smoke that contains particulate matter (PM), unburned hydrocarbon (HCL), carbon monoxide (CO), nitrogen oxides (NOx), sculpture oxides (SOx), and carbon dioxide ($CO_2$) [1–3]. As a result of increasingly stringent regulations to reduce exhaust emissions, this horizon is open as a major area of research in engine development in order to reduce these emissions. Engine manufacturers and designers have adopted modern methods of pollution control devices such as high pressure fuel injection (FIE) equipment, diesel particulate filters (DPF), advanced pressure injector, and associated control systems [4]. However, these technologies are costly to install and cannot be installed on conventional motors to avoid high selling prices. Therefore, there is a growing need for inexpensive technology that can be applied to these current engines [5]. There are several solutions have been used to reduction emissions and increasing performance to diesel engine [4]: directly by improving diesel combustion, and by implementing exhaust gas after treatment systems, as shown in Fig. 1. One of developing methods fuel combustion was blending liquid fuel with gas or water [5–7], improving the injection system by increasing pressure ranges [8], modifying the exhaust gas recirculation (EGR) [9, 10], combustion chamber as well as piston head design, using Bio-diesel fuel [11, 12] and, most recently, using a magnetic field to change the orientation of hydrocarbons and molecules of hydrocarbons (fuel oxidation catalysts along with fuel particulate filters or selective catalytic reduction systems).Generally, there are two major ways: treatment inside the cylinder and treatment outside the cylinder. In the last few years, the homogeneity characteristics and stability for emulsions water-in-diesel or water-in-biodiesel were interesting field, to replace the diesel fuel with new fuel for the engine, to contribute to reducing emissions and improving performance [13].

The W/D emulsions have been studied using a variety of approaches. Hagos et al. [11] used stainless steel and aluminum horizontal surfaces to study water evaporation in diesel and water emulsion in kerosene. The same hot horizontal surface was used to study the partial explosion of the evaporation droplet [12]. Yatsufusa et al. used an air-fired fuel atomization burner to study the combustion and emission properties of water-in-diesel emulsions [13]. Watanabe et al. [14] to explore the breakup features of a secondary atomization of an emulsion, researchers conducted a single droplet test in which the W/D emulsion droplet was suspended on a fine wire, Jeong et al. to investigate a single droplet's auto-ignition and micro-explosion behavior, Jeong and Lee to study the auto-ignition and micro-explosion behaviors of one-dimensional arrays of fuel droplets [11], and Morozumi and Saito [15] to study micro-explosion characteristics of the emulsion droplet. Several actual four-stroke combustion engines have been used to study the effect of W/D emulsions on combustion and emissions [16–22]. Moreover, there has been research on the study of W/D emulsion in a fixed-volume diesel engine combustion chamber with both controllable temperatures and pressures [10, 23, 24] and a rapid pressure expansion machine [25]. In terms of measuring systems and detectors, three-dimensional optical systems and
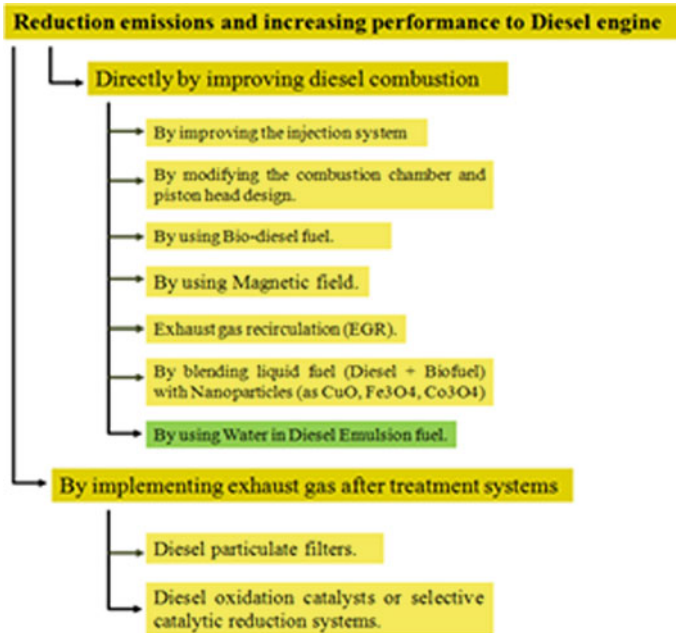
**Fig. 1** Overview for enhancement ways of diesel engine

Schlieren with high-speed imaging, micrographs to measure the properties of emulsion droplets, and nuclear magnetic resonance diffusion quantification were used to examine the water droplet size in the emulsion. While current trends tend more to study the combustion of emulsions in diesel engines including, a constant volume combustion process with variable pressure, direct injection for emulsions, combustion temperature, and ambient gas types to study the spray behavior. Also, combustion characteristics and micro-explosion with the help of an advanced engine diagnostic device such as a Phase Doppler Anemometer (PDA), laser Doppler anemometer (LDA). This chapter will review the research progress in the field of application of W/D emulsions as a fuel and its stability and micro-explosions phenomenon.

## 2 Background on Fuel Emulsion

### 2.1 Preparing Description of Preparation Processes

Many methodologies have been used to study fuel emulsions on diesel engine both inside and outside the engine combustion chamber [24], where the problem of instability of emulsions for a long time was considered the most important problem that

was researched in this field. So, the stabilization of fuel emulsions is influenced significantly by the preparing method, viscosity of fuel, water dosage in emulsion, stirring speed, and concentration of surfactants [24]. Surfactants (sometimes called emulsifiers) are considered one of the materials that are characterized by an equal ratio of polarity, compatible with water, and on the other hand, non-polar or non-hydrophilic; in general, their role is a major role in weakening the surfactant of the medium in which they are dissolved. When mixed into the fuel–water mixture, the polar groups convert to water, and the non-polar groups convert to the fuel thus reducing the surfactant between the two fuel/water phases [26]. Four types of surfactants materials are cationic, anionic, and non-ionic, and these types depend in working on the intensity of surfactant. Normally, it was high option for decreasing surfactant was to enhance a hydrophilic lipophilic balance, with other words (oil–water-lipolytic). Fuel emulsions formed when a surfactant is mixed with the two unbendable fluids water and diesel. Moreover, the combustion of surfactants without increasing emissions such as soot and free of sulfur and nitrogen must be done directly [27]. A few number of literature deals with the study of the effect of surfactant as well as the properties of W/D emulsions in relation to combustion and emissions [26, 28]. Nadeem et al. [29] have tested the water-in-diesel emulsion prepared by adding surfactants on a four-stroke, four-cylinder engine, and concluded that there was a significant reduction in the emission of particulate matter and NOx with the use of other types of fuel emulsion prepared by adding different surfactants. Fuel emulsions are prepared as a result of their effect on mechanical activation resulting from various mechanical devices. Therefore, the methods of mechanical mixing different by several devices, the most important of which are as follows: a supersonic vibrating machine, a vibrating table, a magnetic stirrer, a centrifugal type mixer, etc. Lin and Chen [30] reported that the engine has better performance with lower $CO_2$ emissions by using ultrasonic vibration as fuel emulsion preparation method, and the results were compared to fuel emulsion prepared by mechanical mixing, but this fuel emulsion has a negative influence with HC and NOx emissions. Experiments conducted within one of the research studies that dealt with the effect of the speed of the mechanical homogenizer, where the number of cycles of the homogenizer was changed as a method to study the microscopic structure, showed that the speed has a direct effect on the diameter of the water droplets in the fuel [6]. The choice of emulsification technique is of equal importance, for example, the use of a mechanical agitator or ultrasound. Nowadays, ultrasonic emulsifier is considered to be the best agitator due to its speed, efficacy, and convenient design for effective operation. Determining the optimal procedure for preparing the emulsifier is through the optimal selection of the appropriate agitator, the speed of agitation, and the rotation period, as they are the important factors for the stability of the fuel emulsion for a longer period [31–34]. Wahhab et al. [35] studied the distribution of water droplets in W/D emulsion by used the digital microscopic images processing, and the effects of water dosages and heating on the stabilization of W/D emulsion were tested, as shown in Fig. 2.
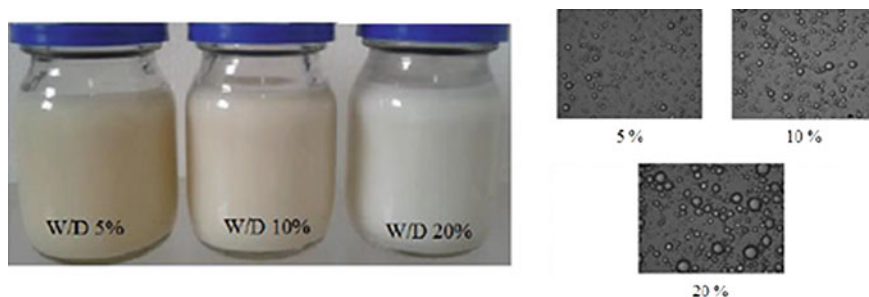
**Fig. 2** Samples of microscopic images captured with the magnification percentage 400X [35]

## 2.2 Emulsion Stability

The emulsification preparing technique, volume fraction of water (dispersed phase), emulsification duration, viscosity of continuous phase (diesel oil), mixing speed (or ultrasonic frequency), and surfactant concentration all have an impact on the W/D emulsion stability. Chen and Tao [34] Using a mechanical agitator, researchers investigated the influence of emulsifier dosage, oil–water ratio, mixing speed, and emulsifying temperature on the stability of water-in-diesel emulsions. They found that increasing the oil to water ratio, stirring speed, and duration improved stability, but increasing the emulsifying temperature had the opposite effect [35]. Experiments with the W/D emulsion showed the stability of the emulsion with better engine performance with lower $CO_2$ emissions reported by [36, 37]. When compared to an emulsion prepared by mechanical agitation, the use of an ultrasonic vibrator improved the emulsion. In the development of stable emulsified fuels, the characteristics of the relevant surfactants, the identification of the optimum agitator frequency, and the agitation period were also deemed to be equally significant properties [31]. Therefore, the surfactant or emulsifier is the most influential feature on the stability of emulsions. In addition to the effect of the water percentage in the emulsion, the intensity of stirring, the duration of stirring, the emulsification temperature, and injection pressure on emulsions stability. Chen et al. [22] Experiments on the influence of emulsifier dosage, water–diesel ratio, mixing speed, time, and emulsifying temperature on the stability of W/D emulsions have been carried out. They found that a 0.5 percent emulsion dose, a 1:1 water-to-diesel volume ratio, a swirling speed of 2500 rpm, duration of 15 min, and an emulsification temperature of 28 °C were ideal for emulsion stability. They also discovered that increasing the diesel-to-water ratio, mixing speed, and duration of up to 15 min improved stability, however, increasing emulsifying heating had the opposite impact. Ghannam and Selim [32] comparable studies to investigate the stability of W/D emulsions and concluded the importance of surfactant in emulsion stability and validated the feasibility of generating a stable emulsion with a larger water content (>30%) by raising the percentage. The 2-4 percent emulsifying agent, with a 15-minute mixing interval and a speed increase to 25,000 rpm was

tested. The emulsifier in a W/D emulsion must have the greatest advantageous benefits of diesel fuel if it is to be used as an alternative fuel for a diesel engine. Because this engine is so crucial in so many applications, a total change in fuel properties, which would necessitate engine reformatting, is not economically possible. Short ignition delay, a sufficiently high Cetane rating to avoid knocking, appropriate atomization at operating range temperatures for good mixing and combustion, easy starting characteristics, little smoke and odor, and a suitable viscosity refueling system are all characteristics of a good CI engine fuel. The gasoline is resistant to wear and corrosion and is simple to use by Ghannam et al. [33] and Ghojel and Tran [34]. The fueling system of a diesel engine is designed to ensure that fuel is delivered to the engine cylinder in an economical and timely manner controlling the emulsion atomization, chemical and physical dissolution, and ignition of the mixture ensures that it operates smoothly to limit exhaust emissions and noise. These are mostly determined by the fuel's physicochemical properties and the injection system's capabilities. As shown in Fig. 3, many researchers concluded that the higher the dose of water in the emulsion, the higher the physical properties such as density, viscosity, modulus of elasticity, and compressibility, as shown in Table 1. Therefore, these changes should be noted since density has a direct impact on the mixing process and viscosity in the injection system.

## 3 Influence of W/D Emulsion on Combustion Process

Numerous experiments were conducted to study the in-cylinder combustion of diesel engines by Dec et al. [36] of a single-cylinder diesel engine under full load working conditions. And depending on the results obtained about the properties of soot formation by applying different optical techniques, a phenomenological model of soot formation and oxidation processes was proposed by Dec [37]. The schematic diagram of this design model is shown in Fig. 4. This model demonstrates that primary soot particles are initially generated at the leading edge of the liquid fuel jet where pre-mixed combustion occurs due to the primary fuel mixing process.

Under the action of the supplementary surfactants in a W/D emulsion, the water charge persists as content within the diesel droplets. When the emulsion charge is injected into the heated combustion chamber, the heat convicts and radiates to the surface of the fuel droplets. The evaporation rates of water and fuel will differ since their boiling temperatures are different. As a result, water droplets reach the hyperheating stage faster than fuel, causing vapor expansion to dissolve [37–42]. At this stage, two phenomena predominate puffiness and microscopic explosion. Microscopic explosion is that the entire drop quickly breaks up into tiny droplets, while in puffiness, the water leaves the droplets in a very fine mist (part of the drop breaks) [15, 27]. These micro-explosions lead to a rapid breakdown, or secondary dissolution, of the fuel droplets which in turn leads to rapid fuel evaporation and thus improved fuel–air mixing as shown in Fig. 3. Therefore, it is equally important to study the basics of micro-explosion of W/D emulsion and its influencing parameters as it plays

**Fig. 3** Diesel engine setup atomization in spray flame of emulsified fuel [33]
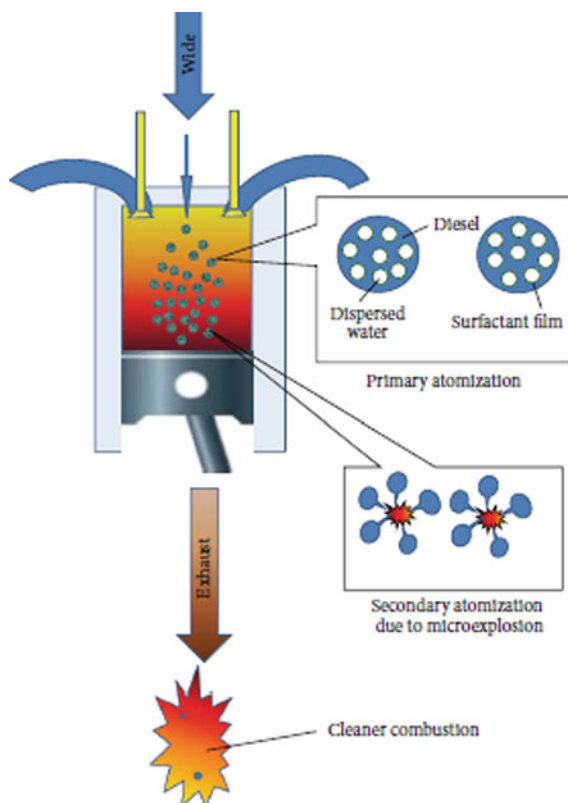


**Table 1** Report for several researches interested of study emulsions stability

| Authors | Water dosage ranges (%) | Remarked |
| --- | --- | --- |
| Ashok and Saravanan [7] | 5–25 | Various fuel injection angles |
| Chen et al. [22] | 2–30 | Mixing speed > 2500 rpm |
| Fingas and Fieldhouse [26] | 5–40 | Measuring viscosity, modulus of elasticity, and compressibility |
| Ghannam and Selim [31] | 5–35 | Measuring physical properties, density |
| Ghannam and Selim [32] | 2, 10 | Measuring physical properties, density |
| Ghannam et al. [33] | 5, 10 | Measuring viscosity, modulus of elasticity, and compressibility |
| Ghojel and Tran [34] | 5–20 | Measuring viscosity, and modulus of elasticity |
| Wahhab et al. [35] | 5–30 | Mixing speed 15,000 rpm, temperature effect |

**Fig. 4** Schematic diagram of the conceptual model for quasi-steady burning fuel Jet, Dec [36]
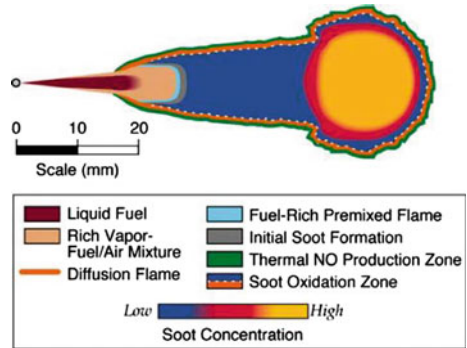
a major role in the combustion improvement. Morozumi and Saito [15] showed that the effect of micro-explosion mainly depends on the fuel used to prepare the emulsion (emulsion type) and the water content. Based on their conclusion, the increasing of emulsion content leads to an increase in the microburst temperature and waiting time. Microburst mechanisms have been extensively tested and relied on the various traits affecting micro-explosions by Fu et al. [28], and they report that both W/D and D/W emulsions can explode under certain conditions. Moreover, they related the diameter of the dispersed liquid to the strength of the micro-explosion through a physical model. Extensive research has been conducted on the performance advantages and emissions of water-in-diesel fuel and the factors affecting micro-explosion. Tanaka et al. [43] suspected that the micro-explosion occurred inside the diesel engine combustion chamber. Based on their conclusions, the emulsion droplet diameter in the combustion chamber is between 20–30 μm, and micro-explosion phenomenon cannot occur with this range of droplet sizes. Although this research is consistent with the research that confirms the effect of the diameter of the size of water molecules on the intensity of the microscopic explosion [28, 42], but it does not agree with most of the results related to the occurrence of microscopic explosion in the diesel engine combustion chamber. Many studies have been carried out experimentally and numerically to understand the phenomenon of micro-explosion. However, there have been few studies of its effects inside the combustion chamber. The behavior of the fuel dispersal fluid is thought to be affected by fuel injection and the passage of emulsified fuel through the injection nozzle's narrow exit. As a result, it is critical to investigate the phenomenon of micro-explosion within the combustion chamber, as well as its impact on combustion processes such secondary atomization, spray penetration, evaporation, and mixed ignition. Injection characteristics, spray penetration, evaporation, chemical and physical atomization, mixture ignition, engine cylinder pressure and temperature, and heat release characteristics are all aspects that affect the combustion process [8, 22, 43, 44]. In terms of fuel injection characteristics, it has been discovered that extending the injection pressure profile across a longer time causes delayed injection timing and a 22–26% increase in injection length [45]. Mahdi et al. [46] prepared a stable emulsion (SE) and an unstable emulsion (UE) with 10% water content by volume and visualized during the Leidenfrost

(a) Experimental test rig and measurement system. different cases.

(b) Micro-explosion behavior during
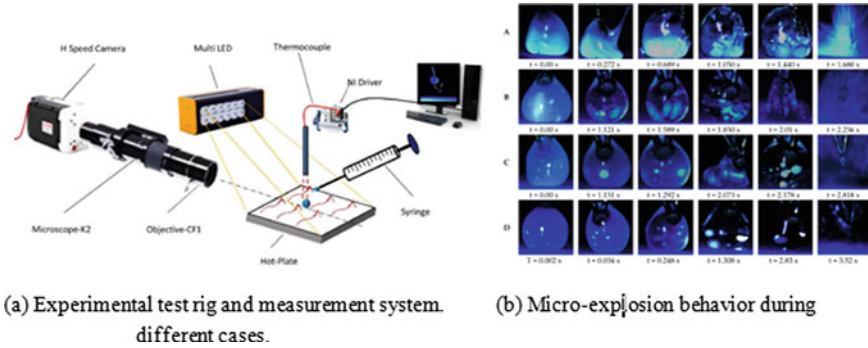
**Fig. 5** Experimental processes for micro-explosion [46]

effect. The results indicate that the strength of the micro-explosion is affected by the rate of fusion, which probably originates from the decomposition of the UE emulsion, which again is probably due to the thermal conductivity of the bound water droplets. This study suggested that the micro-explosion caused the fusion of a few large droplets (in the UE case) rather than the evaporation and cooperation of the micro-droplets to detonate the droplet (in the SE case). Also, the micro-explosion temperature was found to be lower in the UE case than in the SE [46], as shown in Fig. 5. In extensive experiments by Subramanian and Ramesh [47], the ignition retardation with a W/D emulsion is substantially higher than with water injection into the manifold during the intake stroke, according to the researchers. The impact of water dose, atomization pressure, and ambient temperature on ignition delay was investigated by Ghojel and Tran [28]. The ignition delay was considerably affected by the ambient temperature. They also demonstrated how the amount of water in the dose, the atomization pressure, and the ambient temperature affect flame ignition. They discovered that when the injection pressure and water content increased, the firing of flame increased, whereas it reduced as the ambient temperature increased.

# 4 Influence of W/D Emulsion on Engine Performance and Emissions

In fuel-modification technology, performance qualities are critical. As the performance characteristics improve, the economic feasibility of investing in diesel fuel improves. Several tests have been conducted to see how different concentrations of water (5–40%) affect engine performance in terms of thermal brake power (BP), torque, specific brake fuel consumption (BSFC), and thermal efficiency under various conditions. Alahmer et al. [48] concluded the increase in engine brake power with increase in water concentration of emulsions, and this conclusion was confirmed Abu-Zaid [3]. Table 2 reviewed of the latest attempts to improve the performance

of diesel engines by using fuel emulsions [48–68]. The mixing water with diesel fuel is a promising measure as it has significantly reduced nitrogen oxides (NOx) and particulate matter (PM) emissions [3–8]. Therefore, interest in studying diesel emulsions has increased in recent years due to their positive effect on reducing emissions. It has been concluded that 15–20% water in the diesel can give a reduction in nitrogen oxide (NOx) emission of up to 30–35% under regular conditions [66]. Such level of NOx reduction has also been concluded by other authors [6, 67–71], as shown in Table 2. So, it is related to hydrocarbons fractions and diesel with very low nitrogen content. While for fuels with high nitrogen contents, such as some heavy oils, the NOx in the exhaust comes mainly from oxidation of the nitrogen containing fuel components, and in such cases, emulsified water has only a small effect on the NOx level [48].

**Table 2** Review of the latest attempts to improve the performance of diesel engines by using fuel emulsions [48–71]

| Authors | Performance characteristics | Emissions | Remarked |
|---|---|---|---|
| Ithnin et al. [48] Jiao and Burgess [49] Kadota and Yamasaki [50] Kapadia et al. [51] | Max. pressure rise and the longer ignition delay and with using emulsion fuel reduce the network output of the cycle with increase the compression work | Increase (2%-4%) CO, decrease NOx (7–12%) and HC (6–9%) | The oscillations in torque and engine power |
| Kapadia et al. [52] Kerihuel et al. [53] Khalid et al. [54] | Improvement in (BTE) (4–7%), increasing in BSFC (3.3–5%) | lower amounts of polycyclic aromatic hydrocarbons in the flame | Single cylinder engine |
| Liang et al. [55] Mazlan et al. [56] | higher fuel burning in the pre-mixed stage and better BTE | a very large decrease in soot content by mixing in 5% water | Multi-cylinder engine |
| Authors [57, 58] | Increase in flame propagation speed and flame-lift-off length with emulsion fuel | reduction in both NOx and HC along with a decrease in fuel efficiency | Single cylinder engine |
| Ogunkoya et al. [59] Ramalingam et al. [60] | Enhance BTE (5–8%) Increase SFC (8–11%) at 10% water dosage | – | Single cylinder engine |
| Authors [61–71] | Enhance BTE (7–13%) Increase SFC (4–17%) at 5–20% water dosage | 15–20% water in the diesel can give a reduction in nitrogen oxide (NOx) emission of up to 30–35% under regular conditions | Single cylinder engine |
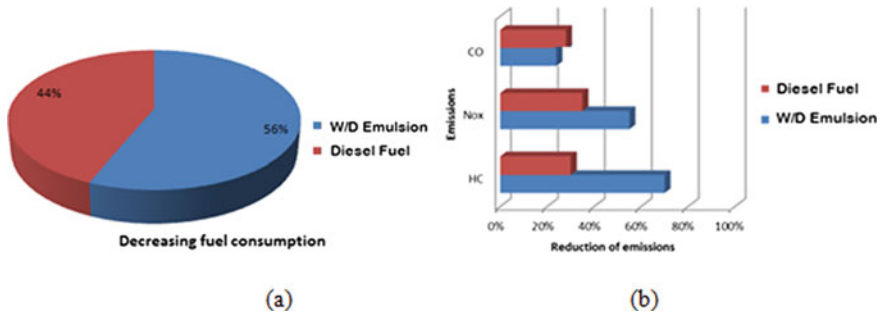
**Fig. 6** General comparison of **a** decreasing fuel consumption, **b** reduction of exhaust emissions, with using emulsions

## 5 Summary

On the basis of the aforesaid literature review, the following observations are made:

The usage of fuel emulsions can improve the amount of energy freed and lead to specific performance changes. In general, water addition treatment of fuel lowers engine fuel consumption and lowers the pace at which gas emissions are released into the atmosphere, resulting in less pollution. After water addition, clear changes in the microstructure of the diesel fuel were noticed, which were greater than changes in the diesel fuel alone. It resulted in a reduction in diesel engine fuel consumption (up to 18%) compared to engines changed by other methods (up to 14%). Figure 6a depicts the comparison between the types of methods utilized (decreasing fuel usage by 56% using W/D emulsions and 44% using diesel fuel) and the change in some fuel qualities caused by adding water to diesel fuel, which resulted in lower emissions in diesel engines; Fig. 6b shows those results.

## 6 Conclusions

Based on what has been reviewed in this paper from the basis of preparing fuel emulsions, their stability characteristics and the impact of their use as fuel on the performance and emissions of CI engines, it was concluded that adding water to diesel fuel represents a good method as an alternative to mixing diesel fuels with gases, so it should be taken as a worthy plan in the future to develop this field. In the short term, it will invest in emulsification method and will go a good way to solve the problem of emissions and reduce the use of hydrocarbons; it will be an "optimal method;" it can be assumed that the combustion engine receives maximum power per liter and that the environment has the lowest possible level of toxic emissions.

# References

1. Abu-Zaid M (2004) An experimental study of the evaporation characteristics of emulsified liquid droplets. Heat Mass Transf 40(9):737–741
2. Abass KI (2017) The impact of various surfactants on the water-in-diesel fuel emulsions. Generations 80:109
3. Abu-Zaid M (2004) Performance of single cylinder, direct injection diesel engine using water fuel emulsions. Energy Convers Manage 45(5):697–705
4. Alahmer A et al (2010) Engine performance using emulsified diesel fuel. Energy Convers Manage 51(8):1708–1713
5. Annamalai M et al (2016) An assessment on performance, combustion and emission behavior of a diesel engine powered by ceria nanoparticle blended emulsified biofuel. Energy Convers Manage 123:372–380
6. Armas O et al (2005) Characterization of light duty diesel engine pollutant emissions using water-emulsified fuel. Fuel 84(7–8):1011–1018
7. Ashok M, Saravanan C (2007) Combustion characteristics of compression engine driven by emulsified fuel under various fuel injection angles
8. Ashok M, Saravanan C (2007) The performance and emission characteristics of emulsified fuel in a direct injection diesel engine. Proc Inst Mech Eng, Part D: J Automobile Eng 221(7):893–900
9. Attia AM, Kulchitskiy A (2014) Influence of the structure of water-in-fuel emulsion on diesel engine performance. Fuel 116:703–708
10. Ballester JM, Fueyo N, Dopazo C (1996) Combustion characteristics of heavy oil-water emulsions. Fuel 75(6):695–705
11. Hagos FY, Aziz ARA, Tan IM (2011) Water-in-diesel emulsion and its micro-explosion phenomenon-review. In: 2011 IEEE 3rd international conference on communication software and networks. IEEE
12. Jeong I, Lee K-H, Kim J (2008) Characteristics of auto-ignition and micro-explosion behavior of a single droplet of water-in-fuel. J Mech Sci Technol 22(1):148–156
13. Yatsufusa T et al (2009) Advantage of using water-emulsified fuel on combustion and emission characteristics. Fuel 5(60)
14. Watanabe H et al (2010) Numerical simulation of emulsified fuel spray combustion with puffing and micro-explosion. Combust Flame 157(5):839–852
15. Morozumi Y, Saito Y (2010) Effect of physical properties on microexplosion occurrence in water-in-oil emulsion droplets. Energy Fuels 24(3):1854–1859
16. Hamadi AS, Dhahad HA, Khudhur AG (2018) An experimental investigation of combustion emissions and diesel engine performance of water in diesel nano emulsion fuel. J Petrol Res Stud 8(3):147–157
17. Basha JS (2015) Preparation of water-biodiesel emulsion fuels with CNT & Alumina nano-additives and their impact on the diesel engine operation. SAE Technical Paper
18. Basha JS (2018) Impact of Carbon Nanotubes and Di-Ethyl Ether as additives with biodiesel emulsion fuels in a diesel engine–an experimental investigation. J Energy Inst 91(2):289–303
19. Basha JS, Anand R (2011) An experimental study in a CI engine using nanoadditive blended water–diesel emulsion fuel. Int J Green Energy 8(3):332–348
20. Basha JS, Anand R (2011) An experimental investigation in a diesel engine using carbon nanotubes blended water–diesel emulsion fuel. Proc Inst Mech Eng, Part A: J Power Energy 225(3):279–288
21. Baskar P, Kumar AS (2017) Experimental investigation on performance characteristics of a diesel engine using diesel-water emulsion with oxygen enriched air. Alex Eng J 56(1):137–146
22. Chen Z et al (2015) Experimental investigation of the performance and emissions of diesel engines by a novel emulsified diesel fuel. Energy Convers Manage 95:334–341
23. Dantas Neto A et al (2011) Alternative fuels composed by blends of nonionic surfactant with diesel and water: engine performance and emissions. Braz J Chem Eng 28(3):521–531

24. Fahd MEA et al (2013) Experimental investigation of the performance and emission characteristics of direct injection diesel engine by water emulsion diesel under varying engine load condition. Appl Energy 102:1042–1049
25. Fingas M, Fieldhouse B (2003) Studies of the formation process of water-in-oil emulsions. Mar Pollut Bull 47(9–12):369–396
26. Fingas M, Fieldhouse B (2004) Formation of water-in-oil emulsions and application to oil spill modelling. J Hazard Mater 107(1–2):37–50
27. Fu WB et al (2002) A unified model for the micro-explosion of emulsified droplets of oil and water. Fuel Process Technol 79(2):107–119
28. Fu W-B et al (2003) A study on ignition characteristics of emulsified oil containing flammable fuel. Fuel Process Technol 80(1):9–21
29. Nadeem M et al (2006) Diesel engine performance and emission evaluation using emulsified fuels stabilized by conventional and gemini surfactants. Fuel 85(14–15):2111–2119
30. Lin CY, Chen LW (2008) Comparison of fuel properties and emission characteristics of two-and three-phase emulsions prepared by ultrasonically vibrating and mechanically homogenizing emulsification methods. Fuel 87(10–11):2154–2161
31. Ghannam M, Selim M (2009) Stability behavior of water-in-diesel fuel emulsion. Pet Sci Technol 27(4):396–411
32. Ghannam MT, Selim MY (2016) Rheological properties of water-in-diesel fuel emulsions. Int J Ambient Energy 37(1):24–28
33. Ghannam MT et al (2019) Flow characteristics of xanthan solutions and their crude oil emulsions in terms of thixotropic behavior. Pet Sci Technol 37(11):1279–1288
34. Ghojel JI, Tran X-T (2010) Ignition characteristics of diesel—water emulsion sprays in a constant-volume vessel: effect of injection pressure and water content. Energy Fuels 24(7):3860–3866
35. Wahhab HA, Mashkour M, Madodi S (2020) Investigation of water-diesel emulsion characteristics using optical technique. J Appl Fluid Mech 13(1):349–355
36. Dec JE, Espey C (1992) Soot and fuel distributions in a D.I. Diesel Engine via 2-D Imaging. SAE Transactions, vol 101, sec 4. SAE Paper 922307, pp 1642–1651
37. Dec JE (1997) A conceptual model of DI diesel combustion based on laser-sheet imaging. SAE Paper 970873
38. Hasannuddin A et al (2016) Durability studies of single cylinder diesel engine running on emulsion fuel. Energy 94:557–568
39. Hasannuddin A et al (2016) Performance, emissions and lubricant oil analysis of diesel engine running on emulsion fuel. Energy Convers Manage 117:548–557
40. Hasannuddin A et al (2018) Performance, emissions and carbon deposit characteristics of diesel engine operating on emulsion fuel. Energy 142:496–506
41. Hegde RR et al (2016) Factors affecting emissions from diesel fuel and water-in-diesel emulsion. Energy Sources, Part A: Recovery, Utilization, Environ Effects 38(12):1771–1778
42. Maiboom A, Tauzia X (2011) NOx and PM emissions reduction on an automotive HSDI Diesel engine with water-in-diesel emulsion and EGR: an experimental study. Fuel 90(11):3179–3192
43. Tanaka H et al (2006) Effect of ambient pressure on micro-explosion of an emulsion droplet evaporating on a hot surface. JSME Int J, Ser B 49(4):1345–1350
44. Lin C-Y, Chen L-W (2006) Emulsification characteristics of three-and two-phase emulsions prepared by the ultrasonic emulsification method. Fuel Process Technol 87(4):309–317
45. Lin C-Y, Wang K-H (2003) The fuel properties of three-phase emulsions as an alternative fuel for diesel engines☆. Fuel 82(11):1367–1375
46. Mhadi AI, Morgan RH, Rashid AA, Cyril C, Mohammed El (2018) The effect of unstable emulsion of water-in-diesel on micro-explosion phenomena. In: AIP conference proceedings vol 2035, p 050007 (2018). https://doi.org/10.1063/1.5075578
47. Subramanian K, Ramesh A (2001) Experimental investigation on the use of water diesel emulsion with oxygen enriched air in a DI diesel engine. SAE Technical Paper
48. Ithnin AM et al (2018) Emulsifier-free Water-in-Diesel emulsion fuel: Its stability behaviour, engine performance and exhaust emission. Fuel 215:454–462

49. Jiao J, Burgess DJ (2003) Rheology and stability of water-in-oil-in-water multiple emulsions containing Span 83 and Tween 80. AAPS PharmSci 5(1):62–73
50. Kadota T, Yamasaki H (2002) Recent advances in the combustion of water fuel emulsion. Prog Energy Combust Sci 28(5):385–404
51. Kapadia H et al (2019) Investigation of emulsion and effect on emission in CI engine by using diesel and bio-diesel fuel: a review. Egypt J Pet 28(4):323–337
52. Kerihuel A et al (2006) Ethanol animal fat emulsions as a diesel engine fuel–Part 1: formulations and influential parameters. Fuel 85(17–18):2640–2645
53. Khalid A et al (2017) Effect of biodiesel-water-air derived from biodiesel crude palm oil using premix injector and mixture formation in burner combustion. Energy Procedia 111:877–884
54. Liang Y et al (2013) Effect of oxygen enriched combustion and water–diesel emulsion on the performance and emissions of turbocharged diesel engine. Energy Convers Manage 73:69–77
55. Mazlan NA et al (2018) Effects of different water percentages in non-surfactant emulsion fuel on performance and exhaust emissions of a light-duty truck. J Clean Prod 179:559–566
56. Mehta RN et al (2015) Study of stability and thermodynamic properties of water-in-diesel nanoemulsion fuels with nano-Al additive. Appl Nanosci 5(8):891–900
57. Nanthagopal K et al (2017) Influence on the effect of zinc oxide and titanium dioxide nanoparticles as an additive with Calophyllum inophyllum methyl ester in a CI engine. Energy Convers Manage 146:8–19
58. Ogunkoya D et al (2015) Performance, combustion, and emissions in a diesel engine operated with fuel-in-water emulsions based on lignin. Appl Energy 154:851–861
59. Ramalingam K et al (2018) An assessment of combustion, performance characteristics and emission control strategy by adding anti-oxidant additive in emulsified fuel. Atmos Pollut Res 9(5):959–967
60. Şahin Z, Tuti M, Durgun O (2014) Experimental investigation of the effects of water adding to the intake air on the engine performance and exhaust emissions in a DI automotive diesel engine. Fuel 115:884–895
61. Suresh V, Amirthagadeswaran K (2015) Combustion and performance characteristics of water-in-diesel emulsion fuel. Energy Sources Part A-Recovery Utilization Environ Effects 37(18):2020–2028
62. Suresh V et al (2014) Emission characteristics of diesel engine using water-in-diesel emulsified fuel and its CFD analysis. Int J Appl Environ Sci 9:2739–2749
63. Syu J-Y et al (2014) Effects of water-emulsified fuel on a diesel engine generator's thermal efficiency and exhaust. J Air Waste Manag Assoc 64(8):970–978
64. Tariq Chaichan M (2013) Enhancement of DI compression ignition engine performance and emission using diesel-water emulsion as fuel-eng. Al-Rafidain Eng. J. (AREJ) 21(4):29–41
65. Vellaiyan S, Amirthagadeswaran K (2016) Zinc oxide incorporated water-in-diesel emulsion fuel: formulation, particle size measurement, and emission characteristics assessment. Petroleum Sci Technol 34(2):114–122
66. Vellaiyan S, Amirthagadeswaran K (2016) The role of water-in-diesel emulsion and its additives on diesel engine performance and emission levels: a retrospective review. Alex Eng J 55(3):2463–2472
67. Vellaiyan S, Amirthagadeswaran K (2016) Influence of water-in-diesel emulsion fuel and compression ratio on combustion, performance and emission characteristics of diesel engine. J Sustain Energy Eng 3(3):238–253
68. Vellaiyan S, Amirthagadeswaran K (2016) Taguchi-Grey relational-based multi-response optimization of the water-in-diesel emulsification process. J Mech Sci Technol 30(3):1399–1404
69. Vigneswaran R et al (2018) Experimental investigation of unmodified diesel engine performance, combustion and emission with multipurpose additive along with water-in-diesel emulsion fuel. Energy Convers Manage 172:370–380
70. Wamankar AK, Murugan S (2014) Experimental investigation of carbon black–water–diesel emulsion in a stationary DI diesel engine. Fuel Process Technol 125:258–266
71. Yilmaz E et al (2014) Preparation of diesel emulsion using auxiliary emulsifier mono ethylene glycol and utilization in a turbocharged diesel engine. Energy Convers Manage 86:973–980

# Investment of Blending Biofuels and Nanoparticles with Conventional Diesel Fuel to Improve Combustion Process—A Review

**Ahmad Fadil, Mahmoud A. Mashkour, and Hasanain A. Abdul Wahhab**

**Abstract** This paper presents the previous literature on the performance and emission behavior of compression ignition engines (CI) through the investment of biofuel and enhances combustion process by nano-additives. Biodiesel is a biofuel in liquid state which can be obtained by chemical reactions from an alcohol with vegetable oils or animal fats and with a catalyst. At current production levels, biodiesel requires a subsidy to compete directly with petroleum fuels. Although biodiesel cannot completely replace petroleum diesel, biodiesel as an alternative fuel is one of the biggest choices among other sources because it has a huge potential to reduce pollutant emissions and used in compression ignition engines, and there are a number of advantages in the use of nanoparticles as fuel additives, such as reducing ignition delay time and emission characteristics. This paper will review research progress in the field of application of using biodiesel as an alternative fuel and enhancing it with nonmaterials to modify combustion processes.

**Keywords** Biofuel · Engine performance · Emissions · Fuel technology

## 1 Introduction

The consumption of petroleum products is increasing day by day with the increasing number of vehicles on the roads. The consumption of hydrocarbon fuels increases environmental pollution. There is a need to solve these twin problems of fuel supply and environmental pollution [1, 2]. Non-renewable fuels emit more hydrocarbon, nitrogen oxides, soot and carbon monoxide emissions than renewable biofuels [2, 3]. Various alternative fuels are considered as alternative fuels for petroleum products, and efforts have been made to analyze and demonstrate the suitability of the fuel [3]. Renewable fuels have received more attention because they reduce environmental pollution (by completing the carbon cycle) and reduce petroleum import [1]. Biofuels are hydrocarbons made by or from an organism that we humans can use to power

A. Fadil · M. A. Mashkour · H. A. Abdul Wahhab (✉)
Mechanical Engineering Department, University of Technology, Baghdad, Iraq
e-mail: 20085@uotechnology.edu.iq

something. This definition of biofuels is fairly formal. Practically, any hydrocarbon fuel that is produced from organic matter (living or living material) in a short period of time (days, weeks, or even months) is considered a biofuel. This contrasts with fossil fuels, which take millions of years to form, and with other fuels that do not depend on hydrocarbons (e.g., nuclear fission). Biofuels in their solid form have been used since humans discovered fire. Wood was the first form of biofuel that the ancients even used for cooking and heating. With the discovery of electricity, humans have discovered another way to use biofuels [4]. Biofuels have been used for a very long time to produce electricity. This type of fuel was discovered even before the discovery of fossil fuels, but with the exploration of fossil fuels such as gas, coal, and oil, the production and use of biofuels suffered a severe impact. With the advantages provided by fossil fuels, it has gained a lot of popularity especially in developed countries. Liquid biofuels have been used in the automotive industry since its inception. To meet the ever-increasing energy demands, there has been a growing interest in alternative fuels such as biodiesel to provide a suitable alternative to diesel oil for internal combustion engines. Biodiesel offers a very promising alternative to diesel oil because it is renewable and has similar properties [5]. Biodiesel does not contain petroleum products but can be blended at any level with petroleum diesel to create a biofuel blend that can be used in most compression ignition engines in its pure form or blended with petroleum-based diesel. Biodiesel is a clean-burning alternative fuel obtained through chemical processes from vegetable oils or animal fats and alcohol. The reaction requires a catalyst, usually a strong base, such as sodium or potassium hydroxide. Table 1 lists the advantages and limitations of biodiesel use [6–13].

Next to their low cost, another undeniable advantage of inedible oils for biodiesel production lies in the fact that no nutrients are expended to produce the fuel [7, 8]. For this reason, experiments with biodiesel production should be conducted in many countries, using non-edible oils such as castor, tung, cotton, jojoba, and *jatropha*.

**Table 1** Report for advantages and limitations of using biodiesel [6–13]

| *Advantages* |
|---|
| A renewable fuel, extracted from vegetable oils or animal fats |
| Low toxicity, as compared with diesel fuel |
| It degrades more quickly than diesel fuel, reducing the environmental consequences of biofuel spills |
| Lower emissions of pollutants: carbon monoxide, particulate matter, polycyclic aromatic hydrocarbons, and aldehydes |
| *Limitations* |
| Low calorific value of biodiesel |
| High production of nitrous oxide (NOx) |
| Unstable |
| They can cause problems in the engine valves and injection systems |

Animal fats are also an interesting option; moreover, high-acid fats from livestock, pork, poultry, and fish can be used [11]. Microalgae appear to be a very important alternative for biodiesel production in the future due to its high oil productivity. However, it must be borne in mind that only some species are useful in the production of biofuels. Water hyacinth (*Eichhornia Crassipes*) is also one most useful feedstock for the production of biofuel. Although the properties of oils and fats used as raw materials may differ, the properties of biodiesel must be the same; it is produced from vegetable oils or animal fats and an alcohol, through a transesterification reaction. Biodiesel is obtained from the purification of the mixture of fatty acid methyl esters (FAME). A catalyst is used to accelerate the reaction according to the catalyst used; transesterification can be basic, acidic, or enzymatic [3]. This paper will review the research progress in the field of application of biodiesel as an alternative fuel and its enhancement with nanomaterials to modify combustion processes.

## 2 Background on Biodiesel Fuel

### 2.1 Biodiesel Production

Transesterification is the process of producing biodiesel. In the transesterification process, methyl esters are produced. These methyl esters are called biodiesel [4, 5]. During biodiesel production, glycerin is produced as a by-product. These methyl esters can be used in diesel engines, alone or blended with diesel oil. At current production levels, biodiesel requires a subsidy to compete directly with petroleum fuels. Although biodiesel cannot completely replace petroleum diesel, there are the following advantages of biodiesel that justify its development [2]. Figure 1 shows a description of the biodiesel production stages [5].

Global biodiesel production is expected to reach 40.5 billion liters by 2026 which is a 12% increase over the 2016 level [4]. Figure 2 shows biodiesel production
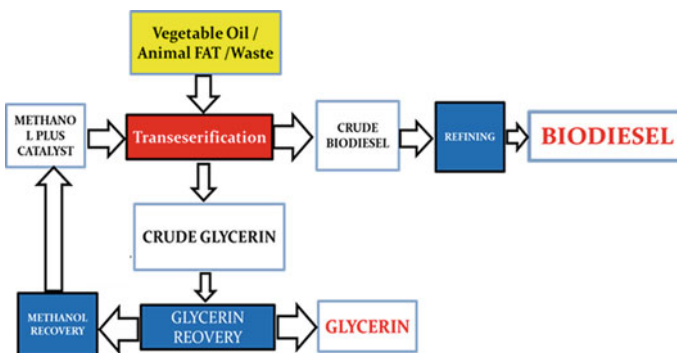


**Fig. 1** Description of biodiesel production stages [5]

ranges and prices, respectively. Policy rather than market forces will continue to influence production patterns. The European Union is expected to remain by far the main producer of biodiesel. Production should reach 13 billion liters by 2026. It is down from 13.3 billion liters in 2016 and 14.3 billion liters in 2020 when the red target is supposed to be met. This is associated with a lower potential for diesel use. Vegetable oil will continue to be the feedstock of choice for biodiesel production, and biodiesel based on waste oil and grease will develop in the European Union and the United States [4, 5]. In the United States, biodiesel production should remain stable around 7.4 billion L. Argentine biodiesel will also help close the US advanced mandate gap, especially in the early years of the projection period. Due to the increase in domestic and international demand, Argentine production should rise from 3.1 billion liters in 2016 to 3.7 billion liters in 2019. The decrease in import demand is supposed to reduce Argentine production to 2.9 billion liters by 2026. Another important players are Brazil, Indonesia, and Thailand. Brazil must contribute 36% of the global expansion of biodiesel production to meet its domestic mandate of 8% and maintain its position as the third largest producer of biodiesel. After a decline in 2015 due to a policy shift, Indonesian biodiesel production recovered in 2016, primarily driven by rising domestic demand. Although this forecast anticipates a slight increase in exports during the forecast period, it will become a less important driver of Indonesian biodiesel production. Indonesian biodiesel production should reach 4.4 billion liters by 2026. The main uncertainty surrounding this increase in biodiesel production is the viability of export duties on crude palm oil (CPO) exports, which finance subsidies for biodiesel producers. Malaysia and the Philippines will continue to expand their biodiesel production. While Malaysia will export about 40% of its production, the Philippines' production is mainly for domestic consumption, and in nominal terms, the global price of biodiesel should increase by 11%. Expressed in real terms, the global price of biodiesel should decline modestly in the final years of the projection period when US and EU demand declines [4].

## 2.2 Physicochemical Properties of Biofuel

Biofuel is a hydrocarbon made by or from an organism that we humans can use to power something. This definition of biofuels is fairly formal [14]. Practically, any hydrocarbon fuel that is produced from organic matter (living or living matter) in a short period of time (days, weeks, or even months) is considered a biofuel [14, 15]. This contrasts with fossil fuels, which take millions of years to form, and with other fuels that do not depend on hydrocarbons (e.g., nuclear fission). The most common biofuels are biodiesel and bioalcohol, including bioethanol and bio-butanol (also called biogasoline) [10]. Liquid biofuels have been used in the automotive industry since its inception. There have been great efforts in many developing countries around the world to extract ethanol from water hyacinth due to its abundance and high biomass production [16]. Water hyacinth (*E. Crassipes* Martius) is a freshwater monocotyledonous aquatic plant, belonging to the family Pontederiaceae, related to
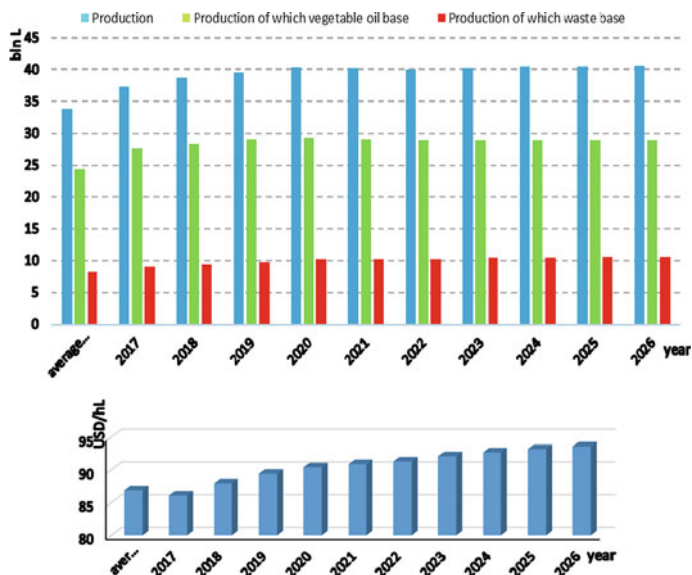
**Fig. 2** Biodiesel production and price ranges

the lily family (Liliaceae) [17]. It is also a well-known aquarium ornamental plant found in water gardens and aquariums. It grows and clogs inland waterways in so warm climates that it is now considered the world's worst aquatic weed. It bears beautiful blue- to purple-colored flowers along with its round to oblong leaves and wax-covered petioles. It grows from a few inches to a height of about a meter [18]. The stems and leaves have air-filled sacs that help them stay afloat in the water. Its rate of spread under certain conditions is very rapid and can spread to invading large areas of water causing practical problems in shipping, fishing, hydroelectric intakes, and irrigation systems. Although water hyacinth is seen in many countries as a weed, it is possible to find useful applications because the plant is rich in energy and protein. Water hyacinth fibers can be used in a variety of applications and products, including paper, fibreboard, yarn, ponchos, basket netting, and as energy raw materials. The fresh plant contains 95.5% moisture, 0.04% N, 1.0% ash, 0.06% $P_2O_5$, 0.20% $K_2O$, and 3.5% organic matter, and various studies have been conducted on the benefits of rose bean [10]. The majority (28%) of the recovery methods are in bioenergy (biogas, bioethanol, briquette), 21% of these materials are used in phytoremediation, 10% are for biofertilizers, 7% are for high-value chemicals (furfurals), and 7% for animal feed, 4% for building insulation panels, 10% for producing enzymes, 10% for biopolymers, and 3% using a combined method (used in plant and bioethanol processing later), as shown in Fig. 3.

Many researchers have concluded that recovering potential bioenergy from anaerobic digestion for water hyacinth, fruit, and vegetable waste as considered an important biofuel source, so in new researches the water hyacinth was described as one
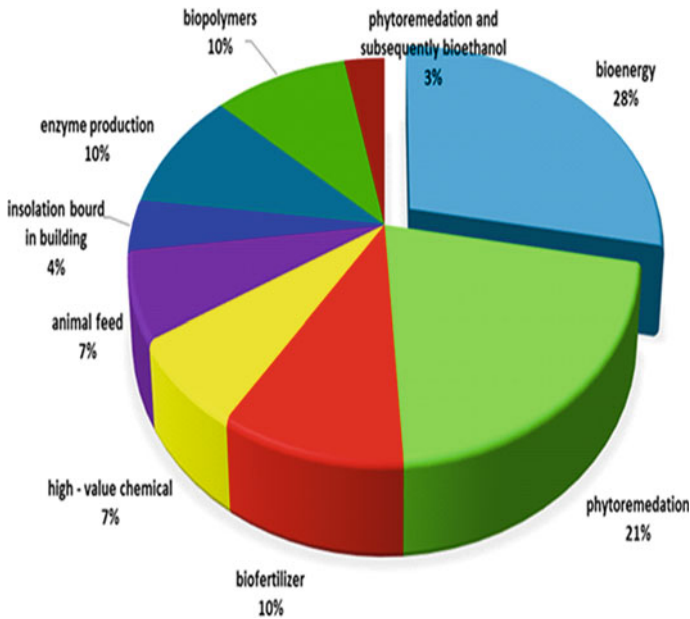
**Fig. 3** A general distribution of invest methods to bioenergy

important source  biofuel production from the  plant. Table 2 Shows several studies used water hyacinth (WH) plant to production biofuel.

## 3   Influence of Nano-Additives on Engine Performance and Emissions

Performance characteristics play a fundamental role in fuel modification technologies. Improved performance features lead to better economic feasibility of investing in diesel fuel. Several studies have been conducted to study the effect of nano-additives with different concentrations of diesel and biodiesel (0–50%) on engine performance in terms of thermal brake power (BP), torque, specific brake fuel consumption (BSFC), and heat. Several studies have been conducted to study the effect of nano additives with different concentrations to diesel and biodiesel (0 to 50%) on engine performance in terms of thermal brake power (BP), torque, specific brake fuel consumption (BSFC) and heat. also, thermal efficiency was studied under same these  conditions. Table 3 reviews recent attempts to improve the performance of diesel engines using nano-additives [38–55]. Engine emissions are mainly divided into two different categories, the first is caused by high combustion chamber temperature such as nitrogen oxides, and the second is caused by incomplete combustion of fuel and low combustion temperature such as HC and $CO_2$ [53]. Carbon

**Table 2** Report for several researches interested of study water hyacinth (WH) as important biofuel source

| Authors | Aim | Remarked |
|---|---|---|
| Pushpa TB et al. [8] Premalatha RP et al. [9] Rahman AKML et al. [10] | Using water hyacinth as biosorbent for removing: basic dyes, or Cr (III), or toxic congo red dye | Biosorbent |
| Canazart DA et al. [11] Gogoi P et al. [12] Nash DAH et al. [13] | Phytoremediation of industrial wastewater, or use of citric acid bound to *E. Crassipes* root powder for bioremediation of total inorganic arsenic and turbidity from polluted water, or phytoremediation of nutrients and organic carbon using WH in Sago mill | Phytoremediation |
| Sayago UFC [14] | Use chromium-laden biomass to assess bioethanol production | Phytoremediation and bioethanol |
| Vasconcelos GA et al. [15] Mahmood S et al. [16] | Evaluation: Consequences of replacing Tifton-85 straw with water hyacinth straw in sheep's diet, or potential for water hyacinth as a water forage for grass carp (Ctenopharyngodon idella) | Animal feed |
| Induekha VP [17] | Using water hyacinth as mulch in turmeric, or a traditional water hyacinth drum compound and vermicompost on soil quality and crop growth for tomato and cabbage plants | Mulch |
| Goswami L et al. [18] Fan R et al. [19] | Feasibility of using water hyacinth manure with pig manure and without pig manure as an alternative to peat, or a compound of water hyacinth drum and conventional vermicompost on soil quality and crop growth for tomato and cabbage plants | Compost |
| Poomsawat W et al. [20] | Possibility of producing furfural from water hyacinth | Furfural |
| Liu X et al. [21] | Converting water hyacinth (WH) to chemicals using $FeCl_3$ as a low-cost, non-toxic oxidant | High-value chemicals |

**Table 2** (continued)

| Authors | Aim | Remarked |
|---------|-----|----------|
| Salas-Ruiz A et al. [22] | The potential use of WH petiole for the manufacture of thermal insulation pellets | Bio-based insulation board for construction |
| Kurup RSC et al. [23], Karmakar M et al. [24], Udeh CB et al. [25], Lalitha P et al. [26] | Investigating the possibility of cellulase production from WH by native bacteria, or enhancing xylanase production from WH using Trichoderma species | Enzymes |
| Saratale RG et al. [27], Sandari MT [28] | The phytochemistry and pharmacological purposes of WH, or the use of WH biomass for the production of poly hydroxybutyrate (PHB) | Biopolymers |
| Setyaningsih L [29] Madian HR et al. [30] | Features of molds produced from mixture of WH and empty fruit | Briquette |
| Rezania S et al. [31], Abdul Wahhab HA [32] | Enhancing bioethanol production from WH by an integrated pretreatment method | Bioethanol |
| Zhang Q et al. [33], Priya P et al. [34] Barua VB et al. [35] Sarto S et al. [36], Mathew AK et al. [37] | Enhancing bioethanol production from WH by an integrated processing method | Biogas |

dioxide is produced as a result of incomplete combustion, reduced engine combustion time, or low combustion chamber temperature [54]. On the other hand, incomplete combustion of diesel or fuel will result in the production of hydrocarbons. Soot is caused by the incomplete combustion of hydrocarbon fuels and is observed in dark exhaust waste. Compared to gasoline-powered engines, a diesel engine emits very low concentrations of hydrocarbons (HC), nitrogen oxides (NOx), and carbon oxides (CO, Cox). But with the help of fuel modifications (nano-additives), these emissions will be further reduced. In the next section, we summarize the effect of various nano-additions using a bio-jojoba fuel blend on engine emissions.

## 4 Summary

Based on the paper reviewed for performance and emissions of CI engines, it was concluded that blending biodiesel and additives to pure diesel fuel is a good alternative to blending diesel fuels with gases, so it should be considered in the future for transportation purpose. Apart from the fuel storage and delivery mechanism, it offers

**Table 3** Review of the latest attempts to improve the performance of diesel engines by using nano-additives [38, 55–70]

| Authors | Performance characteristics | Emissions | Remarked |
| --- | --- | --- | --- |
| Al-kayiem et al. [38] Seela CR et al. [55] Ghafoori M et al. [56] | Increasing in thermal efficiency (6–9%) | Reducing in all emissions ($CO_2$, NOx, and HC). $CO_2$ (2–4%), NOx (7–12%), and HC (6–9%) | Use nano materials: $Fe_3O_4$, ZnO |
| Meshack Hawi et al. [57] Raju VD et al. [58] Radhakrishnan S et al. [59] | Improvement in performance, combustion, and emissions | Reducing unburned hydrocarbon emissions and carbon monoxide, and reducing in NOx | Use nanomaterials: $FeCeO_2$, cerium oxide |
| Authors [60–62] | Increase in flame propagation speed and flame-lift-off length with emulsion fuel | Reduction in both NOx and HC along with a decrease in fuel efficiency | Use nanomaterials: CuO, (20CSBCeO250 and 10CSBCeO250) |
| Nayak S et al. [63] Anbarasu G et al. [67] Kale NW et al. [70] | Enhance BTE (5–8%) Increase SFC (8–11%) at 10% water dosage | Considering greenhouse gases, CO, smoke, HC, and NOx emissions decreased to about 29%, 12.8%, 7.9%, and 9.8%, respectively | Use nanomaterials: silver nanoparticles (20CSBCeO250 and 10CSBCeO250), alumina nanoparticles, and $Al_2O_3$ |

almost similar performance as it has good combustion properties. In the short term, biodiesel production from plants like water hyacinth will go a long way to solving the emissions problem, reducing hydrocarbon resources, and increasing the cost of discovery; It would be a "method to reckon with," and it can be assumed that the combustion engine receives maximum power per liter and that the environment has the lowest possible level of toxic emissions.

# References

1. Bhattacharya A, Kumar P (2010) Water hyacinth as a potential biofuel crop. Electron J Environ Agric Food Chem 9(1):112–122
2. Wauton I, William-Ebi D (2019) Characterization of water hyacinth (*Eichhornia Crassipes*) for the production of thermochemical fuels. J Multi Eng Sci Stud (JMESS) 5(7):2661–2665
3. Shaafi T et al (2015) Effect of dispersion of various nanoadditives on the performance and emission characteristics of a CI engine fuelled with diesel, biodiesel and blends—a review. Renew Sustain Energy Rev 49:563–573

4. Sagar CV, Kumari NA (2013) Sustainable biofuel production from water Hyacinth (*Eicchornia crassipes*). Int J Eng Trends Technol 4(10):4454–4458

5. Rubiat M (2018) Effect of blending various biodiesels with diesel on performance and emissions of diesel engine: a review. World Sci News 94(2):287–297

6. Sengudzwa T et al (2014) Production of bio fuels from *Eichhornia crassipes* algae

7. Ilo OP et al (2020) The benefits of water hyacinth (*Eichhornia crassipes*) for Southern Africa

8. Pushpa TB, Vijayaraghavan J, Vijayaraghavan K, Jegan J (2016) Utilization of effective microorganisms based water hyacinth compost as biosorbent for the removal of basic dyes. Desalin Water Treat 57:24368–24377

9. Premalatha RP, Parameswari E, Davamani V, Malarvizhi P, Avudainayagam S (2019) Biosorption of chromium (III) from aqueous solution by water hyacinth biomass. Madras Agric J 106:12–21

10. Rahman AKML, Al Mamun R, Ahmed N, Sarkar A, Sarkar AM (2019) Removal of toxic Congo red dye using water hyacinth petiole, an efficient and selective adsorbent. J Chem Soc Pak 41:825–833

11. Canazart DA, Nunes AR, da C, Sanches M, Conte H (2017) Phytoremediation agro industrial wastewater of using macrophyte Eichhornia crassipes. Braz J Surg Clin Res BJSCR 17:87–91

12. Gogoi P, Adhikari P, Maji TK (2017) Bioremediation of arsenic from water with citric acid cross-linked water hyacinth (*E. crassipes*) root powder. Environ Monit Assess 189

13. Nash DAH, Abdullah SRS, Hassan HA, Idris M, Muhammad NF, Al-baldwi IA, Ismail NI (2019) Phytoremediation of nutrients and organic carbon from sago mill effluent using water hyacinth (*Eichhornia crassipes*). J Eng Technol Sci 51:573–584

14. Sayago UFC (2019) Design of a sustainable development process between phytoremediation and production of bioethanol with *Eichhornia crassipes.* Environ Monit Assess 191

15. de Vasconcelos GA, Véras RM, de Lima SJ, Cardoso DB, de Castro SP, de Morais NN, Souza AC (2016) Effect of water hyacinth (Eichhornia crassipes) hay inclusion in the diets of sheep. Trop Anim Health Prod 48:539–544

16. Mahmood S, Khan N, Iqbal KJ, Ashraf M, Khalique A (2018) Evaluation of water hyacinth (*Eichhornia crassipes*) supplemented diets on the growth, digestibility and histology of grass carp (Ctenopharyngodon idella) fingerlings. J Appl Anim Res 46:24–28

17. Indulekha VP, Thomas CG (2018) Utilization of water hyacinth as mulch in turmeric. J Trop Agric 56:27–33

18. Goswami L, Nath A, Sutradhar S, Bhattacharya SS, Kalamdhad A, Vellingiri K, Kim K-H (2017) Application of drum compost and vermicompost to improve soil health, growth, and yield parameters for tomato and cabbage plants. J Environ Manag 200:243–252

19. Fan R, Luo J, Yan S, Wang T, Liu L, Gao Y, Zhang Z (2015) Use of water hyacinth (*Eichhornia crassipes*) compost as a peat substitute in soilless growth media. Compost Sci Util 23:237–247

20. Poomsawat W, Tsalidis G, Tsekos C, de Jong W (2019) Experimental studies of furfural production from water hyacinth (*Eichhornia Crassipes*). Energy Sci Eng 7:2155–2164

21. Liu X, Zu X, Liu Y, Sun L, Yi G, Lin W, Wu J (2018) Conversion of waste water hyacinth into high-value chemicals by iron (III) chloride under mild conditions. BioResources 13:2293–2303

22. Salas-Ruiz A, del Mar Barbero-Barrera M, Ruiz-Téllez T (2019) Microstructural and thermo-physical characterization of a water hyacinth petiole for thermal insulation particle board manufacture. Materials, 12:560

23. Kurup RSC, Snishamol C, Prabhu GN (2005) Cellulase production by native bacteria using water hyacinth as substrate under solid state fermentation. Malays J Microbiol 1:25–29

24. Karmakar M, Ray RR (2011) A statistical approach for optimization of simultaneous production of -glucosidase and endoglucanase by rhizopus oryzae from solid-state fermentation of water hyacinth using central composite design. Biotechnol Res Int 2011:574983

25. Udeh CB, Ameh JB, Ado SA, Okoduwa SIR (2017) Optimization of xylanase production from fermentation of water hyacinth (*Eichhornia crassipes*) using Trichoderma species. J Biotechnol Res 3:2413–3256

26. Lalitha P, Sripathi SK, Jayanthi P (2012) Secondary metabolites of *Eichhornia crassipes* (Waterhyacinth): a review (1949 to 2011). Nat Prod Commun 7:1249–1256

27. Saratale RG, Cho SK, Ghodake GS, Shin HS, Saratale GD, Park Y, Lee HS, Bharagava RN, Kim DS (2020) Utilization of noxious weed water hyacinth biomass as a potential feedstock for biopolymers production: a novel approach. Polymers 12:1704

28. Sundari MT, Ramesh A (2012) Isolation and characterization of cellulose nanofibers from the aquatic weed water hyacinth-*Eichhornia crassipes*. Carbohydr Polym 87:1701–1705

29. Setyaningsih L, Satria E, Khoironi H, Dwisari M, Setyowati G, Rachmawati N, Kusuma R, Anggraeni J (2019) Cellulose extracted from water hyacinth and the application in hydrogel. IOP Conf Ser Mater Sci Eng 673

30. Madian HR, Sidkey NM, Elsoud MMA, Hamouda HI, Elazzazy AM (2019) Bioethanol production from water hyacinth hydrolysate by candida tropicalis Y-26. Arab J Sci Eng 44:33–41

31. Rezania S, Din MFM, Kamaruddin SF, Taib SM, Singh L, Yong EL, Dahalan FA (2016) Evaluation of water hyacinth (*Eichhornia crassipes*) as a potential raw material source for briquette production. Energy 111:768–773

32. Abdul Wahhab HA, Al-Kayiem HH (2021) Environmental risk mitigation by biodiesel blending from *Eichhornia crassipes*: performance and emission assessment. Sustainability 13:8274

33. Zhang Q, Wei Y, Han H, Weng C (2018) Enhancing bioethanol production from water hyacinth by new combined pretreatment methods. Bioresour Technol 251:358–363

34. Priya P, Nikhitha SO, Anand C, Nath RSD, Krishnakumar B (2018) Biomethanation of water hyacinth biomass. Bioresour Technol 255:288–292

35. Barua VB, Goud VV, Kalamdhad AS (2018) Microbial pretreatment of water hyacinth for enhanced hydrolysis followed by biogas production. Renew Energy 126:21–29

36. Sarto S, Hildayati R, Syaichurrozi I (2019) Effect of chemical pretreatment using sulfuric acid on biogas production from water hyacinth and kinetics. Renew Energy 132:335–350

37. Mathew AK, Bhui I, Banerjee SN, Goswami R, Chakraborty AK, Shome A, Balachandran S, Chaudhury S (2015) Biogas production from locally available aquatic weeds of Santiniketan through anaerobic digestion. Clean Technol Environ Policy 17:1681–1688

38. Al-Kayiem HH, Abdul Wahhab HA, Magaril E, Abdul-Aziz AR (2018) Performance and emissions investigation of a single cylinder diesel engine using enhanced blend biodiesel by nanoparticles. AIP Conf Proc 2035(1)

39. Muralidharan K, Govindarajan P (2011) The effect of bio-fuel blends and fuel injection pressure on diesel engine emission for sustainable environment. Am J Environ Sci 7(4):377–382

40. Martin M, Prithviraj D (2011) Performance of pre-heated cottonseed oil and diesel fuel blends in a compression ignition engine. Jordan J Mech Indust Eng 5(3):235–240

41. Prbakaran B, Viswanathan D (2016) Experimental investigation of effects of addition of ethanol to bio-diesel on performance, combustion and emission characteristics in CI engine, Alexandria Eng J

42. Liaquat AM, Masjuki HH, Kalam MA, Fattah IR, Hazrat MA, Varman M, Mofijur M, Shahabuddin M (2013) Effect of coconut biodiesel blended fuels on engine performance and emission characteristics. In: Procedia Engineering, vol 56. pp 583–590

43. Machacon HT, Matsumoto Y, Ohkawara C, Shiga S, Karasawa T, Nakamura H (2001) The effect of coconut oil and diesel fuel blends on diesel engine performance and exhaust emissions. JSAE Rev 22(3):349–355

44. Huzayyin AS, Bawady AH, Rady MA, Dawood A (2004) Experimental evaluation of diesel engine performance and emission using blends of jojoba oil and diesel fuel. Energy Convers Manage 45(13–14):2093–2112

45. Pramanik K (2003) Properties and use of jatropha curcas oil and diesel fuel blends in compression ignition engine. Renewable Energy 28(2):239–248

46. Buyukkaya E (2010) Effects of biodiesel on a DI diesel engine performance, emission and combustion characteristics. Fuel 89(10):3099–3105

47. Nwafor OMI (2004) Emission characteristics of diesel engine operating on rapeseed methyl ester. Renew Energy 29(1):119–129

48. Vijayaraj K, Sathiyagnanam AP (2016) Experimental investigation of a diesel engine with methyl ester of mango seed oil and diesel blends. Alex Eng J 55:215–221

49. Özener O, Yüksek L, Ergenç AT, Özkan M (2014) Effects of soybean biodiesel on a DI diesel engine performance, emission and combustion characteristics. Fuel 115:875–883
50. Venkatraman M, Devaradjane G (2011) Computer modeling of a CI engine for optimization of operating parameters such as compression ratio, injection timing and injection pressure for better performance and emission using diesel-diesel biodiesel blends. Am J Appl Sci 8(9):897–902
51. Sujaykumar G, Ravikumar R, Mutalikdesai S, Pujar B, Baddi V, Siddapur D, Santosha PV, Telagadi B (2017) Comparative study of waste cooking oil and cashew nut shell oil bio fuel blends with diesel. Energy Power 7(3):65–69
52. Tesfa B, Gu F, Mishra R, Ball AD (2013) LHV predication models and LHV effect on the performance of CI engine running with biodiesel blends. Energy Convers Manag 71:217–226
53. Lawrence P, Mathews PK, Deepanraj B (2011) Effect of prickly poppy methyl ester blends on CI engine performance and emission characteristics. Am J Environ Sci 7(2):145–149
54. Rahimi H, Ghobadian B, Yusaf T, Najafi G, Khatamifar M (2009) Diesterol: an environment-friendly IC engine fuel. Renew Energy 34(1):335–342
55. Seela CR, Ravi Sankar B (2020) Investigations on CI engine with nano-sized zinc oxide added Mahua Methyl Ester blends. Int J Ambient Energy 41(2):146–151
56. Ghafoori M et al (2015) Effect of nano-particles on the performance and emission of a diesel engine using biodiesel-diesel blend. Int J Automot Mech Eng 12
57. Hawi M et al (2019) Experimental investigation on performance of a compression ignition engine fueled with waste cooking oil biodiesel–diesel blend enhanced with iron-doped cerium oxide nanoparticles. Energies 12(5):798
58. Raju VD et al (2018) An experimental study on the effect of nanoparticles with novel tamarind seed methyl ester for diesel engine applications. Energy Convers Manage 164:655–666
59. Radhakrishnan S et al (2018) Effect of nanoparticle on emission and performance characteristics of a diesel engine fueled with cashew nut shell biodiesel. Energy Sour Part A Recovery Utilization Environ Effects 40(20):2485–2493
60. Perumal V, Ilangkumaran M (2018) The influence of copper oxide nano particle added pongamia methyl ester biodiesel on the performance, combustion and emission of a diesel engine. Fuel 232:791–802
61. Arockiasamy P, Anand RB (2015) Performance, combustion and emission characteristics of a DI diesel engine fuelled with nanoparticle blended jatropha biodiesel. Periodica Polytech Mech Eng 59(2):88–93
62. Patil DS (2018) Experimental investigation of effect of cerium oxide nanoparticles as a fuel additive in cottonseed biodiesel blends. MAYFEB J Mech Eng 1
63. Nayak S et al (2018) Performance evaluation and emission characteristics of a 4 stroke diesel engine using green synthesized silver nanoparticles blended biodiesel. Mater Today: Proc 5(2):7889–7897
64. Attia AM et al (2014) Effects of alumina nanoparticles additives into jojoba methyl ester-diesel mixture on diesel engine performance. In: ASME international mechanical engineering congress and exposition. American Society of Mechanical Engineers
65. EL-Seesy AI et al (2016) The influence of multi-walled carbon nanotubes additives into non-edible biodiesel-diesel fuel blend on diesel engine performance and emissions. Energy Procedia 100(September):166–72
66. Amit KS (2015) Impact on the performance of direct compression ignition engine by adding nano-particle in biodiesel. J Mater Sci Mech Eng 2(7):7–9
67. Jeryrajkumar L, Anbarasu G, Elangovan T (2016) Effects on nano additives on performance and emission characteristics of calophyllim inophyllum biodiesel. Int J ChemTech Res 9(4):210–219
68. Selvan VAM, Anand R, Udayakumar M (2009) Effects of cerium oxide nanoparticle addition in diesel and diesel-biodiesel-ethanol blends on the performance and emission characteristics of a CI engine. J Eng Appl Sci 4(7):1819–6608
69. Loganathan CS (2015) Emission reduction from a diesel engine fueled by cerium oxide nano-additives using SCR with different metal oxides coated catalytic converter. J Eng Sci Technol 10(11):1404–1421

70. Ghogare P, Kale N (2016) Experimental investigation on single cylinder diesel engine fuelled with cotton seed biodiesel blends with nano additives. In: International conference on electrical, electronics, and optimization techniques

# Strategic Maintenance Decision Making Under Adverse Contribution Margins—A Case Study in a Cement Plant

**George Decruz, Habibah Norehan Haron, and Khairur Rijal Jamaludin**

**Abstract** The research in a cement plant on decision-making with respect to improvements to address equipment failure in the kiln utilized the identification of the costs associated with the failure as a precursor to the development of the appropriate strategies. The cost model utilized included the losses related to opportunity losses, the direct losses related to the repair, and the losses that contributed to an increase in variable costs. In this paper, the application of the sum of the latter two components of the model to identify viable maintenance and operational improvements from an economic perspective was carried out. This is extremely relevant when the company is constrained by low-selling price and low demand. Low-selling price translates into low-contribution margins and therefore requires a more prudent allocation of resources to obtain immediate positive results. This is illustrated in this paper based on the case study in a cement kiln covering a five-year period.

**Keywords** Kiln · Clinker · Maintenance · Variable costs · Repair costs · Cost of improvement · Equipment failure · Reliability · Contribution margin

## 1 Introduction

In the manufacture of cement, the production of clinker a semi-finished product requires the highest cost input both from a variable cost perspective as well as from a fixed cost perspective. The production of clinker involves the crushing and grinding of a proportioned mix of limestone, shale, and ferrum-rich material to produce a fine powder referred to as raw meal. This raw meal is then sintered to form clinker

G. Decruz (✉) · H. N. Haron · K. R. Jamaludin
Razak Faculty of Technology and Informatics, Universiti Teknologi Malaysia, Jalan Sultan Yahya Petra, 54100 Kuala Lumpur, Malaysia
e-mail: gedec58@gmail.com

H. N. Haron
e-mail: habibahharon.kl@utm.my

K. R. Jamaludin
e-mail: khairur.kl@utm.my
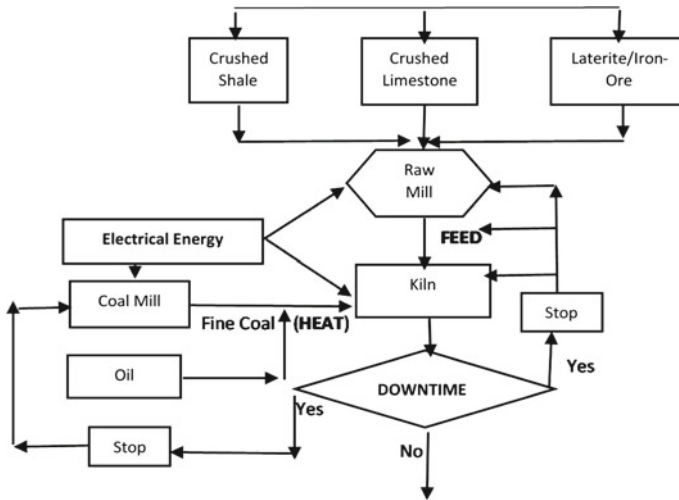
**Fig. 1** Process flow for clinker manufacture with energy inputs

in the pyro-processing unit utilizing coal as the primary fuel and fuel oil and alternative fuels as start-up and secondary fuels, respectively. The final process in the production of cement is the grinding of the clinker and gypsum in a mill, and other cementitious materials are also added according to the relevant standards and specifications. The production of clinker is illustrated in Fig. 1 (1). The manufacture of clinker is an energy intensive process utilizing both thermal and electrical energy. It is maintenance intensive as well requiring heavy expenditure both in preventive, corrective, and repair maintenance; with these having a close relationship with equipment reliability [1, 2].

The utilization of cost of equipment failure as a tool in assessing maintenance performance has been researched and demonstrated. The link between the accurate assessment of downtime costs and financial performance was established in a case study utilizing three cement plants [3]. In research carried out at an energy company in Korea, it was identified that four out of the nine leading maintenance performance indicators were related to maintenance cost [4]. A recent paper published in 2021 has, however, highlighted the paucity of research that establishes the connection between energy efficiency and maintenance [5].

In assessing the cost of equipment failure, various models have been drawn up. One of the early models developed included losses related to the repair costs, production losses as well as variable cost losses related to labor [6]. An improved model composed of direct cost components related to repair and labor, opportunity costs related to loss of production, infant failure costs, and other costs was proposed in research carried out at an electrical transmission facility in Mexico [7]. The overall equipment cost loss (OECL) model was used to determine the cost incurred because of equipment failure based on losses due to non-achievement of overall equipment efficiency (OEE) targets disregarding direct repair costs associated with a failure [8].

The analysis of the relative impact of the various cost dimensions based on the work in Mexico identified that more than 80% of all costs were associated with opportunity cost losses [7]. In that study, no variable cost loss component was studied.

The sole utilization of opportunity losses in identifying improvement strategies that are viable can prove challenging when an industry is faced with a dramatic drop in selling prices. This is because the resulting shrinking opportunity cost losses would make the previous assumptions on cost allocations for improvement strategies non-viable. The importance of aligning maintenance strategy and activities to meet market situations and business objectives has been recognized by researchers [9–11]. To address the adverse market situation, an analysis was carried out in a cement plant to isolate and identify the variable cost losses and direct repair losses associated with specific failures. These findings were then used to identify maintenance and operational improvements under economic conditions of protracted low margins. This paper is an extension of an earlier submitted publication that utilized an overall cost failure model for assessment of maintenance strategies in the same cement plant [2].

## 2   Method

The identification of the variable cost loss related to an equipment failure involved first an identification of the various cost elements related to the consumption of thermal and electrical consumption and assessing if there was any significant correlation of these energy cost elements with equipment failure, where the marker used for equipment failure is kiln downtime. The results of this preliminary correlation study carried out over a five-year period from 2013 to 2017 between energy consumption per unit production and kiln downtime showed that the following cost elements did have a significant correlation with kiln downtime [2]:

i.   specific electrical energy consumption in kilowatt-hour per ton clinker for raw mill grinding
ii.  specific electrical energy consumption in kilowatt-hour per ton clinker for clinker production in the kiln system
iii. specific electrical consumption in kilowatt-hour per ton clinker for coal grinding
iv.  specific heat energy consumption in kilocalorie per ton clinker for clinker production.

This assessment was followed by a more detailed investigation linking the energy consumption to equipment failure utilizing data from 2008 to 2017. The development of the relationship in the case of both heat and electrical energy losses was carried out based on the premise that the total energy consumed during a month can be isolated into energy consumed for production and energy consumed for non-production purposes.

In the case of heat energy, this separation was carried out based on daily heat consumption in calories and production data for days without downtime and

projecting this to estimate the total production heat consumed in a month. The difference between the overall total heat consumed and the heat consumed for production was the heat lost because of equipment failure [2]. This is expressed in Eq. 1 with all symbols used in equations explained in Appendix 1.

$$HC_{effL} = HC - HC_{prod} \tag{1}$$

The cumulative downtime hours for a month were computed from the sum of the different failure events but with each failure event duration capped to 24 h based on heating up schedule after failure [12]. The monthly downtime heat losses were regressed against downtime and other predictors as expressed in Eq. 2 utilizing Minitab 18 [2]. The predictors considered were $D_{K24}$, kiln downtime capped to 24 h, $PR_K$, the mean monthly production rate of clinker production in tons per hour, $C_{CV}$, the mean monthly calorific value of the coal expressed in kilocalories per kg coal, and $N_{FK}$, the monthly number of kiln failures. The costs associated with the losses related to the variable heat energy losses caused by an equipment failure event $i$ in a given month in the year 20YY are expressed in Eq. 3 by utilizing the composite fuel prices during the period when the failure event occurred, $P_{comp,fuel}$ and the price index $P_{index,fuel}$ which standardizes the costs to a common base of December 2017.

$$HC_{effL} = f\left[\sum D_{K24}, PR_K, C_{CV}, N_{FK}\right] \tag{2}$$

$$HC_{effL,cost,mon,20YY,i} = \left(HC_{effL,mon,20YY,i}\right) \times \left(P_{comp,fuel,mon,20YY,i}\right) \\ \times \left(P_{index,fuel,mon,20YY,i}\right) \tag{3}$$

The theoretical basis that supports this can be deduced from the thermal heat balance that has been carried out for rotary kilns which identified the waste energy outputs during production [13, 14]. These waste energy outputs include the waste heat radiated from the hot surfaces in the kiln system as well as the heat contained in waste flue gases which during production constitute 43.9% of total heat input. These waste losses form part of the energy requirements for production. However, when an equipment failure occurs, the kiln will have to be reheated to resume production once the failure has been rectified. During this re-heating, the radiation losses as well as flue gas heat losses continue although as a consequence of the failure event, there is no production. In addition, there is a period prior to the kiln achieving its normal production capacity when the waste heat losses form a higher percentage as that during normal production. The developed model helps to quantify the incremental heat consumed resulting from equipment failure.

In the case of electrical energy losses, the determination of the model required a different approach as hourly electricity consumption readings are not available. The overall monthly specific electrical energy consumed in the relevant operating units was defined as a function of both the specific electrical energy consumed for production and the losses due to failure also expressed in terms of specific energy

losses per ton clinker produced [2]. The significance of separating energy costs for start-ups or warming up from actual production costs has been elaborated on in literature [15]. This provided insight in the development of the model described here. This is expressed in Eqs. 4–6. The monthly specific electrical energy consumed for the various relevant operating unit was tested utilizing regression techniques against various identified predictor variables such as the mean monthly production rates of clinker, raw meal and pulverized coal, kiln downtime hours, number of failures, etc., as expressed in Eqs. 7–9. Research carried out in a plant with high performance with respect to running days established that overall energy losses related to plant stoppage amounted to 0.25 kW-h per ton cement which translates to 0.28 kW-h per ton clinker [16]

$$EC_{spov,K} = f\big[EC_{sp,K}, EC_{speffL,K}\big] \tag{4}$$

$$EC_{spov,RM} = f\big[EC_{sp,RM}, EC_{speffL,RM}\big] \tag{5}$$

$$EC_{spov,CM} = f\big[EC_{sp,CM}, EC_{speffL,CM}\big] \tag{6}$$

$$EC_{spov,K} = f[PR_K, D_K, D_{K24}, N_{FK}] \tag{7}$$

$$EC_{spov,RM} = f[PR_{RM}, D_{K24}, D_{RM}, N_{SRM}, N_{FK}] \tag{8}$$

$$EC_{spov,CM} = f[PR_{CM}, D_{K24}, D_{CM}, C_{CV}, N_{SCM}, N_{FK}] \tag{9}$$

The electrical efficiency losses associated to an equipment failure event $i$ in a given month in the year 20YY is expressed in Eq. 10 [2].

$$
\begin{aligned}
EC_{speffL,cost,mon,20YY,i} = (&EC_{speffL,K,mon,20YY,i} + EC_{speffL,RM,mon,20YY,i} \\
&+ EC_{speffL,CM,mon,20YY,i}) \times (CP, mon, 20YY, i) \\
&\times \big(P_{elect,mon,20YY,i}\big) \times \big(P_{index,elect,mon,20YY,i}\big)
\end{aligned} \tag{10}
$$

The determination of the direct costs related to an equipment failure required firstly the identification of the fixed cost components that have a significant correlation with kiln downtime. The fixed cost components that were tested were manpower costs, overtime costs, and maintenance costs. The actual fixed costs related to an equipment failure $i$ were then determined using fixed cost data extracted from the monthly financial report and related to the fixed cost expense type determined to have a significant relationship [2].

The variable cost losses and fixed cost expenses or direct costs related to each of the failure events were computed utilizing normalization techniques based on December 2017 cost inputs for a five-year period from 2013 to 2017. The cost of

improvements for the failures was mapped against these costs to identify the priority of execution.

## 3   Analysis and Results

The regression relationships obtained relating variable cost component energy losses with downtime are as listed below [2]. The equation for heat efficiency losses presented here was refined from that published earlier where a quadratic log–log relationship had been utilized [2].

$$log_{10}HC_{effL,i} = 4.477 + 0.922(log_{10}D_{K24,i}) \qquad (11)$$

$$EC_{spov,K} = 81.46 - 0.29PR_K + 0.027D_{K96} \qquad (12)$$

$$EC_{speffL,K,i} = 0.027D_{K96,i} \qquad (13)$$

$$EC_{spov,RM} = 44.82 - 0.056PR_{RM} + 0.018D_{K24} + 0.025N_{SRM} \qquad (14)$$

$$EC_{speffL,RM,i} = 0.018D_{K24,i} \qquad (15)$$

$$EC_{spov,CM} = 13.17 - 0.0046PR_K + 0.0036D_{K24} \qquad (16)$$

$$EC_{speffL,CM,i} = 0.0036D_{K24,i} \qquad (17)$$

The energy losses derived from this regression analysis were translated into costs for a given failure, $i$, in a given month of the year. This is expressed in the following equation relating cost of heat energy and electrical energy losses associated with equipment failure. This was done using inputs for fuel cost and electricity energy costs and price indices as defined in Appendix 1. The equations were used to determine the variable cost losses as well as direct repair costs for the five-year period from 2013 to 2017 for different failure events.

$$\Delta C_{VEQF,mon,20YY,i} = \left[ \left[ \begin{array}{c} \left\{ 10^{(4.477+0.922(\log_{10} D_{K24,i}))} \right\} \\ \times P_{comp,fuel,mon,20YY,i} \times P_{index,fuel,mon,20YY,i} \end{array} \right] \right. \\ \left. + \left[ \left\{ \begin{array}{c} [0.027 \times D_{K96,mon,20YY,i}] + [0.018 \times D_{K24,mon,20YY,i}] \\ + [0.0036 \times D_{K24,mon,20YY,i}] \end{array} \right\} \right] \right\}$$

$$\times CP, mon, 20YY, i \times P_{elect,mon,20YY,i} x P_{index,elect,mon,20YY,i} \big]\big] \tag{18}$$

An analysis previously executed for the five-year period identified that only the fixed costs related to maintenance repair had a significant correlation with kiln downtime [2]. This relationship is expressed as follows in Eq. 19 with the various parameters explained in Appendix 1.

$$\Delta C_{Madj,mon,20YY,i} = \Delta C_{M,mon,20YY,i} \times \left( \frac{P_{imp,D17}}{P_{imp.mon,20YY,i}} \right) \tag{19}$$

Equation 18 was used to simulate the variable cost losses related to the different equipment failure for the years 2013–2017 in terms of RM (Ringgit Malaysia currency) per ton clinker. This cost together with the maintenance repair costs expressed in terms of RM per ton clinker was compiled and failures ranked based on total sum of variable cost losses and repair costs. The selection of equipment to be assessed was based on the equipment which were ranked highest in total cost of failure inclusive of opportunity losses as well as equipment failures with the highest combined variable and repair costs of failure. Maintenance strategies were determined based on discussions with subject matter experts to identify steps to address or mitigate these failures. The cost of these strategies was then mapped against the sum of variable cost losses and repair costs. The financial feasibility of each of the strategies was tested based purely on the extent of coverage of cost of the strategy by the savings derived from avoidance of variable and repair cost losses. This compilation of losses and maintenance strategies is shown in Table 1.

## 4 Discussion

The equipment failures identified comprised 52% of the total failure costs over a five-year period from 2013 to 2017. The analysis of the sum of variable cost losses and repair cost losses against the proposed strategies was used to identify a ranking of strategies based on considering returns under market conditions that generate zero contribution margins with low demand. In the case of cyclone blockages, energy variable cost losses are the most significant because of frequency of the occurrences of blockages that requires repetitive heating up. The improvement strategy that was implemented costs only 32% of the total of variable cost losses and repair costs The improvement strategy implemented was identified as the that with the highest priority and was based on the installation of redundant blockage detection systems with an interlock system which mitigates the impact of blockage through the limitation of material clogged within the cyclone.

Cooler grate failures were addressed by strategies based on selection of quality of grate plates as well as scheduled cooler alignments, the costs making up 82% of the variable and repair cost losses. Kiln refractory failure was also addressed

**Table 1** Failure cost losses and strategic intervention costs analysis

| Equipment failure type | Variable cost loss RM per ton clinker | Fixed cost loss for repair RM per ton clinker | Strategic intervention and costs RM per ton clinker | Remarks |
|---|---|---|---|---|
| Cyclone blockage | 0.28 | 0.0 | 0.09 | Improvement cost makes up only 32% of variable cost losses and repair costs |
| Cooler grate failure | 0.09 | 0.08 | 0.14 | Improvement cost makes up 82% of variable cost losses and repair costs |
| Kiln refractory | 0.18 | 0.34 | 0.68 | Variable cost losses and repair costs cover 76.5% of cost of improvement |
| Kiln inlet coating | 0.09 | 0.01 | 0.22 | Variable cost losses and repair costs cover 45% of cost of improvement |
| Snowman | 0.08 | 0.0 | 0.19 | Variable cost losses and repair costs cover 42% of cost of improvement |
| Deep bucket conveyor | 0.09 | 0.02 | 0.5 | Variable cost losses and repair costs cover 22% of cost of improvement |

by implementation of scheduled kiln alignment and revising refractory selection protocols with the variable and repair cost losses covering 82% of the maintenance improvement costs. Variable cost losses and repair costs only addressed 45% of the improvement measures identified. Notwithstanding this lower percentage of coverage improvements were carried out through the installation of special silicon carbide-based refractory to manage stoppages due to kiln inlet coating build-ups and the implementation of preventive maintenance programs to ensure reliability of coating removal equipment.

The snowman failures improvement programs while identified have yet to be implemented based on prioritization of capital expenditure and is scheduled for implementation in 2022. The identified improvements for the deep bucket failures

require the implementation of a scheduled five yearly overhauling of the equipment. However, owing to the prevailing economic situation of low margins and high cost of improvement as well as the impact of COVID-19 which reduced machine running requirement, the maintenance program was scaled down in 2020, and the full overhaul is to be carried out in 2022.

## 5 Conclusions

The computation of variable cost losses isolates the component of equipment failure cost losses from variable costs. These energy failure cost losses have been conventionally lumped into variable losses. Such a revised treatment of the energy cost losses allows the maintenance engineers to correctly understand the true economic impact of equipment failure. Through the computation of the failure cost made up of the sum of energy cost losses and repair costs, decision-making based on viability of improvement strategies under adverse product price regimes was carried out. Literature generally utilizes the potential impact of opportunity losses as the key driver to execute improvement strategies. The highly competitive markets reflected in low to zero contribution margins as well as low-sales volumes places require the utilization of a different measure based on variable and repair cost losses to ensure the proper allocation of resources. The results of the analysis and identification of strategies have showed that immediate improvements of the cost structure and kiln performance are possible through the implementation of strategies that are economically justified based on these failure cost losses.

## Appendix

See Table 2.

**Table 2** Symbols

| Parameter | Description | Parameter | Description |
|---|---|---|---|
| $\Delta C_{VEQF,mon,20YY,i}$ | Incremental variable cost losses resulting from failure event, $i$, for a given month in the year 20YY | $EC_{speffL,cost,mon,20YY,i}$ | Total specific cost of electricity losses, for an event, $i$, in a given month in the year 20YY |
| $\Delta CM_{Madj,mon,20YY,i}$ | Incremental repair maintenance costs adjusted to December 2017 for a failure event $i$ for a given month in the year 20YY | $EC_{speffL,K,mon,20YY,i}$ | Specific electricity losses (kiln) for an event, $i$, in a given month in the year 20YY |
| $\Delta C_{M,mon,20YY,i}$ | Incremental repair maintenance costs for a failure event $i$ for a given month in the year 20YY | $EC_{speffL,RM,mon,20YY,i}$ | Specific electricity losses (raw mill) for an event, $i$, in a given month in the year 20YY |
| $C_{CV}$ kilocalorie/kg | Coal calorific value | $EC_{speffL,CM,mon,20YY,i}$ | Specific electricity losses (coal mill) for an event, $i$, in a given month in the year 20YY |
| $D_{K,i}$ hours | Kiln downtime hours, event $i$ | $HC$ (calories) | Total monthly heat consumed |
| $D_{K24,i}$ hours | Downtime capped to 24 h | $HC_{prod}$ (calories) | Monthly heat consumed for production |
| $D_{K24,mon,20YY,i}$ | Downtime capped to 24 h for event $i$ in a given month in the year 20YY | $HC_{effL}$ (calories) | Monthly heat losses |
| $D_{K96,i}$ | Downtime capped to 96 h | $HC_{effL,cost,mon,20YY,i}$ | Cost of heat losses for event $i$ in a given month in the year 20YY |
| $D_{K96,mon,20YY,i}$ | Downtime capped to 96 h for event $i$ in a given month in the year 20YY | $HC_{effL,mon,2oYY,i}$ | Heat losses for event $I$ in a given month in the year 20YY |
| $D_{RM}$, Hours | Raw mill specific downtime - total raw mill downtime less kiln downtime | $N_{FK}$ | Number of kiln failures |
| $D_{CM}$, hours | Coal mill specific downtime—total coal mill downtime less kiln downtime | $N_{SCM}$ | Number of failures at coal mill (excluding kiln) |

(continued)

**Table 2** (continued)

| Parameter | Description | Parameter | Description |
|---|---|---|---|
| $EC_{spov,K}$ kilowatt-hour (kWh) per ton | Overall kiln specific electricity consumption | $N_{SRM}$ | Number of failures at raw mill (excluding kiln) |
| $EC_{spov,RM}$ kWh/ton | Overall raw mill specific electricity | $PR_{CM}$ (tons/hour) | Pulverized coal production rate |
| $EC_{spov,CM}$ kWh/ton | Overall coal mill specific electricity consumption | $PR_K$ (tons/hour) | Clinker production rate |
| $EC_{sp,K}$ kWh/ton | Kiln electricity consumption for production | $PR_{RM}$ (tons/hour) | Raw meal production rate |
| $EC_{sp,RM}$ kWh/ton | Raw mill electricity consumption for production | $CP_{mon,20YY,I}$ (tons/hour) | Clinker production in the given month in the year 20YY when event $i$ occurs |
| $EC_{sp,CM}$ kWh/ton | Coal mill electricity consumption for production | $P_{comp,fuel,mon,20YY,i}$ | Composite fuel price, event in a given month in the year 20YY |
| $EC_{speffL,K}$ | Specific electricity losses, kiln | $P_{index,fuel,mon,20YY,i}$ | Price index for fuel price adjustment to December 2017 |
| $EC_{speffL,K,i}$ | Specific (kiln) electricity losses,for event $i$ | $P_{elect,mon,.20YY,i}$ | Electrical price in the given month of the year 20YY when the failure event, $i$, occurs |
| $EC_{speffL,RM}$ | Specific electricity losses, raw mill | $P_{index,mon,20YY,i}$ | Price index for electricity price adjustment to December 2017 |
| $EC_{speffL,RM,i}$ | Specific (raw mill) electricity losses, for event $i$ | $P_{imp,D17}$ | Import price index for December 2017 |
| $EC_{speffL,CM}$ | Specific electricity losses, coal mill | $P_{imp,mon,20YY,i}$ | Import price index for a given month in the year when the failure event $i$ occurs |
| $EC_{speffL,CM,i}$ | Specific (coal mill) electricity losses for event $i$ | $RM$ | Ringgit Malaysia |

# References

1. Decruz, Haron HN (2020) The impact of Kiln downtime on variable cost elements of clinker production. In: Proceedings of international conference on Engineering Business Management (ICEBM, 2019), vol 18, issue 1, pp 1–6
2. Decruz G, Haron HN, Jamaludin KR. Cost of equipment failure modelling as a tool for maintenance strategy. Lecture Notes in Mechanical Engineering (under publication)
3. Shafeek H (2014) Continuous improvement of maintenance process for the cement industry case study. J Qual Maint Eng 20(4):333–376
4. Ku S, Kim C (2019) Development of a model for maintenance performance measurement: a case study of a gas terminal. J Qual Maint Eng 26(1):69–86
5. Kappatos V (2021) Maintenance: a key factor for energy efficiency (Chapter 15). In: Mathioulakis M (ed) Aspects of the Energy Union, pp 321–336
6. Creehan KD (2005) Establishing optimal maintenance practices in traditional manufacturing environment. J Chin Inst Ind Eng 22(1):11–18
7. Peimbert-Garcia RE, Vasquez-Serrano JI, Limon-Robles J (2021) The impact of early failures on maintenance costs: an empirical study in Latin America. J Qual Maintenance Eng
8. Wudhikarn R (2016) Implementation of the overall equipment cost loss (OECL) methodology for comparison with overall equipment effectiveness (OEE). J Qual Maint Eng 22(1):81–93
9. Maletič D, Maletič M, Al-Najjar B, Gomišček B (2014) The role of maintenance in improving company's competitiveness and profitability: a case study in a textile company. J Manuf Technol Manag 25(4):441–456
10. Komonen K (2002) A cost model of industrial maintenance for profitability analysis and benchmarking. Int J Prod Econ 79:15–31
11. Kurian MC, Shalij PR, Pramod VR (2019) Maintenance strategy selection in a cement industry using analytic network process. J Qual Maint Eng 26(4):509–525
12. Refratechnik Technical Advisory Pamphlet, Kiln heating-up curve. Refratechnik Cement, Göttingen
13. Atmaca, Yumrutas R (2014) Analysis of the parameters affecting Energy consumption of a rotary kiln. Appl Thermal Eng 66:435–444
14. Alsop PC (2014) The cement plant operations handbook. Sixth Edition Publication Ltd
15. Brundage MP, Chang Q, Zou J, Li Y, Arinez J, Xiao G (2015) Energy economics in the manufacturing industry: a return on investment strategy. Energy 93:1426–1435
16. Virendra R, Kumar DBSP, Babu JS, Kant DR (2015) Detailed energy audit and conservation in a cement plant. Int Res J Eng Technol (IRJET) 2(1):248–256

# Development of Remote Laboratory System with Multi-degree Viewing Access in Support for Distance Learning Initiative

**Mohd Nashrul MohdZubir, Faisal Mahmud, Azfar Hakeem Azman, Mohd Yazed Ahmad, Unaizah Obaidellah, Zuraidah Abdullah, Nahrizul Adib Kadri, Norhafizan Ahmad, and Mohammed A. H. Ali**

**Abstract** The project highlights the work on establishing a remote laboratory system that can be operated via the web as part of the effort to support online distance learning programs. To achieve this objective, integration of the hardware, software, and network communication modules was performed, enabling real-time remote access and interaction between the user and the remote infrastructure. The entire system was locally developed which requires linking between a web application software and server software to ensure uninterrupted online communication during the remote activities. The physical interaction within the lab was realized via human interface machine and microcontroller which translate the command given by the user from the web into set of instructions to control and operate the lab. The current prototype has solved the persisting challenges in implementing web-based remote control systems namely data lagging and false data acquisition via the use of server systems and data transfer algorithms. This strategy ensures data integrity and reliability to be displayed to the user in real-time. A new robotic viewing system has been developed and incorporated within the laboratory infrastructure. This new feature allows more freedom in coordinating user viewing flexibility which is crucial in capturing and

M. N. MohdZubir (✉) · A. Hakeem Azman · N. Ahmad · M. A. H. Ali
Department of Mechanical Engineering, Faculty of Engineering, Universiti Malaya, Kuala Lumpur, Malaysia
e-mail: nashrul@um.edu.my

F. Mahmud
Department of Computer Science (Applied Computing), Faculty of Computer Science and Technology, Universiti Malaya, Kuala Lumpur, Malaysia

M. Yazed Ahmad · N. Adib Kadri
Department of Biomedical Engineering, Faculty of Engineering, Universiti Malaya, Kuala Lumpur, Malaysia

U. Obaidellah
Department of Artificial Intelligence, Faculty of Computer Science and Information Technology, Universiti Malaya, Kuala Lumpur, Malaysia

Z. Abdullah
Department of Educational Management, Planning and Policy, Faculty of Education, Universiti Malaya, Kuala Lumpur, Malaysia

mimicking the user presence in the lab and during the experimental conduct. The above results provide welcoming perception on the impact of implementing remote labs as part of the continuous efforts to liberate the education platform and promote education without boundaries.

**Keywords** Distant learning · Remote laboratory · Online engineering education · Web-based experimentation

## 1  Introduction

It is well acknowledged that rapid progress of internet technology has transformed diverse aspects of human lives. However, within the context of education platform, the nature of conducting laboratory exercises has remained largely unchanged since the dawn of industrial evolution 3.0, where computers and electrical devices dominate in terms of performing activities related to the laboratory routines [1]. In addition, the implementation of "grouping" concept in laboratory activities during this period has not been critically gauged, particularly on the aspect of its effectiveness in stimulating students learning domain [1, 2]. The concern stems from the nature of the laboratory conduct where different levels of engagement from the participants result in students turning into passive observers instead of actively interacting [3]. Moreover, with the sharp increase of students undertaking laboratory courses on the yearly basis, it has become increasingly difficult for the existing experimental facility to provide a convenient learning platform for individual students [4]. In this light, there is a persistent need to transform the current laboratory concept into exciting, engaging, and stimulating program that could reenergize the students' enthusiasm for performing the lab work [5]. The birth of 4G internet revolution has paved a path for students to take the laboratory exercise into a new level, where, combined with automation technology and state-of-the-art sensory devices, a laboratory works are able to be conducted by a tip of a finger using personal communication devices such as laptop and smartphones [6, 7]. It is anticipated that this novel approach will pave new dimension in student learning domain by injecting IR4.0 elements into the laboratory exercise.

It is well known that one of the persisting challenges in realizing experimental exercise under remote conditions is the feeling of absentness within experimental facility. This is predominantly attributed to rigidness in the viewing system which typically uses static cameras to monitor the experimental domain and other physical processes and interactions [8, 9]. This results in deterioration of user cognitive, affective, and psychomotor learning levels. The ability to replicate human viewing mobility which includes perception of depth and perspective at multi-degree angles is essential to maintain the level of thinking, understanding, and sensing required within the experiment which falls under cognitive aspect. On the other hand, rigid viewing mode would undermine the user's affective learning domain when performing the tasks within the experiment to the point that the user would ultimately lose the

connection and enthusiasm to complete the experiment [10]. Ultimately when the above two learning domains are compromised, the psychomotor component of the user learning ability which deals with physical dexterity of the user with the experimental setup would be affected, in such a way that the user fails to feel the excitement and gives involuntary attention and response to the vital sensory cues that govern the experimental activities [11].

In this research, a multi-degree viewing aid system was developed and installed within the existing remote experimental facility to enable users to experience human-like maneuvering, navigation, and coordination of the viewing task. This would help the user to examine and monitor the facility in different angles and positions which are crucial in accomplishing the tasks. Specifically, a camera mounted on a multi-degree of freedom manipulator connected to mobile robotic vehicle was used by which the camera positioning and viewing angle were controlled by the vehicle and manipulator maneuvering action. The control was performed by the host computer via the existing web application interface. Unlike the modules within the experimental setup which are connected directly to the server via Universal Serial Bus (USB) port, the communication between the mobile robot and the server hosting the web application was facilitated via the WIFI module which navigates the data packet transmission to and from the server. In this manner, the newly viewing system can be tied to the existing experimental setup since both facilities are connected to the same server despite having different communication strategies. The ability to mimic human viewing actions will ensure that the users are physically "brought" into the facility and feel the actual environment. This will address the entire learning levels which is dominated by the flexibility in visualizations.

## 2 Method

### 2.1 Development of Viewing Mobility System

This project deals with improving the user viewing flexibility when conducting experiment under remote conditions. The visualization system consists of a camera mounted on a multi-degree of freedom manipulator connected to mobile robotic vehicle. This configuration aims to mimic human physical viewing demands during remotely conducted experiments. This viewing module is part of the integrated remote laboratory facility which would allow the user to conduct laboratory exercises by communicating with the experimental setup via web application. To achieve this task, a robotic rover would undergo a systematic modification that involves placing a manipulator on board the rover platform. This module serves to provide more viewing direction to camera similar to human vision mobility.

The overall prototype design of the camera viewing mobility system is given in Fig. 1. In this configuration, the rover is allowed to move in three directions (i.e., $x$, $y$, and $\psi$) and the camera manipulator is free to move in another three directions (i.e.,
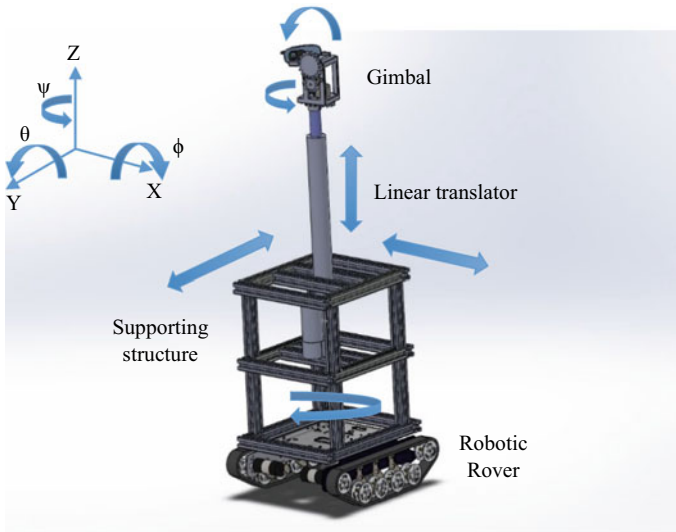
**Fig. 1** Design of vision mobility mechanism

$z$, $\theta$, and $\varphi$), making the total degree of freedom to 6. This arrangement promotes higher flexibility in camera positioning which allow the user to view the experimental facility and adjust the focus on the section of interest during experimental conduct.

## 2.2 Integration of Viewing System into Web Application

The above viewing mechanism was driven by series of microcontrollers whose role is to translate the series of commands from the user into electrical signals that drive the motors. These motors will in turn determine the camera direction and position at the presetting speed. The user will interact with the robot using a custom-built web application that contains interface in the form of buttons to trigger the command to communicate with the motors' microcontrollers. The web application also incorporates viewing window that allows the live streaming of the experimental facility thus giving the user the real-time interaction. This application is hosted in a server which becomes the medium of information exchange between the web and experimental facility.

In order to accomplish the communication loop between the server and the mobile viewing system, a different approach was adopted from the current serial communication via USB connection that supports the information transfer between the server and the electrical components within the experimental facility. On this note, the rover requires wireless communication that uses transmitter–receiver modules that allows the command from the server to be transmitted and detected by the receiver which
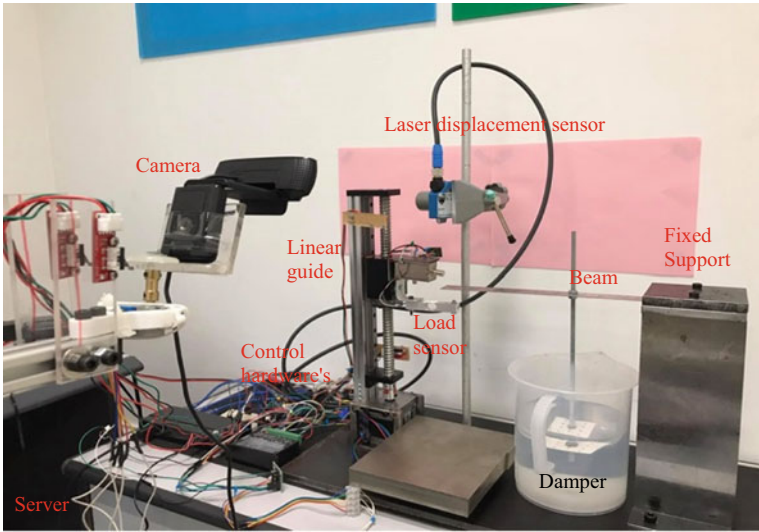
(a)
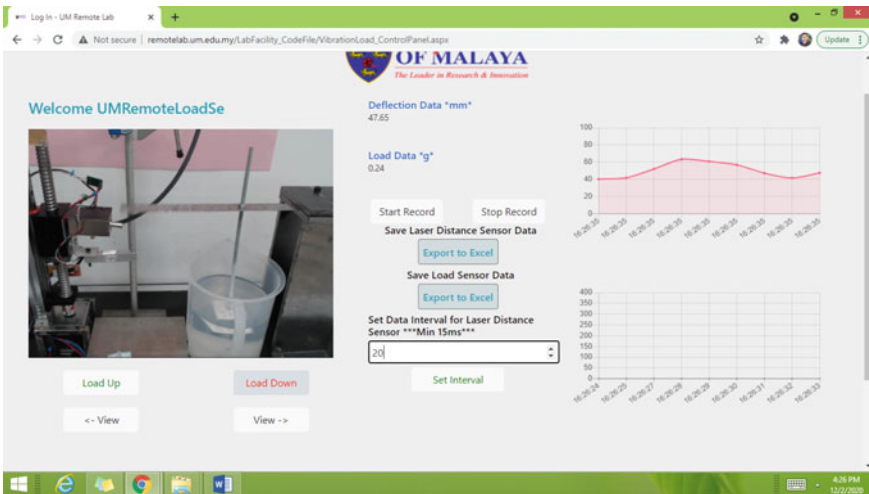


(b)

**Fig. 2** **a** Completed experimental facility and **b** Web application interface

will later flow to the microcontroller to be decoded to represent specific instructions for the robot's movement. This arrangement allows the rover to gain unlimited motion since server-robot communication cables is avoided.

Since the rover is to be made free from any wire connection to server, it is compulsory for video streaming from the camera on board to demonstrate such similar attribute. Further, the streaming has to be made directly to the web which

requires internet communication protocol. Thus, to achieve this task, another onboard computer containing hardware required for internet communication is needed. Here, a Raspberry PI computer was used due to its small size and features modules identical to ordinary computers which include USB connection as well as WIFI and network cards. On this note, the USB camera was connected via the matching port while the data packet representing the video was broadcasted via the wide-area network internet protocol using WIFI-modem communication module.

## 2.3 *Complete Web-Based Laboratory Facility*

The above vision mobility system was integrated into the existing web platform as shown in Fig. 2a. On the other hand, the web application is given in Fig. 2b contains the interfaces necessary for the user to interact with the lab facility while navigating their vision by controlling the rover and onboard manipulators. A laboratory exercise within 3rd-year laboratory subject offered to UM Mechanical Engineering undergraduate students was chosen to demonstrate the web-based remote laboratory idea. Traditionally, under manual operation, the exercise named "Single Degree of Freedom Vibration" requires the user to perform several tasks which involve physical interaction with the experimental setup as well as collecting the data both manually and by using software. These sequences require user's presence in the lab to complete the experiment. Here, under the proposed approach, the laboratory setup was undergone hardware transformation whereby the physical tasks were replaced by series of motor-driven interactions. On the other hand, the measurement of physical properties was performed via sensors that translate these properties into electrical signals to be further interpreted and converted into numerical quantities. Series of microcontrollers were connected to the above sensor and motors hardware to communicate to the server that host the software used to operate the setup. This web application software is broadcasted globally via the internet connection, enabling users to access and execute the experiment upon passing the authorization passage.

## 3   Results and Discussion

Figure 3 shows the prototype of the vision mobility system with onboard computer, microcontroller, and camera. A continuous track system was used to propel the rover since it can provide more stability to the load on the platform. The gimbal mechanism was fabricated using 3D printer. A 16 V 44A battery rechargeable battery was used to power the instruments, computer, electrical components, and driving system of the rover. The viewing height can be adjusted via a linear translator while the left and right glancing motion is accomplished via the gimbal mechanism. The sideways as well as back and forth motion can be performed by driving the motor in either clockwise or
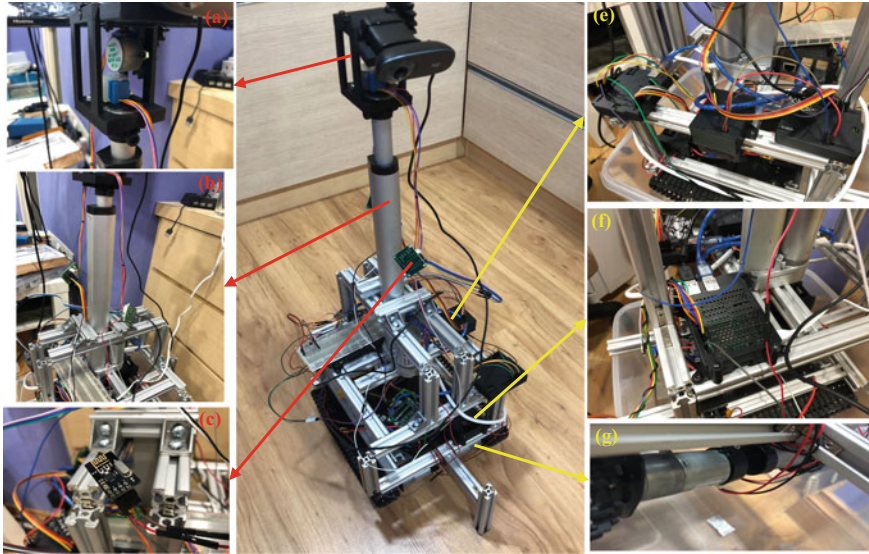
**Fig. 3** Complete prototype of vision mobility system along with the closeup view of **a** Gimbal mechanism **b** Linear translator **c** Radio transmitter **e** Microcontroller **f** Raspberry PI computer and **g** Rover driving motor

anticlockwise direction. The angular change of the rover is accomplished by rotating the motor in opposite direction.

For video transmission from the robot, a video streamer software called Gstreamer was used which allows a generic USB webcam to function within the Raspberry PI computer. A port forwarded IP was assigned, allowing the computer to stream the video via Wi-Fi to the web application and further broadcast to the user connected outside the local network. Gstreamer provides hardware encoding which can provide low latency video transmission and at the same time uses less CPU resource by using the integrated CPU of the PI. From multiple testing, the video stream is set to 1280 × 720 resolution with as frame rate of 30 fps which provides the lowest average latency.

Usually, wireless data transmission comes with a shortfall known as latency. The video feed also has its own latency to and from the Raspberry PI. To further understand on how this may affect the streaming performance, a test was conducted to record the latency of the video transmission. The test involved pointing the rover camera on a monitor which display a stopwatch from a computer. The computer also displays the video fed to the Gstreamer software. In this manner, the difference in time between the video software and the actual display can be observed upon applying window print screen function, thus showing the latency of the video stream. The example is given in Fig. 4.

Figure 4 shows the result of the latency in live streaming process. While the delay was expected the level is in the range of microseconds, indicating that the

Video software window



Computer display window
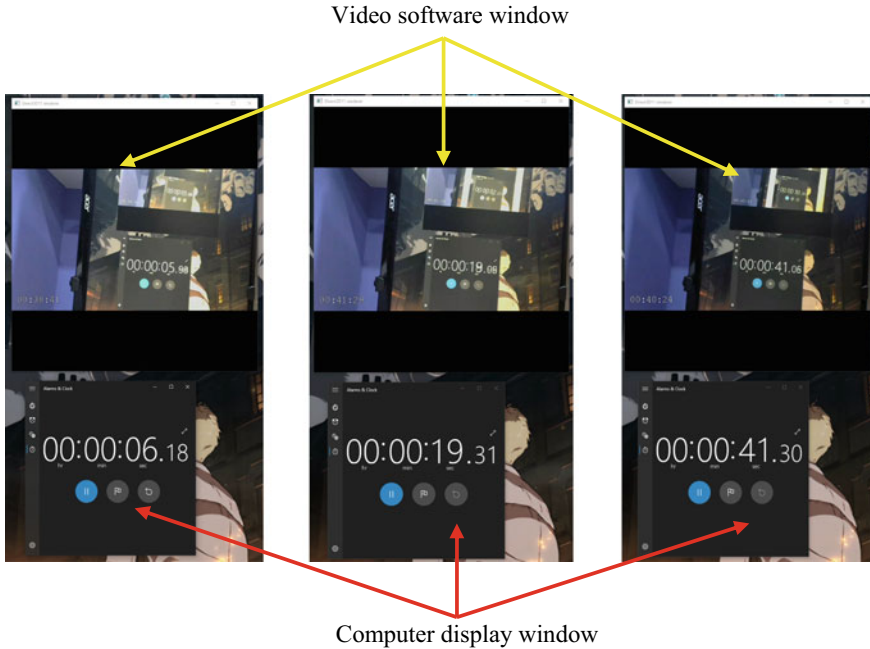
**Fig. 4** Latency test on video streaming by the rover camera for three different snapshot times

current streaming procedure would provide sufficient speed for the user to gain real-time experience without noticeable delay. The average delay was obtained by taking several progressive snapshots and performing the averaging. It was found the average delay recorded was 296 ms which is about the range acceptable for human to perceive real-time interaction, i.e., 180 ms [12].

## 4 Conclusions

This project has demonstrated the development and implementation of web-based remote laboratory system to enable flexible access in performing laboratory exercises and beyond. The focus of the current work dealt with the design and integration of flexible vision mobility system which is crucial to address the problem related to gaining wider and multi-directional viewing access mimicking human vision freedom. The system consists of a camera attached to the manipulator which was mounted on a transport rover vehicle. The motion and direction of the camera is governed by series of motors whose motion is controlled by the micro-controller. A wireless communication was adopted in the form of remote control transmitted-receiver module as well as WIFI system to enable data transfer between the robot/camera and the server established to host the web application. The mobility

system was successfully demonstrated with the ability of the camera to be maneuvered in all 6 Degree of Freedom motions. The camera live video streaming was accomplished using a Raspberry PI microcomputer equipped WIFI function to allow data to be sent to the web application via network IP and further broadcast to the user outside users. Investigation on the latency of video streaming from the rover to the user's computer device revealed a reasonable time lag reaching the user due to the data processing sequence. However, this latency is within acceptable value based on human noticeable vision lag which allows the feed to be perceived as real-time. The establishment of this new educational platform for laboratory conduct would revolutionize the education in terms of information sharing and knowledge dissemination to break the boundary of exclusiveness in learning and promote andragogy learning attributes with the support from latest internet technology.

# References

1. Feisel LD, Rosa AJ (2005) The role of the laboratory in undergraduate engineering education. J Eng Educ 94(1):121–130
2. Beck C, Butler A, Burke da Silva K (2014) Promoting inquiry-based teaching in laboratory courses: are we meeting the grade? CBE—Life Sci Educ 13(3):444–452
3. Abdulwahed M, Nagy ZK (2013) Developing the TriLab, a triple access mode (hands-on, virtual, remote) laboratory, of a process control rig using LabVIEW and Joomla. Comput Appl Eng Educ 21(4):614–626
4. Abdulwahed M, Nagy ZK (2011) The TriLab, a novel ICT based triple access mode laboratory education model. Comput Educ 56(1):262–274
5. Ma J, Nickerson JV (2006) Hands-on, simulated, and remote laboratories: a comparative literature review. ACM Comput Surv (CSUR) 38(3):7-es
6. Gubsky DS, Kleschenkov AB, Mamay IV (2019) Virtual laboratory for microwave measurements. Comput Appl Eng Educ 27(6):1496–1505
7. Tripathi PK, Mohan J, Gangadharan KV (2012) Design and implementation of web based remote laboratory for engineering education. Int J Eng Technol 2(2):270–278
8. Šafarič R, Truntič M, Hercog D, Pačnik G (2005) Control and robotics remote laboratory for engineering education. Int J Online Eng 1(1):1–8
9. Ortelt TR, Sadiki A, Pleul C, Becker C, Chatti S, Tekkaya AE (2014) Development of a tele-operative testing cell as a remote lab for material characterization. In: 2014 international conference on interactive collaborative learning (ICL). IEEE, pp 977–982
10. Fawzi K, Fadi D, Franck L, Benoit L (2018) Quadcopter control using on-board monocular camera for enriching remote laboratory facilities. In: 2018 IEEE international conference on automation, quality and testing, robotics (AQTR). IEEE, pp 1–6
11. Müller D, Erbe HH (2007) Collaborative remote laboratories in engineering education: challenges and visions. Adv Remote Lab e-learn Expe 35–59
12. Wardle DA (1998) The time delay in human vision. Phys Teacher 36(7):442–444

# Design and Fabrication of a Gasifier for the Production of Liquid Fuel—A Case Study of *Spondias mombin*

**O. L. Rominiyi, O. M. Ikumapayi, E. O. Orumwense, O. S. Fatoba, and E. T. Akinlabi**

**Abstract** Biowaste can be transformed into an environmentally friendly fuel, resulting in a cleaner environment. The use of plum fruit (*Spondias mombin*) as a substrate in a biowaste energy conversion system is a solution to the problem of fossil fuel through gasification. The aim of this research is to design and fabricate a gasifier for liquid fuel production from *S. mombin* (plum seed). This work was achieved by harvesting, drying, and pulverizing of plum seed after which the detailed design of the gasifier was done with the aid of solidworks. Materials were carefully selected and purchased based on availability, cost, thermal properties, mechanical properties, and their physical properties. The reactor system which consists of the reactor, pipes, and bends, shell in tube condenser, and thermocouple were fabricated. The performance evaluation of the gasifier was carried out, and various parameters such as operating time, start-up time, total operating time, fuel combustion rate, specific gasification rate, and combustion zone rate were obtained as 0.167 h, 1.17 h, 1.417 h, 11.98 kg/h, 24.94 kg/m$^2$ h, and 4.7 (m/h) respectively. The heat load of the condenser, the logarithmic mean temperature difference (LMTD), mass flow velocity, Reynold's number of fluid entering the condensing unit, and volume of burning chamber were also obtained as 145 kJ, 25 °C, 0.5 kg/s, 4.5448, and 0.062 m$^3$, respectively. The maximum pressure built up in the reactor was 0.05 bar, and quantity of liquid fuel produced was 10 ml.

**Keywords** Gasifier · *Spondias mombin* · Liquid fuel · Mass flow velocity · LMTD

O. L. Rominiyi · O. M. Ikumapayi (✉) · E. O. Orumwense
Department of Mechanical and Mechatronics Engineering, Afe Babalola University, Ado Ekiti, Nigeria
e-mail: ikumapayi.omolayo@abuad.edu.ng

O. S. Fatoba · E. T. Akinlabi
Department of Mechanical Engineering Science, University of Johannesburg, Johannesburg, South Africa

E. T. Akinlabi
Department of Mechanical Engineering, University of Northumbria, Newcastle, United Kingdom

# 1 Introduction

Gasification is a method of converting organic or naturally preserved remains or remains of animals or plants that lived in the past (fossil-based carbonaceous materials) into carbon monoxide, hydrogen, and carbon dioxide at high temperatures (>700 °C) without combustion. This resulting gas is known as fuel gas or syngas [1]. A gasifier is a high-temperature, high-pressure chamber where oxygen (or air) and steam directly interact with coals or other feed ingredients, triggering a biochemical reaction that transforms the input to syngas and ash (the powdery residue left after the burning of a substance). Syngas is a by-product of the synthetic natural gas production process. This gas is odourless, colourless, and highly flammable, and it has a variety of uses. The hydrogen obtained as a syngas from gasification can be burned to provide heat and water, as well as electricity. Hydrogen derived from coal or other solid fuels can also be used to refine oil or make fertilizer and ammonia. Syngas enhanced with hydrogen can also be used to make gasoline and diesel fuel [2]. Gasification is a feasible alternative to traditional techniques of turning coal, biomass, and some waste streams into energy and other useful products. Because of its benefits in application areas and environments, such as the clean generation of power from coal, gasification may become a more important part of the global energy and industrial sectors [3]. Due to its constant pricing and sufficient supply around the world, coal will be the primary feedstock source for gasification technology in the future. Costs, infrastructure, dependability, maintainability, efficiency, availability, national energy security, environmental concerns, public and government perception and policy, and feedstock and product flexibility will all play a role in whether gasification achieves its full commercial potential [4, 5]. The concept of solid-state gasification is not new. Gasification was originally used to make tar in the late 1700s and early 1800s. Various types of gasification technologies have been developed over the last 20 years and are now in use [6]. It has been used to make a number of fuels, including town or producer gas, a combustible gas produced by gasifying coke in the presence of steam and air. Gasification can be utilized to treat biodegradable-based materials found in municipal solid waste such as paper, card, green trash, and plastics because they have a high carbonaceous content. Noncombustible materials and recyclables (usually metals and glass) are often removed during the pretreatment step because they might reduce the amount of heat available for the process, reducing the process and operational efficiency [7, 8]. Wood, cereals, seaweed, and animal waste are examples of biomass. Biomass is likely the most ancient source of energy we have. Wood has been used to cook food and warming buildings for hundreds of years. The sun provides biomass with its energy. The sun's stored energy can be found in all organic matter. All living matter contains the energy of the sun. Photosynthesis converts water, carbon dioxide, and minerals into oxygen and carbohydrates with the help of the sun [9, 10].

## 2  Materials and Methods

### 2.1  Sample Harvesting

The *Spondias mombin* (plum seed) was the main feedstock used to evaluate the performance of the fabricated gasifier to produce liquid fuel. These plum seeds were collected at Afe Babalola University, behind central workshop. The samples were then sundried in an open atmosphere; thereafter, the moisture content of the dried feedstock was established.

### 2.2  Moisture Content of the Feedstock

The plum seed was pulverized with the aid of a milling machine at the Chemical Engineering Department, Afe Babalola University. Then, the mass of an empty petri dish was obtained with an electrical weighing balance and recorded as $(M_1) = 19.21$ g.

The dried pulverized feedstock was poured into the petri dish, and the mass was recorded as $(M_2) = 32.92$ g.

The petri dish containing the feedstock was heated in a universal oven at 105 °C for two hours, after which the petri dish was removed and cooled; then, its mass was obtained and recorded as $(M_3) = 31.5$ g.

$$\text{Loss in mass} = (M_2 - M_3) = (32.92 - 31.52) \text{ g} = 14 \text{ g}$$

$$\begin{aligned}
\text{Percentage of moisture in feedstock} \\
\text{(pulverized plum seed)} &= \frac{M_2 - M_3}{M_2 - M_1} \times \frac{100}{1} \\
&= \frac{32.92 - 31.52}{32.92 - 19.21} \times \frac{100}{1} = 10.21\%
\end{aligned}$$

$$\text{Percentage of moisture in feedstock} = 10.21\%$$

### 2.3  Material Consideration and Selection

Solidworks were used for the detailed drawing of the gasifier as shown in Fig. 1. The materials used for the fabrication of the reactor include mild steel, angle iron, gas valve, industrial heater, thermocouple, pressure gauge, and fibre glass. Material selection was done based on the following factors: availability, cost, strength and rigidity, durability, ease of cleaning, resistance to fire, and resistance to corrosion [11]. The basic components of the gasifier are the reactor, the air supply unit, feeding unit, gas outlet tube, condenser unit, water supply unit, and the sub-cooler unit.
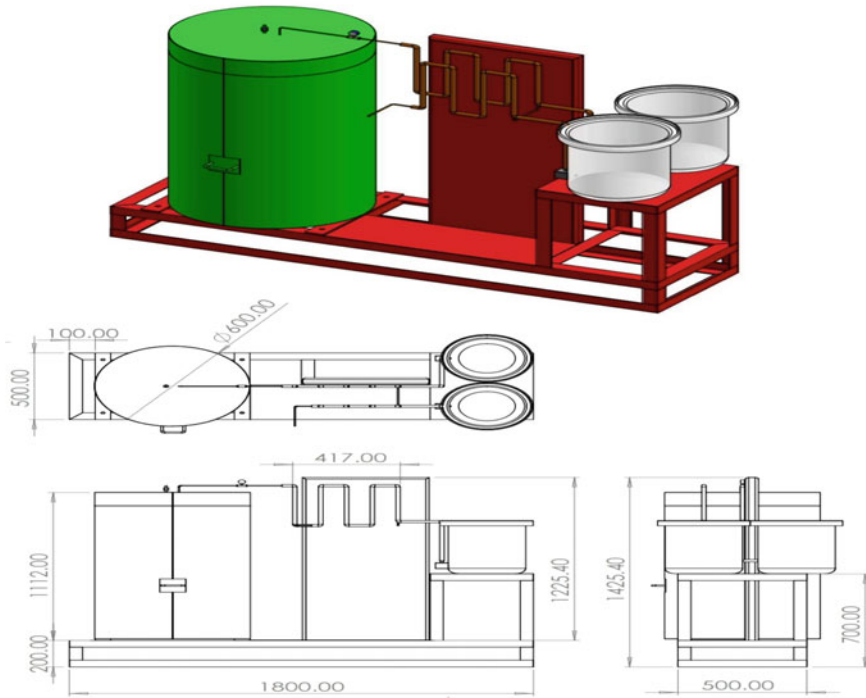
**Fig. 1** 3D model and schematic drawing of the gasifier system

## 2.4   *Analyses and Design Calculations*

The following design calculations and equations were used to develop, design, and fabricate the gasifier as shown in Table 1. The volume of the inner gasifier chamber was obtained using Eq. (1) since the gasifier takes a cylindrical shape. The maximum loading for the inner gasifier chamber was determined using Eq. (2). The circumferential or hoop stress of the gasifier was determined using Eq. (3). In cylinders made of a ductile material, the value of circumferential stress $(\sigma_{t_1})$ is given as 0.8 times the yield point stress $(\sigma_y)$ [12]. The longitudinal stress of the gasifier was obtained using Eq. (4). The longitudinal stress is half of the circumferential or hoop stress [12, 13]. According to maximum shear stress theory as depicted in Eq. (5), the maximum shear stress is half the algebraic difference of the maximum and minimum principal stress [12, 13]. Working or design stress was computed with the use of Eq. (6). It was noted that factor of safety for steel is 4 when the load applied is steady [12]. The amount of heat required to gasify the feedstock was calculated using Eq. (7) [13]. The minimum amount of heat required for the gasification of the feedstock was computed using Eq. (8) [13]. The power required for gasification of the feedstock was obtained using Eq. (9) [14]. The thickness of the reactor $(t_r)$ was determined with the

aid of Eq. (10) [14, 15]. The quantity of burning chamber for the gasification of the feedstock was determined using Eq. (11). The amount of heat load to gasify the feedstock was determined using Eq. (12) [15]. The LMTD was determined using Eq. (13) for one shell pass and one tube pass [16]. The parallel flow was established using Eq. (14). The counter flow was determined using Eq. (15). The LMTD for multiple shell and tube in Eq. (16) was also determined [16]. The true temperature difference in Eq. (17) was established. The surface area of tone tube was determined as shown in Eq. (18), Eq. (19) was applied to other tubes, and the clearance was determined using Eq. (20) [14–16]. The shell area was also calculated using Eq. (21). The Mass Velocity $G_s$ in Eq. (22) was determined. The equivalent diameter of the shell was computed to be 11.87 mm. Reynold's number was computed using Eq. (24).

## 2.5   Determination of Moisture Content of the Feedstock

The moisture content of the feedstock was determined using Eq. (25). Plum seed was collected, sun dried, and pulverized with the aid of a milling machine at the Afe Babalola University Unit Operations Laboratory, Ado Ekiti, Ekiti State, Nigeria as shown in Fig. 2.

The mass of an empty petri dish was obtained with an electrical weighing balance and recorded as $(M_1) = 19.21$ g.

The dried pulverized feedstock was poured into the petri dish, and the mass was recorded as $(M_2) = 32.92$ g.

The petri dish containing the feedstock was heated in a universal oven at 105 °C for two hours, after which the petri dish was removed and cooled; then, its mass was obtained and recorded as $(M_3) = 31.5$ g.

$$\text{Loss in mass} = (M_2 - M_3) = (32.92 - 31.52) \text{ g} = 1.4 \text{ g}$$

$$\begin{aligned}
\text{Percentage of moisture in feedstock} &= \frac{M_2 - M_3}{M_2 - M_1} \times \frac{100}{1} \\
\text{(pulverized plum seed)} \\
&= \frac{32.92 - 31.52}{32.92 - 19.21} \times \frac{100}{1} = 10.21\%
\end{aligned}$$

$$\text{Percentage of moisture in feedstock} = 10.21\% \tag{25}$$

## 2.6   Fabrication Stage

The following are the steps involved in fabricating the machine [17, 18]:

i.  **Marking out**: With the use of making-out instruments like scribers and markers, the metal sheet was marked out to the designed specifications and dimensions

were calculated using the working drawing as a guide. Before cutting, the angle iron used as the machine frame was also dimensioned.

**Table 1** Analysis and design calculation table

| Design parameters | Analysis | Equation | S/N |
|---|---|---|---|
| Volume of the inner gasifier chamber | Where $\pi = 3.142$ <br> $r = 250$ mm $= 0.25$ m; $h = 800$ mm $= 0.8$ m <br> Volume $= 3.142 \times 0.25^2 \times 0.8$ <br> $V = 0.1571$ m$^3 = 1.57 \times 10^8$ mm$^3$ | $\pi r^2 h$ | (1) |
| Maximum loading for the inner gasifier chamber | The density of the pulverized seed (*Spondias mombin*) was obtained to be 0.000464 kg/cm$^3 = 464$ kg/m$^3$. The maximum load of the gasifier then will be $\frac{1}{4}$ of the whole volume, since the volume of the inner gasifier chamber is 0.1571 m$^3$. So, $\frac{1}{4} \times 0.1571 = 0.039275$ m$^3$ <br> Mass $=$ Density $\times$ Volume <br> Mass $= 464 \times 0.039275 = 18.2236$ kg <br> Maximum loading for the gasifier is 18.2236 kg | Density $= \frac{\text{Mass}}{\text{Volume}}$ | (2) |
| Circumferential or hoop stress of the gasifier | The yield point stress ($\sigma_y$) of steel is given as 370 MPa (53,700 psi) <br> $= 0.8 \times 370 = 296$ MPa <br> Circumferential or hoop stress of the gasifier is 296 MPa | $(\sigma_{t_1}) = 0.8 \times (\sigma_y)$ | (3) |
| Longitudinal stress of the gasifier | $= \sigma_{t_2} = \frac{296}{2} = 148$ MPa <br> Longitudinal stress of the gasifier is 148 MPa | $\sigma_{t_2} = \frac{\sigma_{t_1}}{2}$ | (4) |
| Maximum shear stress of the gasifier | Maximum principal stress $=$ hoop stress $(\sigma_{t_1})$ <br> Minimum principal stress $=$ longitudinal stress $(\sigma_{t_2})$ <br> $= \frac{296-148}{2} = 74$ MPa <br> Maximum shear stress of the gasifier is 74 MPa | Maximum shear stress $=$ <br> $\tau_{\max} = \frac{\sigma_{t_1} - \sigma_{t_2}}{2}$ | (5) |
| Working or design stress | Yield point stress for steel $= 370$ MPa (53,700 psi) <br> Working or design stress $=$ <br> $\frac{370}{4} = 92.5$ MPa <br> Working or design stress $= 92.5$ MPa | Factor of safety $=$ <br> $\frac{\text{Yield point stress}}{\text{Working or design stress}}$ | (6) |

**Table 1** (continued)

| Design parameters | Analysis | Equation | S/N |
|---|---|---|---|
| Heat required to gasify the feedstock | Mass of feedstock $= m_f = 2$ kg <br> Specific heat capacity of plum seed <br> $C_p = 3.73$ (kcal/kg °C) <br> $= 15{,}616.764$ (J/kg °C) <br> Change in temperature $=$ <br> $\Delta T = (500 - 30)$ °C $= 470$ °C <br> $= Q_m = 2 \times 15{,}616.764 \times 470$ <br> $= 14{,}679{,}758.2$ J or 3506.2 kcal <br> Heat required to gasify the feedstock $=$ <br> $14{,}679{,}758.2$ J | $= Q_m = m_f C_p \Delta T$ | (7) |
| Minimum heat required for gasification | Mass of feedstock $= m_f = 2$ kg <br> Heat of combustion of plum seed $=$ <br> $h_c = 21{,}210{,}000$ J/kg <br> $= Q_{mc} = 2 \times 21{,}210{,}000 = 42{,}240{,}000$ J <br> Minimum heat required for gasification $=$ <br> $42{,}240{,}000$ J | $= Q_{mc} = m_f h_c$ | (8) |
| Power required for gasification | $= \frac{42{,}240{,}000}{3600} = 11{,}733.333$ W <br> Power required for gasification $=$ <br> $11{,}733.333$ W | $= \frac{Q_{mc}}{3600}$ | (9) |
| Thickness of the reactor | Design pressure $= P_i = 10$ bar $=$ <br> $10 \times 10^5$ N/mm$^2 = 10 \times 10^5$ MPa <br> Internal radius $= R_i = 250$ mm <br> Corrosion allowance $= C_a = 3$ mm <br> Design tensile stress $=$ <br> $\sigma_d = 92.5$ MPa $= 92.5 \times 10^6$ Pa <br> Joint efficiency $= E = 0.9$ <br> $= t_r = \frac{10 \times 10^5 \times 250 + 3}{92.5 \times 10^6 \times 0.9 - 0.6 \times 10 \times 10^5} =$ <br> $3.02$ mm <br> Thickness of the reactor $= 3.02$ mm | $= t_r = \frac{P_i R_i + C_a}{\sigma_d E - 0.6 P_i}$ | (10) |
| Determination of volume of burning chamber | $D =$ diameter of the burning chamber $=$ <br> $0.304$ m <br> $h =$ height of the burning chamber $=$ <br> $0.855$ m <br> $V = \dfrac{3.142 * 0.304^2 * 0.855}{4}$ <br> $V = \dfrac{0.2482}{4}$ <br> $V = 0.062$ m$^3$ | $V = \frac{\pi d^2 h}{4}$ | (11) |

**Table 1** (continued)

| Design parameters | Analysis | Equation | S/N |
|---|---|---|---|
| Determination of heat load | $M$ = mass of substance in kg = 2 kg<br>$C_p$ = specific capacity of feedstock = 1810 J/kg/K<br>$\Delta t$ = change in temperature of cold fluid = $(9-5)\,°C = 4\,°C$<br><br>$Q = 2*1810*4$<br>$Q = 14{,}480$ J<br>$Q = 14.5$ kJ | Heat load $(Q) =$<br>$M*C_p*\Delta t$ | (12) |
| Determination of logarithm mean temperature difference (LMTD) | | $\text{LMTD} = \dfrac{\Delta T_1 - \Delta T_2}{\ln\left(\frac{\Delta T_1}{\Delta T_2}\right)}$ | (13) |
| Parallel flow | The parallel flow was established using Eq. (14)<br>$\Delta T_1$ = Temperature of hot fluid entering − Temperature of cold fluid entering<br>$\Delta T_2$ = Temperature of hot fluid existing − Temperature of cold fluid existing<br><br>$\text{LTMD} = \dfrac{(24)-(26)}{\ln\left(\frac{24}{26}\right)}$<br><br>$\text{LMTD} = \dfrac{-2}{\ln(0.9231)}$<br><br>$\text{LMTD} = \dfrac{-2}{-0.0800}$<br>$\text{LMTD} = 25\,°C$ | $\text{LMTD} = \dfrac{(29-5)-(35-9)}{\ln\left(\frac{29-5}{35-9}\right)}$ | (14) |
| Counter flow | $\Delta T_1$ = Temperature of hot fluid entering − Temperature of cold fluid existing<br>$\Delta T_2$ = Temperature of hot fluid existing − Temperature of cold fluid entering<br><br>$\text{LTMD} = \dfrac{(20)-(30)}{\ln\left(\frac{20}{30}\right)}$<br><br>$\text{LMTD} = \dfrac{-10}{\ln(0.6670)}$<br><br>$\text{LMTD} = \dfrac{-10}{-0.4054}$<br>$\text{LMTD} = 24.6670\,°C$<br>$\text{LMTD} = 25\,°C$ | $\text{LMTD} = \dfrac{(29-9)-(35-5)}{\ln\left(\frac{29-9}{35-5}\right)}$ | (15) |

**Table 1** (continued)

| Design parameters | Analysis | Equation | S/N |
|---|---|---|---|
| Multiple shell and tube | $F_T$ = Correction factor = 0.9 (0.9 was used for the steady operation of the exchangers)<br><br>Recall that $\frac{\Delta T_1 - \Delta T_2}{\ln\left(\frac{\Delta T_1}{\Delta T_2}\right)} = 25$<br><br>So, LMTD = 25 * 0.9<br>LMTD = 22.5 °C | $\text{LMTD} = \frac{\Delta T_1 - \Delta T_2}{\ln\left(\frac{\Delta T_1}{\Delta T_2}\right)} * F_T$ | (16) |
| True temperature difference | $\Delta t$ = True temperature difference<br>$F_T$ = Correction factor = 0.9<br><br>$\Delta T_{\text{LMTD}} = 25$<br>$\quad \Delta t = 0.9 * 25$<br>$\quad \Delta t = 22.5$ | $\Delta t = F_T * \Delta T_{\text{LMTD}}$ | (17) |
| Determination of surface area | $\Delta d_o$ = Tube outside diameter = 12 mm<br>$L$ = Length of tube = 110 mm<br>$A' = 3.142 * 12 * 110$<br>$A' = 4147.44$ mm$^2$<br>$A' = 0.00415$ m$^2$ | $A' = \pi * \Delta d_o * L$ | (18) |
| Surface area of tubes | $Q = 14{,}480$ J<br>$U_d = 200$ (overall $U_d$ is between 200 and 500, by Kern [16])<br>$\Delta t = 22.5$<br><br>$A = \dfrac{14{,}480}{200 * 22.5}$<br>$A = \dfrac{14{,}480}{4500}$<br>$A = 2.1452$ m<br>$A = 2.15$ m | $A = \frac{Q}{U_d * \Delta t}$ | (19) |
| Clearance | The baffle spacing is usually chosen to be within 20–100% of the shell inside diameter<br>$P_t$ = pitch, 1.25 * 12 = 15 mm<br>1.25 = minimum tube pitch (TEMA standard)<br>12 = tube outer diameter<br>$d_o = 12$ mm<br>$C = 15 - 12$<br>$C = 3$ mm<br>The clearance is 3 mm | Clearance, $C = P_t - d_o$ | (20) |

(continued)

**Table 1** (continued)

| Design parameters | Analysis | Equation | S/N |
|---|---|---|---|
| Shell area | $A_s$ = Shell area<br>$B$ = Baffle spacing = 203.2 mm<br>$C$ = Clearance = 3 mm<br>$D_s$ = Shell internal diameter = 100 mm (assumed)<br>$P_t$ = Pitch = 15 mm<br><br>$A_s = \dfrac{203.2 * 3 * 100}{15}$<br>$A_s = \dfrac{60,960}{15}$<br>$A_s = 4064$ mm<br>$A_s = 4.06$ m | $A_s = \dfrac{B*C*D_s}{P_t}$ | (21) |
| Determination of mass velocity $G_s$ | $G_s$ = Mass Velocity<br>$M_s$ = Mass flow rate on the shell side = 2 kg/s<br>$A_s$ = Shell area = 4.06 m<br><br>$G_s = \dfrac{2}{4.06}$<br>$G_s = 0.4926$<br>$G_s = 0.5$ kg/s | $G_s = \dfrac{M_s}{A_s}$ | (22) |
| Determination of equivalent diameter of shell side | $D_e$ = Equivalent diameter of shell side = ?<br>$P_t$ = Pitch = 15 mm<br>$d_o$ = Tube outside diameter = 12 mm<br><br>$D_e = 4 * \left( \dfrac{15 * 15 - \frac{3.142*12*12}{4}}{3.142 * 12} \right)$<br>$D_e = 4 * \left( \dfrac{225 - \frac{452.448}{4}}{37.704} \right)$<br>$D_e = 4 * \left( \dfrac{225 - 113.112}{37.704} \right)$<br>$D_e = 4 * \left( \dfrac{111.888}{37.704} \right)$<br>$D_e = 4 * 2.9675$<br>$D_e = 11.87$ mm | $D_e =$<br><br>$4 * \left( \dfrac{P_t * P_t - \frac{\pi * d_o * d_o}{4}}{\pi * d_o} \right)$ara> | (23) |

**Table 1** (continued)

| Design parameters | Analysis | Equation | S/N |
|---|---|---|---|
| Determination of Reynold's number | $R_e$ = Reynold's number<br>$G_s$ = Mass Velocity = 0.5 kg/s<br>$D_e$ = Shell side diameter = 11.87 mm<br>$\mu$ = Shell fluid dynamic viscosity at the average temperature = 1.3059 °C<br><br>$R_e = \dfrac{0.5 * 11.87}{1.3059}$<br>$R_e = \dfrac{5.935}{1.3059}$<br>$R_e = 4.5448$ | $R_e = \dfrac{G_s - D_e}{\mu}$ | (24) |



**Fig. 2** **a** Collected plum seed **b** the pulverized *Spondias mombin* (plum seed)

ii. **Metal cutting**: In electric hand metal cutting machine, also known as a hand cutter or angle grinder, the metal sheet and angle irons were cut along the prescribed lines. This is accomplished via the machine by using cutting disc.

iii. **Rolling and Folding**: The cylindrical-shaped parts, such as the inner and outer layers of the combustion chamber, were sent to a metal sheet rolling machine for rolling after being cut to size. An electric/hydraulic bending machine was used for folding a few pieces into cylindrical shapes as shown in Fig. 3a.

iv. **Welding**: With the help of an arc welding machine and Gauge 12 mild steel electrode, all of the cut and disjointed members were welded together.

v. **Grinding**: The angles of the welded surfaces were smoothed with a cutting angle grinder. This was accomplished by attaching a grinding disc/stone to the machine.

vi. **Finishing and Painting**: Body filler was used to fill up the grinded surfaces and joints. Emery papers, also known as sandpapers, were used to scrub the

**Fig. 3** **a** Outer and inner layers of the combustion chamber. **b** Lagging with fibre glass. **c** Fabricated and assembled gasifier system

body-filled surfaces. With the help of an air compressor machine, all parts of the machine were painted blue. During and immediately after painting, all necessary precautions were performed. The result of the whole fabrication process is shown in Fig. 3a–c.

## 3 Results and Discussion

The performance evaluation of the system was carried out, and the following parameters were obtained.

### 3.1 Start-Up Time (ST)

This is the amount of time it takes to ignite the feedstock in the burning chamber and produce gas that can be condensed into liquid [19]. This parameter was calculated from the moment the heater was turned on and heat was applied to the feedstock in the reactor until gas was created and visible as a white flame escaping from the reactor. The start-up time is 70 min at temperature range of 100 and 112 °C. Start-up time = 70 min = 1 h 10 min = 1.17 h.

### 3.2 Operating Time (OT)

This is the time from when the gasifier starts producing gas and the gas is cooled through the condenser back to liquid until the process is complete, and no more liquid is obtained. This lasted for 15 min. Operating time = 15 min = 0.167 h.

### 3.3   Total Operating Time (TOT)

This is the duration from the time feedstock is heated up until no more liquid is produced in the gasifier. Basically, it is the sum of the start-up time and the operating time of the gasifier as depicted in Eq. (26).

$$\text{Total operating time} = \text{Start-up time} + \text{Operating time}$$
$$\text{Total operating time} = 70\ \text{min} + 15\ \text{min} = 85\ \text{min or 1 h 25 min} \tag{26}$$

### 3.4   Fuel Consumption Rate (FCR)

The equation for fuel consumption rate is presented in Eq. (27). This is the weight of feedstock used in operating the gasifier divided by the operating time [20].

$$\text{Fuel consumption rate} = \frac{\text{Weight of the feedstock used (kg)}}{\text{Operating time (h)}}$$
$$\text{Fuel consumption rate} = \frac{2}{0.167} = 11.98\ \text{kg/h} \tag{27}$$

The maximum pressure in the reactor was obtained as 0.05 bar = 5000 Pa, and the quantity of the liquid fuel produced was 10 ml.

### 3.5   Specific Gasification Rate (SGR)

The specific gasification was computed using Eq. (28). SGR is the amount of feedstock used per unit time per unit volume of the reactor.

$$\text{Specific gasification rate} = \frac{\text{Weight of feedstock used (kg)}}{\text{Reactor area (m}^2) \times \text{Operating time (h)}}$$
$$\text{Specific gasification rate} = \frac{2}{0.4 \times 0.167} = 24.94\ \text{kg/m}^2\ \text{h} \tag{28}$$

### 3.6   Combustion Zone Rate (CZR)

This is the length of the reactor per unit time

$$\text{Combustion zone rate} = \frac{\text{Length of reactor (m)}}{\text{Operating time (h)}}$$

$$\text{Combustion zone rate} = \frac{0.8}{0.167} = 4.7 \text{ (m/h)} \tag{29}$$

## 4 Conclusion

- In future, the world's deposition of fossil fuels will soon run out, and evidently, the cost of fuel has been increasing drastically over the years as the demand for conventional fuel is increasing daily. We have a sharp shortage of fuel as prices rise every day.
- On the other hand, biomass is cheap and abundantly available everywhere in the world. As we have shown with this research, fuel production from gasification of *S. mombin* is a promising alternative to solve these perennial fuel crises.
- Another fact shown through the analysis carried out on the fuel produced from gasification of *S. mombin* is that it has a low moisture content (10.21% which is far lower than that of coal which is 25% and 20% for lignite and anthracite coal, respectively), hence giving it a good heating value and energy conversion rate coupled with the locally available materials used for the fabrication of this energy conversion system.

## References

1. Natarianto I, Simikins BJ, Kumar A, Huhnke R (2020) Economics of distributed power generation via gasification of biomass and municipal solid waste. Energies 13:3703
2. Alka DK, Vinod AM (2019) Co-gasification of coal and biomass an emerging clean energy technology, status and prospects of development I Indian context. Int J Min Sci Technol 29(2)
3. Ikumapayi OM, Akinlabi ET, Adedeji PA, Akinlabi SA (2021) Preparation, characterization, image segmentation and particle size analysis of cow bone powder for composite applications. In: Trends in manufacturing and engineering management. Lecture notes in mechanical engineering, pp 273–283. https://doi.org/10.1007/978-981-15-4745-4_25
4. Levine JS, Isis F, Daniel JS, Grant B, Robert MD (2015) National energy technology: methodology for estimating the prospective $CO_2$: storage resource of shales at the national and regional scale
5. Oyinbo ST, Ikumapayi OM, Jen TC, Ismail SO (2020) Experimental and numerical prediction of extrusion load at different lubricating conditions of aluminium 6063 alloy in backward cup extrusion. Eng Solid Mech 8(2):119–130. https://doi.org/10.5267/j.esm.2019.10.003
6. Panda AK, Singh RK, Mishra DK (2011) Thermolysis of waste plastics to liquid fuel: a suitable method for plastic waste management and manufacture of value added products—a world prospective. Renew Sustain Energy Rev 14(1):233–248
7. Bhattacharya SC, Hla SS, Leon MA, Weeratunga K (2005) An improved gasifier stove for institutional cooking. Asian Institute of Technology, Thailand

8. Afolalu SA, Ikumapayi OM, Ogedengbe TS, Emetere ME (2021) Performance assessmentof the developed flux powder on the tensile and hardness properties of steels joints using TIG-welding. [Rev Compos Matér Av] J Compos Adv Mater 31(3):153–157. https://doi.org/10.18280/rcma.310306

9. Imeh EO, Mohammed-Dabo IA, Ameh AO, Okoduwa SIA, Fasanya OO (2017) Production and characterization of biomass briquettes from tannery solid waste. MDPI (Recyling) 2(17):1–19

10. Adeoti OM, Dahunsi OA, Awopetu OO, Oladosu KO, Ikumapayi OM (2019) Optimization of clay-bonded graphite crucible using D-optimal design under mixture methodology. Int J Sci Technol Res 8(07):444–461

11. Sonawane Y, Shindikar M, Khaladkar M (2015) Use of catalyst in pyrolysis of polypropylene waste into liquid fuel. Int Res J Environ Sci 4(7):24–28

12. Khurmi RS, Gupta JK (2005) Machine design. In: Handbook of machinery dynamics, issue I, p 11

13. Kumar DS (2013) Heat and mass transfer. S. K. Kataria & Sons, New Delhi

14. Yadav AD, Bhupendra G, Mukesh P (2013) Performance analysis of the constructed updraft biomass gasifier for three different biomass fuels. Int J Mod Eng Res 3(2):56–67

15. Hossain A, Hassan MR, Islam MR (2014) Design fabrication and performance study of a biomass solid waste pyrolysis system for alternative liquid fuel production. Global J Reserve Eng 14(5)

16. Kern DQ (1965) Process heat transfer, Int. edn. McGraw-Hill Book Company; Dutta BK. Heat transfer-principles and applications, 1st edn. PHI Pvt. Ltd., New Delhi

17. Mulaba-Kapinga D, Nyembwe KD, Ikumapayi OM, Akinlabi ET (2020) Mechanical, electrochemical and structural characteristics of friction stir spot welds of aluminium alloy 6063. Manuf Rev 7(25):1–15. https://doi.org/10.1051/mfreview/2020022

18. Aladesanmi VI, Fatoba OS, Akinlabi ET, Ikumapayi OM (2021) Regression analysis of hardness property of laser additive manufactured (LAM) Ti and $TiB_2$ metal matrix composite. Mater Today Proc 44(Part 1):1249–1253. https://doi.org/10.1016/j.matpr.2020.11.252

19. Ates F, Norbert M, Nikolett B (2013) Comparison of real waste (MSW and MPW) pyrolysis in batch reactor over different catalysts. Part I: product yields, gas and pyrolysis oil properties. Bioresour Technol 133:443–454

20. Yinesor G (2008) Gasification of woodchips and hazelnut shells in a downdraft gasifier. FP6 bigpower SSA project. Biogas tech workshop, 9–11th Apr 2008, Gebze, Turkey

# Impact and Hardness Behaviours of Heat-Treated Aluminium 6101 Alloy Quenched in Different Waste Media

O. M. Ikumapayi, O. L. Rominiyi, M. O. Ajisafe, S. A. Afolalu, O. S. Fatoba, and E. T. Akinlabi

**Abstract** Heat treatment process consists of a series of operations that include heating at a specific rate, soaking at a specific level for a long of time, and cooling at a specific rate. The primary goal of this research is to analyse how heat treatment affects the microstructure and mechanical properties of aluminium alloys 6101. The selected quenching media (spent engine oil, coconut juice, air cool, and sugar cane juice) were hence selected as they have been known to increase the general mechanical properties of aluminium alloy 6101. The impact and hardness properties of the heat-treated samples were studied, and their microstructural characterizations were obtained. It was established that from the results obtained and their discussions, impact strength increases as the annealing temperature increases, while hardness of the samples reduced with increase in annealing temperature. Air cooled has a higher impact strength than sugar cane juice cool, while sugar cane juice cool outperformed engine oil medium, and engine oil medium outperformed coconut juice medium.

**Keywords** Aluminium alloy 6101 · Air · Coconut juice · Spent engine oil · Sugar cane juice

## 1 Introduction

The heat treatment process consists of a series of operations that include heating at a specific rate, soaking at a specific level for a long of time, and cooling at a specific rate. The primary goal of this research is to analyse how heat treatment affects the microstructure and mechanical properties of aluminium alloys [1]. The proposed

O. M. Ikumapayi (✉) · O. L. Rominiyi · M. O. Ajisafe · S. A. Afolalu
Department of Mechanical and Mechatronics Engineering, Afe Babalola University, Ado, Nigeria
e-mail: ikumapayi.omolayo@abuad.edu.ng

O. S. Fatoba · E. T. Akinlabi
Department of Mechanical Engineering Science, University of Johannesburg, Johannesburg, South Africa

E. T. Akinlabi
Pan African University of Life and Earth Sciences Institute, Ibadan, Nigeria

methodology of this research project on aluminium alloy 6101 involves strengthening by heat treatment. This process comprises solution heat treatment, quenching and age hardening, annealing, normalizing, ageing, etc. This is then followed by the characterization processes. The aim is to obtain a desirable microstructure to achieve predetermined properties. The heat-treating process is a method of heating and cooling metals in a sequence of operations that prevents the metal from being molten. The main goal of heat treatment is to improve a metal's utility by altering or repairing its mechanical properties. Heat treatment can also improve the strength, hardness, and impact resistance of a metal. Although heat treatment can soften and increase the ductility of metals, one important drawback is that no single heat-treating process can provide all of these properties [2, 3]. Except in its pure state, aluminium is a white, nonferrous, shiny metal that is generally light in weight and exceptionally corrosion resistant. It is non-magnetic, ductile, and malleable. Aluminium alloys, which are utilized in aircraft building, are made up of copper, magnesium, and manganese combined with variable amounts of other metals [4]. Aluminium alloy's lightweight performance offers great advantage in transport applications such as buses, aerospace, trains, cars, and ships. The excellent feature of the metal helps give automotive and other transport users improved driving performance as well as an increase in fuel economy and reduction of emissions. A common significant advantage of aluminium alloy is its resistance to corrosion. This characteristic is valuable for products used in architecture, civil engineering, heat exchangers, construction, transport, and many other applications [5]. Heat treatment is readily accepted by the majority of aluminium alloys. This technique comprises heating the alloy to a predetermined temperature, maintaining it there for a predetermined duration, and then cooling the component to ambient temperature or below. A bigger proportion of the metal's components solidify during the heating process. Rapid quenching maintains this state, resulting in a significant improvement in mechanical performance [6]. Aerospace and electrical fixtures as well as electronics are symbolic uses of the 6101-aluminium alloy. They are also commonly used in automatic components of equipment, precision machining, mould making, electronics and precision instruments, SMT, solder carriers for PC boards, etc. [7].

- Aerospace: 6101 aluminium alloy can be used to manufacture skins for planes, fuselage plates, beams, and rotors.
- Transportation: Aluminium alloy 6101 is also used for vehicles, metro cars, train commuter cars, construction components for high-speed passenger cars, doors and windows, racks, parts for vehicle engines, air conditioners, radiators, body panels, wheels, and structures for boat.
- Packaging: Aluminium alloy 6101 is often used in the form of thin plates and foils, rendered into containers, lids, and books as metal packaging products.
- Printing: It is used mainly to produce PS plates. A modern form of material for the printing industry is aluminium-based PS plates. They are used for printing and automated plate making.

Alloy 6101 is primarily used in the design of frames, doors and windows, suspended walls, wire curtains, perforated sheet metal, decorative surfaces, etc., such

as separate architectural windows and doors. Aluminium alloy 6101 is an aluminium alloy with magnesium and silicon, with traces of manganese and chromium, in sheet and plates. It is highly resistant to corrosion and as a result, it is mainly utilized in marine application and also components of structure in transportation and military applications due to its exceptional performance in extreme conditions [8]. With the sensitization temperature and time, the alloy's mechanical and chemical properties deteriorate. Its chemical properties deteriorate as a result of magnesium-rich particles precipitating at the grain boundary, while its mechanical properties deteriorate as a result of softening caused partly by a reduction in magnesium core and partly by recrystallization at elevated temperatures [9, 10]. Aluminium alloys are used in a broad spectrum of load bearing applications. The atomic mass of aluminium is 26.9815 g/mol, and its density is 2.7 g/cm$^3$. Aluminium is applied/widely used in aerospace, automotive, and marine industries due to its characteristic high strength-weight ratio, general corrosion resistance, and weldability [11]. 6XXX Al-Mg alloys, such as alloy 6101, because of their light weight, weldability, and corrosion resistance, have been commonly used in marine structures. These Al-Mg alloys, which have a variety of useful material properties, are in high demand for use in commercial and military swift sea transportation. While it is well understood that the strength of Al-Mg alloys increases as the Mg content increases, increasing the temperature during the annealing process reduces the strength of Al-Mg alloys [12]. Furthermore, although increasing Mg content can improve strength, it can also lead to a reduction in corrosion resistance. Most engineering materials' mechanical properties, including corrosion behaviour, can be effectively modified by altering their microstructures using various heat treatment procedures, as has long been known. The aluminium 6101 alloy is well known for its exceptional performance in harsh conditions.

## 1.1 Purpose of Heat Treatment

Heat treatment is a process that involves heating and cooling a metal or alloy in order to improve or change its physical and mechanical properties. Hardening is the process of increasing a metal's hardness, resulting in a tougher, more durable item. Alloys were heated to temperatures above the material's critical transition temperature and cooled quickly enough to allow the material to solidify into a much harder, stronger structure [13]. Heat treatment is used to bring in desired improvements in the metallurgical composition and properties of metal components. The differences in volume fraction, shape, scale, and distribution of precipitated particles control properties as well as variations in temperature and time, which are all influenced by the structure's initial state. In wrought products, the initial structure can range from unrecrystallized to recrystallized, with only minor strain from quenching after solution heat treatment. These variables, such as precipitation time and temperature, have an impact on the final structure and mechanical properties. Process details must be established and controlled carefully for each type of product to ensure the desired final characteristics [13].

Heat treating, in a broad context, refers to any cooling or heating operation performed on a metal component with the aim of changing the metallurgical composition or residual stress condition aluminium 6101 alloy is a heat-treatable alloy. They are alloys in which, after specific operations must have been carried out, the strength and hardness of the precipitation-hardenable wrought and cast alloys are increased. Heat treatment operations, on the other hand, can be accomplished by annealing and ageing. Most heat treatment operations are designed to regulate strength and ductility. Maximum strength is also obtained by precipitative hardening at the expense of ductility in AlMgSi and associated alloys. Annealing can improve ductility at the cost of power [14].

### 1.1.1 Annealing

The aluminium 6101 alloy is annealed at 413 °C (775 °F) for 3 h before being cooled in air at 10–260 °C (50–500 °F) each hour. After cold operating at 344 °C (650 °F) and air in cooling, the stress relief annealing mechanism can be used. Annealing treatments carried out on several types of aluminium alloys are employed based on respective different objectives [15, 16]. Two forms of annealing heat treatment processes are full and partial annealing. Because different dislocation configurations in the matrix and the second phase interface have an impact on mechanical and corrosion resistance capabilities, annealing temperature and duration have been optimized to improve these qualities [17, 18]. The goal of annealing is to alter a material's physical and frequently chemical qualities to increase ductility and reduce stiffness, making it simpler to work with. It involves heating a substance over its recrystallization temperature, maintaining it there for a set amount of time, and then cooling it [19, 20].

### 1.1.2 Solution Heat Treatment

The solution heat treatment process is the first step in the heat treatment of aluminium alloys, which is a three-step process. The concept refers to the process of soluble phases dissolving. To fully benefit from the precipitation hardening reaction, a solid solution must first be developed. The aim of this step is to get as many of the soluble hardening elements in the alloy into solid solution as possible. These methods include soaking the alloy at a very high temperature for a long time, long enough to obtain a virtually homogeneous stable solution [21].

### 1.1.3 Quenching

The development of super-saturated alloys is referred to as quenching. In the heat treatment chain, this is the most important step. The key goal of this procedure is

to quickly cool the specimen to a lower temperature to protect the already formed stable solution formed at the solution heat-treating temperature [5, 14, 22].

### 1.1.4 Age Hardening

The ageing (age-hardening) process is a hardening process that involves the precipitation of the solute atoms either at an elevated temperature (artificial ageing or precipitation heat treatment or at room temperature (natural ageing). After completion of solution heat treatment and quenching operations, hardening is then achieved. Natural ageing is a process that is most often used in heavily alloyed members of the 6xxx wrought series, all 2xxx alloys that are almost always solution heat treated and quenched, and some 7xxx copper alloys [8, 23]. Several studies have attempted to sensitize 5xxx series aluminium alloys using IGC and SCC, with critical sensitizing temperatures of these alloys ranging from 450 to 550 °F [24, 25]. The selected quenchants (spent engine oil, coconut juice, air cool, and sugar cane juice) were hence selected as they have been known to increase the general mechanical properties of aluminium alloy 6101. The decision to use these quenching media was based on the fact that they are both cost efficient and environmentally friendly. Furthermore, oil is preferred to water as a quenching medium because it decreases the chance of distortion or splitting by cooling metals more uniformly and rapidly. The purpose of this study is to enhance the mechanical and electrochemical properties of 6101 Al-Mg alloys to increase their service life.

## 2 Materials and Methods

## 2.1 Materials

### 2.1.1 Metal Material

The metal material used for this study is aluminium alloy AA6101 which was cut into a rectangular shape of thickness 6 mm diameter, which was sectioned from 100 mm piece of the aluminium sample. The chemical composition of aluminium alloy 6101 is depicted in Table 1.

**Table 1** Typical chemical composition of aluminium alloy 6101

| Element | Content (%) |
|---|---|
| Aluminium/aluminium, Al | 98.9 |
| Magnesium, Mg | 0.60 |
| Silicon, Si | 0.50 |

### 2.1.2   Quenching Materials

The cooling media used in this research include abundant air cooling (AC), coconut juice (CJ), sugar cane juice (SG), and spent engine oil (EO) which may be considered subsequently as waste material have been proven, from results of previous research works, tend to improve the mechanical properties of aluminium alloy 6101 when used as quenching media. Air cooling is mostly considered as the best and most economic quenching medium for heat treatment of aluminium alloy.

## 2.2   *Methodology*

### 2.2.1   Strengthening by Heat Treatment

The heat treatment process is carried out to increase strength of the specimens. This is a three-step process which involves (1) solution heat treatment—this is the procedure used in order to obtain a solid solution. Since a solid solution is needed first, this method takes full advantage of the precipitation hardening reaction. The procedure involved soaking the aluminium 6101 alloy for 60 min (1 h) at a relatively high temperature, long enough to obtain a nearly homogeneous solid solution. (2) Age hardening (natural ageing): The already prepared aluminium samples were heat treated to an annealing temperature of 413 °C in a muffle furnace, and a stress relief annealing procedure was conducted after cold working at 344 °C, accompanied by cooling in air. This procedure is carried out in order to minimize pressures that could have been caused by machining operations. (3) Annealing process: After the above operations, the prepared samples were then heated to 250 °C, 350 °C, and 450 °C, respectively, for 60 min (1 h) of holding time. The samples were easily removed from the muffle furnace and quenched in various media, which include coconut water, sugar cane juice, air cooling, and spent engine oil.

### 2.2.2   Methods of Annealing

After machining of the samples, the samples were annealed in an electric furnace at temperatures ranging from 250 °C to 350 °C to 450 °C for each quenching medium before the experiments were carried out. It is held at these temperatures for a long enough period of time (1 h) to ensure complete homogeneity. Once the heater has been shut off, it slowly cools down inside the furnace. The specimen is then removed from the furnace after a fair period of steady heat loss, until the furnace temperature has reached the nominal room temperature.

### 2.2.3  Normalizing Process

As soon as the set of machined samples, each sample of the aluminium alloy was placed in the furnace and heated to temperatures between the ranges of 250 °C to 350 °C to 450 °C, respectively. Two (2) pairs of the control samples were normalized in air. The samples were held at these temperatures for 1 h (60 min) in order to complete the transformation process. They were later taken out of the furnace and placed in the open air to cool.

### 2.2.4  Ageing Process

Ageing process of aluminium alloys can be of both natural and artificial forms. In the natural ageing of aluminium alloys, the elements that dissolve the aluminium continued to precipitate out overtime after it has been solution heat treated. This allows the gains to lock into place, increasing the natural strength of the specimen. Some alloys can only harden to a certain degree, and not all alloys achieve adequate hardness from natural ageing at room temperature. This situation could be overcome by precipitation hardening, also known as artificial ageing.

## 2.3  Characterization of Quenched Materials

### 2.3.1  Hardness Testing

The hardness of the various quenched samples, as well as the control sample, was determined using a Brinell hardness tester with a 1.5 mm diameter. This was done to see how much a normal pointed indenter could penetrate a specific area in compliance with the ASTM E384 standard [4, 7, 22]. The specimens were brought into contact with the ball indenter under a preliminary minor load usually 10 kgf. Although the preliminary load is still applied, a 100 N main load is applied, resulting in increased penetration. The load lever was shifted from point A to point B to load the unit after safe precautions had been made; it was then left for 10 s before the hardness values were taken and recorded. The expression for Brinell hardness number is given in Eq. (1)

$$\text{BHN} = \frac{P}{\frac{\pi D}{2}[D - \sqrt{D^2 - d^2}}$$  (1)

where
  '$D$' is the indenter diameter
  '$d$' is the average indent diameter, and
  '$P$' is the applied load.

### 2.3.2 Impact Testing

The Charpy impact tester was used to determine how the samples acted under severe loading, as well as the impact intensity or energy needed to trigger sample for deformation or breakage. According to ASTM E23, the samples are machined into 55 mm × 10 mm × 6 mm Charpy specimens with a central V-notch. For each study, the exercise was performed three times, and the impact intensity (IS) was calculated by averaging the impact energies. The ASTM E23 standard was followed while testing specimens with a V-notch in the fusion region for the purpose of impact test fracturing. The Charpy effect tester was used in this study as an impact measure. This swinging hammer is suspended at an angle of 45° from the horizontal surface [5, 22]. When the arm is released during the test, it hammers the specimen directly on the opposite side of the notch, causing the specimen to break. The impact energy from the hammer can give a clear and visual indication of the material property such as toughness. The specimen which is being tested decelerates the movement of the swinging hammer by direct absorbent of the energy of the impact. The specimen was then positioned on the vice of the impact tester so that the notch was facing away from the hammer. The scale pointer was reset to 0, and safety concerns were taken into account. The release mechanism freed the pendulum, and the effect energy (E) was measured directly on the meter. The research was carried out on notched bar specimens that had been specially prepared. The heat treatment procedure was carried out on 6 mm thick aluminium alloy 6101 bars at varying annealed temperatures of 250 °C, 350 °C, and 450 °C, respectively, for the purpose of this study, and the impact test was carried out on the sample parts. Samples of the fractured materials for impact test are depicted in Fig. 1. The impact strength was then computed based on Eq. (2):

$$\text{Impact strength} = \frac{E}{A} \tag{2}$$

where

$E$ = the amount of energy required to bend or fracture the samples
$A$ = ligament cross-sectional area of the samples under testing in $m^2$

### 2.3.3 Microstructural Preparation

Before microstructural analysis was carried out, sample preparation such as grinding, polishing, and etching was carried out on the heat-treated and unheat-treated aluminium materials. Samples of heat-treated aluminium alloy were ground using silica carbide paper of different grit size on the grinding machine to obtain a smooth surface for metallographic analysis. The metallographic procedure employed during grinding involved selection of SiC paper of different grit varying from 320, 800, 1200, and 4000 with abundance of water for rinsing, and the operation was done

**Fig. 1** Images of fractured specimen after carrying out impact test

at 320 rpm with an applied load of 150 N for 30 s for each emery paper grit used. After the grinding comes polishing. The polishing was done on all the samples to a mirror finish surface. The essence is to remove contaminants, impurities, and scratches from the surface of the heat-treated materials before etching it. The process used for the polishing includes MD-Mol and OP-Chem for initial and final surface polishing, respectively. The suspension used was DiaPro Mol and OP-s for initial and final polishing, respectively. About 150 N applied force was initially used within 4 min while 90 N was applied thereafter at about 2.5 min at both 150 rpm. After the polishing comes etching. Etching was done to reveal the metallographic features after grinding and polishing of the samples; etching was done on the samples used for microstructural analysis. The etchant used is Weck's double etching cycle reagent. The samples were pre-etched for 1 min using 2 g of sodium hydroxide (NaOH) and 100 ml distilled water and immediately deepened in less than 15 s in 4 g of potassium permanganates (KMnO4), 1 g of NaOH, and 100 ml of distilled water [19, 20, 26]. The etchant attacked the grain boundaries and gave a clear image of the size of the grains. The etched samples were analysed under the microscope.

## 2.4 Microstructural Evolution Characterization

Olympus BX51M optical microscope was used for optical microscopy. The microstructures were observed using an Olympus BX51M camera. Olympus stream essential software was used to capture and process the digital output. Optical microscope was used to study the microstructural evolution of the samples of aluminium alloy materials. Images of the microstructural features for different quenching media were taken at a specified magnification on the optical microscope. The microstructural examinations were performed to reveal efficacy of bonding of quenching media on the heated-aluminium alloy.

## 3 Results and Discussion

### 3.1 Impact Test Results

The average energy absorbed by the fractured material in various quenching media is shown in Tables 2, 3, 4 and 5. It was established that Tables 2, 3, 4, 5, 6, 7, 8 and 9 demonstrate the impact test results for various quenching media, such as sugar cane juice cool, coconut juice cool, motor oil cooling, and air cooling, following annealing at various specified temperature of 250 °C–350 °C–450 °C. The impact strengths were computed using Eq. (2) for each medium at various temperatures.

From Fig. 2, it is observed that at an annealing temperature of 250 °C, sugar cane cooled medium yields the highest impact strength with the values of 23.131 J/m$^2$, while coconut juice quenching medium yields 19.697 J/m$^2$ followed by air cooled

**Table 2** Values of impact energy absorbed for samples quenched in coconut juice cool

| S/N | Temperature (°C) | Impact energy (J) | | | Average impact energy (J) |
|-----|------------------|------|------|------|---------------------------|
|     |                  | E1   | E2   | E3   |                           |
| 1   | 250              | 72   | 62   | 61   | 65.000                    |
| 2   | 350              | 87   | 96   | 78   | 87.000                    |
| 3   | 450              | 85   | 59   | 74   | 72.667                    |

**Table 3** Values of impact energy absorbed for quenched in sugar cane juice cool

| S/N | Temperature (°C) | Impact energy (J) | | | Average impact energy (J) |
|-----|------------------|------|------|------|---------------------------|
|     |                  | E1   | E2   | E3   |                           |
| 1   | 250              | 78   | 68   | 83   | 76.333                    |
| 2   | 350              | 68   | 88   | 70   | 75.333                    |
| 3   | 450              | 97   | 74   | 73   | 81.333                    |

**Table 4** Values of impact energy absorbed for samples quenched in engine oil

| S/N | Temperature (°C) | Impact energy (J) | | | Average impact energy (J) |
|-----|------------------|------|------|------|---------------------------|
| | | E1 | E2 | E3 | |
| 1 | 250 | 58 | 66 | 63 | 62.333 |
| 2 | 350 | 90 | 76 | 102.5 | 89.500 |
| 3 | 450 | 75 | 70.5 | 79 | 74.833 |

**Table 5** Values for energy absorbed for each samples normalized in air

| S/N | Temperature (°C) | Energy absorbed (J) | | | Average energy absorbed (J) |
|-----|------------------|------|------|------|-----------------------------|
| | | E1 | E2 | E3 | |
| 1 | 250 | 61 | 70 | 60 | 63.667 |
| 2 | 350 | 97 | 110 | 84 | 97.000 |
| 3 | 450 | 76 | 90 | 80 | 82.000 |

*Note* The geometrical properties of the metal were clearly defined, where the length of the specimen is 55 mm with a breadth of 10 mm. The cross-sectional area of the section is given as:
$A = L \times B \times h = 55 \times 10 \times 6 = 3300 \text{ mm}^2 = 3300 \times 10^{-3} \text{ m}^2$

**Table 6** The results of the impact strengths for samples quenched in coconut juice cool

| S/N | Temperature (°C) | Impact energy (J) $\left(E = \frac{E1+E2+E3}{3}\right)$ | Impact strength (J/m²) $\frac{E}{A}$ |
|-----|------------------|------------------|------------------|
| 1 | 250 | 65.000 | 19.697 |
| 2 | 350 | 84.300 | 25.545 |
| 3 | 450 | 72.667 | 22.020 |
| **Avg. impact strength** | | | **22.421** |

**Table 7** The results of the impact strengths for samples quenched in sugar cane juice cool

| S/N | Temperature (°C) | Impact energy (J) $\left(E = \frac{E1+E2+E3}{3}\right)$ | Impact strength (J/m²) $\frac{E}{A}$ |
|-----|------------------|------------------|------------------|
| 1 | 250 | 76.333 | 23.131 |
| 2 | 350 | 75.333 | 22.828 |
| 3 | 450 | 81.333 | 24.640 |
| **Avg. impact strength** | | | **23.533** |

**Table 8** The results of the impact strengths for samples quenched in spent engine oil cool

| S/N | Temperature (°C) | Impact energy (J) $\left(E = \frac{E1+E2+E3}{3}\right)$ | Impact strength (J/m²) $\frac{E}{A}$ |
|-----|------------------|------------------|------------------|
| 1 | 250 | 62.333 | 18.889 |
| 2 | 350 | 89.500 | 27.121 |
| 3 | 450 | 74.833 | 22.677 |
| **Avg. impact strength** | | | **22.896** |

**Table 9** The results of the impact strengths for samples normalized in air

| S/N | Temperature (°C) | Impact energy (J) $\left(E = \frac{E1+E2+E3}{3}\right)$ | Impact strength (J/m$^2$) $\frac{E}{A}$ |
|-----|------------------|---------------------------------------------------------|------------------------------------------|
| 1 | 250 | 63.667 | 19.293 |
| 2 | 350 | 97.000 | 29.394 |
| 3 | 450 | 82.000 | 24.848 |
| **Avg. impact strength** | | | **24.512** |

with 19.293 J/m$^2$ and the engine oil quenching medium recorded the least value of impact strength with 18.889 J/m$^2$.

From Fig. 3, it was observed that at an annealing temperature of 350 °C, air cooling medium yields a specimen with the highest impact strength of 29.394 J/m$^2$ than the other quenching media. It was noticed that EO yields 27.121 J/m$^2$ and CJ produces 25.545 J/m$^2$ and the least was SG with the impact strength of 22.828 J/m$^2$.

From Fig. 4, it was revealed that at an annealing temperature of 450 °C, air cooled (AC) medium yields a specimen with the highest impact strength of 24.848 J/m$^2$, while sugar cane cooled produced 24.64 J/m$^2$. It was noticed that at 450 °C, both AC and SG had almost the same values. The EO had an impact strength of 22.677 J/m$^2$ and CJ had 22.02 J/m$^2$.



**Fig. 2** Graph comparing impact strength at 250 °C
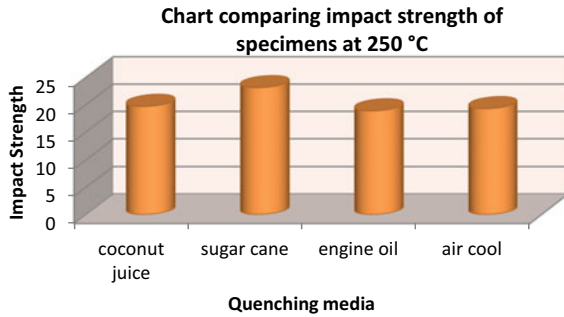


**Fig. 3** Graph comparing impact strength at 350 °C
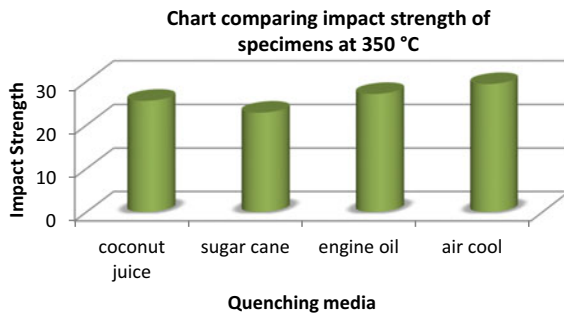
**Fig. 4** Graph comparing impact strength at 450 °C
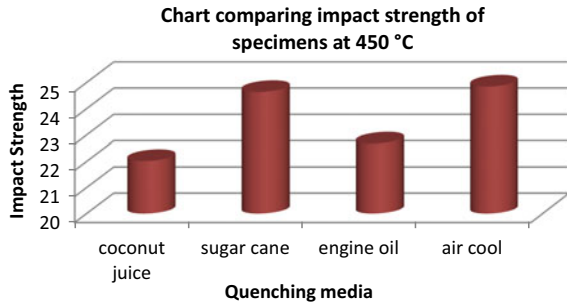


The average impact strength was higher in air cooling medium than sugar cane juice medium; sugar cane juice medium is higher than engine oil medium; and lastly, engine oil medium is higher than coconut juice medium. According to the derived results of impact strength in Table 9 for the specimens quenched in the different media, the 'air cool' form of quenching appears to be tougher and offer more resistance to fracture than any of the other quenching media. Air cooling has been known to be the best form of quenching during heat treatment procedure as they offer higher resistance to fracture. It was observed that the specimens quenched in air are stronger and more resistant to fracture than the others with average strength of 24.512 $J/m^2$.

From Table 7, 'sugar cane juice' as a quenching medium, from the derived results of impact strength, is the next most effective medium for quenching as it also appears to be tougher and offer more resistance to fracture than specimens quenched in engine oil and coconut juice. It was observed that the specimens quenched in 'sugar cane juice' are strong and more resistant to fracture with an average strength of 23.533 $J/m^2$.

Because engine oil cools slower than coconut water, the average impact strength was higher in engine oil medium (22.896 $J/m^2$) than in coconut juice medium (22.421 $J/m^2$). The graphical illustration of the comparison of different quenching media in Fig. 5 demonstrated this. At all annealing temperatures, air cooled specimens absorbed the most impact energy and were more ductile than specimens quenched in other media, and this was also supported by the work reported in [26, 27].

## 3.2   Hardness Test Results

The results for the Brinell hardness test conducted on heat-treated AA6101 quenched in spent engine oil (EO), cool in air (AC), sugar cane cool (SG), coconut juice (CJ), and control (C) samples are shown in Table 10. From the table, specimens quenched in 'engine oil' are seen to have higher hardness properties than the other quenching media at 350 and 450 °C, while specimens quenched in 'coconut juice' appear to have higher hardness properties than the other quenching media at 250 °C.

**Fig. 5** Graph of Charpy impact strength versus annealing temperature of the different quenching media
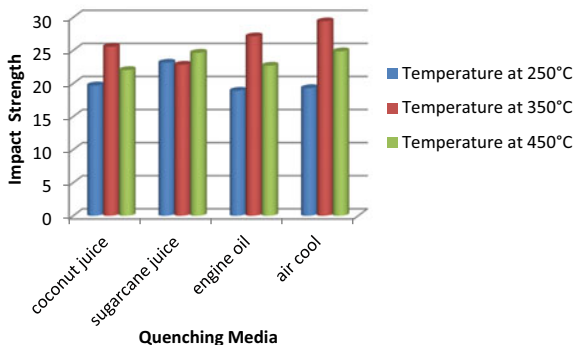


**Table 10** Result of AA6101 hardness test

| S/N | Medium/temperature | $BN_1$ | $BN_2$ | $BN_3$ | $(BHN) = \frac{BN_1 + BN_2 + BN_3}{3}$ |
|-----|--------------------|--------|--------|--------|----------------------------------------|
| 1 | EO250 at 250 °C | 65 | 75 | 75 | 72 |
| 2 | EO350 at 350 °C | 44 | 44 | 39 | 42 |
| 3 | EO450 at 450 °C | 39 | 39 | 39 | 39 |
| 4 | AC250 at 250 °C | 65 | 57 | 65 | 62 |
| 5 | AC350 at 350 °C | 39 | 29 | 39 | 36 |
| 6 | AC450 at 450 °C | 39 | 35 | 35 | 37 |
| 7 | SG250 at 250 °C | 57 | 75 | 57 | 63 |
| 8 | SG350 at 350 °C | 35 | 39 | 42 | 39 |
| 9 | SG450 at 450 °C | 29 | 29 | 39 | 32 |
| 10 | CJ250 at 250 °C | 75 | 88 | 65 | 76 |
| 11 | CJ350 at 350 °C | 32 | 39 | 39 | 37 |
| 12 | CJ450 at 450 °C | 39 | 35 | 35 | 37 |
| 13 | Control (C) | 57 | | 65 | 57 |

• **Diameter of indenter ($D$) = 1.6 mm * Load ($P$) = 100 kgf.**

From Fig. 6, it was noted that specimens quenched in coconut juice and spent engine oil appear to possess higher hardness values of 76 BHN and 72 BHN, respectively, than specimens quenched in sugar cane juice and those cooled in air with BHN of 63 and 62, respectively, at an annealing temperature of 250 °C.

It was established in Fig. 7 that specimens quenched in 'spent engine oil' appear to possess the highest hardness values of 42 HBN, while the one quenched in sugar cane juice had 39 HBN, coconut juice had 37 HBN, and those cooled in air had 36 HBN at an annealing temperature of 350 °C. Specimens quenched in 'sugar cane' also have higher hardness properties than those quenched in coconut juice and dry air.

Figure 8 revealed that specimens quenched in 'spent engine oil' appear to possess highest hardness values of 39 BHN, while coconut juice has 37 BHN, the specimens

**Fig. 6** Comparison of hardness of specimens at 250 °C
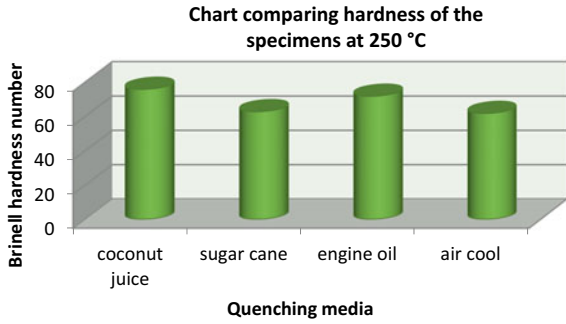


**Fig. 7** Comparison of hardness of specimens at 350 °C
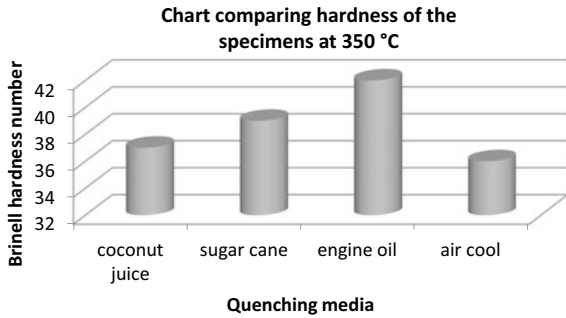
quenched in sugar cane juice have 32 BHN, and the one cooled in air has 37 BHN all at an annealing temperature of 450 °C. Specimens quenched in 'coconut juice' and 'dry air' are observed to have the same value of 37 as the Brinell hardness number.

According to the experimental results, and as shown in Table 10, the Brinell hardness number of the specimens decreases as the annealing temperature rises from 250 to 450 °C. This is comparable to Ikumapayi et al.'s observation that motor oil has greater hardness levels [5] as well as the report in [28]. The four media utilized improved the mechanical characteristics of the AA6101 samples when annealed at 250 °C.



**Fig. 8** Comparison of hardness of specimens at 450 °C
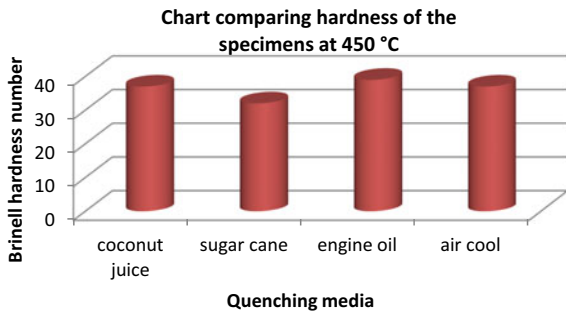
## 3.3   Microstructural Analysis Results

The optical micrograph of both unheated and heat-treated AA6101 is shown in Figs. 9, 10, 11, 12 and 13. The micrograph clearly reveals boundaries and grain size. It was noted that the grain sizes of all the heat-treated samples were almost the same with the untreated sample of AA6101. It was noticed that as the annealing temperatures are increasing, there was reduction in the grain sizes of the samples as noticed from Figs. 10 to 13. Thereafter, rapid cooling of the material using water quenching will avoid the formation of (θ). To put it another way, Cu particles will be confined, resulting in a super-saturated solid solution with the formula ($\alpha$). After that, it allows for homogenous nucleation. The motivating factor is significant consequence of the increasing cooling, resulting in a high rate of nucleation, and this is age hardening, as illustrated in Fig. 12 by the highly distributed particles obtained by raising the temperature for the second annealing phase to 350 and 4500 °C. Because the crystallites are tiny and close together, they will obstruct deformation and raise yield stress over time, resulting in a harder alloy. Because time and temperature are involved in the age-hardening process, if the specimen is left in the annealing furnace for extended periods of time, the grains will continue growing and the specimen will regain most of its ductility as the crystalizes will no longer function as a dislocation and cause any stresses on the crystal lattice, but it will try to eliminate them. With increasing annealing temperatures, the degree of recrystallization rose, particle size distribution became more uniform, and more recrystallized grains formed. After annealing at 350 °C, the microstructure was fine and homogenous, with an equiaxed grain structure. This indicates that the ideal annealing temperature for this material is about 350 °C.



**Fig. 9** Untreated micrograph of AA6101 aluminium alloy
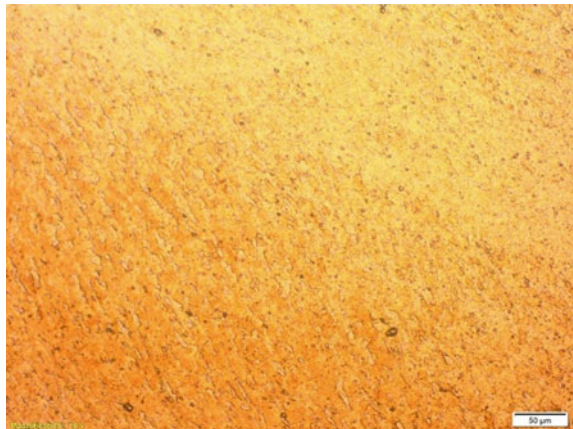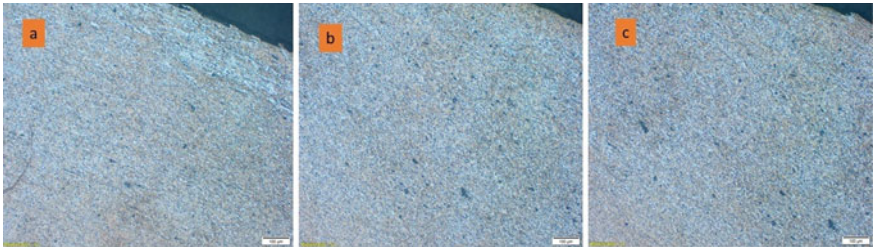
**Fig. 10** Micrograph of heat-treated AA6101 normalized in air **a** 250 °C, **b** 350 °C, and **c** 450 °C
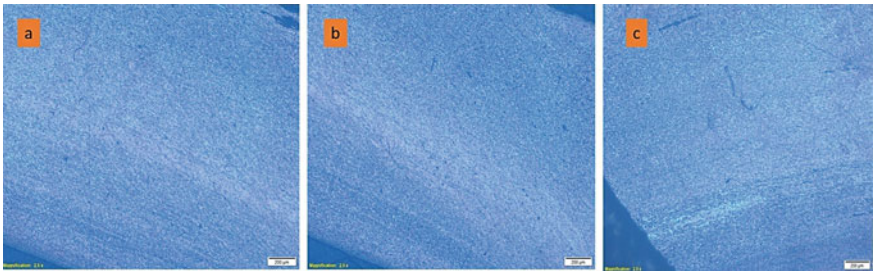


**Fig. 11** Micrograph of heat-treated AA6101 quenched in sugar cane water **a** 250 °C, **b** 350 °C, and **c** 450 °C
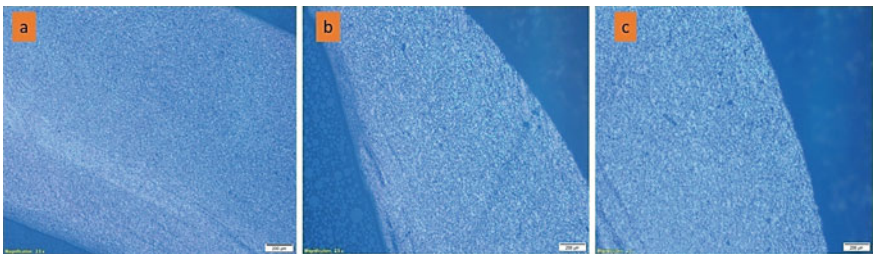


**Fig. 12** Micrograph of heat-treated AA6101 quenched in coconut water **a** 250 °C, **b** 350 °C, and **c** 450 °C
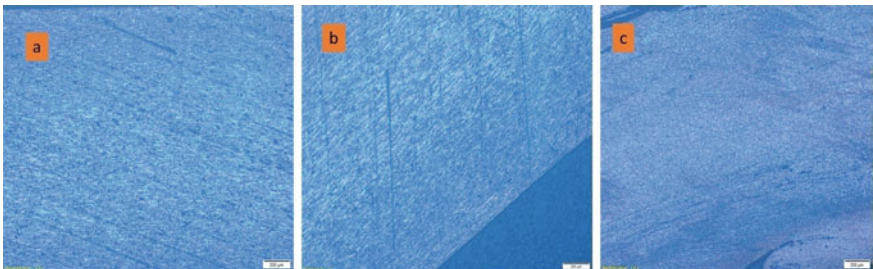


**Fig. 13** Micrograph of heat-treated AA6101 quenched in spent engine oil **a** 250 °C, **b** 350 °C, and **c** 450 °C

# 4 Conclusion

The following conclusions have been reached on the characterization of heat-treated aluminium alloy 6101 quenched in different waste media as a case study.

This research demonstrated how waste items such as sugar cane juice, coconut water, and used engine oil were employed as quenching media to improve the mechanical properties of AA6101. When quenched in the various mediums utilized, the aluminium alloy could harden. From the results obtained and their discussions, impact strength increases as the annealing temperature increases, while hardness of the samples reduced with increase in annealing temperature. Air cooled has a higher impact strength than sugar cane juice cool, sugar cane juice cool outperformed engine oil medium, and engine oil medium outperformed coconut juice medium. For heat-treated AA6101 samples subjected to impact or rapid load, the air cool medium is the best and most cost-effective quenching medium.

# References

1. Chester RJ, Polmear I (1983) The metallurgy of light metals. In: The metallurgy of light metals
2. ASM International, American Institute of Mining (1995) Acta materialia. CrossRef 59(1)
3. Baker H (1998) ASM handbook: alloy phase diagrams, vol 3. In: ASM handbook
4. Akinlabi ET, Ikumapayi OM, Bodunde OP, Adaramola BA, Uchegbu ID, Fatoba SO (2020) Impact of quenching on the hardenability of steels EN-3 (~1015), EN-8 (~1040) and EN-24 (~4340) during Jominy end quench technique. Int J Emerg Technol 11(5):290–297
5. Ikumapayi OM, Okokpujie IP, Afolalu SA, Ajayi OO, Akilabi ET, Bodunde OP (2018) Effects of quenchants on impact strength of single-vee butt welded joint of mild steel. In: IOP conference series: materials science and engineering, vol 391, no 012007. https://doi.org/10.1088/1757-899X/391/1/012007
6. Mudashiru L, Adeodu A, Awodoyin A, Bello A, Oloyede O, Aiyedun P (2020) Evaluation of impact and hardness properties of Al 6063-AgNPs composites produced by stir cast technique. In: IOP conference series: materials science and engineering, vol 805, no 1. https://doi.org/10.1088/1757-899X/805/1/012002
7. Ding F, Jia X, Hong T, Xu Y, Hu Z (2021) Influence of different heat treatment processes on plasticity and hardness of 6061 aluminum alloy. Cailiao Daobao/Mat Rep 35(8). https://doi.org/10.11896/cldb.19120115
8. Karuppusamy T, Velmurugan C, Thirumalaimuthukumaran M (2019) Experimental study on the mechanical properties of heat treated aluminium composites. Mater Res Expr 6(9). https://doi.org/10.1088/2053-1591/ab2ebb
9. Sankaran KK, Mishra RS (2017) Metallurgy and design of alloys with hierarchical microstructures. In: Metallurgy and design of alloys with hierarchical microstructures
10. Lin S, Nie Z, Huang H, Li B (2010) Annealing behavior of a modified 5083 aluminum alloy. Mater Des 31(3). https://doi.org/10.1016/j.matdes.2009.09.004
11. Yahaya SNM, Azmi II, Ng CH, Lai CF, Hashim MY, Adam A, Baehr R, Grote KH (2020) An overview on forming process and heat treatments for heat treatable aluminium alloy. J Adv Res Fluid Mech Therm Sci 70(1). https://doi.org/10.37934/ARFMTS.70.1.112124
12. Prillhofer R, Rank G, Berneder J, Antrekowitsch H, Uggowitzer PJ, Pogatscher S (2014) Property criteria for automotive Al-Mg-Si sheet alloys. Materials 7(7). https://doi.org/10.3390/ma7075047

13. Staley JT (1977) Heat treating of aluminum alloys. Technical paper. Society of Manufacturing Engineers EM
14. Rajaa SM, Abdulhadi HA, Jabur KS, Mohammed GR (2018) Aging time effects on the mechanical properties of Al 6061-T6 alloy. Eng Technol Appl Sci Res 8(4). https://doi.org/10.48084/etasr.2102
15. Afolalu SA, Ikumapayi OM, Emetere ME, Ongbali SO (2021) Investigation of mechanical properties and characterization of a joint using nano flux powder for a-tig welding. In: Material today: proceedings, vol 44, Part 1, pp 2879–2883. https://doi.org/10.1016/j.matpr.2021.01.091
16. Agarana MC, Akinlabi ET, Ikumapayi OM (2021) Dynamic analysis of rectangular aluminium plate under transverse loading using finite difference algorithm.Trends in mechanical and biomedical design, lecture notes in mechanical engineering, pp 223–229.https://doi.org/10.1007/978-981-15-4488-0_20
17. Campbell F (2008) Elements of metallurgy and engineering alloys. ASM Int
18. Bahrami A, Yazdan MM (2019) Modeling electrical resistivity of naturally aged Al–Mg–Si alloys. Metals 9(3):310. https://doi.org/10.3390/met9030310
19. Ku M-H, Hung F-Y, Lui T-S (2019) Examination of the high tensile ductility improvement in an As-solutionized AA7075 alloy with the aid of a friction stir process. Metals 9(2):196. https://doi.org/10.3390/met9020196
20. Fabrizi A, Capuzzi S, De Mori A, Timelli G (2018) Effect of T6 heat treatment on the microstructure and hardness of secondary $AlSi_9Cu_3(Fe)$ alloys produced by semi-solid SEED process. Metals 8:750. https://doi.org/10.3390/met8100750
21. Afolalu SA, Ikumapayi OM, Emetere ME, Ogedengbe TS (2021) Improvement of ASTM A53 steel durability using agrowastes as carburizing agent. Int J Integr Eng 13(6):50–61
22. Ikumapayi OM, Akinlabi ET, Fatoba SO, Kazeem RA, Afolabi SO, Adeoye AOM, Akinlabi SA (2021) Evaluation of fracture energy of aluminium alloy 1050-F and carbon steel EN-3 (~1015) 0.15% C at different temperatures gradient. In: Lecture notes in mechanical engineering, pp 150–168. https://doi.org/10.1007/978-981-16-3641-7_19
23. Essien EV, Udo UE (2016) Development and determination of the age hardening characteristics of Al-Mg-Si based alloy, B.Eng. Degree project submitted to the Department of Mechanical Engineering, University of Uyo, Uyo-Nigeria
24. Hassan SB, Aigbodion VS (2009) The effect of thermal ageing on microstructure and mechanical properties of Al-Si-Fe/Mg alloys. J Alloy Compd 486(1–2):309–314
25. Simar A, Bréchet Y, de Meester B, Denquin A, Pardoen T (2007) Sequential modeling of local precipitation, strength and strain hardening in friction stir welds of an aluminum alloy 6005A-T6. Acta Mater 55(18):6133–6143
26. Qiang RG, Stiller K, Hansen V, Oskarsson A, Danoix F (2002) Influence of aging conditions on the microstructure and tensile strength of aluminium alloy 6063. Forum Mater Sci 396–402:1211–1216
27. Callister W (2015) Materials science and engineering, 9th edn. John Wiley & Sons, NJ 07030, p 446, 603–608
28. Xuexuan X, Zhao Y, Yulong Y, Guangxu W, Xiaolong H (2016) Effects of various Mg/Si ratios on microstructure and performance property of Al-Mg-Si alloy cables. Institute for Materials Microstructure, Central South University, Changsha 410083, United States. https://doi.org/10.1016/J.MATCHAR.2016.07.011

# Investigation of Mechanical Properties of Torrefied Corncob and Rice Husk Briquettes: Modeling and Simulation

Segun E. Ibitoye, Rasheedat M. Mahamood, Tien-Chien Jen, and Esther T. Akinlabi

**Abstract** Energy security and a green environment have called for global concern in recent years. This is due to the increase in global population and unconscious human activities, which has led to the thickening of the infrared radiation layer, emission of greenhouse gases, and global warming. In this study, solid fuel briquette was manufactured from a blend of torrefied corncob and rice husk to mitigate the environmental problem associated with their disposal. Experimental, modeling, and simulation approaches were employed for the investigation. Feedstock samples were prepared and torrefied at 260 °C for 60 min, after which it was pulverized and screened into 1.7, 1, and 0.5 mm. Briquettes were produced at different blending ratios and compaction pressure, and gelatinized starch was used as a binding agent. The mechanical properties (compressive strength and shatter index) of the manufactured briquettes were investigated. Findings show that blending ratio and compaction pressure significantly influence the mechanical properties of the manufactured briquettes. Empirical models developed for 60, 80, and 100 kPa densification pressure were able to predict the trend of the mechanical properties of the manufactured briquettes. The models developed in this study found applications in future biomass briquettes production and product design.

**Keywords** Biomass · Briquette · Corncob · Empirical model · Mechanical property · Rice husk

S. E. Ibitoye (✉) · R. M. Mahamood · T.-C. Jen · E. T. Akinlabi
Department of Mechanical Engineering Science, Faculty of Engineering and the Built Environment, University of Johannesburg, 524, Auckland Park 2006, South Africa
e-mail: ibitoye.s@unilorin.edu.ng

S. E. Ibitoye
Department of Mechanical Engineering, Faculty of Engineering and Technology, University of Ilorin, PMB 1515, Ilorin, Nigeria

R. M. Mahamood
Department of Materials and Metallurgical Engineering, Faculty of Engineering and Technology, University of Ilorin, PMB 1515, Ilorin, Nigeria

E. T. Akinlabi
Pan African University for Life and Earth Sciences Institute, Ibadan, Nigeria

# 1 Introduction

The rising global population and technological advancement have significantly increased the worldwide energy demand. Depletion, unstable global market, non-renewable nature, and environmental implications of fossil fuel utilization have kindled the search for alternative and renewable sources of energy [1]. Many alternatives have been recognized, including tidal, geothermal, solar, wind, hydro, biomass, etc. Among the options, biomass has been documented to display sustainable characteristics [2]. Biomasses are abundantly available in different forms even in remote areas—energy crops, forest trees, sawmill residues, and agricultural residues. However, challenges are limiting the use of biomass, such as agricultural residues for energy generation. Examples are not limited to low bulk and energy densities, low calorific value, high moisture contents, transportation and handling problems, and ample storage space [3–5]. Commonly, farmers dump their residues in an open field or burn them openly, and these have caused several environmental threats to the people. The burning and dumping of agricultural residues in an open field have led to the emission of greenhouse gases, which causes global warming. The conversion of agricultural residues into usable energy will alleviate environmental challenges related to their disposal and advance the economy via employment generation [6].

To efficiently and effectively mitigate the challenges limiting biomass for solid fuel production, researchers recommend application of thermal pretreatment via torrefaction and densification technologies [2, 7]. Biomass densification process applies mechanical force on biomass feedstock to enhance bond formation and biomass density [8]. Biomass densification can be done with or without using a binding agent. Examples of biomass densification processes are briquetting, pelletizing, bailing, and cubing [2]. Densification quality is influenced by two main factors: process parameters and feedstock parameters. The process parameters include densification temperature, pressure, and additives (such as a binding agent), while the feedstock parameters include moisture content, particle size, etc. [9–12]. Torrefaction, on the other hand, is a thermo-chemical process of heating biomass in an inert atmosphere [13, 14]. Torrefaction influence the physical, energy, and chemical properties of biomass—it promotes the biomass hydrophobicity and grindability properties, enhances energy density and thermal properties, and reduces biomass moisture contents [10]. Given the unique advantage of torrefaction and densification, combining the two processes can manufacture solid fuel with enhanced mechanical and combustion properties.

Biomass densification and torrefaction processes have been explored and documented. Wilczyński et al. [9] investigated the effect of compaction conditions on the properties of fuel briquette made from pine sawdust. The optimum briquettes strength was obtained at a process temperature of 150 °C and 10% moisture content. A numerical model was also developed in the study for the prediction of the densification pressure. Yang et al. [10] study the main effect parameter on physicomechanical characteristics of *Pinus radiate* sawdust briquettes via torrefaction. Yang et al. submitted that densification pressure and moisture contents significantly influence the mechanical properties, while the effect of dwelling time was not noticeable. The

effect of feedstock blends on the properties of solid fuel has been investigated [15], and it was opined that feedstock blinding influences solid fuel's physical, mechanical, and combustion characteristics [3]. Boasiako and Acheampong [16] investigate the strength properties of sawdust briquettes, and it was concluded feedstock density substantially influences the strength properties of manufactured briquettes.

Given the foregoing, applying the combination of densification and torrefaction for briquettes production from agricultural residues will improve the global energy mix and enhance the green environment. Furthermore, the blending of biomass feedstock will augment biomass utilization and product properties. Therefore, this study aims to manufacture solid fuel briquettes from torrefied corncob and rice husk and investigate the shatter index and compressive strength properties for energy application. A numerical model was also developed to predict shatter and strength properties for future energy applications and product design.

## 2 Methods

The step-by-step approaches adopted in this study are discussed in this section.

### 2.1 Experimentation

The materials used for this study are corncob, rice husk, and cassava starch. The feedstock (corncob and rice husk) was obtained from maize and rice farm, located at Oro town, Kwara State, Nigeria, while the starch was collected from cassava processing factory, Gaa-Akanbi, Kwara State, Nigeria. The collected feedstock was sorted from unwanted substances, followed by a torrefaction process at 260 °C for 60 min. The torrefied feedstock was pulverized and screened into 1.7, 1, and 0.5 mm fines by the sieve analysis, followed by the densification process. The densification was carried out at different compaction pressure and blending ratios following the aggregate mix shown in Table 1. The feedstock was mixed using an electric mixer (Rico, model: YP103KM1511 000056) at 100 rpm for 5 min and transferred into the prepared mold for the compaction process. Gelatinized starch, 5% of the total blends, was utilized as the binding agent. After the compaction process, the manufactured briquettes were sun-dry for 7 days, after which they were stored in a zip-lock bag for analysis purposes.

### 2.2 Mechanical Properties of the Briquettes

Shattering index: This revealed the briquette's toughness property and the briquettes' capability to resist scrubbing and impact forces during handling and transportation.

**Table 1** Aggregate mix at different densification pressure

| Sample ID | Corncob (%) | Rice husk (%) | Compaction pressure (kPa) |
|---|---|---|---|
| J1 | 90 | 10 | 60 |
| J2 | 90 | 10 | 80 |
| J3 | 90 | 10 | 100 |
| K1 | 80 | 20 | 60 |
| K2 | 80 | 20 | 80 |
| K3 | 80 | 20 | 100 |
| L1 | 70 | 30 | 60 |
| L2 | 70 | 30 | 80 |
| L3 | 70 | 30 | 100 |
| M1 | 60 | 40 | 60 |
| M2 | 60 | 40 | 80 |
| M3 | 60 | 40 | 100 |
| N1 | 50 | 50 | 60 |
| N2 | 50 | 50 | 80 |
| N3 | 50 | 50 | 100 |

The shatter property was determined by dropping briquettes four times continually from an elevation of 1.85 m onto a concrete plate [17]. The shatter index was calculated using Eq. 1.

$$\text{Shattering index (S)} = \frac{\text{weight of briquette in plate after 4 drops}}{\text{the initial weight of the sample}} \times 100\% \quad (1)$$

Compressive strength: Compressive strength is the factor that shows the briquette's ability to withstand crushing forces. It was determined twenty-one days after drying using a Universal Testing Machine (Model: FS5080) in accordance with ASTM standard method [18]. The maximum stress of the briquettes was documented as the compressive strength. The experiment was carried out in duplicate, and the average is reported.

## 2.3 Modeling and Simulation of the Briquettes

When a function consists of two or more parameters, a multivariate approximation is required for integration, differentiation, and interpolation [9]. In addition, quadratic interpolation is promising if a data set has a minimum of three points. Therefore, a polynomial equation given in Eq. 2 is appropriate to create a model of the mechanical properties of the manufactured briquettes [9, 19].
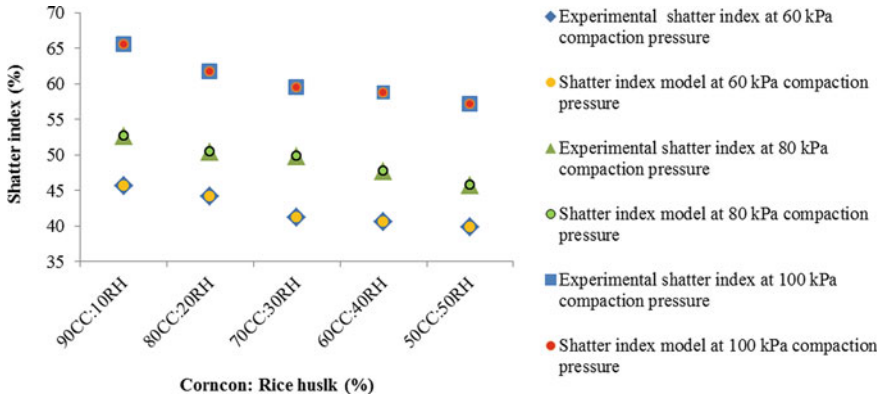
**Fig. 1** Relationship between aggregate mix, compaction pressure, and shatter index
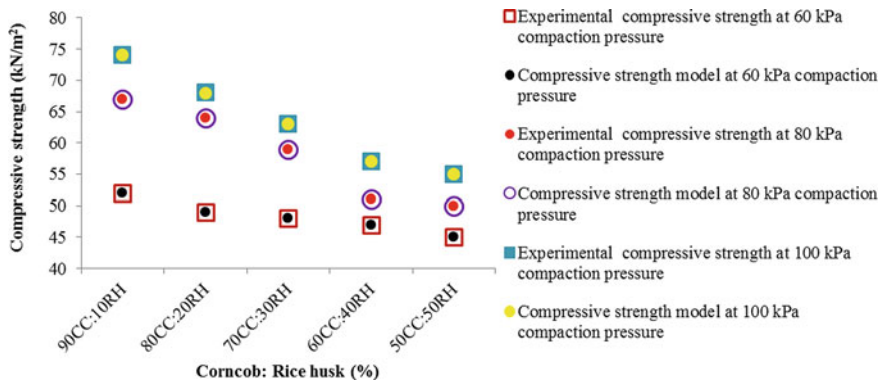


**Fig. 2** Relationship between aggregate mix, compaction pressure, and compressive strength

$$Y = \alpha + \beta_1 X + \beta_2 X^2 + \beta_3 X^3 + \varepsilon \tag{2}$$

where dependent variable $Y$ represents the shatter index and compressive strength, independent variable $X$ denotes the feedstock blending ratio and $\varepsilon$ is the error term. Figures 1 and 2 represent the model curves, and they are determined using Eqs. 4–9 generated using the Microsoft EXCEL spreadsheet.

## 2.4 Coefficient of Correlation

The relationship between two variables is usually measured using the coefficient of correlation and is represented by Eq. 3 [20, 21]. Thus, used to determine each curve presented in Figs. 1 and 2.

$$r = \frac{\sum(X - \overline{X})(Y - \overline{Y})}{\sqrt{\left\{\sum(X - \overline{X})^2\right\}\left\{\sum(Y - \overline{Y})^2\right\}}} \qquad (3)$$

where $\overline{Y}$ and $\overline{X}$ are the averages of $Y$ and $X$, respectively, and $r$ is the coefficient of correlation.

## 3 Results and Discussion

The experimental and empirical model data are presented and discussed in this section.

### 3.1 Shatter Index

Figure 1 shows the effect of aggregate mix and compaction pressure on the shatter index of the manufacture fuel briquettes, while Table 2 shows their respective experimental and empirical model data sets. The highest (65.49%) and lowest (39.87%) shatter index correspond to samples J3 and N1, respectively. The results revealed that shatter index property increases with compaction pressure and decreases as the proportion of rice husk increases in the aggregate. This is because compaction pressure reduces the briquette particles' pore space, thus shortening the intermolecular distance of the briquette particles. This makes the briquette particles interlock, hence, increases the resistance of the briquettes rubbing and impact loads. Analyses of the results show that corncob plays a significant role in improving the shatter index property of the solid fuel briquettes. The shatter index revealed the durability of the briquettes during storage and handling. So, the higher the shatter index value, the better the durability of the manufactured briquettes. The empirical models created for the shatter index at 60, 80, and 100 kPa compaction pressure are shown in Eqs. 4, 5, and 6, respectively. The coefficient of correlation ($r$) and standard error ($\varepsilon$) of the empirical models indicate a strong relationship among the variables.

$$S_{60} = 0.000560x^2 + 0.953113x + 0.969176; r = 0.961168; \varepsilon = \pm 0.000037\% \qquad (4)$$

$$S_{80} = 0.000417x^2 + 0.959708x + 0.969557; r = 0.989808; \varepsilon = \pm 0.000042\% \qquad (5)$$

$$S_{100} = 0.000274x^2 + 0.967055x + 0.98944; r = 0.963467; \varepsilon = \pm 0.000040\% \qquad (6)$$

**Table 2** Experimental and predicted values empirical model for the mechanical properties of briquettes

| Sample ID | Corncob (%) | Banana stalk (%) | Compaction pressure (kPa) | Mechanical properties | | | |
|---|---|---|---|---|---|---|---|
| | | | | Shatter index (%) | | Compressive (kN/m$^2$) | |
| | | | | * | ** | * | ** |
| J1 | 90 | 10 | 60 | 45.650 | 45.655 | 52.000 | 52.001 |
| J2 | 90 | 10 | 80 | 52.750 | 52.755 | 67.000 | 66.999 |
| J3 | 90 | 10 | 100 | 65.490 | 65.495 | 74.000 | 74.002 |
| K1 | 80 | 20 | 60 | 44.220 | 44.220 | 49.000 | 48.999 |
| K2 | 80 | 20 | 80 | 50.530 | 50.529 | 64.000 | 64.000 |
| K3 | 80 | 20 | 100 | 61.750 | 61.748 | 68.000 | 67.990 |
| L1 | 70 | 30 | 60 | 41.190 | 41.187 | 48.000 | 47.999 |
| L2 | 70 | 30 | 80 | 49.890 | 49.888 | 59.000 | 59.001 |
| L3 | 70 | 30 | 100 | 59.530 | 59.528 | 63.000 | 62.991 |
| M1 | 60 | 40 | 60 | 40.590 | 40.588 | 47.000 | 47.000 |
| M2 | 60 | 40 | 80 | 47.730 | 47.727 | 51.000 | 51.000 |
| M3 | 60 | 40 | 100 | 58.810 | 58.808 | 57.000 | 57.005 |
| N1 | 50 | 50 | 60 | 39.870 | 39.869 | 45.000 | 45.001 |
| N2 | 50 | 50 | 80 | 45.810 | 45.809 | 50.000 | 49.999 |
| N3 | 50 | 50 | 100 | 57.140 | 57.140 | 55.000 | 55.013 |

*Experimental; **Empirical model

## 3.2 Compressive Strength

Figure 2 shows the effect of aggregate mix and compaction pressure on the compressive strength of the manufactured briquettes. The experimental and corresponding empirical model data is presented in Table 2. The results showed that the compressive strength of the briquettes decreases with an increase in the percentage of rice husk in the aggregate; however, the strength property improves as the compaction pressure increases. Samples J3 and N1 gave the best and most minor compressive strength of 74 and 45 kN/m$^2$, respectively. It was discovered that compressive strength property increases with compaction pressure. This is because the applied pressure enhances the bonding of the briquettes particles. More so, the combined effect of the binder used for the briquettes production and pressure applied makes the molecules of briquettes particles diffuse at the contact surfaces, thus the formation of solid bridges between the particles. The applied pressure and binder used to hold the briquettes particle together, which improves the compressive strength properties. Equations 7, 8, and 9 are the empirical models developed for the compressive strength at densification pressure of 60, 80, and 100 kPa, respectively. The model's standard error ($\varepsilon$) and correlation coefficient ($r$) show a strong relationship among the variables.

$$C_{60} = 0.000134x^2 + 0.986943x + 0.316478;$$
$$r = 0.977316; \varepsilon = \pm 0.000003 \, \text{kN/m}^2 \tag{7}$$

$$C_{80} = -0.0000263x^2 + 1.0030493x - 0.087391;$$
$$r = 0.978311; \varepsilon = \pm 0.000003 \, \text{kN/m}^2 \tag{8}$$

$$C_{100} = 0.0001935x^2 + 0.9744437x + 0.833355;$$
$$r = 0.989456; \varepsilon = \pm 0.000372 \, \text{kN/m}^2 \tag{9}$$

## 4 Conclusion

The mechanical properties of solid fuel briquettes produced from blends of torrefied corncob and rice husk were investigated in this study using experimental, modeling, and simulation techniques. It could be concluded that blending ratios and compaction pressure influence the mechanical properties of the manufactured briquettes. The mechanical properties improved as the percentage of corncob increases in the aggregates. Samples J3 (90CC:10RH at 100 kPa), and N1 (50CC:50RH at 60 kPa), respectively gave the best and the least mechanical properties. Empirical models were successfully developed for 60, 80, and 100 kPa densification pressure, and the models were able to predict the trend of the mechanical properties of the manufactured briquettes. The models developed in this study found applications in future biomass briquettes production and product design.

## References

1. Oyedepo SO, Dunmade IS, Adekeye T et al (2019) Bioenergy technology development in Nigeria—pathway to sustainable energy development. Int J Environ Sustain Dev 18:175–205
2. Ibitoye SE, Jen T-C, Mahamood RM, Akinlabi ET (2021) Densification of agro-residues for sustainable energy generation: an overview. Bioresour Bioprocess 8:1–19
3. Rajput SP, Jadhav SV, Thorat BN (2020) Methods to improve properties of fuel pellets obtained from different biomass sources: effect of biomass blends and binders. Fuel Process Technol 199:1–12
4. Sirous R, José F, António L (2020) Mixed biomass pelleting potential for Portugal, step forward to circular use of biomass residues. Energ Rep 6:940–945
5. Jelonek Z, Drobniak A, Mastalerz M, Jelonek I (2020) Environmental implications of the quality of charcoal briquettes and lump charcoal used for grilling. Sci Total Environ 747:1–25

6. Albashabsheh NT, Heier JL (2021) Optimization of lignocellulosic biomass-to-biofuel supply chains with densification: literature review. Biomass Bioenerg 144:1–10
7. Ibitoye SE, Jen T-C, Mahamood RM et al (2021) Generation of sustainable energy from agro-residues through thermal pretreatment for developing nations: a review. Adv Energ Sustain Res 2100107:1–15
8. Afra E, Abyaz A, Saraeyan A (2021) The production of bagasse biofuel briquettes and the evaluation of natural binders (LNFC, NFC, and lignin) effects on their technical parameters. J Clean Prod 278:1–5
9. Berdychowski M, Tala K, Wojtkowiak D (2021) Experimental and numerical analysis of the effect of compaction conditions on briquette properties. Fuel 288:1–19
10. Yang I, Cooke-willis M, Song B et al (2021) Densification of torrefied Pinus radiata sawdust as a solid biofuel: effect of key variables on the durability and hydrophobicity of briquettes. Fuel Process Technol 214:1–9
11. Pradhan P, Mahajani SM, Arora A (2021) Pilot scale production of fuel pellets from waste biomass leaves: effect of milling size on pelletization process and pellet quality. Fuel 285:1–7
12. Marques P, Freire F (2020) Life cycle assessment of biomass pellets: a review of methodological choices and results. Renew Sustain Energ Rev 133:1–13
13. Manouchehrinejad M, Mani S (2018) Torrefaction after pelletization (TAP): analysis of torrefied pellet quality and co-products. Biomass Bioenerg 118:93–104
14. Andini A, Bonnet S, Rousset P et al (2018) Torrefaction study of Indonesian crop residues subject to open burning. In: 7th international conference on sustainable energy and environment: technology and innovation for global energy revolution, pp 28–31
15. Andreia M, Mariano T, Perett J et al (2016) Recovery of agricultural and wood wastes: the effect of biomass blends on the quality of pellets. Fuel 284:1–7
16. Antwi-Boasiako C, Acheampong BB (2016) Strength properties and calorific values of sawdust-briquettes as wood-residue energy generation source from tropical hardwoods of different densities. Biomass Bioenerg 85:144–152
17. Odusote JK, Muraina HO (2017) Mechanical and combustion characteristics of oil palm biomass fuel briquette. J Eng Technol 8:14–29
18. ASTM D2166-85 (2008) Standard test methods for compressive strength. ASTM International, West Conshohocken, PA. Available at www.astm.prg
19. Phadke MS (2011) Quality engineering using robust design, pp 1–342
20. Mitchual SJ (2014) Densification of sawdust of tropical hardwoods and maize cobs at room temperature using low compacting pressure without a binder. Ph.D. thesis, Department of Wood Science Technology Kwame Nkrumah University Science Technology, pp 1–264
21. Bird J (2017) Higher engineering mathematics. https://doi.org/10.1201/9781315265025

# Study and Analysis of Challenges in Wind Energy Implementation

**Eden Voon Wu Qian and Elammaran Jayamani**

**Abstract** Wind energy is the most abundant, if not the cleanest, energy available on the Earth. The only obstacle is that it is chaotic and uncontrollable. With rise in demands for renewable energy and the stability of other renewable energy sources, the next logical step would be to harvest wind energy out of thin air. However, implementation of wind energy harvester or wind turbines comes with its own set of challenges. Different region of the world will produce its own set of challenges and needs to be understood before suggesting any implementation. From low wind speed to negative public perceptions, this paper presents an overview of challenges faced by all over the globe and especially in Malaysia.

**Keywords** Wind energy · Implementation · Renewable · Sustainable

## 1 Introduction

Energy is essential. The very core of the world runs on energy in one form or another. Be it thermal, electrical, chemical, kinetic, potential or even nuclear, energy is the very essence that keeps the world alive and moving forward. However, it is also malleable and easily transformed from one form into another wasted form. For example, powering a lightbulb produces useful light but wasted heat and occasionally, sound. These wasted by product will eventually destroy the planet if mishandled. Hence, it is our responsibility to ensure the energy is used wisely and more importantly is generated cleanly and sustainably. This article aims to categorize the challenges found globally and determine if Malaysia has faced such problems. Certain articles may be repeated throughout to aid in facilitating the categorizing presentation.

E. V. W. Qian · E. Jayamani (✉)
Swinburne University of Technology Sarawak Campus, 93350 Kuching, Sarawak, Malaysia
e-mail: ejayamani@swinburne.edu.my

E. V. W. Qian
e-mail: edstudies91@gmail.com

## *1.1 Renewable Energy*

The term "renewable" is defined as not being depleted upon usage. Hence, renewable energy (RE) means energy that stems from sources that can be easily replenished. These sources may include the Sun, the wind, water and the Earth's heat, though it may all be derived just from the Sun as the primary energy source for everything. The importance of RE lies in its ability to stay clean [25]. Given that the global warming increased the Earth's temperature by approximately $1.2\degree$C, and the blame may be placed primarily on the usage of fossil fuels which releases pollutants into the air. On top of that, greenhouse gasses (GHG) produced traps the energy from the Sun, much like a car under a sunny day, contributing more heat to global warming [10]. Should this continue, the Earth may see increasing sea levels that leads to flood, heatwaves bringing drought and worsening of all-weather catastrophes.

Thankfully, RE comes in many forms with many means of harvesting, most of which uses Faraday's law of induction by introducing some sort of kinetic energy into mechanical devices such as a turbine. Starting off would be **hydropower** which harvests energy by converting the potential energy of water dams into kinetic energy to spin turbines, which induces current for power generation. Following that would be the use of organic matter, **bioenergy**, as burning fuel to generate steam for turbine rotation and power generation. Harvesting the Earth's heat gives birth to **geothermal energy** that also utilizes high heat to produce steam for power generation. **Ocean energy** involves the harvesting of tides and waves by exploiting the free oscillation due to the oceanic wind on the surface. One energy that does require turbine for power generation would be **solar energy** as the excitement of electrons inside a photovoltaic cell is its main power source. **Hydrogen**, on the other hand, is a novel energy source where heat is introduced to allow the "reforming" process to occur. Hydrogen then becomes a fuel source for power generation. Lastly, even the fluctuation of air pressure may be harvested as **wind energy** where one form of kinetic energy, air flow, is converted into rotational kinetic energy for the turbines.

## *1.2 Wind Energy*

In simpler terms, wind is basically air flowing about in a certain region due to pressure gradients. Pressure gradients are affected by the thermal gradients that results from the heating and cooling of the atmosphere, where this cycle of heated air rising and cooler air dropping fluctuates pressure in a given area. Just as with many renewable sources, wind is highly unpredictable and may flowing from various direction [7]. The kinetic energy contained in flowing wind can be calculated by utilizing formulae for kinetic energy and mass flow rate. According to [5], the result of the equation is verified by [7] and [6], and the power contained in flowing wind requires the following equation

$$\text{Power in Wind, } P = \frac{1}{2}\rho\, A V^3 (\text{Watt}) \tag{1}$$

Hence, the power in wind is proportionate to the density of air flowing, the area at which air is in collision with the turbine blades and the cubed of air flow velocity.

## 1.3 Wind Turbine

Previously, windmills are used for milling and grinding but in modern years, these devices are known as wind turbines and are primarily used for the generation of electricity. There are primarily two types of wind turbines horizontal axis wind turbines (HAWT) and vertical axis wind turbines (VAWT).

Horizontal axis wind turbines (HAWT) works by utilizing aerodynamic blades fitted to its rotor. As air flows over aerofoiled-shaped blades, the subsequent produced lift force is the contributing factor to its rotational motion. Most HAWTs now include a yaw pitch drive (passive) or utilize an anemometer and some control system (active) to ensure the wind turbine faces the correct wind direction. Vertical axis wind turbines (VAWT), on the other hand, are typically smaller wind turbines with axis of rotation perpendicular to its surface. Unlike HAWTs, this particular arrangement allows wind collection from all directions though this may involve large stress on the machine [12].

As suggested by Eq. (1), an increase in wind speed will result in a cubed increase in power generation. When the speed is low enough to produce little to no power, this is known as "cut-in speed". However, when the speed is at a certain point, any further increase in wind speed will result in damages to the blades and generators with no increase to its power generation capabilities. At maximum point, or its "cut-out speed", a brake must be applied to prevent excessive damage.

The number of blades also affects the power generation in wind turbines. Assuming similar design except for the number of blades, a typical HAWT will produce optimal power at 4 blades, whereas for VAWT works best at less than 4 blades. It was concluded that HAWT is better than VAWT with same number of blades as it produces 4 times more power. However, VAWT is much more suitable for lower speeds as that is the zone where maximum power appears [17].

As wind speed is the major contributing factor, it should be noted that it is affected by the altitude at which the rotors are supposed to rotate. Generally, higher altitude allows for faster wind speeds though. However, there should be a balance between high altitudes nacelle, the housing for electrical and generator components and its serviceability [7]. Though Lee et al. [14] calculate the optimum height for the highest annual net profit is at 103.5 m, it is safe to assume the same applies to maximize power generation. Hence, depending on the accessibility of the site, a fine balance must be understood to maximize efficiency while minimizing operational costs.

Another potential factor to bear in mind when building wind farms, where many wind turbines work together, is the spacing of each wind turbines. Excess spacing

between wind turbines will translate to a waste of land and highly compact wind farms will result in lower efficiency as a whole. A research by Meyers and Meneveau [16] has proven that under desirable conditions, where the land is flat with no topography, about 7D to 15D spacing apart, where D represents the rotor diameter, proves to be the optimal.

### 1.4  Malaysian Climate

According to the Malaysian Meteorology Department (n.d.), the main characteristics of Malaysia revolve around having uniform temperature, high humidity and blessed with lots of rain though with lower than average rated wind speed nationwide. Data from the same source indicates that Malaysia is located close to the equatorial doldrums area. The four seasons in Malaysia are divided into four types of monsoon seasons instead. From November to March, wind speed from 10 knots (5.14 m/s) to 30 knots (15.43 m/s) blows from northeast to southwest. This is known as the northeast monsoon. The opposite southwest monsoon occurs from May to September with wind speed of less than 15 knots (7.72 m/s). Between these periods, late March to early May and October to mid-November, weaker winds are chaotic and bring about heavy rain and strong wind in short bursts.

## 2  Challenges

This section aims to generalize the challenges faced by wind energy harvesting and encompasses political initiatives, societal hindrance and environmental impacts. After this section, it is hoped that a thorough understanding on these challenges will open new ways to innovate the wind energy industry.

### 2.1  Manufacturing Costs

Assuming an average horizontal axis wind turbine, the components and its cost may be broken down into several parts: the rotor, drive train (nacelle), the control system and the main tower. On top of that, the components to build a wind turbine station may be broken down into its foundation, transportation, civil works, installation, electrical connections and the required documentations for the entire project. All in all, the total initial capital cost (ICC) is up to $1,403,000, nearly RM 6 million in the year 2006. The nacelle makes up for 60% of the wind turbine component costs, while the electrical connection and civil work make up for 33 and 23%, respectively, for wind turbine station costs. The chart below shows the distribution of all parts contributing to the huge ICC [8].

In a study done by Gebreslassie (2020), the top ranked challenge would be the lack of investment capital. Given the large cost to not only manufacture wind turbines but to install it as well, this proves to be difficult for investors in Ethiopia. The only financial institution at the time was the Development Bank of Ethiopia (DBE) with insufficient resources to support any wind energy developments. Furthermore, the undeveloped manufacturing industry in the country forces the import of building materials. This puts a heavy toll on the investors who have to pay even higher interests and the country in an overall financial burden. Offshore wind turbines will provide more power generation as compared to onshore wind turbines. However, the complicated procedures to build as well as to maintain put the entire offshore project at about 2.75 times more expensive than onshore projects [2].

## 2.2 Fabrication and Transportation

As previously discussed, the lack of proper raw material manufacturing disrupts Ethiopia's wind energy technology development. The lack of proper programmes and/or trade agreements to fully support any wind energy projects becomes one of the major hurdles to harvest wind energy in due time. This translates to poor and inconsistent supply chain and results in lower product qualities [9]. By using the life cycle assessment (LCA) method, it was discovered that throughout the life of a typical wind turbine from acquiring raw materials to the dismantling of the entire unit, the manufacturing process has the highest environmental impact. Interestingly, it was found that this was due to the cement making process which releases particle to its surrounding. Coming second and third for impacting the environment would be the transportation and operation phase, respectively [21].

## 2.3 Technology and Skills Availability

According to this article, developing energy technologies, including wind energy technologies, all require some sort of core skills to secure its future. As with all other developments, managers and professionals are a must to provide the necessary leadership and direction for the entire team. It was also said that workers in the area must be flexible and willing to travel due to the nature of long distanced wind turbine installations. The skills commonly lacking in the wind energy sector would commonly be project developers, service technicians and data analysts [13]. The same problem may be seen in education systems such as China's. Despite being the leader in wind energy technologies, the lack of educated graduates in this field is due to the inflexibility and long duration of study in university. Even after graduation or for the uneducated, the lack of training centres hinders the development of wind energy harvesting. On top of that, the syllabus covers only the science, engineering and skill training. The lack of coverage on topics such as economy, policy, environment and

planning may disrupt proper planning of wind energy harvesting. Lastly, nearly all of the wind energy education and training is done physically. This means that China has no infrastructure to move classes online, and this may change the mind of those who may be interested in the field but unable to fully commit yet [26]. This leads to situations as found in Ethiopia, lack of Ethiopian technical and soft skills, high turnovers, lack of experience and lack of competency among many other factors. In short, the country is not well prepared nor is it well equipped to introduce or develop wind energy technologies in Ethiopia. Should they wish to import skilled workers, it would relate back to the country's financial status and the need for financial supports [9].

## 2.4 Policies and Implementation

France introduced new policies to help push the development of wind energy even further. However, the framework is unclear which may confuse the actors between purchase agreements. Furthermore, with the circular economy in mind, the proposed contracts did not include any end of life management policy. This means that as the wind turbine approaches the end of its lifetime, the way forward becomes vague and may lead to undesired consequences. On top of that, pre-existing contracts (prior to the new policy introduction) were not given updated clear policy on lifetime extension, repowering or end of life management. Lastly, the lack of social cost assessment for energy production and usage is one of the challenges faced. Because of this, the most suitable RE source becomes uncertain and due to its financial manner, this may push investors out of the RE scene [24]. Similarly, the uncertainty of US governments to move from the profitable fossil fuel to unstable, yet promising RE, is the bane of wind energy development throughout the world. Though some initiative has been done to boost RE, the fact that it is still not profitable sways the government's confidence and as a result, multiple policy is put in place which may cause more confusion than clarity. For example, the government of Germany extended its Production Tax Credit (PTC) policy by 1 year instead of the promised 4 years. This may severely cripple certain companies' initiation towards Research and Development as well as any existing projects [2].

Over in India, several problems surfaced due to the unpredictability of wind availability. The fluctuation in air flow forces power plant to work at lower efficiency as sudden spike in wind load-generation may damage the system. The demands and wind power production are both uncertain as well. This means that during peak demand season, the lack of wind power production will cripple the energy industry. In terms of marketing, the uncertainty of wind power production makes market penetration difficult. Whenever the market requests for certain physical delivery, the seasonal wind power production might be insufficient and the company as a whole risk losing profit. To add to the financial burden, additional infrastructure is required to ensure smooth power output as well as load-generation balancing. Energy storage facilities as well as long-distanced power transmission infrastructure are all costly

and required maintenance during its lifespan [1]. Wind energy harvesting may be done in urban area as well. However, the wind flow in urban areas is classified as highly turbulent due to the irregular building shape or the high roughness of ground surface. This will result in reduction in power output performance and higher noise production. In short, the chaotic aerodynamics of wind in urban settings makes it difficult for HAWT. However, more studies need to be done to determine if VAWTs may be able to alleviate the issues of turbulent air flow [22].

Wind turbine experiences voltage fluctuation which may ultimately reduce the lifespan of any electrical connection as well as becoming an unreliable energy source. This may due to unstable airflow, grid connection issues, operational faults, etc. [21]. As turbine start up, a minor harmonics is produced (which may be minimized by good control algorithm design) which may cause efficiency loss and disturbances in electronic equipment [20]. Furthermore, the intermittent nature of wind energy source, there will be periods of excessive power spikes or drops which need to be smoothen out to be usable. Intermittent wind supply produces unstable power into the power grid which may result in instability there. At times, there may be a surge of high speed providing high power output and vice versa. This would mean additional (or existing) power plant is required to help fill in the gaps should there be low power generation and some sort of controller to ensure the system does not get overloaded. Having this issue also pulls down the confidence of the public towards relying on wind energy and slows the development of RE in general [2]. In the United Kingdoms, a different problem arises altogether, both onshore and offshore wind turbines are affected by an external factor that decreases its overall performance efficiency, build-up of salt for offshore and build-up of grime for onshore wind turbines. Not to mention the degradation of its internal components such as the gearbox and bearings, the combination of these will severely limit the wind turbines' performance [2].

## 3 Wind Turbine Challenges

### 3.1 Flora and Fauna

Wind turbine must be constructed up to a minimum height for the greatest efficiency possible. Doing so brings about the challenge of damage avian animal habitats, especially birds and bats. However, the number of bird death due to wind turbines as compared to birds killed due to destruction of their habitat (deforestation) is very little, even neglectable. Despite this, the chance of bird striking the turbine blades and being critically injured is still there and needs to be taken into consideration [18]. Older wind turbines with shorter rotor diameter which produces higher revolution per minute (RPM) is deadlier than newer and larger wind turbines. Again, the number of bird death due to wind turbine is negligible when compared to other devasting human action towards the ecosystem [21]. On the other hand, offshore wind turbines

pose another kind of threat and damage to marine life. Sensitive marine animals such as dabs or salmons may experience pile-driving pulses whenever near these wind turbines. Though more research needs to be done to understand the extent of the damage, it is another factor that needs to be taken into consideration.

## 3.2    Social View

Despite harvesting clean energy from thin air, wind turbines themselves may pose some medical issues in relation to its working principles. A wind turbine must include a rotational component, the rotors, to aid in the generation of power. However, this does lead to the production of low-frequency aerodynamic noise. Residents living within 2 kms (km) will be especially affected by this phenomenon which may result in sleep disorders as well as damaging the vestibular structure. This is further amplified if there are no structures between the residents and the wind turbine site [18]. In terms of noise, the accumulation of grime into accretions serves to increase sound generation. Along with the complex air flow across each blade, the generated sound may be enough to affect one's physical and mental health the closer the wind turbine is [2]. In terms of visual impacts, stemming from the shape, colour, layout of the wind turbines, proximity to local residents, shadow flickering or even sunlight reflection, only adds on to the public negative perception [21]. Shadow flickering is also detrimental to epilepsy sufferers as the periodic dip in light level caused by shadows is significant. This usually happens when the sun is rising or setting, and hence, the direction of the blades must be taken into consideration. This is made even harder should a yaw system is installed to rotate and face the wind during operations. Even infrastructure needed to connect wind farms to the power grid may pose some visual discomfort to the public unless more finance is allocated to attempt to hide these poles and cables. Wind turbines need to be tall and big to achieve maximum efficiency. However, some would argue that as time progresses, larger and larger wind turbines will affect the local landscape views, especially in large numbers such as a wind farm. Of course, this is a very subjective topic and despite being ugly to some, as the saying goes, "Beauty is in the eyes of the beholder", some may even travel long distance to watch wind turbines at work. The same cannot be said for offshore wind turbines as it is usually not visible to the public eyes on a daily basis. On top of that, tall wind turbines pose a safety risk to aircrafts in the vicinity. The solution was to use navigation beacons which is very bright and may disturb residents at night. These infrastructures also affect farming land as useful rectangular plots are transformed into triangular shaped land [2].

### 3.3 Climate Change

Some preliminary studies indicate that wind turbine brings about a macroclimate change, though negligible globally. The rotation of wind blades mixes the air around it even more and may lead to undesired distribution of temperature and humidity such as having lower humidity on ground levels. More evidence on this is required to properly debunk this myth, but for the time being, the topic of wind turbine contributing to environmental concerns is a topic to debate about [18].

## 4 Malaysia

A study by Suzana et al. [23] to determine the developments of renewable energy sources in Malaysia shows that wind energy is highly inefficient with an efficiency score of 0.001. The highest mean efficiency score is 0.686 which points towards mini hydro. This can be attributed to several factors such as political, societal and environmental.

In Malaysia, wind energy development is generally low due the country's low wind speed hindering the sectors feasibility. Despite having enacted the Renewable Energy Act 2011 to help boost this industry, wind energy is not listed inside the schedule as a renewable energy. Numerous previous studies were done to further understand the possibility of wind energy harvesting in the country but most were either inconclusive or unreliable due to either being studied too near airports, where aircrafts contaminate the airflow in the area or reliance on external parties for data, which turns out to be unevenly distributed. In short, Malaysia needs to focus on its incompetence when it comes to collecting, organizing and distributing wind data for future developments. Researches must be consistent on the elevation, area of collection and avoid areas where air might be easily disturbed for an even mean wind speed data collection. From the Renewable Energy Act 2011, a renewable energy (RE) fund is created to cover the proposed feed-in-tariffs (FiTs). However, it relies on surcharges from electrical consumers which brings about three problems. The first would be the reliance on electrical consumers might not be aggressive enough to support these new RE development. This lack of financial support for other popular RE means there will be even less financial assistance provided for wind energy development. The second problem would be the imposed levies onto consumers. Most consumers would not be willing to pay for externalities and any additional imposed levies can be seen as punishment. No matter how the Sustainable Energy Development Authority (SEDA) tries to promote RE, it will not work if the public perception is negative. Lastly, consumers who consume more electricity is required to pay more. Consumers would not be willing to pay extra which results in less electricity consumed. This ties in to the first problem, where the funding for RE comes from surcharge tariffs. Hence, the lack of surcharge from consumers' preference means less funding for RE development. The government's political support can be seen here in the form

of misplaced priority in the energy field as this only fuels the consumption of fossil fuel [11].

The lack of onshore development is concerning in Malaysia, even more so for offshore wind energy. Across the entire country, there is no single development of offshore research or development despite offshore wind turbines are capable of producing more than onshore wind turbines. In Kijal, Terengganu, an energy analysis found that wind turbines with rated power 850 kW shows the most promising capacity factor (CF) valued at 26.8%. CF is the average power generated over the rated peak power, meaning that power generation from wind turbine might be a wastage of its potential [3]. Due to Malaysia's low inland wind speed, researches have been done to determine the feasibility of wind energy harvesting in offshore conditions. Based on altimetry data from sources such as TOPEX, Poseidon, Jason-1, Jason-2 and Saral, it was determined that the annual mean wind speed ranges from 2.0 to 5.0 m/s with one area reaching up to 6.036 m/s (though this is negligible due to it being in international waters). The results show that areas such as C4 (Terengganu coastline), C9 (Labuan) and D11 (Sabah) are the most suitable offshore spots for wind turbine development for its high annual wind speed and wind energy density. These spots have annual wind speed of 5.364, 5.150 and 5.165 m/s, respectively (Zaman et al. n.d.). These results were shown to align with a research by Ho [11] which showed wind in Kudat, Sabah (D11) and Labuan, Malaysia (C9) to have a maximum diurnal wind speed of 5.55 and 4.65 m/s, respectively.

## 5   Conclusion

The wind energy industry needs more attention to further develop and overcome the various challenges proposed by this paper. This would include clearer policies, innovating wind turbines and revamping the education system to produce more skilled workers. In Malaysia, even more research needs to be done and ideas to be proposed to overcome the country's environmental condition. Though it shows promising result for offshore wind energy, the lack of Malaysian incentive as well as lack of clear data organization is holding the entire industry from moving forward.

## References

1. Abhinav R, Pindoriya NM (2018) 'Opportunities and key challenges for wind energy trading with high penetration in Indian power market'. Energy for Sustain Developm 47:53–61, Elsevier
2. Ahmed NA, Cameron M (2014) 'The challenges and possible solutions of horizontal axis wind turbines as a clean energy solution for the future'. Renew Sustain Energy Rev 38:439–460, Pergamon
3. Albani A, Ibrahim MZ, Yong KH (2014) 'The feasibility study of offshore wind energy potential in Kijal, Malaysia: the new alternative energy source exploration in Malaysia'. Energy Exploration Exploitation 32:329–344

4. Alif Ahmad Zaman A, Ellyza Hashim F, Yaakob O (n.d.) Satellite-based offshore wind energy resource mapping in Malaysia. viewed 6 April, 2021. https://doi.org/10.1007/s11804-019-000 66-w

5. Boyle G (2012) Renewable energy. Oxford University Press, Oxford, Third

6. Carter D (2018) In: Renewable energy: an introduction, Callisto Reference, Forest Hills

7. Dunlap RA (2015) Sustainable energy. Cengage Learning, Stamford, CT

8. Fingersh L, Hand M, Laxson A (2006) 'Wind turbine design cost and scaling model', viewed 21 September, 2021. <http://www.osti.gov/bridge>

9. Gebreslassie MG (2021) 'Development and manufacturing of solar and wind energy technologies in Ethiopia: challenges and policy implications'. Renew Energy 168:107–118, Elsevier Ltd. viewed https://doi.org/10.1016/j.renene.2020.11.042

10. Hansen J, Sato M, Ruedy R, Schmidt G, Lo K, Hendrickson M (2020) 'Global Temperature in 2019', viewed 1 October, 2021, <http://www.columbia.edu/~jeh1/mailings/2020/20200115_ Temperature2019.pdf

11. Ho LW (2016) 'Wind energy in Malaysia: past, present and future'. Renew Sustain Energy Rev 53:279–295, Elsevier. viewed https://doi.org/10.1016/j.rser.2015.08.054

12. Hyams MA (2012) Wind energy in the built environment. In: Metropolitan sustainability: understanding and improving the urban environment, pp 457–499

13. ILO Skills and Employability Department (2011) 'Skills and occupational needs in renewable energy skills and occupational needs in renewable energy transition just'

14. Lee J, Kim DR, Lee KS (2015) 'Optimum hub height of a wind turbine for maximizing annual net profit'. Energy Convers Managem 100:90–96, Elsevier Ltd

15. Malaysian Meteorology Department (n.d.) 'MetMalaysia: Iklim Malaysia', viewed 6 May, 2021, <https://www.met.gov.my/pendidikan/iklim/iklimmalaysia>

16. Meyers J, Meneveau C (2012) Optimal turbine spacing in fully developed wind farm boundary layers. Wind Energy 15(2):305–317

17. Nasab NM, Kilby J, Bakhtiaryfard L (2019) 'Effect of number of blades on generating power in wind turbines'. In: 2019 29th Australasian universities power engineering conference, AUPEC 2019, pp 0–5

18. Nazir MS, Mahdi AJ, Bilal M, Sohail HM, Ali N, Iqbal HMN (2019) Environmental impact and pollution-related challenges of renewable wind energy paradigm—a review. Sci Total Environ 683:436–444

19. Office of Energy Efficiency & Renewable Energy (2017) 'How Do Wind Turbines Survive Severe Storms? | Department of Energy', viewed 7 May, 2021, <https://www.energy.gov/eere/ articles/how-do-wind-turbines-survive-severe-storms>

20. Pinyol R (2016) Harmonics: causes, effects and minimization

21. Shafiullah GM, M.t. Oo A, Shawkat Ali ABM, Wolfs P (2013) 'Potential challenges of integrating large-scale wind energy into the power grid–a review'. Renew Sustain Energy Rev 20:306–321, Pergamon

22. Stathopoulos T, Alrawashdeh H, Al-Quraan A, Blocken B, Dilimulati A, Paraschivoiu, M, Pilay P (2018) Urban wind energy: Some views on potential and challenges. J Wind Eng Indus Aerodynam 179:146–157, Elsevier Ltd viewed <https://doi.org/10.1016/j.jweia.2018.05.018>

23. Suzana F, Chachuli M, Mat S, Ludin NA, Sopian K (2020) 'Performance evaluation of renewable energy R&D activities in Malaysia'. viewed 6 April, 2021. <https://doi.org/10.1016/j.ren ene.2020.08.160>

24. Tazi N, Bouzidi Y (2020) Evolution of wind energy pricing policies in France: opportunities and new challenges. Energy Reports vol 6. Elsevier, pp 687–692

25. Tromly K (2001) Renewable energy: an overview. Energy Efficiency and Renewable Energy Clearinghouse (EREC) Brochure'

26. Xie Y, Feng Y, Qiu Y (2013) The present status and challenges of wind energy education and training in China. Renewable Energy, vol 60. Pergamon, pp 34–41

# Impact of Milling on Hardness and Optical Transmission of PMMA Lenses

## An Experimental and Mathematical Approach

**Job Maveke Wambua, Fredrick M. Mwema, Buddi Tanya, Tien-Chien Jen, and Esther T. Akinlabi**

**Abstract** This study evaluates the impacts of milling on the hardness and optical transmission of PMMA lenses using experimental and mathematical models. Three milling parameters, i.e., spindle speed, depth of cut, and feed rate, were evaluated. The machining levels were obtained from experimental trials. The experiments were designed using the Taguchi method, giving out 16 experiments. Sixteen workpieces were investigated for Shore D Hardness and optical transmission before and after milling, and the change was computed. The experimental analysis identified a reduction in Shore D Hardness and optical transmission after milling. The mathematical analyses using Taguchi analysis and ANOVA found out that for the absolute minimum change in Shore D Hardness, the milling parameters should be 5000 rpm (spindle speed), 0.3 mm (depth of cut), and 0.05 m/min (feed rate). Similarly, for the optical transmission, the parameters should be a spindle speed of 3750 rpm, a depth of cut of 1.2 mm, and a feed rate of 0.1 m/min. The analysis further identified the depth of cut to be the most dominant milling parameter toward the Shore D Hardness and optical transmission of PMMA lenses with a percentage impact of 12.77 and 42.51%, respectively. Thus, this study presents a model for conventional milling of PMMA for optical applications.

J. M. Wambua · F. M. Mwema (✉)
Department of Mechanical Engineering, Dedan Kimathi University of Technology, Private Bag, Nyeri 10143, Kenya
e-mail: fredrick.mwema@dkut.ac.ke

F. M. Mwema · T.-C. Jen · E. T. Akinlabi
Department of Mechanical Engineering Science, University of Johannesburg, Auckland Park 524-2006, South Africa

B. Tanya
Mechanical Engineering Department, Gokaraju Rangaraju Institute of Engineering & Technology, Telangana, Hyderabad 500090, India

E. T. Akinlabi
Pan African University for Life and Earth Sciences Institute, Ibadan, Nigeria

# 1   Introduction

According to the World Health Organization, the number of people experiencing visual impairment or blindness was approximately 2.2 billion as of 2019 [1]. Out of these, about one billion cases could or can be prevented or corrected through surgery and the use of vision correction devices such as spectacles and contact lenses. However, the cost of preventing and treating visual impairment is exceptionally high (approximately USD 14.3 billion globally). This has made it challenging for residents in underdeveloped and developing countries to access visual health care and correction devices.

To address the problem, polycarbonates and other polymeric materials have been adopted in visual correction devices due to their mechanical strength and optical transmission [2]. However, these mechanical and optical properties limit them to machining using advanced methods such as laser cutting, inaccessible to many impoverished countries and communities. CNC machining is a conventional method and is readily available. Various researchers have investigated the impact of milling parameters on the responses of polymers and polymer composites, such as surface roughness, material removal rate, temperature, vibrations, wear, and cutting forces. For example, Sylajakumari et al. evaluated the impact of wear parameters on the dry sliding wear performance of co-continuous composites [3]. The authors concluded that the sliding distance was the dominant factor affecting the sliding wear.

Further, Jahan et al. investigated the impact of milling parameters on the generation of cutting forces during the machining of polycarbonate glass [2]. It was found out that the depth of cut was a significant factor affecting the cutting force. They also concluded that optimization of materials is quite essential for effective manufacturing. Consequently, in machining PLA composites, Langat et al. evaluated the impact of milling parameters on the surface roughness and milling temperatures and obtained the optimal machining parameters [4]. The depth of cut was identified as the most dominant machining parameter.

Despite numerous studies evaluating the impacts of machining parameters on various responses, there are limited studies on how the parameters affect polymers' hardness and optical transmission, especially PMMA. This is the primary contribution of this study. This study was conducted to evaluate the impacts of the milling process parameters on the hardness and optical transmission of PMMA lenses. The analysis was conducted experimentally and through mathematical modeling and analysis to identify the best milling parameters for the least impact or change on the hardness and optical transmission. The experimental analysis was conducted through the comparison of the responses before and after milling. The mathematical modeling and analysis were conducted on the absolute change in responses after milling and adopted to evaluate the impact of each milling parameter on the responses and the contribution of the parameters toward each response.

## 2 Methods

### 2.1 Design of Experiment

To investigate the impacts of milling on the hardness and optical transmission of PMMA lenses, workpieces were obtained from used lenses with approximate dimensions of 45 by 30 by 6 mm. Three milling parameters, i.e., spindle speed, depth of cut, and feed rate, with symbols $S$, $D$, and $F$, were selected from trial experiments conducted. From the trials, four levels were selected for each parameter, as shown in Table 1.

The experiments were then designed using the Taguchi methodology with the three factors and four levels. The design produced an L16 Taguchi array with 16 experimental runs, as shown in Table 2. These runs were adopted as the number of experiments. Therefore, 16 workpieces were selected for experimentation.

**Table 1** Milling parameters and their levels

| Parameter | Level | | | |
|---|---|---|---|---|
| | 1 | 2 | 3 | 4 |
| Spindle speed, $S$ (rpm) | 1250 | 2500 | 3750 | 5000 |
| Depth of cut, $D$ (mm) | 0.3 | 0.6 | 0.9 | 1.2 |
| Feed rate, $F$ (m/min) | 0.05 | 0.10 | 0.20 | 0.35 |

**Table 2** L16 Taguchi array

| Run | $S$ (rpm) | $D$ (mm) | $F$ (m/min) |
|---|---|---|---|
| 1 | 1250 | 0.3 | 0.05 |
| 2 | 1250 | 0.6 | 0.10 |
| 3 | 1250 | 0.9 | 0.20 |
| 4 | 1250 | 1.2 | 0.35 |
| 5 | 2500 | 0.3 | 0.10 |
| 6 | 2500 | 0.6 | 0.05 |
| 7 | 2500 | 0.9 | 0.35 |
| 8 | 2500 | 1.2 | 0.20 |
| 9 | 3750 | 0.3 | 0.20 |
| 10 | 3750 | 0.6 | 0.35 |
| 11 | 3750 | 0.9 | 0.05 |
| 12 | 3750 | 1.2 | 0.10 |
| 13 | 5000 | 0.3 | 0.35 |
| 14 | 5000 | 0.6 | 0.20 |
| 15 | 5000 | 0.9 | 0.10 |
| 16 | 5000 | 1.2 | 0.05 |

## 2.2  Preprocessing

The hardness (HD) and optical transmission (Tr) values were obtained for each workpiece before milling, denoted as $HD_b$ and $Tr_b$, respectively. For the measurement of hardness, a Shore D durometer (Model number 560-10D, Gain Express Holdings Ltd, United Kingdom), with a resolution of 0.5 HD, was used with a modified stand, as shown in Fig. 1.

The workpieces were placed on a flat bench following the ASTM D2240 and ISO 868: 2003 standards. The indenter on the durometer was aligned vertically with the workpiece, and the durometer pressed steadily. The hold button (Fig. 1) was then pressed within one second, and the instantaneous reading was obtained [5]. The procedure was repeated three times. The obtained values ranged between 0 and 100.

Consequently, the optical transmission before milling was also obtained in terms of the light passing through, as shown in the experimental setup in Fig. 2. It was assumed that the reflected and absorbed light by the workpieces was minimal. A laser source (Model number 25-LHR-213–230, Melles Griot, U.S.A) with a wavelength of 632.8 nm shown in Fig. 2 was used to generate the rays passing through the workpieces. The amplified detector (Model number PDA36A-EC SI, Thorlabs, U.S.A) with a wavelength of between 350 and 1100 nm shown in Fig. 2 was used to sense the amount of light. This light was then translated into voltages displayed by the two-channel digital storage oscilloscope with a bandwidth of 40 MHz (Model number TDS1001B, Tektronix, U.S.A) (TCDSO). The initial amount of light in
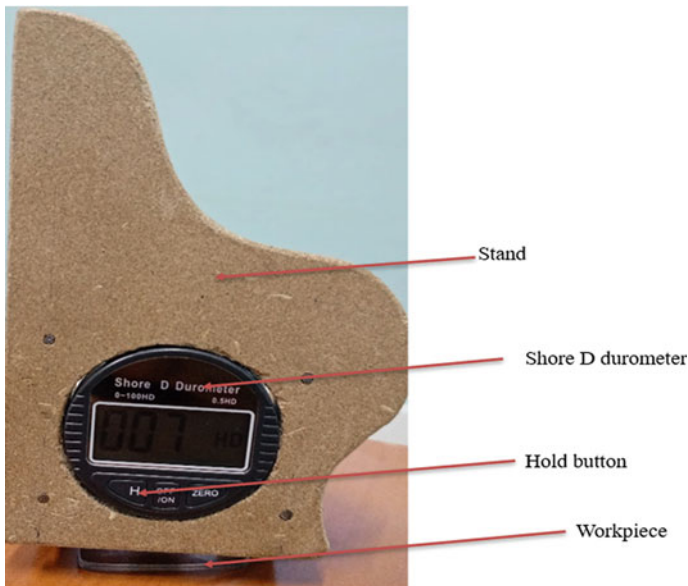


**Fig. 1**  Experimental setup of Shore D durometer with modified stand
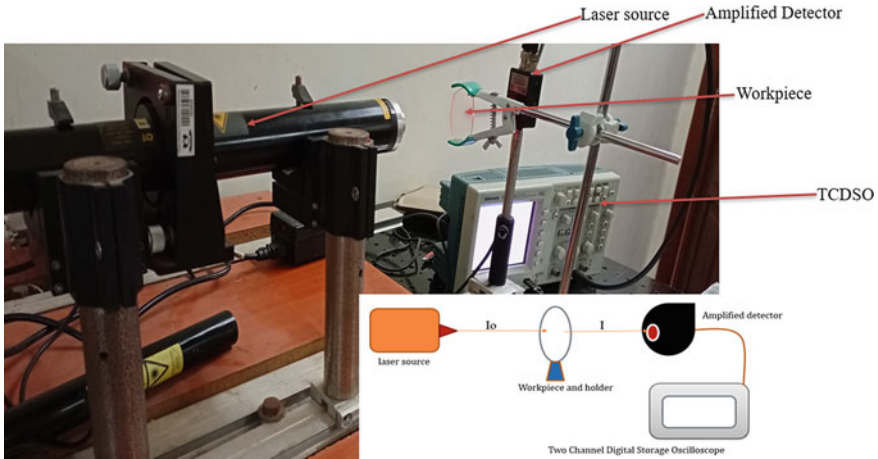
**Fig. 2** Experimental and schematic setup for the measurement of optical transmission

volts (Io) was measured without the workpiece. The final amount of light (I) was then measured as the light penetrated through the workpiece.

The optical transmission was then computed using Eq. 1.

$$Tr = \frac{I}{Io} \times 100 \tag{1}$$

where Tr = Transmission (%).

Io = Initial voltage reading without the workpiece.

*I* = Final voltage reading with the workpiece.

## 2.3 Experimentation and Post-Processing

Sixteen workpieces were machined in a CNC machine (Model—BenchMill 6000, Intelitek, U.S.A) using a 3-mm-diameter multi-edged HSS tool, corresponding to the runs obtained in the Taguchi array (Table 2). After machining, they were cleaned with a piece of cloth dipped in ethanol to remove accumulated chips. Three Shore D Hardness values of the milled surfaces were then obtained (using the setup in Fig. 1) along the tool path ($HD_a$). Similarly, the optical transmission after milling ($Tr_a$) was also obtained using the setup in Fig. 2 and computed from Eq. 1.

**Table 3** Measurement of Shore D Hardness (before and after milling)

| Run | Shore D Hardness, before milling (HD) | | | | Shore D Hardness, after milling (HD) | | | |
|---|---|---|---|---|---|---|---|---|
| | 1 | 2 | 3 | Average | 1 | 2 | 3 | Average |
| 1 | 67.5 | 68.5 | 64.5 | 66.8 | 60.0 | 59.0 | 55.5 | 58.2 |
| 2 | 80.5 | 79.0 | 81.0 | 80.2 | 40.5 | 44.5 | 40.5 | 41.8 |
| 3 | 86.0 | 87.0 | 88.5 | 87.2 | 54.0 | 60.0 | 56.0 | 56.7 |
| 4 | 77.0 | 78.5 | 80.5 | 78.7 | 56.5 | 58.0 | 56.0 | 56.8 |
| 5 | 86.5 | 86.5 | 85.0 | 86.0 | 64.5 | 72.0 | 65.5 | 67.3 |
| 6 | 77.0 | 79.0 | 74.5 | 76.8 | 50.0 | 46.5 | 51.5 | 49.3 |
| 7 | 78.0 | 79.0 | 74.0 | 77.0 | 45.0 | 51.0 | 51.5 | 49.2 |
| 8 | 80.5 | 78.5 | 82.0 | 80.3 | 46.0 | 44.5 | 50.5 | 47.0 |
| 9 | 85.5 | 81.5 | 83.5 | 83.5 | 64.5 | 70.5 | 69.0 | 68.0 |
| 10 | 82.0 | 82.5 | 84.5 | 83.0 | 69.0 | 67.5 | 66.0 | 67.5 |
| 11 | 81.5 | 81.0 | 81.5 | 81.3 | 46.5 | 46.5 | 50.0 | 47.7 |
| 12 | 74.5 | 72.0 | 73.0 | 73.2 | 49.5 | 45.5 | 47.0 | 47.3 |
| 13 | 77.5 | 74.5 | 79.5 | 77.2 | 52.0 | 50.0 | 52.0 | 51.3 |
| 14 | 84.0 | 85.0 | 87.0 | 85.3 | 64.0 | 63.5 | 65.0 | 64.2 |
| 15 | 77.0 | 73.0 | 75.0 | 75.0 | 49.0 | 52.0 | 58.5 | 53.2 |
| 16 | 74.0 | 72.0 | 78.5 | 74.8 | 57.0 | 58.0 | 59.5 | 58.2 |

## 2.4 Results Presentation

The results obtained from the measurement of Shore D Hardness of the workpieces before ($HD_b$) and after ($HD_a$) milling are recorded in Table 3. Similarly, the average values obtained from the measurement of optical transmission before ($Tr_b$) and after ($Tr_a$) are recorded in Table 4.

The average absolute changes in the Shore D Hardness and optical transmission of the PMMA lenses were obtained and recorded in Table 5.

## 3 Analysis and Discussion

## 3.1 Experimental Analysis

After milling the PMMA lenses, it was observed that the Shore D Hardness reduced significantly (Table 3). The highest value of Shore D Hardness was found to be 68.0 (run 9). This was obtained using a spindle speed of 3750 rpm, depth of cut of 0.3 mm, and feed rate of 0.2 m/min. Conversely, the least Shore D Hardness (41.8) in run two was obtained from a parameter combination of 1250 rpm, 0.6 mm, and 0.1 m/min for the spindle speed, axial depth of cut, and feed rate, respectively. The low

**Table 4** Measurement of optical transmission (before and after milling)

| Run | Before milling | | | After milling | | |
|---|---|---|---|---|---|---|
| | $I_O$ (V) | $I$ (V) | Transmission, $T$ (%) | $I_O$ (V) | $I$ (V) | Transmission, $T$ (%) |
| 1 | 44.0 | 38.2 | 86.82 | 44.9 | 15.0 | 33.41 |
| 2 | 44.0 | 40.5 | 92.05 | 45.1 | 20.8 | 46.12 |
| 3 | 43.9 | 41.3 | 94.08 | 44.0 | 24.0 | 54.55 |
| 4 | 43.9 | 38.1 | 86.79 | 44.6 | 24.0 | 53.81 |
| 5 | 43.8 | 40.1 | 91.55 | 45.0 | 20.0 | 44.44 |
| 6 | 43.2 | 40.4 | 93.52 | 45.0 | 12.9 | 28.67 |
| 7 | 43.9 | 38.5 | 87.70 | 44.5 | 20.6 | 46.29 |
| 8 | 44.0 | 38.4 | 87.27 | 44.9 | 20.8 | 46.33 |
| 9 | 43.8 | 39.8 | 90.87 | 44.9 | 18.2 | 40.53 |
| 10 | 43.7 | 41.2 | 94.28 | 45.0 | 16.1 | 35.78 |
| 11 | 43.9 | 34.9 | 79.50 | 45.0 | 18.4 | 40.89 |
| 12 | 43.9 | 38.5 | 87.70 | 44.9 | 33.2 | 73.94 |
| 13 | 43.6 | 38.3 | 87.84 | 44.7 | 17.4 | 38.93 |
| 14 | 44.0 | 38.0 | 86.36 | 44.8 | 12.7 | 28.35 |
| 15 | 42.3 | 40.3 | 95.27 | 44.6 | 14.3 | 32.06 |
| 16 | 44.0 | 37.9 | 86.14 | 44.6 | 31.1 | 69.73 |

**Table 5** Absolute change in Shore D Hardness and optical transmission of PMMA lenses

| Run | Change in Shore D Hardness, $|\Delta HD|$ (HD) | Change in optical transmission, $|\Delta Tr|$ (%) |
|---|---|---|
| 1 | 8.6 | 53.41 |
| 2 | 38.4 | 45.93 |
| 3 | 30.5 | 39.53 |
| 4 | 21.9 | 32.98 |
| 5 | 18.7 | 47.11 |
| 6 | 27.5 | 64.85 |
| 7 | 27.8 | 41.41 |
| 8 | 33.3 | 40.94 |
| 9 | 15.5 | 50.34 |
| 10 | 15.5 | 58.50 |
| 11 | 33.6 | 38.61 |
| 12 | 25.9 | 13.76 |
| 13 | 25.9 | 48.91 |
| 14 | 21.1 | 58.01 |
| 15 | 21.8 | 63.21 |
| 16 | 16.6 | 16.41 |

spindle speed and feed rate increased the machining time, which increased the tool-workpiece contact period. This could have led to stress-induced shear deformations which weakened the workpieces and increased the machining interface temperatures and forces [6]. In addition, weaker milled surfaces led to increased penetration of the indenter and hence a low hardness value.

Additionally, the optical transmission of PMMA lenses was reduced after milling. The highest optical transmission was obtained as 73.94%, which was achieved by combining spindle speed of 3750 rpm, depth of cut of 1.2 mm, and feed rate of 0.1 m/min. The least optical transmission was obtained from a parameter combination of spindle speed of 5000 rpm, depth of cut of 0.6 mm, and feed rate of 0.2 m/min. The high depth of cut was associated with effective heat dissipation, and hence a better surface quality. This led to better surface transparency. An increase in feed rate was also associated with increased tool wear, which deteriorated the surface quality and hence poor light penetration [7].

## *3.2 Mathematical Analysis*

The mathematical analysis was conducted using the Taguchi analysis and two-way analysis of variance (ANOVA). In Taguchi analysis, signal-to-noise (*S/N*) ratios for the changes in Shore D Hardness and optical transmission in relation to the milling parameters were obtained. The Taguchi analysis can be conducted in three criteria, i.e., smaller-is-better, nominal-is-better, and larger-is-better [4, 5]. In this study, the goal of the analysis was to obtain the parameter combination for the lowest change possible. Therefore, the smaller-is-better criterion was adopted to generate the *S/N* ratios. These are displayed in Table 6.

According to the Taguchi analysis, the largest *S/N* ratio depicts the parameter level for the best respective response [8]. For the Shore D Hardness, the highest *S/N* ratios were $-26.48$, $-24.05$, and $-25.60$ for the spindle speed, depth of cut, and feed rate, respectively (Fig. 3). These *S/N* ratios corresponded to parameter levels 4, 1, and 1. This depicts that in order to minimize the change in Shore D Hardness during

**Table 6** Response table for *S/N* ratios of change in Shore D Hardness and optical transmission

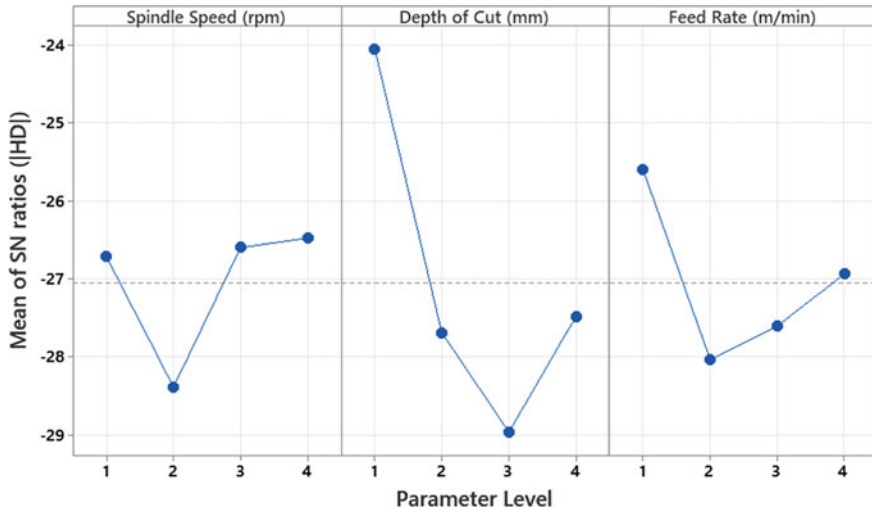| Level | Shore D Hardness | | | Optical transmission | | |
|---|---|---|---|---|---|---|
| | Spindle speed | Depth of cut | Feed rate | Spindle speed | Depth of cut | Feed rate |
| 1 | $-26.72$ | $-24.05$ | $-25.60$ | $-32.52$ | $-33.96$ | $-31.71$ |
| 2 | $-28.39$ | $-27.69$ | $-28.04$ | $-33.57$ | $-35.02$ | $-31.37$ |
| 3 | $-26.60$ | $-28.97$ | $-27.61$ | $-30.97$ | $-33.01$ | $-33.37$ |
| 4 | $-26.48$ | $-27.48$ | $-26.94$ | $-32.34$ | $-27.42$ | $-32.96$ |
| Delta | 1.91 | 4.92 | 2.44 | 2.60 | 7.60 | 2.00 |
| Rank | 3 | 1 | 2 | 2 | 1 | 3 |

**Fig. 3** Main effect plot for the mean of *S/N* ratios for the absolute change in Shore D Hardness verses parameter levels

the milling of PMMA lenses, a spindle speed of 5000 rpm, depth of cut of 0.3 mm, and feed rate of 0.05 m/min should be used. The high spindle speed with a low depth of cut and feed rate ensured smooth chip removal, which led to effective heat dissipation. The removal also reduced the friction and milling force, which reduced the tool's impact on the workpiece. This created less impact on the PMMA lenses.

Similarly, the largest *S/N* ratios for the optical transmission were $-30.97$, $-27.42$, and $-31.37$ for the spindle speed, depth of cut, and feed rate, respectively (Fig. 4). This corresponded to the optimal parameters: 3750 rpm, 1.2 mm, and 0.1 m/min for the spindle speed, depth of cut, and feed rate, respectively. High spindle speed and moderate feed rate led to a better surface cleanup, and hence a better surface finish [9]. A clean surface allowed for more light transmission and less reflection. According to a study conducted by Hossain, when light incidences a surface, it is reflected, refracted, transmitted, or absorbed [10]. A high depth of cut contributed to a reduction in thickness, which reduced the amount of light absorbed by the PMMA lens, and hence more transmission.

The impact of each milling parameter on the Shore D Hardness and optical transmission was also evaluated using the delta values. From Table 6, it was identified that the depth of cut was the dominant parameter affecting both the Shore D Hardness and optical transmission of PMMA lenses. This could be attributed to the high correlation between depth of cut, surface roughness, machining, and friction forces. The feed rate was the second dominant parameter for the Shore D Hardness and, finally, the spindle speed. The second dominant machining parameter for the optical transmission was the spindle speed and, lastly, the feed rate.

An ANOVA was also conducted to evaluate the percentage impacts of each parameter toward the Shore D Hardness and optical transmission of the PMMA lenses and
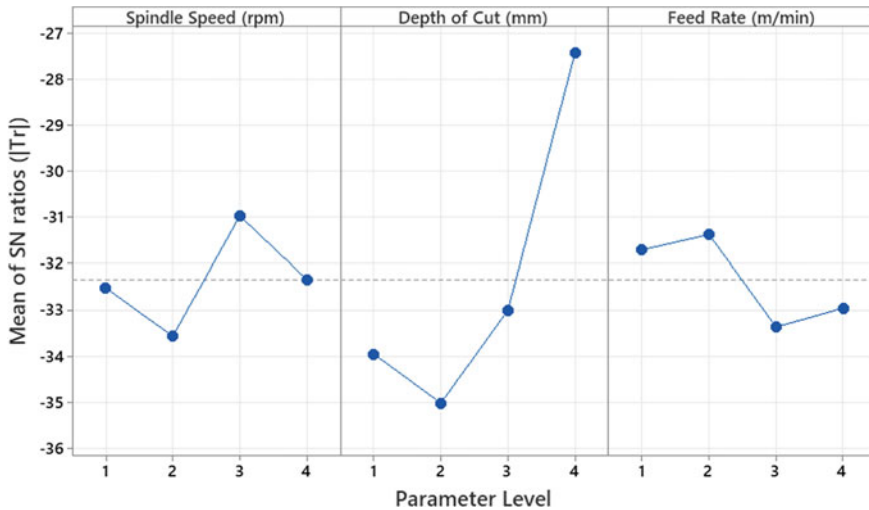
**Fig. 4** Main effect plot for the mean of *S/N* ratios for the absolute change in optical transmission verses parameter levels

to validate the findings obtained from the Taguchi analysis. This is shown in Table 7.

A significance value of 0.05 was adopted in conducting the ANOVA. It was observed that all the milling parameters were insignificant toward the Shore D Hardness with *p-values* more than the significance value (0.430, 0.198, and 0.892 for the

**Table 7** ANOVA for the absolute change of Shore D Hardness and optical transmission

| Source | DF | Adj SS | Adj MS | Percentage impact (%) | *F*-value | *P*-value |
|---|---|---|---|---|---|---|
| *Shore D Hardness* | | | | | | |
| Regression | 3 | 165.008 | 55.003 | | 0.85 | 0.494 |
| Spindle speed (rpm) | 1 | 43.218 | 43.218 | 4.58 | 0.67 | 0.430 |
| Depth of cut (mm) | 1 | 120.540 | 120.540 | 12.77 | 1.86 | 0.198 |
| Feed rate (m/min) | 1 | 1.250 | 1.250 | 0.00 | 0.02 | 0.892 |
| Error | 12 | 779.209 | 64.934 | | | |
| Total | 15 | 944.217 | | | | |
| *Optical transmission* | | | | | | |
| Regression | 3 | 1400.35 | 466.78 | | 3.06 | 0.070 |
| Spindle speed (rpm) | 1 | 1.50 | 1.50 | 0.00 | 0.01 | 0.923 |
| Depth of Cut (mm) | 1 | 1374.23 | 1374.23 | 42.51 | 9.00 | 0.011 |
| Feed rate (m/min) | 1 | 24.61 | 24.61 | 0.01 | 0.16 | 0.695 |
| Error | 12 | 1832.25 | 152.69 | | | |
| Total | 15 | 3232.60 | | | | |

spindle speed, depth of cut, and feed rate, respectively). However, the depth of cut was the highest contributing factor with approximately 12.77%, followed by the spindle speed (4.58%) and, lastly, the feed rate with almost no impact. The depth of cut was also the highest contributing factor toward the optical transmission (42.51%) and the only significant parameter with a *p-value* less than the significance value (0.011). The spindle speed and feed rate have a negligible impact on the optical transmission of PMMA lenses.

## 4 Conclusions

This study aimed to investigate the impact of milling on the Shore D Hardness and optical transmission of PMMA lenses through an experimental and mathematical model. From the findings, several conclusions can be drawn:

1. Milling of PMMA lenses reduces their Shore D Hardness and transmission significantly.
2. The highest Shore D Hardness can be obtained from a parameter combination of 3750 rpm, 0.3 mm, and 0.2 m/min for spindle speed, depth of cut, and feed rate, respectively. Likewise, the highest optical transmission can be obtained from a parameter combination of 3750 rpm, 1.2 mm, and 0.1 m/min for spindle speed, depth of cut, and feed rate, respectively.
3. To minimize the absolute change in Shore D Hardness after milling of PMMA lenses, the milling parameters should be 5000 rpm (spindle speed), 0.3 mm (depth of cut), and 0.05 m/min (feed rate). Similarly, for the optical transmission, the parameters should be a spindle speed of 3750 rpm, a depth of cut of 1.2 mm, and a feed rate of 0.1 m/min.
4. The depth of cut is the most dominant milling parameter toward the Shore D Hardness and optical transmission of PMMA lenses with a percentage impact of 12.77 and 42.51%, respectively.

## References

1. World Health Organization (2019) World Report on Vision. [Online]. Available: https://www.who.int/publications/i/item/9789241516570
2. Jahan MP, Ma J, Hanson C, Chen X, Arbuckle GK (2020) Experimental and numerical investigation of cutting forces in micro-milling of polycarbonate glass. Mach Sci Technol 24(3):366–397. https://doi.org/10.1080/10910344.2019.1698608
3. Sylajakumari PA, Ramakrishnasamy R, Palaniappan G (2018) Taguchi grey relational analysis for multi-response optimization of wear in co-continuous composite. Materials (Basel) 11(9):1–17. https://doi.org/10.3390/ma11091743
4. Langat HK, Mwema FM, Keraita JN, Akinlabi ET, Wambua JM, Jen T (2021) Optimization of milling parameters of unmodified calotropis procera fiber-reinforced PLA composite (UCPFRPC). J Compos Sci 5:261. https://doi.org/10.3390/jcs5100261

5. ISO (2003) Plastics and ebonite—determination of indentation hardness by means of a durometer (shore hardness). [Online]. Available: https://www.iso.org/standard/34804.html

6. Derakhshan ED, Akbari AA (2009) Experimental investigation on the effect of workpiece hardness and cutting speed on surface roughness in hard turning with CBN tools. In: Proceedings of the world congress on engineering, vol 2

7. Parhad P, Likhite A, Bhatt J, Peshwe D (2015) The effect of cutting speed and depth of cut on surface roughness during machining of austempered ductile iron. Trans Indian Inst Met 68(1):99–108. https://doi.org/10.1007/s12666-014-0439-y

8. Elsheikh AH, Deng W, Showaib EA (2019) Improving laser cutting quality of polymethylmethacrylate sheet: experimental investigation and optimization. J Mater Res Technol xx:1–15. https://doi.org/10.1016/j.jmrt.2019.11.059

9. Kumar NS, Shetty A, Shetty A, Ananth K, Shetty H (2012) Effect of spindle speed and feed rate on surface roughness of carbon steels in CNC turning. In: International conference on modeling, optimization, and computing, vol 38, pp 691–697. https://doi.org/10.1016/j.proeng.2012.06.087

10. Hossain S (2019) Optical properties of polymers and their applications. New Jersey Institute of Technology

# Combined Torrefaction and Densification of Rice Husk: Effect of Process Parameters

**Segun E. Ibitoye, Rasheedat M. Mahamood, Tien-Chien Jen, and Esther T. Akinlabi**

**Abstract** Torrefaction and densification technologies have been reported to enhance biomass properties for efficient and effective energy production. The enormous quantity of agricultural residues generated every year globally has threatened the people and the environment due to indiscriminate dumping and burning of the residues. Therefore, this study aims to convert agricultural residues (rice husk) into usable energy through the combined application of torrefaction and densification technology. The collected and sorted rice husk was torrefied at different temperatures (220, 240, 260, and 280 °C) and 60 min as residence time. The densification process was carried out on the torrefied samples at two different pressures (5 and 10 MPa), while the dwelling time was set at 4 min. The densification products' water resistance, shatter index, density, and drop to fracture properties were investigated following the established standards. The results showed that the outcomes of the torrefaction process were influenced by temperature and residence time, though the effect of temperature was more pronounced. Torrefaction biogas, biochar, and bio-oil yields varied between 19.23–26.28, 35.90–53.85, and 26.92–37.82%, respectively. The shatter index and drop to fracture properties increase with densification pressure and decrease with torrefaction temperature. However, the water resistance property increases with torrefaction temperature. The highest and the lowest shatter index and drop to fracture were obtained from the sample produced at 220 °C (10 MPa) and 280 °C (5 MPa), respectively. The briquettes made in this study displayed good fuel properties and can be utilized for different energy purposes.

S. E. Ibitoye (✉) · R. M. Mahamood · T.-C. Jen · E. T. Akinlabi
Department of Mechanical Engineering Science, Faculty of Engineering and the Built Environment, University of Johannesburg, P. O. Box 524, Auckland Park 2006, South Africa
e-mail: ibitoye.s@unilorin.edu.ng

S. E. Ibitoye
Department of Mechanical Engineering, Faculty of Engineering and Technology, University of Ilorin, P. M. B. 1515, Ilorin, Nigeria

R. M. Mahamood
Department of Materials and Metallurgical Engineering, Faculty of Engineering and Technology, University of Ilorin, P. M. B. 1515, Ilorin, Nigeria

E. T. Akinlabi
Pan African University for Life and Earth Sciences Institute, Ibadan, Nigeria

**Keywords** Briquettes · Densification · Drop to fracture · Shatter index ·
Torrefaction · Water resistance

## 1 Introduction

Wood is one of the most popular biomass used for energy generation. But due to
the increase in global energy demand as a result of technological advancement and
rising world population, energy production industries have begun to utilize non-
woody biomass material for energy purposes. This development is related to the
upsurge in deforestation and environmental challenges resulting from the dumping
and burning of non-woody wastes in an open field. An example of non-woody waste
is agricultural residues.

In 2017, Asonja et al. [1] reported that about 2000 billion tons of agricultural
residues are generated globally every year. The dumping and burning of agricultural
residues have constituted a threat to the people-emission of greenhouse gases, which
causes global warming and an increase in the global mean temperature. Conversion of
agricultural residues into usable energy will help reduce the use of woody biomass
for energy production and mitigation to the dumping and burning of agricultural
residues in an open field. In addition, the converted products will serve as a substitute
for fossil fuels, which will reduce the overdependence on fossil fuel and act as carbon
dioxide-neutral energy material; thus, enhancing the green environment [2].

An efficient and effective method of converting agricultural residues into usable
energy is the application densification and thermal pretreatment technologies [3,
4]. Biomass densification process is the application of forces on biomass feed-
stock with the aim of improving the fuel properties. Biomass densification can
generally be classified as briquetting and pelletizing, depending on the shape and
size of the densification products [4]. Densification eliminates some of the draw-
backs limiting biomass utilization for energy generation-low bulk and energy densi-
ties, high-moisture contents, low-combustion efficiency, handling and transportation
problems, etc. On the other hand, biomass thermal pretreatment is the process of
heating biomass in an inert atmosphere at a specific temperature range. Depending
on the operating temperature, biomass thermal pretreatment can be categorized into
carbonization, pyrolysis, gasification, and torrefaction [3, 5, 6]. Torrefaction is the
process of heating biomass feedstock in an inert atmosphere between the temperature
ranges of 200–300 °C [7, 8]. Torrefaction improves biomass' thermal, grindability,
hydrophobicity, density, and combustion properties. The combined application of
densification and thermal pretreatment technologies will substantially enhance the
biomass properties for energy utilization.

Densification and thermal pretreatment technologies have been applied in biomass
energy production, some of which are testified in literature [9–12]. The effect of
mixing ratio and binder additive on densification products has been investigated [9,
13]. It was opined that blending of feedstock and varying the percentage of binder
influences the properties of densification products. Increasing the percentage of

binder up to 6% enhances the physico-mechanical properties, beyond which the properties begin to decrease [14]. Also, Trubetskaya et al. [15] submitted that increasing the percentage of the binder has no noticeable effect on the heating property of densification products. Pua et al. [16] studied the properties of pellets produced from blends of different biomass. The findings showed that the densification of single biomass displayed better fuel properties than blending of different biomass.

Works of literature have shown that torrefaction yields, and characteristics are influenced mainly by process temperature and residence time, while the effect of particle sizes is negligible [5, 12, 17]. A comprehensive review of the application, principle, current challenges, and possible solutions of biomass thermal pretreatment and densification can be found in Ibitoye et al. [3], Ibitoye et al. [4], and Chen et al. [18]. The study conducted by Kaoma and Gheewala [19] revealed that the energy required for domestic cooking and heating could economically be generated through the densification process. It was added that viable rural electricity could be generated through the gasification process by utilizing densification products as feedstock. Thermal pretreatment of biomass before densification will enhance their thermal and combustion properties. Therefore, this study aims to generate sustainable energy from rice husk via combined torrefaction and densification processes as a substitute for fossil fuel for domestic and industrial applications. This study is expected to reduce overdependence on fossil fuels as the primary energy source and promote green environment.

## 2 Materials and Methods

### 2.1 Materials

The feedstock used for this study is rice husk, and cassava starch was utilized as a binding agent. The rice husk was collected from the Entrepreneurship Grooming Institute rice mining plants, located at Fate Road, Ilorin, Kwara State, Nigeria. The cassava starch was obtained from the Gari Making industry, Gaa-Akanbi, Ilorin, Kwara State, Nigeria.

### 2.2 Methods

#### 2.2.1 Materials Preparation and Preliminary Characterization

The collected rice husk feedstock was sorted to remove foreign substances such as grasses and stones, and the sorted feedstock was sun-dry to eliminate surface moisture. Preliminary characterization was carried out on the prepared feedstock

following the established standards [19–24]. These include thermogravimetric, proximate, and ultimate analyzes and calorific value determination. These were done to be acquitted with the feedstock properties and to help in the setting of the torrefaction process parameters.

### 2.2.2 Torrefaction Process

The torrefaction process was carried out following the method used by Ibitoye et al. [5]. Based on the thermogravimetric analysis results, the rice husk feedstock was torrefied at four different temperatures (220, 240, 260, and 280 °C). At the same time, the residence time of 60 min was observed for all the torrefaction temperatures, and nitrogen gas was utilized to create an inert environment. The rice husk feedstock was torrefied as collected without further particle reduction. The condensable gases were collected throughout the torrefaction process. After observing the residence time, the biochar was collected and transferred into a desiccator for cooling to the ambient temperature. The torrefaction yields are estimated using Eqs. 1, 2and3 [12].

$$\text{Biochar} = \frac{W_c}{W_f} \times 100\% \tag{1}$$

$$\text{Bio} - \text{oil} = \frac{W_o}{W_r} \times 100\% \tag{2}$$

$$\text{Biogas} = 100 - (\text{Bio} - \text{oil} + \text{Biochar})\% \tag{3}$$

where $W_r$ is the weight of rice husk feedstock, $W_c$ is the weight of the solid yield, and $W_o$ is the weight of the liquid yield.

### 2.2.3 Densification Process

After the torrefaction process, densification of the torrefied rice husk was carryout to form solid fuel briquettes without pulverizing the torrefied samples. The briquetting process was performed at two different pressures (5 and 10 MPa), using 5% gelatinized starch as a binding agent. The torrefied feedstock was mixed with the binder using an electric mixer at 100 rpm, and mixing of the feedstock and binder was done without adding water. After mixing for 5 min, the blend was transferred into the mode for compaction. A particle reduction was noticed after mixing the feedstock and binder. Compression was done using a 40 MPa briquetting machine (Patent number: NG/P/2022/194), and 4 min of residence time were observed for all the briquettes produced. The briquette was ejected from the mold and sun-dry for 7 days. The sun-dried briquettes were stored in air-tight bags for further analysis.

### 2.2.4 Characterization of the Produced Briquettes

*Density:* The mass and geometry of the briquette were measured immediately after ejection from the mold and after sun-drying for 7 days to calculate the green and relaxed densities, respectively. The density was determined as the ratio of the mass to the calculated volume of the briquettes. Each compaction pressure was repeated four times, and the average density is reported.

*Shatter index:* The shatter index property revealed the ability of the briquettes to withstand crushing and rubbing loads during handling. It displayed the durability characteristics of the produced briquettes. The shatter index was determined by dropping the briquette from a height of 1.8 m onto a concrete floor, and it was calculated using Eq. 4 [4, 25]. The experiment was conducted in duplicate, and the average is reported.

$$\frac{\text{Weight of the sample in plate after 4 drops}}{\text{The initial weight of the sample}} \times 100\% \tag{4}$$

*Drop to fracture:* It revealed the ability of the briquettes to withstand impact forces. It was estimated by dropping the briquettes from a height of 1.8 m on to concrete floor until the briquettes fail or crumble. The number of drops required for the briquette to crumble was recorded as the drop to fracture. The experiment was conducted in duplicate, and the average was recorded.

*Water resistance:* It revealed the hydrophobicity properties of the produced fuel briquettes. The water resistance property was determined by immersing the briquettes in water and observing the disintegration rate of the briquettes in the water.

## 3 Results and Discussion

### 3.1 Characterization of the Raw Rice Husk

#### 3.1.1 Thermogravimetric Analysis

Figure 1 shows the results of the thermogravimetric analysis (TGA) of the raw sample. The TGA revealed that the onset temperature of the raw rice husk is about 531 °C. This is the temperature at which the feedstock begins to disintegrate under heating. The onset temperature is an indication of the thermal stability of a material. At any temperature higher than 531 °C, the raw rice husk becomes thermally unstable. Higher onset temperature indicates better thermal stability properties. The onset temperature of rice husk is higher than that of corncob (389 °C) reported by Ibitoye et al. [5]. Therefore, rice husk is more thermally stable than corncob feedstock. TGA serves as a guide in the setting of the torrefaction temperature. When the onset temperature is lower than the torrefaction temperature (200–300 °C), conducting a
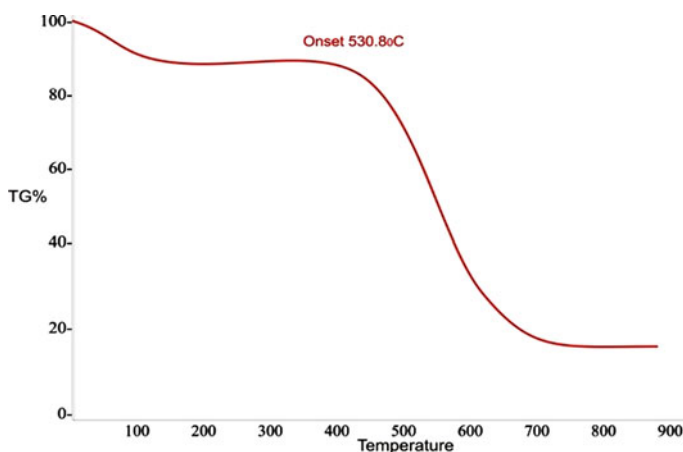
**Fig. 1** Thermogravimetric analysis of the raw rice husk

torrefaction experiment on the feedstock becomes very difficult. Happily, the onset temperature of rice husk is higher than torrefaction temperature.

### 3.1.2 Ultimate and Proximate and Calorific Value Analyzes

Table 1 shows the ultimate and proximate and calorific value analyzes results of the raw rice husk. The ash, moisture, volatile matter, and fixed carbon contents are 16.98, 9.55, 65.45, and 9.92%, respectively. The carbon, hydrogen, nitrogen, and oxygen component of the ultimate analysis are 48.72, 4.46, 0.79, 28.11%, respectively, while the calorific value is 14.89 kJ/kg. Studies of the preliminary results revealed the potential of rice husk for energy production. The results of the fixed carbon (9.92%), carbon (48.72%), and calorific value (14.89%) revealed the combustion and thermal properties of the rice husk. Although the ash content was observed to be somewhat high, the ash content is expected to reduce with the application of torrefaction and densification technology.

**Table 1** Ultimate and proximate and calorific value analyzes of the raw rice husk

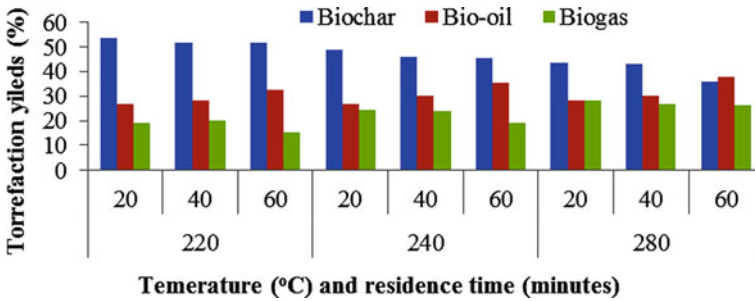| Proximate analysis (%) | | | | Ultimate analysis (%) | | | | Calorific value (kJ/kg) |
|---|---|---|---|---|---|---|---|---|
| Ash | Moisture | Volatile matter | Fixed carbon | Carbon | Hydrogen | Nitrogen | Oxygen | |
| 16.98 | 9.55 | 65.45 | 9.92 | 48.72 | 4.46 | 0.79 | 28.11 | 14.89 |

**Fig. 2** Effect temperature and residence time of torrefaction yields

## 3.2 Torrefaction Yields

Figure 2 shows the effect of residence time and temperature on torrefaction yields. The biogas, biochar, and bio-oil yields are in the range of 19.23–26.28, 35.90–53.85, and 26.92–37.82%, respectively. The results show that the biochar yield decreases as the torrefaction temperature and residence time increase. Though, bio-oil and biogas yields increase with residence time and temperature. This is because higher temperature and residence time lead to emission of volatile content and breakdown of the structural component of the rice husk. The emitted contents are condensed as bio-oil and biogas, which results in a decrease in biochar yield. The biochar yield was higher than bio-oil yield; though, the bio-oil yield was more than biogas yield. The observation and inference made in the study are in agreement with the reports of Zheng et al. [26], Odusote et al. [17], and Manouchehrinejad and Mani [27].

## 3.3 Characterization of the Densification Products

### 3.3.1 Density

The effect of densification pressure and torrefaction temperature on the briquette density is shown in Fig. 3. The green density is the density of the wet briquette, while relaxed density is the density of the sun-dried briquettes. The results presented in Fig. 3 show that the green and relaxed density varied between 0.914–1.194 and 0.549–0.747 g/cm$^3$, respectively. It was observed that the compaction pressure and torrefaction temperature affect the density of the produced briquettes, but the effect of compaction pressure was more pronounced than torrefaction temperature. Higher compaction pressure makes the briquettes particles to be closely parked; thus, reducing the distance and pore spaces between briquette particles. Furthermore, at constant mass, the applied pressure leads to a reduction in the calculated volume of the briquette and an increase in the mass per unit volume of the produced briquettes. The reduction in the intermolecular distance due to the applied pressure enhances the
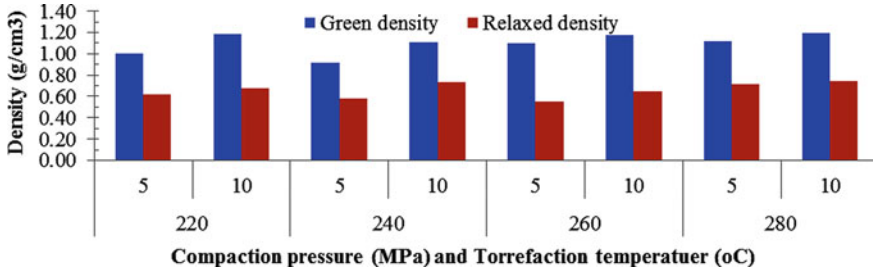
**Fig. 3** Variation of the green and relaxed density with temperature and densification pressure

adhesive force and intermolecular bonding between the briquette particles. Higher torrefaction temperature leads to loss of mass and in turn, a drop in the density of the briquettes. This is because of the disintegration and liberation of volatile matters during torrefaction. This observation is also linked with the results of the torrefaction yields (Fig. 2).

### 3.3.2 Shatter Index and Drop to Fracture

Figure 4 shows the results of shatter indices and drop to fracture at different compaction pressure and torrefaction temperature. The shatter index ranges from 99.83 to 99.93%, while the drop to fracture ranges from 250 to 300 drops.

The highest and the lowest shatter index and drop to fracture were obtained from the sample produced at 220 °C (10 MPa) and 280 °C (5 MPa), respectively. Generally, the briquettes manufactured at 10 MPa displayed better shatter index and drop to fracture properties than those manufactured and 5 MPa. This is because higher compaction pressure enhances the formation of solid bridges and inter-particle bonding, which improves the strength properties of the briquettes. Analyzes of the results show that drop to fracture and shatter index properties decrease as the torrefaction temperature increases. This is because torrefaction reduces the binding capability
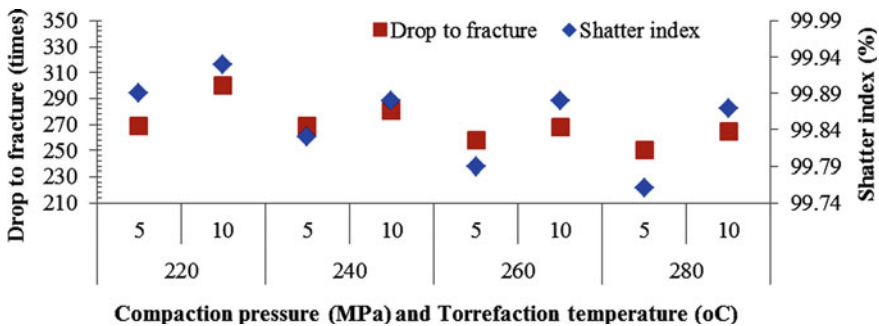


**Fig. 4** Variation of shatter index and drop to fracture with temperature and densification pressure

of the natural binding agent (lignin) inherent in the feedstock. Higher torrefaction temperature weakens the lignin and strength of the resulting briquettes. Although, briquettes strength can be improved by increasing the percentage of binder [9, 13]. At a constant percentage of binder, briquette manufactured at a lower torrefaction temperature exhibits better strength properties than those manufactured at higher torrefaction temperature.

### 3.3.3   Water Resistance

The water resistance property of the produced briquettes was also investigated. At 0 min, the samples of the briquettes floated on the water, which showed that the briquettes had not absorbed water. The briquettes floated on the water for up to about 60 min, after which they began to sink. The briquettes sunk about 120 min of immersion, but there was no noticeable disintegration after tapping the briquettes in the water. The briquettes sample began to disintegrate in water after about 7 h of immersion. It was observed that the water resistance capability of the briquettes increases with torrefaction temperature and compaction pressure. This is because torrefaction improves the hydrophobicity properties of the briquettes. The hydrophobicity nature and absorption of atmospheric moisture are significantly enhanced after torrefaction. During densification, the applied pressure reduces the pore spaces between briquettes particles, reducing the water percolation and capillary when the briquettes are immersed in water. The observation made revealed the stability of the briquettes during storage and when exposed to a humid environment.

## 4   Conclusion

The effect of process parameters on combined torrefaction and densification was investigated in this study using rice husk feedstock. Rice husk feedstock is thermally stable up to about 531 °C. Both torrefaction temperature and residence time affect the torrefaction yields, though the effect of temperature was more pronounced than residence time. Torrefaction biogas, biochar, and bio-oil yields varied between 19.23–26.28, 35.90–53.85, and 26.92–37.82%, respectively. The characteristics of the densification are influenced by pressure and torrefaction temperature. The higher the densification pressure, the better the density, shatter index, and drop to fracture property of the produced fuel briquettes. Higher torrefaction temperature results to better water resistance properties. However, briquettes density, shatter index, and drop to fracture properties decrease with an increase in torrefaction temperature.

# References

1. Asonja A, Desnica E, Radovanovic L (2017) Energy efficiency analysis of corn cob used as a fuel. Energy Sources, Part B Econ Planning, Policy 12:1–7
2. Sirous R, José F, António L (2020) Mixed biomass pelleting potential for Portugal, step forward to circular use of biomass residues. Energy Rep 6:940–945
3. Ibitoye SE, Jen T-C, Mahamood RM et al (2021) Generation of sustainable energy from agro-residues through thermal pretreatment for developing nations: a review. Adv Energy Sustain Res 2100107:1–15
4. Ibitoye SE, Jen T-C, Mahamood RM et al (2021) Densification of agro-residues for sustainable energy generation: an overview. Bioresour Bioprocess 8:1–19
5. Ibitoye SE, Jen T-C, Mahamood RM et al (2021) Improving the combustion properties of corncob biomass via torrefaction for solid fuel applications. J Compos Sci 5:1–15
6. Rezania S, Oryani B, Cho J et al (2020) Different pretreatment technologies of lignocellulosic biomass for bioethanol production: an overview. Energy 199:117457
7. Babinszki B, Jakab E, Sebestyén Z et al (2020) Journal of analytical and applied pyrolysis comparison of hydrothermal carbonization and torrefaction of azolla biomass: analysis of the solid products. J Anal Appl Pyrolysis 149:104844
8. Pahla G, Ntuli F, Muzenda E (2020) Torrefaction of landfill food waste for possible application in biomass. Waste Manag 71:512–520
9. Ajimotokan HA, Ibitoye SE, Odusote JK (2019) Physico-mechanical properties of composite Briquettes from Corncob and rice husk. J Bioresour Bioprod 4:159–165
10. Ajimotokan HA, Ibitoye SE, Odusote JK et al (2019) Physico-mechanical characterisation of fuel briquettes made from blends of corncob and rice husk. J Phys Conf Ser 1378(02200):1–12
11. Adeleke AA, Odusote JK, Ikubanni PP et al (2020) The ignitability, fuel ratio and ash fusion temperatures of torrefied woody biomass. Heliyon 6:e03582
12. Kongto P, Palamanit A, Chaiprapat S et al (2021) Enhancing the fuel properties of rubberwood biomass by moving bed torrefaction process for further applications. Renew Energy RENE 14903:1–30
13. Rajput SP, Jadhav SV, Thorat BN (2020) Methods to improve properties of fuel pellets obtained from different biomass sources: effect of biomass blends and binders. Fuel Process Technol 199:1–12
14. Deshannavar UB, Hegde PG, Dhalayat Z et al (2018) Production and characterization of agro-based briquettes and estimation of calorific value by regression analysis: an energy application. Mater Sci Energy Technol 1:175–181
15. Trubetskaya A, Leahy JJ, Yazhenskikh E et al (2019) Characterization of woodstove briquettes from torrefied biomass and coal. Energy 171:853–865
16. Pua F, Syahmi M, Ean L, Gowri S (2020) Characterization of biomass fuel pellets made from Malaysia tea waste and oil palm empty fruit bunch. Mater Today Proc 31:187–190
17. Odusote JK, Adeleke AA, Lasode OA et al (2019) Thermal and compositional properties of treated Tectona grandis. Biomass Convers Biorefinery
18. Chen W, Lin B, Lin Y et al (2021) Progress in biomass torrefaction: principles, applications and challenges. Prog Energy Combust Sci 82:1–34
19. ASTM D5373-16 (2016) Standard test methods for determination of carbon, hydrogen and nitrogen in analysis samples of coal and carbon in analysis samples of coal and coke. ASTM International, West Conshohocken, PA. Available at: www.astm.org
20. ASTM D5865-04 (2004) Standard test method for gross calorific value of coal and coke. ASTM International, West Conshohocken, PA. Available at: www.astm.org. Accessed 10 Apr 2021
21. ASTM D3175-11 (2013) Standard test method 0f volatile matter in biomass. ASTM International, West Conshohocken, PA. Available at: www.astm.org. Accessed: 10 Apr 2021
22. ASTM E871-82 (2013) Standard test method for moisture analysis of particulate wood fuels. ASTM International, West Conshohocken, PA. Available at: www.astm.org. Accessed 10 Apr 2021

23. ASTM D3172-07 (2013) Standard test methods of fixed carbon in biomass. ASTM International, West Conshohocken, PA. Available at: www.astm.org. Accessed 10 Apr 2021
24. ASTM E1755-01 (2015) Standard test method for ash in biomass. ASTM International, West Conshohocken, PA. Available at: www.astm.org. Accessed 10 Apr 2021
25. Odusote JK, Muraina HO (2017) Mechanical and combustion characteristics of oil palm biomass fuel briquette. J Eng Technol 8:14–29
26. Zheng A, Zhao Z, Chang S et al (2013) Effect of torrefaction on structure and fast pyrolysis behavior of corncobs. Bioresour Technol 128:370–377
27. Manouchehrinejad M, Mani S (2018) Torrefaction after pelletization (TAP): analysis of torrefied pellet quality and co-products. Biomass Bioenergy 118:93–104

# Noise Sensitivity of Mode Shape and Mode Shape Difference to Damage Detection

Muyideen Abdulkareem and Abideen Ganiyu

**Abstract** Wavelet transform (WT) has become a reliable tool in detecting damage in structures. Owing to its reliability, various researchers have applied WT to identify singularities in mode shapes and their derivatives to identify damage. Recently, the idea of WT analysis of mode shape differences to detect damage in structures was proposed. This involved applying the difference between the mode shape of the undamaged and damaged structure. In this study, a WT noise sensitivity of mode shapes and mode shape differences to damage detection in plate structures is presented. A numerical model of a square steel plate with different boundary conditions (one, two, and four sides fixed) is applied in this study. The damage is imposed at different locations in the plate models by reducing thickness at the damage locations to mimic corrosion. The damage detectability of both methods is then analyzed and evaluated. The results show that mode shape differences provided better and more accurate detection than mode shapes. The problem of border distortion was visible in the coefficients when mode shape was applied. The parametric analysis showed that mode shape differences performed better when the signals were polluted with noise.

**Keywords** Wavelet transform · Plate · Noise · Damage · Mode shapes · Mode shape differences

## 1 Introduction

Early detection of damage in structure at all stages can save lives, prevent destructions, and reduce cost of maintenance. Decades ago, the most common nondestructive method (NDT) of detecting damage in structure was visual inspection. This method

M. Abdulkareem (✉)
Department of Civil and Environmental Engineering, Faculty of Engineering, Technology and Built Environment, UCSI University, Kuala Lumpur, Malaysia
e-mail: abdulkareem@ucsiuniversity.edu.my

A. Ganiyu
Military Technological College, Muscat, Oman

lacks the ability to provide adequate health status of structures, especially when dealing with large and complex structures. For example, access to some areas may not be possible to inspectors, and moreover, inspection depends so much on personal judgment and experience of the inspector. In order to detect the presence of damage in such structures, researchers came up with the idea of vibration-based damage detection (VBDD) techniques. These techniques utilize the vibration responses of structures to identify damage.

The wavelet transform (WT) is a VBDD technique for precise analysis of signal that overcomes drawbacks inhibited by other techniques [1]. These hindrances may lead to incorrect detections as seen in frequency methods [2, 3] by temperature and environmental effects or long computational efforts in artificial neural network (ANN) method [4, 5]. The attractiveness of WT sterns from its ability to extract information from different varieties of data [6, 7]. Unlike techniques based of Fourier transform, WT localizes data in both time and frequency, hence able to examine local data that allow locating and detecting local damages [1, 8, 9].

In view of the versatility of WT, several researchers have applied WTs to analyze mode shapes and their derivatives to detect damage in structures. For example, Douka et al. [10] proposed a technique to identify crack characteristics in plates with an "all-over part-through" crack parallel to one of the edges. The vibration modes of a plate were analyzed using continuous wavelet transform (CWT) to estimate the cracks properties. An intensity factor that correlates to the wavelet coefficients was applied to estimate the crack depth. Quek et al. [11] presented a wavelet technique sensitivity analysis to detect cracks in beams. Different crack characteristics, boundary conditions, and wavelet functions were examined. The crack properties were evaluated through wavelet analysis of the vibration modes of the beam. In Umesha et al. [12], WT was applied to identify crack damage characteristics by using the static deflection profile. The size and location of cracks were varied, as well as the load intensity, flexural rigidity, and beam length. Ruka [13] presented a CWT method to identify cracks in a cantilever beam by using higher modes of the damaged experimental and numerical models of the beam.

Xiang and Liang [14] proposed a two-step crack detection technique for beams structures. The first step involved WT analysis of the mode shape data to detect and locate damage in the beam, while the second entailed applying the measure natural frequencies to quantify the severity of the crack depth from an established data. Zhong and Oyadiji [15] detected cracks by using CWT of reconstructed modal data of beams. Their approach was based on establishing the difference of the CWTs of two sets of mode shape data. Jiang et al. [16] applied complex continuous wavelet transform (Complex CWT) to analyze the mode shape slope to detect cracks in beams. Nikravesh and Chegini [17] presented a method to identify multiple all-over part-through cracks in a plate model by discrete wavelet transform (DWT) analysis of the mode shape data. The depths and positions of the cracks were varied to evaluate the sensitivity of the proposed method. Reddy and Swarnamani [18] applied CWT to detect and locate damage in a plate structure by suing mode shape and strain energy data. Recently, Xu et al. [19] applied WT to detect multiple damages in the curvature

mode shapes of a cantilever beam. The aim was to detect damage by applying noisy signal.

The literatures above show the reliability of WT analysis of mode shapes and their derivatives to detect damage in structures. However, an alternative to mode shapes for damage detection is to use mode shape differences. This method has recently been explored to detect damage in plate structures [20]. The method involves decomposition of the difference between the undamaged and damage structure's mode shape. The authors applied the difference between the first mode shapes of a plate structure. Similarly, Vafaei and Alih [21] showed the adequacy of the first mode shape differences to detect damage by using ANN.

In this paper, a sensitivity study is carried out to evaluate the wavelet transform performance of both mode shape and mode shape difference to damage detection. The CWT is then applied to decompose but signals to identify the location of damage. A square plate is modeled numerically with three different boundary conditions: all sides fixed, two opposite sides fixed, and one side fixed (cantilever). The damage imposed on the plate is modeled by reducing the thickness at various locations of damage. This is on the assumption that the damage is in the form of corrosion. The first mode shape is implored though higher modes contain better damage prints; however, higher modes are difficult to obtain in practice. Since the presence of noise is inevitable in practice, and to further evaluate these techniques, a detailed parametric study is carried out to evaluate the effect of varying noise levels, damage sizes and depth, as well as damage locations.

## 2  Two-Dimensional Continuous Wavelet Transform

A mother wavelet function $\psi(x)$ creates a wavelet family $\psi_u, s(x)$.

$$\psi_{uv}(x) = \frac{1}{\sqrt{v}}\psi\frac{(x-u)}{v},\tag{1}$$

where $v$ and $u$ are scale and position, respectively.

Mallat [22] defined the 1D CWT of a signal $f(x)$ as

$$Wf(u, v) = \frac{1}{\sqrt{v}}\int\limits_{-\infty}^{+\infty} f(x)\psi\left(\frac{x-u}{v}\right)\mathrm{d}x\tag{2}$$

$Wf(u, v)$ is wavelet coefficient of the wavelet $\psi_{u,v}(x)$.

According to Rucka and Wilde [23], the 2D CWT of a signal $f(x, y)$ is given as

$$W^i f(u, z, v) = \frac{1}{v} \int\limits_{-\infty}^{\infty} \int\limits_{-\infty}^{\infty} f(x, y) \psi^i \left( \frac{(x - u)}{v}, \frac{y - z}{v} \right) dx dy$$

$$= \frac{1}{v} f * \psi^i \left( \frac{-u}{v}, \frac{-z}{v} \right) = f * \overline{\psi}_v(u, z), \quad i = 1, 2 \qquad (3)$$

where $f * \overline{\psi}_v$ denotes a convolution of functions.

## 3   Plate Numerical Models and Continuous Wavelet Transform Analysis

The square plate is modeled by using a finite element software, SAP2000 [24]. The plate is made up of 784 square thin shell elements that are 20 mm by 200 mm. The three different boundaries conditions are as follows: four sides fixed, two opposite sited fixed, and one side fixed (cantilever plate). The material properties of the plate are mass density $\rho = 7850$ kg/m$^3$, modulus of elasticity $E = 200$ Gpa, and Poisson's ratio $v = 0.3$, while the plate's dimensions are length $l = 560$ mm, width $b = 560$ mm, and thickness $h = 2$ mm. The damage in the plate model is taken as corrosion and modeled by reducing the thickness of the plate at the location of damage. The thickness is reduced from 2 to 1.5 mm, indicating a 25% reduction of the thickness. The damage is square and has dimensions of 80 mm by 80 mm corresponding to 2.041% of the plate's total area. A cross-section of the plat model is shown in Fig. 1 indicating the orientation of the middle damage. The different types of boundaries of the plate models applied in this study as stated above and the various locations of damage in each plate model are shown in Fig. 2. Table 1 highlights the damage locations in each plate.

The first mode shapes of the three plates are shown in Fig. 3. Though higher modes contain more damage prints, the choice for using the first mode shapes stems from its ease to obtain in practice. Another reason is the presence of dead zones which submerge damage [13], and these zones increase as the mode increases. From the numerical analysis, the mode shapes are obtained, and the mode shape differences are obtained by subtracting the damaged plate's mode shape from the undamaged. Both mode shapes and mode shape differences are normalized to values between + 1 and −1.

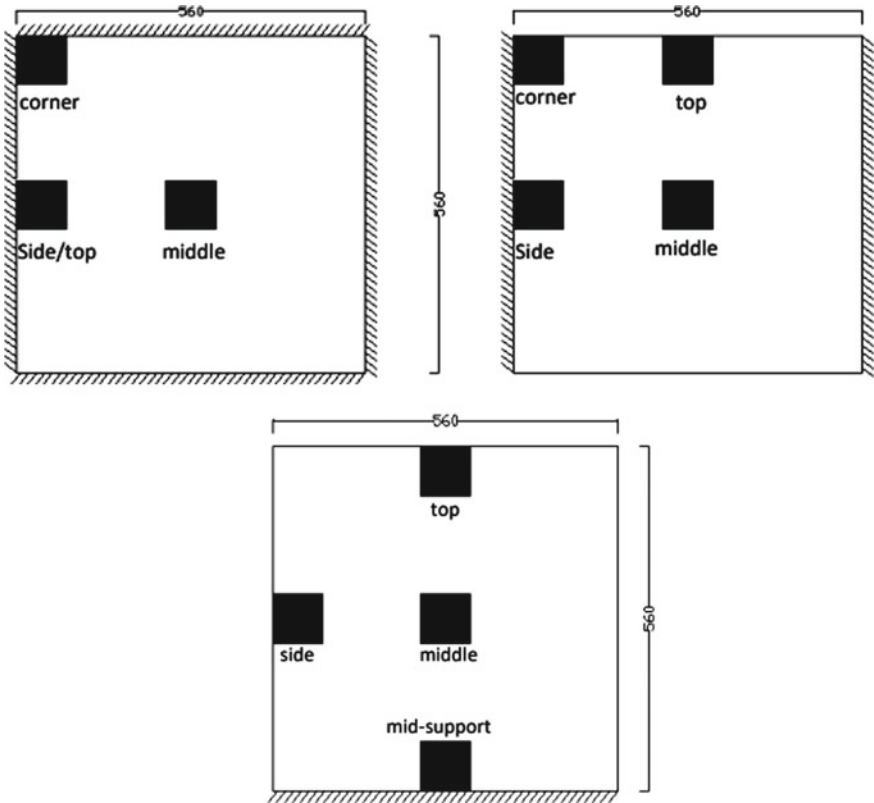**Fig. 1** Cross-section showing damage
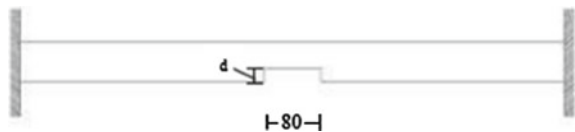
**Fig. 2** Square plate with **a** four sides fixed; **b** two opposite sides fixed; **c** one side fixed

| Plate model | Damage locations |
|---|---|
| **Table 1** Location of damage in plate models | |
| Plate model | Damage locations |
| Four sides fixed | Middle, corner, side |
| Two sides fixed | Middle, corner, side, top |
| One side fixed | Top, mid-support, middle, side |



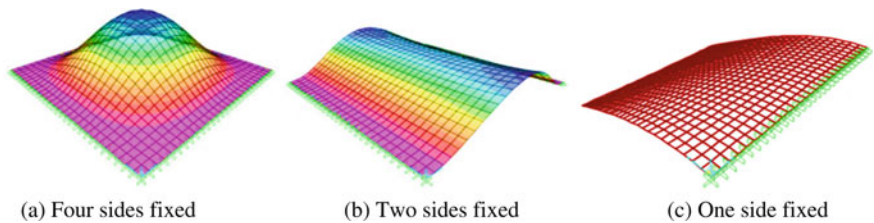(a) Four sides fixed        (b) Two sides fixed        (c) One side fixed

**Fig. 3** First mode shapes

The WT analysis is executed by using the Wavelet Toolbox in Matlab R2015a. The selected mother wavelet is Paul wavelet, while the scale and angle indexes are 3 and 1, respectively. The selection is arrived at by applying trial and error method to choose the best combination of mother wavelet, scale, and angle indexes for the best damage detection [21, 22]. The mode shapes and mode shape differences are decomposed by using the 2D CWT as shown in Eqs. 4 and 5 for the horizontal and vertical components, respectively.

## 4 Wavelet Transform Analysis Results

### 4.1 Plate with Four Sides Fixed

This section presents the results of damage detection in the plate with four side fixed. In Fig. 4, the result of the wavelet coefficients of the decomposed mode shape differences are presented. It is clearly seen that the middle, corner, and side/top damages are detected precisely. The coordinates of the detected damages are (280,280), (40,520), and (40,280), respectively, and these values correspond to the actual damage locations. Similarly, the effects of border distortion and false damage detection are not visible. Border distortion effects are eliminated by reducing the stiffness change at the boundaries by applying mode shape differences. However, from the mode shape decomposition shown in Fig. 5, only, the middle and side/top damages are accurately detected with no visible border distortion and no false detection. The coefficient of the corner damage as seen in Fig. 5b gives inaccurate and false detection with the effect of border distortion visible. The middle and side/top damage effect on the stiffness of the plate submerges the effect of border distortion, but not enough when damage occurs at the corner damage.
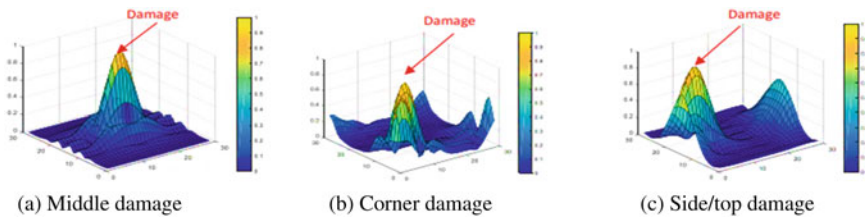


(a) Middle damage     (b) Corner damage     (c) Side/top damage

**Fig. 4** Wavelet coefficients of numerical plate model using mode shape difference (four sides fixed)

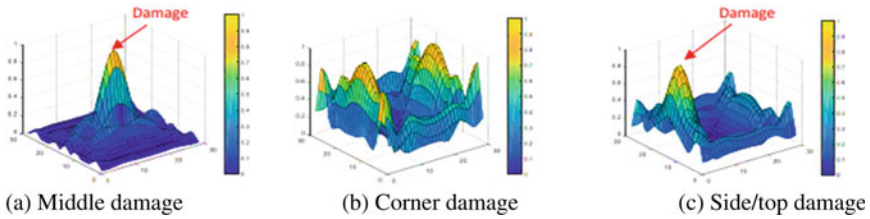(a) Middle damage          (b) Corner damage          (c) Side/top damage

**Fig. 5** Wavelet coefficients of numerical plate model using mode shape (four sides fixed)

## 4.2 Plate with Two Opposite Sides Fixed

In Fig. 6, the wavelet coefficients of the plate with two opposite sides fixed using mode shape differences are presented. The four damage locations are accurately detected with no false damage detection. However, the effect of border distortion can be seen in Fig. 6b but no sufficient enough to submerge the damage coefficient in locating the corner damage. The absence of border distortion in the other coefficients indicates the reduction of sudden change in stiffness experienced at the boundary due to applying mode shape differences. The locations of the detected middle, corner, side, and top damages are defined by their coordinates as (280,280), (40,520), (40,280), and (280,520), respectively. The mode shape decomposition results shown in Fig. 7 indicate that only the top and corner damages are accurately detected. Although Fig. 7b shows the detection of corner damage, effect of border distortion is visible as seen in Fig. 6b. The middle and side damages (Fig. 7a and c) are not detectable due to border distortion dominance in these coefficients. This shows that presence of damage at the middle and side locations in the plate does not have enough effect on the plate's stiffness to prompt detection of these damages when the mode shape decomposition is utilized. Results in this section indicate that applying mode shape differences to detect damage in plate with this boundary condition is advisable.

## 4.3 Plate with One Side Fixed

Figures 8 and 9 show the WT coefficients of the plate with one fixed side by using mode shape and mode shape difference, respectively. In Fig. 8, the four damage locations are accurate, however, an additional false damage is included in Fig. 8d. Border distortion can visible but very minimal and has no effect in the damage detection. In Fig. 9a, b and c, the top, mid-support, and middle damages are not detected. The effects of border distortion occur in these coefficients submerging the damages. In Fig. 9d, the side damage is detected correctly in the coefficient; however, the presence of a false damage and border distortion can be seen. This result indicates that wavelet transform decomposition of mode shape for damage detection is not suitable when cantilever plate structure is considered. Thus, wavelets transform
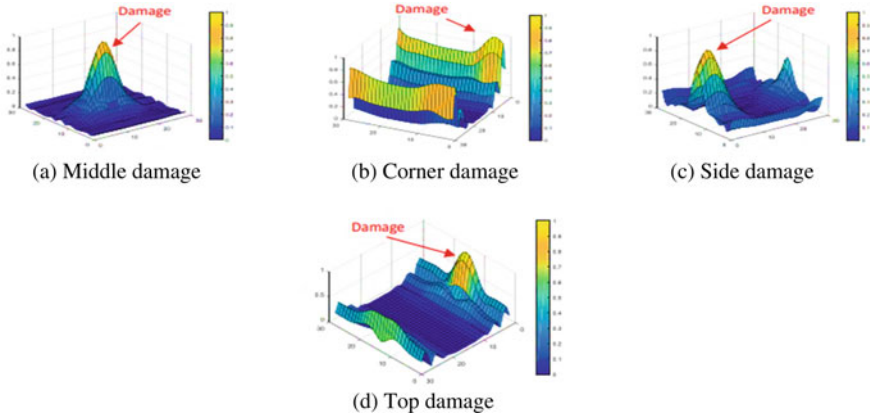
(a) Middle damage        (b) Corner damage        (c) Side damage



(d) Top damage

**Fig. 6** Wavelet coefficients of numerical plate model using mode shape difference (two opposite sides fixed)



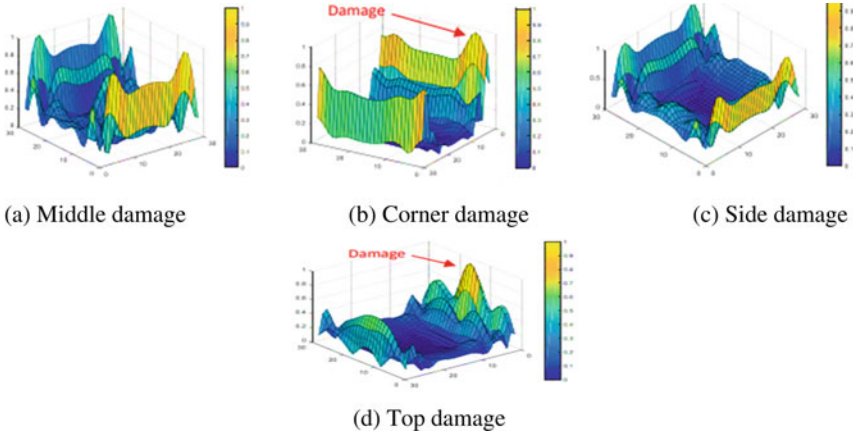(a) Middle damage        (b) Corner damage        (c) Side damage



(d) Top damage

**Fig. 7** Wavelet coefficients of numerical plate model using mode shape (two opposite sides fixed)

decomposition of mode shape differences of cantilever plate is more suitable than mode shape for identification of damage.

## 5 Parametric Study

This section provides a more detailed study on the comparison of the capabilities of mode shape and mode shape differences to detect damage through wavelet transform decomposition. Since the effects of noise are inevitable in real structures, the main parameter considered is noise. In addition to noise, the damage area and thickness
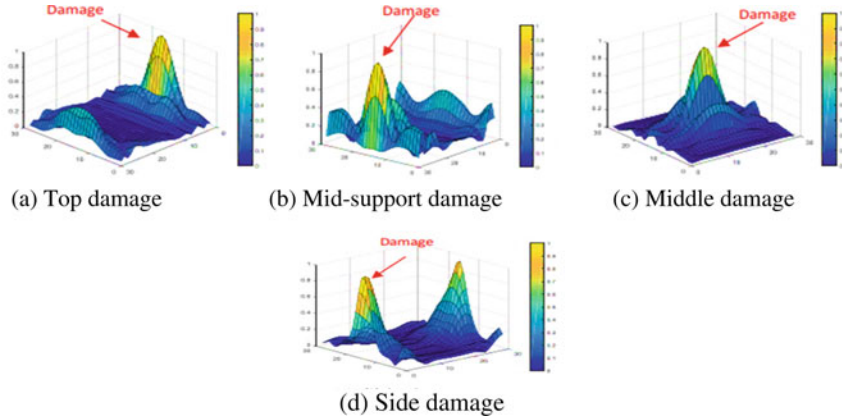
(a) Top damage          (b) Mid-support damage          (c) Middle damage

(d) Side damage

**Fig. 8** Wavelet coefficients of numerical plate model using mode shape difference (one side fixed)



(a) Top damage          (b) Mid-support damage          (c) Middle damage
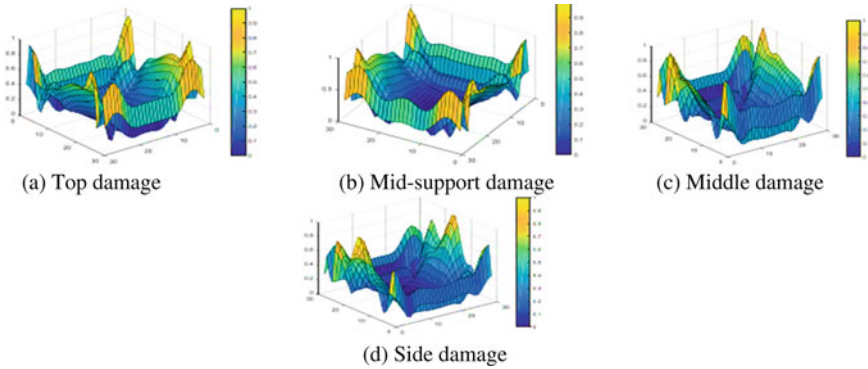
(d) Side damage

**Fig. 9** Wavelet coefficients of numerical plate model using mode shape (one side fixed)

reduction (severity) are also varied, and the results are presented graphically. The damage areas are varied between 0.51 and 2.51% of the plate's area, while the severities are between 5 and 87.5%. Table 2 shows the damage severities (damage cases) considered. The damage characteristics, i.e., location, size, and severity, are combined, and noise is added to each obtained signal. The noise-inflicted signal is then decomposed to identify damage location. This is done to obtain the maximum allowable noise that can be added to the signal before damage becomes undetectable due to the noise added to the signal. Noise is added to the signal by using the equation given as:

$$e = 20 \log 10 \left( 1 / m \right) \tag{4}$$

$$x_m = awgn(x, e) \tag{5}$$

**Table 2** Thickness reduction of plate

| Case | 1 | 2 | 3 | 4 | 5 |
|---|---|---|---|---|---|
| Thickness reduction (%) | 5 | 25 | 50 | 75 | 87.5 |
| Plate thickness $d$ (mm) | 1.90 | 1.50 | 1.00 | 0.50 | 0.25 |

where $e$ is signal-to-noise ratio and $m$ is noise level.

In the graphs in this section, the $x$- and $y$-axes represent the damage area and noise level, respectively. The curves represent the maximum allowable noise level to detect damage for different damage characteristics. The area below each curve represents the allowable noise level to detect damage, while the area above represents the unallowable noise level.

## 5.1  Plate with Four Sides Fixed

The graphs in Figs. 10 and 11 show the maximum allowable noise levels for damage in plate with four sides fixed. In Fig. 10, the mode shape is applied, and the damage locations considered are middle and side/top. These two locations are considered because the third damage location (corner) is undetectable in the wavelet coefficient of the mode shape. The trend in the graphs shows that middle damage has higher allowable noise levels than side/top damage except when the severity is 5% (Case 1) where allowable noise is 0%. It shows that at a very minute severity, the side/top damage has higher effect on the plate's stiffness than the middle damage. However, this turns around when the severity increases to 25% (Case 2) and above. For example, in Fig. 10b, the allowable noise level when damage area is 2.041% for middle damage is 3%, while side/top is 2%. This means that middle damage has greater effect on the plate's stiffness than side/top damage. In addition to this, the allowable noise levels of both damage locations increase as the damage severity and size increases. This is actually an expected trend, and it is due to greater effect on plate's stiffness as the damage severity increases. Taking severity, for example, the allowable noise at 0.51% middle damage area is 1% in Case 2 (Fig. 10b) increases to 2% in Case 5 (Fig. 10e). Similarly, in consideration of damage size in Case 2, the allowable noise level at 0.51% middle damage area is 1%, and this increases to 3% at 2.51% middle damage area.

In Fig. 11, the maximum allowable noise levels for damage detection when applying mode shape difference are presented by considering the three damage locations are represented. From the graphs in Fig. 11, corner damage has the highest allowable noise level, then middle damage, while the side/top damage has the least. For example, when damage severity is 5% (Case 1) and area is 0.51% plate's area, the allowable noise level for corner, middle, and side/top damages is 23%, 17%, and 14%, respectively. This is an indication that the impact on stiffness of the plate in the mode shape difference is highest when damage occurs at the corner, with
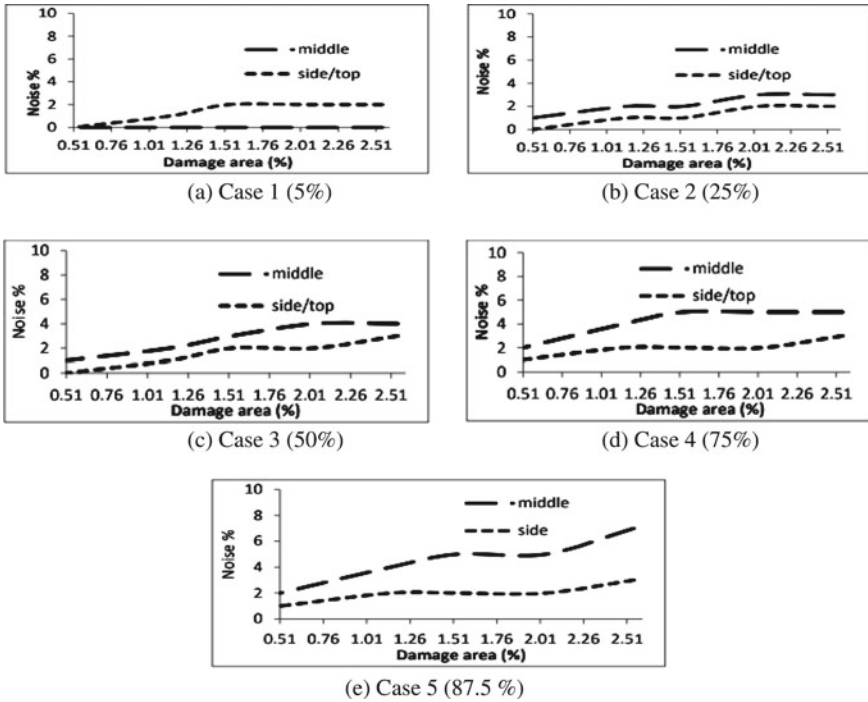
(a) Case 1 (5%)

(b) Case 2 (25%)

(c) Case 3 (50%)

(d) Case 4 (75%)

(e) Case 5 (87.5 %)

**Fig. 10** Damage detectability with respect to noise and damage severities (mode shape) (four sides fixed)

middle damage next and side/top damage having the least. Similarly, the allowable noise levels of the three damage locations increase as the damage severity and size increases. This is as expected and seen when we have corner damage of 0.51% plate's area, the allowable noise level increases from 23% at severity of 5% (Case 1) to 30% at severity of 87.5% (Case 5). The allowable noise increases from 23 to 28% when corner damage size increases from 0.51 to 2.51% of plate's area at severity of 5% (Case 1).

From these Figs. 10 and 11, we can see that the maximum allowable noise levels are higher when mode shape differences are applied than mode shape. This is a trend applicable to all damage locations. For example, at severity of 75% (Case d), the mode shape of middle and side/top damages at 0.51% damage area has allowable noise levels of 2% and 1%, respectively, while these values for mode shape difference are 21% and 22%, respectively. The resilience to noise as seen in the application of mode shape differences results from the overall reduction of stiffness all through the signal causing high coefficient at the point of damage.
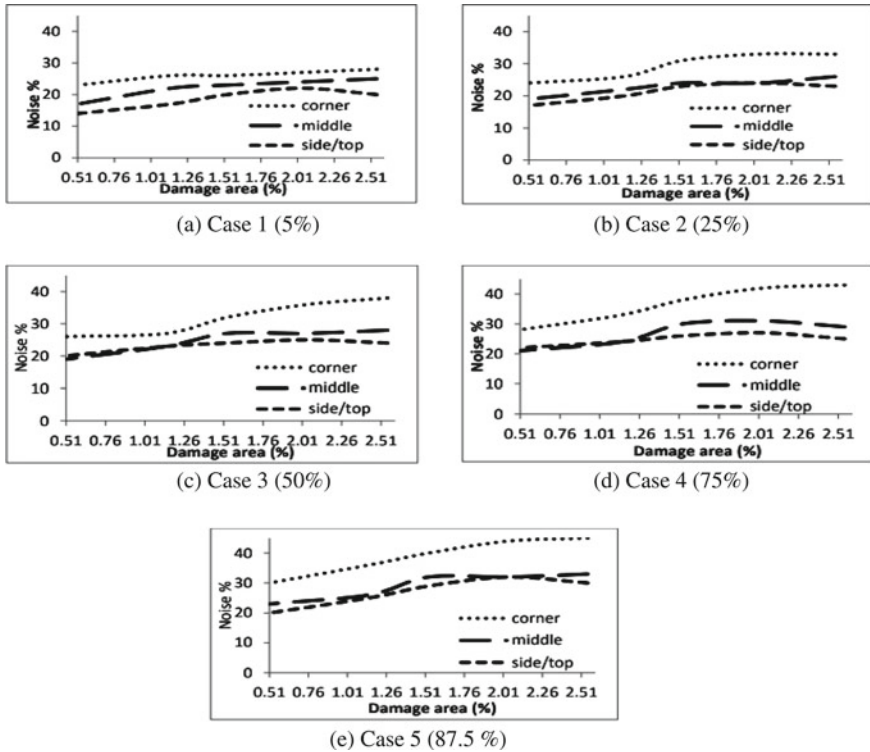
**Fig. 11** Damage detectability with respect to noise and damage severities (mode shape diff) (four sides fixed)

## 5.2 Plate with Two Opposite Sides Fixed

The results in the section show the maximum allowable noise levels to detect damage in a plate with two opposite sides fixed. Figures 12 and 13 highlight the performance of mode shape and mode shape difference, respectively. From Fig. 12, only, the top and corner damage locations are represented in the graphs. The other two locations (middle and side) are undetectable by decomposing mode shapes of this plate structure; hence, no maximum allowable noise level for damage detection is presented. Figure 13a shows that the maximum allowable noise level for corner and top damages with severity of 5% (Case 1) is zero. This means that addition of noise to mode shape signal with 5% severity is undetectable. Generally, the corner damage is more resilient to noise than top damage. In Fig. 12b, the allowable noise levels at 1.148% damage area are 2% and 1% for corner and top damages, respectively. This means that corner damage has higher wavelet coefficient than top damage as a result of the effect on the plate's stiffness. The trend in the graphs in Fig. 13 also shows that allowable noise levels increase as the damage severity and area increases. These increments are expected as higher damage severity and size have higher coefficients indicating

damage. For example, the maximum allowable noise level for corner damage at 1.148% damage area and 25% severity (Case 2) is 2%, and this increases to 4% at the same damage area but as severity increases to 87.5% (Case 5). Similarly, the allowable noise level increases from 2 to 4% when the corner damage area increases from 1.148 to 2.041% as seen in Fig. 12c (Case 3).

In Fig. 13, the maximum allowable noise levels to detect damage in plate when mode shape differences are decomposed are shown. The curves represent all the four damage locations. The top damage is the most resilient to noise in this structure as mode shape difference is employed. This is followed by side, middle, and corner damages. The trend in these graphs shows that allowable noise levels also increases as the severity of damage increases. For example, the allowable noise level at 2.041% top damage area is 25% when severity is 5% (Case), and this increases to 35% when severity increases to 87.5% (Case 5). Similarly, the allowable noise level increases as the damage severity increases. However, in the middle damage, the allowable noise
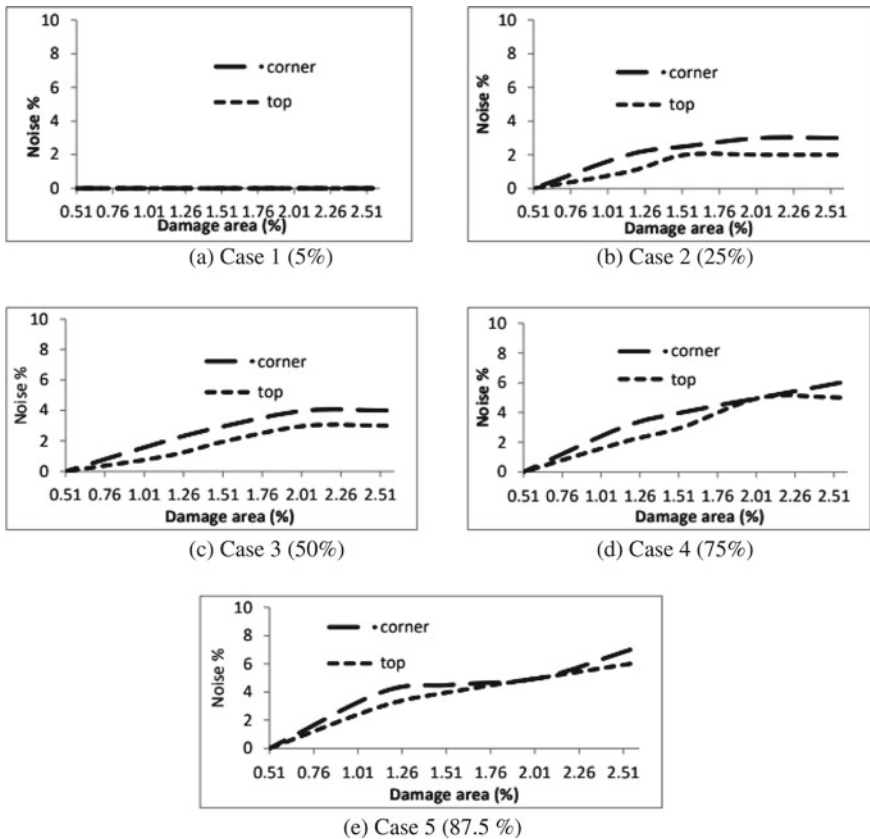


**Fig. 12** Damage detectability with respect to noise and damage severities (mode shape) (two opposite sides fixed)

(a) Case 1 (5%)

(b) Case 2 (25%)

(c) Case 3 (50%)
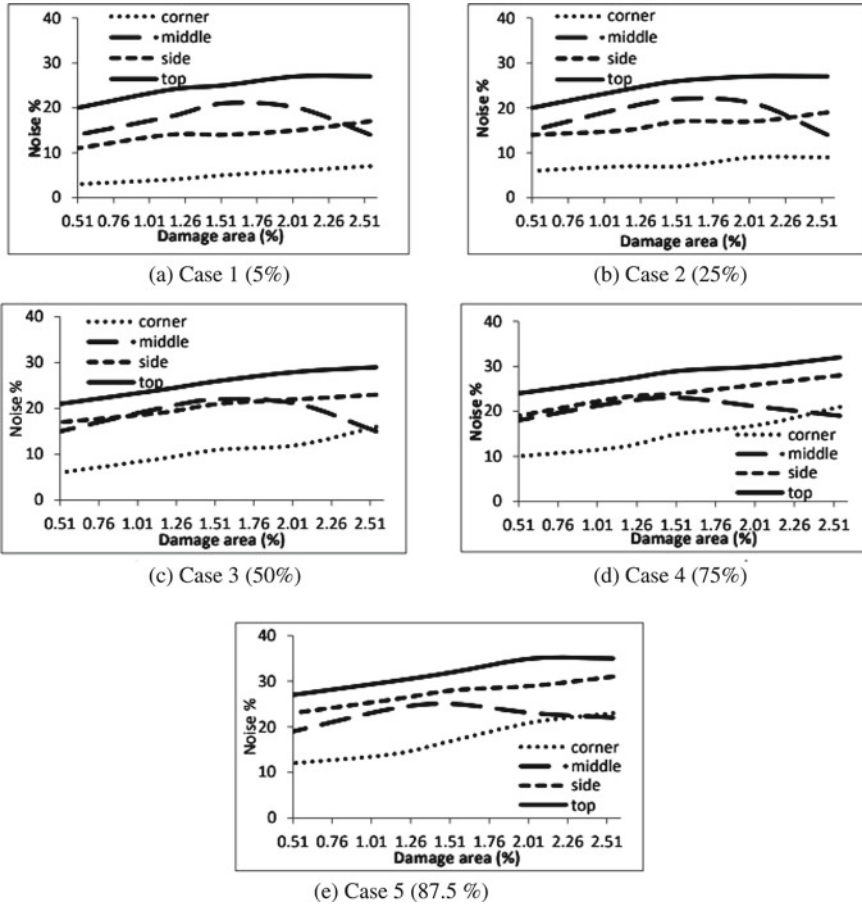
(d) Case 4 (75%)

(e) Case 5 (87.5 %)

**Fig. 13** Damage detectability with respect to noise and damage severities (mode shape diff) (two opposite sides fixed)

level increases, gets to a peak, then decreases. The allowable noise level increments seen in the top, side, and corner damages increase from 24%, 19%, and 10% to 32%, 28%, and 21%, respectively, at damage area 0.51% to 2.51% when the severity is 75% (Case 4) as shown in Fig. 13d. On the other hand, in Fig. 13d, the allowable noise level at 0.51, 1.531, and 2.51% damage areas are 19, 23, and 18%. This indicates that the effect of middle damage on the plate's mode shape difference increases until the middle damage area gets to 1.53%, and a further increment in the middle damage area leads to decrease in the effect of stiffness, thus lowering the damage coefficient. This has shown that the location of damage can play a role in the level of noise resilience.

This section shows that mode shape differences perform better than mode shape when noisy data are applied to detect damage in wavelet transform coefficients. It

also shows that the corner damage is more resilient to noise than top damage when mode shape is applied, whereas, top damage is more resilient when mode shape difference is applied.

## 5.3 Plate with One Side Fixed

Decomposition of mode shapes obtained from cantilever structures is unable to give damage locations; thus, this section shows only results from mode shape differences. The damage locations are top, middle, mid-support, and free end of the plate structure. The graphs in Fig. 14 show the maximum allowable noise levels for each location with other damage parameters. From Fig. 14, the trend shows that top damage is more resilient to noise than other damage locations. This is followed by middle, mid-support, and free-end locations. In this view, top damage has the highest wavelet coefficient do detect damage due to the sudden perturbation in the decomposed signal caused by the effect of stiffness. Similarly, in Fig. 14, it can be deduced that the maximum allowable noise levels of the damage locations increase as damage area and severity increases. This is due to the normal effect on structures stiffness that reduces as damage area and severity increases. By increasing damage (area or severity), the perturbation causing damage increase, and this submerges the presence of noise until it reaches the maximum allowable noise level. A close look at Fig. 14 shows that the smallest free-end damage area that is detectable is 0.765% plate's area. This shows that damage less than 0.765% plate's area is undetectable, and the stiffness effect of such damage is not enough to produce perturbation that can be captured in the wavelet coefficients. Similarly, Fig. 14a shows that when mid-support damage severity is 5% (Case 1), damage area less than 0.765 is undetectable; however, Fig. 14b shows that free-end damage area of 0.51% is detectable when severity is 25% (Case 2).

## 6 Conclusions

In this study, an evaluation of damage detection performance of wavelet transforms analysis of first mode shapes and first mode shape differences of plate structures is presented. A parametric study is also presented to study the effects of varying levels of noise, damage size, and damage severity. Numerical models of a square plate with three different boundary conditions with damage at different location are applied. The boundary conditions are four sides fixed, two sides fixed, and one side fixed. The results showed that wavelet analysis of mode shape differences provided more reliable results than mode shapes. Damage locations in the plates were accurately identified when the mode shape differences were applied; however, accurate results were not obtained when the mode shapes were applied. Damage locations in the plate with one side fixed were undetected when mode shape was applied. Generally, the
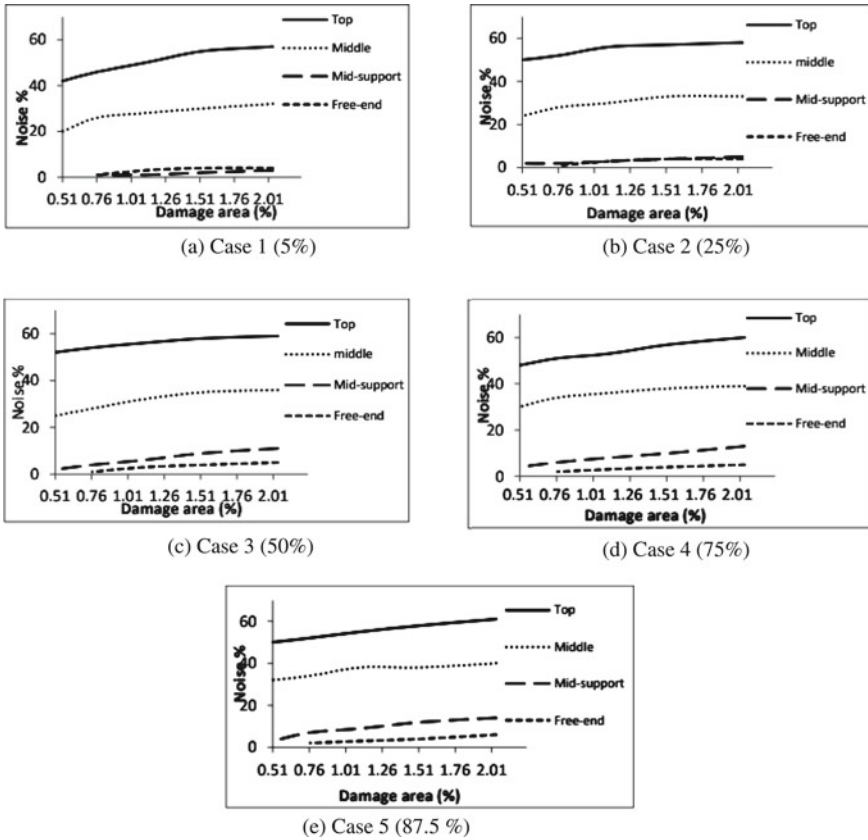
**Fig. 14** Detectable damage level with respect to noise for different levels of damage severity (mode shape diff) (one side fixed)

effect of border distortion resulted to inaccurate and false damage detection when applying mode shapes. The parametric study showed that mode shape differences give better and accurate results than mode shape in wavelet analysis.

## References

1. Bagheri A et al (2011) Structural damage identification of plates based on modal data using 2D discrete wavelet transform. Struct Eng Mech 1:13–28
2. Kim J-T, Yun C-B, Yi J-H (2003) Temperature effects on frequency-based damage detection in plate-girder bridges. KSCE J Civil Eng 6:725–733
3. Park J-W et al (2015) Development of temperature-robust damage factor based on sensor fusion for a wind turbine structure. Front Struct Civil Eng 1:42–47
4. Lai WF, Miang MN, Min YH (2016) Anticipating the logistics companies' preference on technology adoption: AHP approach. Int'l J Bus Sys Res 2–4:346–363

5. Abdulkareem M, Ganiyu A, Abd Majid MZ (2019) Damage identification in plate using wavelet transform and artificial neural network. IOP Conf Ser: Mater Sci Eng 1:012015

6. Andreaus U et al (2016) Experimental damage evaluation of open and fatigue cracks of multi-cracked beams by using wavelet transform of static response via image analysis. Struct Control Health Monit

7. Yousefi J et al (2014) Damage categorization of glass/epoxy composite material under mode II delamination using acoustic emission data: a clustering approach to elucidate wavelet transformation analysis. Arab J Sci Eng 2:1325–1335

8. Abdulkareem M, Ganiyu A, Nathaniel O et al (2021) Interval analysis of mode shapes to identify damage in beam structure. Materialwiss Werkstofftech 10:1064–1072

9. Tan HR, Lum KM, Mok VH (2007) Performance evaluation of coifman wavelet for ECG signal denoising. In: 3rd Kuala Lumpur International Conference on Biomedical Engineering, pp 419–422

10. Douka E, Loutridis S, Trochidis A (2004) Crack identification in plates using wavelet analysis. J Sound Vib 1–2:279–295

11. Quek ST et al (2001) Sensitivity analysis of crack detection in beams by wavelet technique. Int J Mech Sci 12:2899–2910

12. Umesha P, Ravichandran R, Sivasubramanian K (2009) Crack detection and quantification in beams using wavelets. Comput Aided Civil Infrastruct Eng 24:593–607

13. Rucka M (2011) Damage detection in beams using wavelet transform on higher vibration modes. J Theor Appl Mech 49:399–417

14. Xiang J, Liang M (2012) Wavelet-based detection of beam cracks using modal shape and frequency measurements. Comput Aided Civil Infrastruct Eng 27:439–454

15. Zhong S, Oyadiji SO (2011) Detection of cracks in simply-supported beams by continuous wavelet transform of reconstructed modal data. Comput Struct 89:127–148

16. Jiang X, Ma ZJ, Ren WX (2012) Crack detection from the slope of the mode shape using complex continuous wavelet transform. Comput Aided Civil Infrastruct Eng 27:187–201

17. Nikravesh SMY, Chegini SN (2013) Crack identification in double cracked plates using wavelet analysis. Meccanica 48:2075–2098

18. Reddy DM, Swarnamani S (2012) Damage detection and identification in structures by spatial wavelet based approach. Int'l J Appl Sci Eng 10:69–87

19. Xu W et al (2015) Two-dimensional curvature mode shape method based on wavelets and teager energy for damage detection in plates. J Sound Vib 347:266–278

20. Abdulkareem M, Kasali ME et al (2019) Optimal sensor distance for damage detection considering wavelet sensitivity & uncertainties. IOP Conf Ser: Mater Sci Eng 513:012018

21. Vafaei M, Alih SC (2017) Adequacy of first mode shape differences for damage identification of cantilever structures using neural networks. Neural Comput Appl

22. Mallat S (1998) A wavelet tour of signal processing. Academic, New York

23. Rucka M, Wilde K (2006) Application of continuous wavelet transform in vibration based damage detection method for beams and plates. J Sound Vib 297:536–550

24. Computers and structures (2014) i SAP2000. Version 17.1.1

# Conversion of Industrial Steel Waste to Smart Lightweight Structures Toward Sustainable Development Goal 12

**V. Vijaya Prakash and J. Shamini**

**Abstract** This study evaluated the suitable percentage of replacing natural coarse aggregate with industrial steel waste generated from metal roofing fabrication industry to produce G35 grade eco-friendly concrete. Experimental design mix for the wasted steel substitution with crushed granite was prepared at 10%, 15% and 20% where the control mix specimen was used as reference for mechanical strength comparison. Through compressive strength tests, the mechanical strengths were observed with the increasing of curing age, but the strengths were reduced with the increment of wasted steel in the mixture. 10% of wasted steel substitution gave the optimum mechanical strength values where the values slipped drastically for 15% wasted steel substitution and above. Acid–base reaction between cement and steel coating in the concrete mixture generated hydrogen gas, which reduced the compressive strength. The higher the percentage of steel in the concrete mixture, the weaker the mechanical strengths were obtained. By recycling the steel waste, the eco-friendly concrete encourages lightweight structures for sustainable environment.

**Keywords** Lightweight · SDG12 · Industrial steel waste · G35 concrete · Compressive strength

## 1 Introduction

Increased production rates of iron and steel promoted economic wealth. However, they imposed challenges toward sustainable development, due to emissions associated with iron and steelmaking, and increasing usage of resources [1]. To satisfy the human greed to maximize profit, natural resources were exploited, which have led to its extinction. Therefore, it is important for the manufacturing companies

V. Vijaya Prakash (✉)
Department of Environmental Sciences, Faculty of Forestry and Environment, Universiti Putra Malaysia, UPM Serdang, 43400 Selangor, Malaysia
e-mail: vijaya5982@gmail.com

J. Shamini
Centre for Advanced Materials and Intelligent Manufacturing, Faculty of Engineering, Built Environment and IT, SEGi University, Sdn Bhd, 47810 Petaling Jaya, Selangor, Malaysia

to contribute through a corporate social responsibility program, to promote reuse or recycling of such wastes [2]. In the current era, the Industry Revolution 4.0 has promoted the manufacturing industry to force themselves into the evolution of the way these industries run their business. The challenges of the Industry 4.0 are divided into four different scenarios: deployment, operation cum technologies, integration and compliance with the Sustainable Development Goals, as well as long-run scenarios. From all these scenarios, basic production input–output flow such as raw material, energy information consumption, product and waste disposal has an important role to play [3].

The processes involved in recycling of wasted steel are tedious. Molten steel needs a critically high temperature of about 1450–1550 °C. Water quenching is a traditional heat recovery technology, which uses cold water to cool down slag. However, this technology consumes a huge amount of water, yet fails to recover the sensible heat of the slag [4]. Critically, high power consumption and other natural resources need to be forfeited for the recycling processes to be carried out. However, if the waste is not handled tactfully, it will end up in the environment. Some researchers identified wasted steels, which can stay in the environment and will have prolonged contact with environmental components, such as soil and deep water. Subsequently, it might promote the release of dangerous substances for both human health and the environment [5]. Mutagenic and genotoxic substances can be found in aquatic and soil environments, which can have an adverse effect toward living creatures, through drinking water and the food chain, leading to serious public health concerns which go beyond a few generations [3]. Pollution occurs when there is a high concentration of heavy metal, which can be catastrophic toward microbes. The leachate (soaked water from the solid waste) produced from heavy metal is unavoidable, especially in developing countries, which can flow into water streams involved in the daily usage of the communities [6].

Studies show that heavy metals can be classified as substantial pollutants due to the high density, even at low concentrations, which can be highly toxic. Eight heavy metals, such as lead (Pb), zinc (Zn), nickel (Ni), arsenic (As), chromium (Cr), copper (Cu), mercury (Hg) and cadmium (Cd), are listed as highly spread heavy metals in the environment [7]. To reuse this wastage into useful products, this research has been conducted. Coated steels which are mainly used in roofing and wall cladding industry as a support in buildings were used for this research study. The factory is producing average of three percent (3%) coated steel wastages which is approximately eight metric ton (8 mt) monthly from their production. The inability to recover the wastages will end up in land filling. This needs to be handled tactfully to avoid unwanted waste. In this study, the wastage was reused as a replacement of coarse aggregate to produce G35 concrete.

## 2 Experimental Material and Method

### 2.1 Material Preparation

The material used in this study consisted of water, cement, river sand, rock aggregate and wasted coated steel as partial replacement of coarse aggregate. Aggregates from rock quarries with 20 mm particle size were used as coarse aggregate to act as structural filler and occupying majority volume of the concrete to increase the strength and workability purposes [8]. The wasted coated steel is protected with resin coating thickness of 0.05 mm on both top and bottom surfaces [9]. Initially, the wasted coated steel came in roll form to Production Department for roofing and wall cladding forming. Before the roll forming took place, it is a normal practice to cut off the beginning and ending portions to meet the 8 feet supplier's recommendations. These two parts of metal sheet in the roll have a high potential to get damaged (scratches and dented) due to unavoidable transportation issue from the supplier. These wastages were later slit into strip form with the width of 20 mm by using digital control hydraulic shearing machine. Next, the strips were cut into 20 mm length, which made the sample dimension of 20 mm × 20 mm × 0.6 mm.

### 2.2 Compressive Strength Test

The ability of hardened concrete to withstand maximum compressive load was determined through compressive strength test. Substitution of the wasted steel was kept at 10%, 15% and 20% for 1 day, 7 days, 14 days, 21 days and 28 days over the period of curing age [10]. Concrete specimens were cured by air and water, of which the day 1 concrete mixture was cured by air. Meanwhile, specimen for day 7 to day 28 was cured in water. Three sample strengths were tested for each mixed batch to determine the average strength of the hardened concrete.

Cube-shaped concrete specimen was used to test the compression load using compression testing machine, where the reading was taken for all mixed batches until the compression reaches the failure point. The strength values can be determined by using Eq. 1 during the compressive strength test.

$$C_S = \frac{M_l}{A_S} \tag{1}$$

where
$C_s$ = compressive strength, MPa
$M_l$ = maximum load at failure point, N
$A_s$ = specimen cross-sectional area, mm$^2$.

## 3    Results and Discussion

### 3.1    Strength Test

Figure 1 shows the mechanical strength across various testing periods, from day 1 to day 28, for concrete batches with 10%, 15% and 20% waste substitution, with crushed granite. The compressive strength increased due to the concrete aging process and displayed a continuing decrease in workability of the partially replaced coarse aggregate concrete specimen when the amount of waste increased. The 35 MPa targeted strength of G35 concrete on 28th day of water curing was obtained for control mix specimen with the compressive strength achieved at 36.16 MPa, which is 3.3% higher than projected mechanical strength. For the 10% waste replacement, the obtained mechanical strength was 34.80 MPa, which was 99.43% of the targeted compressive strength value. This value was acceptable, as the expected outcome needed to be at 99% comparatively with that of the base concrete strength, which is 35 MPa [11]. There was an increase in strength by sixfold on day 28, compared to day 1 curing for the 10% substitution sample. This was because the day 1 specimen was still wet and weak. The same trend was observed for another percentage of the wasted replacement from day 1 to day 28, but the sudden strength decline was detected for the wasted substitution 15% and onwards. The compressive strengths were 25.73 MPa and 20.43 MPa, for the 15% and 20% substitution, respectively, on the 28th day of the curing process.

Figure 2 shows the cracked concrete sample after the compression test, which demonstrated a regular rupture for all mixed batches. The main crack was observed on the edge of the specimen and stretched toward the middle point of the sample. This
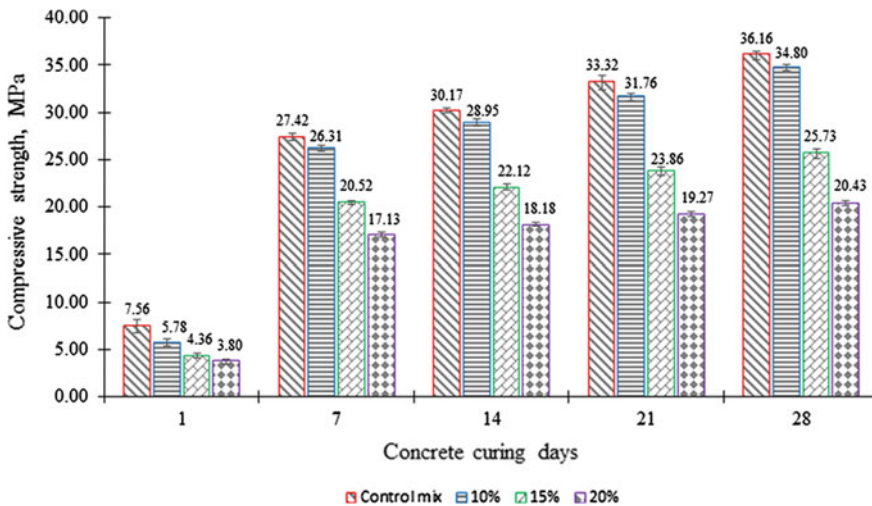


**Fig. 1** Compressive strength tested for **a** day 1; **b** day 7; **c** day 14; **d** day 21; and **e** day 28
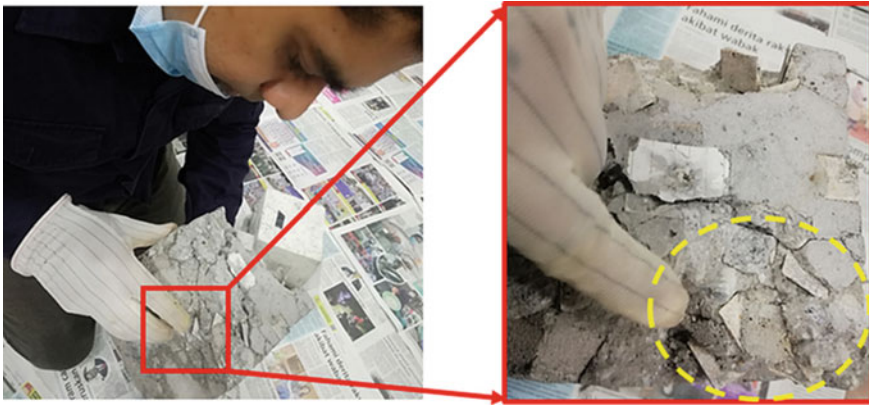
**Fig. 2** Crushed hardened concrete specimen

indicates that the wasted steel had bound well in the mixture, as seen at the yellow emphasized circle, to form a rigid concrete structure. Chemical reaction between the cement (alkali, $OH^-$) and the Zincalume coating (aluminum, $Al^{3+}$) generated hydrogen gas, $H_2$, which caused swelling in the concrete and reduced the compressive strength. The higher the amount of wasted steel added, more hydrogen gas generated through the chemical reaction and weakened the material binding in concrete [12]. Equation 2 shows the chemical reaction, where the hydrogen gas released has an adverse impact to the compressive strength. Except for 10% replacement concrete with wasted steel, other mixes of the concrete have not met the compressive strength test. Hence, it is not advisable to run a mass production with 15% and 20% mixtures.

$$(OH^-) + (Al^{3+}) = Al_2O_3 + H_2O + H_2(gas) \tag{2}$$
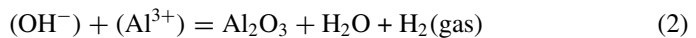
## 3.2 Impact Assessment

With the concept of cradle to grave, most of the non-recyclable solid wastes typically end up in landfills, which is what is being practiced globally. This is seen as a cost reduction method for waste disposal. However, the adverse impact of landfill activities causes damage toward the environment. Harmful and potent contaminants will enter the soil and pollute both the soil particles and groundwater, through leachate generation [13].

The rapidly increasing number of landfills due to inadequate solid waste management has limited the available land for development purposes. The speedy population growths and urbanization caused by the increase in the demand for infrastructures and housing have created competing states for property buyers to acquire properties.

Hence, the land value has increased by multiple folds, which reduces the affordability for low-income group people to purchase land and properties on the land. This increases the number of squatter settlements around these areas [14].

The number of health impact-related cases pertaining to landfills attributes to low birth weight, respiratory diseases and congenital anomalies. It also brings about a poor odor in the air, which causes poor eating appetite among local communities. Greenhouse gases released from landfills promote air pollution and smog, which causes poor air quality and which affects the respiratory system [15].

## 4 Conclusions

This research showcased the importance of achieving sustainability through recycling of steel wastes, to support light-weighted structures. The conclusions for this research work are stated below:

- The results obtained showed that the 10% wasted steel substitution portraits an optimum compressive strength. The mechanical strengths were observed to display a downward trend when the percentage of waste increased beyond 15% in the concrete mixture.
- The morphology of waste and the chemical reaction between the cement and the steel coating in the concrete mixture weakened the strengths.
- Recycling steel wastes helped to reduce the adverse effects on human health, the environment and the socio-economy.
- As an alternative for conventional concrete, this eco-friendly concrete can be considered for light-weight to middle-weight range concrete application such as for pavement constructions.

## References

1. Bali N, Panta MP, Antelo M (2019) Sustainable performance-oriented production practices in the Indian iron and steel industry: an empirical investigation. J Clean Prod 226:379–391
2. Ardjmand M, Daneshfar MA (2020) Selecting a suitable model for collecting, transferring, and recycling drilling wastes produced in the operational areas of the Iranian offshore oil company (IOOC) using analytical hierarchy process (AHP). J Environ Manage 259. https://doi.org/10.1016/j.jenvman.2019.109791
3. Benassi L, Alias C, Feretti D, Gelatti U, Piovani G, Zerbini I, Sorlini S (2019) Ecotoxicity and genotoxicity of steel slags: preliminary results. Detritus 6:32–38

4. Wang XQ, Tao Z, Hassan MK (2020) Post-fire behaviour of high-strength quenched and tempered steel under various heating conditions. J Constr Steel Res 164:105785
5. Primavera A, Pontoni L, Mombelli D, Barella S, Mapelli C (2016) EAF slag treatment for inert materials' production. J Sustain Metall 2(1):3–12
6. Jayanthi B, Emenike CU, Agamuthu P, Simarani K, Mohamad S, Fauziah SH (2016) Selected microbial diversity of contaminated landfill soil of Peninsular Malaysia and the behavior towards heavy metal exposure. CATENA 147:25–31
7. Selvi A, Rajasekar A, Theerthagiri J, Ananthaselvam A, Sathishkumar K, Madhavan, J, Rahman PK (2019) Integrated remediation processes toward heavy metal removal/recovery from various environments–a review. Front Environmen Sci 7:66
8. British Standard (2002) BS EN 12620:2002+A1:2008 Aggregates for concrete. British Standard Institution, London
9. McKenzie R (2018) BlueScope Steel Limited (BSL). Equity 32(3):11
10. British Standard (2019) BS EN 12390-3:2019 Testing hardened concrete. Compressive strength of test specimens. British Standard Institution, London
11. Assefa S, Dessalegn M (2019) Production of lightweight concrete using corncob ash as replacement of cement in concrete. Am J Civil Eng 7(1):17–20
12. Alzubaidi R (2017) Recycling of Aluminum Byproduct waste in concrete production. Jordan J Civil Eng 11(1):15–29
13. Teta C, Hikwa T (2017) Heavy metal contamination of ground water from an unlined landfill in Bulawayo, Zimbabwe. J Health Pollution 7(15):18–27
14. Olawoye AO, Akinola Olusola O, Stephen AT (2019) The socio-economic and environmental implications of residential buildings in proximate distance to landfill site. A case of Olususun Landfill, Ojota Lagos. J Environ Earth Sci 9(6):99–115
15. Shaddick G, Ranzi A, Thomas ML, Aguirre-Perez R, Dunbar MB-N, Parmagnani F, Martuzzi M (2018) Towards an assessment of the health impact of industrially contaminated sites: waste landfills in Europe. Epidemiol Prev 42:69–75

# Strategy to Manage Rock Quarries by Reducing Harvested Aggregates Towards Eco-Building Concept

**V. Vijaya Prakash and J. Shamini**

**Abstract**   Rock quarries for aggregate harvesting are a major concern to ensure that the environment surrounding the quarries is not affected badly. This study evaluated suitable percentage of replacing natural aggregate with coated steel for concrete fabrication. Coated steel was substituted at 10, 15, and 20% and tested for splitting tensile strength test. The mechanical strengths were observed with the increasing of curing age, but reduced with the increment of coated steel in mixture. 10% substitution gave optimum mechanical tensile strength. The higher the percentage of coated steel in the concrete mixture, the weaker the mechanical strengths. Through this material replacement, the environment is protected by reduced aggregate mining.

**Keywords**   Rock quarry · Coated steel · Natural coarse aggregate · Tensile strength · Eco-building

## 1   Introduction

Promotion of a sustainable environment is a major concern in the current era, as preserving the environment for future generations seems to be extremely important. In September 2015, more than 190 world leaders unanimously committed to 17 sustainable development goals, which were to be met by 2030, in order to lend a hand in fixing global climate change issues. One of the goals (Goal 12, Responsible Consumption and Production) was to ensure sustainable consumption and production patterns, which targeted the substantial reduction of waste generation, through prevention, reduction, recycling, and reuse, by strengthening the scientific and technological capacity to move towards more sustainable patterns of consumption and

V. Vijaya Prakash (✉)
Department of Environmental Sciences, Faculty of Forestry and Environment, Universiti Putra Malaysia (UPM), 43400 Serdang, Selangor, Malaysia
e-mail: vijaya5982@gmail.com

J. Shamini
Centre for Advanced Materials and Intelligent Manufacturing, Faculty of Engineering, Built Environment & IT, SEGi University, 47810 Petaling Jaya, Selangor, Malaysia

production [1]. The challenges for the goals to be achieved are the proposal, execution, and monitoring of the techniques. A systematic structure was needed to reduce the waste produced by manufacturing companies, without leaving anyone behind [2].

Besides being affected by wasted metals in the environment, the coarse aggregate harvested from rock quarries is not an insignificant issue to be overlooked. In 2009, Malaysia had 314 active quarries, but only 3.8% of it (12 quarries) were practicing sustainable green efforts. The rehabilitation of quarries is important to prevent pollution, as the economic growth from a quarry is huge. According to the Mineral and Geoscience Department of Malaysia, in 2016, the quarry industry was the prime industry in the construction sector. In 2016, the mineral industry contributed US$1.8 billion to the nation's GDP and granite (non-renewable resources) had been identified as one of the 33 types of world class minerals [3]. In addition to ensuring rehabilitation, the pollution from quarries needs to be handled discreetly without compromising human health. Crushing hard rock is one of the techniques to produce coarse aggregates for concrete production. However, the dust concentration can cover up to a 5 m distance from the drilling area [4]. Recent studies across different sites of a typical quarry showed that noise pollution and dust pollution from crushing, drilling, and blasting areas can affect 88% of the quarry worker's hearing and cause respiratory problems [5].

In terms of reducing the above-mentioned issues, the replacement of partial rock aggregates with that of industrial waste has been studied by various researchers. Ceramic waste, recycled concrete aggregates, and e-plastic waste are some of the materials used to replace coarse aggregates partially, for a sustainable environment [6]. Specifically, for steel waste, it was found that most of the studies were conducted using steel slag, which had an almost similar morphology with that of natural rock aggregates [7]. The mechanical properties of the concrete with steel slag, which had been replaced partially, instead of the natural aggregates, had been proven to have better mechanical properties. Improvements in the compressive strength, flexural strength, and the modulus of elasticity had been identified when steel slags were used as substitutes for the coarse aggregates. Various research works have been conducted to replace coarse aggregate with steel slags, and positive outcomes have been identified [8]. However, less research has been conducted on substituting coated steels for that rock aggregates.

## 2 Experimental Material and Method

### 2.1 Material Preparation

For the concrete fabrication, water, cement, river sand, rock aggregate, and wasted coated steel were used as partial replacement of rock aggregates. Table 1 shows the design mix while substituting the rock aggregate.

**Table 1** Concrete design mix for substituting rock aggregate for split tensile strength test

| Wasted steels replacement (%) | 0 | 10 | 15 | 20 |
|---|---|---|---|---|
| Rock aggregate (%) | 100 | 90 | 85 | 80 |

## 2.2  Splitting Tensile Strength

The split tensile strength test was conducted for hardened concrete specimen with 7, 14, 21, and 28 days of curing age with wasted steel substituted. Cylindrical shape hardened concrete was tested for this strength test. An average strength was evaluated by conducting three samplings of each mix batch specimen [9].

Strength test was conducted by using compression testing machine. The concrete specimens were positioned horizontally in the compression machine where the load was imposed progressively until the concrete split. The failure load was recorded to evaluate the split tensile strength, and the split tensile strength values can be determined by using Eq. 1.

$$T = 2P\pi l d \tag{1}$$

where
$T$ splitting tensile strength (MPa)
$P$ maximum applied load at failure point (N)
$l$ length (mm)
$d$ diameter (mm)

## 3  Results and Discussions

## 3.1  Splitting Tensile Strength

Figure 1 represents the tensile strength results of concrete containing the wasted steel, and the control mix concrete, where the tests conducted for 7 days to 28 days, with 7 days' interval for each mixed batch. The strength was observed to reduce gradually when the percentile of waste steel increased. Splitting tensile test is not advisable to be conducted on day 1 after casting the specimen, as it would only be partially hardened. The overall split tensile strength increased over time due to the concrete aging process.

The standard split tensile test was at 2.81 MPa, where the control mix specimen achieved 2.84 MPa, which was 1.07% greater than the standard [9]. The 10% of the steel waste gave a strength of above 90%, compared to the standard, which achieved 2.53 MPa, and was acceptable for the concrete fabrication. Sudden decrease of strength was observed for the 15% and 20% mixed concrete, which was 85% and
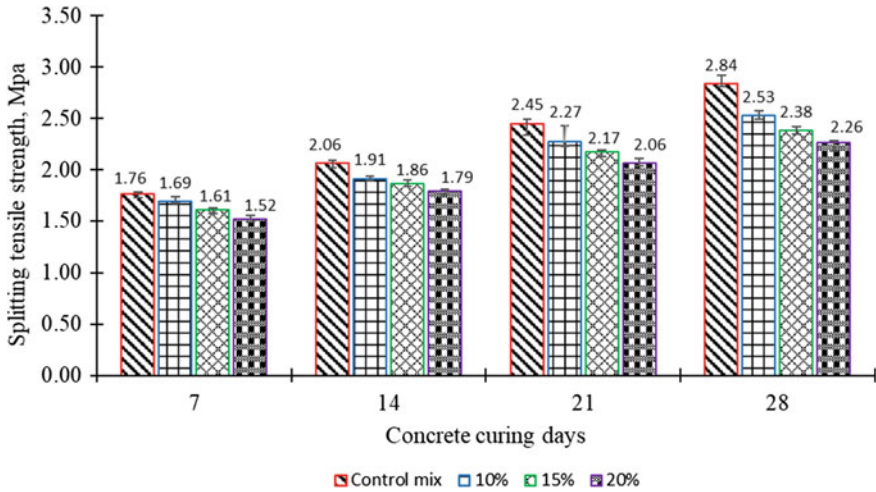
**Fig. 1** Splitting tensile strength tested for **a** day 7; **b** day 14; **c** day 21; and **d** day 28

80%, respectively. The non-angular waste steel samples had a small surface area, and reduced superficial pores, leading to more voids in the hardened concrete. It weakened the mechanical strength of the splitting tensile test [10].

## 3.2 Impact Assessment

Landfills and large-scale quarrying activities for aggregate harvesting will have a significant adverse impact towards the environment, human health, ecology, and socio-economy of local community and their surroundings. Toxins generated in the landfills such as pose contaminants have a direct impact towards the degradation of the soil's quality and the natural water resources. The demand for natural aggregates as construction material has increased, to expedite the infrastructure development, mainly for developed and developing nations. Likewise, the increase in steel material production will lead to a high volume of steel waste, which ends up in landfills. Soil pollution and groundwater pollution occur due to leachate production, which results from the reaction between steel materials and the environment [11].

Rock quarrying sites have shown a massive growth, to cater for the demand of crushed granite. The process of looking for a suitable quarry location, hard rock extraction, and cleaning after extraction leads to environmental and atmospheric damage. The extraction of natural aggregates through rock blasting causes air, water, and noise pollution. The quarry activities directly destroy the wildlife's natural habitat [12]. The vibration through the heavy-duty machineries and noise from heavy vehicles, equipment, and activities involving explosives have the potential to unbalance

the local communities and the wildlife animals, including the birds, through the destruction of their natural habitat.

Water pollution has become new normal, mainly in the river basin near landfill and quarries, where the impacts are much more significant towards local communities, who highly depend on river water as their daily source for drinking, washing, and agricultural use. The lowering of water table in the river catchments will vanish, which will affect the natural drainage, and causes floods during heavy rainfall [13]. Greenhouse gases such as $CO_2$, $CO$, $NO_x$, $SO_x$, $CH_4$, and other particulate materials, such as $PM_{10}$ and $PM_{2.5}$, were determined in high concentration near the quarries, which led to air pollution. Damages such as terrestrial acidification and photochemical smog, which formed from the quarrying emissions, lead to a poor quality of life for the local communities and cause significant health-related issues to them due to prolonged exposure with air pollutants [14]. Reducing the usage of natural aggregates by substituting waste steel will reduce the quarrying activities to help reserve the natural resources.

## 4  Conclusions

This research proved the significance of achieving sustainability through retaining rock quarries for aggregate harvesting, by replacing wasted steels with rock aggregates. The results obtained showed that the 10% wasted steel substitution with crushed granite contributed ideal splitting tensile strengths. The strengths showed descending trend when the steel percentage increased beyond 15% in the concrete mixture. Recycling steel wastes help to reduce the rock harvesting from quarries and help to sustain them. The extraction of natural aggregates can be diminished, where the pollutions related to rock quarrying and landfilling can be controlled to protect the environment. Subsequently, the health and safety of human and other living things near the quarry and landfills will improve. As an alternative for conventional concrete, this strategy can be considered as one of the techniques to save the excessive rock quarries for harvesting.

## References

1. Pradhan P, Costa L, Rybski D, Lucht W, Kropp JP (2017) A systematic study of sustainable development goal (SDG) interactions. Earth's Future 5(11):1169–1179
2. Diaz-Sarachaga JM, Jato-Espino D, Castro-Fresno D (2018) Is the sustainable development goals (SDG) index an adequate framework to measure the progress of the 2030 agenda? Sustain Dev 26(6):663–671

3. Yahya ZB, Ariffin M, Abdullah SH (2018) Legislative analysis on quarry rehabilitation in Selangor, Malaysia. Res Pol 55:1–8
4. Sairanen M, Rinne M (2019) Dust emission from crushing of hard rock aggregates. Atmos Pollut Res 10(2):656–664
5. Mutha VR, Yasobant S, Boondesh N (2017) Occupational and environmental impacts of granite quarry activities in Chittoor District of Andhra Pradesh. SSRN, India. https://doi.org/10.2139/ssrn.3015128
6. Khalid FS, Azmi NB, Sumandi KASM, Mazenan PN (2017) Mechanical properties of concrete containing recycled concrete aggregate (RCA) and ceramic waste as coarse aggregate replacement. AIP Conf Proc 3–5 April, 020079
7. Palankar N, Shankar AUR, Mithun BM (2016) Durability studies on eco-friendly concrete mixes incorporating steel slag as coarse aggregates. J Clean Prod 129:437–448
8. Saxena S, Tembhurkar AR (2018) Impact of use of steel slag as coarse aggregate and wastewater on fresh and hardened properties of concrete. Constr Build Mater 165:126–137
9. American Society for Testing and Materials (2017) ASTM C496/C496M-17 standard test method for splitting tensile strength of cylindrical concrete specimens. ASTM International, West Conshohocken, PA
10. Dhir RK, de Brito J, Silva RV, Lye CQ (2019) Sustainable construction materials: recycled aggregates. Woodhead Publishing Series, Kidlington, United Kingdom
11. Jayanthi B, Emenike CU, Agamuthu P, Simarani K, Mohamad S, Fauziah SH (2016) Selected microbial diversity of contaminated landfill soil of Peninsular Malaysia and the behavior towards heavy metal exposure. CATENA 147:25–31
12. Emmanuel D (2018) Environmental impact of quarry activities in Supare-Akoko, Ondo State Nigeria. Geography Planning Sci 3(1):101–111
13. Vandana M, John SE, Maya K, Padmalal D (2020) Environmental impact of quarrying of building stones and laterite blocks: a comparative study of two river basins
14. Fugiel A, Burchart-Korol D, Czaplicka-Kolarz K, Smoliński A (2017) Environmental impact and damage categories caused by air pollution emissions from mining and quarrying sectors of European countries. J Clean Prod 143:159–168

# Access Control System for Safety Feature of Lock: A Review

**Zhang Huan, S. Yaw Yoong, and J. Shamini**

**Abstract**  Access control system is a system to control the forbidden passage, which involves many fields such as electronics, machinery, communication and so on. Its structure is not complex, but it has strong practicability and great market demand. Many scholars have improved and studied the door access control system, and the application of biometric recognition to the access control system is the main research direction at present. Biometric access control system is based on fingerprint, face, iris, voice, vein and other human biometrics for identity recognition and authentication. Compared with the traditional access control system, the access control system based on biometrics has better security, convenience and functionality. At present, there are three recognition methods used most in access control system: fingerprint recognition, face recognition and iris recognition. Based on a large number of documents, this paper summarizes the main research contents, development status and research results of various recognition methods. The advantages and disadvantages of various technologies at present are pointed out, and the future development trend is prospected.

**Keywords** Safety lock · Fingerprint · Face recognition · Iris recognition

## 1   Introduction

Access control system, also known as access management control system, is a comprehensive system. Traditional access control system uses call confirmation and fixed password for identification, but there are still problems of low adaptability and security performance. Today, with the rapid development of economy, people's living standards are improving rapidly and private property is becoming richer and richer,

Z. Huan · S. Yaw Yoong
Faculty of Engineering, Built Environment & IT, Centre for Modelling and Simulation, SEGi University, 47810 Petaling Jaya, Selangor, Malaysia

J. Shamini (✉)
Faculty of Engineering, Built Environment & IT, Centre for Advanced Materials and Intelligent Manufacturing, SEGi University, 47810 Petaling Jaya, Selangor, Malaysia
e-mail: shaminijanasekaran@segi.edu.my

which also puts forward higher and higher requirements for the security system represented by the access control system. How to use the scientific, effective, simple and practical access control system identity recognition method with high security has become the focus and focus of access control system research.

With the continuous development of computer vision technology and biometric extraction technology, the combination of these two technologies in access control system has become the development direction of social identity authentication. Biometric access control system is an access control system based on human biometrics, mainly including face recognition, fingerprint recognition, iris recognition, palm print recognition, vein recognition, voiceprint recognition, etc. At present, there are three recognition methods mostly used in the access control system: fingerprint recognition, face recognition and iris recognition.

As the earliest biometric recognition method, fingerprint recognition is also a recent research hotspot. Everyone's fingerprint features are unique, and the fingerprint lines, intersections and breakpoints are different and stable [1]. The access control system based on fingerprint identification uses the fingerprint of the human body's own finger as the key to open the door and judges whether to open the door according to the characteristic matching of the input fingerprint. It not only improves the security of the access control system, but also brings great convenience and more humanized experience to users.

Face recognition is a research hotspot in many fields, such as pattern recognition, computer image, artificial intelligence and so on. As a way of biometric comparison, facial features are unique [2]. Compared with other recognition technologies, face recognition technology has unique advantages in the application process. For example, it is more convenient in the process of image information acquisition. It has gradually become the most direct and natural biometric technology. It has become the focus of artificial intelligence and pattern recognition and has also been widely used in access control system.

Iris recognition was proposed in the late 1990s. Iris recognition access control system is to determine people's identity and whether to open the door by comparing the similarity between iris image features. Compared with other biological characteristics of human body, iris has obvious uniqueness, and the iris structure of different people is different, which has been determined by human individuals during embryonic development [3]. Therefore, the authentication of human identity through iris recognition has strong reliability and unforgeability.

This paper mainly analyzes the improvement of various identification methods and related technologies of the access control system, so as to provide reference for the further improvement and review of the access control system in the future.

## 2 Review of Recognition

### 2.1 Fingerprint Recognition

Wang et al. [4] proposed a hidden fingerprint access control system based on smart phones and application software. The system is controlled by a smart phone and a micro PC with Wi-Fi communication function. Smart phones and micro PCs establish keys through Diffie–Hellman key exchange (DH) and digital signature algorithm (DSA). The smartphone encrypts the fingerprint biometric data, and then transmits it to the micro PC for verification. The system can prevent the fingerprint reading device from being damaged to a great extent, and greatly improve the confidentiality of fingerprint residual information. However, the normal operation of the system largely depends on the stability of Wi-Fi network. Therefore, the applicable environment requirements of the access control system are relatively strict.

Tshomo et al. [5] designed a double door lock system using radio frequency identification and fingerprint identification. The system is based on Arduino Mega 2560 microcontroller. It has two ways to unlock. One is to obtain fingerprints through fingerprint scanner for matching. The other is to compare the ID of the RF card with the authorization ID. TTL camera is installed in the system. Any person who tries to enter but is not registered and authorized will be photographed and stored in SD card. The advantage of the system is that it has two unlocking methods, which complement each other. However, because the system uses RF card identification, it inevitably brings the risk of house theft due to the loss or theft of RF card.

Wang et al. [6] designed a biometric access control system based on fingerprint identification technology. The system takes C8051F020 single chip microcomputer as the core control chip. The hardware block diagram is shown in Fig. 1. When the fingerprint sensor detects the user, the main controller will call the comparison algorithm to match the received information. If the matching is successful, you can enter. At the same time, the relay will close for about two seconds. Therefore, after the door lock is opened, it will close automatically in a period of time. The system is designed based on low-power devices and chip packaging components, which reduces the area of PCB and improves the anti-interference of the circuit. However, the design does not completely test the fingerprint identification algorithm. In this paper, only the software and hardware of fingerprint acquisition are designed, and the algorithm of fingerprint identification is only verified on PC.

Chen et al. [7] designed an intelligent access control system based on fingerprint identification. STC89C52 is used as the CPU in the hardware design of the system. It mainly makes in-depth research on fingerprint identification algorithm, and its algorithm flow is shown in Fig. 2. Firstly, the contrast and gray of fingerprint image are adjusted to a fixed level. Then, through Gabor filter, the fingerprint is enhanced by using directional field image. Finally, a fingerprint matching algorithm based on string distance is proposed. Through MATLAB application simulation, the results show that the algorithm runs well and has high accuracy. The disadvantage is that in the process of fingerprint feature extraction, the reference point selected by the
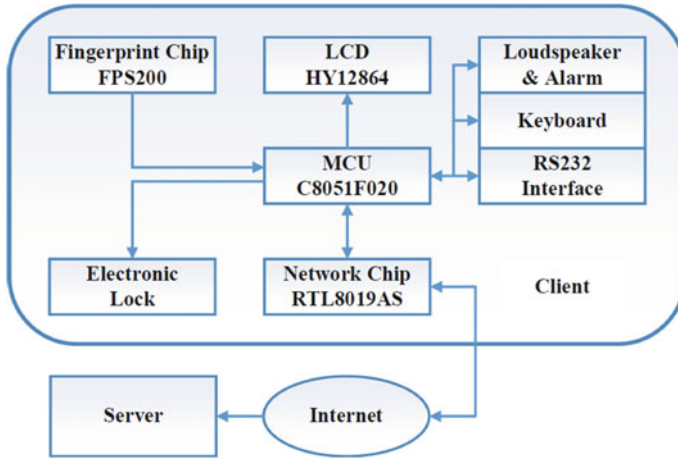
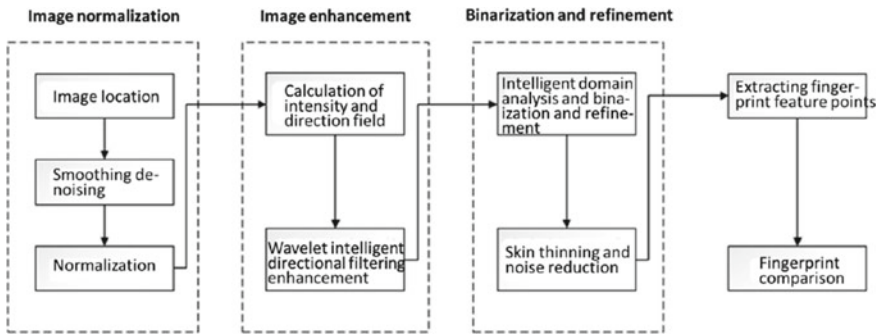**Fig. 1** Hardware block diagram [6]



**Fig. 2** Algorithm flow [7]

system is the center point of fingerprint. If the quality of the collected fingerprint is not high, it is impossible to determine how the center point is adaptive. Selecting the appropriate reference point needs further research.

## 2.2 Face Recognition

Hu [8] designed a home intelligent access control system based on cloud platform. The system takes STM32F103RCT6 single chip microcomputer as the core control unit, and Raspberry Pi 3B+ as the sub control system. Raspberry Pi recognizes the result, and it will be sent to the main control chip STM32 of ARM Cortex-M3 core to control the door lock to complete the switching operation. The terminal device

will send the collected relevant data to the cloud platform for storage to ensure that the mobile application can be accessed at any time. Through the system, users can remotely open the camera in real time to view the information outside the door, and remotely open and close the door lock. The disadvantage is that the system uses Bluetooth connection. However, Bluetooth unlocking can only be carried out in a certain area with limited distance. 4G transmission module or other remote wireless transmission module can be considered in the future.

Lin and Huang [9] implemented an access control system for the elderly based on LBP face recognition. The system is based on Raspberry Pi embedded platform. Raspberry Pi connects to Logitech C310 USB camera to obtain images. The system architecture is shown in Fig. 3. The system uses the cascade classifier provided by open CV to classify and locate the captured images. Then LBP algorithm is used to extract local features from the input image. Finally, the recognition results are divided into three categories: family members, visitors and strangers. The system has high recognition accuracy and low cost, and is very suitable for improving the safety of the elderly living alone. The disadvantage is that in the system experimental test, the facial expression is more conventional and lacks human spontaneous expression. Later, more complex face images may be used for further testing.

Based on multi-task cascaded convolutional neural network (CNN) and improved face recognition algorithm *k*-nearest neighbor (KNN), Shi et al. [10] designed an intelligent access control system based on machine vision. The overall design flow chart of the system is shown in Fig. 4. Firstly, the face information database is established. After collecting the face images of all users, image analysis and unified annotation are carried out. After the machine vision system, the interaction module confirms that the current detection object is a living body, and the feature points of the face image are extracted and matched with the face information database. The system solves the problem of identity forgery attack. Only after confirming that the
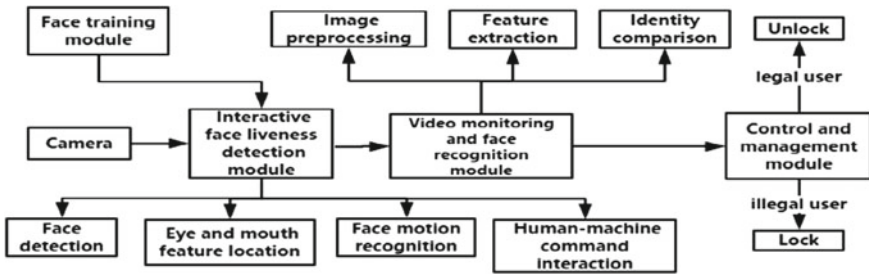
**Fig. 3** System architecture [9]
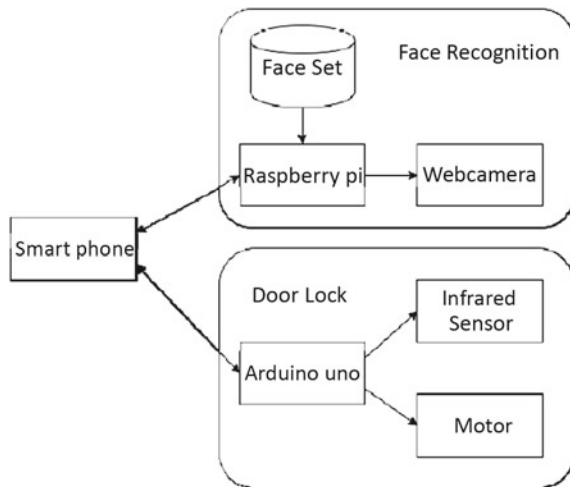
**Fig. 4** Overall design flow chart [10]

detection object is a living body and the facial information is matched successfully can the door lock be opened. The disadvantage is that the defense ability of the interactive face activity detection method proposed in this paper is very weak in the face of 3D face model attack.

Ganjoo and Purohit [11] designed an anti-theft door lock based on face recognition and blink detection. The system takes raspberry pie as the main control core and uses support vector machine model to compile Raspberry Pi face recognition program. Histogram of oriented gradient (HOG) feature extractor is used to detect the face in the image, and SVM classifier is used to recognize the face. The blink mechanism calculates the opening and closing degree of the eyes in the normalized image through face detection and eye location, and establishes a model for judging the blink action to check people's vitality. The design uses a single camera for living detection, which can effectively avoid photo or model deception, and increase the security and reliability. The disadvantage is that blink detection requires the user's active cooperation, and the detection time is too long.

## 2.3 Iris Recognition

Noma-Osaghae et al. [12] designed an access control system based on iris biometric system. The system takes ATmega128 chip as the core of embedded system. The system design includes two stages, registration stage and verification stage. Once an individual registers to enter the system, the user can enter the door. Identity recognition means one to many matching, which needs to provide the user's iris as an identity recognition means. The iris samples provided are compared with the information previously stored in the database. After iris recognition experiment and loading all modules, the system can achieve the expected effect, and the recognition accuracy is very high. However, the human–computer interaction of the access control system designed by the system is not friendly. In the subsequent improvement process, we can consider adding graphical interface to make the product more humanized and conducive to practical application.

Minacova and Petrov [13] proposed a preliminary iris location method in biometric access control system. This method is based on iris to stabilize the brightness feature in human eye image. The iris on the image has a series of consistent features, which can be used for preliminary search. The area around the iris has high brightness in most cases. At the same time, the pupil in the iris is dark. The brightness change between eye elements allows a stable mode to be selected as a basis for iris search. The preliminary search method provided allows the iris recognition area to be reduced. This method shortens the recognition time of existing recognition methods. The disadvantage is that in some cases, the boundary between sclera and iris can hardly be distinguished, which will affect the test accuracy.

Ma [14] developed an access control and attendance system based on iris recognition. The system takes DM8168 as the core processor. The system uses Ethernet as the transmission medium and connects all iris recognition terminals of the company to the same LAN through the switch. The iris recognition terminal transmits the access control signal through the Wigan protocol, controls the access control switch and transmits the data to the system server through the network to record the access control record. This mode is easy to transplant and maintain. Users only need to install a browser and log in to the system through the network. The disadvantage is that the recognition speed of the system is low, and only the iris recognition function is preliminarily realized. The rainbow recognition algorithm can be further optimized in the future.

## 3 Other Methods

### 3.1 Voice Recognition

Raj et al. [15] describes a speech processing method combining MATLAB and Arduino. The door lock system operates through Arduino, and fast Fourier transform (FFT) performs voice detection by checking the nearest pitch value of a given voice sample. Then, the given speech is checked in the speech processing area (MATLAB). If the sound matches the database, Arduino will run the motor according to the instructions given to the motor driver. The rotation of the motor will cause the door lock to open and close according to its forward and reverse rotation. The system block diagram is shown in Fig. 5. The whole system is based on simple and concise calculation. It is not only fast, but also very suitable for hardware implementation. However, human activities such as diet, exercise and work will change human voice, resulting in problems in voice recognition. This problem will be the main direction to be studied and solved in the future.
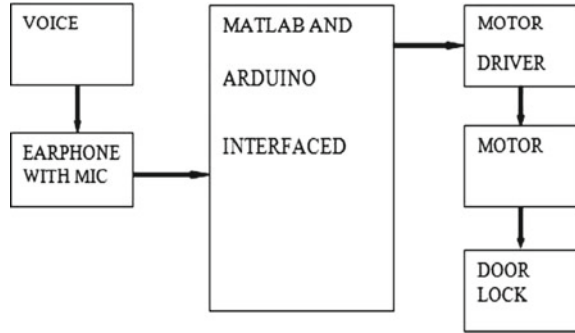
## 3.2 Palm Vein Recognition

Yin [16] designed a palm vein access control system with client based on ARM platform and server using x86 system for unified data management. The system device reads vein graphics data through Fujitsu's palm secure vein sensor. The arm board and the server are installed with sensor drivers, transplanted with the palm vein system and authentication library, and call the third-party interface to realize the registration, identification and authentication functions of the access control system. The client controls the access controller through the Wigan interface and communicates with the server through HTTP protocol. The equipment can be used as enterprise access control and attendance machine to provide users with higher security level authentication and has broad market prospects. The disadvantage is that the system designed in this paper is currently used on Android mobile phones and cannot be applied to IOS system, which needs further development.

## 4 Conclusions

The structure of access control system is not complex, but it has strong practicability and great market demand. At present, many scholars have improved the door access control system, and the application field of access control system is becoming more and more extensive. However, people's requirements are also constantly improving. There is still a lot of room for development in terms of security, convenience and functional perfection of access control system. In the future research field of identity recognition, biometric-based recognition technology will continue to develop, mainly focusing on improving the accuracy and speed of identity recognition. In addition, identity recognition technology will also develop in a diversified direction with the development of near-field communication and two-dimensional code technology, so as to make this technology more perfect in terms of security, convenience and functionality.

# References

1. Singla N, Kaur M, Sofat S (2020) Automated latent fingerprint identification system: a review. Forensic Sci Int 309:110187
2. Lin Y, Xie H (2020) Face gender recognition based on face recognition feature vectors. In: 2020 IEEE 3rd International conference on information systems and computer aided education (ICISCAE), 27–29 Sept 2020, pp 162–166
3. Gangwar A, Joshi A (2016) DeepIrisNet: deep iris representation with applications in iris recognition and cross-sensor iris recognition. In: 2016 IEEE International conference on image processing (ICIP), 25–28 Sept 2016, pp 2301–2305
4. Wang CC, Wang JW, Cheng TC (2020) A design of a concealed fingerprint access control system based on commodity smartphones and APP software. In: 2020 IEEE 9th Global conference on consumer electronics (GCCE), 13–16 Oct 2020, pp 341–342
5. Tshomo K, Tshering K, Gyeltshen D, Yeshi J, Muramatsu K (2019) Dual door lock system using radio-frequency identification and fingerprint recognition. In: 2019 IEEE 5th International conference for convergence in technology (I2CT)
6. Wang H, Wang Z, Sun G, Zhang L, Gao Y, Zhang Y, Bi C (2021) Design of a biometric access control system based on fingerprint identification technology. In: Artificial intelligence in china, pp 34–42
7. Chen SJ, Qu N, Bai HL (2019) Intelligent access control system based on fingerprint identification. In: 2018 7th International conference on advanced materials and computer science (ICAMCS 2018), pp 20–24
8. Hu F (2020) Design of home intelligent access control system based on cloud platform. Master, Huaibei Normal University
9. Lin JJ, Huang SC (2017) The implementation of the visitor access control system for the senior citizen based on the LBP face recognition. In: 2017 International conference on fuzzy theory and its applications (IFUZZY)
10. Shi W, Li J, Ding Y, Zhou K (2019) Research on intelligent access control system based on interactive face liveness detection and machine vision. In: The second international conference on advanced electronic materials, computers and materials engineering (AEMCME 2019), Changsha, Hunan, China, p 8
11. Ganjoo R, Purohit A (2021) Anti-spoofing door lock using face recognition and blink detection. In: 2021 6th International conference on inventive computation technologies (ICICT), 20–22 Jan 2021, pp 1090–1096
12. Noma-Osaghae E, Robert O, Okereke C, Okesola OJ, Okokpujie K (2017) Design and implementation of an iris biometric door access control system. In: 2017 International conference on computational science and computational intelligence (CSCI), 14–16 Dec 2017, pp 590–593
13. Minacova N, Petrov I (2015) Method of preliminary localization of the iris in biometric access control systems. IOP Conf Ser Mater Sci Eng 93(1)
14. Ma QC (2017) Research and development of access control and attendance system based on iris recognition. Master, China University of Petroleum (East China)
15. Raj LDW, Santhosh K, Subash S, Sujin C, Tharun P (2019) Voice controlled door lock system using Matlab and Arduino. In: 2019 IEEE International conference on system, computation, automation and networking (ICSCAN), 29–30 Mar 2019, pp 1–6
16. Yin JL (2019) Research and application of palm vein access control system. Master, Chengdu University of Technology

# Selection of Materials Based on Thermo-Mechanical Properties of Thermal Barrier Coatings and Their Failures—A Review

**Ali Raza, Faiz Ahmad, Thar M. Badri, M. R. Raza, Khurshid Malik, and Saad Ali**

**Abstract** Thermal barrier coatings (TBCs) are particularly designed to detain the degradation of material as a result of high heat flux. Thermal barrier coating is a process in which fine particles of a material in non-metal or metal form are deposited on the surface of a substrate in semi-molten or molten state. During service, degradation in the form of thermal or mechanical performance of a component can happen. Therefore, it is very important to understand the material requirements and failures of TBCs. In this paper, the properties of material to be used in TBC and the failure mechanisms caused by hot corrosion, residual stress, sintering reaction, calcium-magnesium-aluminosilicate attack and interdiffusion and oxidation are discussed. This review correlates the properties and structure of TBCs and reasons of failures which would be beneficial for designing TBC for future applications.

**Keywords** Thermal barrier coatings · Thermal and mechanical properties of thermal barrier coatings · Hot corrosion · Oxidation · Sintering · Residual stress

## 1 Introduction

By decelerating the extent and rate of deprivation experienced by the component, operating efficiency of a power producing unit or gas turbine may be improved. Failure of a component can be avoided by the use of claddings or protective coatings that are resistant to the high-temperature deprivation [1]. Nevertheless, it is not recommended to use claddings because it can change the microstructure of the basic substrate that can expose it to the other means of failure [2]. For this reason, thermal

A. Raza · F. Ahmad (✉) · T. M. Badri · K. Malik · S. Ali
Department of Mechanical Engineering, Universiti Teknologi PETRONAS, Seri Iskandar, Malaysia
e-mail: faizahmad@utp.edu.my

A. Raza
e-mail: er.aliraza1993@gmail.com

M. R. Raza
Department of Mechanical Engineering, CUI, Sahiwal, Pakistan

spray coatings are broadly used, and thermal barrier coatings (TBCs) are particularly designed to detain the degradation of material as a result of high heat flux [3]. Many researchers have suggested to use TBCs for protection of gas turbines from various failures [4–6]. Thermal spray coating is the most adaptable process that can be useful for apparatuses of any dimension. In contrast to the laser cladding process and welding, this coating technique does not change the microstructure of substrate.

Thermal spray is the general name for a coating process, in which a material is melted by using hot gaseous medium and at the same time deposited onto a substrate with high velocity where it deposits to form required coating. The material to be coated can be deposited in various states including wire, powders, rods, suspension or molten form. Torch is used to convert particles depending on the energy supplied into a hot gas stream. Fuel and oxygen recommended by manufacturer of spray gun are mixed in the mixing zone of gun and then directed on the way by carrier gas to combustion chamber. Chemical reaction occurs during ignition in combustion chamber due to which heat energy is released. Pressure inside combustion chamber increases as the combustion continues and hot gases start to flow with the high velocity. The fuel used is acetylene, propylene, oxygen or propane, and as carrier gas, nitrogen or other inert gas is used. A chemical reaction between acetylene and oxygen gases and nitrogen as carrier gas is presented in Eq. 1.

$$C_2H_2 + 2.5(O_2 + 3.76N_2) \rightarrow 2CO_2 + H_2O + 9.4N_2 \tag{1}$$

Thermal spray coatings were first commercialized by Schoop who devised devices to melt zinc or tin and to project metal in molten form by using compressed air in 1910. After that in the mid of 1920s, thermal spraying started to be used in fifteen countries [7]. In 1947, the first paper on ceramic coatings for turbine blades was published by NACA. In 1948, frit coating was tested on turbine blades of an engine. Later on, in 50s and 60s, this coating was tested by air force. In 1960, thermal barrier coatings made from zirconia were used in nozzles of rocket engine. Sal Grisaffe conducted research on thermal spray and founded the first group of coatings in 1960. In the mid of 1970, modern thermal spray coating was developed which consisted of 12 YSZ top-coat and NiCrAlY bond coat in a research-based gas turbine engine [8, 9]. Until now, much of the work has been done on thermal barrier coatings but there is very less literature available, in which properties to be considered while selecting the materials, failures of coatings and methods to avoid these failures are discussed [10, 11].

In this review article, first section contains details about the history and working of thermal spray coatings. Second section deals with the requirements of a material to be used in thermal barrier coatings. In the third section, properties of top-coat, bond coat, substrate and thermally grown oxide layer are described that must be kept in mind while selecting the materials. In the last section, failures of TBC coatings and methods to measure and avoid these failures are discussed.

## 2 Material Requirements for TBCs

The factors for efficiency improvement of mechanical systems especially gas turbines are high operating efficiency, reduced emissions and extended operating life. The efficiency of a gas turbine depends on the temperature difference between inlet and outlet. For every increase of 56 °C in the turbine inlet temperature, there will be an increase of 1.5% efficiency and 10% work output [12]. In order to meet these situations, by increasing the entry temperature of turbine to enhance the thermodynamic efficiency which is very effective, there is a chance of extreme operating environment as a result of increase in operating temperature, that can damage the core parts [13]. In a modern gas turbine, the temperature of inlet may reach 1600 °C [14]. The temperature of components can be reduced to nearly 100–300 °C, by using the coatings which have low thermal conductivity on parts like blades. Many features like no phase alteration between working temperature and room temperature, excessive melting point, chemical inertness, low thermal conductivity, better adherence to substrate, thermal expansion coefficient match with substrate, lower sintering rate [15], capital, thickness, surface roughness requirement, performance and process cost per part must be kept in mind while selecting a TBC process [16].

## 3 Material Properties

### 3.1 Top-Coat

The main purpose of top-coat is to offer thermal insulation between the hot gases and the substrate. This can be achieved by using low thermal conductivity material [17]. Low thermal conductivity is achieved by pores inside the top coat material, but porosity must not be greater than 8% [13]. Its thickness ranges from 100 to 400 µm. Also, topcoat should have following properties:

- It should be phase stable when exposed to high temperature, because phase transformation and volume change can occur which can damage the material [18].
- It must be resistant to erosion attack and sintering when subjected to high temperature in the presence of oxidized environment [19].
- It must have resistance to fracture and tolerance of strain throughout the process of thermal cycling.
- It should be thermodynamically compatible with the material of TGO for better adhesion.
- There should be match of coefficient of thermal expansion between top-coat and substrate in order to avoid strain during thermal cycling.
- Its stiffness and elastic modulus should not increase when subjected to high temperature (greater than 1200 °C).

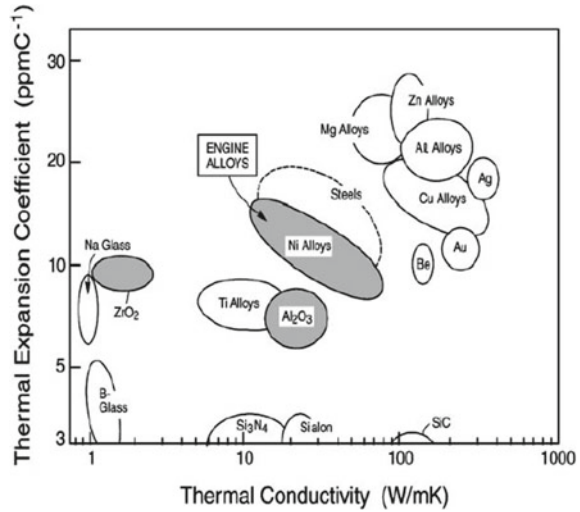**Fig. 1** Thermal conductivity and coefficient of thermal expansion of materials used for top coat [17]



Figure 1 shows different alloys of substrate and coating materials. It can be seen that for Ni-based alloys, zirconia is the best material for top-coat because it has low thermal conductivity and its coefficient of thermal expansion is matching with the Ni alloys.

## 3.2 Bond Coat

Bond coats are applied directly to the substrate before top-coat to avoid oxidation at high temperature. This coat provides resistance for substrate against oxidation by means of a protective TGO layer which is developed on the bond coat and grows slowly when it gets oxidized at high temperature. Generally, bond coat is made of two basic types of alloys. The first one is platinum-modified Ni aluminide, and second one is MCrAlY. Yield strength of MCrAlY bond coat is higher than platinum aluminide bond. Generally, its thickness varies from 75 to 200 μm. A bond coat should have following properties:

- It should have high creep strength to avoid failure due to compressive stress originated in the TGO. These stresses are developed in the TGO if the cooling rate is extremely high, and due to compressive stress, tensile stresses are produced which can cause spallation of top coat [20].
- It should have moderate strength and ductility at both low and high temperatures. If the bond coat is weak and not much ductile, then it can be unstable and TGO buckling can be the cause of crack in the layer [21].
- The oxidation property of bond coat should be such that it can produce and maintain the TGO layer normally (alpha-alumina).

- Its chemical composition should be homogeneous [22].

A bond coat is also anticipated to lessen the interdiffusion with the substrate based on Ni superalloy [23].

## 3.3  Thermally Grown Oxide

At temperature above 700 °C, the bond coat starts to get oxidized and a third layer called thermally grown oxide starts to develop between the topcoat and bond coat. The thickness of TGO is between 1 and 10 µm, and the maximum value can be 20 µm [24]. If the thickness is more than 5 µm, then it can introduce high magnitude stresses and can cause detachment of coating which is the reason of premature failure of coating. An ideal bond coat should have a TGO layer of $\alpha$-$Al_2O_3$ because its oxygen ion diffusivity is very low, and it is an excellent barrier against diffusion which stops further oxidation of bond coat. It should have following properties:

- For the top coat to be thermodynamic stable at high temperature for long time, the phase of TGO material must be compatible with it [17].
- The rate of its growing should be slow and stable at high temperature. If the growing rate is fast, then thick layer will be formed which can cause spallation [17].
- It should not allow oxygen to diffuse through it. Otherwise, oxygen will diffuse through this layer to the substrate material and oxidize it [22].
- It must be dense and mechanically strong to have resistance against fracture at high cycle loads.

## 3.4  Substrate

It is the actual material of blade in gas turbine on which coating is deposited. As it is exposed to high temperature and mechanical load for long period, it should have high fatigue and creep strength, hot corrosion and oxidation resistance and ductility. On the other hand, its thermal conductivity should be high because higher thermal conductivity will help to dissipate heat at higher rate that is necessary to cool the blade [13]. Ni-based superalloys are currently being used along with 11 or 10 alloying elements as a substrate for applications where temperature is more than 800 °C [25]. Figure 2 is the schematic diagram of a TBC system which shows the structure and composition.
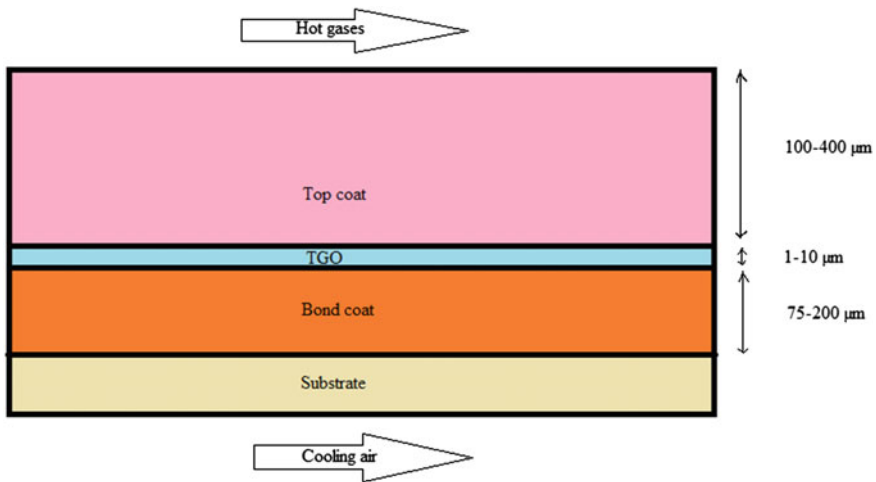
**Fig. 2** Structure of TBC

## 4 Types of Failures in TBCs

In case of gas turbines, the temperature can reach to 1500 °C. Typically, the material used for coating is made of YSZ which is stable up to 1200 °C. Above this temperature, coating starts to damage. Due to which, lifetime of a turbine is decreased at high temperature. There are many types of damages which can occur during service life of a turbine. These failures are listed below.

### 4.1 Hot Corrosion

Corrosion of superalloys or materials in the presence of oxidizing gas due to molten salt at high temperature of range 700–925 °C is called hot corrosion. The rate of oxidation is fast at this temperature when alloys and metals are contaminated with salts. As a result of which, protective oxide layer breaks down and salts reach the metal surface causing degradation [26]. Due to this degradation, bond coat and topcoat are both affected due to the porosity of APS method in YSZ coating. Through the pores and cracks, molten salt infiltrates the YSZ and reacts with bond coat [27]. It is different from corrosion at low temperature. If the hot corrosion occurs at temperature equal to melting point of salt layers, then it is hot corrosion of type-1 and the corrosion occurring at the temperature less than the melting point of salt layers is called type-2 hot corrosion. Corrosion in topcoat is because of the occurrence of lead (Pb) and vanadium in the fuel. Despite from the fuel or air, corrosion can also be produced after combustion due to the contaminants in the fuel that deposit on the surface.

## 4.2  Residuary Stress

These are produced during coating deposition process. There are two main reasons of residual stresses in thermal coating. First one is rapid cooling, in which the temperature of particles is reduced from higher to the temperature of substrate during deposition. The stress induced in this type is tensile in nature. The second reason for stress is the mismatch between coefficient of thermal expansion of substrate and coating. When the temperature of coating reaches from average temperature after deposition to the room temperature, the residual stresses are produced due to the difference in thermal shrinkage of coating and substrate. If coefficient of thermal expansion of substrate is greater than coating, then stresses produced are compressive and tensile stresses are produced for opposite case [28]. Compressive stresses are favorable to a certain limit than tensile stresses because tensile stress is more dangerous and can cause initiation of crack and adhesion loss. Besides this, there are other reasons for residual stresses like coating thickness and temperature, speed of deposition, phase transformation, thermally grown oxide and grain morphology. The various methods to examine these stresses include modeling, diffraction technique, spectroscopy technique, high energy X-ray, curvature measurement and finite element modeling [29].

## 4.3  Sintering Reaction

Sintering can be the cause of failure in case of thermal barrier coatings if the temperature of application is greater than 1000 °C. Microstructure of coating is altered due to sintering which includes change of properties such as thermal conductivity, hardness and elastic modulus. Sintering occurs at high temperature during service that results an increase in hardness and elastic modulus, and this is dangerous for coating system because it fills the pores of coating due to which thermal conductivity of top coat increases. Stiffness also increases due to sintering which increases thermal stress that leads to spallation of coating. This issue is common for YSZ coatings at temperature greater than 1000 °C. The problem of sintering can be controlled by using appropriate powder and time in a deposition technique as well as coating material and stabilizer [29]. Nanostructured coating is found to be suitable for this problem.

## 4.4  Calcium-Magnesium-Aluminosilicate Attack

In a gas turbine, when temperature reaches to higher value, coating on blades starts to be corroded because of silicates in molten form which is comprised of calcium-magnesium-aluminosilicate abbreviated as CMAS. During the service of a turbine, CMAS sticks on the topcoat of blade in solid form, and when the temperature

reaches above the melting point (1200 °C) of CMAS, it starts to penetrate through the microstructure of topcoat in molten form. As a result, elastic modulus of ceramic top coat increases, which causes high stress. Crack is initiated and propagated in top coat due to mismatch in the thermal expansion coefficient between CMAS and ceramic top coat [29]. Many authors have investigated the relationship between stress and CMAS penetration depth. They found that the regions which are away from CMAS have low stress than the regions which are close to it. Also, as the depth of penetration increases, strain energy of the layer decreases and this results in degradation of the coating layer during thermal cycling [30]. The failure due to CMAS can be avoided by following ways:

(a)  to increase the surface area of top-coat by modifying pore geometry
(b)  to enhance the level of porosity
(c)  to select new and appropriate materials for the top-coat
(d)  to block the CMAS penetration by using dense layer upon the top-coat surface.

## *4.5 Interdiffusion and Oxidation*

During the thermal cycle fatigue period at high temperature, the bond coat starts to get oxidized and thermally grown oxide layer begins to develop at the interface of bond coat and topcoat. If this situation continues for long time, then oxide layer thickness will increase due to which stresses will develop. There are two reasons for these stresses; first one is mismatch of the coefficient of thermal expansion between TGO and the coating layer, and second reason is the conversion of metal from high density to oxide of low density that generates growth stress. Residual stresses in TGO are the sum of stress produced due to mismatch of CTE and stress due to TGO growth. There is a limit of thickness for oxide layer growth which is 5 μm. When the value of this thickness is greater than this value, stresses of high magnitude will be introduced which will detach the top coat along with oxide layer from bond coat and life of coating will end [31]. There is also a chance of chemical failure due to low thickness of TGO. This failure is due to the low aluminum amount in bond coat. When the amount of aluminum is low, the protective oxide layer which is made of α-alumina develops no longer and other alloying elements will start to be oxidized. In the absence of α-alumina oxide layer, oxygen may diffuse into the bond coat which is known as internal oxidation. Due to this diffusion, the mismatch of coefficient of thermal expansion between bond coat and top coat made of YSZ is reduced, and hence, thermal stresses are also reduced [32].

## 5  Conclusion

In this review, a brief history of thermal barrier coatings and working of thermal spray process is discussed. The main points are as follows:

- While selecting a TBC process, many features like no phase alteration between working temperature and room temperature, excessive melting point, chemical inertness, low thermal conductivity of top-coat, better adherence to substrate, thermal expansion coefficient match with substrate, lower sintering rate, thickness, surface roughness requirement, performance and process cost per part must be kept in mind.
- The failures associated with TBC are hot corrosion, sintering reaction, oxidation and interdiffusion, residual stress and CMAS attack.
- The problem of sintering can be controlled by using appropriate powder and time in a deposition technique as well as coating material and stabilizer.
- By selecting new and appropriate materials for the topcoat and using dense layer upon the topcoat surface, CMAS attack can be controlled.
- There should be match between coefficient of thermal expansion of TGO and the coating layer to avoid interdiffusion and oxidation.

# References

1. Wang L, Zhao Y, Zhong X et al (2014) Influence of "island-like" oxides in the bond-coat on the stress and failure patterns of the thermal-barrier coatings fabricated by atmospheric plasma spraying during long-term high temperature oxidation. J Therm Spray Technol 23:431–446
2. Yakout M, Elbestawi MA, Veldhuis SC et al (2019) Density and mechanical properties in selective laser melting of Invar 36 and stainless steel 316L. J Mater Process Technol 266:397–420
3. Ziaei-Asl A, Ramezanlou MT et al (2019) Thermo-mechanical behavior of gas turbine blade equipped with cooling ducts and protective coating with different thicknesses. Int J Mech Sci 150:656–664
4. Wee S, Do J, Kim K et al (2020) Review on mechanical thermal properties of superalloys and thermal barrier coating used in gas turbines. Appl Sci 10:5476
5. Miller RA et al (2009) History of thermal barrier coatings for gas turbine engines. National Aeronautics and Space Administration
6. Reed RC et al (2008) The superalloys: fundamentals and applications. Cambridge University Press
7. Zhang G, Fan, Xu R et al (2018)Transient thermal stress due to the penetration of calcium-magnesium-alumino-silicate in EB-PVD thermal barrier coating system.Ceram Int44:12655–12663
8. Rani S, Agrawal AK, Rastogi V et al (2017) Failure analysis of a first stage IN738 gas turbine blade tip cracking in a thermal power plant. Case Stud Eng Fail Anal 8:1–10
9. Sun J, Fu Q-G, Yuan R-M et al (2017) Corrosion and thermal cycling behavior of plasma sprayed thermal barrier coatings on die steel. Mater Des 114:537–545

10. Leyens C, Wright IG, Pint BA et al (2000) Hot corrosion of an EB-PVD thermal-barrier coating system at 950°C. Oxid Met 54:401–424
11. Breeze P et al (2016) Chapter 4—Gas turbines. In: Gas turbine power generation, pp 31–42
12. Yakout M, Elbestawi MA, Veldhuis SC et al (2018) On the characterization of stainless steel 316L parts produced by selective laser melting. Int J Adv Manuf Technol 95:1953–1974
13. Bose S et al (2007) Chapter 5—High-temperature corrosion. In: High temperature coatings, pp 53–70
14. Cook L, Wolfenden A, Brindley W et al (1994) Temperature dependence of dynamic Young's modulus and internal friction in LPPS NiCrAlY. J Mater Sci 29:5104–5108
15. Liu Q, Huang S, He A et al (2019) Composite ceramics thermal barrier coatings of yttria stabilized zirconia for aero-engines. J Mater Sci Technol 35:2814–2823
16. Pollock T, Lipkin D, Hemker K et al (2012) Multifunctional coating interlayers for thermal-barrier systems. MRS Bull 37:923–931
17. Feuerstein A, Knapp J, Taylor T et al (2008)Technical and economical aspects of current thermal barrier coating systems for gas turbine engines by thermal spray and EBPVD: a review.J Therm Spray Technol 17:199–213
18. Evans AG, Mumm D, Hutchinson J et al (2001) Mechanisms controlling the durability of thermal barrier coatings. Prog Mater Sci 46:505–553
19. Karlsson AM, Xu T, Evans A et al (2002) The effect of the thermal barrier coating on the displacement instability in thermal barrier systems. Acta Mater 50:1211–1218
20. Ghadami F, Aghdam ASR, Ghadami SJV et al (2020) Microstructural characteristics and oxidation behavior of the modified MCrAlX coatings: a critical review. Vacuum 109980
21. Mehboob G, Liu M-J, Xu T et al2020)A review on failure mechanism of thermal barrier coatings and strategies to extend their lifetime.Ceram Int 46:8497–8521
22. Habibi MH, Wang L, Liang J et al (2013) An investigation on hot corrosion behavior of YSZ-Ta2O5 in Na2SO4+V2O5 salt at 1100°C. Corros Sci 75:409–414
23. Thakare JG, Pandey C, Mahapatra M et al (2020) Thermal barrier coatings—a state of the art review. Met Mater Int
24. Tan JC et al (1997) Optimisation of the HVOF thermal spray process for coating, forming and repair of components. Dublin City University
25. Wu S, Zhao Y, Li W et al (2021) Research progresses on ceramic materials of thermal barrier coatings on gas turbine. Coatings 11:79
26. Clarke D, Levi C et al (2003) Materials design for the next generation thermal barrier coatings. Annu Rev Mater Res 33:383–417
27. Miller RA et al (1997) Thermal barrier coatings for aircraft engines: history and directions. J Therm Spray Technol 6:35–42
28. Chen Y et al (2015) Study of bond coats for thermal barrier coating applications
29. Rana N, Mahapatra MM, Jayaganthan R et al (2015) High-temperature oxidation and hot corrosion studies on NiCrAlY coatings deposited by flame-spray technique. J Therm Spray Technol 24:769–777
30. Soares C et al (2015) Chapter 3—Gas turbine configurations and heat cycles. In: Gas turbines, 2nd edn, pp 93–171
31. Ali MY, Nusier SQ, Newaz GM et al (2001) Mechanics of damage initiation and growth in a TBC/superalloy system. Int J Solids Struct 38:3329–3340
32. Arif AFM, Al-Athel KS, Mostaghimi J et al (2017) 3.4 Residual stresses in thermal spray coating, pp 56–70

# A New Methodology to Investigate the Removal Crater Volume in the Particles Blended of Electrical Discharge Operation (EDO)

**Mohammed Abdulridha Abbas, Ola Mohammed Merzah, Ahmed Dheyaa Jawad, Dhafer Manea Hachim, Ghassan Shaker Abdul Ridha, and Bahaa Abdulhur Hatem**

**Abstract** A crater volume is considered a function of the removal rate and roughness in the Electrical Discharge Operation (EDO) medium. From here, the researchers have suffered from measuring the craters' topology using Atomic Force Microscopy (AFM) since it is not locally available. Besides, the numerical model to specify this volume is aging. Accordingly, this study aims to present a new methodology to compute the crater volume. This methodology is a hybrid of the polynomial-fitting (Poly-Fit) technique of the nodes of the melted elements resulted from Finite Elements Analysis (FEA) and rules of Simpson or trapezoidal. The model generated by the poly-fit uses one of these rules to determine the crater volume. Hence, it compares the size resulting from each rule with the traditional disk rule. In addition, these volumes produced from these rules are utilized to compute the removal rate of Inconel 718 and are compared to the adopted experimental values of this rate. As a result, it is remarked that Simpson's rule is more suitable than other rules since the average error ratio equals to 6.34% as compared to others.

M. A. Abbas (✉) · B. A. Hatem
Aeronautical Techniques Engineering Department, Engineering Technical College/Najaf, Al-Furat Al-Awsat Technical University (ATU), Najaf 54001, Iraq
e-mail: mohd.a.abbas@atu.edu.iq; hd160087@siswa.uthm.edu.my

M. A. Abbas
Sustainable Manufacturing and Recycling Technology, Advanced Manufacturing and Materials Center (SMART-AMMC), Universiti Tun Hussein Onn Malaysia (UTHM), 86400 Parit Raja, Malaysia

A. D. Jawad · D. M. Hachim
Power Mechanics Techniques Engineering Department, Engineering Technical College/Najaf, Al-Furat Al-Awsat Technical University (ATU), Najaf 54001, Iraq

O. M. Merzah
Air Conditioning and Refrigeration Techniques Engineering Department, Al-Mustaqbal University College, Babylon 51001, Iraq

G. S. A. Ridha
Department of Mechanical Technical/Production, Kut Technical Institute, Middle Technical University, Baghdad, Iraq
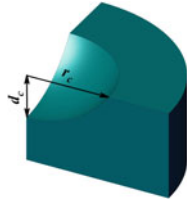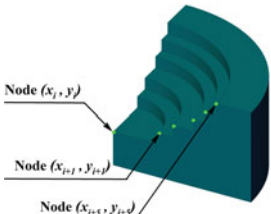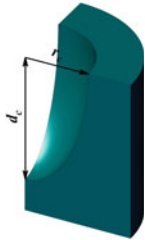
# 1 Introduction

The particles blended medium in the Electrical Discharge Operation (EDO) was contributed to enhancing electrical erosion of complex materials [1]. However, this contribution did not fully boost the machined surface and removal rate quality in this operation [2, 3]. As proof, the mounting of current in this medium strengthened the spark power, thereby yielding large craters [4–6]. Furthermore, the diameter of these craters is affected by the amount of additive powder. The growth of this amount led to expanded diameter resulting from the erosion in the EDO [7–9]. On the other hand, just as the powder amount played a meaningful role in widening the diameter of craters, the nanosize of powder has diminished these craters' size [10, 11]. Accordingly, the peak current with both the amount and size of the powder is difficult to control in the EDO medium for producing the best quality of removal [12]. From here, it turns out that by increasing these factors leads to rising the energy of electrical erosion and removal operation. At the same time, this increment produced an unacceptable roughness depending on the expansion of the craters [13–15].

It's no secret that, through these experimental studies and other studies, the Atomic Force Microscopy (AFM) strongly contributed in detecting the topology and dimensions of craters produced by EDO [16, 17]. Nevertheless, the crater topology has been presented as a spherical dome, disc, or circular paraboloid to investigate the Material Removal Rate (MRR) based on Finite Element Analysis (FEA) [18–23]. Obviously, in Table 1, the volume of disk topology dominated to investigate MRR compared to other topologies. Since AFM examination is always unavailable to examine the quality of the machined area and recognize the roughness, this exam wastes time and money, although it supplies promising outcomes [24–26]. Moreover, the disk topology resulted from the EDO of the craters is considered an elderly rule in the numerical investigation. Hence, it is necessary to present a volumetric rule of the crater topology in place of disk topology. Accordingly, this study introduces a new methodology for computing the crater volume by adopting the polynomial technique with Simpson and Trapezoidal rules. Outputs of FEA have represented this technique to calculate the removal crater depending on disk topology. Hence, the nodes of removal edges of this crater in EDO were employed to fit the curve to generate a polynomial model. Consequently, this model utilized these rules to create the removal volume. Finally, the volume induced by disk, Simpsons, and trapezoidal is exploited to compute MRR, which is then compared with the chosen experimental outcomes.

Depending on aforesaid, this study has adopted the experimental outputs of MRR conducted by Jadam et al. [27]. It employed Inconel 718 and Multi-Walled Carbon Nano Tubes (MWCNTs) as the workpiece and blended particles in EDO, respectively. Hence, it is essential to clarify these outputs used in the investigation context. Furthermore, it demonstrates the thermal inputs and boundary conditions utilized in the present work. Additionally, the new methodology adopted in the current research shows a description of the proposed model of crater topology.

**Table 1** Traditional volumetric of crater topology models produced by EDO

| Reference No | Description of topology | Crater volume ($V_c$) ($\mu m^3$) | Equation No |
|---|---|---|---|
| [19, 21] | <br>Spherical dome volume | $\pi/6(3r_c^2 + d_c^2),$ | (1) |
| [20, 22, 23] | <br>Node $(x_i, y_i)$<br>Node $(x_{i+1}, y_{i+1})$<br>Node $(x_{i+s}, y_{i+s})$<br>Disk volume | $\sum_{i=0}^{n-1} \frac{\pi(x_i + x_{i+1})^2}{4(y_{i+1} - y_i)},$ | (2) |
| [18, 20] | <br>Circular Paraboloid volume | $\pi/2(d_c r_c^2),$ | (3) |

where $r_c$ indicates the crater radius ($\mu m$), $d_c$ refers to the crater depth ($\mu m$), while $x_i$ and $y_i$ are $x$ and $y$ coordinates of the edge node of the first removed disk radius. Moreover, $x_{i+1}$ and $y_{i+1}$ denote the succeeding node coordinates of the other radius, etc

## 2 Investigation Environment

The investigation environment adopted in the present study, as aforementioned, is the experimental outcomes performed by Jadam et al. [27]. Inconel 718 is one of the best and advanced materials in aeroplane and aerospace fabrication. It has unique features, especially related to the melting temperature and superior hardness. Hence, the EDO technique is one of the efficient systems to operate this alloy without physical forces. Additionally, MWCNTs particles have excellently achieved the finest results

**Table 2** Work materials properties

| Work materials | Density (g/cc) | Melting point (K) | Thermal conductivity (W/m K) | Specific heat capacity (J/g K) |
|---|---|---|---|---|
| Inconel 718 | 8.9 | 1608 | 11.2 | 0.435 |
| MWCNTs | 1.2 | 3823 | 400 | 2 |

**Table 3** Experimental outcomes of MRR of Inconel 718 [27]

| Peak current (A) | Experimental MRR (mm³/min) | |
|---|---|---|
| | At 0.5 g/L | At 1 g/L |
| 2 | 0.9667 | 0.8755 |
| 4 | 3.6663 | 2.0976 |
| 6 | 4.7424 | 4.0129 |
| 8 | 7.7703 | 7.0408 |

in machining Inconel 718 by this system [28]. Accordingly, these reasons lead to the selected work materials by Jadam et al. [27].

According to this adopted study, the parameters' levels utilized are 2, 4, 6, 8 A, and 0.5, 1 g/L for peak current and concentration of MWCNTs particles, respectively. Furthermore, the voltage and both on and off duration for each pulse are 140 V, 10 µs, and 10 µs, accordingly. On the other hand, it is remarked as the notable application to the distance of gap among the copper pole and Inconel 718, where this distance is 50 µm [27]. Observably, the properties of work materials and the experimental values of MRR of this alloy were demonstrated in Tables 2 and 3, individually.

The numerical procedure using FEA in the current study depends on these experimental data. Consequently, it is crucial to clarify the crater topology proposed, besides the input and boundaries employed with the thermal spark of EDO to machining this material.

## 3 Model of Crater Topology

In FEA-Simulation of EDO, the crater volume is determined following the simulation stage [29, 30]. Hereby, the crater volume is computed depending on the form of the topology. Moreover, the disk volume has performed the best numerical results of MRR as contrasted to other topologies [1, 20, 22, 23]. Thus, it was elected to compare with the existing aimed topology.

The volumetric topology of the removed disk by the EDO system includes a total of all of the removed sub-disks according to Eq. 2. Here, these disks represent the killed-melted elements based on FEA. Consequently, the rate of removed material resulted from this total can be estimated by [23, 31]

$$MRR = \frac{47.1239}{(\text{on}_t + \text{off}_t)} \sum_{i=0}^{n-1} \frac{(x_i + x_{i+1})^2}{(y_{i+1} - y_i)}, \quad (4)$$

where $\text{on}_t$ and $\text{off}_t$ are on-time and off-time of pulse in the EDO system, respectively. The aimed topology in the current study presents revolutionary development of the disk topology. It employees the revolved volume resulted from the poly-fit technique of cutting edges nodes. These nodes are produced from melted elements of each sub-disk after the simulation is achieved. In Fig. 1a, b, the difference between the crater of the disk and poly-fit can be observed. Therefore, the steps to establish this topology consists of the following:

- Assigning the nodes of cutting edges of melted elements, where the total coordinates of these elements represent the final distance of these nodes. Note that these elements generate the removed sub-disk. Accordingly, the whole of the removed sub-disks reflects the final crater volume, as depicted in Fig. 1a, b.
- Generating a polynomial model from these nodes, as demonstrated in Fig. 1b. This model leads to producing the polynomial equation by the curve fitting technique.
- Exploiting this equation with Simpson or Trapezoidal rules to specify the crater volume, as illustrated in Eqs. 5 and 6 [32, 33]. Hence, this volume is utilized to validate the experimental MRR values according to Eqs. 7 and 8.

$$V_{CS} = D/3\big[A_i + A_l + 4(A_{i+1} + A_{i+3} + \cdots) + 2(A_{i+2} + A_{i+4} + \cdots)\big], \quad (5)$$

$$V_{CT} = D/2\big[A_i + A_l + 2(A_{i+1} + A_{i+2} + A_{i+3} + A_{i+4} + \cdots)\big], \quad (6)$$

$$MRR = \frac{20D\big[A_i + A_l + 4(A_{i+1} + A_{i+3} + \cdots) + 2(A_{i+2} + A_{i+4} + \cdots)\big]}{(\text{on}_t + \text{off}_t)}, \quad (7)$$

$$MRR = \frac{30D\big[A_i + A_l + 2(A_{i+1} + A_{i+2} + A_{i+3} + A_{i+4} + \cdots)\big]}{(\text{on}_t + \text{off}_t)}, \quad (8)$$
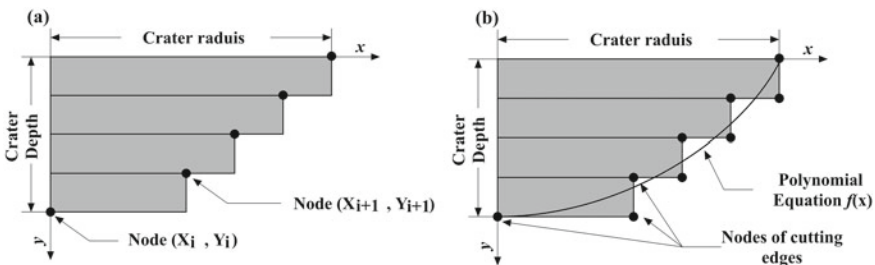


**Fig. 1** Comparison among traditional and novel topology of the crater. *Notes* **a** Disk crater topology; **b** poly-fit crater topology

where $V_{CS}$ is the crater volume depending on the Simpson's rule ($\mu$m$^3$), $V_{CT}$ is the crater volume based on the trapezoidal rule ($\mu$m$^3$), and $D$ denotes the distance between elements' nodes of the cutting edges. To estimate the subareas ($A_i, A_{i+1}, A_{i+2}, \ldots, A_l$) mentioned in Eqs. 5–8, the crater radiuses ($x_i, x_{i+1}, x_{i+2}, \ldots, x_{i+n}$) illustrated in Fig. 1a are exploited to calculate it after the simulation operation according to Eq. 9:

$$A_{\text{sub}} = \pi (x_{i+n})^2 \tag{9}$$

After the view of the variance between the traditional crater topology represented by the disk technique and the poly-fit technique presented in the current study, it is significant to understand the thermal role of spark in the EDO system. Thus, it is vital to cover the thermal inputs, boundaries, and heat flux applied in this study.

## 4 Thermal Inputs and Boundaries

Through showing both the models of crater topologies, it is becoming clear the role of the thermal simulation to understand the melted elements to form the crater topology according to the FEA technique. Therefore, the heat transient mode model is applied to describe the thermal effect of the eroding spark in the EDO medium. This model is deemed as a basis to establish the thermal inputs depending on Fourier's expression reported in Eq. 10 [34]:

$$\frac{\rho C_p}{K} \left( \frac{\partial T}{\partial t} \right) = \frac{\partial^2 T}{\partial r^2} + \frac{\partial^2 T}{\partial z^2}, \tag{10}$$

where $K$ is the thermal conductivity, $C_P$ is the specific heat capacity, $\rho$ is the density of work material, $T$ is the applied temperature, and $t$ is the duration of machining. At the same time, $r$ and $z$ indicate the coordinate axes, as demonstrated in Fig. 2. Likewise, in Fig. 2, OA-vector refers to the spark radius, whereas OB-vector represents the $r$-axis direction. Furthermore, AB-vector is the heat convection direction occasioned from the dielectric liquid. Hence, the final global element model of Eq. 10 developed by the Finite Elements Method (FEM) is expressed as [34]:

$$\{q_g\} = \{K_g\}\{T_g\} + \{C_{\text{pg}}\}\{\overline{T}_g\}, \tag{11}$$

where $\{q_g\}$, $\{K_g\}$, and $\{Tg\}$ are the global vectors of heat flux, thermal conductivity, and applied temperature, respectively. Meanwhile, $\{C_{\text{pg}}\}$ and $\{\overline{T}_g\}$ are the vectors of heat capacity and rate of thermal applied, separately.

The boundaries are applied to complete the numerical analysis of electrical erosion in EDO based on FEM in accordance with Fig. 2 and Eq. 11 as follows [4, 31]:
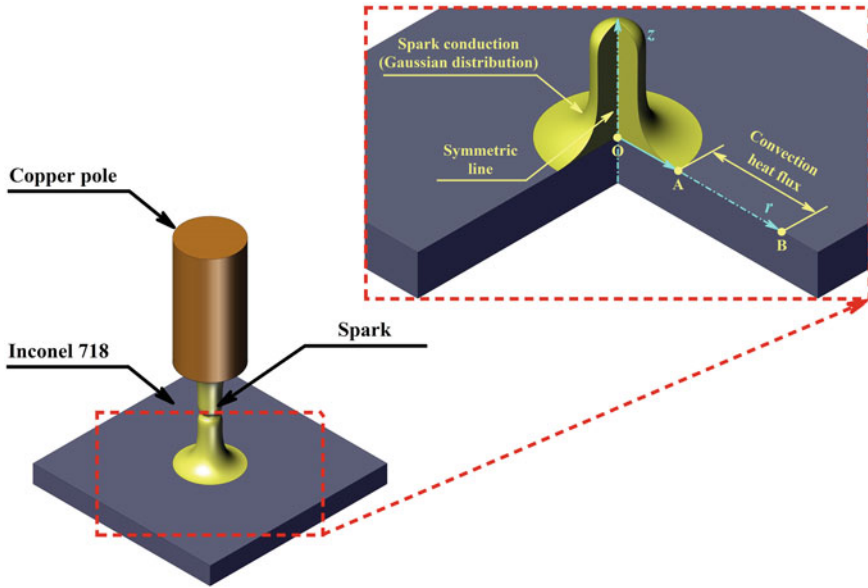
**Fig. 2** Spark mechanism to machining Inconel 718 in EDO system

$$K\left(\frac{\partial T}{\partial t}\right) = \begin{cases} h\Delta T & \text{at (AB-Vector)} \\ q(r) = \left[51.967\, C_{PS}\, F_H\, G_D^2\, P_I/10^{12}\pi\,(S_r \text{on}_t)^2\right]\exp(-4.5\, r^2/S_r^2) & \text{at (OA-Vector)} \end{cases},$$

$$(12)$$

where $C_{PS}$ refers to the concentration of blended particles, $F_H$ denotes the fraction of heat and approach to 0.09, $G_D$ indicates the gap distance, $P_I$ is the peak current applied in the EDO system, and $S_r$ is the spark radius. Note that this radius is described by the following model [4]:

$$S_r = (2.04\,e - 3)\,P_I^{0.43}\text{on}_t^{0.44} \tag{13}$$

This brief and concentrated explanation provided a comprehensive vision of the investigation environment and the crater model targeted. Consequently, Fig. 3 reveals this vision by a scenario of the MRR investigation. Wherein this scenario depends on the types of craters' topology followed in the current research. Therefore, the meshing size according to Eq. 11 is 5 μm using the mapping style in the FEA technique. Accordingly, this scenario is considered as a starting point to determine the results of craters' volume. Hence, these outcomes employ to investigate the experimental values of MRR.
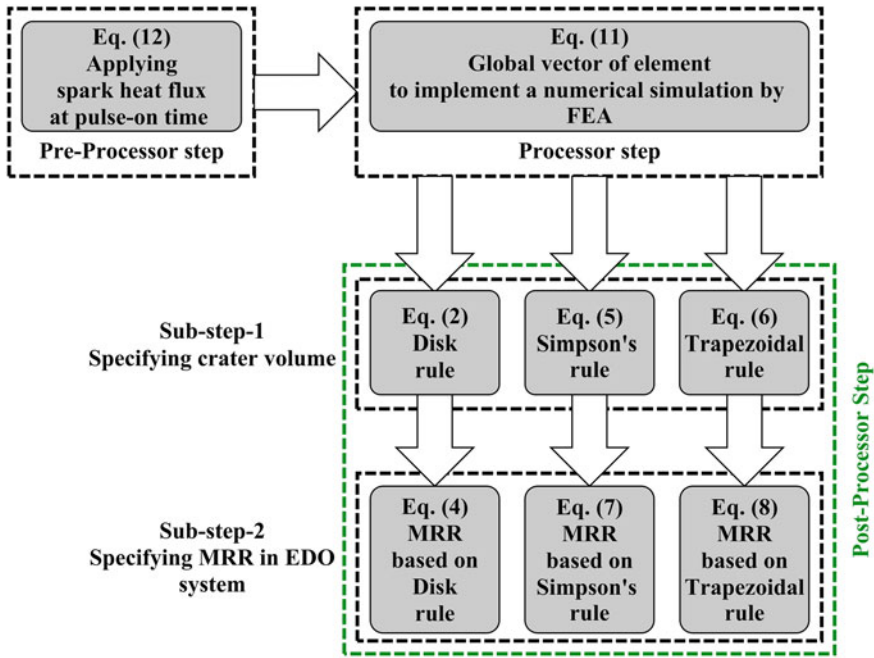
**Fig. 3** Investigation scenario of MRR in EDO system depending on the type of crater topology

## 5   Results and Discussion

As aforementioned, the methodology presented in this study included both the environment of investigation, the crater topology proposed, and the thermal inputs. Thus, this methodology led to present an adequate concept to specify the volume of the crater depending on the rules of the disk, Simpson, and trapezoidal. Accordingly, this concept contributes to determining the numerical values of the removal rate of Inconel 718 in EDO to be validated together with the experimental values of this rate.

From here, the polynomial models obtained via the poly-fit technique were observably listed in Table 4. That's where these models have been conducted by curve fitting of melted elements nodes of cutting edges after FEA is applied, as has been explained [35]. Furthermore, the correlation factor in Table 4 ranges from 0.9211 to 0.9633 for these models. Hence, this range strongly exhibits the correlation between these models to these nodes at each run. Depending on this step, these models are employed, as in the next step, in the rules of Simpson and trapezoidal to compare with disk rule since this rule is highly reliable in the numerical investigation of the EDO system [23]. Therefore, it can be observed that this comparison exists among these rules in Table 5. Hence, the average error ratio of craters resulting from disk and Simpson rules is less than the trapezoidal rule.

**Table 4** Polynomial models at each run

| Concentration of MWCNTs (g/L) | Case No | Polynomial model | $R^{2a}$ |
|---|---|---|---|
| 0.5 | 1 | $f(x) = 2841.1x^2 + 0.2454x - 2 \times 10^{-5}$ | 0.9344 |
| | 2 | $f(x) = 6201.9x^2 + 0.1259x - 2 \times 10^{-5}$ | 0.9577 |
| | 3 | $f(x) = 10^8 x^3 - 2669.4x^2 + 0.1209x - 2 \times 10^{-5}$ | 0.9211 |
| | 4 | $f(x) = 8116.2x^2 - 0.0349x - 2 \times 10^{-5}$ | 0.9348 |
| 1 | 1 | $f(x) = 6 \times 10^{11}x^4 + 3 \times 10^8 x^3 - 24485x^2 + 0.6464x - 2 \times 10^{-5}$ | 0.9394 |
| | 2 | $f(x) = -6 \times 10^7 x^3 + 10877x^2 - 0.0216x - 2 \times 10^{-5}$ | 0.9633 |
| | 3 | $f(x) = 6575.4x^2 + 0.1233x - 2 \times 10^{-5}$ | 0.9597 |
| | 4 | $f(x) = 10016x^2 - 0.1465x - 2 \times 10^{-5}$ | 0.9475 |

$^a R^2$: Correlation factor

**Table 5** Craters volumes resulting from the disk, Simpson, and trapezoidal rules

| Concentration of MWCNTs (g/L) | Case No | $V_{CD}$* (mm³) | $V_{CS}$ (mm³) | %$\epsilon$** | $V_{CT}$ (mm³) | %$\epsilon$ |
|---|---|---|---|---|---|---|
| 0.5 | 1 | 0.2962 | 0.3461 | 16.85 | 0.4370 | 47.53 |
| | 2 | 1.3497 | 1.3153 | 2.55 | 1.6515 | 22.36 |
| | 3 | 1.4762 | 1.7277 | 17.04 | 2.2888 | 55.05 |
| | 4 | 2.6542 | 2.7741 | 4.52 | 3.6553 | 37.72 |
| 1 | 1 | 0.3199 | 0.3045 | 4.79 | 0.4089 | 27.84 |
| | 2 | 0.7535 | 0.7578 | 0.57 | 0.9231 | 22.50 |
| | 3 | 1.3026 | 1.4044 | 7.81 | 1.7986 | 38.08 |
| | 4 | 2.5966 | 2.3839 | 8.19 | 3.3144 | 27.64 |
| Average %$\epsilon$ | | | | 7.79 | | 34.84 |

*$V_{CD}$: Crater volume by disk rule; **%$\epsilon$: Error ratio

According to Tables 4 and 5, Fig. 4 summarizes computing the crater volume in the EDO system. It interprets the steps of locating and fitting the nodes of melted elements following the simulation by FEA. Consequently, this summary displays one of these outcomes stated in Tables 4 and 5. This outcome represents run No. 1 at 2 A and 0.5 g/L of peak current and MWCNTs concentration. In turn, according to Fig. 4, under these conditions, crater volume is witnessed based on disk and Simpson rules as the second and third steps, sequentially. Moreover, after locating these nodes, as

the first step, these steps were applied. Hence, steps 1–3 are replicated in the other runs mentioned in Tables 4 and 5.

The outcomes of the crater volumes illustrated in Table 5 have cast a shadow on the numerical results of MRR, as demonstrated in Table 6 and Fig. 5. These results have an average error ratio equal to 7.28, 6.34, and 38.06% with the experimental values of MRR, as depicted in Table 6, according to disk, Simpsons, and trapezoidal rules, respectively. As observed in Fig. 5, these volumes and MRR possess the same behavior toward the growth of pulse current. Accordingly, this growth has contributed to an increase in the crater volume and MRR [36]. Thus, this behavior has endorsed that a rise in pulse current led to increased pulse energy [37]. In turn, this energy assists in extending the volume of the crater and the rate of Inconel 718 removal. Moreover, this resulted volume has primarily helped to raise the roughness [38, 39]. These truths and the outputs of the average error ratios showed that the best-adapted topology to investigate MRR and the roughness of the machined surface is Simpson's rule with the poly-fit technique.

This article has presented a new vision to predict and compute the crater volume using the polynomial technique, depending on these outputs. From here, this technique has proved that Simpson's rule is more precise in determining this volume in the EDO, as compared to the other studied formulas. Hence, the poly-fit and this rule as a hybrid technique have aided in enhancing the numerical method to compute the crater dimensions.

## 6 Conclusions

The crater volume in the EDO system is a challenge posed to the authors for computing the removal rate and the roughness of the workpiece. Accordingly, the traditional models of the crater must be updated by a new numerical model to enhance this volume. Therefore, this study endeavored to present a new methodology by linking the poly-fit technique with Simpson and trapezoidal rules, individually, instead of the disk model. Consequently, this hybrid linking has concluded to following:

i. The poly-fit technique is efficient with Simpson's rule to compute the volume of craters and investigate the removal rate of Inconel 718. Therefore, this methodology is considered a promising technique to specify the crater volume, in contrast to the rules of disk and trapezoidal. Moreover, as a hybrid method, this technique has achieved an average of 6.34 of the error ratio.
ii. This hybrid technique can be beneficial as a function of surface roughness. Thus, it can employ to compute the dimensions of the removal crater in the EDO system.

Depending on the concluded outputs of the current study, the poly-fit technique and rule of Simpson are deemed an efficient hybrid and novel in computing the crater dimensions. Consequently, this study strongly recommends adopting this method to
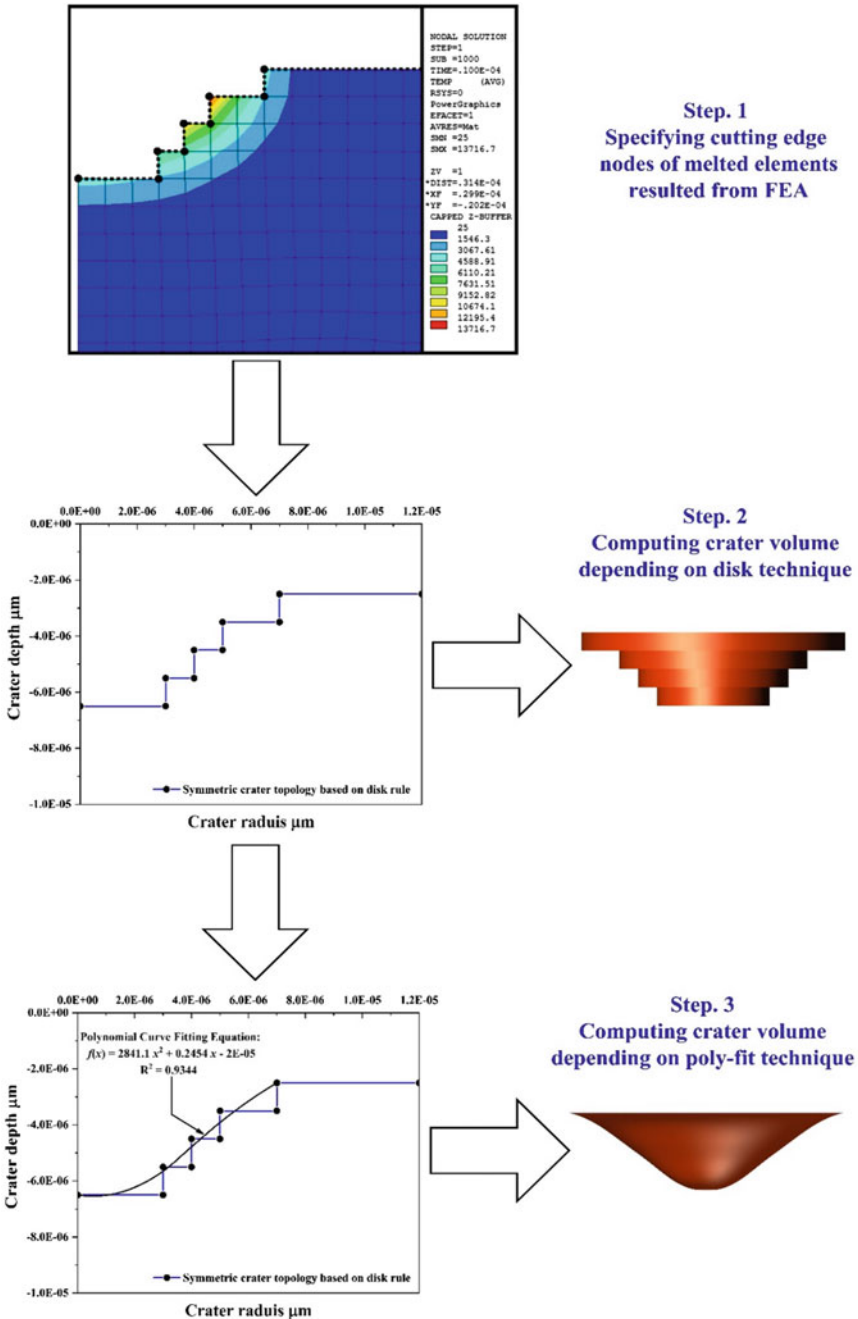
**Fig. 4** Summary of computing the crater volume in the EDO system. Step (1) The cutting edges nodes of melted elements of simulated model; Step (2) The traditional technique to compute the crater by disk rule; Step (3) The novel technique to compute the crater relying on the poly-fit technique of these nodes

**Table 6** Comparison of numerical and experimental values of Inconel 718's MRR

| Concentration of MWCNTs (g/L) | Exp. MRR (mm³/min) | Num. MRR (mm³/min) | | | | | |
|---|---|---|---|---|---|---|---|
| | | With disk rule | %ϵ | With Simpson's rule | %ϵ | With Trapezoidal rule | %ϵ |
| 0.5 | 0.966 | 0.888 | 8.08 | 1.038 | 7.41 | 1.310 | 35.61 |
| | 3.666 | 4.049 | 10.44 | 3.946 | 7.63 | 4.954 | 35.14 |
| | 4.742 | 4.428 | 6.62 | 5.183 | 9.29 | 6.866 | 44.79 |
| | 7.770 | 7.962 | 2.48 | 8.322 | 7.11 | 10.965 | 41.13 |
| 1 | 0.875 | 0.959 | 9.61 | 0.913 | 4.35 | 1.226 | 40.12 |
| | 2.097 | 2.260 | 7.77 | 2.273 | 8.39 | 2.769 | 32.02 |
| | 4.012 | 3.907 | 2.62 | 4.213 | 4.99 | 5.395 | 34.46 |
| | 7.040 | 7.789 | 10.64 | 7.151 | 1.58 | 9.943 | 41.22 |
| Average %ϵ | | | 7.28 | | 6.34 | | 38.06 |
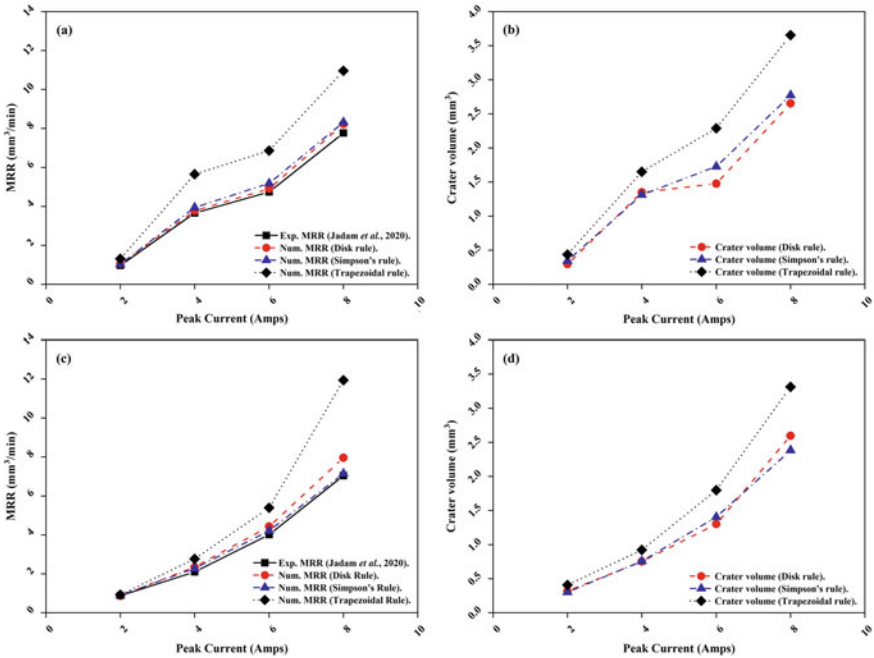


**Fig. 5** Influence of peak current on MRR and volume of the crater in EDO system. Observed the role of the gradient of peak current with: 0.5 g/L of MWCNTs on **a** MRR and **b** crater volume; 1 g/L of MWCNTs on **c** MRR and **d** crater volume

predict the MRR and roughness of the machined surface in the EDO system to avoid the cost, time, and effort in the experimental field.

# References

1. Abbas MA, Lajis MA, Abdul Ridha GS (2019) A new methodology for predicting quantity of agglomeration between electrodes in PMEDM environment. Int J Mech Eng Technol 10:1461–1479
2. Abbas DR, Lajis MA, Abbas MA (2020) Comparison of the removal rate in EDM based on the mixed environment. In: Lecture notes in mechanical engineering. Adv Manuf Eng 25–33
3. Abbas MA, Lajis MA (2020) Influence of the agglomeration phenomenon on the recast surface in PMEDM environment. In: Lecture notes in mechanical engineering. Adv Manuf Eng 11–24
4. Abbas MA, Lajis MA, Jawad AD et al (2019) Influence of the spark heat on the electrode behavior in Powder Mixed-EDM environment. J Mech Eng Sci 13:6125–6143
5. Hong TT, Van Cuong N, Danh BT et al (2021) Multi-objective optimization of PMEDM process of 90CrSi alloy steel for minimum electrode wear rate and maximum material removal rate with silicon carbide powder. Mater Sci Forum 51–58
6. Sahu SK, Jadam T, Datta S et al (2018) Application of SiC powder added in kerosene dielectric media for electro-discharge machining of Inconel 718 super alloys: effect of powder concentration. Mater Today Proc 5:20297–20305
7. Abdudeen A, Abu Qudeiri JE, Kareem A et al (2020) Recent advances and perceptive insights into powder-mixed dielectric fluid of EDM. Micromachines 11:754
8. Kumar S, Goud M, Suri NM (2020) Experimental investigation of magnetic-field-assisted electric discharge machining by silicon-based dielectric of Inconel 706 superalloy. Sādhanā 45:1–8
9. Sajeevan R, Dubey AK (2021) Parametric study of die-sinking electric discharge machining on aluminium based metal matrix composite. Mater Today Proc 44:930–934
10. Hosni NAJ, Lajis MA (2020) Experimental investigation and economic analysis of surfactant (Span-20) in powder mixed electrical discharge machining (PMEDM) of AISI D2 hardened steel. Mach Sci Technol 24:398–424
11. Pillai KVA, Hariharan P (2021) Experimental investigation on surface and machining characteristics of micro ED milling of Ti-6Al-4 V with different nano powder mixed dielectrics. Silicon 1–24
12. Abbas MA, Lajis MA, Abbas DR et al (2020) Influence of additive materials on the roughness of AISI D2 steel in electrical discharge machining (EDM) environment. Materwiss. Werksttech 51:719–724
13. Devgan S, Sidhu SS (2019) Evolution of surface modification trends in bone related biomaterials: a review. Mater Chem Phys 233:68–78
14. Lamichhane Y, Singh G, Bhui AS et al (2019) Surface modification of 316L SS with HAp nano-particles using PMEDM for enhanced biocompatibility. Mater Today Proc 15:336–343

15. Singh G, Singh G, Bains PS et al (2019) Surface evaluation of ED machined 316L stainless steel in $TiO_2$ nano-powder mixed dielectric medium. Mater Today Proc 18:1297–1303
16. Ali P, Walia RS, Murtaza Q et al (2020) Material removal analysis of hybrid EDM-assisted centrifugal abrasive flow machining process for performance enhancement. J Braz Soc Mech Sci Eng 42:1–28
17. Babbar A, Prakash C, Singh S et al (2020) Application of hybrid nature-inspired algorithm: single and bi-objective constrained optimization of magnetic abrasive finishing process parameters. J Mater Res Technol Eng 9:7961–7974
18. Salonitis K, Stournaras A, Stavropoulos P et al (2009) Thermal modelling of the material removal rate and surface roughness for die-sinking EDM. Int J Adv Manuf Technol 40:316–323
19. Jatti VS, Bagane S (2017) Thermo-electric modelling, simulation and experimental validation of powder mixed electric discharge machining (PMEDM) of BeCu alloys. Alexandria Eng J 57:643–653
20. Shabgard M, Oliaei SNB, Seyedzavvar M et al (2011) Experimental investigation and 3D finite element prediction of the white layer thickness, heat affected zone, and surface roughness in EDM process. J Mech Sci Technol 25:3173–3183
21. Bhattacharya A, Batish A, Singh K (2012) FE simulation and experimental validation of powder mixed EDM process for estimating the temperature distribution and volume removed in single crater. Int J Model Simul Sci Comput 3:1250006
22. Joshi SN, Pande SS (2010) Thermophysical modelling of die-sinking EDM process. J Manuf Process 12:45–56
23. Kumar A, Bagal DK, Maity KP (2014) Numerical modeling of wire electrical discharge machining of super alloy Inconel 718. Procedia Eng 1512–1523
24. Farré M, Barceló D (2012) Introduction to the analysis and risk of nanomaterials in environmental and food samples. Compr Anal Chem 1–32
25. Chiappini C, Almeida C (2014) Silicon nanoneedles for drug delivery. In: Semiconducting silicon nanowires for biomedical applications, pp 144–167
26. De Sousa FDB, Scuracchio CH (2014) The use of atomic force microscopy as an important technique to analyze the dispersion of nanometric fillers and morphology in nanocomposites and polymer blends based on elastomers. Polímeros 24:661–672
27. Jadam T, Sahu SK, Datta S et al (2020) Powder-mixed electro-discharge machining performance of Inconel 718: effect of concentration of multi-walled carbon nanotube added to the dielectric media. Sādhanā 45:1–16
28. Jadam T, Sahu SK, Datta S et al (2019) EDM performance of Inconel 718 superalloy: application of multi-walled carbon nanotube (MWCNT) added dielectric media. J Braz Soc Mech Sci Eng 41:1–20
29. Li C, Ge P, Bi W (2021) Thermal simulation of the single discharge for electro-spark deposition diamond wire saw. Int J Adv Manuf Technol 1–8
30. Wandra R (2021) Finite element analysis of powder mixed electric discharge machining on Ti-alloy. Mater Today Proc
31. Abbas MA, Lajis MA (2020) The effect of the gap distance between electrodes on removal rate in PMEDM using FEA. In: Lecture notes in mechanical engineering. Adv. Manuf. Eng 7–16
32. Bird J (2012) Newnes engineering mathematics pocket book, 3rd ed. Taylor & Francis, pp 102–105
33. Virdi S, Baker R, Virdi NK (2014) Construction mathematics. CRC Press, p 227
34. Kansal HK, Singh S, Kumar P (2008) Numerical simulation of powder mixed electric discharge machining (PMEDM) using finite element method. Math Comput Model 47:1217–1237
35. González-Castaño C, Lorente-Leyva LL, Muñoz J et al (2021) An MPPT strategy based on a surface-based polynomial fitting for solar photovoltaic systems using real-time hardware. Electronics 10:206
36. Razak MA, Abdul-Rani AM, Nanimina AM (2015) Improving EDM efficiency with silicon carbide powder-mixed dielectric fluid. Int J Mater Mech Manuf 3:40–43
37. Rezaei Ashtiani HR, Hojati F (2021) The influences of spark energy density on the electrical discharge machining (EDM). Adv Mater Process Technol 1–17

38. Taherkhania A, Ilani MA, Ebrahimi F, Nguyen PH et al (2021) Investigation of surface quality in cost of goods manufactured (COGM) method of $\mu$-$Al_2O_3$ powder-mixed-EDM process on machining of Ti-6Al-4V. Rev Int J Adv Manuf Technol
39. Haque R, Sekh M, Kibria G et al (2021) Improvement of surface quality of Ti-6al-4v alloy by powder mixed electrical discharge machining using copper powder. Facta Universitatis Series Mechanical Engineering, p 19

# Time-Dependent Corrosion Resistance Investigation of Hydrophobic Magnesium Alloys

**Hasan Koten and Ozge Kamaci**

**Abstract** In this study, the corrosion resistance of AZ31B magnesium alloy was evaluated against time. Because of its sensitivity to corrosion, AZ31B magnesium alloy was chosen to be coated with elephoretic coating method. With the electrophoretic coating method, it is possible to coat the alloy surfaces practically with biocompatible materials in one step. The characterization of the alloy surfaces has been changed in order to eliminate the susceptibility of magnesium to corrosion. Surface characterization has been made superhydrophobic and hydrophobic by coating the alloys. Stearic acid and magnesium nitart-containing coating materials are aimed to reduce the surface energy of alloys. It has been shown that the corrosion resistance of the surface coated alloys is higher than the uncoated alloy samples. To discuss the authenticity of the thesis, it was observed for the first time that AZ31B alloys were kept in corrosive liquids for a long time and preserved their hydrophobic properties thanks to the coating. Since AZ31B alloy is used as a bio-implant raw material, corrosion has been evaluated for the first time in an environment simulating body conditions. Coated AZ31B samples have been shown to retain their stabilization in DMEM for approximately one month. It has been shown that K.10AZ31B and K.12AZ31B alloys taken as coating samples have superhydrophobic surface characterization, and K.8AZ31B and K.D.10AZ31B samples are hydrophobic coated. For the first time, AZ31B samples were coated at these concentrations. It has been shown that the coating samples were made successfully and the coatings continued for a long time both in 3.5% NaCl environment and in DMEM containing antibiotics.

**Keywords** AZ31B · Corrosion resistance · Electrophoretic coating · Stearic acid · Bio-implant

H. Koten (✉)
Mechanical Engineering Department, Istanbul Medeniyet University, Istanbul, Turkey
e-mail: hasan.koten@medeniyet.edu.tr

O. Kamaci
Institute of Graduate Education, Istanbul Medeniyet University, Istanbul, Turkey

# 1   Introduction

Electrophoretic coating consists of two processes under the electric field as a system. It consists of suspended liquid, charged particles, and electrodes. In the first process, the charged particles suspended in the air in the suspended system move towards the opposite side of their charge under the electric field. The electrode with which they move is the opposite of their charge. In the second stage, the particles deposited on the electrode, which is completely opposite to their own charge, form the coating material here. The film layer they form is generally referred to as homogeneous. The size of the charged particles used for coating is 30 µm small. If no pores are desired on the coated substrates, the pores can be closed with a hot working material.

In addition, the purpose of the system is to ensure that the particles in suspension remain in a stabilized state. When talking about stabilization, it means holding the particles in suspension together with van der Waals forces. As soon as the particles overcome the electrostatic attraction force between themselves, they become ready to be stored with the help of the current electric field of the system.

This system has many different advantages over other coating systems. It can be controlled from the outside. The substrates to be coated can be in the desired shapes. It is a method that is open to continuous development, since its usage area is very large. In addition, one of the reasons for its widespread use is the choice of cost-effective materials and their practical application (Randal, 2006; Besra et al., 2008), [3].

Metallic materials are coated with EPD system in order to increase their resistance against corrosion. Considering that magnesium alloys have a wide usage area, increasing their resistance to corrosion is the first condition.

In this study, only the coating of magnesium alloys with EPD will be explained. Coating of magnesium alloys with EPD systems is most common in biodegradable alloys. This is because magenzum is a light element in physical structure and is suitable for disintegration. The biodegradation mechanism refers to the biocorrosion mechanism.

Metallic materials have certain usage limits and deficiencies in terms of their structures. Especially, stainless steel, titanium, and cobalt-based materials are frequently used in orthopaedic surgery. However, especially the elastic modulus values of these materials do not meet the flexural modulus of a real bone. For this reason, magnesium and its alloys, which are closer to bone, have been used in orthopaedic surgery. However, the main problem in the usage of magnesium alloys in orthopaedic surgery is the rapid corrosion of the material. Whilst magnesium corrodes, it quickly causes gas cavitation. In this case, the second undesirable problem is the rapid corrosion problem of the material [41] (Fig. 1).

Parameters affecting the electrophoretic coating; particles have to be of a certain size. Even though the particles are very large in size, they may not be uniformly distributed. In addition, any opener used in suspension solution has its own dielectric constant. Any material added to the suspension disrupts the dielectric system of the system. Each particle also has its own dielectric constant. In addition to these

**Fig. 1** Electrophoretic storage system [3]
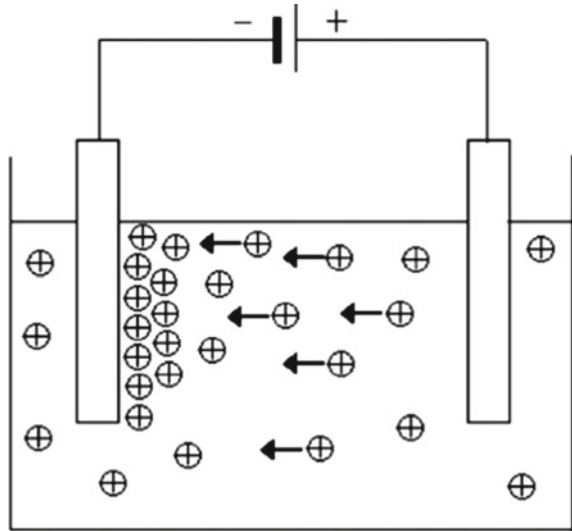
parametric data, there are also different parameters related to the external electricity of the system. These parameters affect the time and amount of storage in the electrodes in the system [1, 2].

In this study, the variation of the coatings of magnesium alloys at different concentrations according to the parametric data will be examined.

## 2 Material and Method

In this study, AZ31B magnesium alloy, stearic acid $CH_3(CH_2)16COOH$, magnesium nitrate $Mg(NO_3)_2$. $6H_2O$, pure ethanol ($C_2H_5OH$), NaCl, magnetic stirrer, precision balance, electrodes, electrolysis bath, DC power supply, silicon carbide, and ultrasonic bath are used. AZ31B samples are first cut in the specified dimensions. Then comes the cleaning process. AZ31B samples are first cleaned of the corrosive residues on them with 180P and then 800P silicon carbide paper. The cleaned samples were cleaned separately in an ultrasonic cleaner with distilled water and anhydrous ethanol.

The completely cleaned samples were coated with the magnesium stearate compound prepared at SA:Mg+ 2 (15:1 and 8:1) concentrations. Magnesium stearate in the concentrations prepared in the process was put into the electrolysis bath. AZ31B alloy samples were attached to the electrodes. Coating was done at 30 V for 30 min.

Each coated sample was re-cleaned with anhydrous ethanol. From the coated samples, SA:Mg+ 2 (15:1) was left in a 3.5% NaCl solution for one week. For comparison, SA/Mg+ 2 (8:1) which was coated but not put into 3.5% NaCl was kept at room conditions for one day.

SEM images of the samples obtained at both concentrations were taken and evaluated.

## 3    Case Studies

Various morphological images are formed due to magnesium and stearic acid in many different materials.

Figure 2 The coated sample is not corroded. Magnesium stearate [80] stated in their similar study that morphological SEM images will be formed in the form of cauliflower, rose petal, or thorn as a result of stearic acid [80].

Looking at Fig. 3, this situation is clearly explained in this image, since one electrode in the EPD system can be studied by the method of giving electrons and the other electrode receiving electrons. Morphological distortions have occurred in the cathode, which is the electron donor side.

The AZ31B samples, which were increased in the concentration of the coating and left in 3.5% NaCl solution, are as follows.

In the example shown in Fig. 4, when SA:Mg+ 2 (15:1) is subtracted, it is seen that the coating did not occur in the sample. There are different reasons for this situation. First of all, since the parametric data will be discussed, the ethanol used in the suspension solution was prepared with 95% ethanol. That is, 5% water is present in the suspension solution. In this case, the solutions are expected to be pure, as discussed in the parametric data of the EPD system. As soon as the stability of
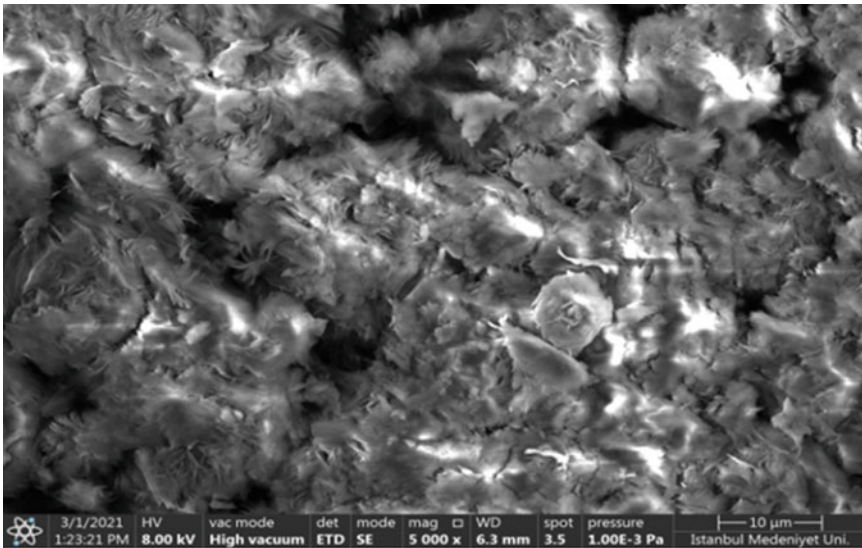


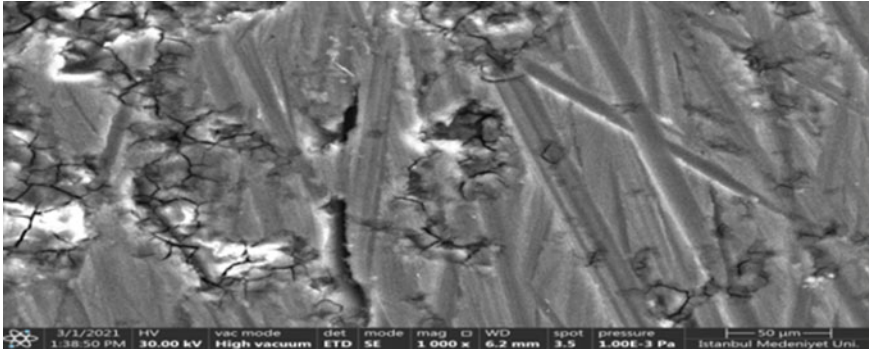**Fig. 2**  SA:Mg+ 2 (8:1) anode one day after coating

**Fig. 3** SA:Mg+ 2 (8:1) uncoated cathode

each suspension solution deteriorates, the EPD system deteriorates, coating is not possible. Since ethanol is not pure in this way, it completely affects the dielectric constant of the suspension, and there are differences in the loading of particles in the coating.

The samples with concentrations of SA/Mg+ 2 (8/1, 10/1) were kept in corrosive 3.5% NaCl solution, and SEM images were taken at the 1st and 4th weeks. SA/Mg+ 2 (12/1) samples were kept in 3.5% NaCl solution, and SEM images were taken at the end of the 1st and 3rd week. Since the samples were highly concentrated, it was thought that the image might deteriorate in the 4th week. As a matter of fact,
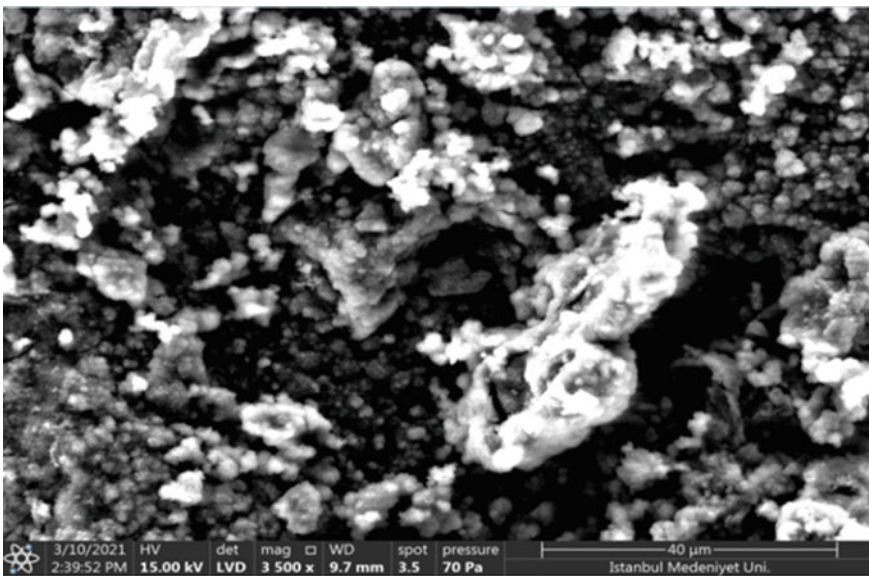


**Fig. 4** Sample coated with 4 SA:1 Mg +2 (15:1) and left in 3.5% NaCl solution for 1 week

as of the 3rd week in the image given, it was seen that the protective layer formed in the image of the SA/Mg+ 2 (12/1) sample and the layer could not protect itself. SEM was performed in SA/Mg +2 (15/1) sample for comparison and trial purposes. For example, since there is an error in the coating solution, it will not be taken as data in the experiment. Samples with SA/Mg+ 2 (10/1) were kept in DMEM for 1 and 3 weeks, and SEM was taken. Uncoated samples were again kept in 3.5% NaCl solution for 1 and 4 weeks, and SEM shots were taken.

When SEM images are examined, respectively; in Fig. 32, SEM imaging was applied one day after the coating of K.8.AZ31B magnesium alloy. The rose petal motif given in literature studies on coatings with stearic acid is seen in the image. Related literature studies will be discussed in the discussion section. However, looking at the image, it can be said that the surface coating of the sample with stearic acid and magnesium nitrate has taken place. The sample was not left in a corrosive environment. The SEM image of the electron donating cathode after electrostorage is given. In the image, it is seen in the image that the cathode is exposed to the electric field, and because it is in the electron donor position, it undergoes crevice corrosion or stress corrosion. The lines in the middle and around the cathode show scratches in the SEM image because the materials were sanded before the coating process. The cathode has not been left in a corrosive environment.

The K.8.AZ31B sample was kept in room conditions for about two weeks due to laboratory conditions, and then kept in a 3.5% wt% NaCl corrosive solution for 1 week, and then, SEM was taken. In the image, it was revealed that the plates were formed from microstructures and nano-spindle structures, and the coating became thorny. Even if the coating stays in room conditions for 2 weeks and stays in a corrosive environment for 1 week, its coating continues. In the sample of K.8.AZ31B, the cauliflower image showing the superhydrophobic coating surface model, which is formed as a result of coatings with stearic acid in the literature studies, was formed on the coating. From here comes the idea that the surface is covered. The stability of this desired coating form in the corrosive environment, even at the end of the 4th week, shows that a successful coating model is obtained.

The image of (10/1) K.10.AZ31B sample in the corrosive medium with 3.5% NaCl at the 1st week; when the coating concentration is increased, a hierarchical view of the coating in which micro- and nano-structured coating form is obtained. An image similar to the SEM image in the reference source related to the thesis study is shown. But the micro- and nano-structures are more discretely aligned. Although the K.10.AZ31B sample remained in 3.5% NaCl solution for 4 weeks, micro- and nano-structures still exist in the image. There is no opening or disintegration in the coating. This shows us that there is no morphological defect in the coating, although it is kept in a corrosive environment for the longest time amongst the related literature studies. The SEM image obtained after the K.12.AZ31B sample was kept in a corrosive, 3.5% NaCl solution for 1 week; micro- and nano-structures coexist separately in layers. Again, the cauliflower image was obtained at this concentration. This time, spindle structures are also present in the image. Morphologically, it can be said that the alloy has been successfully coated. Considering the SEM image of K.12.AZ31B

sample at the end of the 3rd week in Fig. 39, it is thought that a corrosive 3.5% NaCl solution has penetrated the coating. There was some deterioration in the coating.

The K.S.AZ31B sample, uncoated, was drawn in a large scale of 50 µm in the SEM image after it was kept in a corrosive 3.5% NaCl solution for 1 week. As the image is not 10 µm like all other SEM shots, it is insufficient for comparison. However, in the discussion section, it is understood from the photo taken after the coating is corroded. The K.S.AZ31B sample remained in a corrosive, 3.5% NaCl solution for 3 weeks. In the uncoated AZ31B sample, corrosion products formed prickly crystal structures in layers. For this reason, it can be concluded that an uncoated magnesium alloy corrodes rapidly after 3 weeks.

The SEM image of the K.15.AZ31B sample was taken only because the image that would appear on the coating surface at high concentration was curious. In addition, since this sample could not be prepared with 100% pure ethanol, cracks formed on the coating surface and H2 release occurred after 1 week after being coated and left in a corrosive environment. For this reason, it will not be compared with other examples.

In Fig. 5, in the SEM image of K.D.10.AZ31B, the coated magnesium alloy sample kept in DMEM 1 week later, a cauliflower-shaped surface coating was formed. Since this image is similar to the previous reference SEM images, it gives the impression that the coating has been done successfully.

In Figs. 6 and 7, SEM image of K.D.10.AZ31B sample taken after 3 weeks of soaking in DMEM, it was observed that the cauliflower-shaped surface coating
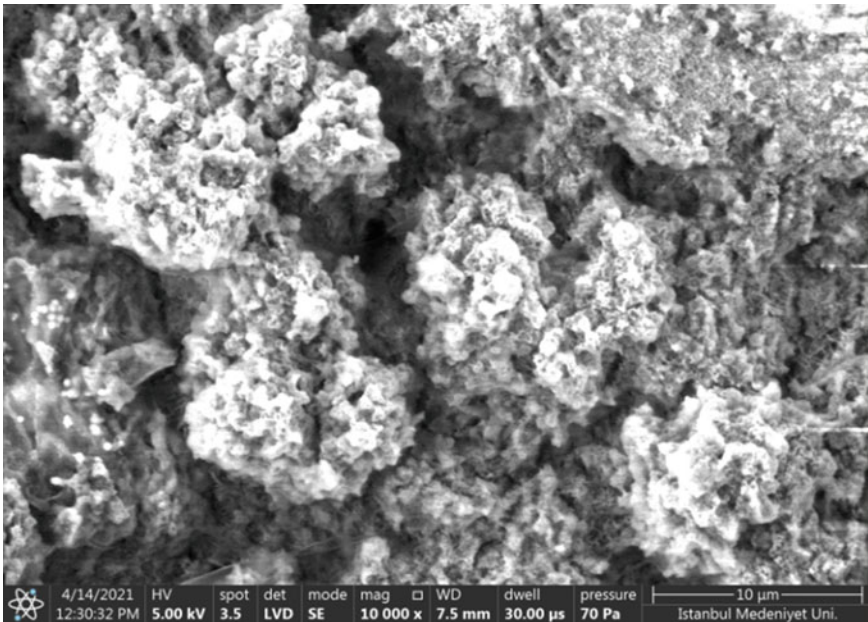


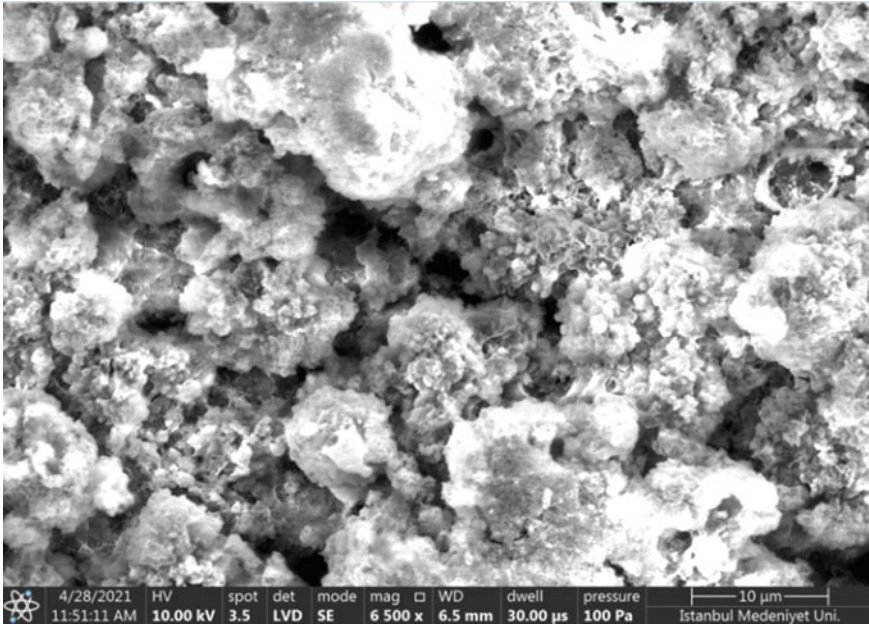**Fig. 5** K.D.10.AZ31B SA/Mg + 2: (10/1) 1.Week, immersed image in DMEM

**Fig. 6** K.D.10.AZ31B SA/Mg+ 2: (10/1) At the end of the 3rd week, the image stored in DMEM

morphology preserves the stability of its structure. However, there is a suspicion that there may be slight dispersion at the edges in the 5 $\mu$m detailed image. However, it retained a long-term surface stable morphology.

## 4 Conclusion

Magnesium alloys are materials that are always open to corrosion due to their physical properties. Various methods have been used to prevent this situation. In this study, electrophoretic coating process, which is an economically convenient and practical application, was carried out. Two concentration trials were conducted in the study. In one study, SA: Mg+ 2, 8.1 trial was conducted just to discuss the morphological appearance of the coating. It is understood that the coating is stable when looking at the SEM image. In this respect, it is thought that it would be appropriate to prepare materials at this coating concentration against corrosion. However, it is seen in SA: Mg + 2, 15:1 that a stable coating cannot be obtained when a certain concentration limit is exceeded based on the coating parameters, and impure materials are used in the coating material. For this reason, it is seen that the use of pure organic openers in the preparation of coating materials is essential for the movement of particles to the substrate to be coated.
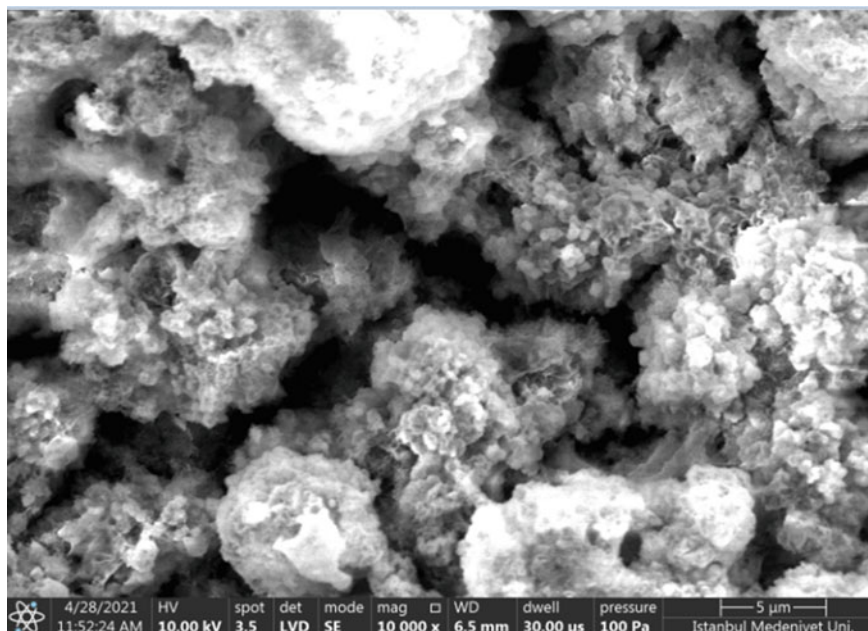
**Fig. 7** K.D.10.AZ31B SA/Mg+ 2: (10/1) Close-up view at the end of the 3rd week kept in DMEM

# References

1. Amrollah P et al (2015) Electrophoretic deposition (EPD): fundamentals and applications from nano-to micro-scale structures. In: Handbook of Nanoelectrochemistry, Springer International Publishing Switzerland
2. Besra L, Liu M (2007) A review on fundamentals and applications of electrophoretic deposition (EPD). Prog Mater Sci 52(1):1–61
3. Corni I, Ryan MP, Boccaccini AR (2008) Electrophoretic deposition: From traditional ceramics to nanotechnology. J Eur Ceram Soc 28(7):1353–1367
4. Hutchings IM (1992) Tribology: friction and wear of engineering materials: Edward Arnold,(Fax:+ 44 (0) 732 461321), pp 352, £19. 95 paperback, ISBN 0 340 56184
5. Jafarpour M, Aghajani H (2019) Electrophoretic deposition of bi-layered nano-sized silicon carbide/mullite coating from stabilized suspensions. J Australian Ceramic Soc 1–10
6. Jayabharathy S, Mathiazhagan P (2019) Study of erosion corrosion behaviour of magnesium and its alloys
7. Joseph KR, Neto C (2010) On the superhydrophobic properties of crystallized stearic acid. Aust J Chem 63(3):525–528
8. Juliadmi D, Fauzi VR, Gunawarman HN, Idris MH (2017) Hydroxyapatite coating on titanium alloy Ti-6Al-4V with electrophoretic deposition (EPD) for dental root application. Int J Adv Sci Eng Inform Technol 7(6):2152–2158
9. Kamachimudali U, Sridhar TM, Raj B (2003) Corrosion of bio implants. Sadhana 28(3):601–637
10. Kamrani S, Fleck C (2019) Biodegradable magnesium alloys as temporary orthopaedic implants: a review. Biometals 32(2):185–193
11. Kang CW, Fang FZ (2018) State of the art of bioimplants manufacturing: part I. Adv Manuf 6(1):20–40

12. Kannan MB, Dietzel W, Blawert C, Atrens A, Lyon P (2008) Stress corrosion cracking of rare-earth containing magnesium alloys ZE41, QE22 and Elektron 21 (EV31A) compared with AZ80. Mater Sci Eng, A 480(1–2):529–539
13. Karambakhsh A, Afshar A, Malekinejad P (2012) Corrosion resistance and color properties of anodized Ti-6Al-4V. J Mater Eng Perform 21(1):121–127
14. Khalifeh A (2019) Stress corrosion cracking damages. Failure Analysis, pp 25
15. Kiełbus A (2007) Corrosion resistance of Elektron 21 magnesium alloy. J Achievem Mater Manuf Eng 22(1):29–32
16. Kuruvila R, Kumaran ST, Khan MA, Uthayakumar M (2018) A brief review on the erosion-corrosion behavior of engineering materials. Corros Rev 36(5):435–447
17. Laska A, Bartmański M (2020) Parameters of the electrophoretic deposition process and its influence on the morphology of hydroxyapatite coatings. Review Inżynieria Materiałowa 20–25
18. Li P, Gao G, Wang Y, Ma Y (2010) Crystal structures and exotic behavior of magnesium under pressure. J Phys Chem C 114(49):21745–21749
19. Liao Q, Hu W, Le Q, Chen X, Hu K, Cheng C, Hu C (2020) Microstructure, mechanical properties and texture evolution of Mg–Al–Zn–La–Gd–Y magnesium alloy by hot extrusion and multi-pass rolling. Acta Metallurgica Sinica (English Letters) 33:1359–1368
20. Liu C, Ren Z, Xu Y, Pang S, Zhao X, Zhao Y (2018) Biodegradable magnesium alloys developed as bone repair materials: a review. Scanning
21. Loto CA (2017) Stress corrosion cracking: characteristics, mechanisms and experimental study. Int J Adv Manuf Technol 93(9):3567–3582
22. Luo AA (2014) Alloy development, manufacturing and design for magnesium applications. In: Magnesium technology, Springer, Cham, pp 5–5
23. Manakari V, Parande G, Gupta M (2017) Selective laser melting of magnesium and magnesium alloy powders: a review. Metals 7(1):2
24. Manivasagam G, Dhinasekaran D, Rajamanickam A (2010) Biomedical implants: corrosion and its prevention-a review. Recent Patents On Corrosion Sci
25. Mao L, Yuan G, Wang S, Niu J, Wu G, Ding W (2012) A novel biodegradable Mg–Nd–Zn–Zr alloy with uniform corrosion behavior in artificial plasma. Mater Lett 88:1–4
26. Martínez-Viademonte MP, Abrahami ST, Hack T, Burchardt M, Terryn H (2020) A review on anodizing of aerospace aluminum alloys for corrosion protection. Coatings (Basel) 10(11):1cp-1cp
27. McCafferty E (2001) Effect of ion implantation on the corrosion behavior of iron, stainless steels, and aluminum—a review. Corrosion 57(12):1011–1029
28. Mei D, Lamaka SV, Lu X, Zheludkevich ML (2020) Selecting medium for corrosion testing of bioabsorbable magnesium and other metals–a critical review. Corrosion Sci 108722
29. Mercieca S, Caligari Conti M, Buhagiar J, Camilleri J (2018) Assessment of corrosion resistance of cast cobalt-and nickel-chromium dental alloys in acidic environments. J Appl Biomater Funct Mater 16(1):47–54
30. Minagar S, Berndt CC, Wang J, Ivanova E, Wen C (2012) A review of the application of anodization for the fabrication of nanotubes on metal implant surfaces. Acta Biomater 8(8):2875–2888
31. Mitchell J, Crow N, Nieto A (2020) Effect of surface roughness on pitting corrosion of AZ31 Mg alloy. Metals 10(5):651
32. Miwa M, Nakajima A, Fujishima A, Hashimoto K, Watanabe T (2000) Effects of the surface roughness on sliding angles of water droplets on superhydrophobic surfaces. Langmuir 16(13):5754–5760
33. Moldovan P, Stanica CN, Ciobanu G, Ungureanu I, Iorga GM, Buţu M (2014) Intergranular corrosion of AA 5083–H321 aluminum alloy. UPB Sci Bull Series B 76(3):169–180
34. Moosbrugger C (2017) Introduction to magnesium alloys. ASM International, 1À10
35. Mundotiya BM, Ullah W (2018) Morphology controlled synthesis of the nanostructured gold by electrodeposition techniques. In: Novel metal electrodeposition and the recent application. London, UK, IntechOpen

36. Nayak S, Bhushan B, Jayaganthan R, Gopinath P, Agarwal RD, Lahiri D (2016) Strengthening of Mg based alloy through grain refinement for orthopaedic application. J Mech Behav Biomed Mater 59:57–70
37. Oldani C, Dominguez A (2012) Titanium as a biomaterial for implants. Recent Adv Arthroplasty 218:149–162
38. Parida P, Behera A, Mishra SC (2012) Classification of biomaterials used in medicine
39. Pehkonen SO, Yuan S (2018) Superhydrophobic film coatings for corrosion inhibition. In: Interface science and technology, vol 23. Elsevier, pp 133–184
40. Prosek T, Nazarov A, Bexell U, Thierry D, Serak J (2008) Corrosion mechanism of model zinc–magnesium alloys in atmospheric conditions. Corros Sci 50(8):2216–2231
41. Qi H, Heise S, Zhou J, Schuhladen K, Yang Y, Cui N, Lu T (2019) Electrophoretic deposition of bioadaptive drug delivery coatings on magnesium alloy for bone repair. ACS Appl Mater Interf 11(8):8625–8634
42. Rashidi N, Alavi-Soltani SR, Asmatulu R (2007) Crevice corrosion theory, mechanisms and prevention methods
43. Razavi M, Fathi M, Savabi O, Razavi SM, Beni BH, Vashaee D, Tayebi L (2014) Controlling the degradation rate of bioactive magnesium implants by electrophoretic deposition of akermanite coating. Ceram Int 40(3):3865–3872
44. Rehman U, Atiq M (2020) Zein/bioactive glass coatings with controlled degradation of magnesium under physiological conditions: designed for orthopedic implants. Prosthesis 2(3):211–224
45. Safarpour M, Hosseini SA, Ahadani-Targhi F, Vašina P, Alishahi M (2020) A transition from petal-state to lotus-state in AZ91 magnesium surface by tailoring the microstructure. Surf Coat Technol 383:125239
46. Sato N (2012) Basics of corrosion chemistry. Green Corrosion Chemistry and Engineering, pp 1
47. Schilling T, Bauer M, LaLonde L, Maier HJ, Haverich A, Hassel T (2017) Cardiovascular applications of magnesium alloys. Magnesium Alloys 191
48. Sevvel P, Jaiganesh V (2016) Impact of tool profile on mechanical properties of AZ31B mg alloy during FSW using optimized parameters. FME Trans 44(1):43–49
49. Sezer N, Evis Z, Kayhan SM, Tahmasebifar A, Koç M (2018) Review of magnesium-based biomaterials and their applications. J Magnesium and Alloys 6(1):23–43
50. Shao L, Li H, Jiang B, Liu C, Gu X, Chen D (2018) A comparative study of corrosion behavior of hard anodized and micro-arc oxidation coatings on 7050 aluminum alloy. Metals 8(3):165
51. She Z, Li Q, Wang Z, Li L, Chen F, Zhou J (2013) Researching the fabrication of anticorrosion superhydrophobic surface on magnesium alloy and its mechanical stability and durability. Chem Eng J 228:415–424
52. Sherif EM (2012) Corrosion behavior of magnesium in naturally aerated stagnant seawater and 3.5% sodium chloride solutions. Int J Electrochem Sci 7:4235–4249
53. Simandl GJ, Schultes H, Simandl J, Paradis S (2007) Magnesium-raw materials, metal extraction and economics-global picture. In: Digging deeper, proceedings of the ninth biennial SGA meeting, pp 827–831
54. Škugor Rončević I, Vladislavić N, Buzuk M, Buljac M (2020) Electrodeposition of hydroxyapatite coating on Mg alloy modified with organic acid self-assembled monolayers. J Chem Res 44(3–4):212–220
55. Song F, Wu C, Chen H, Liu Q, Liu J, Chen R, Wang J (2017) Water-repellent and corrosion-resistance properties of superhydrophobic and lubricant-infused super slippery surfaces. RSC Adv 7(70):44239–44246
56. Stack MM, Jana BD, Abdelrahman SM (2011) Models and mechanisms of erosion–corrosion in metals. In: Tribocorrosion of passive metals and coatings, Woodhead Publishing, pp 153–187e
57. StJohn DH, Qian MA, Easton MA, Cao P, Hildebrand Z (2005) Grain refinement of magnesium alloys. Metall and Mater Trans A 36(7):1669–1679
58. Tang J, Wang J, Xie X, Zhang P, Lai Y, Li Y, Qin L (2013) Surface coating reduces degradation rate of magnesium alloy developed for orthopaedic applications. J Orthopaedic Transl 1(1):41–48

59. Teng FZ (2017) Magnesium isotope geochemistry. Rev Mineral Geochem 82(1):219–287
60. Tholstrup T, Vessby B, Sandstrom B (2003) Difference in effect of myristic and stearic acid on plasma HDL cholesterol within 24 h in young men. Eur J Clin Nutr 57(6):735–742
61. Tian P, Liu X (2015) Surface modification of biodegradable magnesium and its alloys for biomedical applications. Regenerative Biomater 2(2):135–151
62. Van Tassel JJ, Randall CA (2006) Mechanisms of electrophoretic deposition. In: Key engineering materials, vol 314. Trans Tech Publications Ltd, pp 167–174
63. Vilarinho PM, Fu Z, Wu A, Kingon AI (2013) Critical role of suspension media in electrophoretic deposition: the example of low loss dielectric $BaNd_2Ti_5O_{14}$ thick films. J Phys Chem B 117(6):1670–1679
64. Waizy H, Seitz JM, Reifenrath J, Weizbauer A, Bach FW, Meyer-Lindenberg A, Windhagen H (2013) Biodegradable magnesium implants for orthopedic applications. J Mater Sci 48(1):39–50
65. Walsh FC, Ponce de Leon C (2014) A review of the electrodeposition of metal matrix composite coatings by inclusion of particles in a metal layer: an established and diversifying technology. Transactions of the IMF 92(2):83–98
66. Wen C, Guan S, Peng L, Ren C, Wang X, Hu Z (2009) Characterization and degradation behavior of AZ31 alloy surface modified by bone-like hydroxyapatite for implant applications. Appl Surf Sci 255(13–14):6433–6438
67. Wielage B, Alisch G, Lampke T, Nickel D (2008) Anodizing–a key for surface treatment of aluminium. In: Key engineering materials, vol 384. Trans Tech Publications Ltd, pp 263–281
68. Wiles P (1958) The surgery of the osteo-arthritic hip. Br J Surg 45(193):488–497
69. Witte F (2015) Reprint of: The history of biodegradable magnesium implants: a review. Acta Biomater 23:S28–S40
70. Wu C, Wen Z, Dai C, Lu Y, Yang F (2010) Fabrication of calcium phosphate/chitosan coatings on AZ91D magnesium alloy with a novel method. Surf Coat Technol 204(20):3336–3347
71. Wu J, Lee B, Saha P, Kumta NP (2019) A feasibility study of biodegradable magnesium-aluminum-zinc-calcium-manganese (AZXM) alloys for tracheal stent application. J Biomater Appl 33(8):1080–1093
72. Xiao H, Hu A, Hang T, Li M (2015) Electrodeposited nanostructured cobalt film and its dual modulation of both superhydrophobic property and adhesiveness. Appl Surf Sci 324:319–323
73. Xiong J, Sarkar DK, Chen XG (2017) Superhydrophobic honeycomb-like cobalt stearate thin films on aluminum with excellent anti-corrosion properties. Appl Surf Sci 407:361–370
74. Xu N et al (2016) Superhydrophobic copper stearate/copper oxide thin films by a simple one-step electrochemical process and their corrosion resistance properties. RSC Adv 6.42:35466–35478
75. Yang Z, Li JP, Zhang JX, Lorimer GW, Robson JAMSEL (2008) Review on research and development of magnesium alloys. Acta metallurgica sinica (English letters) 21(5):313–328
76. Yin Z, Liu F, Song D, He S, Lin J, Yu F (2018) Stress corrosion cracking of a forged Mg-Al-Zn alloy with different surface conditions. J Chem
77. Yun T, Yang LJ, Li YF, Wei YH, Hou LF, Li YG, Murakami RI (2011) Corrosion behaviour of die-cast AZ91D magnesium alloys in sodium sulphate solutions with different pH values. Trans Nonferrous Metals Soc of China 21(4):912–920
78. Zaman HA, Sharif S, Idris MH, Kamarudin A (2015) Metallic biomaterials for medical implant applications: a review. In: Applied mechanics and materials, vol 735. pp 19–25, Trans Tech Publications Ltd
79. Zangari G (2015) Electrodeposition of alloys and compounds in the era of microelectronics and energy conversion technology. Coatings 5(2):195–218
80. Zheng T et al (2019) Fabrication of corrosion-resistant superhydrophobic coating on magnesium alloy by one-step electrodeposition method. J Magnesium Alloys 7.2:193–202
81. Zhu S, Gibson M, Easton M, Zhen Z, Abbott T (2012) Creep resistant magnesium alloys and their properties. METAL Casting Technologies, pp 21–25. https://publications.csiro.au/rpr/download

# A Hybrid Control Scheme for Magnetorheological Elastomer Under Impact Loading Application

**Mohd Sabirin Rahmat, Ho Shuh Huey, Aidil Azlan Ahmad Zamri, Siti Afifa Anuar, Nur Atiqah Ramlan, Najmi Haziq Badrulhisam, and Mohd Noor Hariz Mohd Hilmin**

**Abstract** This paper presents a prediction performance of magnetorheological elastomer isolator device (MREID) associated with hybrid controller for impact loading application. The MREID performance is evaluated numerically by using MATLAB Simulink software. In order to predict the performance of MREID, the modelling of MREID is developed by using adaptive neuro-fuzzy inference system (ANFIS). Then, a single-degree-of-freedom (SDOF) of impact dynamic system is developed as a plant of control structure. For improving the performance of MREID, a hybrid control is proposed. The current generator is developed by using inverse ANFIS method to provide accurate amount of input current to the MREID coils. Performances of the proposed hybrid controller are evaluated by comparing performance between passive system and skyhook controller. The results of the proposed hybrid controller show better response compared to skyhook controller, thus improving the stability and effective in enhancing the MREID performance.

## 1 Introduction

Magnetorheological elastomer (MREs) is a material with rheological properties that can be controlled by regulating the magnetic field within the material. MREs are mainly composed of rubber and micron-sized carbonyl iron particles, which forms a chain-like structure. By applying external input of electric current to device coils, the electromagnetic field can be generated, and thus introducing variable resistance amongst the chain-like particles. Changing the supplied input current will change the resistance and therefore, the overall stiffness and damping properties of the material can be changed. This concept enables the construction of controllable elastomeric component that is suitable for vibrational and impact isolator, as well as for controllable suspension systems.

M. S. Rahmat (✉) · H. S. Huey · A. A. A. Zamri · S. A. Anuar · N. A. Ramlan ·
N. H. Badrulhisam · M. N. H. M. Hilmin
Department of Mechanical Engineering, Faculty of Engineering and Built Environment, MAHSA University, Jalan SP 2, Bandar Saujana Putra, 42610 Jenjarom, Selangor, Malaysia
e-mail: mohdsabirin@mahsa.edu.my

Recent studies on MRE, many researchers focussed on preparation methods for material, mechanical test, and physical modelling of MRE [1]. However, studies that proposed an accurate modelling and MRE control strategy are considered limited. Due to the variety of molecular structure and the randomness of magnetic particles formation, MRE isolator possesses non-linearity, hysteresis property, and uncertainty properties [2, 3]. Thus, despite studies for control algorithm of MRE, the control schemes are completely different due to the difference for damping and stiffness properties.

Motivated by recent studies on MRE study presented in this paper has focussed on investigating the control strategy for MREID. Firstly, the MREID is characterized by evaluating its responses under impact loadings using impact pendulum test rig. The characteristics data are used by developing MREID model using ANFIS method. Then, a SDOF impact dynamic system is developed as the plant model for evaluating control performance. A hybrid controller is designed using the developed model in order to accurately regulating input current depending on desired stiffness and damping values. In order to supply accurate amount of input current, a current generator is developed by using inverse ANFIS method. The performance of MREID associated with hybrid control is evaluated by analyzing performance criteria which is jerk, acceleration, velocity, and force responses against passive and skyhook controller.

This paper is organized as follows: The first section contains a brief introduction and some previous developments on control strategy for MRE. Section two presents the modelling of MRE isolator device. This is followed the description of the proposed control strategy for MRE isolator device due to impact loadings application in section three. Section four elaborates on the experimental setup to measure the behaviour of the MRE isolator device. Section five discusses the simulation results to evaluate the effectiveness of the control strategy. Finally, the last section presents the conclusion and findings of this study.

## 2 Modelling of Magnetorheological Isolator Device Under Impact Loading

The modelling of the MREID is developed by ANFIS method. Before that, MRE characterization is performed with varying impact energy by using pendulum impact test rig. Then, the modelling of MREID is developed by using characterization data through ANFIS method [4]. The four data of displacement, input current, and impact energy from experiments are used as the input, and MRE damping force is set as the model output for ANFIS. Then, the data obtained from the experimental work were used to train the ANFIS to establish a relationship between the three inputs and its output. The diagram for ANFIS is shown in Fig. 1. The training procedure similar approach as proposed in Al-Hmouz [5].

**Fig. 1** ANFIS model
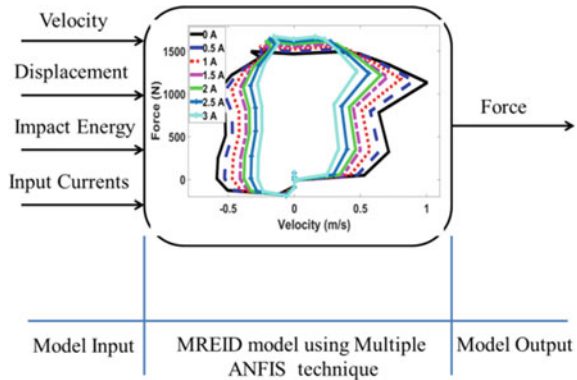
## 3 Control Scheme

In this study, a hybrid control strategy is proposed for the MREID controller in improving the performance of MREID. The hybrid controller is developed by adopting skyhook control and active force control (AFC). These two control strategies are combined to improve stability of acceleration responses by the MREID. Then, the amount of damping force from the controller output is required by the current generator. The current generator is used to supply an accurate amount of input current to the MREID coils. Then, in order to examine the performance of the controller, a single-degree-of-freedom (SDOF) impact dynamic system is developed. Figure 2 shows the diagram for SDOF of impact dynamic system in developing mathematical model**.**

According to the Newton's second law, the dynamic model can be derived as

$$M\ddot{x} + c\dot{x} + \text{MRE}x = F_{\text{impact}} \tag{1}$$

**Fig. 2** SDOF of impact dynamic system
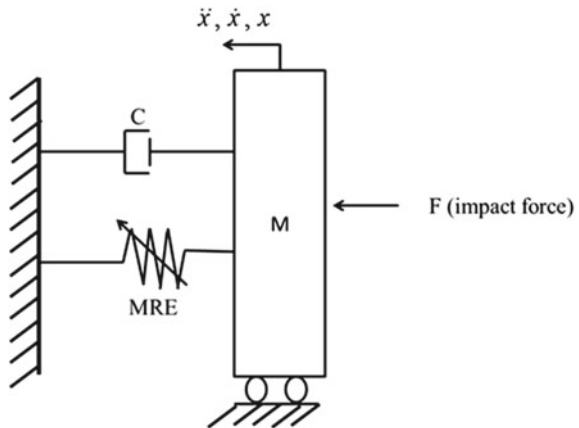
From Fig. 2, the mass, *M,* is connected with MRE and damping, *c,* to the rigid structure.

### 3.1 Skyhook Controller

Generally, skyhook control is one of the most popular control strategies in semi-active suspension system for disturbance rejection control and dynamic system stability improvements [6, 7]. In the skyhook control system, an imaginary damper is virtually placed between the movable mass and a fictitious stationary sky as an effort to eliminate the motion of the movable mass when dynamic system is subjected to impact force. General equation for skyhook control can be described as

$$F = -C_{\text{sky}} \cdot \dot{x} \tag{2}$$

Where $C_{\text{sky}}$, $\dot{x}$, and $F$ represented the damping value of the fictitious damper, body velocity, and force from control algorithm.

### 3.2 Active Force Control (AFC)

Active force control was introduced by Hewit and Burdess [8]. The AFC control is the effective way to eliminate external disturbance practically due to reduced complexity in its control algorithm. Thus, it can be operated on the physical measurement or on the estimated parameters [9, 10], which easier to implement in real-time applications. The control algorithm for AFC scheme to obtain the estimated impact force in the AFC loop is as follows:

$$F_e = \frac{1}{K}(F_a - E_m \cdot \ddot{x}) \tag{3}$$

Here, $F_e$, $F_a$, $E_m$, and $\ddot{x}$ denote the desired force, actuator force, estimated mass, and body acceleration, respectively. These two controllers are combined as the hybrid control strategy in controlling the MRE on a SDOF impact dynamic system. The control structure of hybrid control is shown in Fig. 3.

### 3.3 Current Generator

In this study, current generator is developed by using inverse ANFIS method to estimate the desired amount of input current to the MRE isolator device coil. A detailed description for developing current generator is reported by Rahmat et al.
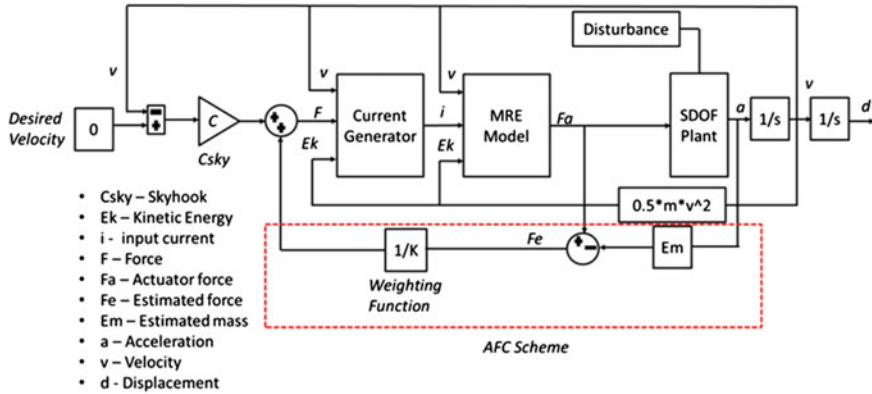
**Fig. 3** Control structure of hybrid control

[11]. Through the controller output, the current generator is able to determine a suitable input current based on the kinetic energy, displacement SDOF body, and the damping estimated by hybrid controller.

## 4 Results and Discussion

This section describes the simulation results of the MREID using hybrid control strategy. The performance of the controller is evaluated in terms of jerk, acceleration, velocity, and force dissipated by the MREID. The impact force or input force of the simulation is designed as square input by using signal builder source in MATLAB Simulink software. The response time of the square input started at time, 7–7.5 s. This relative time is considered to allow the MRE material properties to stabilize after given the input current. The simulation results of the proposed control scheme compared to passive and skyhook control are shown in following figures, where Fig. 3 shows the jerk responses, Fig. 4 displays the acceleration, Fig. 5 presents the velocities, and Fig. 6 shows the force responses for all three simulations (Fig. 7).

From the graphs, the results show that the hybrid controller was able to enhance the stability of the impact dynamic system by using MREID. It was seen to reduce all responses compared to both the skyhook and passive solutions. The proposed hybrid controller and skyhook control were capable in reducing jerk, acceleration, velocities, and force up to 50%, respectively, compared to passive damper. Therefore, it can be concluded that the performance of MREID was improved by using hybrid control strategy and able to implement for real application.
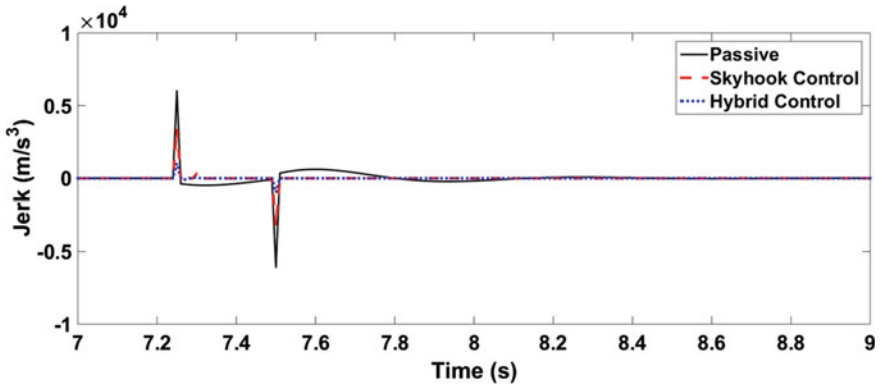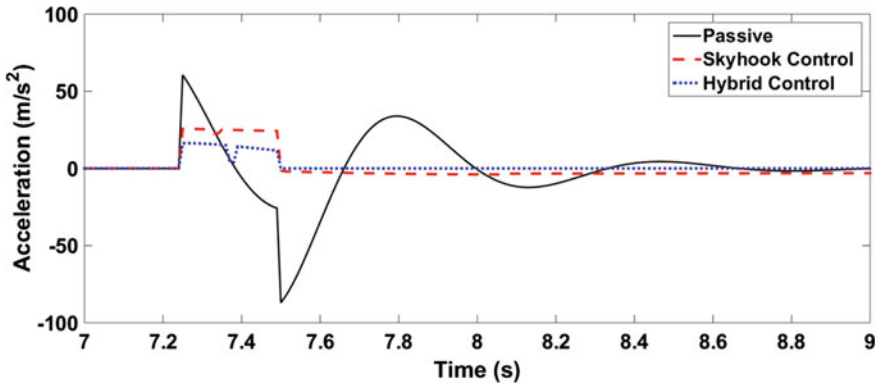
**Fig. 4** Jerk versus time



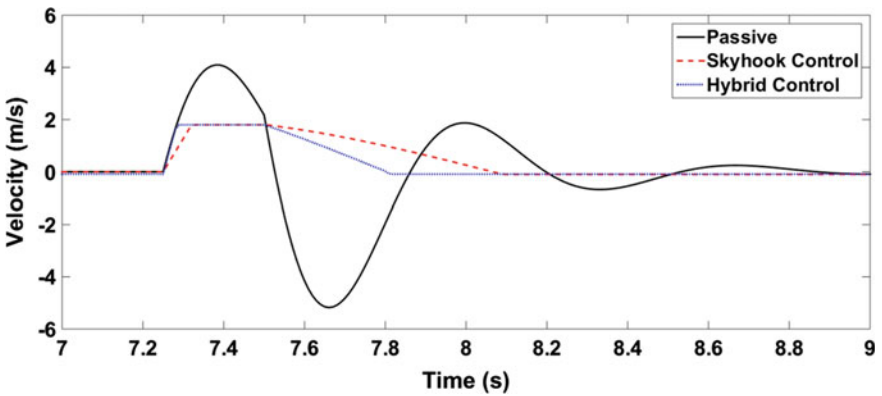**Fig. 5** Acceleration versus time
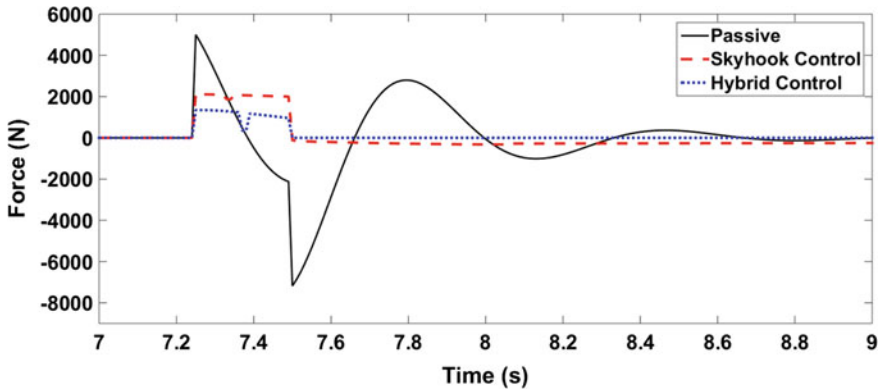


**Fig. 6** Velocity versus time

**Fig. 7** Force versus time

## 5 Conclusions

The hybrid of skyhook and active force control for MREID has been successfully analyzed by comparing it performance between passive system and skyhook controller. The modelling of MREID was developed by using ANFIS. Then, SDOF of impact dynamic system was developed, and a hybrid control was proposed. The current generator is developed by using inverse ANFIS method to provide accurate amount of input current to the MREID coils. Performances of the proposed hybrid controller were evaluated by comparing performance between passive system and skyhook controller. Based on the result, the hybrid controller for MRE isolator device was suitable for improving the stability for dynamic system and reducing structural failure up to 50%. This control strategy was provided the best control solution for MREID controller under impact loadings applications.

## References

1. Sun TL, Gong XL, Jiang WQ, Li JF, Xu ZB, Li WH (2008) Study on the damping properties of magnetorheological elastomers based on CIS-polybutadiene rubber. Polym Test 27(4):520–526
2. Ubaidillah B, Sutrisno J, Purwanto A, Mazlan SA (2014) Recent progress on magnetorheological solids: materials, fabrication, testing, and applications **. Adv Eng Mater 17(5):1–35
3. Ubaidillah IF, Li Y, Mazlan SA, Sutrisno J, Koga T, Choi S-B (2016) A new class of magnetorheological elastomers based on waste tire rubber and the characterization of their properties. Smart Mater Struct 25(11):1–15
4. Rahmat MS, Hudha K, Kadir ZA, Amer NH, Abd Rahman MLH, Abdullah S (2020) Modelling and validation of magneto-rheological fluid damper behaviour under impact loading using

   interpolated multiple adaptive neuro-fuzzy inference system. Multidiscip Model Mater Struct
   In Press:1–22

5. Al-Hmouz A, Shen J, Al-Hmouz R, Yan J (2012) Modeling and simulation of an adaptive neuro-
   fuzzy inference system (ANFIS) for mobile learning. IEEE Trans Learn Technol 5(3):226–237

6. Amer NH, Ramli R, Mahadi WNL, Abidin MAZ (2011) A review on control strategies for
   passenger car intelligent suspension system. In: ECCE 2011—international conference on
   electrical, control and computer engineering, pp 404–409

7. Hudha K, Jamaluddin H, Samin PM, Rahman RA (2005) Effects of control techniques and
   damper constraint on the performance of a semi-active magnetorheological damper. Int J Veh
   Auton Syst 3(2):230

8. Hewit JR, Burdess JS (1981) Fast dynamic decoupled control for robotics, using active force
   control. Mech Mach Theory 16(5):535–542

9. Mailah M, Yoong CS (2008) Disturbance rejection control applied to a gantry crane. Jurnal
   Mekanikal 25(June 2008):64–79

10. Priyandoko G, Mailah M, Jamaluddin H (2009) Vehicle active suspension system using skyhook
    adaptive neuro active force control. Mech Syst Signal Process 23(3):855–868

11. Rahmat MS, Hudha K, Kadir ZA, Amer NH, Nuri NRM, Abdullah S (2019) Modelling and
    characterisation of a magneto-rheological elastomer isolator device under impact loadings
    using interpolated multiple adaptive neuro fuzzy inference system structure. Int J Mater Struct
    Integrity 13(4):215–241

# Influence of the Polymethylmethacrylate (PMMA) Content Variation on the Microstructure, Density, and Compressive Properties of Established Porous Magnesium (Mg)

**Nur Ayuni Jamal, Zainal Amir Hasan, Farazila Yusof, Yusilawati Ahmad, Hazleen Anuar, and Norhuda Hidayah Nordin**

**Abstract**  In the present work, porous Mg was fabricated via powder metallurgy technique with the aids of polymethylmethacrylate (PMMA) as the space holder material in establishing a desirable porous structure at various proportions of 10 wt%, 30 wt%, and 50 wt%, respectively. The microstructure of porous Mg revealed a complete spherical closed-cell structure with the addition of 10 wt% and 30 wt% of PMMA whereas irregular open-cell structure were observed with the addition of 50 wt% of PMMA. On the other hand, the densities of sintered porous Mg decreased from 1.209 g/cm$^3$ to 0.923 g/cm$^3$ when the PMMA content was increased from 10 wt% to 50 wt%, respectively. In contrast, the porosities of porous Mg increased from 9.88% to 48.40% as the content of PMMA was increased from 10 wt% to 50 wt%, respectively. Moreover, XRD analysis detected the formation of Mg and MgO phases. Finally, the compressive strength and energy absorption of the established porous Mg enhanced from 17.67 MPa and 1.18 MJ/m$^3$ to 55.44 MPa and 2.42 MJ/m$^3$ when the PMMA was increased from 10 wt% to 30 wt%, respectively. However, the addition of 50 wt% of PMMA reduced the compressive strength and energy absorption of established porous Mg to 8.79 MPa and 0.97 MJ/m$^3$ due to the formation of irregular open-celled pores that easily propagate thus fractured at much lower stress. Therefore, based on the current findings, 30 wt% of PMMA content was considered as the optimum in establishing porous Mg with desirable microstructure, density, and compressive properties.

N. A. Jamal (✉) · Z. A. Hasan · H. Anuar · N. H. Nordin
Manufacturing and Materials Engineering Department, Kulliyyah of Engineering International Islamic University Malaysia, PO BOX 10, 50728 Kuala Lumpur, Malaysia
e-mail: ayuni_jamal@iium.edu.my

Y. Ahmad
Chemical Engineering and Sustainability Department, Kulliyyah of Engineering International Islamic University Malaysia, PO BOX 10, 50728 Kuala Lumpur, Malaysia

F. Yusof
Centre of Advanced Manufacturing and Materials Processing (AMMP), Faculty of Engineering, University of Malaya, 50603 Kuala Lumpur, Malaysia

## 1   Introduction

Lightweight, high stiffness, high strength-to-weight ratio, and excellent energy absorption capacity are among the unique combination of physical and mechanical properties of porous metals that have attracted various attention, especially in the sectors of automotive, aerospace, and biomedical [1–4]. In this context, porous metals with different porosity levels between 10 and 70% can be designed which often resulted in porous structures that consist of either open-celled structure, closed-cell structure, or combination of these two structures [3].

Magnesium (Mg) is one of the ideal candidates to be developed into porous metals as it has the lowest density as compared to other metallic materials and little attention has been directed toward the development of porous Mg [4]. Porous Mg is often fabricated by powder metallurgy technique based on solid state or liquid state route [2–5]. Powder metallurgy technique based on solid-state route was implemented in the current study to develop porous Mg owing to the simplicity of this process and excellent control of porosity level [1–5].

In order to ensure successful fabrication of porous Mg, the application of space holder or pore creator is commonly exploited to design a desirable porous structure. Combination of different manufacturing processes and space holder material is often responsible in designing the required architecture and geometrical morphology of the resultant porous structure. Commonly used space holder materials including urea (carbamide), wax, ammonium bicarbonates ($NH_4HCO_3$), and culinary salt (NaCl) often require secondary processing to be completely removed from the matrix material, thus contributing to higher processing cost [1–5]. Polymethylmethacrylate (PMMA) on the other side offers low decomposition temperature of PMMA (360–400 °C) in which can be completely decomposed during sintering hence eliminate the need of additional processing. Therefore, PMMA at various content of 10, 30, and 50 wt% was introduced as a porous agent or space holder material in the current study to fabricate porous Mg.

The successful fabrication of porous metals including porous Mg by exploiting PMMA as the space holder has been recorded in the previous studies [2–7]. However, the existing data on materials characterizations and processing techniques of porous Mg development are still limited especially involving the usage of PMMA as the space holder material. Therefore, current study was initiated to develop porous Mg by powder metallurgy technique and the effects of various PMMA content on the density, porosity, strength, and energy absorption behavior of porous Mg were investigated accordingly.

## 2 Raw Materials and Processing of Porous Mg via Powder Metallurgy Technique

### 2.1 Raw Materials

Three different types of starting materials were utilized in the current study including metallic powders of magnesium (Mg), zinc (Zn), and manganese (Mn) and space holder particles as seen in Fig. 1. In this study, Mg powder of 97.5 wt% was employed as a matrix component having an average particle size of 45 $\mu$m with 99.99% purity. Moreover, 2 wt% of Zn powder having an average particle size of 17 $\mu$m with 99.9% purity was introduced as a sintering additive to facilitate liquid phase sintering of porous Mg while 0.5 wt% of Mn powder having an average particle size of 17 $\mu$m with 99.9% purity was added to minimize the impurities of the resultant porous Mg specimen during fabrication. A complete spherical shape of polymethylmethacrylate (PMMA) having an average particle size of 150 $\mu$m with 99.9% purity was exploited as a space holder particle and its content was varied between 10 wt%, 30 wt%, and 50 wt%, respectively. These metallic powders and PMMA space holders were supplied by NovaScientific Resources Malaysia Sdn Bhd. Finally, small amount of ethanol ($C_2H_5OH$) having 95% purity of ethyl alcohol and molarity of 46.07 g/mol supplied by Classic Chemical Sdn Bhd was introduced as a binder to reduce the segregation of powders mixture during processing.
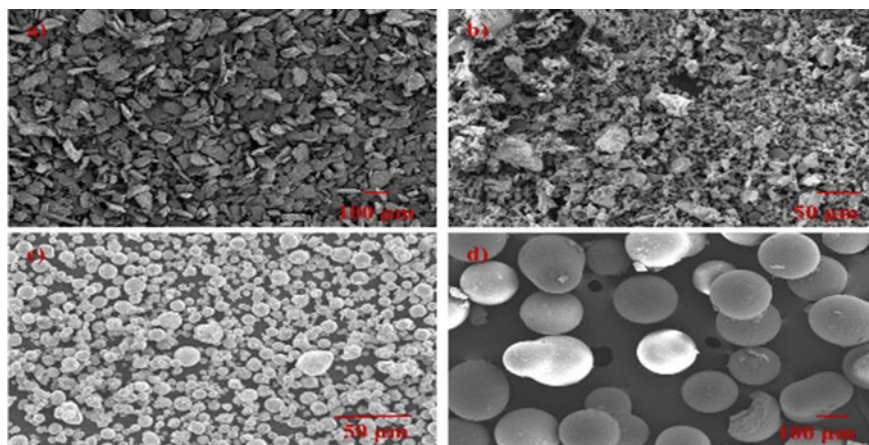


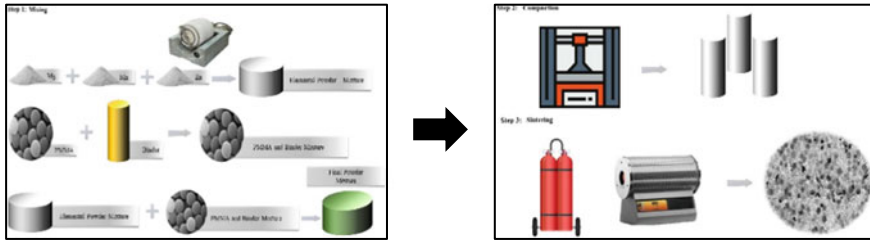**Fig. 1** Microstructure of starting powders of **a** Mg, **b** Zn, **c** Mn and PMMA

**Fig. 2** Schematic illustration of porous Mg preparation via powder metallurgy technique

## 2.2 Sample Preparation via Powder Metallurgy Technique

Three main steps were involved in this powder metallurgy technique including mixing, compacting, and sintering as schematically shown in Fig. 2. Metallic powders of Mg, Zn, and Mn were firstly mixed by horizontal ball milling to produce the elemental powder mixture. These metallic powders were mixed for about 12 h at constant milling speed of 250 rpm with ball to powder ratio of 1:7. Next, the resultant elemental powder mixture and PMMA space holder with the presence of binder were mixed for another 2 h prior to prepare final powder mixture. The resultant final powder mixture was then uniaxially compacted in a die having diameter of 10 mm at given constant pressure of 250 MPa. Lastly, the compacted specimen was sintered at 450 °C for 1 h to remove the space holder (PMMA) content followed by sintering of the specimens at 530 °C for 2 h under argon (Ar) environment. The sintered specimens were then rinsed with acetone and dried in an oven at 100 °C for 4 h to remove impurities followed by characterizations.

## 3 Results and Discussion

### 3.1 Microstructure of Porous Mg at Different PMMA Content

Fabrication of porous Mg via powder metallurgy method by utilizing PMMA particle as a space holder material has successfully resulted in the formation of homogeneous spherical macro pores having closed-cell structure in the case of 10 and 30 wt% of PMMA content addition as shown in Fig. 3. Moreover, the resultant closed-cell structure was found to be spherical in shape and homogeneously distributed within the Mg matrix. Additionally, this closed-cell structure was found to replicate the morphology of starting PMMA particles in terms of size and shape. It has been reported that the resultant porous structure that mimics the original shape and size of space holder material is essential in obtaining optimum physical and mechanical properties of porous metals [8]. On the contrary, an open-celled structure that demonstrated irregular pores shape was observed when 50 wt% of PMMA content was added in the
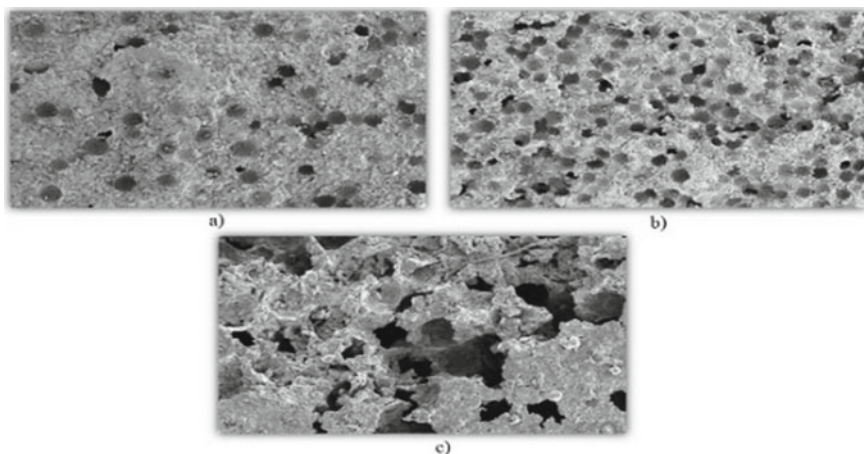
**Fig. 3** Microstructure of porous Mg at different PMMA content of **a** 10 wt%, **b** 30 wt% and **c** 50 wt%

Mg matrix. It was also discovered that the number of the resultant pores for both closed-cell and open-celled structures increased with increasing PMMA content.

## 3.2  Sintered Density and Porosity of Porous Mg

The sintered densities and porosities of Mg with different PMMA content are depicted in Fig. 4. It can be observed that the sintered density of the porous Mg decreased, and the porosity of the porous Mg increased with increasing PMMA content. The sintered densities of the porous Mg decreased from 1.209 g/cm$^3$ to 0.923 g/cm$^3$ when the PMMA content was increased from 10 wt% to 50 wt%, respectively. In contrast, the porosity level of the porous Mg increased from 9.88% to 48.40% as the content of PMMA was increased from 10 wt% to 50 wt%, respectively. These indicate that the density of the porous Mg reduced whereas the porosity increased with the addition of PMMA particles as the space holder. Hence, further addition of PMMA particles contributed to the additional spaces within the sintered microstructure that further increased the porosity level.

## 3.3  X-ray Diffraction (XRD) Analysis

XRD patterns of porous Mg at various PMMA content confirmed the existence of peak characteristics of Mg and MgO phases after sintering as depicted in Fig. 5. The presence of an inherited by-product of MgO phases implying oxidation phenomena
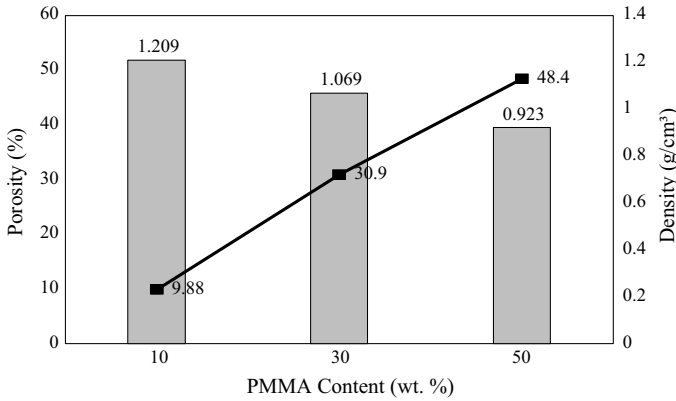
**Fig. 4** Sintered densities and porosities of Porous Mg at various PMMA content of 10, 20 and 50 wt%

during sintering [9]. This could be due to the combination of high reactivity of Mg and PMMA space holder that led to oxidation, especially with increasing PMMA content from 10 wt% to 50 wt%, respectively. Moreover, the presence of MgO also resulted in difficulty of creating a dense structure of porous Mg as a result of sintering obstruction [10, 11]. Finally, the presence of Zn and Mn phases was unable to be detected, probably due to the small addition of these powder during processing [12].
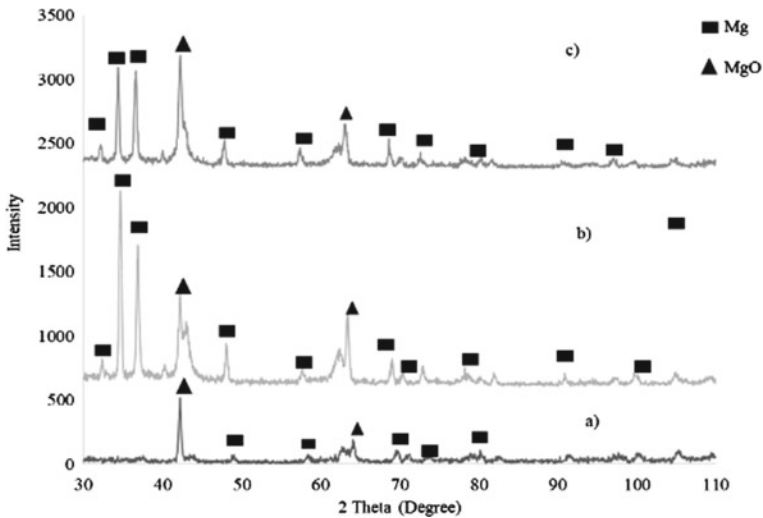


**Fig. 5** XRD analysis of porous Mg at various PMMA content of 50, 30, and 10 wt%

## 3.4 Compressive Behavior of Porous Mg

The stress–strain curve of porous Mg conformed the characteristic pattern of porous metals that includes the regions of elastic, plateau, and densification as shown in Fig. 6. On the hand, the energy absorption capacity of porous Mg at various PMMA content was calculated from the area under the stress–strain curve. The stress–strain curve of porous Mg showed the increasing trend in the yield strength from 17.67 MPa to 55.44 MPa with increasing PMMA content from 10 wt% to 50 wt%, as indicated in Fig. 6. Similarly, the energy absorption capacity of porous Mg increased from 1.18 MJ/m$^3$ to 2.42 MJ/m$^3$ with increasing PMMA content as tabulated in Table 1. However, as the PMMA content was further increased to 50 wt%, the yield strength, and energy absorption capacity of porous Mg decreased to 8.79 MPa and 0.97 MJ/m$^3$, respectively. This could be attributed to the formation of open-celled structure with irregular interconnected pores that acted as an initial crack site hence propagate at much lower stress [13]. Moreover, it has been reported that higher amount of space holder increased the interconnected pores in the porous Mg in which later resulted in higher number of total pores and thinner cell walls of Mg or thinner skeleton of Mg wall [13]. It is important to note that low energy absorption capacity of porous Mg is associated with the highest PMMA content of 50 wt% might be due the lowest value of yield strength, implying less dense of cell wall and low bending deformation resistance that arises from the formation of cell structure [14, 15]. However, 10 wt% of PMMA content also demonstrated lower value of yield strength and energy absorption capacity as compared to 30 wt% of PMMA content. This could be due to the completely enclosed of PMMA particles by the Mg matrix during processing, especially with the low addition of PMMA content [16]. Moreover, these enclosed particles were incapable to disperse into the liquid phase during sintering hence became trapped in the Mg matrix. Consequently, sintering process became retarded together with the formation of MgO element as evidenced in XRD analysis [16].

## 4 Conclusion

Fabrication of porous Mg via powder metallurgy method using PMMA particle as the space holder material had successfully resulted in the formation of homogeneous spherical macro pores with closed-cell structure for 10 wt% and 30 wt% of PMMA content and open-celled structure for 50 wt% of PMMA content. In relation to this, the sintered density of porous Mg decreased, and porosity level increased with increasing PMMA from 10 wt% to 30 wt% and 50 wt%, respectively. Additionally, XRD patterns confirmed the existence of Mg and MgO peaks after sintering. In this context, the formation of MgO phases was pronounced with increasing PMMA content from 10 wt% to 50 wt%, suggesting oxidation phenomenon. Finally, the compressive stress–strain curve showed the increasing trend in the yield strength and energy absorption capacity with increasing PMMA content from 10 wt% to 30 wt% followed by a
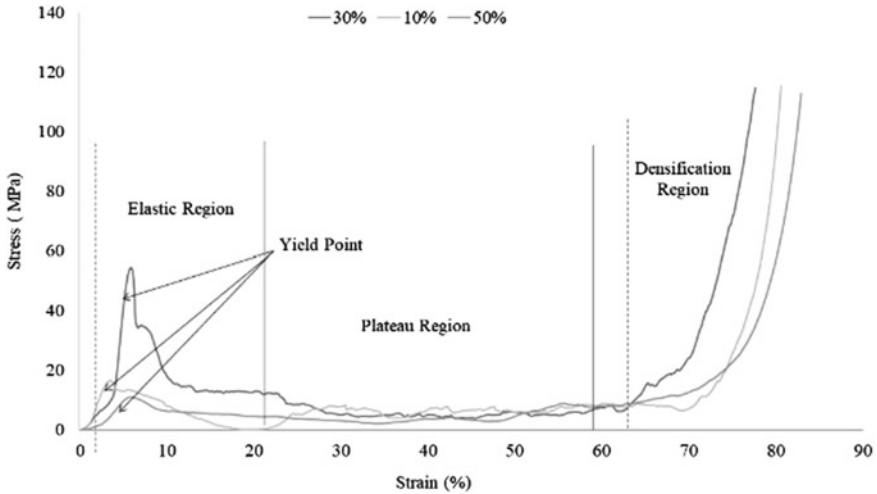
**Fig. 6** Stress–strain curve of porous Mg at various PMMA content

**Table 1** Yield strength and energy absorption capacity values of porous Mg

| PMMA content (wt %) | Yield stress (MPa) | Energy absorption capability (MJ/m$^3$) |
| --- | --- | --- |
| 10 | 17.67 ± 0.55 | 1.18 ± 0.51 |
| 30 | 55.44 ± 0.49 | 2.42 ± 0.44 |
| 50 | 8.79 ± 0.69 | 0.97 ± 0.65 |

decreasing trend of the established porous Mg containing 50 wt% of PMMA. In view of this, maximum compressive strength of 55.44 MPa and energy absorption capacity of 2.42 MJ/m$^3$ were recorded with the addition of 30 wt% of PMMA space holder. Therefore, it can be concluded that 30 wt% of PMMA addition exhibited the ideal performance for the established porous Mg in the current study in terms of microstructure, density, porosity, yield strength as well as energy absorption capacity.

# References

1. Kennedy A (2012) Porous metals and metal foams made from powders. Powder Metall 2:31–46
2. Wen CE, Yamada Y, Shimojima K et al (2004) Compressibility of porous magnesium foam: dependency on porosity and pore size. Mater Lett 58:357–360

3. Wen CE, Mabuchi M, Yamada Y et al (2001) Processing of biocompatible porous Ti and Mg. Scripta Mater 45:1147–1153
4. Yilong L, Guibao Q, Yang Y (2016) Preparation and compressive properties of magnesium foam. Rare Metal Mater Eng 45:2498–2502
5. Jha N, Mondal DP, Majumdar JD, Badkul A et al (2013) Highly porous open cell Ti-foam using NaCl as temporary space holder through powder metallurgy route. Mater Des 47:810–819
6. Li YH, Shang XY, Li YJ (2020) Fabrication and characterization of TiMoCu/PMMA composite for biomedical application. Mater Lett 27:1–3
7. Kucharczyk A, Naplocha K, Kaczmar JW et al (2018) Current status and recent developments in porous magnesium fabrication. Adv Eng Mater 20:1–16
8. Sathaiah S, Dubey R, Pandey A et al (2021) Effect of spherical and cubical space holders on the microstructural characteristics and its consequences on mechanical and thermal properties of open-cell aluminum foam. Mater Chem Phys 273:125115
9. Qiao JC, Xi ZP, Wang JY et al (2008) Compressive property and energy absorption of porous sintered fiber metals. Mater Trans 49:2919–2921
10. Amal MI, Annur D, Lestari FP et al (2016) Processing of porous Mg-Zn-Ca alloy via powder metallurgy. In: AIP conference proceeding, vol 1778, pp 030010-1–030010-5
11. Kartika I, Risanti DD, Laksana HRP et al (2021) Fabrication of porous Mg–Ca–Zn alloy by high energy milling for bone implants. Lect Notes Electr Eng 746:711–722
12. Xia XC, Chen XW, Zhang Z et al (2013) Effects of porosity and pore size on the compressive properties of closed-cell Mg alloy foam. J Magnes Alloy 1:330–335
13. Kowalski K, Nowak M, Jakubowicz J et al (2016) The effects of hydroxyapatite addition on the properties of the mechanically alloyed and sintered Mg-RE-Zr alloy. J Mater Eng Perform 25:4469–4477
14. Markaki AE, Clyne TW (2001) The effect of cell wall microstructure on the deformation and fracture of aluminium-based foams. Acta mater 49:1677–1686
15. Bi Y, Zheng Y, Li Y (2015) Microstructure and mechanical properties of sintered porous magnesium using polymethyl methacrylate as the space holder. Mater Lett 161:583–586
16. Mustapha F, Mustapha M, Noorsal K (2010) Preliminary study on the fabrication of aluminium foam through pressure assisted sintering dissolution process. J Mater Process Technol 210:1598–1612

# Comparison of Joint Configuration for Aluminum 6061 Tailor Welded Blank with Dissimilar Thicknesses Using Friction Stir Welding

**Amer Isyraqi Hussin and Ahmad Baharuddin Abdullah**

**Abstract** The current study investigates the comparison of joint configuration between square butt welding and scarf welding of aluminum 6061 and their effect on mechanical properties. Two aluminum plates with a different thickness of 2.0 mm on the advancing side and 1.5 mm on the retreating side were welded together using the Friction Stir Welding (FSW) method with the identical parameters of welding speed, spindle rotation, tool tilt angle, and tool profile. All four comparisons are conducted using the fix parameter for different rolling angles, which are 0°/0°, 90°/90°, 0°/90° and 90°/0°. Based on tensile test results, it is found that the ultimate tensile strength (UTS) for the scarf joint is higher than square butt joint configuration by 2–5%. On the microhardness, it was observed that the scarf joint had a higher Vickers hardness value than the square butt joint configuration, which was identified in the stir zone. Based on the comparison results, it was discovered that the scarf joint configuration is stronger and may facilitate advancements in the automotive industry, particularly in terms of crashworthiness.

**Keywords** Friction Stir Welding · Scarf joint · Square butt joint

## 1 Introduction

Friction Stir Welding (FSW), which was initially introduced at The Welding Institute in the United Kingdom, is a solid state joining technology in which the pieces are welded together without the base material fusing [1]. Because of its advantages over fusion welding, FSW is widely employed in industries such as metal forming and automotive [2], space, aviation, and ocean engineering [3], structural [4], and others. Most FSW processes employ joint configurations similar to fusion weldings, such as butt joints, T-joints, and lap joints [5–7]. Furthermore, rolling angle is a factor that can influence the mechanical properties of a joint configuration's value [8]. Combining a variety of rolling angles and joint configurations is expected to

A. I. Hussin (✉) · A. B. Abdullah
Metal Forming Research Lab, School of Mechanical Engineering, USM Engineering Campus, 14300 Nibong Tebal Penang, Malaysia
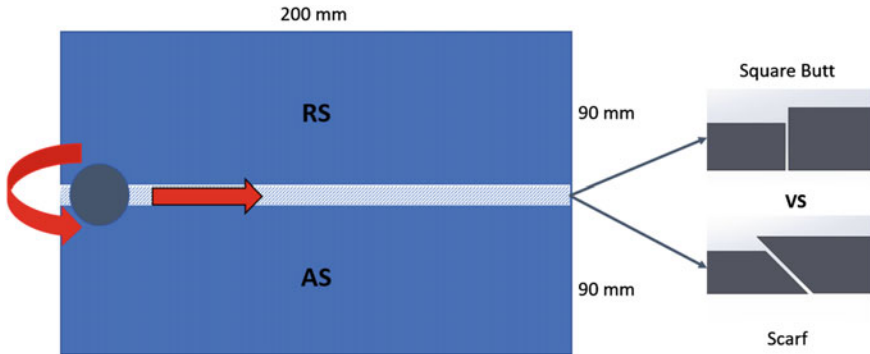e-mail: isyraqi@student.usm.my

**Fig. 1** Processes for square butt and scarf joint configurations using FSW

produce good mechanical qualities for this purpose. Scarf joint is a modification on the square butt joint configuration which is used to improve the welding contact area by chamfering or tilting the edges of two touching surfaces. Figure 1 showed the difference between scarf and square butt joint configuration during FSW process. Scarf joint configuration, according to prior research of AA6061 FSW, allows for a 13% increase in joint strength when compared to square butt joints configuration [9]. The scarf joint has the advantage that the abutting surface is inclined to the tool axis, which can help to alleviate difficulties that cause various FSW defects [10]. However, to date, it is believed that no comprehensive investigations into scarf joints for materials of dissimilar thicknesses have been conducted.

## 2 Experiment Procedure

Aluminum 6061 was used as comparison for the join configuration due to good welding quality compared to other aluminum series. Dimension of the advancing side (AS) is 200 × 90 × 2.0 mm and for the retreating side (RS) is 200 × 90 × 1.5 mm. A universal milling machine is used to perform the friction stir process using a fix parameter. The spindle speed was set to 865 rpm, the welding speed was set to 90 mm/min, and the tool tilt angle was set to 3°. The FSW tool features a straight cylindrical profile with a 10 mm shoulder diameter and a 5 mm pin diameter. The tool pin has a length of 1 mm, making it appropriate for welding thicknesses of 2.0 and 1.0 mm. The tool was made of D2 high carbon steel that had been hardened to 62 HRC and polished to prevent hot material from sticking to the tool surface. Table 1 presents the types of specimens according to their joint configuration and rolling angle. The tensile testing was carried out according to the ASTM E8 standard. A Vickers hardness tester was used to measure the cross-section of a polished workpiece along welding zones.

| Specimens | | Rolling angle (°) | |
|---|---|---|---|
| Square butt | Scarf | Retreat side | Advance side |
| A | E | 0 | 0 |
| B | F | 90 | 90 |
| C | G | 0 | 90 |
| D | H | 90 | 0 |

**Table 1** Specimens of the scarf and square butt joint according to the rolling angle

## 3  Results and Discussion

The discussion is split into two sub-sections, by focusing on the tensile strength and microhardness of the produced joints.

### 3.1  Tensile Result

Tensile specimens were tested with the weld perpendicular to the loading direction. Figure 2 illustrates the tensile specimen following a tensile test with a universal tensile machine (UTM). The first comparison for specimens *A* and *E* was made by placing them side by side and measuring the failure location from the welding center line. For specimen *A*, the location of failure is closed to the AS which is away from the welding line's center. In comparison to specimen *E*, the failure location is at the welding area's center line. The breaking profile for specimen *A* is a straight line parallel to the welding direction, however, the breaking line profile for specimen *E* is slightly slanted up toward the RS. For specimens *B* and *F*, both of failure locations displayed a straight breaking line parallel to the welding direction. At specimen *F*, the breaking point occurred in the center of the welding line, whereas in specimen *B*, it happened in the AS area. The failure locations for specimens *C* and *G* are slightly different, with the *C* specimen's breaking point moving a bit from the welding line's center to the AS. Aside from that, the *G* specimen's breaking line was in the middle of the welding line. The failure positions in the center of the welding lines were identical in specimens *D* and *H*. The failure location seems to be unaffected by the join configuration. These observations showed that the majority of square butt join configuration specimens failed at AS, where the thickness of this side was thicker than the RS side.

Figure 3 presents different ultimate tensile strengths (UTS) between square butt and scarf join configurations for all types of rolling angles. The value of UTS for specimen *E* is higher than specimen *A*. The same results can be seen in all subsequent sample comparisons where specimen *F* has a higher UTS value than specimen *B*, *G* has a higher UTS value than *C*, and *H* has a higher UTS value than *D*. The results also revealed that specimen *D* has the highest UTS value for a square butt joint, while specimen *H* had the highest UTS value for a scarf joint. According to the comparison
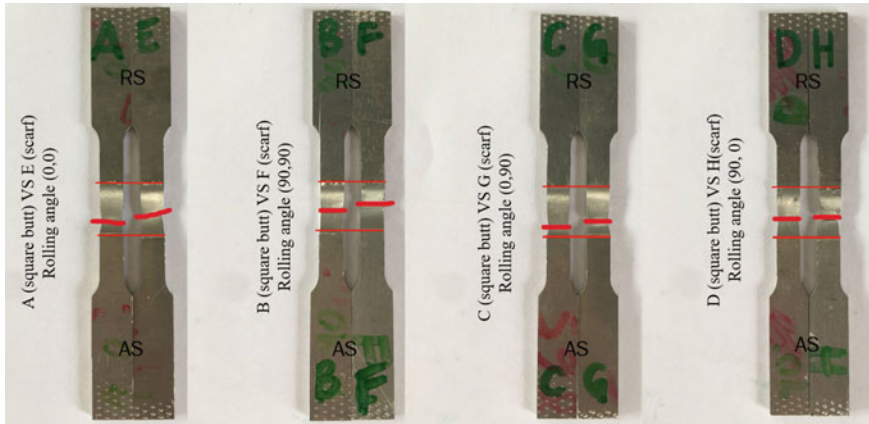
**Fig. 2** Tensile specimen failure location

chart, it was found that all scarf joint configurations exceed the square butt joint configuration. The most significant difference value is obtained between specimens B and F for rolling angles of 90° and 0°, with a different value of 5.4%. The smallest change between specimens *D* and *H* was determined to be a 2% improvement in UTS value. The other two differences, specimens *A* and *E* by 3.4% and specimens *C* and *G* by 4.9%, each had a distinct value increase. Moreover, it was discovered that the direction of the rolling angle between the specimens influences the value of UTS, even when the geometric factor of the joint configuration is ignored. This is demonstrated by the differences in specimen combinations with varying values, with 90° and 0° having the highest rolling angle combination, followed by 0° and 90°, 0° and 0°, and finally 90° and 90°.

## 3.2 Hardness Result

Figure 4 presents the hardness profile for all four comparison types of joint. For all of the specimens, the profile revealed that the hardness value was not significantly different. However, the value of hardness at the center of the welding shows that the scarf joint has a better hardness value than butt welding. The gap at the center from 0 to 2 mm around the stir zone proved that the hardness of the scarf joint is better than the square butt joint and that there was no major effect on the hardness value outside the stir zone to the base material.
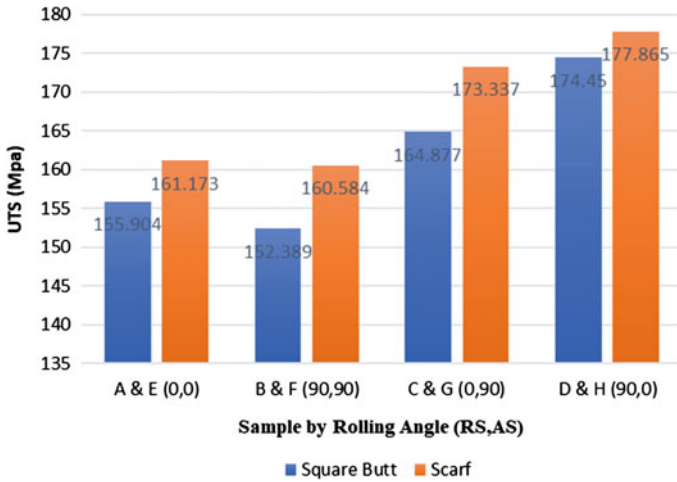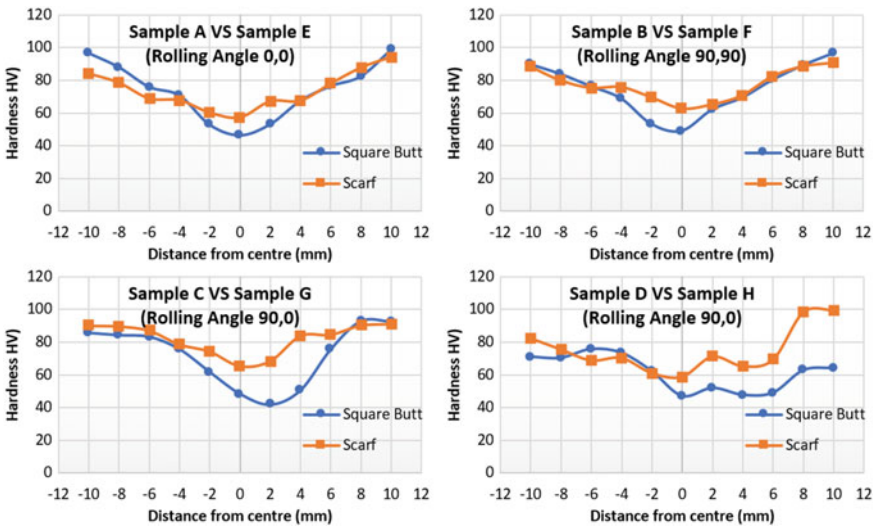
**Fig. 3** Ultimate tensile test result



**Fig. 4** Hardness profile for all specimen

## 4   Conclusions

The scarf joint configuration is a promising technique to replace the square butt join configuration. According to the results of the experiment, specimen H, which had a scarf joint configuration with a rolling angle combination of 90° and 0°, had the highest UTS value. Based on tensile results, it was found that the UST for the scarf

joint is better than square butt configuration by 2–5%. The value of the Vickers hardness for scarf joint is better than square butt joint was found at the stir zone. The hardness profile from ±2 mm to the base material is slightly different, indicating that the hardness value did not have a significant impact on the area outside of the stir zone for both joint configurations. Based on the results, the scarf joint is better than the square butt configuration in terms of mechanical properties. Due to the effectiveness of mechanical properties compared to the square butt joint configuration, the scarf joint configuration has the potential to be used in several areas of the automotive industry, particularly crashworthiness in car structures. Improvements in parameter optimization should be addressed in future work to improve the tensile and microhardness values of the scarf joint configuration.

# References

1. El-sayed MM, Shash AY, Abd-rabou M et al (2021) Welding and processing of metallic materials by using friction stir technique : a review. J Adv Joining Process 3(March)
2. Rizlan MZ, Abdullah AB, Hussain Z (2021) A comprehensive review on pre- and post-forming evaluation of aluminum to steel blanks via friction stir welding. Int J Adv Manuf Technol 114(7–8):1871–1892. https://doi.org/10.1007/s00170-021-06963-1
3. Gao F, Guo Y, Yu W et al (2021) Materials characterization microstructure evolution of friction stir welding of Ti6321 titanium alloy based on the weld temperature below microstructure transformation temperature. 177(December 2020)
4. Kamalvand E, Jabbari A, Reza M et al (2021) Effect of friction stir welding parameters on the deep drawing of tailor-welded blanks (TWBs). CIRP J Manuf Sci Technol 33:91–99
5. Tewari M, Jadoun RS, Kumar S (2021) Effect of process parameters on tensile strength of Friction stir welded butt joints of thick AA1350 aluminum plates using Taguchi experimental design. Mater Today : Proc 44:2721–2725
6. Sabry I, El-Kassas AM, Mourad AHI et al (2019) Friction stir welding of T-joints: experimental and statistical analysis. J Manuf Mater Process 3(2). https://doi.org/10.3390/jmmp3020038
7. Infante V, Braga DFO, Duarte F et al (2016) Study of the fatigue behaviour of dissimilar aluminium joints produced by friction stir welding. Int J Fatigue 82:310–316. https://doi.org/10.1016/j.ijfatigue.2015.06.020
8. Pauzi AF, Abdullah AB, Jamaludin MF (2019) Pre-forming evaluation of dissimilar aluminium alloys blank fabricated using friction stir welding technique. IOP Conf Ser Mater Sci Eng 670(1). https://doi.org/10.1088/1757-899X/670/1/012077
9. Sethi D, Acharya U, Shekhar S et al (2021) Applicability of unique scarf joint configuration in friction stir welding of AA6061-T6: analysis of torque, force, microstructure and mechanical properties. Def Technol xxxx. https://doi.org/10.1016/j.dt.2021.03.010
10. Goel P, Noor A, Id S et al (2021) Investigation on the effect of tool pin profiles on mechanical and microstructural properties of friction stir butt and scarf welded aluminium alloy 6063. pp 1–15. https://doi.org/10.3390/met8010074

# An Evaluation Model of Lean Technique Implementation in Remanufacturing Process

**Anas Zeyad Yousef, Tze Fong Go, and Shamini Janasekaran**

**Abstract**  The project aims to show the importance of waste-free remanufacturing and its modern technologies and systems, and their application to the remanufacturing process of air compressors for a specific company. Waste will be reduced by implementing some lean techniques in manufacturing as well as remanufacturing process. This paper presents an evaluation model of lean technique implementation in remanufacturing process. 5S, Kaizen and VSM to be considered in the evaluation. After comparison before and after implementation of lean remanufacturing, 20.5% improvement be obtained. Remanufacturing and lean technique share the same aim which is circular economic; therefore, combination of lean remanufacturing is the trend for the sustainable manufacturing in the future.

## 1   Introduction

The issue of waste-free production is one of the modern topics, as it is considered one of the methods and techniques of modern management of production and operations, and one of the important mechanisms through which the company can achieve a sustainable competitive advantage in a business environment characterized by rapid changes in technology, the diversity of customer needs and desires, and the intensity of competition between companies [1].

Remanufacturing is a viable option for recycling used materials and bringing them back to life. Despite the fact that the manufacturing sector includes anything from heavy equipment to automobiles, furniture, and information technology, it faces challenges [2]. The problems derive from the remanufacture properties that have no influence (product used or part of it), high product variety, low production sizes, and high manufacturing speeds. Any of the problems in remanufacturing seem like procedure challenges that require a longer time to remanufacture and more wastes to minimize

A. Z. Yousef · T. F. Go (✉) · S. Janasekaran
Center for Advance Materials and Intelligent Manufacturing, Faculty of Engineering, Built Environment and Information Technology, SEGi University, Selangor, Malaysia
e-mail: gotzefong@segi.edu.my

[3]. Therefore, this paper provides an evaluation model for lean remanufacturing techniques.

The remaining of the paper is organized as follows: Sect. 2 presents materials and methods which the flow of the project and equation of lean technique be implemented. Sections 3 and 4 indicate results and discussion with a case study. Finally, Sect. 5 concludes the findings of this paper.

## 2  Methods

This section explains the activities that are being carried out to achieve the objectives of the research, the procedures being followed, how to measure progress, and what constitutes success (Fig. 1).

### 2.1  Case Study

Remanufacturing of the car air conditioner compressors has been selected. Lean manufacturing will be applied to its remanufacturing process. Company is named as 'Advanced Compressor Engineering Services Limited' (ACES) located in UK. The processes involved in complete remanufacturing process of a compressor.

### 2.2  Lean Tools Score Equation

5S, Kaizen, and VSM to be considered in the lean implementation evaluation. The equations are used to evaluate the remanufacturing process before and after the implementation of lean technique in the remanufacturing process of car AC compressors. Total four equations are explained in this section.

#### 2.2.1  5S Score Assessment

For the 5S, major points of scope in the areas are considered for this study such as sorting of parts, availability of tools, and its placement in assigned places derived from a generic 5S checklist items goal [4]. Table 1 shows the 5S checklist for the remanufacturing process of car AC compressors for before and after lean implementation.
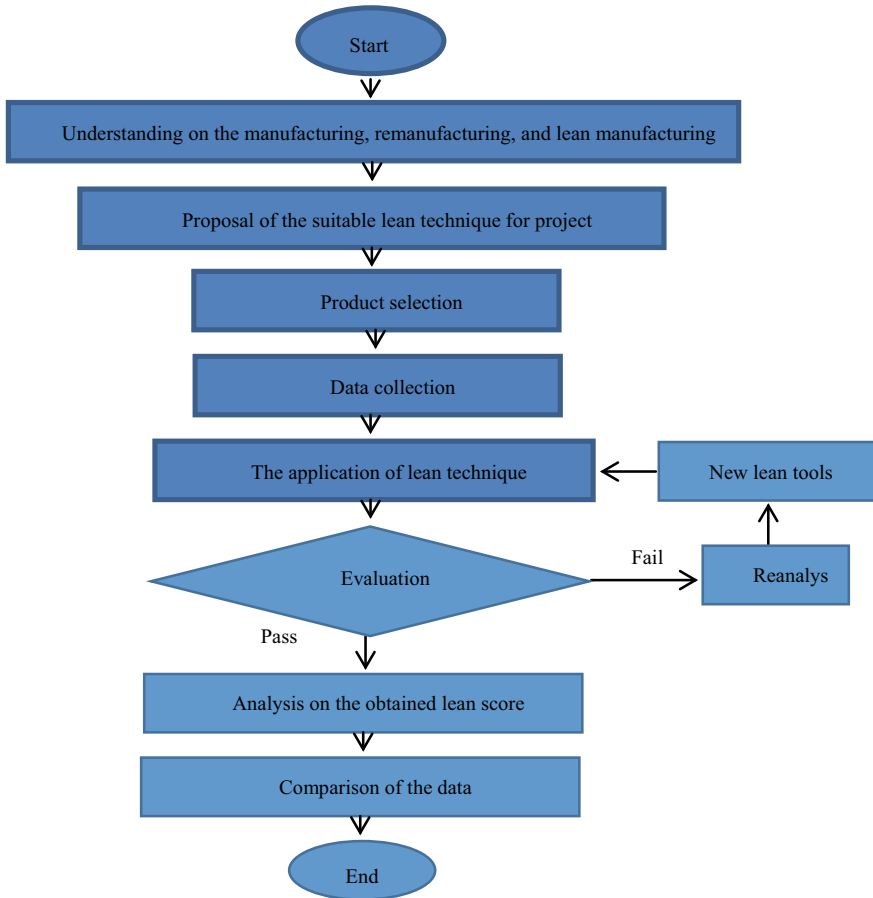
From [5]

**Fig. 1** Flowchart of the study

$$5S \text{ score} = \sum_{i=1}^{n} X_i \tag{1}$$

where
$X$ audit point grade mark (i.e., 1 for compliance and 0 for incompliances)
$i$ the 5S assessment points
$n$ number of 5S assessment questions.

### 2.2.2 Kaizen Score Assessment

From [6]

**Table 1** 5S checklist

| | Before | After |
|---|---|---|
| *S1—Sort—SEIRI* | 1/ 0/NA | |
| 1. No unnecessary items are left or stored in the workplace | 1 | 1 |
| 2. All machines and pieces of equipment are in regular use | 1 | 1 |
| 3. All tools, fixtures, and fittings are in regular use | 1 | 1 |
| 4. Storage area is defined to store broken, unusable, or occasionally used items | 1 | 1 |
| 5. Standards for eliminating unnecessary items exist and are being followed | 0 | 0 |
| *S2—Set in order—SEITON* | | |
| 6. Locations of tools and equipment are clear and well organized | 1 | 1 |
| 7. Locations of materials and products are clear and well organized | 0 | 1 |
| 8. Labels exist to indicate locations, containers, boxes, shelves, and stored items | 0 | 0 |
| 9. Evidence of inventory control exists (i.e., Kanban cards, FIFO, minimum/maximum, etc.) | 0 | 1 |
| 10. Dividing lines are clearly identified and clean as per standard | 0 | 1 |
| 11. Safety equipment and supplies are clear and in good condition | 1 | 1 |
| *S3—Shining—SEISO* | | |
| 12. Floors, walls, ceilings, and pipework are in good condition and free from dirt and dust | 0 | 1 |
| 13. Racks, cabinets, and shelves are kept clean | 0 | 1 |
| 14. Machines, equipment, and tools are kept clean | 1 | 1 |
| 15. Stored items, materials, and products are kept clean | 1 | 1 |
| 16. Lighting is enough, and all lighting is free from dust | 0 | 0 |
| 17. Good movement of air exists through the room (to limit the spread of viruses) | 1 | 0 |
| 18. Pest control exists and effective | 1 | 1 |
| 19. Cleaning tools and materials are easily accessible | 0 | 1 |
| 20. Cleaning assignments are defined and are being followed | 1 | 1 |
| *S4—Standardize—SEIKETSU* | | |
| 21. Information displays, signs, color coding, and other markings are established | 0 | 0 |
| 22. Procedures for maintaining the first three S's are being displayed | 1 | 1 |
| 23. 5S checklists, schedules, and routines are defined and being used | 1 | 0 |
| 24. Everyone knows his responsibilities, when and how | 0 | 1 |
| 25. Regular audits are carried out using checklists and measures | 1 | 1 |
| *S5—Sustain—SHITSUKE* | | |
| 26. 5S seems to be the way of life rather than just a routine | 0 | 1 |
| 27. Success stories are being displayed (i.e., before and after pictures) | 0 | 0 |

(continued)

**Table 1** (continued)

|  | Before | After |
|---|---|---|
| 28. Rewards and recognition are part of the 5S system | 0 | 1 |

$$K = \sum_{f=1}^{f=d} P_f * S_f \tag{2}$$

where
*f* Kaizen project being implemented
*d* maximum number of Kaizen projects that
*S* individual phase weight of the project
*P* Weight of Kaizen project.

### 2.2.3 VSM Score Assessment

From [7]

$$\text{V.S.M score} = 1 - \sum_{q=1}^{q=r} \left( \frac{\text{Non value added time}}{\text{Total cycle time}} \right) * W_q \tag{3}$$

where
*r* number of non-added value processes
*q* non-value-added time process time
$W_q$ weight of corresponding non-value-added time.

### 2.2.4 Overall Lean Score

After the three lean assessment, an overall assessment shall be done by

$$\text{OLS} = \sum_{a=1}^{a=b} \text{LT}_a * H_m \tag{4}$$

where
*a* lean tool being implemented
*b* number of lean tools being implemented
LT lean tool 'a' score
*H* weight of lean tool '*a*'.

## 3   Result

This section presents the results of the lean score for remanufacturing process of a compressor as per mentioned in Sect. 3.

### 3.1   5S Assessment Score

Based on checklist shown in Table 1, applicable verbs from the list are denoted (1) and inapplicable events with the number 0. So, adding up all the ones, the 5S score is $\frac{23}{28}$. The maximum 5S score that can be attained is $\frac{28}{28}$., so the obtained score of $\frac{23}{28}$ shows that now we have more than 82% of the maximum possible score has been attained. When we have complied most of scores in the 5S with percentage of 82%.

### 3.2   Kaizen Assessment Score

For this project, two (2) simple projects have been proposed with a time span of two weeks each. These two projects cover areas in the remanufacturing processes. Table 2 presents the project phases and weight for these projects.

The Kaizen score for the first week will be as follows;

$$K = [0.9 * ((1 \times 0.3) + (1 \times 0.3) + (1 \times 0.2))]$$
$$+ [0.95 \times ((1 \times 0.3) + (1 \times 0.2) + (1 \times 0.20))]$$
$$= 1.44 \text{ or } 144.6\%$$

The Kaizen score for the second week will be as follows;

**Table 2** Project phases and weights for Kaizen assessment

| Project No | No phase | Weightage |
|---|---|---|
| Project one | Phase1 | 30% |
| Project one | Phase2 | 30% |
| Project one | Phase3 | 20% |
| Project one | Phase4 | 10% |
| Project one | Phase5 | 10% |
| Project two | Phase1 | 30% |
| Project two | Phase2 | 20% |
| Project two | Phase3 | 20% |
| Project two | Phase4 | 20% |
| Project two | Phase5 | 10% |

$$K = [0.9 \times ((1 \times 0.1) + (1 \times 0.1))] + [0.95 \times (1 \times 0.2)] = 0.37 \text{ or } 37\%$$

The subtotal for the two week is $= \frac{(144+37)}{2} = 90.5\%$

So, the Kaizen score for the two weeks is 90.5%.

## 3.3 VSM Assessment Score

Table 3 shows the time needed for each step in remanufacturing process of compressor.

For the best-case scenario, the compressor passes the test, and no re-inspection and repair is required. For that case, the V.S.M score is as below;

$$\text{VSM} = 1 - \frac{(20 * 0.4) + (18 * 0.15) + (10 * 0.05) + (15 * 0.1) + (10 * 0.25) + (5 * 0.15)}{88}$$

$$= 0.82 \times 100 = 82\%$$

However, for the worst case possible, both the re-inspection and second repair are taken into consideration giving a V.S.M score as below;

$$\text{VSM} = 1 - \frac{(20 * 0.4) + (18 * 0.15) + (10 * 0.05) + (15 * 0.1) + (10 * 0.25) + (5 * 0.15) + (15 * 0.3) + (8 * 0.15)}{111}$$

$$= 0.81 \times 100 = 81\%$$

**Table 3** Remanufacturing process time take per one compressor

| Stage | Cycle time (minutes) | Non value-added time ratio |
|---|---|---|
| Complete strip down | 10 | 0 |
| Inspection of parts | 20 | 40 |
| Replace and remanufacture | 18 | 15 |
| Rewinding | 10 | 5 |
| Cleaning | 15 | 10 |
| Reassembly | 10 | 25 |
| Testing | 5 | 15 |
| Total maximum cycle time | 88 | |
| In case it fails the test | | |
| Reinsertion | 15 | 30 |
| Repair | 8 | 15 |
| Max cycle time (2) | 111 | |

**Table 4** Lean score comparison

| Lean tool | Datum score (%) | Implementation score (%) | Progress rate (%) |
|-----------|-----------------|--------------------------|-------------------|
| 5S | 50 | 82 | 32 |
| Kaizen | 77.5 | 90.5 | 13 |
| VSM | 60 | 81 | 21 |
| OLS | 62 | 85 | 23 |
| Average | | | 20.5 |

## 3.4 The Overall Lean Score

By compiling the obtained results, Kaizen score is 90.5%; 5S is 82% score, and the V.S.M. score with one repair cycle of is 81%. It will be assumed 30%, 30%, and 40% are the respective weights for the 5S score, Kaizen score, and V.S.M. score, respectively. Then, OLS can be counted, and Table 4 presents the lean score comparison between before (datum) and after lean implementation in remanufacturing process.

$$OLS = (0.3 \times 0.905) + (0.3 \times 0.82) + (0.4 \times 0.81)$$
$$= 0.84 \times 100 = 85\%$$

## 4 Discussion

As shown in Table 4, in the case of the 5S grading system, the questions were organized around the points that are checked in the region and get a score of up to 82% that can be increased until we reach a 100% application rate with a 32% progress rate. As for the Kaizen result, a score of 90.5 was achieved for both weeks, with a 13% progression score. This therefore means that a Kaizen score can be a very powerful contributor to a total score, OLS. As for VSM, a score of 81% was achieved, and this would indicate a strong climate improving in an organization that seeks rapid growth in its poor implementation [8].

Therefore, the remanufacturing process flow layout proposed based on the implementation of the lean technique shown Fig. 2b. The remaining compressor oil is drained as the draining process has been developed by adding a drain machine. The development in the process of conveying the dismantled parts, which was used as an electric conveyor belt conveyor, was in the stage of disassembly and inspection. In the cleaning section, the space used was reduced, which reduces movement and with the restriction of the four machines used to clean and disperse them in different colors.
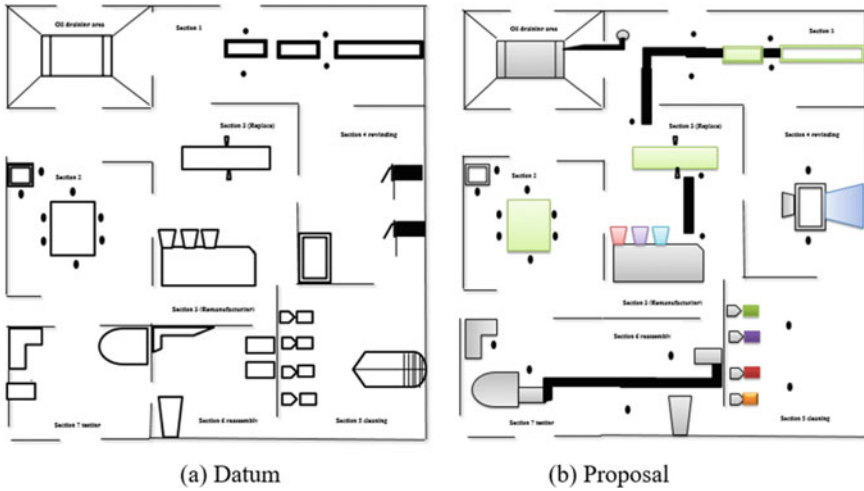
**Fig. 2** Remanufacturing process flow layout

## 5 Conclusions

The use of lean manufacturing processes and technologies has recently sparked the interest of car air conditioner compressor makers. Lean manufacturing has been applied to the process, which includes many of its tools that help reduce losses. Three tools were selected for the application of lean manufacturing, namely 5S, Kaizen, and VSM. All of these tools were initially evaluated and then evaluated after the application process. The application of these tools has shown a great development in the project and in the remanufacturing process in particular. These tools must be taken into account in any of the manufacturing processes to obtain the highest and most efficient results possible.

## References

1. Pech M, Vaněček D (2018) Methods of lean production to improve quality in manufacturing. Qual Innov Prosperity 22(2):01–15
2. Heyward J, Stanfield P (2019) Analysis of lean scheduling practices in a remanufacturing environment. In: IISE annual conference and expo 2019
3. Liu C, He K, Zhang Y et al (2018) Research on data mining technology for the connotation and measurement of uncertainty for reassembly dimensions. Int J High Performance Syst Archit 8(1–2):13–21

4. Bharambe V, Patel S, Moradiya P (2020) Implementation of 5S in industry: a review. Multidisc Int Res J Gujarat Technol Univ 2(1):12–27
5. Ghali MGB (2018) Metrics for assessment and management of lean manufacturing implementation. Diss. University of Windsor (Canada)
6. Chandrayan B, Solanki AK, Sharma R (2019) Study of 5S lean technique: a review paper. Int J Prod Qual Manage 26(4):469–491
7. Riek LD (2017) Healthcare robotics. Commun ACM 60(11):68–78
8. Sunk A, Kuhlang P, Edtmayr T et al (2017) Developments of traditional value stream mapping to enhance personal and organisational system and methods competencies. Int J Prod Res 55(13):3732–3746

# Design for Assembly and Disassembly on Product Design of Flat Panel Display

**V. K. Y. Chong, T. F. Go, D. A. Wahab, and L. K. Moey**

**Abstract** Nowadays, one of the challenges facing by the world is the excess waste of electronic products. The product design with high complexity increases the difficulty during disassembly process. Besides, it increases the disassembly time. Thus, the purpose of this paper is to achieve the goals of sustainable product development via enhancement of ease of assembly and disassembly. Modifications of snap fit be focused. MOST sequence is used to determine the disassembly time. Analysis of assembly and disassembly force is used to obtain the force requires to assemble and disassemble the product. The results showed the modified design requires 4.8 s and 21.72 N to disassemble the plastic covers. In addition, the disassembly time of modified design reduced 62.5% where the assembly and disassembly force reduced with an average of 6.51%. The findings show the design of snap fit is important because it defines the assembly and disassembly force and disassembly time of a product. The disassembly time and disassembly force are reduced which eventually reduce amount of e-waste.

**Keywords** Disassembly · Assembly · Sustainable design · MOST sequence

V. K. Y. Chong
Faculty of Engineering, Built Environment and Information Technology, SEGi University, Selangor, Malaysia

T. F. Go (✉)
Center for Advance Materials and Intelligent Manufacturing, Faculty of Engineering, Built Environment and Information Technology, SEGi University, Selangor, Malaysia
e-mail: gotzefong@segi.edu.my

D. A. Wahab
Center for Automotive Research (CAR), Faculty of Engineering and Built Environment, Universiti Kebangsaan Malaysia, UKM Bangi, 43600 Selangor, Malaysia

L. K. Moey
Center for Modeling and Simulation, Faculty of Engineering, Built Environment and Information Technology, SEGi University, Selangor, Malaysia

# 1 Introduction

In the era of advanced of science and technology, the development of technology has brought convenience to our life. Electrical and electronic equipment (EEE) has become an essential product which plays key role in our daily life. Due to the fact, the worldwide distribution of electronic waste (e-waste) is 44.75 million tons in the year of 2016 [1]. Disassembly effort of end-of-life (EoL) products is important in parts recovery because it increases disassembly efficiency and reduce labor cost.

In addition, design for assembly (DFA) is a technique or tool that is used to assemble product automatically and manually. It is used to propose good design and assembly sequence for product design [2]. Rosli et al. [3] studied on the design efficiency based on an analysis of an old bicycle tire inflator. Melckenbeeck et al. [4] studied on the optimal sequence from the loose parts of an EoL products. Moreover, design for disassembly (DFD) is used to retrieve used parts or components from EoL products [5]. It proposes optimal disassembly methods for product disassembly. It incorporates with DFA to disassemble a product to reduce parts destruction during disassembly process [6]. Foo et al. [7] proposed a non-destructive disassembly method, screw detection for disassembly.

General case refers to a complete disassembly process, while selective case refers to selective disassembly, or it can be said retrieval of one or more components at one time [8]. Method time measurement (MTM) and Maynard operation sequence technique (MOST) are suitable methods for manual disassembly operations [9].

This paper focuses on the disassembly time and disassembly force of a modified product design. The modifications of product design are applied on a datum in order to study the accessibility of ease of assembly/disassembly of the product. The remaining of the paper is organized as follows: Sect. 2 outlines the methodology of this project. Followed by Sect. 3 describes the results of disassembly, and Sect. 4 goes discussions. Lastly, Sect. 4 is the conclusion of the paper.

# 2 Methodology

This section explains on the methodology. First the disassembly time calculation method. Then, assembly and disassembly force analysis model. Lastly, modifications done on the fasteners of the flat panel display. The enhancement of disassembly time eventually can be determined. In addition, an analysis for assembly and disassembly time is conducted. Comparison of disassembly time and disassembly force of datum and modified design was conducted.

## 2.1 Disassembly Time

MOST sequence is used to obtain the disassembly time of fasteners [10]. Disassembly force is required before proceed to disassembly time. Disassembly force shall be obtained by using the equations in Tables 1, 2 and 3. The equations are used to determine forces for one fastener only. Due to the amount of fastener, Eq. 1 shall be used to get the total disassembly time of the product.

$$\text{Total Disassembly Time} = \text{Disassembly Time} \times \text{Quantity of Fastener} \quad (1)$$

## 2.2 Assembly and Disassembly Force Analysis Model

Modifications of product were done in aspect of dimension, geometry shape, and type of beam. The mechanical properties of the plastic materials shall be chosen precisely as it should able to withstand the maximum deflection of the snap fit beam during insertion and separation process. Table 1 shows the parameters for analysis of maximum deflection force for cantilever straight beam behavior. Equations for analysis for straight beam behavior are shown in Table 2. Whereby, Table 3 shows the equations for assembly and disassembly force. Take note that for both assembly and disassembly force, they actually using the same spreadsheet due to the insertion and retention angle are the same. Thus, equations shall be used to determine the total assembly/disassembly force of the snap fit.

## 2.3 Case Study

In this paper, a flat panel display is used as datum. It is a 14 inches LCD Philips monitor of 2002. "Study for a method to assess the ease of disassembly of electrical and electronic equipment" by [9] was taken as datum. The modifications of product design are done on Autodesk Inventor.

## 3 Results

## 3.1 Enhancement of Disassembly Time

The results showed the modification has reduced the total disassembly time. There were 2 types of fasteners used in datum product which are snap fit type 1 and hinge type 2. According to MOST sequence [9], disassembly time for snap fit type 1

**Table 1** Parameters for analysis of maximum deflection force

| Steps | Parameters | Justifications/Explanation/Equation |
|---|---|---|
| 1 | Secant Modulus, $E_s$<br>Yield Strain, % | • These are the materials properties if this plastic which obtained from the datasheet in [11] |
| 2 | Beam Length, $L_b$<br>Beam Thickness, $T_b$<br>Beam Width, $W_b$<br>Fillet Radius, $R_w$ | • Assumptions were made for dimensions of the snap fit |
| 3 | Stress Concentration Factor, K | • It indicates the stress located in the connection between the beam and the wall<br>• It can be obtained from Eq. 2:<br><br>$K = \frac{R_w}{T_b}$ (2)<br><br>• According to [12], the fillet radius should be as small as possible where it should not less than 0.381 mm<br>• Stress concentration factor reduced as the fillet radius reduced |
| 4 | Target Strain, $\varepsilon_{\text{target}}$ | • It is the desired strain of the material. The final calculated strain shall not exceed target strain<br>• It can be obtained by using Eq. 3:<br><br>$\varepsilon_{\text{target}} = \frac{E_s}{K}$ (3) |
| 5 | Design Deflection, $\delta_{\text{design}}$ | • It indicates the beam deflection during mating and separating action<br>• It can be obtained by using Eq. 4:<br><br>$\delta_{\text{design}} = 0.67 \cdot \frac{E_s (L_b)^2}{T_b}$ (4)<br><br>• Note: The equation is only applicable for cantilever beam with rectangular shape |
| 6 | Initial Calculation, $\varepsilon_{\text{initial}}$ | • It is compared with the target strain based on the dimensions of snap fit that were set earlier<br>• It can be obtained by using Eq. 5:<br><br>$\varepsilon_{\text{initial}} = 1.5 \cdot \frac{T_b (\delta_{\text{design}})}{(L_b)^2}$ (5)<br><br>• The calculated strain value should greater than design strain |
| 7 | Aspect Ratio, $L/T$ | • It determines Q-value<br>• It can be obtained by using Eq. 6:<br><br>Aspect ratio $= \frac{L_b}{T_b}$ (6)<br><br>• It is recommended to design the beam with aspect ratio in a range of 5–10 |

(continued)

**Table 1** (continued)

| Steps | Parameters | Justifications/Explanation/Equation |
|---|---|---|
| 8 | Q-Factor for Value for Wall Deflection, Q | • It is used to reduce calculated beam deflection force<br>• It can be obtained from [13]<br>• Beam to part configurations and beam shape do not use the same table for Q-factor values |
| 9 | Strain Adjusted for Wall Deflection, $\varepsilon_{\text{calc-Q}}$ | • It is used to indicate the Q-factor adjustment<br>• It can be obtained by using Eq. 7:<br>$\varepsilon_{\text{calc}-Q} = \frac{\varepsilon_{\text{initial}}}{Q}$ (7) |
| 10 | Maximum Deflection Force, $F_{\text{p-Q}}$ | • To determine the maximum beam deflection force<br>• It can be obtained by using Eq. 8:<br>$F_{p-Q} = \frac{W_b \times T_b^2 \times E_s \times \varepsilon_{\text{calc}-Q}}{6L_b}$ (8) |

**Table 2** Equation of analysis spreadsheet for straight beam behavior

| Variables | Formulas/Equations |
|---|---|
| Target Strain | $\frac{\text{Secant Modulus}}{\text{Stress Concentration Factor}} = \frac{E_s}{K}$ (9) |
| Design deflection, $\delta_{\text{design}}$ | $0.67 \cdot \frac{E_s (L_b)^2}{T_b}$ (10) |
| Initial calculation, $\varepsilon_{\text{initial}}$ | $1.5 \cdot \frac{T_b (\delta_{\text{design}})}{(L_b)^2}$ (11) |
| Aspect ratio | $\frac{L_b}{T_b}$ (12) |
| Strain adjusted for wall deflection, $\varepsilon_{\text{calc-Q}}$ | $\frac{\varepsilon_{\text{initial}}}{Q}$ (13) |
| Maximum deflection force, $F_{\text{p-Q}}$ | $\frac{W_b \times T_b^2 \times E_s \times \varepsilon_{(\text{calc}-Q)}}{6 \times L_b}$ (14) |

**Table 3** Equation of assembly and disassembly force

| Variables | Formulas/Equations |
|---|---|
| Assembly/Disassembly Force | $F_{p-Q} \cdot \frac{\mu + \tan\alpha}{1 - \mu \tan\alpha}$ (15) |

and hinge type 2 was 0.4 s and 1.1 s, respectively. The disassembly time for datum product eventually was greater than disassembly time of modification design product, as shown in Table 4. This was because snap fit type 1 was used in the modifications design. The design consisted 12 pieces of snap fit type 1 and therefore reduced the disassembly time. Details for the modification of snap fit can be found in Table 5.

**Table 4**  Types of fastener used and disassembly time of datum

| Datum design | Type of fasteners used | Quantity of fasteners | Disassembly time (s) | Total disassembly time (s) |
|---|---|---|---|---|
| Front Cover and Back Cover | Snap fit type 1 | 3 | 0.4 | 1.2 |
|  | Hinge type 2 | 6 | 1.1 | 6.6 |
| Total disassembly time of the design (s) | – | – | – | 7.8 |

**Table 5**  Types of fastener used and disassembly time of modified design

| Modification design | Type of fasteners used | Quantity of fasteners | Disassembly time (s) | Total disassembly time (s) |
|---|---|---|---|---|
| Front Cover and Back Cover | Snap fit type 1 | 12 | 0.4 | 4.8 |

## 3.2  Assembly and Disassembly Force Analysis

The insertion and retention angle for mating and separating process was studied for the purpose of determine assembly and disassembly force. Since this was a loop style lock, thus, the angle was designed onto the static catch. Hence, a table was made with different angles and beam length in order to determine the assembly and disassembly force. Due to the angle was the same for both insertion and retention angle, the assembly and disassembly force was to be the same. In this study, two type snap fit configuration be considered as shown in Fig. 1. Table 6 lists the assembly and disassembly force for beam configuration Type A and Type B. From Fig. 2, the assembly and disassembly force can be observed; it is directly proportional to the insertion/retention angle. From both Table 6 and Fig. 2, the overall forces required for type A were slightly greater than type B regardless of the same snap fit dimensions and insertion/retention angles.

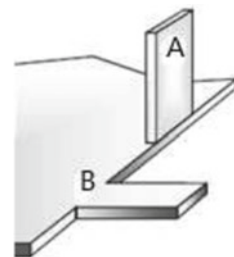**Fig. 1**  Two types of snap fit configurations

**Table 6** Assembly and disassembly force for beam configuration Type A and Type B

| $\alpha$ Design | $\delta$ | $L_b$ | $W_b$ | Assembly and Disassembly force (N) | | Ratio (refer to Type B) (%) |
| --- | --- | --- | --- | --- | --- | --- |
| | | | | Type A | Type B | |
| 0.5 | 1.29 | 8.0 | 8.0 | 1.78 | 1.68 | 5.95 |
| 1.0 | 1.29 | 8.0 | 8.0 | 1.85 | 1.74 | 6.32 |
| 1.5 | 1.29 | 8.0 | 8.0 | 1.93 | 1.81 | 6.63 |
| 2.0 | 1.29 | 8.0 | 8.0 | 2.00 | 1.87 | 6.95 |
| 2.5 | 1.29 | 8.0 | 8.0 | 2.07 | 1.94 | 6.70 |
| | | | | | Average ratio = | 6.51 |
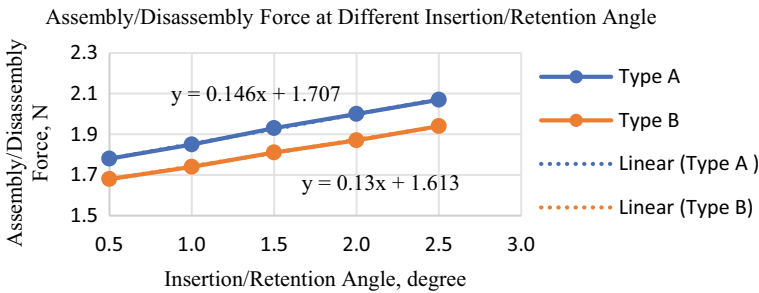


**Fig. 2** Assembly and disassembly force at different insertion/retention angles

## 4 Discussion and Conclusion

The modifications of product design are focused on the front cover and back cover of the flat panel display. Bayblend T65 XF, a mixture of PC and ABS plastics, was chosen as the material for back cover and front cover. The thickness of plastic frame of the front and back cover should follow the thickness of fasteners. Moreover, the number of fasteners and types of fastener should be decided based on the structure and the purpose of the product. By doing so, it is ease to assembly, disassembly, and remanufacture. The appearance of the product design is taken into consideration. Observation was done on the size of monitor bezel where it is reduced in size from year 2015. As mentioned in Sect. 3, the total disassembly time for datum and modified design is 7.8 s and 4.8 s, respectively. From results obtained, time required to disassemble the product for modified design is reduced 62.5%. This is due to the modified design only implements one type of fasteners which is snap fit type 1 where datum uses snap fit type 1 and hinge type 1.

When it comes to assembly and disassembly force, a range of 0.5°–2.5° was used as insertion and retention angle for the angle of static catch. The angle considered is regarding to the geometry structure of the snap fit. As shown in Fig. 2, type B requires lower assembly/disassembly force than type A. It shows the longer the beam length, the force required to assemble/disassemble increases. Moreover, the

average ratio of assembly/disassembly force obtained is 6.51%. In other words, type A required 6.51% of assembly and disassembly force for each snap fit. The overall assembly/disassembly force of type B is smaller than type A. For these reasons, beam type B is better than type A.

The ease of assembly/disassembly and ease of remanufacturing of modified design were assessable than datum due to its snap fit design. The type of fasteners and number of fasteners used in the design shall not influence the efficiency of assembly and disassembly. In modified design, the components or fasteners used are customize specifically for ease of assembly and disassembly. Nevertheless, in view of the fact that datum design was an electronic product of year 2000 where the design concepts and design equipment were comparably weaker. So, the accessibility of fasteners might not that satisfied. In spite of everything, the appearance of the product was also important. Datum design has a thick monitor design due to the skills of designing. Moreover, modified design scored in thickness of plastic frame as well. Plastic frame thickness shall consider the snap fit design feature. Yet, it should not be too thick as it might influence the ease of assembly/disassembly and ease of remanufacturing.

Summarized the results obtained, modified design of snap fit with cantilever beam length of 8.0 mm is chosen as the dimension. The insertion/retention angle for stationary catch is 1.5°. The total assembly/disassembly force for 12 pieces of snap fit is 21.72 N.

# References

1. Authored CP, Forti V, Gray V et al (2017) Quantities, flows, and resources. The Global E-waste
2. Murali GB, Deepak BBV, Biswal BB (2017) A novel design for assembly approach for modified topology of industrial products. Int J Performability Eng 13(7):1013–1019
3. Rosli MF, Effendi MSM, Shayfull Z et al (2020) Design for assembly (DFA) analysis of old bicycle tire inflator. In: AIP Conference Proceedings 2291
4. Melckenbeeck I, Burggraeve S, Van Doninck B et al (2020) Optimal assembly sequence based on design for assembly (DFA) rules. Proc CIRP 91:646–652
5. Abuzied H, Senbel H, Awad M et al (2020) A review of advances in design for disassembly with active disassembly applications. Eng Sci Technol Int J 23(3):618–624
6. Desai A, Mital A (2017) An interactive system framework to enable design for disassembly. J Manuf Technol Manag 28(6):749–771
7. Foo G, Kara S, Pagnucco M (2021) Screw detection for disassembly of electronic waste using reasoning and re-training of a deep learning model. Proc CIRP 98:666–671
8. Kim HW, Lee DH (2017) An optimal algorithm for selective disassembly sequencing with sequence-dependent set-ups in parallel disassembly environment. Int J Prod Res 55(24):7317–7333
9. Vanegas P, Peeters J, Cattrysse D et al (2016) Study for a method to assess the ease of disassembly of electrical and electronic equipment. Method development and application to a flat panel display case study

10. Peeters JR, Tecchio P, Ardente F et al (2018) eDIM: further development of the method to assess the ease of disassembly and reassembly of products—application to notebook computers
11. Covestro Deutschland AG (2020) CAMPUS ® Datasheet
12. Bayer MaterialScience (2016) Snap-fit joints for plastic parts (Online). Available: http://fab.cba.mit.edu/classes/S62.12/people/vernelle.noel/Plastic_Snap_fit_design.pdf. Last accessed Jan 2021
13. Bonenberger PR (2005) The first snap-fit handbook

# Flexural Strength Optimization for Hybrid Glass/Jute Fiber Reinforced Epoxy Composite Fabricated via Vacuum Infusion

**Mohd Fadli bin Hassan, Abu Bakar B. Sulong, Khalina bt. Abdan, and Nabilah Afiqah Mohd Radzuan**

**Abstract**   In this study an attempt was made to develop a green composite, hybridization glass/jute fiber was reinforced with epoxy matrix by vacuum infusion technique. The process parameters of vacuum infusion technique such as supply pressure, soaking time, and use of flow media were investigated. Processed samples of hybrid glass/jute fiber reinforced epoxy composite were tested for their strength by flexural testing recommended by ASTM D790-03 standard. The flexural properties of hybrid glass/jute fiber reinforced epoxy composite was optimized by response surface methodology by two-level factorials. This analysis showed that the flexural strength significantly at coefficient of determination, $R^2$ 0.9812, and flexural modulus significantly with coefficient of determination, $R^2$ 0.9111. The flexural strength of ~106 MPa and flexural modulus of ~10.6 GPa were achieved at optimum parameter of 500 kPa pressure, 120 min soaking time with the utilization of low media during vacuum infusion process.

**Keywords** Hybridization · Flexural strength · Vacuum infusion · Process parameters

M. F. bin Hassan · A. B. B. Sulong (✉) · N. A. M. Radzuan
Department of Mechanical & Manufacturing Engineering, Faculty of Engineering & Built
Environment, Universiti Kebangsaan Malaysia (UKM), 43600 Bangi, Selangor Darul Ehsan,
Malaysia
e-mail: abubakar@ukm.edu.my

K. bt. Abdan
Department of Biological and Agricultural Engineering, Faculty of Engineering, Universiti Putra
Malaysia (UPM), 43400 Serdang, Selangor Darul Ehsan, Malaysia

M. F. bin Hassan
Department of Polymer Composite Engineering Technology, Kolej Kemahiran Tinggi MARA
Masjid Tanah, KM1 Persiaran Paya Lebar, Ramuan China Besar, 78300 Masjid Tanah, Melaka,
Malaysia

# 1 Introduction

Introduction of natural fibers (jute fiber) with partial replacement of synthetic fibers (carbon/glass) in these composite materials could lead to new ventures in composite industries. This is partly due to the environmental concern about limitations of recyclability of synthetic fiber-made composites, but mostly due to their potential in cost reduction. The green composite tooling also offers a number of advantages such as lightweight, low manufacturing cost, and low thermal mass [1, 2].

Hybridization process of glass fiber with natural fibers with epoxy resin will be performed via vacuum infusion technique. The infusion process was the cheapest among composite manufacturing processes [3]. The infusion technique wields a vacuum bag process and it gives this process the low-cost equipment for the manufacture of large composite structures for high-performance applications, compared with other processes using a rigid mold [3, 4].

Mechanical properties such as elastic modulus and flexural test of hybrid glass/jute fibers reinforced epoxy composites in the forms of laminates will be determined. The hybrid composites will exhibit combination of physical and mechanical properties of both glass and jute fiber reinforced thermoset resin. However, the properties will be higher than observed for solely jute fiber reinforced composites but lower than solely glass fiber reinforced composites [1, 5]. Fabricated hybrid composite via the infusion technique studied by controlling the process parameters. The process parameters studied were pressure supply, soaking time, and use of the media flow.

# 2 Experimental

## 2.1 Materials

Jute fiber mat was produced from Indarsen Shamlal Pvt. Ltd., Kolkata, India. The epoxy resin DM15 (F3) A is an unmodified basic liquid epoxy resin made from Bisphenole-A and Epichlorohydrin, having a medium viscosity and low molecular weight, was used in a thermoset matrix. Hardener DM 15 (F3) B is a low viscosity modified liquid amine epoxy hardener were used as catalyst and accelerator for epoxy system in laminating. Both the epoxy resin and commercial curing agent were obtained from Zarm Scientific & Supplies Sdn. Bhd., Malaysia. Other reinforcement materials used were e-glass woven.

## 2.2 Processing

The Hardener DM 15 (F3) B was added to the resin DM 15 (F3) A with using formulation by ratio of 1:5, respectively. The hybrid laminated composites were

fabricated in the following sequence: Glass/Jute/Glass/Jute/Glass/Jute/Glass. The sequence staking orientations were to respect the symmetry construction to give the best mechanical properties of hybrid composite [3].

Specimens for mechanical (flexural) testing were cut and prepared according to ASTM D790-03 standard [6]. The flexural testing using the three-point bend configuration was performed using a universal testing machine (Instron 50 kN) equipped with a flexural test fixture. Testing was carried out in accordance with procedure of the ASTM D790-03 standard [6].

## 2.3  Design of Experiments

Design experiments were carried out using Design Expert software (Statistic Made Easy, version 6.0.10, Stat-Ease, Inc., Minneapolis, MN). The two-level factorial design experiments for three independent variables carried out the total of 12 sets of experiment for this study [7].

## 3  Results and Discussion

The result was analyzed with ANOVA as an appropriate method for experimental design used. The regression equation (Eqs. 1 and 2) were obtained after the ANOVA was completed. This gave the flexural strength and elastic modulus of hybrid composite as a function of different variables: the pressure ($X_1$; kPa), the soaking time ($X_2$; min), and use of the flow media. All terms, regardless of their significance, are included in the following equation below.

For flexural strength:

$$Y = 186.81 + 0.95X_1 - 16.59X_2 - 15.02X_3 - 15.51X_1X_2 \\ - 25.09X_1X_3 - 9.51X_2X_3 \tag{1}$$

For elastic modulus:

$$Y = 7484.89 - 1389.13X_1 + 4537.57X_2 \tag{2}$$

The predicted result of flexural strength and elastic modulus using Eqs. (1) and (2) is given in Table 1 along with the experimental data. From that result, the design of experiment predicted and proposed the best parameter value were predicted number 1 (Table 1).

Effect of process parameter on flexural properties

**Table 1** Observed respond and predicted values

| Number | Pressure | Soaking time | Flow media | Flexural strength | Elastic modulus | Desirability |
|---|---|---|---|---|---|---|
| **1** | **500.000** | **120.000** | **With** | **106.050** | **10,633.334** | **0.839** |
| 2 | 499.999 | 119.733 | With | 106.346 | 10,601.042 | 0.837 |
| 3 | 499.999 | 118.216 | With | 108.030 | 10,417.482 | 0.824 |
| 4 | 134.640 | 120.000 | With | 178.476 | 13,170.996 | 0.663 |
| 5 | 100.000 | 120.000 | Without | 184.218 | 13,411.581 | 0.642 |
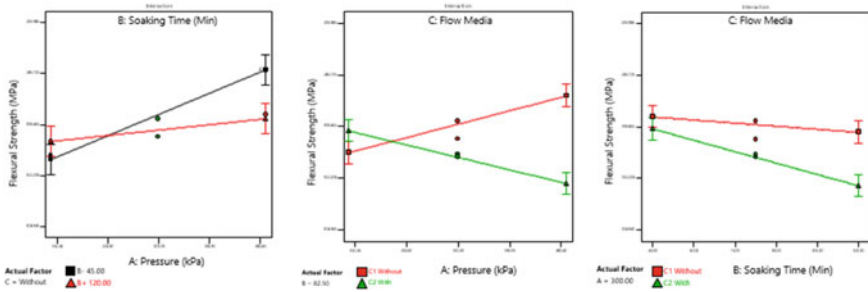


**Fig. 1** Effect of process parameter on flexural strength

The influence of soaking time and pressure on the flexural strength has been presented in Fig. 1. Under same pressure but increasing the soaking time either with or without using flow media, the flexural strength will drop by increasing the soaking time. Flexural strength will increase by increasing the pressure without using flow media but under the same soaking time, but when observed process with parameters under same soaking time and with flow media, the flexural strength will decrease with increasing the pressure value. This effect was attributed to the poor wettability of epoxy resin.

Figure 1 illustrated the relationship between pressure and flow media applied during infusion process and effect on the flexural strength. The minimum soaking time without using flow media gave the positive result for flexural strength. It also could explain the relationship if using high pressure and long soaking time will affect the flexural strength of the hybrid laminate. It describes the combined use of the long soaking time and high pressure as well as the use of media flow negatively impact flexural strength.

Effect of process parameter on elastic modulus

The influence of process parameter during infusion process on the elastic modulus have been illustrated in Fig. 2. The increasing the pressure process will drop the value of elastic modulus. But if maximize the soaking time will give good results for elastic modulus. Increasing the pressure will be affected and cause the poor permeability of resin flow during process. Therefore poor permeability will generate the starvation
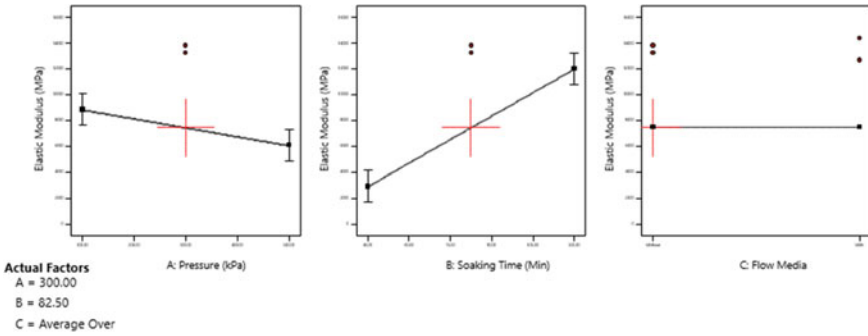
**Fig. 2** Effect of process parameters on elastic modulus

resin on the hybrid composite [3]. Thus, the decrease in elastic modulus for specimen was attributed to the flow of matrix and pressure during process. And it can conclude that the flow media does not influence the elastic modulus result.

## 4 Conclusions

Design experiments were carried out using Design Expert software and determining the optimum process parameters to produce a product with good flexural properties. The best process parameters proposed by design of experiment are process conduct with 500 kPa pressure and using flow media under 120 min of soaking time. The combination of process parameters is used to achieve the highest or optimum flexural properties.

## References

1. Cicala G, Cristaldi G, Recca G, Ziegmann G, El-Sabbagh A, Dicjert M (2009) Properties and performances of various hybrid glass/natural fibre composites for curved pipes. Mater Des 30:2538–2542
2. Arrakhiz FZ, El Achaby M, Malha M, Bensalah MO, Fassi-Fehri O (2013) Mechanical and thermal properties of natural fibers reinforced polymer composites: Doum/low density polyethylene. Mater Des 43:200–205
3. Njionhou Kepnang A, Berthet F, Castanie B. Parameters affecting mechanical properties of composite manufactured by liquid resin infusion (LRI)
4. Beckwith WS (2007) Resin infusion technology: part 1, 2–3. Sample J 43(1, 3–4)

5. Dong C, Davies IJ (2014) Flexural and tensile moduli of unidirectional hybrid epoxy composites reinforced by S-2 glass and T700S carbon fibres. Mater Des 54:893–899
6. (2005) Annual book of ASTM standard, vol 08-01. ASTM Int., West Conshohocken
7. Montgomery DC (1999) Experimental design for product and process design and development. Stat 48(part 2):159–177

# Specific Strength of Sandwich-Structured Composite of Open-Cell Metallic Foam/Resin Joined by Friction Stir Incremental Forming

**Ryo Matsumoto, Harutaka Sakaguchi, Masaaki Otsu, and Hiroshi Utsunomiya**

**Abstract** The compressive deformation behavior of an open-cell nickel foam joined with polymethyl methacrylate (PMMA) sheets by friction stir incremental forming (FSIF) process was investigated with uniaxial compression test. The sheet was joined on each side face of the foam for fabrication of the foam/sheet composite for uniaxial compression test. In FSIF process, the bottom of the sheet was mechanically interlocked to the surface pores of the foam by plastic flow of the frictionally heated sheet. In uniaxial compression test, the cubic foam/sheet composite was compressed with an initial strain rate of $1.0 \times 10^{-3}$ s$^{-1}$. The compressive specific strength of the foam/sheet composite was approximately 30 times higher than that of the foam. This was due to not only high specific strength of the sheet but also the sandwich structure of the foam/sheet composite.

**Keywords** Plastic joining · Nickel foam · Polymethyl methacrylate · Composite structure · Strength-mass relationship

## 1 Introduction

Metallic foams are lightweight due to their low density, however, their strengths are generally low. In order to use metallic foams for structural components, improvement of the strength-mass relationship of component with metallic foam is essential. One of effective means for the improvement of the strength-mass relationship is sandwich-structured composite. Some fabrication processes for the sandwich-structured composite are proposed for foam materials. Concerning joining process of resin sheet on metallic foam or metal with porous surface, friction welding [1, 2], hot pressing [3], and incremental forming [4] have been reported. We applied friction stir incremental forming (FSIF) process to join resin sheet with open-cell

R. Matsumoto (✉) · H. Sakaguchi · H. Utsunomiya
Division of Materials and Manufacturing Science, Osaka University, Osaka, Japan
e-mail: ryo@mat.eng.osaka-u.ac.jp

M. Otsu
Department of Mechanical Engineering, University of Fukui, Fukui, Japan
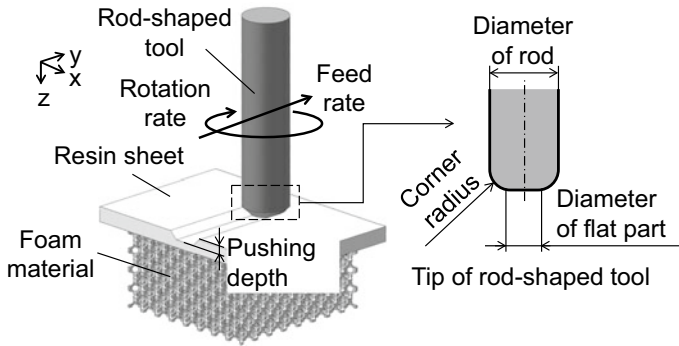
**Fig. 1** Schematic illustration of friction stir incremental forming (FSIF) process for joining of open-cell foam and resin sheet [5]

foam [5]. The sheet was joined by mechanically interlocking to the porous structure of the foam by the plastic flow of the heated and softened resin sheet.

In this study, compressive deformation behavior of an open-cell type nickel foam joined with PMMA sheets by FSIF process is investigated with uniaxial compression test. The specific compressive strength of the sandwich-structured foam/sheet composite is compared with that of uniform mixture of nickel foam and PMMA.

## 2 Joining of Open-Cell Foam and Resin Sheet by Friction Stir Incremental Forming (FSIF)

Friction stir incremental forming (FSIF) process was originally developed for incremental sheet metal forming [6]. FSIF process was applied to join resin sheet with open-cell foam [5]. Figure 1 shows the schematic illustration of FSIF process for joining of open-cell foam and resin sheet. A rotating rod-shaped tool with a flat end is vertically pushed and horizontally fed against the sheet on the foam. The sheet is frictionally heated and incrementally deformed by the rotation and feed of the tool, while the foam is not plastically deformed.

## 3 Experimental Conditions

### 3.1 Open-Cell Foam and Resin Sheet

A commercial open-cell nickel foam (Celmet®, Fig. 2a) was used as substrate. The mean pore diameter and bulk density of the foam were 0.8 mm and $\rho_f = 0.42$ Mg/m³, respectively. The relative density (bulk/buoyant density) was lower than 0.1. A
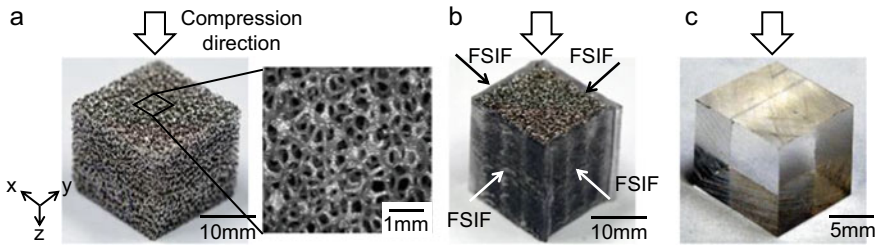
**Fig. 2** Photographs of specimens for compression test. **a** Open-cell nickel foam (Celmet®), **b** nickel foam/PMMA sheet composite, **c** PMMA

commercial transparent polymethyl methacrylate (PMMA) sheet with a thickness of 1.0 mm (Delaglass™ A) was used as resin. The density of the sheet was $\rho_s = 1.19$ Mg/m$^3$.

## 3.2 FSIF Conditions

FSIF process was carried out for fabricating the nickel foam/PMMA composite specimen for compression test. In FSIF process, the flat end diameter of the tool was ϕ4 mm, and the tool was scanned with a rotation rate of 6000 rpm, a feed rate of 10 mm/min and a feed pitch of 4 mm, and a pushing depth of 0.5 mm.

The sheet was put on the foam with 15.5 mm × 15.5 mm × 20 mm in rectangular parallelepiped before FSIF process at each surface of the foam. FSIF process was carried out on the top face of the specimen. After finish of FSIF process on one face of the specimen, the specimen was turned from the top to the bottom or the side. Then FSIF process was carried out on new top face of the specimen. The sheet was joined on each side face of the foam with a cross-section of 15.5 mm × 15.5 mm by repeating this operation (Fig. 2b). After FSIF process, the specimen was cut with 16 mm × 16 mm × 16 mm in cube. The bulk density of the foam/sheet composite specimen was $\rho_c = 0.59$ Mg/m$^3$.

## 3.3 Compression Test Conditions

Compressive deformation behaviors of nickel foam without joining PMMA sheet, nickel foam joined with the PMMA sheets (nickel foam/PMMA sheet composite) and PMMA were investigated by uniaxial compression (Fig. 2). The initial shape of the foam and foam/sheet composite specimens was 16 mm × 16 mm × 16 mm in cube, while that of the PMMA specimen was 10 mm × 10 mm × 10 mm in cube. The specimens were compressed between mirror finish parallel platens with a speed of 1 mm/min under dry condition at room temperature.
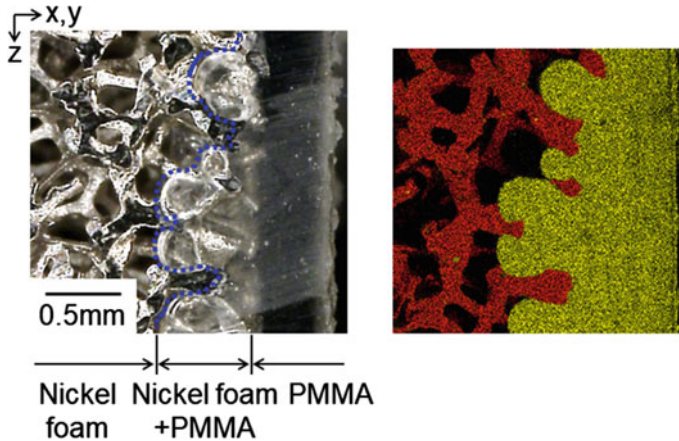
**Fig. 3** Photograph and element map of cross-section of interface of nickel foam/PMMA sheet joined by FSIF process (red area: nickel, green area: carbon)

The nominal compressive stress ($\sigma$) was calculated by dividing the compression load by the initial cross-sectional area of the specimen. The nominal compressive strain ($\varepsilon$) was calculated by dividing the crosshead stroke of the material testing machine by the initial height of the specimen.

## 4 Experimental Results

### 4.1 Interface of Foam/Resin

Figure 3 shows the photograph and the element map of the cross-section of the interface of the nickel foam/PMMA sheet joined by FSIF process. Here the elements of nickel and carbon (PMMA) were detected by energy dispersive X-ray spectrometry (EDX) analysis. The PMMA sheet was confirmed to be plastically flowed into the surface pores of the foam. The mean flow thickness of PMMA was 0.56 mm. It is concluded that the nickel foam is mechanically interlocked with the PMMA sheet.

### 4.2 Compressive Deformation Behavior

Figure 4 shows the photographs of the specimens during compression test. Due to buckling and bending of the cellular matrix of the foam, the plastic deformation was locally concentrated from the early stage of compression in the nickel foam specimen. In the nickel foam/PMMA sheet composite specimen, the delamination
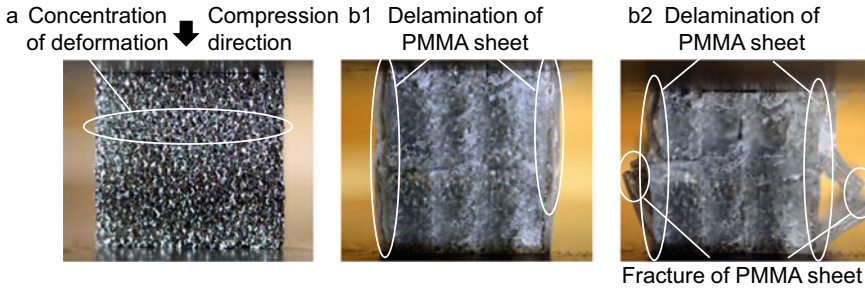
**Fig. 4** Appearances of specimens during uniaxial compression. **a** Nickel foam at nominal compressive strain $\varepsilon = 0.05$, **b1** nickel foam/PMMA sheet composite at $\varepsilon = 0.05$, **b2** nickel foam/PMMA sheet composite at $\varepsilon = 0.2$

of the sheet from the foam occurred at early stage of compression due to bending of the sheet. After that, fracture of the sheet started.

The specific nominal compressive stress–strain curves of the specimens in compression test are shown in Fig. 5. Here each compression test was carried out with two specimens under the same conditions because of the scatters of the pore shape and size of the foam. The specific nominal compressive stress was calculated by dividing the nominal compressive stress ($\sigma$) by the initial bulk density ($\rho$) of the specimen. This is due to the removal of the influence of the weight of the specimen. The stress–strain curve of the foam specimen was lowest among that of the specimens, however, the stress increased with increasing strain. This is the typical deformation behavior of the foam [7]. The stress of the foam/sheet composite specimen increased with increasing strain of $\varepsilon < 0.05$–0.07. This is resulted from bending of the sheet. The stress was suddenly dropped after peaking at $\varepsilon = 0.05$–0.07 due to the fracture of the sheet, and then the stress was almost the same with that of the foam specimen. From the stress–strain curves, the specific nominal compressive stress of the foam ($\sigma_f/\rho_f$), foam/sheet composite ($\sigma_c/\rho_c$), and PMMA ($\sigma_s/\rho_s$) was 0.7 MPa·m³/Mg, 22 MPa·m³/Mg and 111 MPa·m³/Mg at $\varepsilon = 0.05$, respectively. The specific strength of the foam–sheet composite was approximately 30 times higher than that of the foam.

## 5 Discussion on Improvement of Specific Strength of Nickel Foam/Resin Sheet Composite

The specific strength of the uniform mixture of nickel foam/PMMA was estimated by the following mixture rule:

$$X_{\text{f-s}} = \phi \cdot X_{\text{f}} + (1 - \phi) \cdot X_{\text{s}} \tag{1}$$
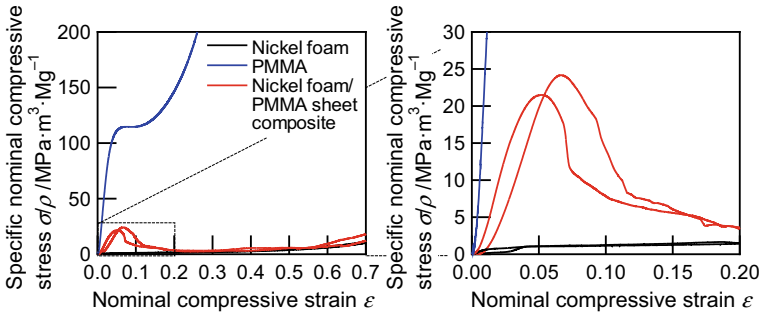
**Fig. 5** Specific nominal compressive stress–strain curves of nickel foam, nickel foam/PMMA sheet composite, and PMMA in uniaxial compression

where $X_{f\text{-}s}$, $X_f$, and $X_s$ were the properties (stress and bulk density) of uniform mixture of nickel foam/PMMA, nickel foam, and PMMA, respectively. $\phi$ was the volume fraction of the nickel foam, and it was 0.87 in the nickel foam/PMMA sheet composite specimen for compression test.

The specific strength of the uniform mixture of nickel foam/PMMA was calculated as $\sigma_{f\text{-}s}/\rho_{f\text{-}s} = 14$ MPa·m$^3$/Mg by Eq. (1). The specific strength of the uniform mixture was lower than that of the foam/sheet composite ($\sigma_c/\rho_c = 22$ MPa·m$^3$/Mg, see Sect. 4.2). Therefore the improvement of the specific strength of the foam/sheet composite was concluded to be due to not only high specific strength of PMMA but also sandwich structure with the sheet joined on the faces of the foam parallel to the compression direction.

## 6   Conclusion

The compressive deformation behavior of an open-cell type nickel foam joined with PMMA sheets by FSIF process was investigated with uniaxial compression test. The compressive specific strength of the foam/sheet composite was approximately 30 times higher than that of the foam. This was due to not only high specific strength of the sheet but also the sandwich structure of the foam/sheet composite. It is concluded the sandwich-structured composite of the foam joined with the sheet is effective to improve the strength-mass relationship.

# References

1. Chen K, Chen B, Zhang S et al (2017) Friction spot welding between porous TC4 titanium alloy and ultra high molecular weight polyethylene. Mater Des 132:178–187
2. Hangai Y, Kishimoto R, Ando M et al (2021) Friction welding of porous aluminum and polycarbonate plate. Mater Lett 304:130610
3. Kim SG, Suzuki A, Takata N et al (2019) Joining of metals and polymers using powder metallurgy with laser irradiation. J Mater Process Technol 270:1–7
4. Yang Z, Chen F, Chen L (2022) A new method for joining of polymer sheet and open-cell metal foam by thermal assisted incremental forming. Int J Adv Manuf Technol (in press)
5. Matsumoto R, Sakaguchi H, Otsu M et al (2020) Plastic joining of open-cell nickel foam and polymethyl methacrylate (PMMA) by friction stir incremental forming. J Mater Process Technol 282:116691
6. Otsu M, Matsuo H, Matsuda M et al (2010) Friction stir incremental forming of aluminum alloy sheets. Steel Res Int 81:942–945
7. Kim WY, Matsumoto R, Utsunomiya H (2017) Deformation and density change of open-cell nickel foam in compression test. Mater Trans 58:1373–1378

# Interface Damage and Delamination Behaviour Prediction of HAp Coating in Artificial Femoral Stem Component of Total Hip Replacement

**R. Holim, M. Nagentrau, and N. R. Rajendran Royan**

**Abstract** The application of artificial joints is rapidly growing in most of the developed countries due to rapid ageing of population. Present study addresses the interface damage and delamination behaviour of hydroxyapatite (HAp) coating on Ti-6Al-4V artificial femoral stem component using cohesive zone modelling (CZM) approach. A simple two-dimensional flat-on-flat contact configuration finite element model consist of contact pad (bone), Ti-6Al-4V substrate and HAp coating is employed throughout the study. The influence of various parameters such as coating thickness, bone elastic modulus, coefficient of friction (COF) and implant elastic modulus subjected to different stress ratios on HAp coating delamination behaviours is focused. The outcome of the finite element analysis clearly indicates that higher bone elastic modulus with lower friction coefficient, coating thickness and artificial implant elastic modulus results in significant interface damage and delamination.

**Keywords** Artificial joints · Delamination · Interface damage · HAp · Ti-6Al-4V

## 1 Introduction

Hip may be vulnerable to some medical conditions such as osteoarthritis [1, 2]. Osteoarthritis is one of the most common forms of arthritis, which is a progressive disorder medical condition that is potentially affecting millions of ageing people worldwide [3, 4]. In order to solve this issue, the utilization of various artificial joints (such as hip joints, knee joints, etc.) has been continuously increasing due to the rapid ageing of population in most of the developed countries [5]. The artificial joints are mainly made up of titanium alloy due to its interesting properties such as

R. Holim · N. R. Rajendran Royan
School of Engineering, UOW Malaysia KDU University College, Shah Alam, Malaysia

M. Nagentrau (✉)
School of Engineering, Faculty of Innovation and Technology, Taylor's University, Taylor's Lakeside Campus, Subang Jaya, Selangor, Malaysia
e-mail: nagentrau.rau17@yahoo.com

the high strength, lightweight, corrosion resistance and good biocompatibility which confirms it as one of the most appropriate materials for artificial joint application [6].

There is a great requirement for a suitable coating material to promote the bond between bone and titanium alloy artificial implants [7]. Hydroxyapatite (Hap:$Ca_{10}(PO_4)_6(OH)_2$) is widely used in biomedical field to promote the bond between artificial implants and bone [8]. Plasma-sprayed Hydroxyapatite (HAp) coating is a bioceramic material that contains main composition of a human bone [9]. Furthermore, HAp coating is promising material as it could promote the bone tissue ingrowth as well [10]. The long-term usage of HAp coating is still a challenging problem as its efficiency is affected [8]. HAp coating can experience failure due to brittle fracture, fatigue cracks, wear by fretting or corrosion and, etc. [6]. Fretting fatigue in the artificial femoral stem component due to human activities will lead to HAp coating through thickness crack until the interface as HAp coating contains microspores. Next, interface damage and delamination will be initiated. Delamination is known as one of the most common failure modes in coated substrates [11]. The delaminated interface which is subjected to contact slip and contact pressure can accelerate the fretting wear behaviour of HAp coating. Moreover, fretting wear powders mixed with body fluid can cause activation of inflammation at the surrounding organs, loosening of implants or subsequent failures that can lead to revision surgery. The revision surgery is costly and can risk the life of the patient.

This paper addresses the interface damage and delamination behaviour at HAp-Ti-6Al-4V interface of artificial femoral stem components using cohesive zone modelling finite element methodology. The influence of HAp coating thickness, bone elastic modulus, coefficient of friction (COF) and implant elastic modulus subjected to different stress ratios on interface damage and delamination behaviour will be examined.

## 2 Material

Ti-6Al-4V and HAp materials are assigned as substrate and coating in present study. Meanwhile, PU foam material as a contact pad is allocated to represent human bone. The material properties that are utilized throughout this research is presented in Table 1. There is total of six cohesive element properties are assigned to represent damage behaviour of HAp-Ti-6Al-4V interface in terms of interfacial strength, energy release rate and interface stiffness in normal and shear directions as shown in Table 2.

**Table 1** FE simulation material properties data

| Material | Young's modulus, $E$ (GPa) | Poisson's ratio, $v$ |
|---|---|---|
| Bone (contact pad) | 0.1–20 | 0.35 |
| HAp coating | 70 | 0.24 |
| Ti-6Al-4V | 110 | 0.33 |

**Table 2** Cohesive element properties

| $t_N^0$ (MPa) | $t_\tau^0$ (MPa) | $G_N^c$ (mJ/mm$^2$) | $G_\tau^c$ (mJ/mm$^2$) | $K_N$(MPa/mm) | $K_\tau$(MPa/mm) |
|---|---|---|---|---|---|
| 12 | 12 | 0.0453 | 0.0453 | 85,000 | 85,000 |

## 3  Finite Element (FE) Simulation Approach

Static finite element (FE) simulation model is created with ABAQUS Standard 6.13 to predict interface damage and delamination behaviour at HAp-Ti-6Al-4V interface. The FE model is modelled based on dog-bone specimen physical model which is widely utilized in fretting fatigue experimental test as shown in Fig. 1.

A two-dimensional 1/4 symmetric finite element model is modelled under plane strain conditions. The dimension of Ti-6Al-4V substrate, HAp coating and PU foam (contact pad) are 4 mm (w) × 2 mm (h), 3 mm (w) × 0.15 mm (h) and 3 mm (w) × 4.5 mm (h), respectively. A cohesive layer (yellow line) in between HAp coating and Ti-6Al-4V substrate is introduced to represent interface. The created parts are then portioned to assign material sections and allocate materials properties along with mesh optimization. The complete assembly of FE model with loading and boundary conditions is shown in Fig. 2.

The displacement and rotational movements of bottom and lateral regions are restricted in the *y*-axis and *x*-axis, respectively. Additionally, tie constraints for HAp-PU foam (contact pad) and HAp-Ti-6Al-4V interface are introduced to represent
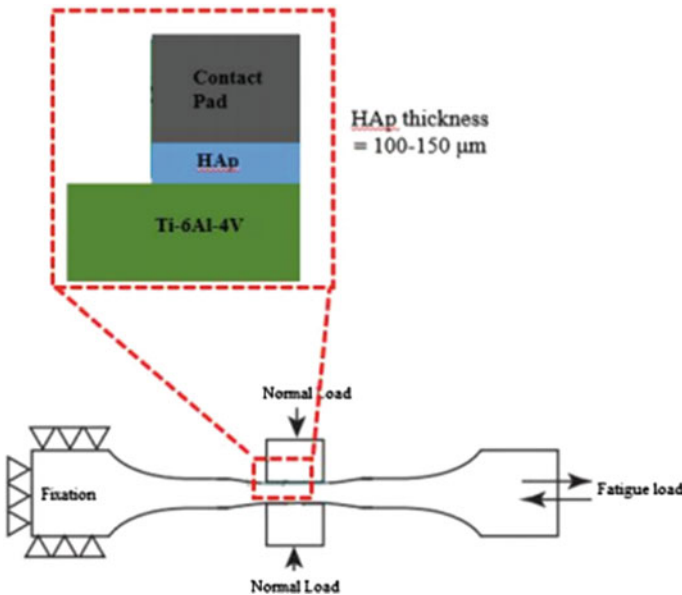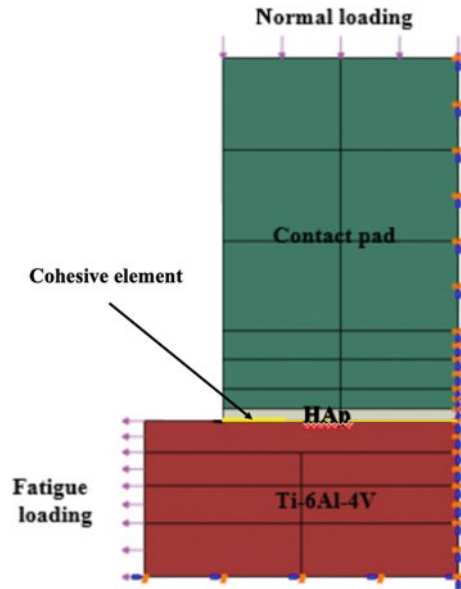


**Fig. 1** Schematic view of contact configuration model

**Fig. 2** FE model with
loading and boundary
conditions



perfect adhesion without any surface slippage to occur. For both interfaces, the former
is designated as the slave and the later is designated as the master surface using
the Lagrangian multiplier contact algorithm. Friction coefficient for HAp-PU foam
(contact pad) and HAp-Ti-6Al-4V interface are set as 0.4 and 0.7, respectively [12–
14]. The finite element mesh module is illustrated in Fig. 3. Linear quadrilateral plane
strain element is assigned via edge seed approach with refinement from coarse to fine
elements towards the contact region. The appropriate element size of 0.05 mm$^2$ at
contact region and 0.01 mm$^2$ at cohesive elements are assigned. The optimized mesh
with proper mesh transition is to ensure inexpensive computational time without
degrading the accuracy of the FE results [15–17].

Static simulation is executed by utilizing static general step with one (1) second
time period and hundred (100) maximum increments. Normal loading (Step-1),
maximum fatigue loading (Step-2) and minimum fatigue loading (Step-3) are applied
accordingly. The applied stress for normal loading, maximum fatigue loading and
minimum fatigue loading are 20 MPa, 550 MPa and 55 MPa, respectively. This
loading condition represents the artificial femoral stem component stress state when
subjected to various human activities and movement. Among the range of parame-
ters that have been assigned in present simulation are HAp coating thickness (0.05–
0.3 mm), stress ratio ($R = 0.1, R = -1, R = 10$), porous bone elastic modulus (0.2–1
GPa), cortical bone elastic modulus (5–10 GPa), coefficient of friction (0.3–0.7) and
implant elastic modulus (110–250 GPa). The interface damage and delamination
results are extracted using path-line technique. Predicted interface damage (SDEG)
reached the value of 1 when delamination is initiated.

**Fig. 3** FE mesh module
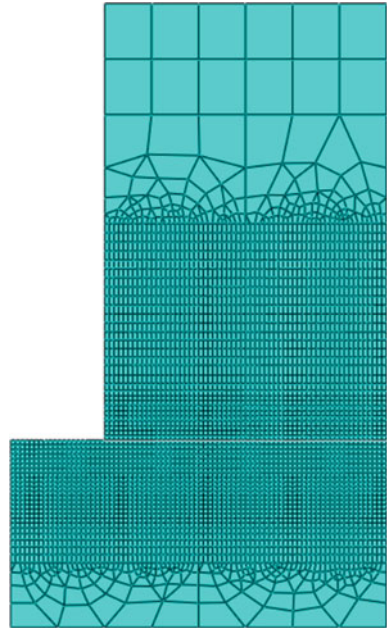


## 4 Results and Discussion

### 4.1 FE Model Validation

FE model validation of interface damage and delamination behaviour at HAp-Ti-6Al-4V interface is performed by comparing with reported experimental result of plasma-sprayed HAp coating on Ti-6Al-4V alloy [6]. Present cohesive zone FE model validated with reported experimental SEM image as shown in Fig. 4. Good agreement is achieved between present cohesive zone model and experimental result as simulation result clearly revealed that delamination is initiated at contact edge.

### 4.2 The Influence of Coating Thickness

Figure 5 illustrates the effect of coating thickness on interface damage and delamination under different stress ratios. The results revealed that HAp all the coating thickness cases experience significant interface damage and delamination near the contact edge region. Higher interface damage and delamination is recorded for least coating thickness (0.05 mm) meanwhile no delamination is observed for coating thickness (0.3 mm) under all three types of stress ratios. Moreover, minimal interface damage is registered at the contact edge region for $R = 0.1$ and $R = -1$ and no
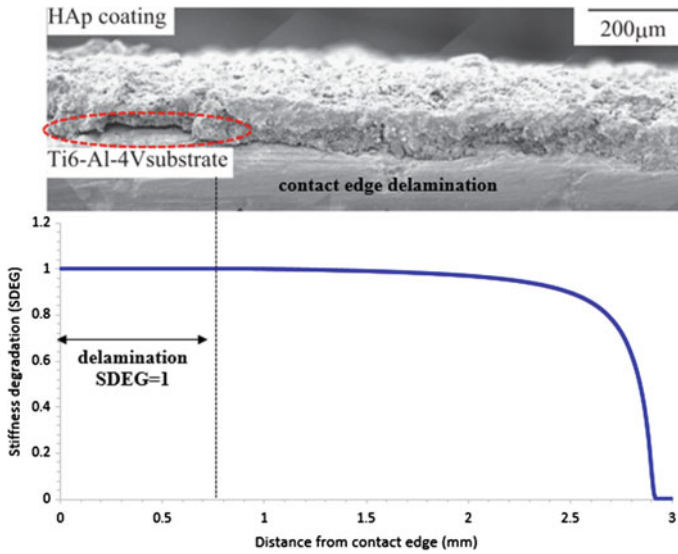
**Fig. 4** Predicted interface and delamination of FE model validation

interface damage is experienced for $R = 10$. This clearly indicates interface damage and delamination is significant in compressive loading compared to tensile loading.

## 4.3   The Influence of Porous Bone Elastic Modulus

Figure 6 shows the effect of porous bone elastic modulus on interface damage and delamination under different stress ratios. The maximum interface damage is recorded at the contact edge for all cases. The higher porous elastic bone modulus (1 GPa) results in significant interface damage and delamination initiation. Similar trend is observed for all the stress ratio cases and again compressive type of loading condition results in noteworthy interface damage and delamination compared to tensile loading.

## 4.4   The Influence of Cortical Bone Elastic Modulus

Figure 7 exhibits the effect the cortical bone elastic modulus on interface damage and delamination under different stress ratios. The findings are quite revealing that significant interface damage is registered at contact edge. The higher cortical bone
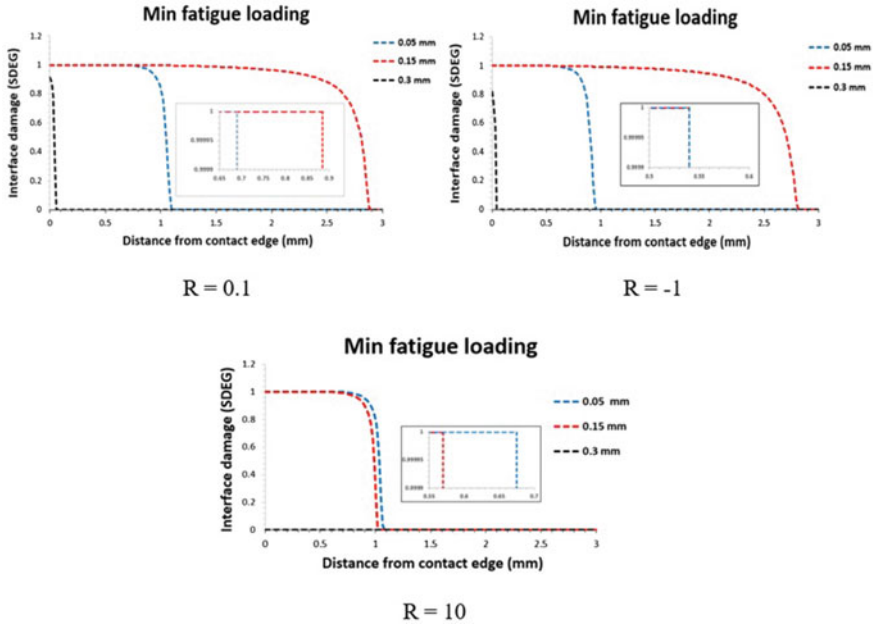
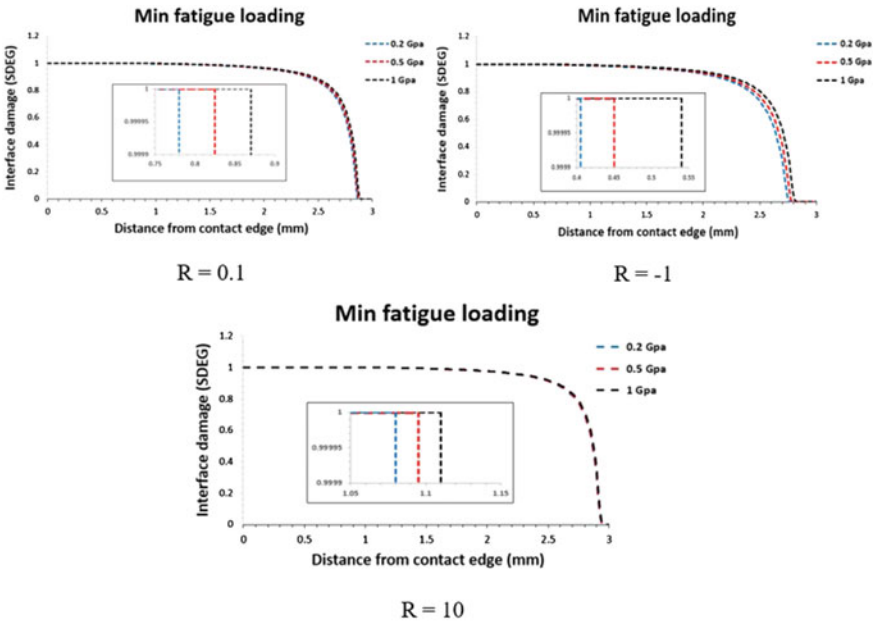**Fig. 5** Effect of coating thickness on interface damage and delamination under different stress ratios



**Fig. 6** Effect of porous bone elastic modulus on interface damage and delamination under different stress ratios
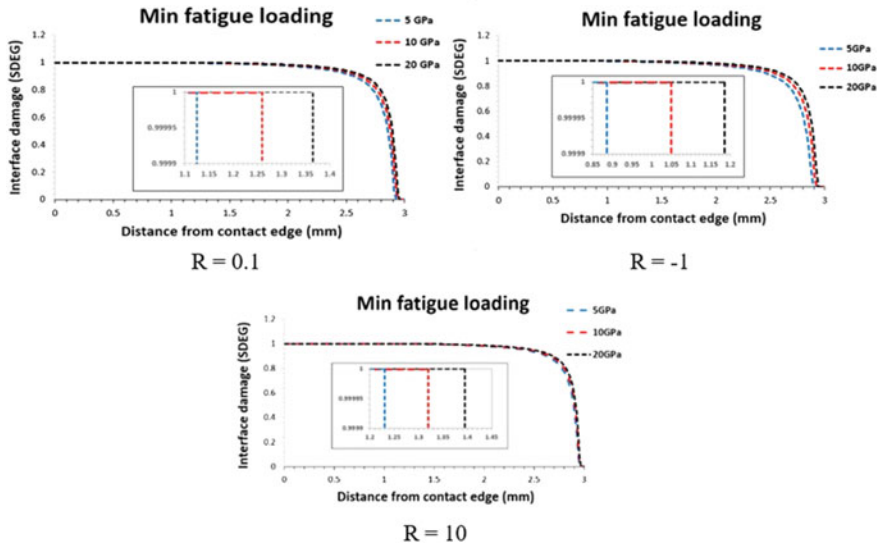
**Fig. 7** Effect of cortical bone elastic modulus on interface damage and delamination under different stress ratios

elastic modulus (20 GPa) results in higher interface damage and delamination initiation for all the stress ratio cases. The compressive type loading ($R = 10$) registered higher delamination length compared to tensile loading ($R = 0.1$ and $R = -1$).

## 4.5  The Influence of Friction Coefficient

Figure 8 illustrates the effect of coefficient on interface damage and delamination under different stress ratios. The findings clearly show significant interface damage and delamination is noted at the contact edge region. Lower coefficient of friction (0.3) shows high interface damage and delamination initiation compared to higher COF values for all stress ratio conditions. The compressive type of loading ($R = 10$) exhibits significant interface damage and delamination compared to tensile loading cases.

## 4.6  The Influence of Hip Implant Material

Figure 9 displays the effect of implant material on interface damage and delamination under different stress ratios. The higher elastic modulus implant material (Co–Cr alloys) results in insignificant interface damage and delamination initiation compared
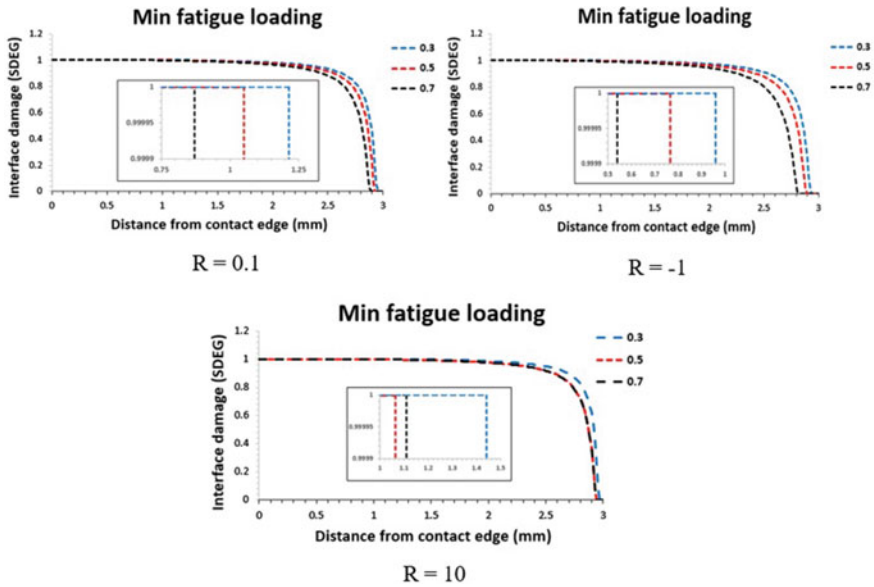
**Fig. 8** Effect of friction coefficient on interface damage and delamination under different stress ratios

to lower elastic modulus implant material (Ti-6Al-4V). To delamination, initiation is registered for Co–Cr and Stainless alloys for all stress ration conditions. Meanwhile, noteworthy delamination is recorded for Ti-6Al-4V in compressive loading cases ($R = 10$).

## 4.7 Discussion

The findings clearly reveal that significant interface damage and delamination are registered at contact edge for all conditions of stress ratio due to stress singularity effect sharp contact edge experiencing higher magnitude of contact pressure and shear stress. In addition, HAp-Ti-6Al-4V interface experiencing combined normal loading and compressive fatigue loading which promotes interface traction to initiate interface damage and delamination compared to tensile loading cases. Higher HAp coating thickness cases experiencing through thickness stress distribution and prevent the stress focused at the interface region. This is clearly evident from least interface damage and delamination initiation is recorded for thick coatings.

Meanwhile, higher bone elastic modulus for both porous and cortical cases record significant interface damage and delamination initiation as stress relaxation conditions. Stress relaxation condition is due to reduced elastic mismatch between HAp coating and Ti-6Al-4V substrate which significantly increases the slip amplitude at
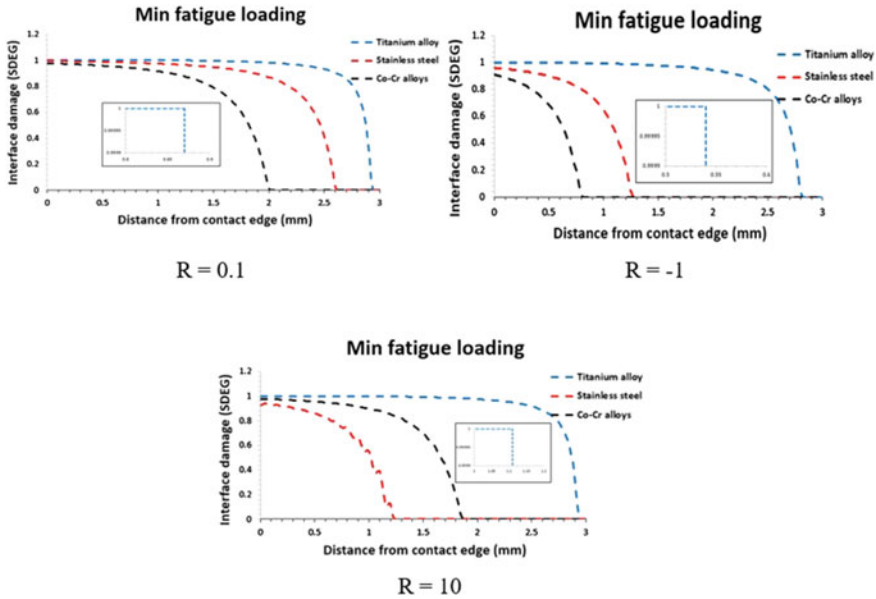
**Fig. 9** Effect of implant material on interface damage and delamination under different stress ratios

interface region. The higher coefficient of friction exhibits least interface damage and delamination initiation as it promotes stick behaviour at interface which minimizes slip behaviour which can lead to delamination initiation. Last but not least, Ti-6Al-4V implant material is less stiff compared to stainless steel and Co–Cr alloy. Thus, lower contact pressure is experienced at interface of HAp-Ti-6Al-4V which demotes stick behaviour along with promotes slip and leads to significant interface damage and delamination initiation.

## 5 Conclusions

The influence of different HAp coating thickness, porous bone modulus, cortical bone modulus, coefficient of friction and hip implant elastic modulus on interface damage and delamination behaviour at HAp-Ti-6Al-4V interface under different stress ratio conditions is analyzed in this FE simulation. The predicted finite element (FE) analysis results allow following conclusion as below:

- Significant interface damage is recorded at the contact edge region due to the stress singularity at sharp edge contact.
- Higher porous and cortical bone elastic modulus results in significant interface damage and delamination initiation.

- Lower friction coefficient, coating thickness and artificial implant elastic modulus results in significant interface damage and delamination.

# References

1. Sato T, Sato N (2015) Clinical relevance of the hip joint: Part I—Review of the anatomy of the hip joint. Int Musculoskeletal Med 37(4):141–145
2. Lespasio MJ, Sultan AA, Piuzzi NS, Khlopas A, Husni ME, Muschler GF, Mont A (2018) Hip osteoarthritis: a primer. Permanente J 22:89–94
3. Sheridan GA, Cashman J (2018) Osteoarthritis of the hip joint. Intech 32:137–144
4. Ray M (2017) Knee osteoarthritis psychological complication: an important overlooked disease correlate. Novel Tech Arthritis Bone Res 1(4):1–11
5. Sivasankar M, Arunkumar S, Bakkiyaraj V, Muruganandam A, Sathishkumar S (2016) A review on total hip replacement. Int Res J Adv Eng Technol 589–642
6. Otsuka Y, Kawaguchi H, Mutoh Y (2016) Cyclic delamination behavior of plasma-sprayed hydroxyapatite coating on Ti-6Al-4V substrates in simulated body fluid. Mater Sci Eng C 67:533–541
7. Otsuka Y, Miyashita Y, Mutoh Y (2016) Effects of delamination on fretting wear behaviors of plasma-sprayed hydroxyapatite coating. Japan Soc Mech Eng 3(2):1–11
8. Nagentrau M, Tobi ALM, Jamian S, Otsuka Y (2019) Contact slip prediction in HAp coated artificial hip implant using finite element analysis. Mech Eng J 6(3):1–10
9. Otsuka Y, Miyashita Y, Mutoh Y (2016) Effects of delamination on fretting wear behaviors of plasma-sprayed hydroxyapatite coating. Mech Eng J 3(2):15–00573
10. Laonapakul T, Rakngarm Nimkerdphol A, Otsuka Y, Mutoh Y (2012) Failure behavior of plasma-sprayed HAp coating on commercially pure titanium substrate in simulated body fluid (SBF) under bending load. J Mech Behav Biomed Mater 15:153–154
11. Saeedifar M, Ahmadi Najafabadi M, Yousefi J, Mohammadi R, Hosseini Toudeshky H, Minak G (2017) Delamination analysis in composite laminates by means of Acoustic Emission and bi-linear/tri-linear Cohesive Zone Modeling. Compos Struct 161:505–512
12. Shockey JS, Von Fraunhofer JA, Seligson D (1985) A measurement of the coefficient of static friction of human long bones. Surface Technol 25(2):167–173
13. Nagentrau M, Tobi AM, Jamian S, Otsuka Y, Hussin R (2021) Delamination-fretting wear failure evaluation at HAp-Ti-6Al–4V interface of uncemented artificial hip implant. J Mech Behavior Biomed Mater 104657
14. Nagentrau M, Tobi ALM, Jamian S, Otsuka Y (2020) HAp coated hip prosthesis contact pressure prediction using FEM analysis. In: Materials science forum, vol 991. Trans Tech Publications Ltd, pp 53–61
15. Siswanto WA, Nagentrau M, Tobi AM, Tamin MN (2016) Prediction of plastic deformation under contact condition by quasi-static and dynamic simulations using explicit finite element analysis. J Mech Sci Technol 30(11):5093–5101
16. Nagentrau M, Siswanto WA, Tobi M, Latif A (2016) Predicting the sliding amplitude of plastic deformation in the reciprocating sliding contact. ARPN J Eng Appl Sci 11(4):2266–2271
17. Siswanto WA, Nagentrau M, Tobi M, Latif A (2015) Prediction of residual stress using explicit finite element method. J Mech Eng Sci 9:1556–1570

# Mechanical Properties of Injection-Molded Poly-Lactic Acid (PLA) Reinforced with Magnesium Hydroxide for Biomedical Application

**Nashrah Hani Jamadon, Mohd Azwan Ahmad, Hanis Najiah Mohd Fuad, and Sharifah Adzila**

**Abstract** The combination of poly-lactic acid/magnesium hydroxide (PLA/Mg(OH)$_2$) with low weight, biodegradability, and favorable mechanical properties make it an ideal material for a biomedical application. In this work, the combination of these two materials was carried out using the injection molding method. Different parameters of 100% PLA, 99% PLA/1% Mg(OH)$_2$, 98.5% PLA/1.5% Mg(OH)$_2$ and 98% PLA/2% Mg(OH)$_2$ were employed. The characterization of PLA/Mg(OH)$_2$ biocomposite was studied using Fourier Transform Infrared Spectrometry (FTIR) to identify the functional groups of the composition. The mechanical properties were determined through the three-point flexural test and Charpy Impact test. The results show that the flexural and Charpy Impact strength of the composites increases with the addition of 1wt% of Mg(OH)$_2$ into the PLA matrix. However, different conditions were observed at the higher rate of Mg(OH)$_2$ (2wt%) in which decreased the flexural strength and impact strength of the PLA. This result is supported by sample autopsy through SEM and EDS. Based on all findings, it can be concluded that the combination of PLA/Mg(OH)$_2$ had produced a positive outcome and can be used as one of the biomedical resources in bone implant application.

**Keywords** Poly-lactic acid · Magnesium hydroxide · Injection molding · Mechanical properties

N. H. Jamadon
Department of Mechanical and Manufacturing Engineering, Faculty of Engineering and Built Environment, Universiti Kebangsaan Malaysia (UKM), 43600 Bangi, Selangor, Malaysia
e-mail: nashrahhani@ukm.edu.my

M. A. Ahmad
Department of Environmental Health, Faculty of Health Sciences, Mahsa University, 42610 Jenjarom, Selangor, Malaysia
e-mail: m.azwan@yahoo.com

H. N. M. Fuad · S. Adzila (✉)
Department of Manufacturing Engineering, Faculty of Mechanical Engineering and Manufacturing, Universiti Tun Hussein Onn Malaysia (UTHM), 86400 Batu Pahat, Johor, Malaysia
e-mail: adzila@uthm.edu.my

# 1   Introduction

In recent years, the advanced technologies in the medical field in utilizing bioma-
terials for the restoration of damaged tissue and organ has become world attention
[1–3]. These materials were used to supplant a segment of the physiological func-
tions of the support or the human body. Biomaterials interrelate with human cells,
tissues, or organs and occasionally perform their roles [4, 5]. Due to the advancement
of human understanding of the biological qualities desired in a biomedical material,
novel material features are being discovered on a regular basis to restore various
infections and so maximize human life quality [6, 7].

Biomaterial assembly is typically an essential subject for improving reliability,
reducing the risk of body rejection, increase the quality of life and longevity of
human beings [8]. In another study on biocompatible material for medical implants,
they have successfully proved that the combination of graphene oxide (GO) with
hydroxyapatite (HA) was able to stimulate the adsorption of protein fibronectin
on the GO-HA surface. This result suggested that the combination of GO-HA can
accelerate the adhesion, proliferation, and produce more significant interaction with
proteins to yield biomaterials that have high biocompatibility for future implantation
applications [9]. Several studies have been conducted to evaluate the efficacy of
reinforced natural fiber polymer composites in a variety of fields [10, 11]. Several
treatments have recently been developed to improve interfacial bonding, mechanical
properties, and water resistance of natural fibers [12, 13].

Poly-lactic acid or PLA is one of the most synthetic polymers regularly used
in the biomedical field [14]. The main advantages of using PLA for biomedical
applications is due to its properties such as flexibility, biodegradability, biocompat-
ibility, and minimal side effects [15]. PLA can be degraded to lactic acid through
hydrolysis as a natural intermediate in the metabolism of carbohydrates and has
excellent biocompatibility and mechanical [16]. Magnesium hydroxide, on the other
hand, is a basic inorganic compound with the chemical formula hydrated $Mg(OH)_2$
[17]. It may be utilized to reinforce the PLA, which is a critical aspect in achieving
successful mechanical properties improvement. However, the high concentration
of $Mg(OH)_2$ may impair the final composite material's mechanical performance
[18]. In this study, the use of poly-lactic acid (PLA) based composite reinforced
with magnesium hydroxide, $Mg(OH)_2$ composite for biomedical application will be
studied.

# 2   Methods

In this work, the Poly-lactic acid (PLA) was used as a matrix and magnesium
hydroxide $(Mg(OH)_2)$ as a reinforcement. Both of material were categorized into
difference types of parameter, such as 100% PLA, 99% PLA/1% $Mg(OH)_2$, 98.5%
PLA/1.5% $Mg(OH)_2$ and 98% PLA/2% $Mg(OH)_2$. The raw material of PLA and

Mg(OH)$_2$ was in pellets and powder form. The blend composition with Mg(OH)$_2$ ratios of 100/0, 99/1, 98.5/1.5, and 98/2.0, respectively, were prepared by mixing the two powders in two roll mills at 190°C with the speed of 570 rpm followed by crushing the compound into pellets. After that, Nissei Injection Molding machine was utilized to fabricate PLA/Mg(OH)$_2$ composites with Mg(OH)$_2$ contents of 0, 1, 1.5 and 2wt%. The rectangle-shaped bar for flexural test and the notched rectangle-shaped bar for impact test was fabricated by injection molding. The fabrication of the composite was taken at 190°C. The mechanical tests were carried out on the samples included three-point flexural test and Charpy Impact test. The FTIR (Perkin-Elmer Spectrum 2000, USA) machine was used to determine and identify the chemical compositions in the mixed compound at a resolution of 4 cm$^{-1}$. The SEM (Hitachi VP-SEM SU1510, Tokyo, Japan) machine was then used to identify the microstructure of PLA/Mg(OH)$_2$ biocomposite after undergoes the impact test.

## 3 Results and Discussions

### 3.1 Fourier Transform Infrared Spectrometry

In this experiment, the Fourier Transform Infrared Spectroscopy (FTIR) was utilized to identify the functional group element in the PLA/Mg(OH)$_2$ composite with four distinctive types of parameters and the region wave number that was used and measured in the range of 4000–600 cm$^{-1}$. The resolution used was 4 cm$^{-1}$.

Figure 1a shows the consequence for pure PLA sample. According to Fig. 1, 1453.22 cm$^{-1}$ showed the bending vibration of OH- bond. The bands located at 2947 cm$^{-1}$ representing stretching vibrations of C-H bond. While, at the peak of 1747.49 cm$^{-1}$ representing carbonyl group (C = O), and at a range of 1181.23 to 1042.34 cm$^{-1}$, the bands representing carbon-carbonyl-oxygen (C–CO-O) group. Moreover, a sharp peak was observed at wavenumber of 1082.98 cm$^{-1}$ representing the oxygen-carbon-carbonyl (O-C–CO). Figure 1b represents the result for the composition of 100% magnesium hydroxide (Mg(OH)$_2$) powder. From the result, strong sharp peak can be observed at 3695.09 cm$^{-1}$ and small peak at 1473 cm$^{-1}$ that indicates the presence of hydroxyl (OH-) group which is OH- antisymmetric stretching vibration in the composite. Figure 1 (c) demonstrates the graph for all compositions on FTIR examination in this research study. All the compositions of PLA composite with different compositions of Mg(OH)$_2$ which are 99% PLA/1% Mg(OH)$_2$, 98.5% PLA/1.5% Mg(OH)$_2$, and 98% PLA/2% Mg(OH)$_2$ has observed the bending vibration of OH- bond at small peak of 1451.53, 1455.59, 1452.19 and at 1473 cm$^{-1}$.

Based on the results, the presence of hydroxyl (OH-), hydrocarbon (C-H), carbonyl (C = O), carbon-carbonyl-oxygen (C–CO-O) and oxygen-carbon-carbonyl (O-C–CO) groups in 99% PLA/1% Mg(OH)$_2$, 98.5% PLA/1.5% Mg(OH)$_2$ and
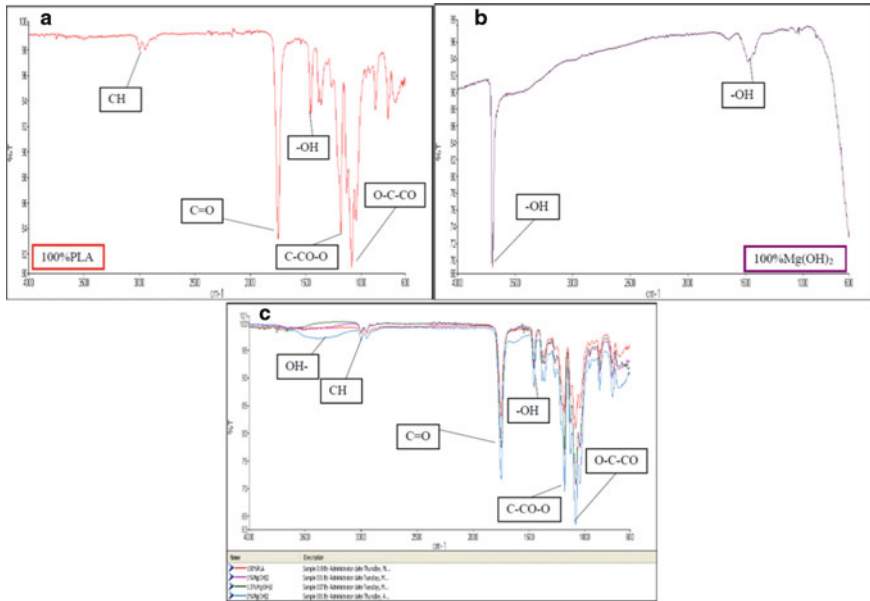
**Fig. 1** FTIR results of **a** PLA 100%, **b** Mg(OH)$_2$ powder and **c** of PLA/Mg(OH)$_2$ composite on FTIR

98% PLA/2% Mg(OH)$_2$ shows the dispersion between the PLA matrix and the reinforcement.

## 3.2 Mechanical Testing

### 3.2.1 Three-Point Flexural Test

Figure 2 shows the flexural strength for the PLA and PLA/Mg(OH)$_2$ composites. The introduction of magnesium hydroxide powder into PLA significantly increased the impact strength of the composites. The flexural strength for 100% PLA, 99% PLA/1% Mg(OH)$_2$, 98.5% PLA/1.5% Mg(OH)$_2$ and 98% PLA/2% Mg(OH)$_2$ samples are 9.78, 10.28, 9.76 and 9.12 MPa accordingly. The addition of 1% of magnesium hydroxide increased the strength by 0.5 MPa. However, further addition of magnesium hydroxide to PLA blends decreased the strength of PLA. This outcome is due to the brittle properties of magnesium hydroxide. The results of the flexural strength of PLA/Mg(OH)$_2$ composites are comparable with the previous findings of PP/Mg(OH)$_2$ composites by Liang et al. [19].

**Fig. 2** Flexural strength of
PLA/Mg(OH)$_2$ composites
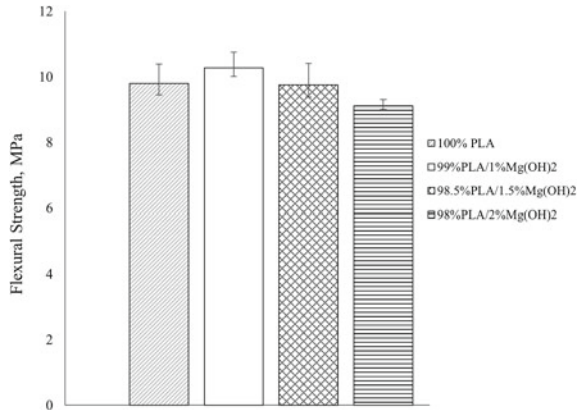


### 3.2.2 Impact Test

Figure 3 shows the Charpy notched impact strength for the PLA and PLA/Mg(OH)$_2$
composites. Under impact, the mechanical properties of composites are better than
that of pure PLA. The introduction of magnesium hydroxide powder into PLA signif-
icantly increases the impact strength of the composites. Pure PLA sample exhibits
the lowest impact strength among all, which is 0.097 J/m. The addition of 1wt% of
magnesium hydroxide increases the strength by 0.003 J/m. The impact strength for
99% PLA/1% Mg(OH)$_2$, 98.5% PLA/1.5% Mg(OH)$_2$ and 98% PLA/2% Mg(OH)$_2$
samples are 0.13, 0.12 and 0.11 J/m, respectively. The best behavior is detected
when the content of Mg(OH)$_2$ is 1wt%. At higher contents, 1.5 and 2wt%, compos-
ites properties decreased in comparison to 1wt%. Nevertheless, the impact strength
of PLA/Mg(OH)$_2$ is higher compared to that of pure PLA.

**Fig. 3** Charpy Impact
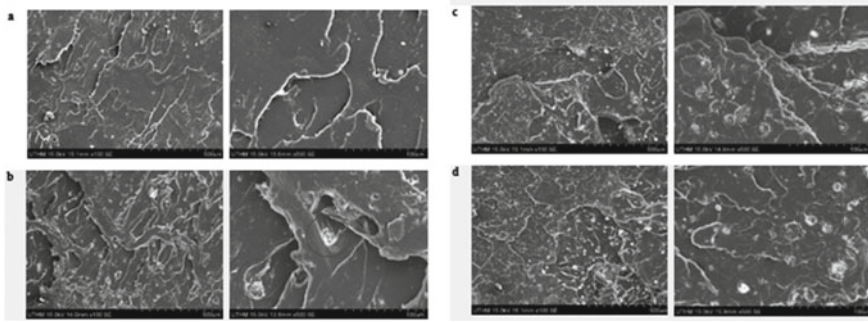strength of PLA/Mg(OH)$_2$
composites
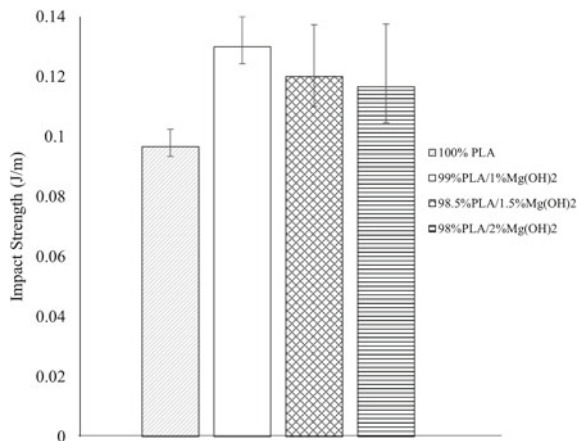
**Fig. 4** SEM images of fracture surface PLA composites; **a** 100% PLA, **b** 99% PLA/1% Mg(OH)$_2$, **c** 98.5% PLA/1.5% Mg(OH)$_2$, and **d** 98% PLA/2% Mg(OH)$_2$

## 3.3 Scanning Electron Microscope (SEM)

Scanning Electron Microscope (SEM) Hitachi VP-SEM SU1510 machine was used to analyze the morphology of fracture surfaces of PLA/Mg(OH)$_2$ composites. The samples were coated with gold (Au) to reduce the charging effect and for better visualization. SEM images of fracture surfaces with the magnification of 100X and 500X with an accelerating voltage of 15.0 kV were captured.

Figure 4 shows the SEM images captured after the PLA composites undergo the impact test. The fracture surface of the specimens was captured and analyzed. The contrast and boundaries of PLA matrix and Mg(OH)$_2$ reinforcement is obviously can be seen. Based on the observation, it shows that in 1wt%, 1.5wt %, and 2wt%, agglomeration of the magnesium hydroxide particles were detected. As the number of fillers increased, more agglomeration in the composite can be seen. The agglomeration shows the spectrum of magnesium, Mg, and oxygen, O$_2$.

The micrographs obtained also indicate that the magnesium particulates are homogeneously dispersed on the fractured surfaces of the polymer matrix. In addition, the findings can be supported by similar research on magnesium composite. The micrograph images show that this kind of particles has a tendency to form agglomerates.

Figure 5 shows the EDS analysis on PLA composites undergoes the impact test. Based on the results obtained from EDS analysis, the existence of C, Mg, and O$_2$ is confirmed in the PLA/Mg(OH)$_2$ composites. These existing elements refer to the composition of poly-lactic acid and magnesium hydroxide. It is noted that the reaction of Mg element with the CO$_3$ group in solution had formed the Mg(OH)$_2$ composites. Meanwhile, for the pure PLA sample, the EDS analysis indicated the absence of magnesium hydroxide, but some foreign elements were detected in the composites. This may happen due to the presence of foreign materials during the material preparation process. However, the existence of the foreign elements is neglected.
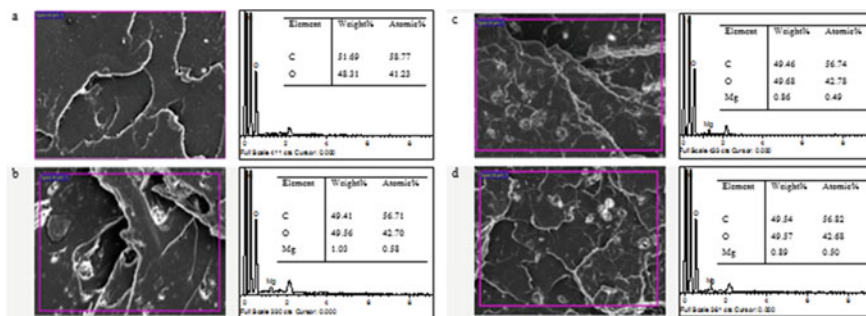
**Fig. 5** EDS analysis on PLA composites; **a** 100% PLA, **b** 99% PLA/1% Mg(OH)$_2$, **c** 98.5% PLA/1.5% Mg(OH)$_2$, **d** 98% PLA/2% Mg(OH)$_2$

## 4 Conclusions

The characterization analysis of PLA/Mg(OH)$_2$ biocomposite by FTIR shows the presence of hydroxyl (OH-), hydrocarbon (C-H), carbonyl (C = O), carbon-carbonyl-oxygen (C–CO-O) and oxygen-carbon-carbonyl (O-C–CO) groups that proved the presence of poly-lactic acid and magnesium hydroxide. Both flexural and impact test results show that the addition of 1wt% of magnesium hydroxide into the poly-lactic acid matrix improves the mechanical strength. The obvious boundaries and contrast between the poly-lactic acid and magnesium hydroxide can be observed throughout the SEM experiment. The SEM images of composites consist of agglomeration of magnesium hydroxide at some places, and this was proven by using EDS analysis. The EDS analysis shows that the agglomeration includes magnesium, Mg and oxygen, and O$_2$ elements that indicate the formation of magnesium hydroxide.

## References

1. Lah NAC, Hussin MH (2019) Titanium and titanium based alloys as metallic biomaterials in medical applications—spine implant case study
2. George P, Hamid ZA, Zakaria MZAB et al (2019) A short review on cockle shells as biomaterials in the context of bone scaffold fabrication. Sains Malaysiana 48:1539–1545
3. Fadilah NIM, Isa ILM, Zaman WSWK et al (2022) The effect of nanoparticle-incorporated natural-based biomaterials towards cells on activated pathways: a systematic review. Polymers (Basel) 14:476
4. Cassady, AI, Hidzir NM, Grøndahl L (2014) Enhancing expanded poly(tetrafluoroethylene) (ePTFE) for biomaterials applications. J Appl Polym Sci 131

5. Bhi, R (2014) Biocompatibility screening of biomaterials for bone tissue engineering—study of the osteogenic cell morphology 3:171–172
6. Morshed M, Chowdhury BR, Latif JY et al (2014) The current available biomaterials being used for skin tissue engineering
7. Zawani M, Fauzi MB (2021) Epigallocatechin gallate: the emerging wound healing potential of multifunctional biomaterials for future precision medicine treatment strategies. Polymers (Basel) 13
8. Chozhanathmisra M, Pandian K, Govindaraj D et al (2019) Halloysite nanotube-reinforced ion-incorporated hydroxyapatite-chitosan composite coating on Ti-6Al-4 V alloy for implant application. J Chem 7472058
9. Che Hashim N, Sawal N, Mohamed Rafie SM et al (2018) Adsorption of Extracellular Matrix Protein Fibronectin on the Surface of the Nanocomposite Particle of Graphene Oxide-Hydroxyapatite. J Kejuruter SI1:15–25
10. Abdullah MSP, Noordin MI, Mohd Ismail SI et al (2018) Recent advances in the use of animal-sourced gelatine as natural polymers for food, cosmetics and pharmaceutical applications. Sains Malaysiana 47:323–336
11. Nurazzi NM, Asyraf MRM, Fatimah Athiyah S, Shazleen SS, Rafiqah SA, Harussani MM, Kamarudin SH, Razman MR et al (2021) A review on mechanical performance of hybrid natural fiber polymer composites for structural applications. Polymers (Basel) 13:1–47
12. Ilyas RA, Sapuan SM, Harussani MM et al (2021) Polylactic acid (Pla) biocomposite: processing, additive manufacturing and advanced applications. Polymers (Basel) 13
13. Anita Lett J, Sagadevan S, Fatimah I et al (2021) Recent advances in natural polymer-based hydroxyapatite scaffolds: properties and applications. Eur Polym J 148:110360
14. Abu Hassan NA, Ahmad S, Chen RS (2020) Density measurement, tensile, and morphology properties of polylactic acid biocomposites foam reinforced with different kenaf filler loading. Sains Malaysiana 49:2293–2300
15. Virlan MJR, Miricescu D, Totan A et al (2015) Current uses of poly(lactic-co-glycolic acid) in the dental field: a comprehensive review. J Chem
16. Salem SA, Hwei NM, Bin Saim A et al (2013) Polylactic-co-glycolic acid mesh coated with fibrin or collagen and biological adhesive substance as a prefabricated, degradable, biocompatible, and functional scaffold for regeneration of the urinary bladder wall. J Biomed Mater Res A 101:2237–2247
17. Chen RS, Mohd Amran NA, Ahmad S (2019) Reinforcement effect of nanocomposites with single/hybrid graphene nanoplatelets and magnesium hydroxide: Thermal stability, flame retardancy and mechanical performance. J Therm Anal Calorim 137:79–92
18. Chen RS, Ahmad S (2020) Impact and fire resistance properties of polypropylene filled with graphene/Mg(OH)2 nanoparticles 1641–1645
19. Liang JZ (2017) Tensile and flexural properties of polypropylene composites filled with highly effective flame retardant magnesium hydroxide. Polym Test 60:110–116

# Development of Composite Aerostructure for UAV Application

**Shahrul Malek Faizsal Shahrul Hairi, Siti Juita Mastura Binti Mohd Saleh, Ahmad Hamdan, and Zamri Bin Omar**

**Abstract** Composite material offers excellent high strength-to-weight ratios suitable for UAV structure. This study aims to fabricate and analyse the synthetic fibre structure for the Universiti Tun Hussein Onn Malaysia Cargo Drone (C-Drone) landing gear. The quasi-static compression test was conducted on the S-glass fibre tube and aluminium alloy tube. The tubes with a dimension of 50 mm outer diameter, 3 mm thickness, and 150 mm height were tested on a universal testing machine (UTM). Both materials were compressed up to 30 mm at a 3 mm/min rate following the requirement in ASTM D-3410. The result shows that fibreglass with brittle properties can withstand an amount of load 35% lower and reduced weight up to 10% compared to aluminium alloy. This research proves that composite material such as glass fibre-reinforced plastic (GFRP) can substitute the current material, aluminium alloy 6061-T6, due to its extensive strength-to-weight ratio, low density, and reasonable price in the market.

**Keywords** Composite material · Glass fibre-reinforced plastic (GFRP) · C-Drone · UAV · Lightweight · Performances

## 1 Introduction

Much extensive research has been done to increase the performance, either increasing the payload or the flight time of the unmanned aerial vehicle (UAV). To achieve those performances, several materials such as carbon fibre-reinforced composites (CRFCs), biomaterial, glass fibre, and aluminium alloy have been applied not only for UAVs but also for aerospace and aeronautical. The materials focus on excellent strength-to-weight ratio, lightweight, and easy to shape into a complex part [1].

S. M. F. Shahrul Hairi · S. J. M. B. M. Saleh · A. Hamdan (✉) · Z. B. Omar
Faculty of Mechanical and Manufacturing Engineering, Universiti Tun Hussein Onn Malaysia (UTHM), Parit Raja, 86400 Batu Pahat, Johor Darul Takzim, Malaysia
e-mail: ahmadh@uthm.edu.my

S. J. M. B. M. Saleh · A. Hamdan
Research Centre for Unmanned Vehicle (ReCUV), Universiti Tun Hussein Onn Malaysia (UTHM), Parit Raja, 86400 Batu Pahat, Johor Darul Takzim, Malaysia

Composite materials can be defined as a material structure consisting of two macroscopically identifiable materials that work together to accomplish a superior result and consist of relatively strong, stiff fibres in a tough resin matrix and produce unique composite properties [2].

Universiti Tun Hussein Onn Malaysia (UTHM) took this opportunity to develop a cargo drone, as shown in Fig. 1a, whose structure is mainly made of aluminium alloy 6061-T6. The C-Drone was designed to carry a 180 kg payload. The weight of aluminium alloy 6061-T6 is too significant and could affect the flight time and reduce the weight of the payload. Lighter material was proposed, and this study was focused on the landing gear part, as in Fig. 1b.

For

Table 1, the glass fibre has an approximate range of between 100 to 328 MPa, nearly the same as aluminium alloy with lower density, which could be advantageous in reducing the weight with the same compressive strength. There is also research that shows that glass fibre can absorb energy higher, which is in between 10.84 and 11.43 J and also have the highest average Charpy impact test, which is between 260.34 and 285.70 kJ/m$^2$ compared to other composites such as carbon fibre and hybrid fibre [3].

In most of research reviews, the outputs cover only general applications. However, the application of composite for C-Drone application needs further investigation.
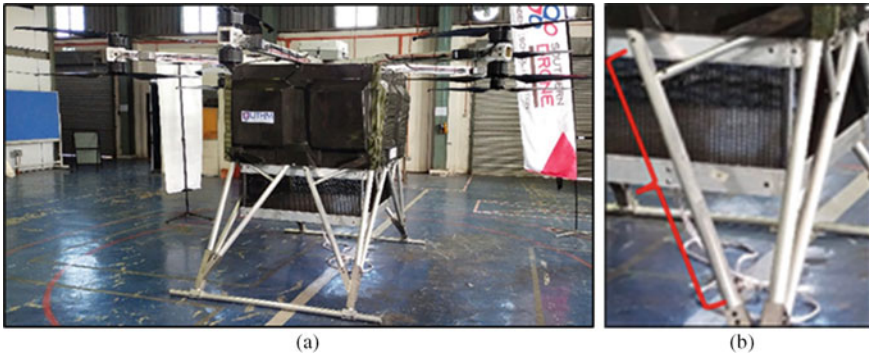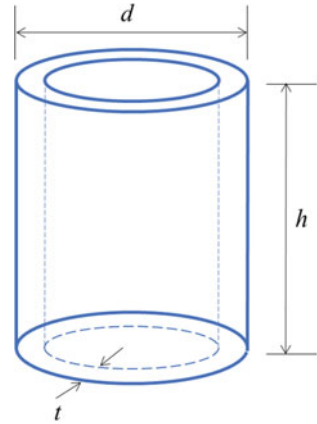


**Fig. 1** Picture of C-Drone, **a** Picture of the whole structure. **b** Landing gear of C-Drone UTHM labelled in red

**Table 1** Compressive strength of different material

| Material | Compressive strength, MPa | Reference |
|---|---|---|
| Carbon fibre | 396–869 | [4, 5] |
| Glass fibre | 100–328 | [5, 6] |
| Aluminium alloy 6061-T6 | 100–483 | [7] |

**Fig. 2** Schematic diagram
of the hollow tube



Therefore, this research investigates the quasi-static compression characteristics of composite material for C-Drone application.

## 2 Methods

Hollow tubes with a dimension of 50 mm outer diameter (*d*), 3 mm thickness (*t*) and 15 0mm height (*h*) as illustrated in Fig. 2 according to the ASTM D-3401 [8]. The Ez Dynamic Sdn. Bhd supplied the aluminium alloy 6061-T6 hollow tubes. The innovative Pultrusion Sdn. Bhd supplied the fibreglass tube hollow.

The samples were tested via universal testing machine (UTM) (manufactured by Daeyeong M.T.C Co) at Jamilus Research Centre, UTHM and the schematic diagram is illustrated in Fig. 3. The quasi-static compress test was set at 3 mm/min compress speed and up to 30 mm at a rate. The experiment was repeated three times to increase the precision of data obtained by having the average value for each material. The result of a load-displacement graph was plotted and recorded on the computer.

## 3 Results and Discussion

By comparing both results from Fig. 4, aluminium alloy tube has higher load can be exerted on the material which the peak load is 86.16 kN, while fibreglass tube only 53.98 kN which the percentage difference is approximately 35%. This happened due to the properties of the materials influencing the behaviour of graph which aluminium alloy is ductile while glass fibre is brittle.

Figure 5 shows the stress verses strain graph being plotted and shows metal or alloy such as aluminium alloy 6061-T6 properties has ductility properties. This property
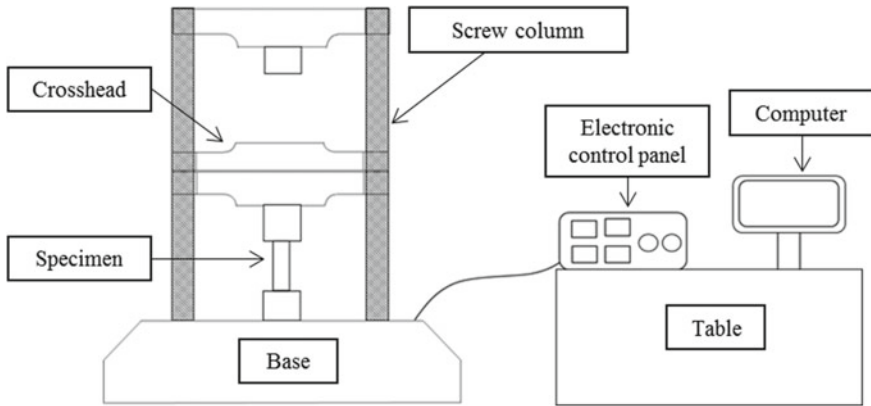
**Fig. 3** Schematic diagram of the quasi-static compression test using UTM machine
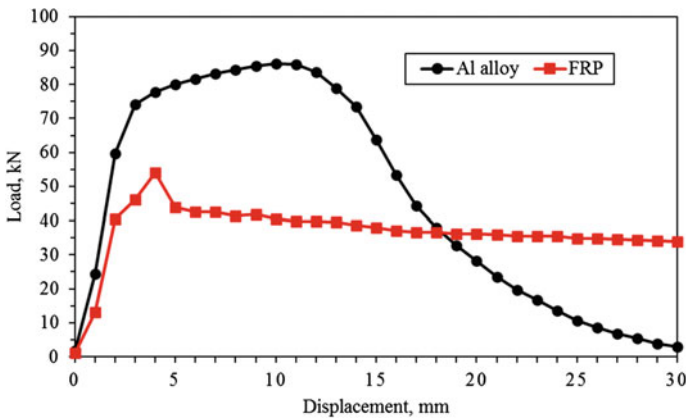


**Fig. 4** Load verses displacement graph plotted for both materials

lets the material receive a high load before failure through yielding. The aluminium alloy can withstand a huge amount of stress before failing, with the ultimate strength of 194.51 MPa at a strain of 0.093. The yield point of aluminium alloy is high, which can occur between 134.66 and 167.19 MPa with a strain rate between 0.013 and 0.027 before the material undergoes the nonlinear deformation phase. The Young modulus of the material can be obtained from the slope using the formula $E = \frac{\text{Stress}}{\text{Strain}}$ and obtained 13.29 GPa.

Figure 6 shows that the fibreglass tube is less ductile and close to brittle than aluminium alloy [9]. The fibreglass can withstand stress but is lower than aluminium alloy before failing with the ultimate strength of 121.87 MPa at a strain rate of 0.027. The yield point of aluminium alloy can occur between 91.48 and 104.40 MPa with a strain rate between 0.013 and 0.020 before the material undergoes a nonlinear
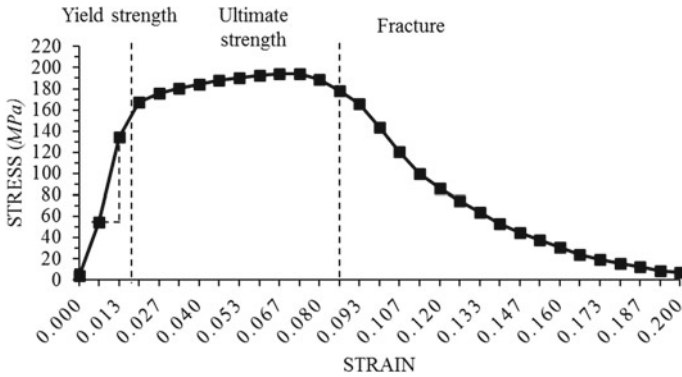
**Fig. 5** Stress verses strain graph of aluminium alloy 6061-T6 tube

deformation phase. The Young modulus of the material is obtained from the slope is 10.33 GPa which is slightly lower than aluminium alloy.

Substitute the value of yield stress from the result and the working design that is being calculated, which is 3.6 MPa, into the formula Factor of Safety, $FOS = \frac{Yield\ strength}{Working\ stress}$. The FOS obtained is 25 for fibreglass while for aluminium alloy, it would be 37.4. The FOS of aluminium alloy is higher than fibreglass by approximately 50%. In this case, the FOS for both materials shows that the yield stress provided to the working stress is overly designed. The aeronautical sector usually imposes 1.5–2.0 FOS as the ideal design safety factor. With that, choosing other materials with reasonable prices and suitable strength in designing is required to prevent overdesign.
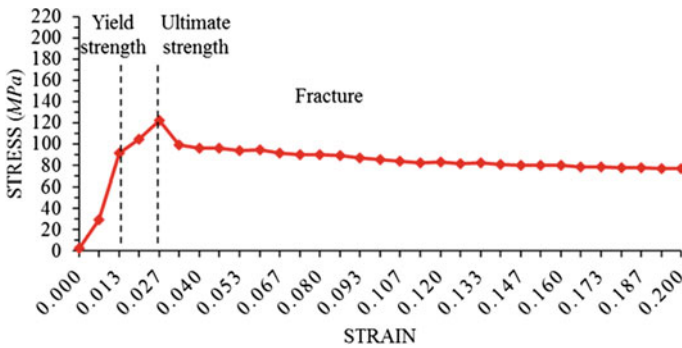


**Fig. 6** Stress verses strain of fibreglass tube

## 4 Conclusions

This research proves that GFRP could be a potential material to be substituted with the current material which is aluminium alloy 6061-T6 due to the economic aspect and also this material could impose high strength as close as aluminium alloy by 35%. The weight of the landing gear structure using current material is 114.54 kg, while imposing glass fibre could reduce weight up to 104.52 kg which leads to a 10% weight reduction. In terms of the economic aspect, S-glass fibre is easy to purchase at a reasonable price compared to other types of composites and metal. This could achieve precision cost-effectiveness and prevent overspending in designing or developing material.

## References

1. Wade Lanning (2019) What drones are made of? MatMatch. [Online]. Available: https://matmatch.com/blog/what-are-drones-made-of/. Accessed 29 May 2021
2. Hafizal Hamidon M, Sultan MTH, Hamdan Ariffin A (2019) Investigation of mechanical testing on hybrid composite materials. In: Jawaid M, Thariq M, NBT-FA. in B. Saba Fibre-Reinforced Composites and Hybrid Composites (eds) Woodhead publishing series in composites science and engineering. Woodhead Publishing, pp 133–156
3. Uzay C, Boztepe MH, Geren N (2016) Impact energy absorption capacity of fiber reinforced polymer matrix (FRP) composites. Conf Int J Arts Sci 09(June):211–220
4. Kumar IP, Mohite PM, Kamle S (2013) Axial compressive strength testing of single carbon fibres. Arch Mech 65(1):27–43
5. Babazadeh J, Rahmani K, Hashemi SJ, Sadooghi A (2021) Effect of glass, carbon, and kevlar fibers on mechanical properties for polymeric composite tubes produced by a unidirectional winding method. Mater Res Exp 8(4):045301. https://doi.org/10.1088/2053-1591/abf0ba
6. Wonderly C, Grenestedt J, Fernlund G, Cěpus E (2005) Comparison of mechanical properties of glass fiber/vinyl ester and carbon fiber/vinyl ester composites. Compos Part B Eng 36(5):417–426. https://doi.org/10.1016/j.compositesb.2005.01.004
7. Senapati AK, Kumar A, Kumar A (2018) Investigation on mechanical properties of Al-6061 alloy based MMC. IOP Conf Ser Mater Sci Eng 410(1):012016. https://doi.org/10.1088/1757-899X/410/1/012016
8. Sampath HP, Srinivasa CV, Naik V (2020) Study of quasi-static compression behaviour of hollow tubes made of glass/epoxy composite. IOP Conf Ser Mater Sci Eng 925(1):012045. https://doi.org/10.1088/1757-899X/925/1/012045
9. Khalid MY, Al Rashid A, Arif ZU, Akram N, Arshad H, Márquez FPG (2021) Characterization of failure strain in fiber reinforced composites: under on-axis and off-axis loading. Crystals 11(2):1–11. https://doi.org/10.3390/cryst11020216

# AC Pipe Structural Dynamic Characterization in On–Off Vehicle Conditions

**Muhammad Safwan Abdul Aziz and Ahmad Zhafran Ahmad Mazlan**

**Abstract** The dynamic behavior of heating, ventilation, and air-conditioning (HVAC) components can influence the vibration and noise been generated in the vehicle. Air conditional (AC) pipe is one of the most critical components in the vehicle HVAC system as it used to transfer different vapor and liquid conditions (high or low pressure) from the compressor to the evaporator. It is important to characterize the dynamic behavior of AC pipe in terms of natural frequencies, mode shapes, and frequency response function (FRF) to investigate the root cause of vibration and noise that been generated in the vehicle HVAC system such as hissing, humming, and clicking. This study will characterize the dynamic behavior of AC pipe in two different conditions, on and off-vehicle. Before installing the AC pipe to the vehicle HVAC system, its structural dynamic behavior will be investigated using an experimental modal analysis (EMA) in free-free condition (off-vehicle) to determine the dominant natural frequencies, mode shapes, and FRF. Then, after the installation, the EMA is conducted again as the mounted AC pipe to the vehicle engine bay structure (on-vehicle) may influence the original FRF. From the result, the first peak of AC pipe natural frequency has been shifted from 148 to 106 Hz with a decreased FRF amplitude due to effect of mounting in the vehicle engine bay. This result is important as it will contributed to the vibration and noise that been generated in the vehicle HVAC system during operation. Further, investigation on the different vibration and noise characteristics can be carried out to determine the root cause of the problems that been affected by the structural dynamic behavior of AC pipe.

## 1 Introduction

Heating, ventilation, and air-conditioning (HVAC) system is one of the most important features inside a vehicle. It helps in providing a comfortable feeling for the driver

M. S. A. Aziz · A. Z. A. Mazlan (✉)
School of Mechanical Engineering, Universiti Sains Malaysia, 14300 Nibong Tebal, Penang, Malaysia
e-mail: zhafran@usm.my

and passengers while driving the vehicle [1]. Nowadays, with the advanced technologies of vehicle in reducing thermal engine noise and silent electric vehicles, noises of HVAC system are becoming more prominent and major problem to be solved [2]. Vehicle HVAC is generally a closed system which made up of four main components, namely as compressor, condenser, thermal expansion valve, and evaporator. All these components are connected using several air conditional (AC) pipes which used to transfer different states of vapor and liquid such as in high- or low-pressure conditions. Each of HVAC components can contributed to the different noises such as hissing, humming, and clicking [3–5]. Some of these noises such as humming is generated due to redundancy of engine operating speed and the AC pipe structural dynamic behavior, such as the natural frequencies of the structure [3]. Hence, it is important to characterize the dynamic behavior of each HVAC components in order to determine the root cause of these noise problems [3].

Experimental modal analysis (EMA) is a general procedure that can be applied to investigate the structural dynamic behavior such as natural frequencies, mode shapes, and frequency response function (FRF) [6]. This method is widely used in automotive, aerospace, and machinery industries in developing their products [7–9]. For example, EMA has been conducted to determine the natural frequencies of engine mount before applying to the petrol-driven grass trimmer. This study is important to avoid the risk of resonance occurrence if the natural frequencies of the engine mount coincide with the engine speed which subsequently affected the performance of the mounts in absorbing the vibration of the engine [9].

This study will characterize the structural dynamic behavior of AC pipe in two different conditions, in on and off-vehicle. Firstly, an EMA is carried out in free-free condition (off-vehicle) to determine the original natural frequencies, mode shapes, and FRF of the AC pipe, prior of installing to the vehicle engine bay (on-vehicle). The results of both AC pipe structural dynamic behaviors will be compared and analyzed in preparing the root cause of the vibration and noise problems that will be generated in the vehicle HVAC system.

## 2 Methodology

### 2.1 Geometry Modeling

Structural dynamic characterization of AC pipe involves several steps such as geometry modeling, impact testing, and structural response analysis. Figure 1a, b shows the geometry model and the actual AC pipe of the vehicle HVAC system.

In Fig. 1a, the geometry of the actual AC pipe is measured and modeled as 2D model in the LMS TestLab software using a coordinate system. There is total of 5 points that been drawn in the software which then connected using a line to represent the actual AC pipe structure. The similar points have also been labeled on the actual AC pipe as shown in Fig. 1b. These points are important as it will be used for the
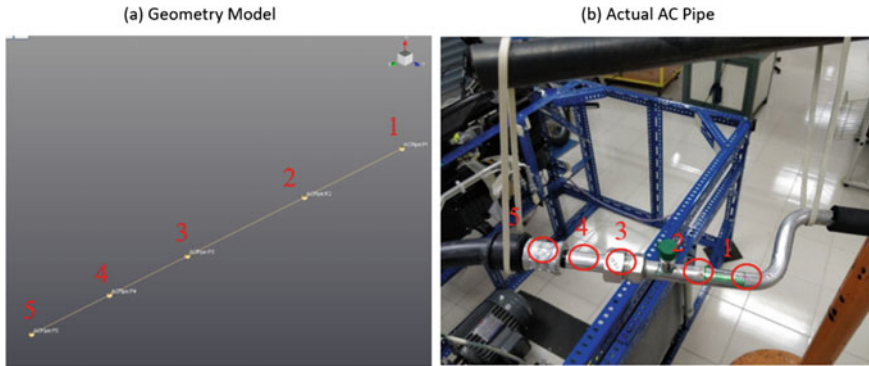
**Fig. 1** **a** Geometry model and. **b** Actual AC pipe (off-vehicle)

impact testing in the next subsection on EMA. Figure 1b also shows the EMA setup of AC pipe in the off-vehicle condition.

## 2.2 Experimental Modal Analysis (EMA)

In this study, the EMA is conducted to determine the AC pipe structural dynamic characteristics in terms of natural frequencies, mode shapes, and FRF. This experiment is important as the result parameters can be used to investigate the root cause of vibration and noise that been generated from the vehicle HVAC system, such as hissing, humming, and clicking [3–5].

The EMA is conducted in two different conditions, on and off-vehicle. For the off-vehicle condition, the AC pipe is hanged using two rubber bands to the stiff stand as a free-free condition shown in Fig. 1b, previously. Meanwhile, for the on-vehicle condition, the AC pipe is mounted in the vehicle engine bay as in actual HVAC system of the vehicle. The detail setup for the EMA is shown in Fig. 2. In this experiment, an impact hammer is used to provide an input (impact force) to the AC pipe structure. Then, an accelerometer is used to measure the output (acceleration response) of the AC pipe, and the signal is sent to the LMS SCADAS DAQ system that integrated with the LMS TestLab software for the result analysis. The roving hammer impact testing method is used in this study, whereby the accelerometer is fixed at one point, and the impact hammer is roving around at all five points.

The relationship between the input force $F(\omega)$ and output vibration $X(\omega)$ of the EMA can be shown using the following equations:

$$X(\omega) = H(\omega)F(\omega) \tag{1}$$

**Fig. 2** EMA setup with AC pipe mounted on-vehicle engine bay (on-vehicle)
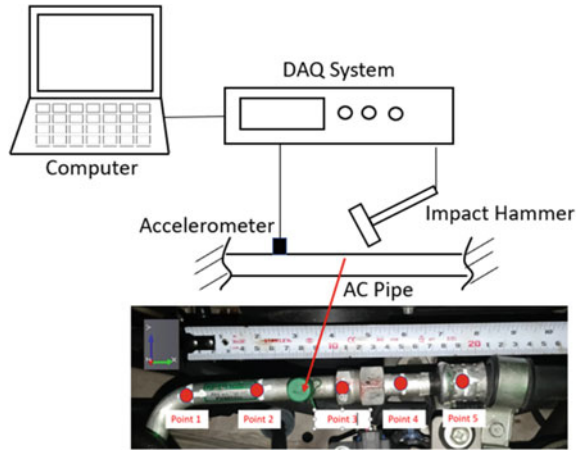
where $H(\omega)$ is the transfer function of the measured system (AC pipe), and the result is represented as FRF curve in the next section.

## 3    Results and Discussion

### 3.1    Frequency Response Function (FRF)

Figure 3 shows the FRF result of AC pipe for both off and on-vehicle conditions. From the figure, it can be observed that the FRF curve of AC pipe in off-vehicle condition has produced several natural frequency peaks between 0 and 600 Hz, whereby the first peak at 148 Hz is the most dominant with vibration amplitude of about 14 m/s$^2$N. For the case of AC pipe mounted in the actual vehicle engine bay (on-vehicle), four natural frequency peaks can be seen at 106 Hz, 173 Hz, 249 Hz, and 338 Hz, respectively. The first peak of natural frequency for the AC pipe has been shifted from 148 to 106 Hz with a reduced vibration amplitude of about 8.5 m/s$^2$N, due to effect of mounting in vehicle engine bay. This result is important as several HVAC noise and vibration problems can be induced between this frequency range, and the structural dynamic behavior of AC pipe can be one of the root causes for these problems [3]. Table 1 highlights the first natural frequency values of AC pipe for both on and off-vehicle conditions.
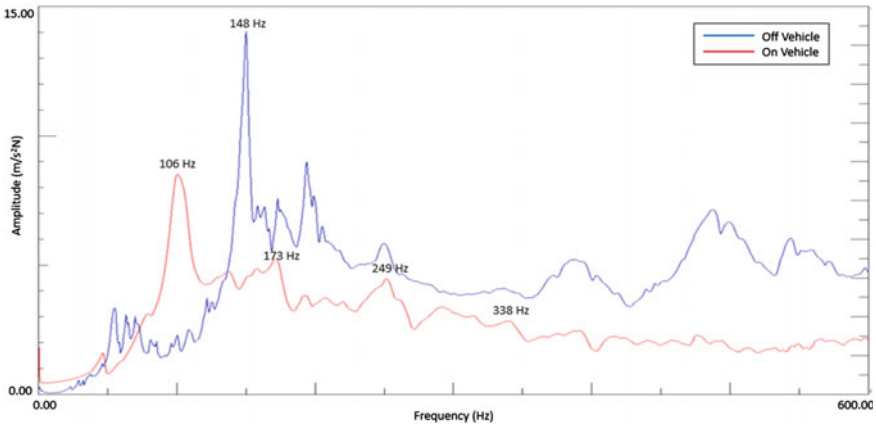
**Fig. 3** AC pipe FRF comparison in on and off-vehicle conditions

**Table 1** List of first AC pipe natural frequency for both on and off-vehicle conditions

| Conditions | 1st Natural frequency (Hz) |
|---|---|
| Off-vehicle | 148 |
| On-vehicle | 106 |

## 3.2 Mode Shapes

Based on the FRF curve result in Fig. 3, the corresponded mode shapes for each natural frequency in on-vehicle condition are extracted and shown in Fig. 4. From the figure, it can be observed that each natural frequency (mode) has produced different mode shape to the AC pipe structure. The 1st mode at 106 Hz shows the first bending deflection for the AC pipe in the vertical direction. The second, third, and fourth bending deflections are shown by the subsequent modes at 173, 249, and 338 Hz. As the modes number goes higher, the more significant defection will be experienced by the AC pipe structure. It is important to avoid any redundancy in operating the vehicle HVAC system with these mode values as it will generate resonance phenomenon and subsequently creating the varied noise and vibration problems to the HVAC system.

## 4 Conclusion

In this study, the structural dynamic characteristics of HVAC AC pipe in terms of natural frequencies, mode shapes, and FRF have been experimentally determined. The EMA has been carried out in two different conditions, on and off-vehicle. From the results, it can be concluded that the mounted AC pipe in the vehicle engine bay has produced different FRF curves with the shifted first natural frequency value from
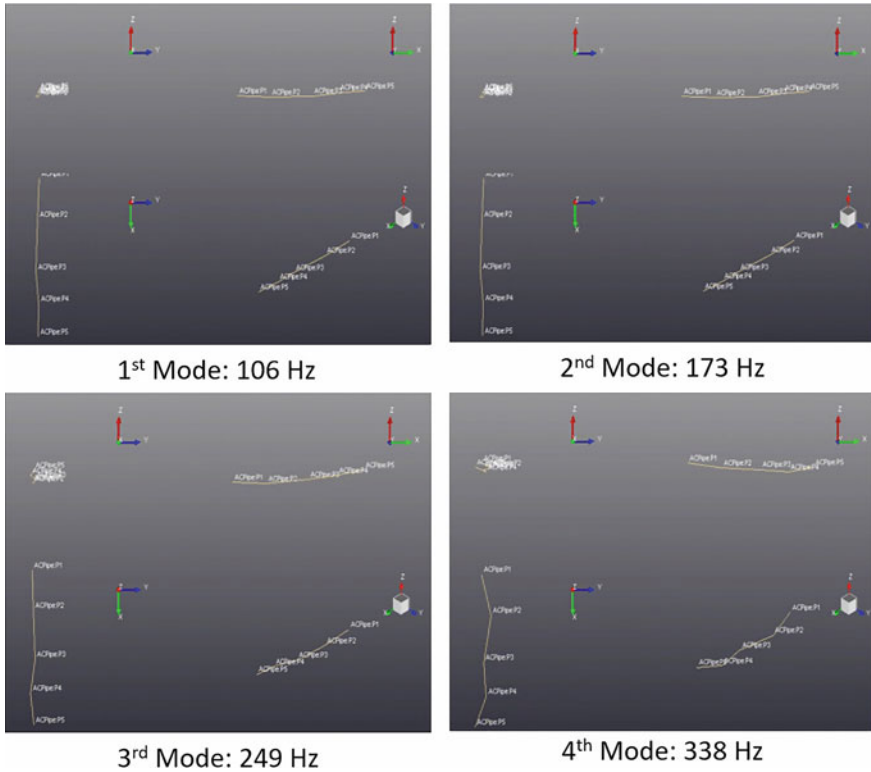
**Fig. 4** Mode shapes of AC pipe at different bending modes (on-vehicle)

148 to 106 Hz. This subsequently produced different mode shapes for each natural frequency value for the AC pipe structure. This result is important as the natural frequency values can contributed to vibration and noise in the vehicle HVAC system during operation, and AC pipe can be one of the root causes for these problems.

# References

1. Bennouna S, Matharan T, Cheriaux O (2018) Automotive HVAC noise reduction (No. 2018-01-1519). SAE Technical Paper
2. Xi J, Feng Z, Wang G et al (2015) Vibration and noise source identification methods for a diesel engine. J Mech Sci Technol 29:181–189
3. Satar MHA, Mazlan AZA, Hamdan MH et al (2021) Experimental validation of the HVAC humming-type noise and vibration in model and vehicle system levels. Archives Acoust 375–385

4. Satar MHA, Mazlan AZA, Hamdan MH et al (2021) A lab-scale HVAC hissing-type noise characterization with vehicle system validation. Archives Acoust 365–373
5. Satar MHA, Mazlan AZA, Hamdan MH et al (2021) Validation of clicking-type noise and vibration in automotive HVAC system. Int J Automotive Mech Eng 18:8489–8497
6. Avitabile P (2001) Experimental modal analysis. Sound Vib 35:20–31
7. Storck H, Sumali H, Pu Y (2001) Experimental modal analysis of automotive exhaust structures (No. 2001-01-0662). SAE Technical Paper
8. Fuellekrug U, Goege D (2012) Identification of weak non-linearities within complex aerospace structures. Aerosp Sci Technol 23:53–62
9. Lee TY, Ooi LE, Mohd Ripin Z (2015) Design of the mounting system of a grass trimmer engine for minimum handle vibration response based on frequency-dependent stiffness and loss factor properties. J Vibroengineering 17:2155–2166

# The Numerical Simulation for Evaluation of Dimensions of Bead Geometry and Heat-Affected Zone (HAZ) of the Weld Joint

**Walisijiang Tayier, Vin Cent Tai, and Shamini Janasekaran**

**Abstract** Bead geometry which includes bead width and depth as well as heat-affected zone, are important physical properties to help determine the weldment quality. However, the dimensions of bead geometry and heat-affected zone are hard to predict without proper computer modeling. In this study, numerical simulation was employed to solve the three-dimensional heat transfer finite element model to predict the bead geometry and heat-affected zone for automated-based shielded metal arc welding. The simulation results showed good agreement with experimental results, with less than 5% of error on average. From the simulation results, the maximum temperatures of the arc crater produced using a variety of electrode diameters were 3300 °C, 3600 °C, and 4000 °C, respectively. The results also indicated that the temperature profile significantly increased when heat source crossed the observation line.

**Keywords** Numerical simulation · Penetration depth · Bead width · Heat-affected zone · Automated-based shielded metal arc welding

## 1 Introduction

Bead geometry is an important factor in determining weldment quality. It includes penetration depth and bead width. However, it is difficult to predict the weldment quality during the welding process. With the aid of computer modeling, three-dimensional finite element models and heat transfer models can be used to numerically simulate heat flow in the weld zone, while essential algorithms such as heat source, and boundary conditions can be created and implemented to obtain the desired

W. Tayier · S. Janasekaran
Centre for Advanced Materials and Intelligent Manufacturing, Faculty of Engineering, SEGi University, Built Environment and IT, 47810 Petaling Jaya, Malaysia

V. C. Tai (✉)
Centre for Modelling and Simulation, Faculty of Engineering, SEGi University, Built Environment and IT, 47810 Petaling Jaya, Malaysia
e-mail: taivincent@segi.edu.my

weldment. Numerical simulation is one of the powerful tools for mechanical applications which are used to compute many numerical models (algorithms) such as heat transfer [1]. In some simulation processes, the dynamic heat model is rarely applied by researchers to simulate the arc welding process. The convection effect and buoyancy force were investigated that a three-dimensional heat model could be used to estimate bead shapes in the weld zone [2, 3]. Finite element model analysis for T-joint weldment of a submerged arc welding [4]. The three-dimensional (heat source) could predict the weld dimensions and deformations with high accuracy [5]. However, to the best of the found knowledge, there is no existing literature on the application of finite element model to predict the bead geometry for shielded metal arc welding. Therefore, this study aimed to develop the mathematical model to predict the bead geometry and heat-affected zone for automated-based shielded metal arc welding and subsequently validate the results against the experimental data to quantify the accuracy of the model.

## 2 Experimental Designs

### 2.1 Materials

Two mild steel AISI 1018 plates (34 mm × 30 mm × 6 mm) were butt joined with automated-based shielded metal arc welding. The welding samples were clamped or fixed to avoid distortion. The configuration of welding samples is depicted, in Fig. 1, while the chemical properties of the metal (0.15–0.2% of C, 0.6–0.9% of Mn, 0.05% of P and S, and 98.81–99.26% of Fe), and experimental parameter setting are tabulated such as welding speed (ranges from 3.19 to 4.6 mm/s) and electrode diameter (ranges from 2.6 to 4 mm).



Fig. 1 Diagram for butt joint. **a** Font view. **b** Top view
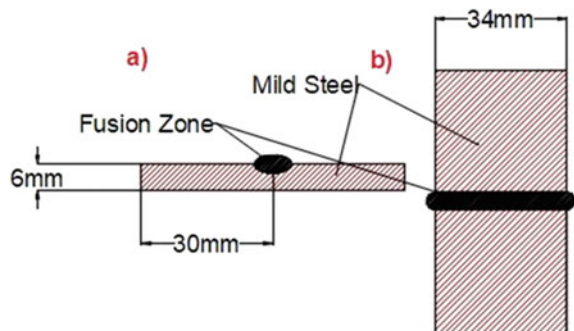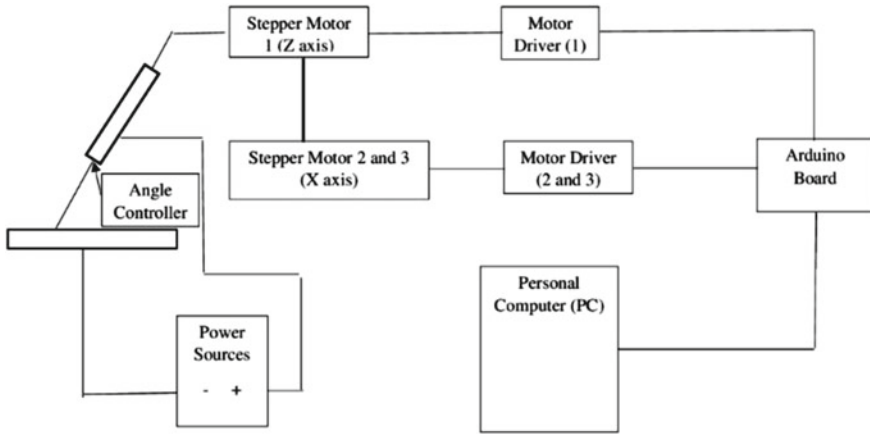
**Fig. 2** Diagram for ABSMAW

## 2.2 Arc Welding

The setup of automated-based shielded metal arc welding used in this study, Arc 200 shielded metal arc welding was connected to Arduino motherboard for data control and data transfer to a personal computer. A constant arc current of 90 A and 26.4 V of constant arc voltage were supplied to the automated-based shielded metal arc welding, Fig. 2.

## 2.3 Characteristics for Material Joint

The welding samples were cut perpendicular, and the samples in cross-sections were ground (220, 1000, and 2000 grit), polished (diamond suspension), and etched ferric chloride. The bead geometries in cross-sections of metal were observed using a digital microscope (Celestron Micro Direct 1080 HDMI), Fig. 3.

**Fig. 3** Diagram for bead geometries and HAZ. *T1-Deph of penetration, T2-Thichness of HAZ, D1-bead width
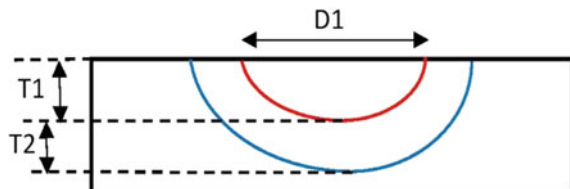
## 3 Numerical Simulations

### 3.1 Heat Transfer Model

The three-dimensional thermal conduction model was used to model the conduction between the metals, Eq. (1) [7]:

$$\frac{\partial}{\partial_x}\left(K_x \frac{\partial T}{\partial x}\right) + \frac{\partial}{\partial_y}\left(K_y \frac{\partial T}{\partial y}\right)$$
$$+ \frac{\partial}{\partial_z}\left(K_z \frac{\partial T}{\partial z}\right) + Q_r(x, y, z, t) = \rho C_p \left(\frac{\partial T}{\partial t} - V\frac{\partial T}{\partial x}\right) \quad (1)$$

where $T$ denotes temperature, $Q_r(x, y, z, t)$ is heating power per unit volume generated by the arc; $K_x$, $K_y$, and, $K_z$ are thermal conductivities from the spatial coordinates $x$, $y$, and $z$; $\rho$ is material density, $C_p$ is specific heat of material; $V$ is the moving speed of the heat source; and $t$ denotes the time instance.

The room temperature of 25 °C was applied to the initial condition at $t = 0$ s. The boundary conditions described by Eq. (2) [8] were applied to the model as depicted, in Fig. 5c.

$$K\frac{\partial T}{\partial x}nx + K\frac{\partial T}{\partial y}ny + K\frac{\partial T}{\partial x}nx + K\frac{\partial T}{\partial z}nz$$
$$+ q_r + h_c(T - T_\infty) + \sigma \varepsilon F\left(T^4 - T_r^4\right) = 0 \quad (2)$$

where, $nx$, $ny$, and $nz$ are outward normal vectors in $x$-, $y$-, and $z$- directions, respectively; $q_r$ is the boundary heat flux on the model; $h_c$ is convective heat transfer coefficient of air, which is 15 Wm$^{-1}$ K$^{-1}$ adopted in this study to simulate free convection [8]; $\sigma = 5.6 \times 10^{-8}$ Wm$^{-2}$ K$^{-4}$ is Stefan-Boltzmann constant; $\varepsilon = 0.4$, which is radiation emissivity of AISI/SAE 1080 steel [6]; and $F = 1$ is radiation view factor.

### 3.2 Heat Source Model

In this study, the principal heat was produced by a fixed torch in the shielded metal arc welding. The heat source was defined through the Goldak model [9, 10], whereby the shape of the heat source was designed by the ellipsoid energy (ellipsoidal shape) and the power density is defined as in Eq. (3):
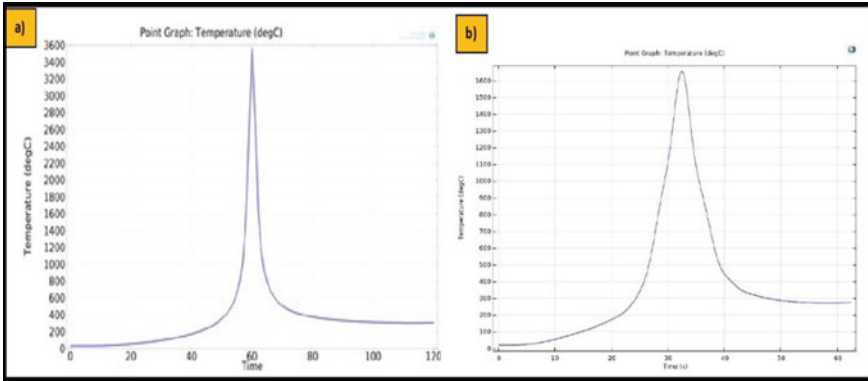
**Fig. 4** Validation, **a** references from literature review and **b** presents study

$$Q_r = \frac{6\sqrt{3} \times f \times \mu \times Q}{a \times b \times c \times \pi\sqrt{\pi}} \times \exp\left(\frac{-3(x - x_0 - V_{in} * t)^2}{a^2} + \frac{-3y^2}{b^2} + \frac{-3z^2}{c^2}\right) \tag{3}$$

where the heat energy is defined as $Q = VI$, $V$ is arc voltage and $I$ is arc current; $V_{in}$ is welding speed; $x_0$ is arc transient position; $\mu$ is arc welding efficiency ($\mu = 0.84$) [11]. The heat deposition is defined by the faction $f = 0.8$ for the front-rear [12]. The crater (weld bead) shape is defined by $a$, $b$, and $c$. In this study, the depth of penetration and bead width was experimentally measured via DM. The values of $a$, $b$, and $c$ recorded were 2 mm, 2 mm, and 6 mm, respectively. The heat source was moving on the heat flux domain at fixed welding speed for 12 s of simulation time with time-step size of $\Delta t = 0.01$ s.

## 3.3 Simulation Setup

In this study, the numerical simulation was implemented in COMSOL Multiphysics 5.6, and the simulation settings were compared with reference [8], Fig. 4. The material properties are given in Table 1.

### 3.3.1 Geometry and Mesh

The 34 mm × 60 mm × 6 mm mild steel plate was created and was the heat source profile $Q_r$ was applied to the weld zone, Fig. 5a.

The accuracy of results depends on mesh quality. Therefore, mesh refinement was performed until the mesh quality was acceptable and the results were independent
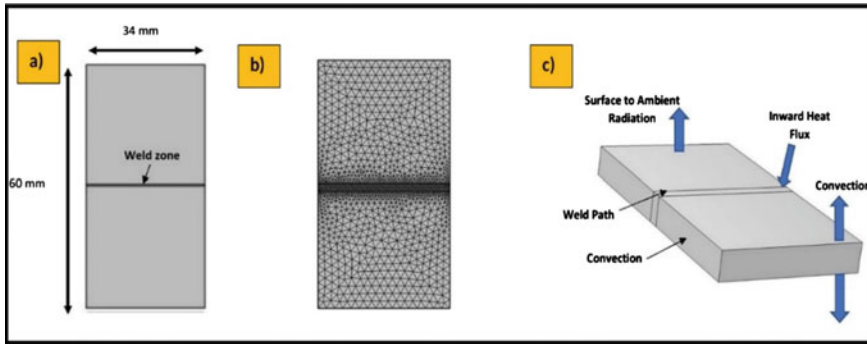
**Fig. 5** Diagram for simulation setup, **a** geometry profile, **b** mesh, **c** boundary conditions

**Table 1** Material properties [13]

| Property | Value | Unit |
|---|---|---|
| Heat capacity ($C_p$) | 486 | J/(k$_g$*K) |
| Density ($\rho$) | 7870 | k$_g$/m$^3$ |
| Thermal conductivity ($k$) | 51.9 | W/(m*K) |
| Young's modulus ($E$) | 205e9 | Pa |
| Poisson's ratio ($\mu$) | 0.29 | / |

of mesh size. The final mesh profile is shown, in Fig. 5b. It consisted of 97,503 tetrahedral and 10,816 triangle elements of quadratic order. The minimum element quality achieved was 0.2007 and average element quality was 0.6632, which satisfied the minimum quality requirement of 0.1 according to [8].

### 3.3.2 Boundary Conditions

In this study, the boundary conditions defined by Eqs. (1), (2) and (3) were applied to the model, Fig. 5c. The weld bead domain dimensions were defined by the electrode diameter and values of *a*, *b*, and *c* in the shape of a crater is as shown, in Eq. 4.

## 4 Validation of Numerical Simulation

The sizes of bead geometries and heat-affected zone obtained from the numerical simulation were validated against the experimental data, Table 2. The physical automated-based shielded metal arc welding experiments were carried out. The range of peak welding current and welding voltage was 90 A and 26.4 V, respectively. Other parameters of the experiments are presented. The melting point of base material (around 1350–1530 °C), the penetration depth, heat-affected zone, and bead

**Table 2** Validation of bead geometries and HAZ dimensions

| Trial No | Bead width (mm) | | | Heat-affected zone (HAZ) (mm) | | | Penetration depth (mm) | | |
|---|---|---|---|---|---|---|---|---|---|
| | Exp | Simu | Error (%) | Exp | Simu | Error (%) | Exp | Simu | Error (%) |
| 1 | 4.863 | 4.864 | 0.02 | 1.328 | 1.384 | 4.2 | 1.119 | 1.135 | 1.4 |
| 2 | 5.558 | 5.418 | 2.5 | 1.33 | 1.312 | 1.4 | 0.766 | 0.806 | 13.1 |
| 3 | 5.834 | 5.912 | 1.3 | 1.319 | 1.314 | 0.4 | 0.703 | 0.744 | 5.8 |
| 4 | 5.769 | 5.288 | 8.3 | 1.351 | 1.246 | 7.8 | 1.587 | 1.438 | 9.4 |
| 5 | 6.325 | 6.239 | 1.4 | 1.629 | 1.537 | 5.6 | 1.329 | 1.318 | 0.8 |
| 6 | 5.702 | 5.891 | 3.3 | 1.334 | 1.228 | 7.9 | 0.775 | 0.815 | 5.2 |
| 7 | 7.118 | 6.807 | 4.4 | 1.554 | 1.562 | 0.05 | 1.649 | 1.596 | 3.2 |
| 8 | 5.767 | 5.739 | 0.5 | 1.317 | 1.329 | 0.9 | 0.991 | 1.027 | 3.6 |
| 9 | 6.507 | 6.343 | 2.5 | 1.586 | 1.353 | 14.7 | 0.813 | 0.804 | 1.1 |
| Ave | | | 2.7 | | | 4.8 | | | 4.8 |

*Exp—Experimental, Simu—Simulation, Ave—Average

width were obtained and compared with the simulation results. Errors between the experimental and simulation outputs were calculated in Table 4.

The numerical setup was to control bead width, penetration depth, and size of heat-affected zone during the simulation [14]. According to the bead geometry's point of view, shapes of bead width, penetration, and heat-affected zone were significantly different because of the different parameter settings. For example, from the shapes of bead width with different electrode diameters, the narrow bead width was produced at 2.6 mm of electrode diameters as the low-temperature distribution. In contrast, the 4 mm electrode was generated by the high bead width in the weld zone, Fig. 7. From the error distributions between experimental and simulation, the average error for each factor did not exceed 5%, while the minimum average error for all factors were 2.7%. Simulation results were significantly reached to the experimental results as the low error and high accuracy distributions and experimental output results were verified through the numerical simulation of high validity, Fig. 6. The experimental and simulation results for the cross-sectioned bead geometries and heat-affected zone under different parameters are presented in Fig. 7. Observed that the bead width dimension increased when the electrode diameter generally increased. The welding speed was also influenced by penetration depth under the constant welding current and voltage.

## 5 Results and Discussion

The numerical simulation predicted the bead width, penetration, and heat-affected zone in the automated-based shielded metal arc welding. Simulation techniques could
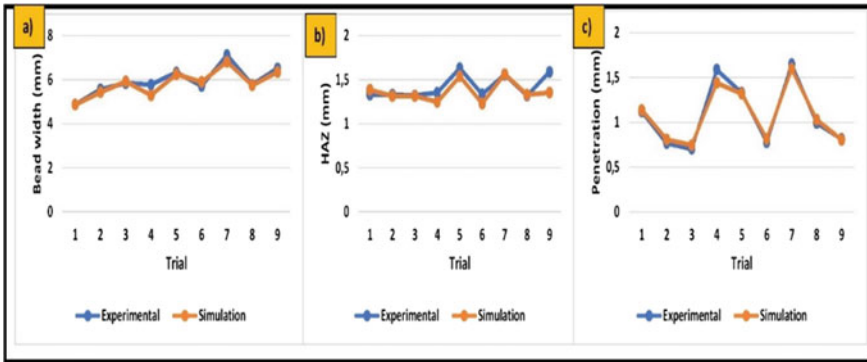
**Fig. 6** Diagram for validation of **a** bead width, **b** HAZ, and **c** penetration depth

change or edit material properties, geometry specifications, and parameter settings. The simulation model estimated depth penetration, bead width, and size of heat-affected zone in the weld zone. Simulation and experimental results showed that when electrode diameter increased, the bead width generally increased from 4.253 to 6.439 mm at constant 90 A of welding current and 26.4 V of welding voltage, However, the depth of penetration decreased from 1.635 to 0.766 mm at the constant 4.6 mm/s of welding speed. In addition, the size of heat-affected zone was also observed, in which the thickness of heat-affected zone generally decreased when the welding speed decreased, Fig. 7.

## 6 Conclusions

An AISI/SAE 1080 steel plate has been successfully joined and simulated. Goldak model was defined for heat source of arc welding and three-dimensional heat transfer model was applied to the finite element model simulation.

During the validation process, low error value (size of bead geometry and heat-affected zone) was produced between the experimental and simulation testing at an average of between 2.7 and 5%.

D1= 4.864 mm          T2= 1.384 mm          D2= 4.863 mm          T2= 1.328 mm

T1= 1.135 mm                                T1= 1.119mm

D1= 5.418 mm          T2= 1.312 mm          D2= 5.558 mm          T2= 1.330 mm

T1= 0.806 mm                                T1= 0.766 mm

D1= 5.912 mm          T2= 1.314 mm          D2= 5.834 mm          T2= 1.319 mm

T1= 0.744 mm                                T1= 0.703 mm
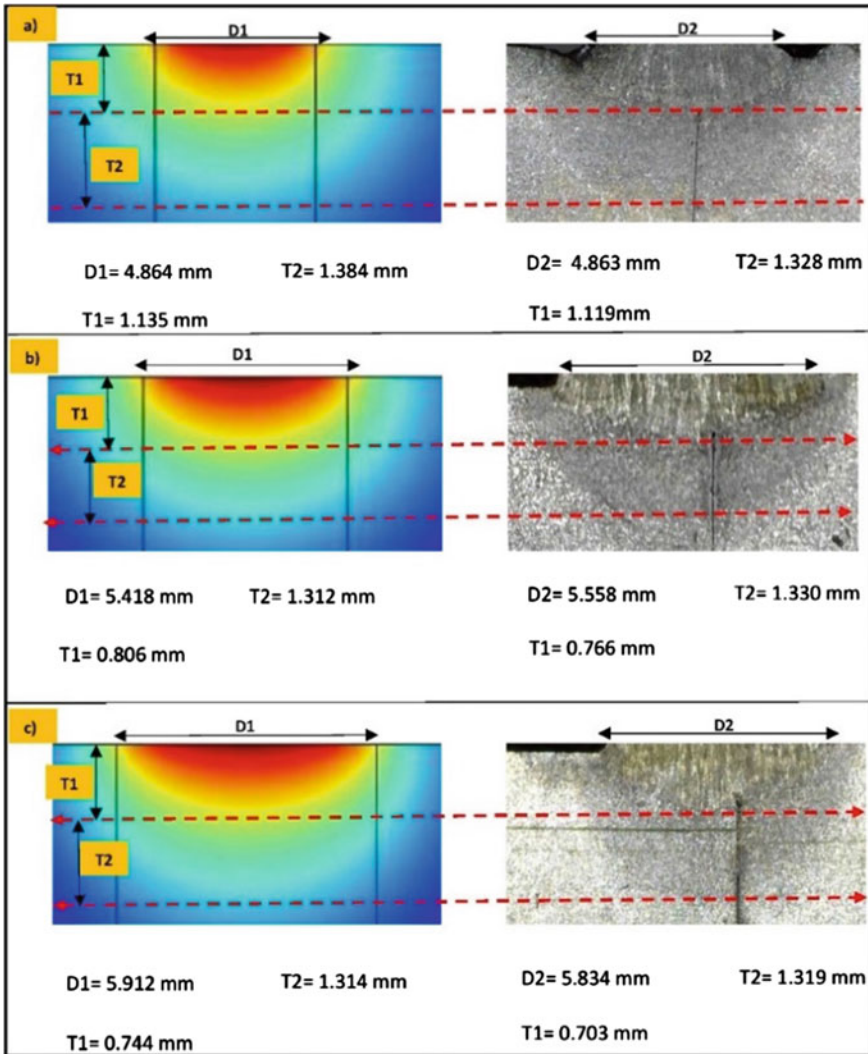
**Fig. 7** Experimental and simulation diagram for bead geometries and HAZ in ABSMAW at **a** 2.6 mm of ED with the 4.6 mm/s of WS, **b** 3.2 mm of ED with the 4.6 mm/s of WS and **c** 4 mm of ED with 4.6 mm/sec of WS. ED-electrode diameter, WS-welding speed, T1-depth of penetration, T2-thickness of HAZ, D1-bead width (simulation), D2-bead width (experimental)

**Conflict of Interest**   The authors declare no financial or commercial conflict of interest.

# References

1. Jianfeng Y, Xiaoting D, Rui G, Wenji L, Liangyu L (2019) Numerical simulation of equivalent heat source temperature field of asymmetrical fillet root welds. Int J Heat Mass Transfer 130:42–49
2. Won-Ik C, Suck-Joo N, Thomy C, Vollertsen F (2017) Numerical simulation of molten pool dynamics in high power disk laser welding. J Mater Process 262–275
3. Mickael C, Carin M, Masson P, Gaied S, Balabane M (2018) A complete model of keyhole and melt pool dynamics to analyze instabilities and collapse during laser welding. J Laser Appl 26
4. Mondal A, Pankaj B, Swarup B (2017) Experimental and FE analysis of submerged arc weld induced residual stress and angular deformation of single and double sided fillet welded joint. Int J Steel Struct 17:9–18
5. Perić M, Srećko Š (2018) Numerical analysis and experimental investigation of welding residual stresses and distortions in a T-joint fillet weld. Mater Des 53:1052–1063
6. Navid N, Jill U, Mohammad A (2017) Hardness and residual stress modeling of powder injection laser cladding of P420 coating on AISI 1018 substrate. Int J Adv Manuf 93:3485–3503
7. Johnso I, Iguchi M, Wahnsiedler W (2015) Mathematical and physical modelling of materials processing operations. Chapman & Hall/CRC
8. Josserand E, Jullien J, Nelias D, Deloison D (2007) Numerical simulation of welding-induced distortions taking into account industrial clamping conditions. Math Model Weld Phenom 8:1105–1124
9. Goldak J, Akhlaghi M (2005) Computational welding mechanics. Springer Science Business Media, New York
10. Goldak J, Chakravarti A (1985) A new finite element model for welding heat sources. Metall Mater Trans B 15:299–305
11. Dupont J, Marder A (1995) Thermal efficiency of arc welding processes. Weld J 74
12. Tomasz K (2020) Computational techniques in numerical simulations of arc and laser welding processes. Materials 608:1–19
13. Kumar S, Singh R (2020) Investigation of tensile properties of shielded metal arc weldments of AISI 1018 mild steel with preheating process. Mater Today: Proc 26
14. Deng D, Liang W, Murakawa H (2018) Determination of welding deformation in fillet-welded joint by means of numerical simulation and comparison with experimental measurements. J Mater Process Technol 183:219–225

# Corrosion Behavior of Laser-Welded Ti6Al4V in 3.5%Wt NaCl

**P. O. Omoniyi, R. M. Mahamood, N. Arthur, S. Pityana, S. Skhosane, T. C. Jen, and E. T. Akinlabi**

**Abstract** Titanium and its alloys, especially Ti6Al4V, have greatly revolutionized the manufacturing industry. Ti6Al4V, the workhorse of industries, has been widely used in the aerospace, automobile, and marine industry due to its outstanding corrosion resistance and good strength-to-weight ratio. This article investigates the corrosion potentials of Ti6Al4V joined using laser welding in 3.5%wt sodium chloride (NaCl) and compares it with an unwelded Ti6Al4V sheet. The samples were characterized using the Tafel curve, open-circuit potential, and scanning electron (SEM) images. Results showed that the unwelded sample exhibited higher corrosion resistance when compared to the laser-welded sample.

**Keywords** Corrosion · Laser welding · Microstructure · NaCl · Ti6Al4V

## 1 Introduction

The joining of metals, especially welding, has been used in various industries due to its strength over brazing and fasteners such as rivets, bolts, and nuts. Welding Ti6Al4V in recent decades has been perfected to an appreciable stage, with the use of laser welding, which offers a great advantage of small heat-affected zone over

P. O. Omoniyi (✉) · R. M. Mahamood · T. C. Jen · E. T. Akinlabi
Mechanical Engineering Science Department, University of Johannesburg, Johannesburg 2092, South Africa
e-mail: omoniyi.po@unilorin.edu.ng

P. O. Omoniyi
Mechanical Engineering Department, University of Ilorin, PMB 1515, Ilorin, Nigeria

R. M. Mahamood
Department of Materials and Metallurgical Engineering, University of Ilorin, PMB 1515, Ilorin, Nigeria

N. Arthur · S. Pityana · S. Skhosane
CSIR, National Laser Center, P. O. Box 395, Pretoria, South Africa

E. T. Akinlabi
Pan Africa University for Life and Earth Sciences Institute, Ibadan 200005, Nigeria

other fusion welding such as gas tungsten arc welding (GTAW) and gas metal arc welding (GMAW) [1, 2]. However, due to the heat required in joining these metals, changes in microstructure and atmospheric contaminations are bound to occur [3]. The change in microstructure at the weld zone (heat-affected zone and fusion zone) has been reported to affect the corrosion resistance of Ti6Al4V [4]. The acicular $\alpha'$ and martensitic microstructure have been reported as the primary source of pitting corrosion in Ti6Al4V [5]. Even though Ti6Al4V is known to have high corrosion resistance, due to the passive film of titanium dioxide ($TiO_2$) formed on its surface, the breakage of the film could be a result of environmental conditions [6]. Works of literature have reported the dissolution of the passive film formed on Ti6Al4V in halide ions. Chloride ion ($Cl^-$) has been reported to deplete the oxide layer and exposes Ti6Al4V to aggressive pitting [3].

This research aims to study the effect of sodium chloride (NaCl) solution on the passive film formed on laser-welded Ti6Al4V alloy. It further investigates the microstructure of the laser-welded Ti6Al4V. This research will give a good guide on numerical studies and simulation of corrosion of Ti6Al4V in the marine environment.

## 2   Methods

### 2.1   Laser Welding of Ti6Al4V

Titanium alloy (Ti6Al4V) sheets with a chemical composition consisting of 6.1% aluminum, 4% vanadium, 0.15% iron, and the remaining titanium, were joined using a 3 kW CW YLS-2000-TR ytterbium laser system. Each Ti6Al4V sheet measured 100 mm × 60 mm × 1 mm and was joined in butt configuration. Prior to welding, the faying surfaces were cleaned with acetone to remove contaminations. Argon gas with a 15 L min$^{-1}$ flow rate was used as a shield to protect the welds from atmospheric contamination. Laser power of 2.6 kW and welding speed of 2.6 m min$^{-1}$ were used in joining the Ti6Al4V sheets. The choice of parameters was made as a result of an ongoing study [1], where the welding parameters used exhibited the highest tensile strength. Optical images of the microstructure of the welded metals were captured using Olympus DP 25 microscope.

### 2.2   Corrosion Studies

Samples measuring 20 mm × 10 mm × 1 mm were cut out of the Ti6Al4V sheets for corrosion studies. Each sample was mounted on a cold setting epoxy resin with a copper wire soldered to an end of the metal sample. The samples were grinded using SiC papers ranging from #320 to #4000, cleaned with acetone and rinsed in distilled water. The experimental setup consisted of the sample as the working

electrode, Ag/AgCl as the reference electrode, and the counter electrode was platinum rods. To obtain a stable open-circuit potential, a 200 mm$^2$ surface area was exposed to the sodium chloride (NaCl) solution for two hours at ambient temperature (open-circuit potential, OCP). The corrosion potentials were measured using a DY2300 model potentiostat with DY2300EN software. The potentiodynamic polarization experiment used dynamic potential values ranging from $-0.25$ to $+0.25$ V, and the potentiodynamic scan rate was 1.0 mV/s. Corrosion current ($I_{corr}$ A) and corrosion potential are also measured ($E_{corr}$ V).

## 3   Results and Discussion

### 3.1   Microstructure of Laser-Welded Samples

The microstructure of the laser-welded sample is characterized into three zones, namely: heat-affected zone (HAZ), base metal (BM), and fusion zone (FZ) Fig. 1. The BM comprises the white alpha ($\alpha$) and black beta ($\beta$) phases [2, 7, 8]. Furthermore, the HAZ is categorized into far HAZ and near HAZ. The far HAZ is made of the blocky α microstructure and some untransformed β phases, while the near HAZ is close to the FZ [9]. The near HAZ contains acicular $\alpha'$ microstructure resulting from the zone attaining temperature above the $\beta$ transus temperature of 995 ºC then cooling rapidly in the air [10]. The FZ contains $\alpha$ martensitic microstructure resulting from the zone attaining the liquidus temperature then cooling above the critical cooling temperature rate of 410 ºCs$^{-1}$ [1, 11–13].

### 3.2   Corrosion Analyses

The scanning electron microscopy (SEM) observation of the unwelded sample Fig. 2 and that of the welded sample Fig. 3 after exposure to 3.5%wt sodium chloride (NaCl) solution shows no corrosion attack on the surface except the carbon particles picked up during grinding operation using the silicon carbide (SiC) papers, as shown in the energy dispersive spectroscopy (EDS) chart. The lack of corrosion attack could be attributed to the passive film formed by the metal on its surface. A similar occurrence was also observed by [5].

Tafel curve plot depicted the rate of corrosion in the welded Ti6Al4V is higher than the unwelded samples Fig. 4. The unwelded sample exhibiting a lower corrosion rate could be attributed to the microstructure of the material. The equiaxed $\alpha$ and $\beta$ phases show a higher volume fraction of $\beta$ in it than the welded zone. Works of literature attributed the $\beta$ phase to be the significant cause of an enhanced corrosion resistance in Ti6Al4V alloy [14]. The corrosion performance of the unwelded sample could further be ascribed to the passive film formed on the material's surface, thereby resulting
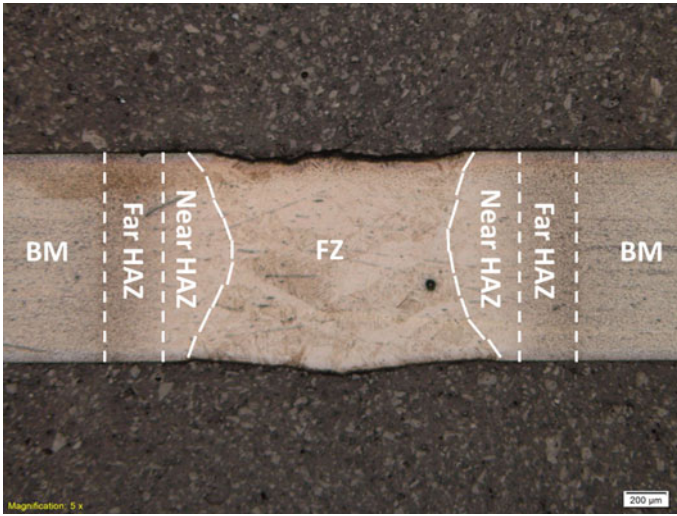
**Fig. 1** Microstructure of laser-welded Ti6Al4V



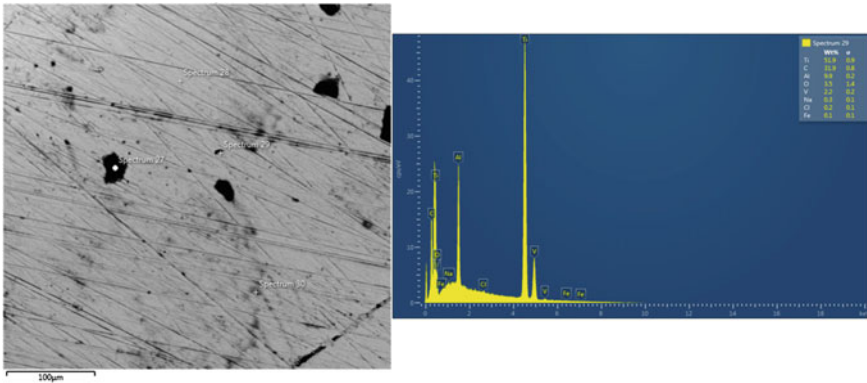**Fig. 2** Unwelded Ti6Al4V surface after corrosion test

in a higher corrosion current ($i_{corr}$) value of 499 µA cm$^{-2}$ than the welded sample 152 µA cm$^{-2}$. The corrosion potential ($E_{corr}$) value for the welded and unwelded are −0.471 V and 0.006 V, respectively. Generally, the corrosion rates for both samples are within the perfectly stable range of <10$^{-3}$ mm year$^{-1}$ [14, 15].
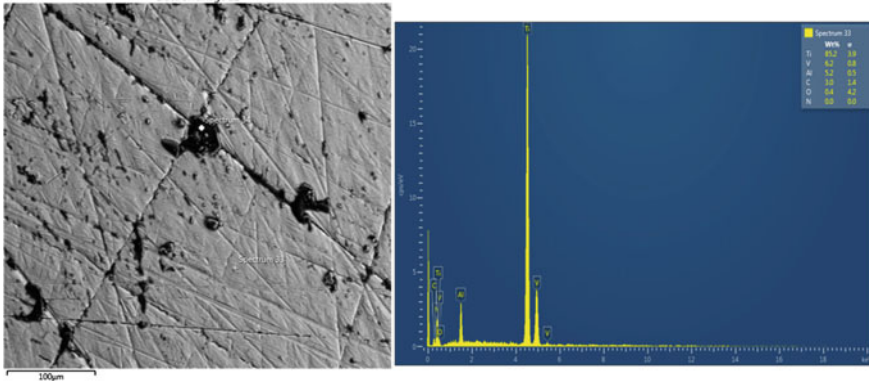
**Fig. 3** Laser-welded Ti6Al4V surface after corrosion test

**Fig. 4** Tafel curves of welded and unwelded samples
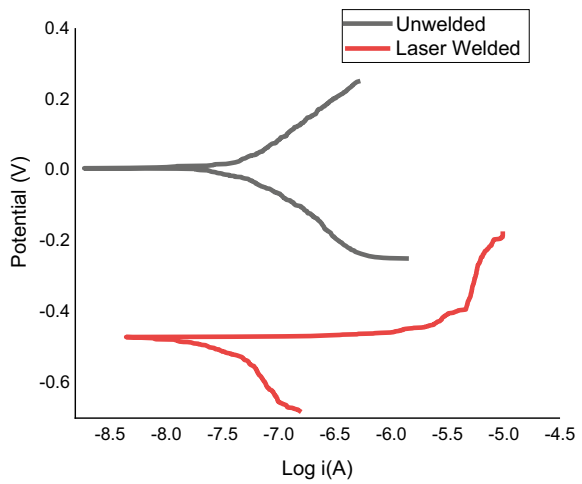


## 4 Conclusions

Laser welding and corrosion studies have been carried out on Ti6Al4V submerged in sodium chloride (NaCl) solution. The following conclusions are drawn from the research.

1. The welded sample's fusion zone comprises a martensitic microstructure, and the heat-affected zone contains an acicular $\alpha'$ microstructure.
2. The unwelded sample had a higher resistance to corrosion than the welded sample.
3. All samples performed perfectly stable in 3.5%wt NaCl, i.e., the corrosion rate is less than $10^{-3}$ mmyear$^{-1}$.

# References

1. Casalino G, Mortello M, Campanelli SL (2015) Ytterbium fiber laser welding of Ti6Al4V alloy. J Manuf Process 20:250–256
2. Ferdinandov NV, Gospodinov DD, Ilieva MD, Radev RH (2018) Structure and pitting corrosion of Ti-6Al-4V alloy and Ti-6Al-4V welds. In: Proceedings of the 7th international conference on advanced materials and systems, pp 325–330
3. Gao XL, Zhang LJ, Liu J et al (2014) Effects of weld cross-section profiles and microstructure on properties of pulsed Nd:YAG laser welding of Ti6Al4V sheet. Int J Adv Manuf Technol 72:895–903
4. Kabir ASH, Cao X, Medraj M et al (2010) Effect of welding speed and defocusing distance on the quality of laser welded Ti-6A1-4V. Mater Sci Technol 4:2787–2797
5. Liu J, Gao XL, Zhang LJ et al (2014) A study of fatigue damage evolution on pulsed Nd: YAG Ti6Al4V laser welded joints. Eng Fract Mech 117:84–93
6. Omoniyi PO, Akinlabi ET, Mahamood RM (2021) Heat treatments of Ti6Al4V alloys for industrial applications : an overview. In: 4th international conference on engineering for sustainable world. https://doi.org/10.1088/1757-899X/1107/1/012094
7. Omoniyi PO, Akinlabi ET, Mahamood RM et al (2021) Corrosion resistance of heat treated Ti6Al4V in NaCl. Chem Data Collect. https://doi.org/10.1016/j.cdc.2021.100780
8. Omoniyi PO, Mahamood RM, Akinlabi ET (2021) Impact of process parameters of laser welding on the mechanical properties of Ti6Al4V: a review. J Chem Technol Metall 56:1074–1081
9. Omoniyi PO, Mahamood RM, Arthur N et al (2021) Investigation of the mechanical and microstructural properties of TIG welded Ti6Al4V alloy. Adv Mater Sci Eng Sel Artic ICMMPE 2020:111–118
10. Omoniyi P, Mahamood R, Arthur N et al (2021) Laser butt welding of thin Ti6Al4V sheets: effects of welding parameters. J Compos Sci 5:1–9
11. Raja VKB, Palanikumar K, Sai AS et al (2019) Pitting corrosion studies on Ti6Al4V alloy weldments in marine environment. Indian J Geo-Marine Sci 48:1179–1182
12. Shamir M, Junaid M, Nawaz F et al (2019) A comparative study of electrochemical corrosion behavior in laser and TIG welded Ti—5Al—2. 5Sn alloy. J Mater Res Technol 8:87–98
13. Squillace A, Prisco U, Ciliberto S et al (2012) Effect of welding parameters on morphology and mechanical properties of Ti-6Al-4V laser beam welded butt joints. J Mater Process Technol 212:427–436
14. Yang J, Yang H, Yu H et al (2017) Corrosion Behavior of additive manufactured Ti-6Al-4V alloy in NaCl solution. Metall Mater Trans A Phys Metall Mater Sci 48:3583–3593
15. Zhang Y, Feng L, Zhang T et al (2021) Heat treatment of additively manufactured Ti-6Al-4V alloy: microstructure and electrochemical properties. J Alloys Compd 888:161602

# Electrochemical Studies on the Effect of Concentration on the Polyvinylpyrrolidone-Cysteine Inhibition Efficiency in an Acidic Solution

**C. K. Nsakabwebwe, M. E. Makhatha, A. D. Baruwa, and E. T. Akinlabi**

**Abstract** This paper studies the inhibition efficiency of mild steel in 1 molar hydrochloric acid in the presence and absence of an inhibitor by means of potentio-dynamic polarization and electrochemical impedance spectroscopy. The immersion time and temperature were 3 h and 25 °C, respectively. The inhibitor concentration was 25, 100, 300, 500 and 700 ppm, respectively. The results of the two analyses exhibited a maximum efficiency at 700 ppm concentration and a constant exposure time. The potentiodynamic polarization results demonstrated that the polymer composite assured both the anodic and cathodic protection of the mild steel. The electrochemistry equivalent circuit fitted around a simplified $R_1 + R_2/Q_2$ circuit derived from the electrochemical impedance spectroscopy data and the Randles equivalent cell.

**Keywords** Concentration · Electrochemical · Inhibition · Polyvinylpyrrolidone-cysteine

## 1 Introduction

Excellent mechanical properties, affordability, cast repeatability and availability posed mild steel as the most sought material [1, 2]. Although applicability is enormous, its susceptibility to corrosion cannot be neglected. Any little exposure to an aggressive environment would cause degradation of the material. The progressive

---

C. K. Nsakabwebwe (✉) · M. E. Makhatha · A. D. Baruwa
Department of Metallurgy, University of Johannesburg, Johannesburg, South Africa

M. E. Makhatha
e-mail: emakhatha@uj.ac.za

A. D. Baruwa
e-mail: drebaruwa@gmail.com

E. T. Akinlabi
Pan African University for Life and Earth Sciences, Ibadan, Nigeria

Department of Mechanical Engineering Science, University of Johannesburg, Johannesburg, South Africa

degradation process of the mild steel in an aggressive environment is usually caused by a phenomenon known as an electrochemical reaction. This process causes mild steel loss of inherent mechanical properties [3, 4]. Properties' degradation informed the decision to develop means of inhibiting, prohibiting or eliminating the rate at which corrosion occurs [5].

Many corrosion inhibitive techniques have been applied to date, and some have demonstrated their efficacies, while others have their limitations in terms of required efficiency [6]. Among them is the application of synthesized inhibitors to specific areas of intention [7]. In fact, many inhibitors have been developed and tested in diverse acidic and non-acidic solutions [8]. The present research investigates the application of a water-soluble polymer composite—polyvinylpyrrolidone. Polyvinylpyrrolidone is a synthetic polymer with diverse properties such as non-toxicity, film-forming ability and high biocompatibility. It is useful in food industries, medicine, coating and paint and adhesive [9]. The immense properties exhibited by polyvinylpyrrolidone caught our attention and drove us to investigate its applicability. However, the polyvinylpyrrolidone is weak in its original form to act as an inhibitor; therefore, it requires doping materials or additions [10].

In this study, cysteine is added to polyvinylpyrrolidone to form a composite. The polyvinylpyrrolidone-cysteine polymer composite inhibits the mild steel susceptibility to corrosion in a molar of hydrochloric acid. The electrochemical techniques investigated in the current study are potentiodynamic polarization and electrochemical impedance spectroscopy.

## 2 Materials and Methods

The elementary mild steel chemical composition used was determined through arc spark optical emission spectroscopy, Table 1. Polyvinylpyrrolidone, cysteine, ammonium persulfate, oxalic acid, ammonium hydroxide, hydrochloric acid (32%) and acetone were used for the synthesis and inhibition.

Potentiodynamic and electrochemical impedance spectroscopy tests were conducted. The polarization setup was composed of three electrodes vis-à-vis: the counter electrode (platinum), the calomel standard electrode and the working electrode was mild steel. The EC-lab workstation was used to conduct the experiment.

The open-circuit potential test was run for 3 h. The current density was determined through the Tafel plots using a corrosion potential in the range of −250 to 250 mV applied at a scan rate of 1 mV/s. The capability of the polymer composite was evaluated as a function of both current density and the applied current potential. The

**Table 1** The chemical composition of mild steel

| Element | Fe | C | Mn | Al | P | Cu | Cr | Mo | Ni | Co |
|---------|------|------|------|------|-------|------|------|------|------|------|
| Wt.% | 99.3 | 0.06 | 0.25 | 0.05 | 0.009 | 0.01 | 0.04 | 0.01 | 0.02 | 0.01 |

inhibition efficiency is calculated using Eq. (1).

$$\text{Inhibition Efficiency} = \frac{I_{\text{corr}} - I'_{\text{corr}}}{I_{\text{corr}}} * 100 \tag{1}$$

where $I_{\text{corr}}$ equals the current density of the inhibited solution and $I'_{\text{corr}}$ equals the current density of the uninhibited solution.

The data generated by the instrument were used to calculate the impedance spectroscopy using Eq. (2).

$$Z(jw) = \frac{V(jw)}{I(jw)} \tag{2}$$

where $Z, v, I, j$ and $w$ are the electrochemical impedance, the supplied potential, imaginary impedance current and angular frequency, respectively. The charge transfer resistance was also used to determine the corrosion inhibition efficiency, as shown in Eq. (3).

$$\text{IE} = \frac{R_{\text{ct}} - R'_{\text{ct}}}{R_{\text{ct}}} * 100 \tag{3}$$

where $R_{\text{ct}}$ is the charge transfer resistance in the inhibited hydrochloric acid solution and $R'_{\text{ct}}$ the charge transfer resistance in the absence of inhibition.

In this study, the Nyquist plot was generated from the electrochemical impedance data from the simplified Randles circuit. It should be noted that the Nyquist curve is a plot showing the correlation between the real and the imaginary parts of the circuit impedance. In addition, the Nyquist plot facilitated the determination of other electrochemical parameters such as the charge transfer resistance, the solution resistivity and time constants.

## 3   Results and Discussions

### 3.1   *Potentiodynamic Polarization*

The exposure of the mild steel to various inhabited electrolytes resulted in both current and potential shifts, as shown in the Tafel plot (Fig. 1). The parameters such as corrosion potential, current density and anodic and cathodic slopes were derived from the plot, whereas the protection efficiency was evaluated from the corrosion current density values using Eq. (1). The Tafel parameters obtained from mild steel dissolution show the effect of concentration, as shown in Table 2.

Results revealed that the corrosion current density is inversely proportional to the concentration of inhibitor. Consequently, the increase in the inhibitor concentration

**Fig. 1** Potentiodynamic polarization curves of mild steel in both uninhibited and inhibited 1 molar hydrochloric acid solution at various concentrations
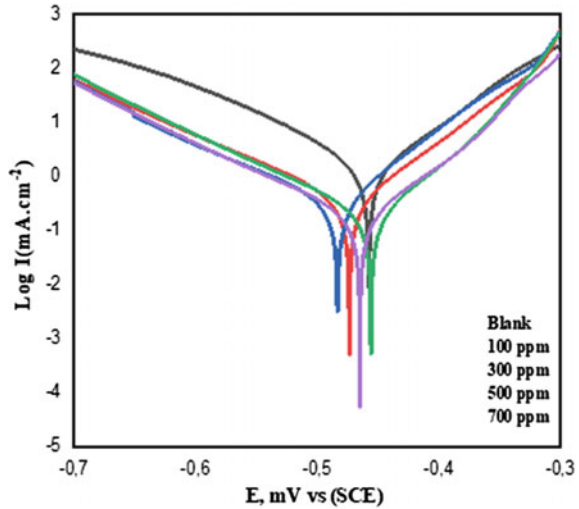


**Table 2** Potentiodynamic polarization parameters of mild steel dissolution in both uninhibited and inhibited 1 molar hydrochloric acid solution

| Sample | $E_{corr}$ (mV) | $I_{corr}$ (mA cm$^{-2}$) | $\beta a$ 1/mV | $\beta c$ 1/mV | $C_R$ 1/mpy | $\theta$ | IE (%) |
|---|---|---|---|---|---|---|---|
| Bare | −457.62 ± 6.31 | 783.87 ± 9.37 | 52.10 ± 2.11 | 55.60 ± 2.67 | 35.7325 ± 2.0008 | – | – |
| 100 ppm | −473.70 ± 5.72 | 177.73 ± 8.81 | 45.70 ± 1.95 | 55.70 ± 2.08 | 08.1017 ± 0.0468 | 0.77 ± 0.88 | 77.33 ± 0.88 |
| 300 ppm | −464.84 ± 4.89 | 149.51 ± 7.77 | 44.00 ± 1.72 | 65.20 ± 1.93 | 06.8154 ± 0.0385 | 0.81 ± 0.97 | 80.93 ± 0.97 |
| 500 ppm | −455.88 ± 4.18 | 137.06 ± 7.21 | 52.70 ± 1.51 | 72.90 ± 1.82 | 06.2478 ± 0.0351 | 0.83 ± 1.28 | 82.52 ± 1.28 |
| 700 ppm | −464.98 ± 0.25 | 084.86 ± 0.84 | 41.40 ± 1.08 | 50.50 ± 01.47 | 03.8684 ± 0.0028 | 0.89 ± 2.37 | 89.17 ± 2.37 |

resulted in a decrease in the current density. The behaviour could be explained on the basis that there is limited transfer of an electron from the anode to the cathode due to the presence of the inhibitor at the metal-solution interface. The film layer of inhibitor at the monitored surface blocks reactions taking place at the anode and cathode, which consequently alleviates the dissolution of bulk material [11, 12]. From the results, it can also be noticed a change in the $\beta_a$ and $\beta_c$ slopes with an increase in the concentration of the inhibitor. The behaviour indicates that the inhibitory layer affects both anodic and cathodic reactions occurring on mild steel surfaces.

Further investigation revealed that progressive changes in the concentration of inhibitor led to a substantial shift of potential from the anodic to the cathodic. Such

deviation in the potential is due to an active inhibitive film formed on the surface. The layer inhibits the mild steel against its eventual dissolution and, thus, enhances the shift in the corrosion potential [13]. However, it has been established by other researchers that when the activated potential value is different from 85 mV for mild steel, the inhibitor is referred to as a mixed-type inhibitor [14, 15]. In this investigation, the shift in the corrosion potential as a result of the inhibitive effect was found to be 16.1 mV at the anode side. The finding demonstrates that the mild dissolution was mainly promoted by iron oxidation. The utmost inhibition efficiency derived from Tafel plots was 89.1% demonstrating that anodic reactions were predominantly controlled by the presence of an inhibitive layer [16].

## 3.2 Electrochemical Impedance Spectroscopy (EIS)

EIS is a technique that is often used to evaluate a material's charge transfer resistance. In this case, it was employed to measure the substrate's corrosion rate when exposed to a varied inhibitor concentration. The significance of the impedance data was demonstrated using the Nyquist plot represented in Fig. 2. The imaginary part of the impedance was plotted against the real part of the same impedance to evaluate the Nyquist curves. The data include charge transfer resistance obtained from inhibitor concentrations ranging from the blank solution to a 700 ppm inhibitor-containing solution. The immersion time was kept at room temperature for an hour for all the concentrations considered.

From the results obtained from the mild steel, a proportional increase in the charge transfer resistance was noticed with the increase of inhibitor concentration within



**Fig. 2** The Nyquist plot of various concentrations in inhibited and uninhibited 1 M HCl solution
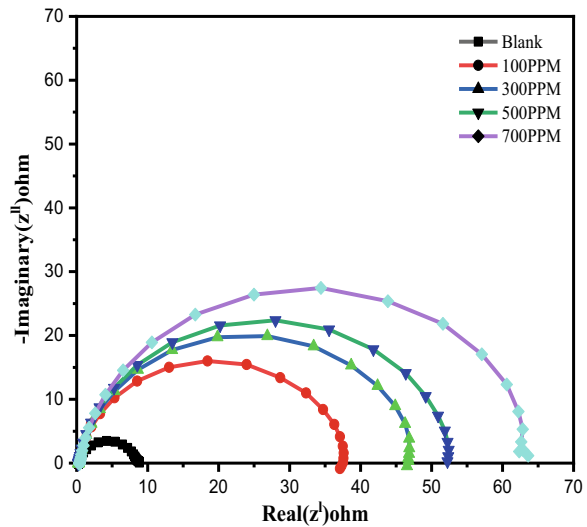
**Table 3** Electrochemical impedance spectroscopy extraction from the fitted circuit

| Concentration | $R_1$ ($\Omega$) | $Q_2$ ($F \times 10^{-3}$) | $a_2$ | $R_2$ ($\Omega$) | (%) IE |
|---|---|---|---|---|---|
| Bare | 0.2840 ± 0.0142 | 1.5980 ± 0.0128 | 0.8747 | 8.377 ± 1.082 | – |
| 100 ppm | 0.1820 ± 0.0092 | 0.6388 ± 0.0087 | 0.8935 | 34.26 ± 2.309 | 75.55 ± 2.08 |
| 300 ppm | 0.3223 ± 0.0112 | 0.5447 ± 0.0217 | 0.9104 | 47.00 ± 2.627 | 82.18 ± 1.11 |
| 500 ppm | 0.2923 ± 0.0097 | 0.7739 ± 0.0339 | 0.9058 | 52.58 ± 3.111 | 84.10 ± 1.24 |
| 700 ppm | 0.5060 ± 0.0231 | 0.5990 ± 0.0264 | 0.9104 | 63.31 ± 3.862 | 86.77 ± 2.31 |

the electrolyte. The increase in the charge transfer resistance was characterized by an extension of the semicircles on the Nyquist plot. The extension of the semicircles ascertained the presence of a thin layer of inhibitor at the metal-solution interface [17]. The outcome demonstrates that the presence of the inhibitive films at the mild steel interface promotes the extension of the semicircles and, therefore, the alleviation of the oxidation characterized by the electron withdrawal from the mild steel substrate surface. Charge transfer resistance is inversely proportional to corrosion rate and is thus proportional to the semicircle radius. The lower the resistance to charge transfer, the greater the metal dissolution and the smaller the semicircles.

Furthermore, the barrier efficiency of the polymer composite was determined according to Eq. (3) and the results are presented in Table 3. The results revealed a proportional increase of the inhibition efficiency with an increase in the concentration of inhibitor. The increase in the concentration of the inhibitor led to the increase of the charge transfer resistance and, therefore, to an extended inhibitive layer which significantly hindered the flow of electrons from the mild steel surface characterized by the metal dissolution. This is in line with the previous findings [18].

### 3.3 Equivalent Circuit

The electrochemical equivalent circuit is presented in Fig. 3. The model explains the electrochemical behaviour of the corrosion cell. The Randles cell model, among others, was selected to best fit the experimental data based on the simplified Randles cell model.

The experimental impedance data obtained from the equivalent fitting revealed led to the different inhibition efficiencies shown in Table 3. The element $R_1$ corresponds to the solution resistivity, whereas charge transfer resistance is the $R_2$. The constant phase element corresponds to the capacitance degree of depression relative to the mild steel surface imperfections, reaction rate discontinuity and the variance in the current distribution to the corrosion cell [19, 20].
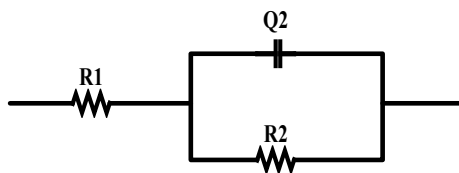
The results show that an increase in the concentration of inhibitors causes a proportional decrease in the constant phase element values. This indicates that the reduction in the corrosion rate is primarily characterized by the significant charges stored at the solution-metal interface [21]. The electronic double layer (EDL) reduction is ascribed to a critical resistance to the electron flow from the mild steel to the hydrochloric acid. Therefore, the more the charges are withdrawn from the mild steel, the higher the rate of corrosion occurrence and the higher the constant phase element stored energy [21–23].

However, it can be observed that the increase in the solution resistivity is proportional to the increase in the concentration of the inhibitor. Such an increase is a consequence of the existence of dissolved inhibitor molecules in the acid. The higher the concentration of dissolved inhibitor in the solution, the more viscous is the electrolyte. However, the viscosity has no influence on the charge conductivity because the PVP inhibitor in the solution is expected to exhibit electrical conductivity.

As shown in Table 3, the results show that the protection efficiencies increase proportionally with the inhibitor's charge transfer resistance and concentration. The protection efficiencies obtained from the electrochemical impedance are in line with the inhibition efficiencies obtained from the Tafel analysis. The inhibition efficiencies are in the range of 75–90% [21, 24].

## 4    Conclusion

This research investigation assessed the corrosion behaviour of mild steel substrate subjected to 1 M of HCl solution with and without inhibitor. The potentiodynamic polarization and the electrochemical impedance spectroscopy were used to investigate the protection efficiency of the polyvinylpyrrolidone-cysteine inhibitor. Results revealed that the utmost protection efficiency of 89.1% was obtained from an optimum inhibition concentration of 700 ppm. The Tafel results indicated that the inhibitor displayed a mixed type, though it was mostly characterized by the anodic protection. Furthermore, the electrochemical equivalent circuit designed from the experimental data best fitted the simplified Randles cell model, which consisted of the solution and charge transfer resistances in parallel with the constant phase element.

**Conflict of Interest**    All the authors state that there is no conflict of interest whatsoever.

# References

1. Chinwko EC, Odio BO, Chukwuneke J, Sinebe JE (2014) Investigation of the effect of corrosion on mild steel in five different environments. Int J Sci Technol Res 3(7)
2. Alaneme KK, Odoni BU (2016) Mechanical properties, wear and corrosion behavior of copper matrix composites reinforced with steel machining chips. Int J Eng Sci Technol 19(3):1593–1599
3. El Ibrahimi B, Jmiai A, Bazzi L, El Issami S (2020) Amino acids and their derivatives as corrosion inhibitors for metals and alloys. Arab J Chem 13(1):740–771
4. Sabirneeza AA, Fathima, Subhashini S (2014) Poly(vinyl alcohol-proline) as corrosion inhibitor for mild steel in 1M hydrochloric acid. Int J Ind Chem 5(3–4):111–120
5. Tezdogan T, Demirel YK (2014) An overview of marine corrosion protection with a focus on cathodic protection and coatings. Brodogradnja/Shipbuilding 65(2):49–59
6. Umoren S (2009) Polymers as corrosion inhibitors for metals in different media—a review. Open Corros J 2:175–188
7. Umoren SA, Solomon MM, Ali SA, Dafalla HD (2019) Synthesis, characterization, and utilization of a diallylmethylamine-basedcyclopolymer for corrosion mitigation in simulated acidizing environment. Mater Sci Eng C 100:897–914
8. Patni N, Agarwal S, Shah P (2013) Greener approach towards corrosion inhibition. Chin J Eng 2013:1–10
9. Nešić A, Ružić J, Gordić M, Ostojić S, Micić D, Onjia A (2017) Pectin-polyvinylpyrrolidone films: a sustainable approach to the development of biobased packaging materials. Compos B Eng 110:56–61
10. Sriyanti V, Edikresnha D, Rahma A, Muni MM, Rachmawati H, Khairurrijal K (2017) Correlation between structures and antioxidant activities of polyvinylpyrrolidone/garcinia mangostana L. Extract composite nanofiber mats prepared using electrospinning. J Nanomater 2017
11. Al Juhaiman LA, Mustafa AA, Mekhamer WK (2012) Polyvinyl pyrrolidone as a green corrosion inhibitor of carbon steel in neutral solutions containing NaCl: electrochemical and thermodynamic study. Int J Electrochem Sci 7:8578–8596
12. Amin M, Hazzazi O, Kandemirli F, Saracoglu M (2012) Inhibition performance and adsorptive behavior three amino acids on cold-rolled steel in 1.0 M HCl-chemical, electrochemical, and morphological studies. Corrosion 68:688–698
13. Tsoeunyane MG, Makhatha ME, Arotiba OA (2019) Corrosion inhibition of mild steel by poly(butylene succinate)-L-histidine extended with 1,6-diisocynatohexane polymer composite in 1 M HCl. Int J Corros 2019
14. Al-Amiery A, Kadhum A, Alobaidy AH, Mohamad A, Hoon P (2014) Novel corrosion inhibitor for mild steel in HCl. Materials 7:662–672
15. Thiu B, Advincula RC (2015) Polymeric corrosion inhibitors for the oil and gas industry: design principles and mechanism. React Funct Polym 95:25–45
16. Singh A, Quraishi M (2010) Piroxicam; a novel corrosion inhibitor for mild steel corrosion in HCl acid solution. J Mater Environ Sci 1(2):101–110
17. Umoren SA, Obot IB, Madhankumar A, Gasem ZM (2015) Performance evaluation of pectin as ecofriendly corrosion inhibitor for X60 pipeline steel in acid medium: experimental and theoretical approaches. Carbohydr Polym 124:280–291
18. Karthikaiselvi R, Subhashini S (2017) The water soluble composite poly(vinylpyrrolidone–methylaniline): a new class of corrosion inhibitors of mild steel in hydrochloric acid media. Arab J Chem 10(1):627–635

19. Singh KR, Devivaraprasad R, Kar T, Chakraborty A, Neergat M (2015) Electrochemical impedance spectroscopy of oxygen reduction reaction (ORR) in a rotating disk electrode configuration: effect of ionomer content and carbon-support. J Electrochem Soc 162(6):F489-F498
20. Bera B, Kar T, Chakraborty A, Neergat M (2017) Influence of nitrogen-doping in carbon on equivalent distributed resistance and capacitance-implications to electrocathalisis of oxygen reduction reaction. J Electroanal Chem 805:184–192
21. Lgaz H, Masroor S, Chafiq M, Damej M, Brahmia A, Salghi R, Benmessaoud M, Ali IH, Alghamdi MM, Chaouiki A, Chung IM (2020) Evaluation of 2-mercaptobenzimidazole derivatives as corrosion inhibitors for mild steel in hydrochloric acid. Metals 10(357):1–14
22. Chaouiki A, Lgaz H, Chung IM, Ali IH, Gaonkar SL, Bhat KS, Salghi R, Oudda H, Khan MI (2018) Understanding corrosion inhibition of mild steel in acid medium by new benzonitriles: insights from experimental and computational studies. J Mol Liq 266:603–616
23. Niass S, Touhami M, Hajjaji N, Srhiri A, Takenouti H (2001) The inhibiting effect of quaternary phosphine on Ni–P alloys in 1 M H2SO4. J Appl Electrochem 31(1):85–92
24. Shukla SK, Quraishi MA, Ebenso EE (2011) Adsorption and corrosion inhibition properties of cefadroxil on mild steel in hydrochloric acid. Int J Electrochem Sci 6(2011):2912–2931